1992

Research on Self Adjusting Back-Pressure Mechanism of Scroll Compressor

J. Zhu
Xi'an Jiaotong University; P. R. China

D. Wang
Xi'an Jiaotong University; P. R. China

D. Zhang
Xi'an Jiaotong University; P. R. China

RESEARCH ON SELF ADJUSTING BACK-PRESSURE MECHANISM OF SCROLL COMPRESSOR

Zhu Jie, Wang Disheng and Zhang Dongjun
Department of Power Machinery Engineering
Xi'an Jiaotong University, P. R. CHINA

ABSTRACT

Forces acting on the orbiting scroll are analysed in detail on the basis of the principle of the self adjusting back-pressure mechanism. The stable condition of the orbiting scroll movement is also discussed. The mathematical model is developed for the scroll compressor. The effects of the constructional parameters of the back-pressure chamber on its pressure and then on the compressor performance are obtained according to the results of calculation and experiment. The proper range of the pressure and the dimensiones of the back-pressure chamber are presented, which are useful to the design of scroll compressor with self adjusting back-pressure mechanism.

INTRODUCTION

The scroll compressor with self adjusting back-pressure mechanism to support the orbiting scroll will operate at high efficiency because of the less frition loss and the prefect sealing property. There are several meshing lines between the orbiting scroll and the fixed one during the compressor working process. In order to keep the proper clearances in these meshing positions, it is necessary to make the orbiting scroll move stably. when the working medium is compressed, there are many forces acting on the orbiting scroll. The forces make the orbiting scroll separate from the fixed one and incline, these will result in the great leakage and the more friction loss, the orbiting scroll will not work properly on serious occasion. The axial gas force leads to the friction loss in the orbiting scroll baseplate, the radial gas force and the tangential gas force cause the overturn moment acting on the orbiting scroll, the moment makes the orbiting scroll incline, this increases the leakage in the flank meshing positions. Therefore, the balances of the axial force and the overturn moment are of great importance to the scroll compressor from the point of view of thermodynamics and dynamics.

BACK-PRESSURE CALCULATION

The theoretic value of the back-pressure is calculated according to the dynamic equilibrium of the orbiting scroll. The analysis of the forces acting on the orbiting scroll is carried out as shown in Fig. 1, the force F_0 is engendered by the pressure of the clearance between the orbiting scroll baseplate and the fixed scroll surface, it is the sealing force. According to the reference [1], the distribution of the pressure in this clearance is given by

$$\frac{dp}{dr} = \frac{6\nu_m}{\pi r\delta_1^3}\frac{dm_1}{dt}$$

then integrated

$$P = P_b + \frac{6\nu_m}{\pi\delta_1^3} ln\frac{r}{R_2}\frac{dm_1}{dt}$$

where ν_m is the viscosity factor of the oil-gas mixture, P_b is the back-pressure, δ_1 is the clearance value, $\frac{dm_1}{dt}$ is the leakage rate, according to the expression of $\frac{dm_1}{dt}$ in reference [1], F_0 is obtained as follows:

$$F_0 = \pi[P_b R_2^2 - P_s R_1^2 - \frac{(P_b - P_s)(R_2^2 - R_1^2)}{2ln\frac{R_2}{R_1}}]$$

where P_s is the suction pressure.

When the friction forces are neglected, the force equilibriums are given by

$$M \cdot g + F_a + F_0 + F_1 + F_2 - F_b = 0$$

$$F_r - R_r - ME\omega^2 + O_{2r} - O_{1r} = 0$$

$$R_t - F_t + O_{1t} - O_{2t} = 0$$

where M is the orbiting scroll mass, F_a is the axial gas force, F_1 . F_2 are the forces acting on the baseplate edge, F_b is the force produced by the back-pressure chamber, F_r is the radial gas force, F_t is the tangential gas force, R_r . R_t are the reaction forces at the crankshaft, ω is the angular velocity, O_{1t} , O_{2t} , O_{1r} , O_{2r} are the reaction forces at the Oldam ring. Because the mass of the Oldam ring is small, when the mass is neglected, $O_{1t} = O_{2t}$ $O_{1r} = O_{2r}$. accordingly , the axial force of the back-pressure and the reaction forces at the crankshaft are given as follows:

$$F_b = M \cdot g + F_a + F_0 + F_1 + F_2$$

$$R_r = F_r - ME\omega^2$$

$$R_t = F_t$$

the moment equlilbriums are given as follows:

$$M_z(F_1, F_2) = F_t \cdot \frac{h}{2} + R_t \cdot h_2$$

$$M_t(F_1,F_2)=F_r\cdot\frac{h}{2}+F_a\cdot\frac{E}{2}+R_rh_2-ME\omega^2h_1$$

then

$$M_r(F_1,F_2)=F_t\left(\frac{h}{2}+h_2\right)$$

$$M_t(F_1,F_2)=F_r\left(\frac{h}{2}+h_2\right)+F_a\cdot\frac{E}{2}-ME\omega^2(h_1+h_2)$$

M_r (F_1 , F_2) and M_t (F_1 , F_2) are the unbalanced overturn moments, they must be balanced by the moment of the forces F_1 and F_2 , as shown in Fig. 2.

$$(F_1-F_2)R\sin\beta=M_t(F_1,F_2)$$

$$(F_1-F_2)R\cos\beta=M_r(F_1,F_2)$$

where $\beta=arctg\dfrac{M_t}{M_r}$

then $$F_1+F_2=\frac{\sqrt{M_t^2(F_1,F_2)+M_r^2(F_1,F_2)}}{R}+2F_2$$

When F_1 、 and F_2 are the positive value, their directions are downward, this means the orbiting scroll meshes with the fixed one properly. If one of them is zero, this indicates that one side of the orbiting scroll baseplate will separate from the fixed scroll surface, and the orbiting scroll will incline to this side. so the stable operating condition of the orbiting scroll is as follows:

$$Min(F_1,F_2)>0$$

or $$(F_1+F_2)_{min}=\frac{\sqrt{M_t^2(F_1,F_2)+M_r^2(F_1,F_2)}}{R}$$

therefore $$F_{bmin}=M\cdot g+F_a+F_o+\frac{\sqrt{M_t^2(F_1,F_2)+M_r^2(F_1,F_2)}}{R}$$

There two pressure distributed in the back of the orbiting scroll baseplate, one is the oil-supply pressure which is equal to the discharge one approximately, the other is the back-pressure, so

$$F_{bmin}=P_d\pi r_1^2+P_{bth}\pi(R_2^2-r_1^2)$$

obtained $$P_{bth}=\frac{F_{bmin}-P_d\pi r_1^2}{\pi(R_2^2-r_1^2)}$$

where P_{bth} is the minimum back-pressure to support the orbiting scroll, which is computed in light of the orbiting scroll dynamic equilibrium.

WORKING PROCESS MODEL

Compression Pocket

The meshing condition of the scroll wraps (N = 3) is shown in Fig. 3, when the crank angle increases from o to 2π, the unsealed volumes in the outsied become the closed ones. When the crank angle increases from $2\ \pi$ to $[2(N-1)+\theta^*]$ (θ^* is the discharge angle), the sucked medium is compressed in working pocket 3 and 2 successively. The compression pockets 3 and 2 communicate with the back-pressure chamber in a certain angle range respectively, the analytical model of the working porcess is shown in Fig. 4, The crank angle corresponding to the back-pressure port postion is θ_b , when the angle is in between ($2\pi+\theta_b$) and 4π, the pocket 3 communicates with the back-pressure chamber, the pocket 2 does not. When the angle is in between 4π to ($4\pi+\theta_b$), the pocket 2 communicates with the chamber, the pocket 3 does not. Because the diameter of the back-pressure port is small, the port may be covered in a certain range.

Because there are too many factors influencing the working process. In order to simplify the calculation, the following assumptions are made.

(1) The medium is treated as the ideal gas with a constant specific heat and its state is homogenous.

(2) The compression process is regarded as the adiabatic one, the flow of the medium is instaneous steady.

(3) Gravitational and kinematic energies of the medium are neglected.

The following fundamental equations discribing the medium properties are given according to the laws of conservation of energy and mass.

$$dP = \frac{kR}{mv}\sum(T_{in} - T)dm_{in} - \frac{dP}{v}dv$$

$$dV = mdv + vdm$$

$$dm = dm_{in} - dm_{out}$$

$$\frac{dP}{P} + \frac{dV}{V} = \frac{dm}{m} + \frac{dT}{T}$$

$$P(O) = P_s$$

$$T(O) = T_s$$

$$V(O) = o$$

where k is the adiabatic exponent, R is the gas constant, T_s is the suction temperature, m_{in} and m_{out} are the leakage masses which are obtained in light of the leak model in reference [2].

Back-Pressure Chamber

The analytical model of the back-pressure chamber is given in reference [1].

SIMULATIVE CALCULATION

The simulative calculation is carried out on the basis of the analytical models of the working process and the back–pressure chamber, the flow diagram of the computer program is shown in Fig. 5, The input parameters of this program are the scroll basic dimensions , the operating condition, the properties of the media and so on. The differential equations are solved by means of the Runge–kutta method. The function of the program is to caluclate the state parameters of the working media, the back–pressure and the compressor efficiency, etc. The properties of the media in the adiabtic process without leakage and back–pressure port are regarded as the initial value, the pressures are regarded as the convergent criteria. The mass conservations of the gas and oil in a cycle are additional criteria to the back–pressure chamber.

RESULT ANALYSIS

In order to analyze the effect of the back–pressure chamber on the compressor efficiency and the effect of the structure parameters of the chamber on the back–pressure, the experiment is carried out. The variations of the back–pressure with the port position and diameter are measured, the influences of back–pressure on the compressor displacement and power are presented.

Effect of the Back–Pressure Chamber.

The pressure curve of the working pocket is shown in Fig. 6, the dotted line P_1 represents the compression process without the back–pressure chamber, the real line P_2 represents one with the chamber. These two lines duplicate each other in the range from O to θ_b , this means that the chamber does not communicate with the analysed pocket in this range. The line P_2 increases abruptly in the range from θ_b to θ_a , the back–pressure chamber communicates with the compression pocket, the media flow from the chamber to the pocket, so the media mass and temperature of the compression pocket increase, accordingly, P_2 is greater than P_1 . There is a turning point θ_a in line P_2 , the flow direction via the back–pressure port is reverse after θ_a , the media flow from the compression pocket to the chamber in the range ($\theta_a \sim \theta_c$), owing to the mass decrease, the compression line increases slowly. The variations of the line P_1 and P_2 are similar each other after θ_c , but P_2 is lower than P_1 , the reason is that the media coming from the compression pocket leak out through the clearance of the back–pressure chamber. As shown in this figure, the compression power with back–pressure is greater than that without the pressure.

Flow through the Back–Pressure Port

The flow condition is discribed in Fig. 7, the square between the curve and the abscissa is the product of the mass flow rate and the angular velocity ω. when the square is positive, it means that the media flow into the back–pressure chamber, when the area is negative, the flow direction is reverse. During a cycle, the positive square is greater than the absolute value of the negative one, the difference is the product of the chamber leakage and ω. There are two ports in

orbiting scroll baseplate, owing to the effect of the scroll wrap thickness, there is the difference between the communicating angles of two ports, so only one port is communicating at θ_b , the other port is open at θ_d . The closing condition is similar to the opening's, only one port is close at θ_e , two ports are both close at θ_c . The ports are covered in the range from θ_c to $(2\pi+\theta_b)$. The variation of the back-pressure is shown in Fig. 8. the slow variation of the back-pressure is caused by the leakage of the chamber in the range $[(-2\pi+\theta_c)\sim\theta_b]$.

Effect of the Back-Pressure Port Position

The change of the back-pressure with the port position is shown in Fig. 9, the position is the main factor effecting the back-pressure. When the port angle α_0 (shown in Fig. 3) increases, the back-pressure decreases, the leakage of the back-pressure chamber is small, so the curve of the back-pressure is concave-upward. The maximum error between the values of calculation and experiment is 3.5%. The variation of the volumetric efficiency with the port position is shown in Fig. 10, The efficiency increases slightly as the port angle rises. one reason is that the back-pressure decreases and so does the leakag of the chamber, the other is that the oil flowing into the working pocket gets more, therefore the sealing property of the working pocket is improved. The comparison between the theoretic value P_{bth} and the experimental result P_b at the port angle 225 ° is shown in Fig. 11, when the pressure ratio of P_b to P_{bthmax} is in the range from 1.05 to 1.15, the orbiting scroll moves stably and the friction loss is less. when the port angle is great than or equal to 280 ° , the axial froce and overturn moment are both unbalanced, the compressor can not work properly. The variation of the work input with the port angle is shown in Fig. 12, although the power decreases slightly as the port angle increases, this increases the unstable degree of the orbiting scroll.

Effect of the Back-Pressure Port Diameter and the Chamber Volume

The variatoins of the back-pressure fluctuation and its average with the port diameter are shown in Fig. 13, 14 respectivly, the variations of the back-pressure fluctuation and its average with the chamber volume are shown in Fig. 15 and 16 respetively. According to these figures, the port diameter and the chamber volume have little influence on the back-pressure average, but they effect the back-pressure fluctuation, if the port diameter decreases from 2 mm to 1mm, the fluctuation ratio P_b / P_{bo} decreases from 2.8% to 2.2%, but if the back-pressure chamber volume increases from V_{th} (The displacement volume)to $5V_{th}$, the ratio P_b / P_{bo} decreases from 10% to 2.5%. According to the results of calculation and experiment, the range of the back-pressure port diameter and the chamber volume are recommended as follows:

$$\frac{\pi D^2}{4} / \omega \cdot V_{th} = (1.4 \sim 4.0) \times 10^{-4} \qquad (s/m)$$

$$V_b / V_{th} = 2.0 \sim 4.0$$

CONCLUSION

(1). The appropriate range of the back-pressure is (1.05~ 1.15) times the theoretic maximum.

(2) The diameter range of the back-pressure port is recommended as follows:

$$\frac{\pi D^2}{4} / \omega \cdot V_{th} = (1.4 \sim 4.0) \times 10^{-4} \qquad (s/m)$$

(3) The volume range of the back-pressure chamber is recommended as follows:

$$\frac{V_b}{V_{th}} = 2.0 \sim 4.0$$

REFERENCE

[1] Zhu jie, ect. "Theoretic Model of Back-Pressure Chamber for Scroll Compressor" 1992 Purdue Compressor Conference.

[2] Zhu jie, ect. " A Research of Scroll Compressor Working Process Computer Simulation and Testing" 1990 Purdue Compressor Conference.

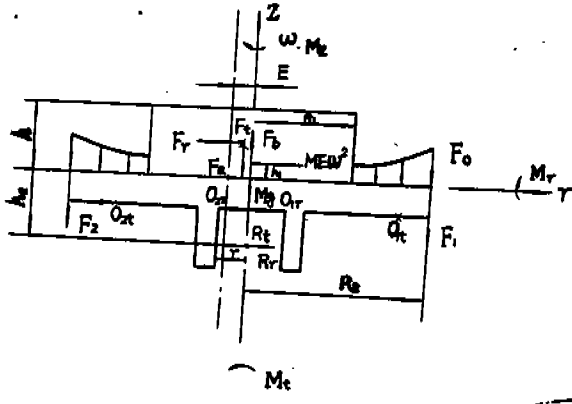

Fig.1 Force analysis

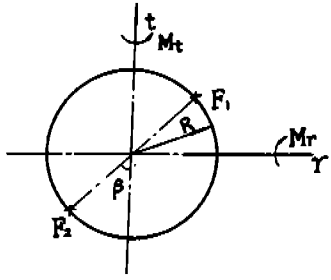

Fig.2 Balancing force

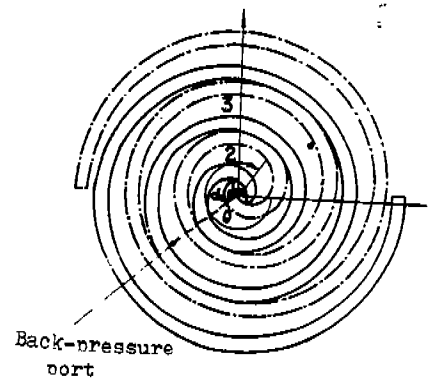

Fig.3 Working pocket

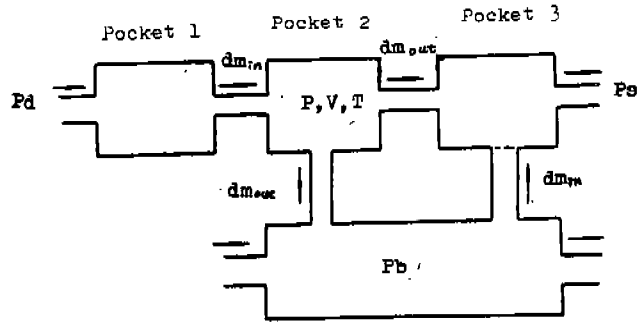

Back-pressure chamber

Fig.4 Analytical model

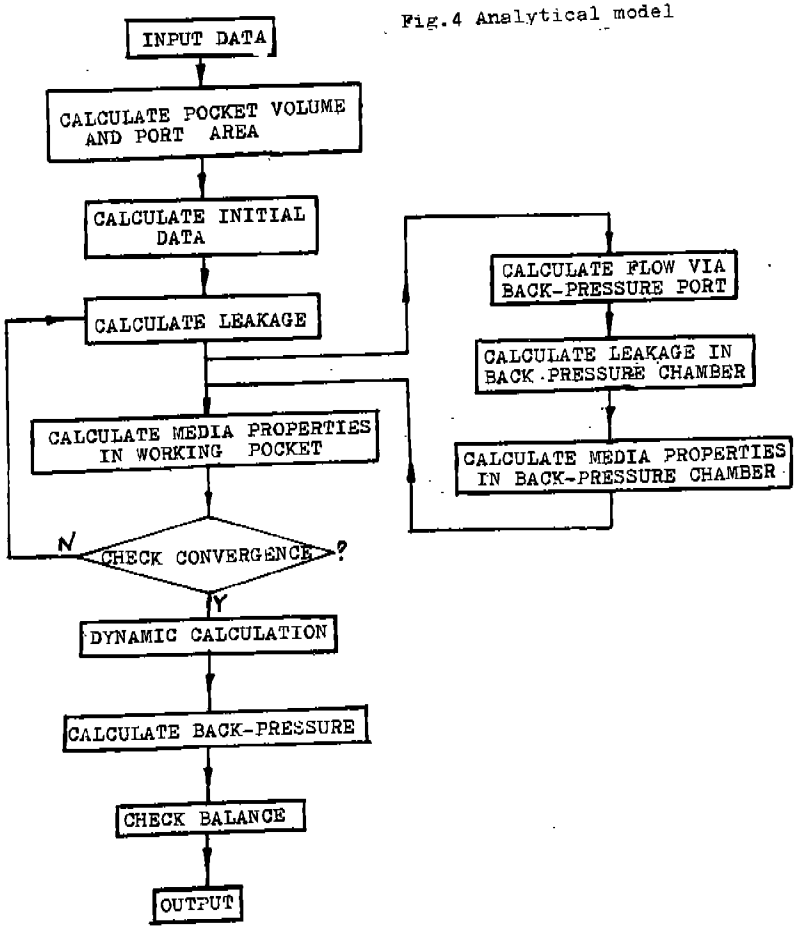

Fig.5 Computer Program

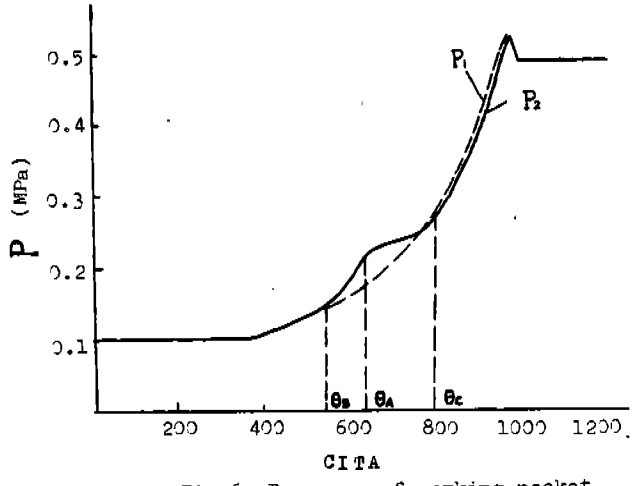

Fig.6 Pressure of working pocket

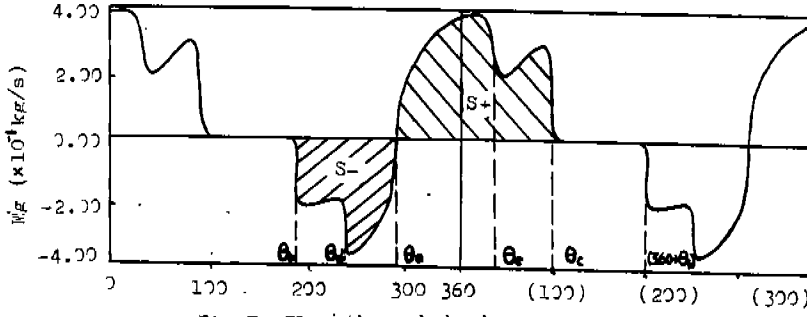

Fig.7 Flow through back-pressure port

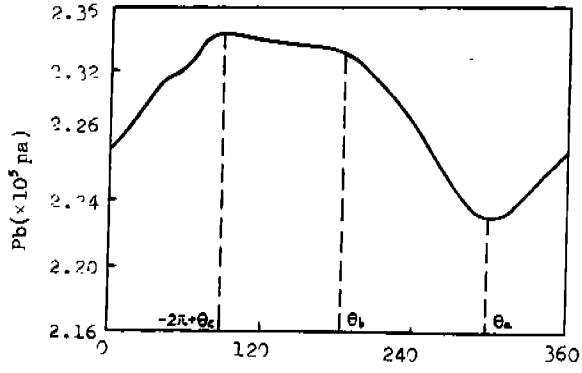

Fig.8 Back-pressure

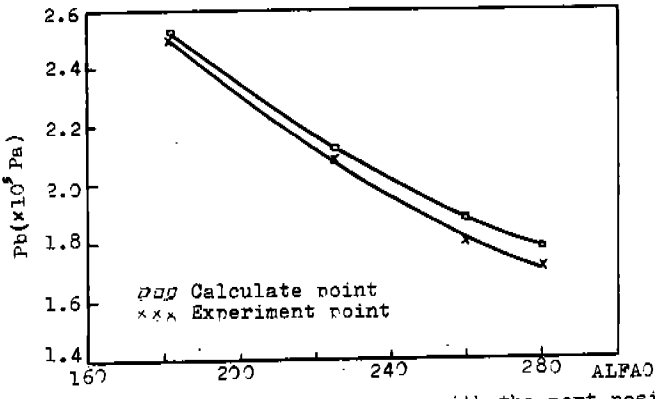

Fig.9 Variation of back-pressure with the port position

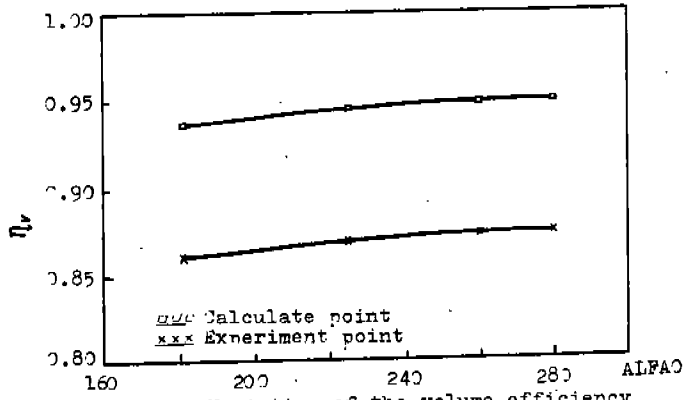

Fig.10 Variation of the volume efficiency with the port position

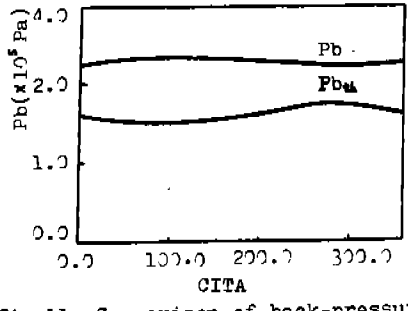

Fig.11 Comparison of back-pressure

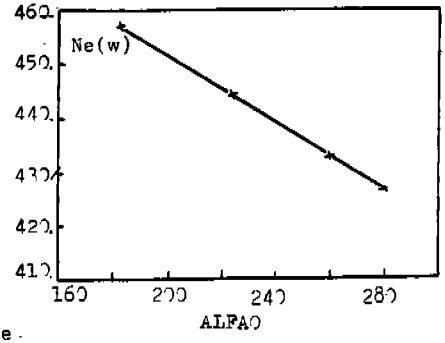

Fig.12 Variation of the power with the port position

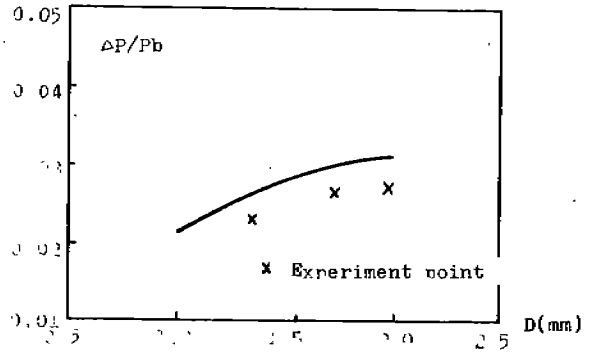

Fig.13 Back-pressure fluctuation

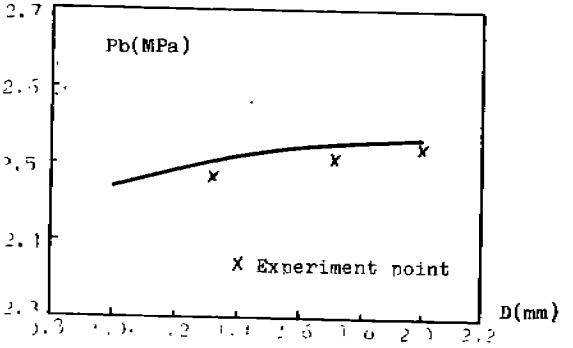

Fig.14 Back-pressure average

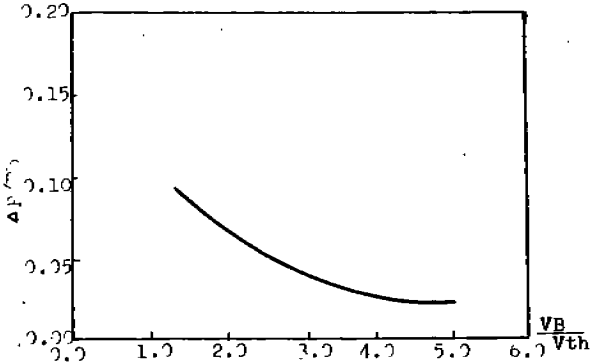

Fig.15 Back-pressure fluctuation

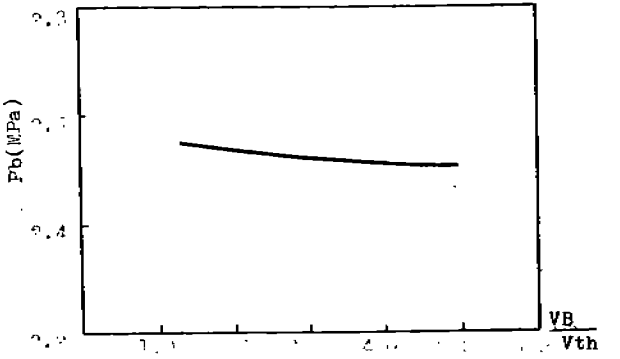

Fig.16 Back-pressure average

Cooperative Societies and Representatives

Air Conditioning Contractors of America, J. P. Norris, representative
Air-Conditioning and Refrigeration Institute (ARI), H. Phillips, representative
The American Society of Heating, Refrigerating, and Air-Conditioning Engineers (ASHRAE), J. R. Wright, representative
The American Society of Mechanical Engineers (ASME)
- Design Engineering Division, D. A. Beaty, representative
- Fluids Engineering Division, K. E. Hickman, representative

Association of Home Appliance Manufacturers (AHAM), J. Weizeorick and L. Swatkowski, representatives
Compressed Air and Gas Institute (CAGI), J. H. Addington, representative
Deutscher Kalte-und Klimatechnischer Verein (DKV), H. Kruse, representative
Gas Research Institute (GRI), S. Freedman, representative
ICI Americas Inc., T. W. Dekleva, representative
International Institute of Ammonia Refrigeration (IIAR), K. Anderson, representative
International Institute of Refrigeration (IIR), L. Lucas, representative
Japanese Association of Refrigeration (JAR), S. Hotani, representative
Japan Society of Mechanical Engineers (JSME), A. Futakawa, representative

Advisory Committee

J. Bergstrom, Uddeholm AB, Sweden
M. A. Di Flora, Vice President, Engineering, Bristol Compressors, USA
R. Dusil, President, J. N. Eberle & Cie. GmbH, Germany
E. H. Eisele, Vice President, Overseas Industrial Operations, Whirlpool Corporation, USA
A. Futakawa, Deputy General Manager of Nagasaki Workes and Manager of Development, Engineering Department, Mitsubishi Electric Corporation, Japan
K. Graunke, Manager, Research and Development, Sulzer-Burckhardt Engineering Works Ltd., Switzerland
E. Heinzelmann, Director, Research and Development, Embraco S/A, Brazil
J. J. Jacobs, Director, Commercial Compressor Engineering, United Technologies-Carrier Corporation, USA
N. J. Josiassen, Vice President, Technology, Danfoss Flensburg GmbH, Germany
E. Korfitsen, Manager, Research and Development, SABROE Refrigeration, Denmark
H. Kruse, DKV-President, Universitat Hannover, Germany
Y. Kuramitsu, General Manager, Airconditioning Systems Division, Toshiba Corporation, Japan
A. Lundberg, Vice President, Marketing and Engineering, STAL Refrigeration, Sweden
E. B. Muir, Senior Vice President, Engineering and Research, Copeland Corporation, USA
S. Olsson, Manager, Development-Strip Products, Sandvik Steel, Sweden
H. Phillips, Vice President, Engineering, Air-Conditioning and Refrigeration Institute, USA
C. F. Speich, Staff Engineer, Screw Compressor Technology, The Trane Company, USA
R. L. Swadner, Staff Engineer, Harrison Radiator Division, General Motors Corporation, USA
P. G. Szymaszek, Vice President, Engineering, Vilter Manufacturing Corporation, USA
J. K. Taulbee, Vice President, Engineering, Americold, USA
S. Touber, Faculty of Mechanical Engineering, University of Technology-Delft, The Netherlands
A. B. Tramschek, Dean, Faculty of Engineering, University of Strathclyde, Scotland
R. R. Wisner, Group Vice President, Refrigeration Engineering, Tecumseh Products Company, USA
D. Woollatt, Manager, Advanced Engineering, Dresser-Rand Company, USA
J. R. Wright, Director of Technology, ASHRAE, USA
Y. Yu, Professor and Head, Chemical Engineering Department, Xi'an Jiaotong University, P. R. China
L. Zhang, Manager, International Projects, Wuxi Compressor Works, P. R. China

4-17, 1992
e University
Lafayette, Indiana, USA

ceedings - Volume IV

2 International Compressor
ineering Conference
urdue

erence Chairman and Editor
es F. Hamilton

dinator
nond Cohen

sored by
W. Herrick Laboratories
ol of Mechanical Engineering

Proceedings of the

1992 International Compressor Engineering Conference at Purdue

Volume IV

July 14-17, 1992
Purdue University
West Lafayette, Indiana, USA

Conference Chairman and Editor
James F. Hamilton

Coordinator
Raymond Cohen

Sponsored by
Ray W. Herrick Laboratories
School of Mechanical Engineering

Table of Contents

C-1: Compressor Design

Chairperson: R. T. S. Ferreira, Federal University of Santa Catarina, Brazil

C-2: Scroll Compressor I - Performance

Chairperson: J. D. Jones, Purdue University

C-3: Compressor Valves I - Dynamics

Chairperson: J. S. Fleming, University of Strathclyde, Scotland

C-4: Screw Compressor I - Performance

Chairperson: P. G. Szymaszek, Vilter Manufacturing Corporation

C-5: Screw Compressor II - Experimental Studies

Chairperson: J. J. Jacobs, United Technologies-Carrier Corporation

C-6: Compressor Simulation

Chairperson: J. H. Kim, University of Cincinnati

C-7: Compressor Noise Control I

Chairperson: J. S. Bolton, Purdue University

C-8: Rotary Compressor I - Performance

Chairperson: C. M. Costa, Embraco, Brazil

C-9: Screw Compressor III - Geometry

Chairperson: J. Sauls, The Trane Company

C-10: Friction Effects - Tribology

Chairperson: S. K. Padhy, General Electric Company

C-11: Lubrication - Bearings

Chairperson: F. Sadeghi, Purdue University

C-12: Scroll Compressor II - Development

Chairperson: J. P. Elson, Copeland Corporation

C-13: Design - Rotary and Reciprocating Compressors

Chairperson: J. A. McGovern, University of Dublin, North Ireland

C-14: Gas Pulsations

Chairperson: L. A. Newberg, De-Sta-Co

C-15: Compressor Vibration I

Chairperson: P. E. Hansen, Danfoss-Flensburg GmbH, Germany

C-16: Alternate Refrigerants I

Chairperson: H. S. Spauschus, Spauschus Associates Inc.

C-17: Scroll Compressor III

Chairperson: J. J. Nieter, United Technologies Research Center

C-18: Compressor Valves II - Reliability

Chairperson: D. Woollatt, Dresser-Rand

C-19: Compressor Noise Control II

Chairperson: C. F. Speich, The Trane Company

C-20: Alternate Refrigerants II

Chairperson: K. Taulbee, Americold Company

C-21: Scroll Compressor IV - Design, Manufacture

Chairperson: A. Futakawa, Mitsubishi Electric Corporation

C-22: Scroll Compressor V - Loading

Chairperson: E. G. Muir, Copeland Corporation

C-23: Rotary Compressor II - Sliding Vane

Chairperson: R. Riffe, Americold Company

C-24: Compressor Valves III - Flow

Chairperson: S. Tauber, Delft University of Technology, The Netherlands

C-25: Compressor Vibration II

Chairperson: C. N. Johnson, Emerson Electric

C-26: Compressor Optimization

Chairperson: P. Davies, Purdue University

C-27: Thermal/Heat Transfer

Chairperson: G. W. Gatecliff, Tecumseh Products Company

C-28: Compressor Motor and Starters

Chairperson: D. G. Smith, Noise Cancellation Technologies Inc.

C-29: Compressor Noise Control III

Chairperson: M. Brown, Americold Company

Appendix A: Additional papers from the 1990 International Compressor Engineering Conference at Purdue

Cooperative Societies and Representatives

Air Conditioning Contractors of America, J. P. Norris, representative
Air-Conditioning and Refrigeration Institute (ARI), H. Phillips, representative
The American Society of Heating, Refrigerating, and Air-Conditioning Engineers (ASHRAE), J. R. Wright, representative
The American Society of Mechanical Engineers (ASME)
- Design Engineering Division, D. A. Beaty, representative
- Fluids Engineering Division, K. E. Hickman, representative

Association of Home Appliance Manufacturers (AHAM), J. Weizeorick and L. Swatkowski, representatives
Compressed Air and Gas Institute (CAGI), J. H. Addington, representative
Deutscher Kalte-und Klimatechnischer Verein (DKV), H. Kruse, representative
Gas Research Institute (GRI), S. Freedman, representative
ICI Americas Inc., T. W. Dekleva, representative
International Institute of Ammonia Refrigeration (IIAR), K. Anderson, representative
International Institute of Refrigeration (IIR), L. Lucas, representative
Japanese Association of Refrigeration (JAR), S. Hotani, representative
Japan Society of Mechanical Engineers (JSME), A. Futakawa, representative

Advisory Committee

J. Bergstrom, Uddeholm AB, Sweden
M. A. Di Flora, Vice President, Engineering, Bristol Compressors, USA
R. Dusil, President, J. N. Eberle & Cie. GmbH, Germany
E. H. Eisele, Vice President, Overseas Industrial Operations, Whirlpool Corporation, USA
A. Futakawa, Deputy General Manager of Nagasaki Workes and Manager of Development, Engineering Department, Mitsubishi Electric Corporation, Japan
K. Graunke, Manager, Research and Development, Sulzer-Burckhardt Engineering Works Ltd., Switzerland
E. Heinzelmann, Director, Research and Development, Embraco S/A, Brazil
J. J. Jacobs, Director, Commercial Compressor Engineering, United Technologies-Carrier Corporation, USA
N. J. Josiassen, Vice President, Technology, Danfoss Flensburg GmbH, Germany
E. Korfitsen, Manager, Research and Development, SABROE Refrigeration, Denmark
H. Kruse, DKV-President, Universitat Hannover, Germany
Y. Kuramitsu, General Manager, Airconditioning Systems Division, Toshiba Corporation, Japan
A. Lundberg, Vice President, Marketing and Engineering, STAL Refrigeration, Sweden
E. B. Muir, Senior Vice President, Engineering and Research, Copeland Corporation, USA
S. Olsson, Manager, Development-Strip Products, Sandvik Steel, Sweden
H. Phillips, Vice President, Engineering, Air-Conditioning and Refrigeration Institute, USA
C. F. Speich, Staff Engineer, Screw Compressor Technology, The Trane Company, USA
R. L. Swadner, Staff Engineer, Harrison Radiator Division, General Motors Corporation, USA
P. G. Szymaszek, Vice President, Engineering, Vilter Manufacturing Corporation, USA
J. K. Taulbee, Vice President, Engineering, Americold, USA
S. Touber, Faculty of Mechanical Engineering, University of Technology-Delft, The Netherlands
A. B. Tramschek, Dean, Faculty of Engineering, University of Strathclyde, Scotland
R. R. Wisner, Group Vice President, Refrigeration Engineering, Tecumseh Products Company, USA
D. Woollatt, Manager, Advanced Engineering, Dresser-Rand Company, USA
J. R. Wright, Director of Technology, ASHRAE, USA
Y. Yu, Professor and Head, Chemical Engineering Department, Xi'an Jiaotong University, P. R. China
L. Zhang, Manager, International Projects, Wuxi Compressor Works, P. R. China

Preface

The 1992 International Compressor Engineering Conference at Purdue (1992 ICECP) is the eleventh biennial conference of this series, which started in 1972 under the name of Purdue Compressor Technology Conference. The name change occurred in 1986 to more accurately reflect the change in the nature of the conference. The conference will be run in parallel with the 1992 International Refrigeration Conference - Energy Efficiency and New Refrigerants. The two conferences are available to attendees with registration at either one conferring attendance and proceedings privileges to both. Proceedings of the individual conferences are available as individual publications.

The goals of the conference remain the same as for the previous conferences:

- to present research and design results in positive displacement compressors,
- to review the state-of-the-art of compressor development and application,
- to educate engineers starting in the compressor field, and
- to provide an easily accessible reference for compressor engineers.

The proceedings are organized by sessions as they were presented in the conference. Papers which arrived too late for inclusion may appear in the proceedings of the 1994 conference. Appendix A of these proceedings contains late papers from the 1990 conference.

Many of the papers presented at the conference could well have fit in more than one technical session. It is advisable for the reader to scan all sessions and papers carefully for applicability to his individual interests. An author index and keyword index have been provided in addition to the table of contents to assist the reader.

The established page limit of ten pages was enforced to a reasonable degree. Papers submitted with 11 pages were usually accepted, and papers with 12 pages were accepted in very special circumstances. I recognize how difficult this page limit was for the authors, and I wish to thank them for their efforts.

On behalf of the organizing committee, I would like to thank the members of the advisory committee, the cooperating professional societies and their representatives, all authors and session chairpersons, and all industrial and academic organizations who have given assistance in many ways. I would especially like to thank Phyllis Hurst, our conference secretary; her assistant, Donna Miller; and John Wellman, the conference coordinator; for their invaluable assistance.

The 1994 International Compressor Engineering Conference at Purdue is tentatively planned for July, 1994, West Lafayette, Indiana.

James F. Hamilton
Professor of Mechanical Engineering
and Conference Chairman

Policy for Publishing Conference Papers in Archival Journals

The organizing committee recommends to all authors who have papers which satisfy the criteria for archival journal articles to submit them to such journals for publication. Because of the relatively small number of copies, publication in the proceedings of the International Compressor Engineering Conference at Purdue does not constitute prior publication as far as many journal editors are concerned. If in doubt, an inquiry should be made. In most cases, the limit of 10 pages will require the creation of an expanded journal article version, which would qualify as a new publication anyway.

The criteria for archival papers are that they should contain original, quantitative, detailed scientific materials which are placed in proper perspective relative to prior work and are supported by references to the appropriate literature. Thus, not all conference papers are suitable. Some describe present practice; or report on procedures that were applied first by someone else; or report design features which, although important to conference participants, have relatively short temporal interest.

The organizing committee requests that authors who choose to submit their papers to archival journals acknowledge that those papers were presented at the 1992 conference and send a copy of each submitted manuscript to the organizing committee.

Purdue University sponsors this conference to provide a forum for the free exchange of ideas on the engineering state-of-the-art in the compressor field. The ideas expressed are those of the author(s) and do not necessarily represent the opinions or policies of the University or the cooperating organizations. The papers are not subject to the formal review procedures of the separate cooperating organizations as they would be if they were to be published by the cooperating societies. Instead, they are subject to the review procedures of the organizing committee.

Keyword Index

BACK-PRESSURE MECHANISM OF SCROLL COMPRESSOR

Qian Zhongliang
Xi'an Jiaotong University
Xi'an, Shaanxi, China

Zhang Zhiheng
General Machinery Research Institute
Anhui, China

ABSTRACT

On the principle of changeable mass thermodynamics, a thermodynamic model of working process for scroll compressor with self-adjusting back-pressure mechanism is established in this paper. General motion law of back-pressure ports position is developed by solving thermodynamic model of compressor and carrying out dynamical computation. In this method, the guarantee of higher volumetric and mechanical efficiency is regarded as the confined condition.

SYMBOLS

- b: polar radius of the centre of the backpressure port, m
- β: polar angle of the centre of the backpressure port, (^{o})
- r_o: eccentricity of the crank, m
- θ: angle of rotation (^{o})
- e: radius of the backpressure port, m
- $S(\theta)$: connected area between the backpressure chamber and compression chamber, m^2
- m: mass of the gas in the compression chamber, kg
- u: specific internal energy of the gas in the compression chamber, kJ/kg
- h_i: specific enthalpy of the gas flowing into the compression chamber, kJ/kg
- h_o: specific enthalphy of the gas flowing out of the compression chamber, kJ/kg
- ω: angular velocity, rad/s
- dm_i: mass of the gas microelement flowing into the compressor chamber, kg
- dm_o: mass of the gas microelement flowing out of the compression chamber, kg
- dm_b: mass of the gas microelement flowing between the backpressure chamber and compression chamber, kg
- T: temperature of the gas in the compression chamber, K
- v: specific volume of the gas in the compression chamber, m^3/kg
- P: pressure of the gas in the compression chamber, (10^5Pa)
- P_b: pressure of the gas in the backpressure chamber (10^5Pa)
- a: radius of basic circle for involute, m
- φ_A: expanding angle of point A on the Wrap, rad
- d: starting angle of the involute, rad
- b_o: polar radius of the backpressure port tangential to the Wrap
- δ: increment of b_o, which is chosen according to the machining requirements of backpressure port, m
- ψ: included angle between an arbitrary point on the circule of the backpressure port and the horizontal axis, rad

INTRODUCTION

One of the key technologies of the scroll compressor is the appropriate balance of the axial force, which not only gurantees that the mating scrolls do not separate in the compression and prevents gas from radial leakage, but also ensures that the acting force on the contact surfaces of the mating scrolls is not too great, and prevents the mechanical officiency decreasing. Currently , there are mainly three methods to balance the axial gas force, i.e., exerting an axial bearing counter-force, a spring force or a backpressure gas force on the back of the orbiting scroll. The last method can not only compensate automatically the wear between the mating scrolls, but also adjust the pressure of the backpressure gas whenever the working condition changes. Therefore it has found wide application in scroll compressors.

When the third method is adopted to balance the axial gas force, the central compression chamber and backpressure chamber are connected by the backpressure port on the orbiting scroll, and the backpressure of the gas in the backpressure chamber depends wholly on the position and geometrical dimensions of the port. This paper geometrically studies the orbit of the backpressure port relative to the static scroll and the law of the flow area change of the port; it finds out the relationship between the pressure in the backpressure chamber and the position and flow area of the backpressure port by applying the basic law of thermodynamics and the principle of mass conservation; it also carries out dynamic computation to determine the optimal position and geometrical dimensions of the backpressure port with the confining condition of enough volumetric and mechanical effeiency of the compressor.

LAW OF MOTION OF THE BACKPRESSUR PORT AND CHANGE OF THE FLOW AREA

Mass exchange of the actuating medium between the compression chamber and backpressure chamber of the scroll compressor is carried out through the backpressure port. Mass flow rate between the two chambers is mainly determined by the pressure ratio $\tau_i(\theta)$ and flow area $S(\theta)$, and the pressure ratio $\tau_i(\theta)$ between the two chambers is connected closely with the flow area $S(\theta)$ and the position and diameter of the backpressure port. To learn about the pressure change in the backpressure chamber when the compressor is working, we must find out the orbit of the backpressure port relative to the static scroll and solve for the law of the flow area of the backpressure port changing with the orbiting angle.

Usually, two backpressure ports are made in the end plate of the orbiting scroll in the scroll compressors with self-adjusting backpressure mechanism , which have a diameter of 2 mm and are 180° out of phase. During the operation of the orbiting scroll, the motion of the backpressure port's center relative to the static scroll is governed by the same law as the relative motion of an arbitrary point on the orbiting scroll. The motion orbit is shown in Fig. 1.

The coordinates of the port center on the orbiting scroll are $(b_{oI}\cos\beta, -b_{oI}\sin\beta)$ and $(-b_{oI}\cos\beta, b_{oI}\sin\beta)$ respectively.Now examine the port in the fourth quadrant. Projected to the static scroll,the orbit of the port center is a circle whose center is at $(b_{oI}\cos\beta, -b_{oI}\sin\beta)$ and radius equals the eccentricity of the crank r_o. Thus, the equation is:

$$x = b_{oI}\cos\beta + r_o\cos\theta \qquad (1)$$

$$y = -b_{oI}\sin\beta - r_o\sin\theta$$

In addition, the orbit of an arbitrary point on the boundary circle of the port is also a circle of the same radius r_o , and only the center of the circle is in

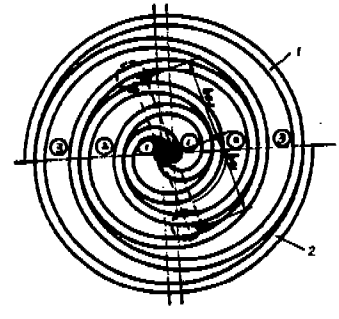

Fig. 1 Orbit of the center of the backpressure port
1.orbiting scroll 2.static croll

a different position, as shown in Fig. 2. The equation of its orbit is,

$$x = b_{01}\cos\beta + r_0\cos\theta + e\cos$$

$$y = -b_{01}\sin\beta - r_0\sin\theta - e\sin \qquad (2)$$

During the operation of the orbiting scroll, the backpressure port may be covered partially or totally by the wall of the Wrap on the static scroll (See the dash area in Fig. 2), which may result in the change in the flow area $S(\theta)$ between the backpressure chamber and compression chamber. It may be acquired by solving the insolute equation of the static scroll and Eq.(2) simultaneously.

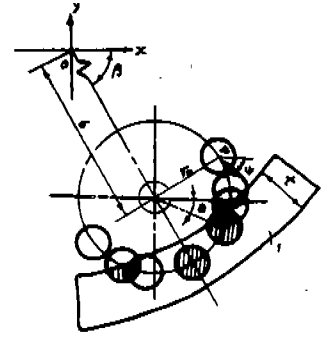

Fig. 2 Orbit of the backpressure port and law of the flow arta change

1. static scroll

Assume the port radius e and chamber volume V_d constant. The pressure in the backpressure chamber is mainly determiined by the position of the port. In a motion period, the port does not move in one compression chamber only, which is determined by the characteristic of the backpressure chamber for balancing the axial force.If the backpressure port moves in the first compression chamber or the second compression chamber,the gas pressure in the backpressure chamber, $P_b(\theta)$ has a range of $P_2(\theta) < P_b(\theta) < P_d$; and such a high backpressure would increase the contact wear between the end surfaces of the mating scrolls, and fail to ensure a high mechanical efficiency. If the port moves in the outermost compression chamber, then $P_3(\theta) < P_b(\theta) < P_2(\theta)$; and such a low backpressure could not ensure the fit of the orbiting scroll to static scroll in operation and could hardly ensure the volumetric efficiency. Therefore,the backpressure port can only move in the second or third compression chambers. Thus, with β determined, selection of b should satisfy the followin conditions:

A. When $0 \leqslant \theta \leqslant \beta$, the port is in the second compression chamber, or is covered by the static scroll

B. When $\beta \leqslant \theta \leqslant 2\pi$ the port is in the third compression chamber, or is covered by the static scroll

The position of the backpressure port in the compression chamber with different angle of rotation θ is shown in Fig. 3.

It can be seen from Fig. 3 that given β , b is

$$b = b_0 + \delta$$

where $b_0 = \sqrt{1 + \varphi_A^2} - r_0 + e$

and can be gained by

$$tg\,B = \frac{\varphi_A(\cos(\varphi_A+\alpha) - \sin(\varphi_A+\alpha)}{A\sin(\varphi_A+\alpha) + \cos(\varphi_A+\alpha)}$$

ANALYSIS OF THE THERMODYNAMIC PROCESS

In order to determine the optimal position and geometric dimensions of the backpressure port, it is necessary to find out the pressure of the gas in the compression and backpressure chambers and law of its change,and analyze the axial force and overturning moment on the orbiting scroll. Therefore the thermodynamic model of the chambers must be established and solved.

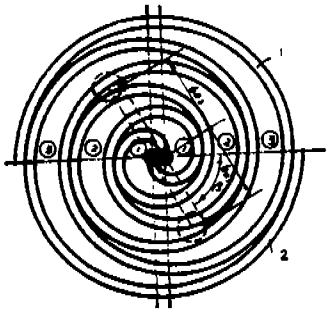

a) Position of the port when $\theta < \beta$

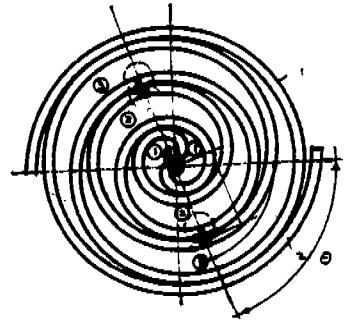

b) Position of the port when $\theta = \beta$

1. Thermodynamic Model of the Compression Chamber

The compression chamber connected with the backpressure chamber is taken as the control volume, the connected system is shown in Fig. 4. Assume that the volumes of the suction and discharge chambers are indefinitely great, and gas flow in the suction, discharge and leakage process and mass exchange between the two chambers is all steady flow, and ignore the effect of the lubricating oil on the performance of the actuating medium and potential energy and kinetic energy of the medium, then, we have the following equation by applying the first law of thermodynamics:

$$d(mu) = dQ + d\theta_b^* - h^* dm_b + h_i dm_i - h_o dm_o - dw \qquad (3)$$

where $d\theta_b^*$ is the heat transfer microelement between the compression chamber and backpressure chamber.

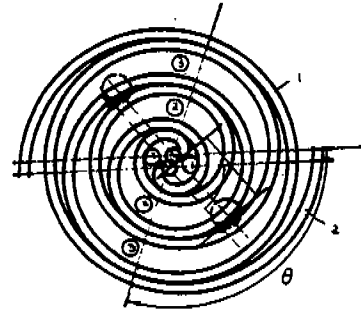

c) Position of the port when $\theta > \beta$

Fig. 3 Analytical gragh of the relationship between θ and β

1. orbiting scroll
2. static scroll

dQ is the heat transfer microelement between the compression chamber and the outside system.

h^* is the specific enthalpy of the gas flowing between the two chambers.

dm_b is positive, and $h^* = h_i$ when $P(\theta) > P_b(\theta)$,

dm_b is negative, and $h^* = h_b$. when $P(\theta) < P_b(\theta)$,

dw is the compression microelement work.

$$dw = -PdV_c ,$$

and V_c is the volume of the compression chamber.

When the rotating velocity of the crank is constant, $\theta = \omega\tau$, $d\theta = \omega d\tau$. Hence Eq.(3) can also be expressed as the following differential form of θ.

$$m\frac{du}{d\theta} + u\frac{dm}{d\theta} = \frac{dQ}{d\theta} + \frac{d\theta_b^*}{d\theta} - h^*\frac{dm_b}{d\theta} + h_i\frac{dm_i}{d\theta} - h_o\frac{dm_o}{d\theta} - P\frac{dV_c}{d\theta} \qquad (4)$$

Apply the total derivative relationship: $\frac{du}{d\theta} = (\frac{\partial u}{\partial T})_v \frac{dT}{d\theta} + (\frac{\partial u}{\partial v})_T \frac{dv}{d\theta}$ and $h_o = h$. Then Eq.(4) can be converted into:

$$\frac{dT}{d\theta} = \left[\frac{dQ}{d\theta} + \frac{d\theta^*_h}{d\theta} - h^*\frac{dm_b}{d\theta} + h_i\frac{dm_i}{d\theta} - h\frac{dm_o}{d\theta} - p\frac{dv_c}{d\theta} - u\frac{dm}{d\theta} - m(\frac{\partial u}{\partial v})_T \frac{dv}{d\theta}\right] / (m(\frac{\partial u}{\partial T})_v) \quad (5)$$

where $\frac{dv}{d\theta} = d(v_c/m)/d\theta = \frac{1}{m}\frac{dv_c}{d\theta} - \frac{v_c}{m^2}\frac{dm}{d\theta}$ (5)

$$\frac{dm}{d\theta} = \frac{dm_i}{d\theta} - \frac{dm_o}{d\theta} - \frac{dm_b}{d\theta}$$

and $m = m_{(o)} + \int_o^\theta (\frac{dm}{d\theta})\, d\theta$

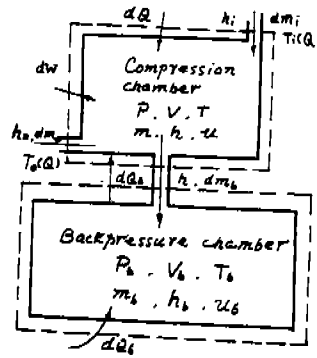

Fig. 4 Thermodynamic model

The above Eq.(5) is thus the basic equation of the thermodynamic model of the compression chamber.

2. Thermodynamic Model of the Backpressure Chamber

Here the backpressure chamber indicated in Fig. 4 is taken as the control volume for analysing the thermodynamic process of the backpressure chamber. Apply the first law of thermodynamics. Then,

$$d(m_b u_b) = dQ_b - \Sigma dQ^*_b + h^* dm_b \quad (6)$$

where dQ_b is the heat transfer microelement between the backpressure chamber and system. When the chamber absorbs heat, dQ_b is positive; otherwise, it is negative.

Apply the total derivative relationship. Then Eq.(6) can be written

$$\frac{dT_b}{d\theta} = \left[\frac{dQ_b}{d\theta} - \Sigma\frac{dQ^*_b}{d\theta} + h^*\frac{dm_b}{d\theta} - u_b\frac{dm_b}{d\theta} - m_b(\frac{\partial u_b}{\partial v_b})_{T_b}\frac{dv_b}{d\theta}\right] / \left[m_b(\frac{\partial u_b}{\partial T_b})_{v_b}\right] \quad (7)$$

where $\frac{dv_b}{d\theta} = \frac{d(v_d/m_b)}{d\theta} = \frac{-v_d}{m_b^2}\frac{dm_b}{d\theta}$;

$$m_b = m_b(o) + \int_o^\theta \frac{dm_b}{d\theta} d\theta$$

where v_d is the volume of the backpressure chamber.

Ignore the effect of oil deposition on the volume, then

$$v_d = C$$

Eq. (7) is thus the basic equation of the thermodynamic model of the backpressure chamber.

The scroll compressor is characterized with the continuous multi-chamber compression, and the parameters of the gas condition in the backpressure chamber are in periodical variation. Therefore the compression process must satisfy the following convergence conditions:

$$\begin{aligned} m_3(360^\circ) &= m_2\ (0^\circ) \\ T_3(360^\circ) &= T_2\ (0^\circ) \\ P_b(0^\circ) &= P_b(360^\circ) \\ T_b(0^\circ) &= T_b(360^\circ) \end{aligned} \quad (8)$$

where m_3, T_3 are the mass and temperature of the gas in the third compression

chamber respectively. m_2 and T_2 are the mass and temperature of the gas in the second compression chamber respectively.

Combining the equations (5), (7) and (8), we obtain the basic equations of the thermodynamic model of the scroll compressor with self-adjusting backpressure mechanism. Solving them, we can find out the pressure of the gas in the compression and backpressure chambers and law of its change.

DETERMINATION OF THE OPTIMAL POSITION OF THE BACKPRESSURE PORT

1. Minium Backpressure P_{bmin} to Ensure the Mating Scrolls do not Separate

Prerequisites of determination of the port position is the calculation of the minimum backpressure P_{bmin} which ensure the mating scrolls do not separate in the operation, to test whether the parameters of the position (b,β) meet the requirements or not. Therefore the axial gas force F_t and overturning moment exerted on the orbiting scroll should be solved for from the pressure distribution in the compression chamber obtained by solving the above thermodynamic model. Then P_{bmin} can be obtained from the balance of the axial forces on the orbiting scroll.

The pressure distribution on orbiting scroll and self-adjusting backpressure mechanism is shown in Fig. 5. Since the contact surfaces of the mating scrolls are not very wide, we can consider it to be linear distribution of pressure here. Then

$$F_{po} = \frac{1}{2}(P_b + P_a)(A_b - A_c) \qquad (9)$$

where A_b is the axial projected area of the orbiting scroll. $A_b = \frac{\pi}{4} D^2$ (where D is the diameter of the end plate of orbiting scroll.)

And A_c is the axial projected area of the suction pressure, compression chamber pressure, and central chamber pressure acting on the orbiting scroll.

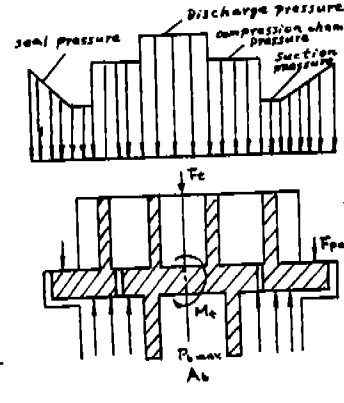

Fig. 5 Sketch of the self-adjusting backpressure mechanism and pressure distribution on orbiting scroll

Assume that the backpressure chamber pressure is just in equilibrium with the axial force and overturning moment at a instant. Then the axial force equilibrium equation of the orbiting scroll is

$$P_{bmin} \cdot A_b = F_t + F_{po} + \frac{2M_t}{D} \qquad (10)$$

Substitute Eq.(9) into Eq. (10), and note that at the moment, $P_b = P_{bmin}$. Then,

$$P_{bmin} = \frac{2F_t}{A_b+A_c} + \frac{A_b-A_c}{A_b+A_c} \cdot P_s + \frac{4M_t}{D(A_b+A_c)} \qquad (11)$$

From Eq.(11), under given working conditions, with A_b and A_c constant and M_t only varying slightly, the variation of P_{bmin} is mainly affected by the axial force F_t. When F_t increases, P_{bmin} increases as well. When $\theta = \theta^*$ (where θ^* is the exhaust angle of the compressor), and F_t is the maximum, P_{bmin} reaches its maximum as well.

2. Determination Method of the Port Position

Minimum backpressure P_{bmin} provides the basis for testing whether the chosen port position (b,β) meets the requirements or not. If with the first chosen β, the thermodynamic and dynamic computations prove that $P_b(\theta)$ is greater

than P_{bmin}, the determination of the position is then reasonable. Otherwise, β should be increased until the above requirements are met. However it should be noted that too high a chamber pressure $P_b(\theta)$ would increase the friction between the contact surfaces of the mating scrolls and result in the decline in the mechanical efficiency of the compressor η_m.

Therefore the determination of the port position should conform to the following principle.

When selecting the proper β, we should first guarantee $P_b(\theta) \geqslant P_{bmin}$ and the volumetric efficiency η_v, and at the same time restrict $P_b(\theta)$, to prevent the apparent decline in the mechanical efficiency η_m. The relationship between the polar angle of the port β and the efficiency of the compressor is shown in Fig. 6. It would be most ideal if the chosen β could always ensure $P_b(\theta) = P_{bmin}$; however, it is impossible to do so because $P_b(\theta)$ and P_{bmin} both vary with θ, and their variations are both very complex. Therefore, the following condition should be satisfied in the determination of the backpressure port position (b, β):

$$\beta_{min} \leqslant \beta \leqslant \beta_{max}$$

where β_{min} is the minimum β to ensure the mating scrolls do not separate.

and β_{max} is the maximum β to ensure the mechanical wear will not be too great.

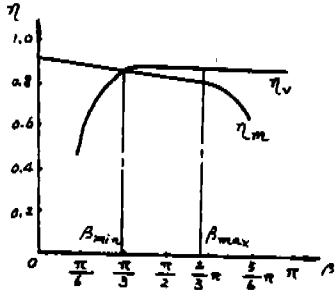

Fig. 6 Relationship between the polar angle of the port and efficiency

CASE ANALYSIS

The above method has been applied to analyse the backpressure port position in our scroll compressor, and the result is shown in Fig. 7.

From Fig. 7, when $\beta = 30^\circ$ or 45°, it cannot be ensured that $P_b(\theta) \geqslant P_{bmin}$; therefore it is not reasonable that $\beta = 30^\circ$ or 45°. when β 60°, it is ensured that $P_b(\theta) \geqslant P_{bmin}$; therefore $\beta_{min} = 60^\circ$ is appropriate to choose. When β contimues to increase, $P_b(\theta) - P_{bmin}$ will increase as well. From Fig. 8, we know η_m will decrease, and when $\beta = 105^\circ$, η_m will have had an apparent decrease. Therefore the selection of β should satisfy: $60^\circ \leqslant \beta \leqslant 105^\circ$. Considering the reliability of the compressor, it is proper to select $\beta = 75^\circ$. Analysis and computation show that the proper positions of the pair of backpressure port centers on the orbiting scroll are at $O_1(34mm, 75^\circ)$ and $O_2(34mm, 255^\circ)$ respectively, as shown in Fig. 9.

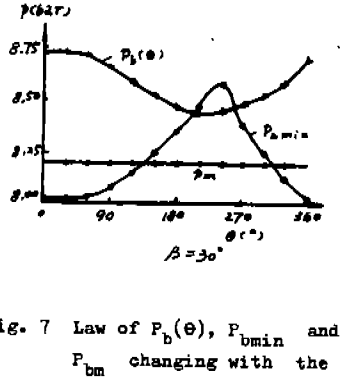

Fig. 7 Law of $P_b(\theta)$, P_{bmin} and P_{bm} changing with the angle of retation θ

(P_m is the average gas pressure in the compression chamber connected with the backpressure chamber in a cycle)

CONCLUSION

1. Backpressure mechanism is widely applied to balance the axial gas force in scroll compressors, which guarantees the compressor's ability to adjust to the changing working conditions.

2. Reasonableness of the backpressure mechanism is mainly demonstrated in

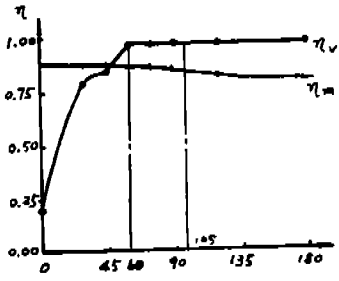

Fig. 8 Effect of B on the volumetric efficiency and mechanical efficiency

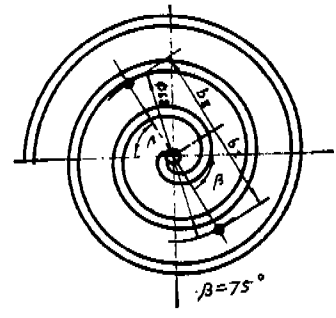

Fig. 9 Position of the backpressure port in the speciman compressor

1. orbiting scroll

the ability of the pressure in backpressure chamber to balance the axial gas force exerted on the orbiting scroll.

3. With the given chamber volume and port radius e, the gas pressure in the backpressure chamber depends on the position of the port (b, β).

4. b is determined by β , which has a proper range of $\beta_{min} \leq \beta \leq \beta_{max}$, thus ensuring the great volumetric and mechanical efficiency of the compressor.

REFERENCES

[1] Morishita E. et al: Scroll Dynamics (1 st Report) Bulletin of JSME 29-248 (1986.2)

[2] M.Ikegawa et al: Scroll Compressor with Self-Adjusting Back-pressure mechanism, Pro. of the JSME No. 830-12, 1983.

[3] Hirano, T. et al: Development of High Efficiency Scroll Compressors for Air Conditions, Pro. of the 1988 Intern. Compr. Eng. Conf. (Purdue)(1988.7) 65

ANALYSIS OF LEAKAGE FLOW THROUGH CLEARANCE ON ROTOR FACE IN VANE COMPRESSORS

Mitsuhiro FUKUTA, Research Associate
Tadashi YANAGISAWA, Associate Professor
Takashi SHIMIZU, Professor

Department of Energy and Mechanical Engineering,
Faculty of Engineering, Shizuoka University,
3-5-1, Johoku, Hamamatsu, 432, JAPAN

ABSTRACT

Performance of vane compressors used for automotive air conditioners is affected greatly by leakage which flows through a clearance between a rotor face and a sideplate. We analyze an instantaneous leakage flow and a time averaged one through the clearance on the rotor face under pressure boundary conditions changing periodically with rotation of the rotor. The flow field on the rotor face at each moment can be evaluated under a quasi-steady condition with an instantaneous pressure distribution on the rotor circumference. On the other hand, the average flow field on the rotor face must be analyzed under an averaged boundary condition which is an average of the pressure changing periodically on the rotor circumference.

NOMENCLATURE

A_k, B_k : Fourier coefficients
a_0, b_0 : Fourier coefficients
h : clearance on rotor face
n : approximate order of Fourier series
P : pressure
P_b : oil supply pressure ($= P_1$)
r : radius
t : time
v : velocity
z : ordinate of clearance height
θ : angular position on rotor face from axial seal
μ : coefficient of viscosity of oil
ν : coefficient of kinematic viscosity of oil
ρ : density of oil
ϕ : rotational angle of rotor
ω : angular velocity of rotor

Subscripts
b : boundary between gas and oil regions
r : radial direction
θ : tangential direction
1 : inner circumference of rotor
2 : outer circumference of rotor

Superscript
$\bar{}$: averaged value in height direction

INTRODUCTION

In recent years, a vane compressor is used for an automotive air conditioners by taking advantages of its small size and its light weight. Leakage which flows through a clearance between a rotor face and a sideplate greatly affects performance of the compressor /(1)/. There have been some studies which analyzed distributions of pressure and velocity on the rotor face based on the Navier-Stokes equation by applying the perturbation technique /(2)/, the Finite Element Method /(3)/ or the Finite Difference Method /(4)/. But in these studies, the flow field was analyzed under some special boundary pressure condition on the rotor circumference, and discussion about a practical leakage flow occurring under the periodic changing boundary pressure condition

on the rotor circumference was insufficient.

In this study, we analyze an instantaneous leakage flow at each moment through the clearance on the rotor face based on the Navier-Stokes equation by applying the Fourier series analysis /(2)/, and examine an appropriate manner of a decision of the boundary pressure condition on the rotor circumference to analyze an averaged leakage flow.

THEORETICAL ANALYSIS

Pressure Distribution

Figure 1 shows a schematic view of the vane compressor and a modeling of the flow field between the rotor face and the sideplate. Lubricating oil is supplied from an oil groove on the sideplate to the rotor face. The flow field of leakage flow through the clearance on the rotor face is modeled as that between a stationary disc and a rotating disc on which circumference the pressure changes periodically with the rotor rotation. The leakage flow in this flow field is governed by the Navier-Stokes equations and an equation of continuity, and these equations are expressed as follows since the clearance is very small by comparison with the flow field.

$$\frac{\partial v_r}{\partial t} + v_r\frac{\partial v_r}{\partial r} + \frac{v_\theta}{r}\frac{\partial v_r}{\partial \theta} - \frac{v_\theta^2}{r} = -\frac{1}{\rho}\frac{\partial p}{\partial r} + \nu\frac{\partial^2 v_r}{\partial z^2} \tag{1}$$

$$\frac{\partial v_\theta}{\partial t} + v_r\frac{\partial v_\theta}{\partial r} + \frac{v_\theta}{r}\frac{\partial v_\theta}{\partial \theta} + \frac{v_r v_\theta}{r} = -\frac{1}{\rho r}\frac{\partial p}{\partial \theta} + \nu\frac{\partial^2 v_\theta}{\partial z^2} \tag{2}$$

$$\partial(rv_r)/\partial r + \partial v_\theta/\partial\theta = 0 \tag{3}$$

In the above Navier-Stokes equations, an inertial term, a centrifugal term and a coriolis term are assumed to be negligible since the clearance on the rotor face is very small. By integrating equations (1) and (2) respectively and substituting boundary conditions on both the stationary and the rotational discs into those equations, radial and tangential velocities are derived as follows.

$$v_r = (z^2 - hz)(\partial p/\partial r)/(2\mu) \tag{4}$$

$$v_\theta = (z^2 - hz)(\partial p/\partial\theta)/(2\mu r) + zr\omega/h \tag{5}$$

Substituting equations (4) and (5) into equation (3), we obtain the Laplace equation for pressure.

$$\partial(r\partial p/\partial r)/\partial r + (\partial^2 p/\partial\theta^2)/r = 0 \tag{6}$$

The Laplace equation for what is called the Dirichlet problem is solved by applying the Fourier series /(2)/. The pressure on an inner circumference is assumed to be constant ($=P_b$) and that on an outer circumference of the rotor is expressed as follows.

$$p_2 = A_0 + \sum_{k=1}^{n}(A_k\cos k\theta + B_k\sin k\theta) \tag{7}$$

Where, coefficients in equation (7) are derived by discrete Fourier approximation using sampled data of the pressure on the rotor circumference. By using these boundary pressure distributions, the pressure distribution on the rotor face is derived as follows.

$$p = a_0 + b_0\log r + \sum_{k=1}^{n}(A_k\cos k\theta + B_k\sin k\theta)\frac{(r/r_1)^k - (r_1/r)^k}{(r_2/r_1)^k - (r_1/r_2)^k} \tag{8}$$

where

$$a_0 = (A_0\log r_1 - P_b\log r_2)/\log(r_1/r_2)$$

$$b_0 = (P_b - A_0)/\log(r_1/r_2)$$

Velocity Distribution

In this study, we will express the velocity distribution with an averaged one in

height direction. The radial and tangential average velocities are derived as follows by integrating equations (4) and (5) respectively.

$$\overline{v_r} = -(\partial P/\partial r)h^2/(12\mu) \tag{9}$$

$$\overline{v_\theta} = -(\partial P/\partial \theta)h^2/(12\mu r) + r\omega/2 \tag{10}$$

In the above equations, pressure gradients are given by differentiating equation (8). In the Fourier analysis, in general, it is not appropriate to use the gradient obtained by differentiating a function expressed by the Fourier series, and we will discuss this problem at the later section.

Gas Flow Region

In the neighborhood of an axial seal, refrigerant gas as a working fluid flows through the clearance on the rotor face from a high pressure compression chamber into a suction chamber, and the leakage greatly affects the performance of the compressor. In a practical use, the gas flow region on the rotor face near the axial seal can be solved sufficiently under a flow field with a single phase of oil by approximation with a group of streamlines which have the velocity of inner direction on the rotor circumference /(5)/. In the present study, we analyze the average gas flow region using the average velocity distribution. A boundary line between the gas and the oil regions is obtained by solving the following equations applying the Runge-Kutta method with an initial position where the gas begins to enter the clearance on the rotor face.

$$\left.\begin{aligned} dr_b/dt &= \overline{v_r} \\ d\theta_b/dt &= \overline{v_\theta}/r \end{aligned}\right\} \tag{11}$$

Boundary Pressure Condition

Since the rotor circumference faces the compression chambers, the pressure on the rotor circumference changes periodically with the rotor rotation. Table 1 shows specifications of the compressor studied here and analytical conditions, and Figure 2 shows volume and pressure changes of the compression chamber leading a vane located at rotational angle of ϕ.

Taking into account of periodic pressure change with the rotor rotation, we analyzed the leakage flow through the clearance on the rotor face under the following three different boundary pressure conditions on the rotor circumference. The first boundary condition is an instantaneous pressure distribution corresponding to the rotor rotation (denoted as Boundary condition 1). The pressure distribution on the rotor circumference changes periodically every $2\pi/3$ rad, since the compressor studied here has three vanes. Figure 3 shows the instantaneous pressure distribution on the rotor circumference corresponding to the rotational angle of 0, $\pi/6$, $\pi/3$ and $\pi/2$ rad. In this figure, the pressure distribution at positions of the vane and the axial seal is assumed to be linear.

The second one is an average pressure distribution that the pressure at each angular position on the rotor circumference is equal to the time average of the pressure in the compression chamber which is facing that position. It is shown in Figure 4 with a solid line (Boundary condition 2).

The last one is a linear pressure distribution from the suction side to the discharge side which is employed in the past studies /(2)-(4)/, and shown in Figure 4 with a broken line (Boundary condition 3). The analytical results corresponding to the each boundary conditions are compared with one another.

RESULTS AND DISCUSSION

Accuracy of Pressure Gradient

At first, we discuss accuracy of the pressure gradient obtained by differentiating the function expressed by the Fourier series. As an example, we calculate the tangential pressure gradient on the rotor circumference by differentiating equation (7) when the rotational angle of the rotor is $\pi/2$ rad, and compare it with an analytical pres-

sure gradient. Figure 5 shows the analytical pressure gradient and the pressure gradients which are obtained by differentiating equation (7) whose number of sampling points is 360 and approximate order is 180 and 120 respectively. As shown in these figures, the pressure gradients obtained by differentiating equation (7) fluctuate at the position where the pressure gradient changes abruptly. The fluctuation of the pressure gradient depends on the number of sampling points and the approximate order of the Fourier series, and they must be selected carefully. But an error of the velocity caused by the error of the pressure gradient is much smaller than the second term on the right hand of equation (10), and this error disappears when we integrate the velocity to estimate the leakage flow rate. The velocity distribution, therefore, can be solved sufficiently by differentiating the Fourier series in a practical use. Once the pressure and velocity distributions are expressed by the Fourier series, it is useful that the center of pressure, flow rate and shearing force of oil for an arbitrary rotational angle of the rotor can be expressed by the Fourier series. In the following analysis, we employ the Fourier series whose number of sampling points is 360 and the approximate order is 120.

Instantaneous Flow Fields

Figure 6(a)-(d) show the instantaneous pressure and velocity distributions on the rotor face under the boundary pressure condition 1 (rotational angle ϕ = 0, $\pi/6$, $\pi/3$ and $\pi/2$ rad). In these figures, mark 'V' indicates the position of the axial seal (θ = 0 rad), and mark ']' indicates the position of the vane at each moment. As shown in these figures, lubricating oil flows from the inside to the outside of the rotor for the most part, and high pressure refrigerant gas passes through the clearance on the rotor face into the suction side in the neighborhood of the axial seal.

The pressure and velocity distributions shown in Figure 6 are steady flow fields under each boundary conditions shown in Figure 3, and these can be regarded as the instantaneous flow field only when the inertial force is as small as negligible. Figure 7 shows magnitude of the inertial force in radial direction against the viscous force about fluid element existing at middle height of the clearance on the rotor circumference when the rotational angle of the rotor is $\pi/2$ rad. Figure 7(a) is radial velocity at the middle height of the clearance on the rotor circumference, (b) is magnitude of unsteady term of inertial force which is the first term on the left hand of equation (1), and (c) is magnitude of convective term of inertial force which is the second and the third terms on the left hand of equation (1). These figures show that the radial velocity and the inertial force have sharp peaks at the positions of the vane (θ = $7\pi/6$, $11\pi/6$ rad) and the axial seal (θ = 0 rad). However, even when the rotational speed and the clearance increase, portions where the inertial force is big are local and have little influence on whole flow field and whole flow rate. The flow field on the rotor face at each moment, therefore, can be evaluated under the quasi-steady condition with the instantaneous pressure distribution on the rotor circumference.

Average Flow Fields

Figure 8 and 9 show the average pressure and velocity distributions corresponding to the second and the third boundary conditions respectively. In the case of boundary condition 2, the lubricating oil flows from the inside to the outside of the rotor at most of the rotor face. On the other hand, the oil which flows from the outside to the inside of the rotor increases under boundary condition 3 since the high pressure region on the rotor circumference is larger than that of the boundary condition 2. The flow rate of the leakage oil which flows out from the clearance on the rotor face estimated by integrating the radial velocity on the rotor circumference is 3.40 cm^3/s under the boundary condition 2 and 1.16 cm^3/s under the boundary condition 3. The average leakage flow rate estimated as the average of the instantaneous flow rate at each moment is equal to that under boundary condition 2.

Figure 10 shows the gas flow regions on the rotor face estimated by using the average velocity distributions under the boundary conditions 2 and 3 respectively. The gas flow regions which have great influence on the performance of the compressor are quite different from each other. Thus when we analyze the average flow field on the rotor face, it is appropriate to use the boundary condition that the pressure at each angular position on the rotor circumference is equal to the time average of the pressure in the compression chamber which is facing that position.

CONCLUSIONS

Based on the Navier-Stokes equation, we analyzed the instantaneous and time averaged leakage fields on the rotor face clearance by applying the Fourier series analysis under the more realistic boundary pressure conditions which changes periodically with the rotor rotation. The results are summarized as follows.

(1) In the practical use, once the number of sampling points and the approximate order of the Fourier series are selected adequately, the velocity distribution can be solved sufficiently by applying the differentiation of the Fourier series.

(2) The flow field on the rotor face at each moment can be evaluated under the quasi-steady condition with the instantaneous boundary pressure distribution on the rotor circumference because of less influence of the inertial force than that of the viscous force.

(3) The average flow field on the rotor face must be analyzed under the boundary condition that the pressure at each angular position on the rotor circumference is equal to the time average of the pressure in the compression chamber which is facing that position.

REFERENCES

(1) Honda, I., et al., "A Study on a Vane-Type Compressor (Relation between Gap Clearance and Performance)", Trans. JSME (in Japanese), Series B, Vol. 57, No. 534, 1991, 564.

(2) Bein, M., et al., "Nonaxisymmetric Flow in the Narrow Gap between a Rotating and a Stationary Disk", Trans. ASME, J. Fluid Eng., Vol. 98, No. 2, 1976,217.

(3) Hirano, T., et al., "Finite Element Method Analysis of Leakage Flow in the Narrow Clearance between the Rotor and Side Plates of a Sliding Vane Rotary Compressor", Proc. 1982 Purdue Comp. Tech. Eng. Conf., 1982, 305.

(4) Honda, I., et al., "Analysis of a Gap Flow on the Side Plate for Rotary Vane Compressor", Trans. JSME (in Japanese), Series B, Vol. 56, No. 526, 1990, 1607.

(5) Hagimoto, K., et al., "Analysis of Tow-Phase Flow in the Narrow Clearance Between a Rotor End Face and a Stationary Plate", Mitsubishi Heavy Industries Tech. Report (in Japanese), Vol. 23, No. 2, 1986, 160.

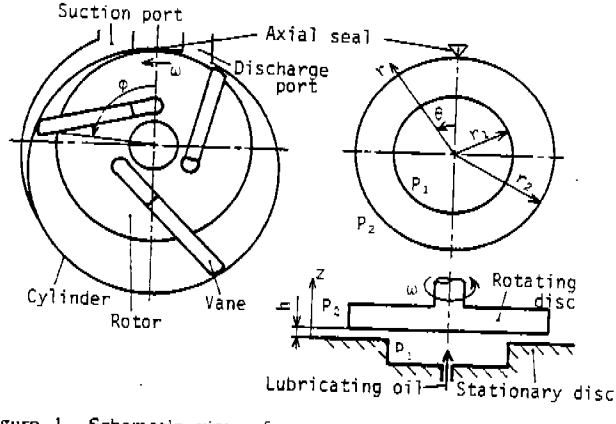

Figure 1 Schematic view of vane compressor and analytical model

Table 1 Specifications of compressor and analytical condition

Number of vane		3	
Cylinder radius	r_c	36.3	mm
Rotor radius	r_2	28.8	mm
Oil groove radius	r_1	20.0	mm
Gap height	h	30.0	μm
Suction pressure	P_s	0.309	MPa
Discharge pressure	P_d	1.52	MPa
Oil supply pressure	P_b	1.06	MPa
Oil viscosity	μ	0.005	Pa-s
Rotational speed	N	2000	rpm

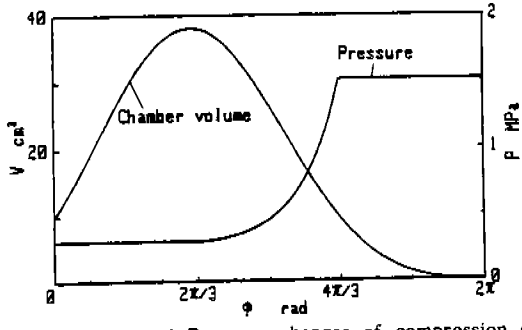

Figure 2 Volume and Pressure changes of compression chamber

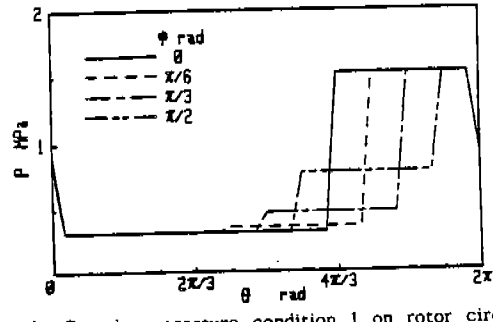

Figure 3 Boundary pressure condition 1 on rotor circumference

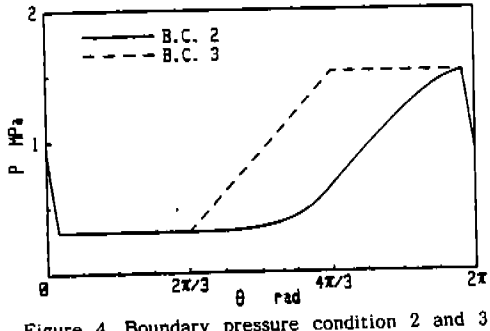

Figure 4 Boundary pressure condition 2 and 3 on rotor circumference

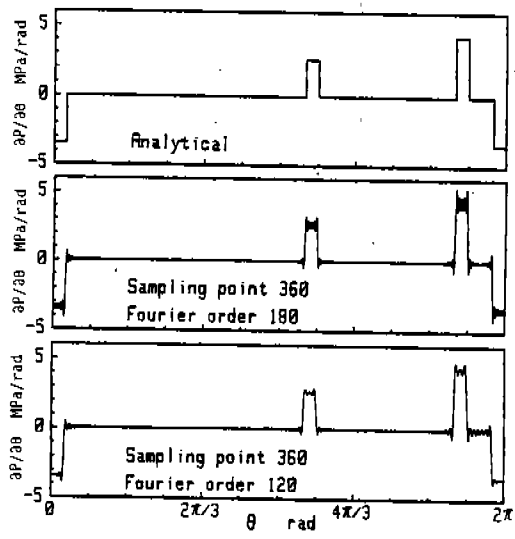

Figure 5 Pressure gradients obtained by differentiating Fourier series ($\phi = \pi/2$ rad)

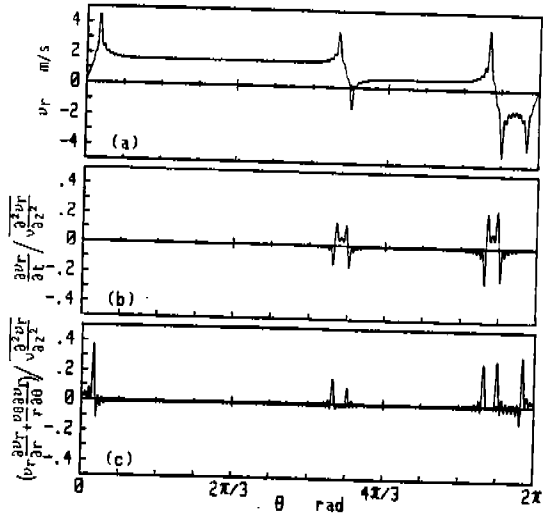

Figure 7 Magnitude of inertial force against viscous force ($\phi = \pi/2$ rad, $z = h/2$)

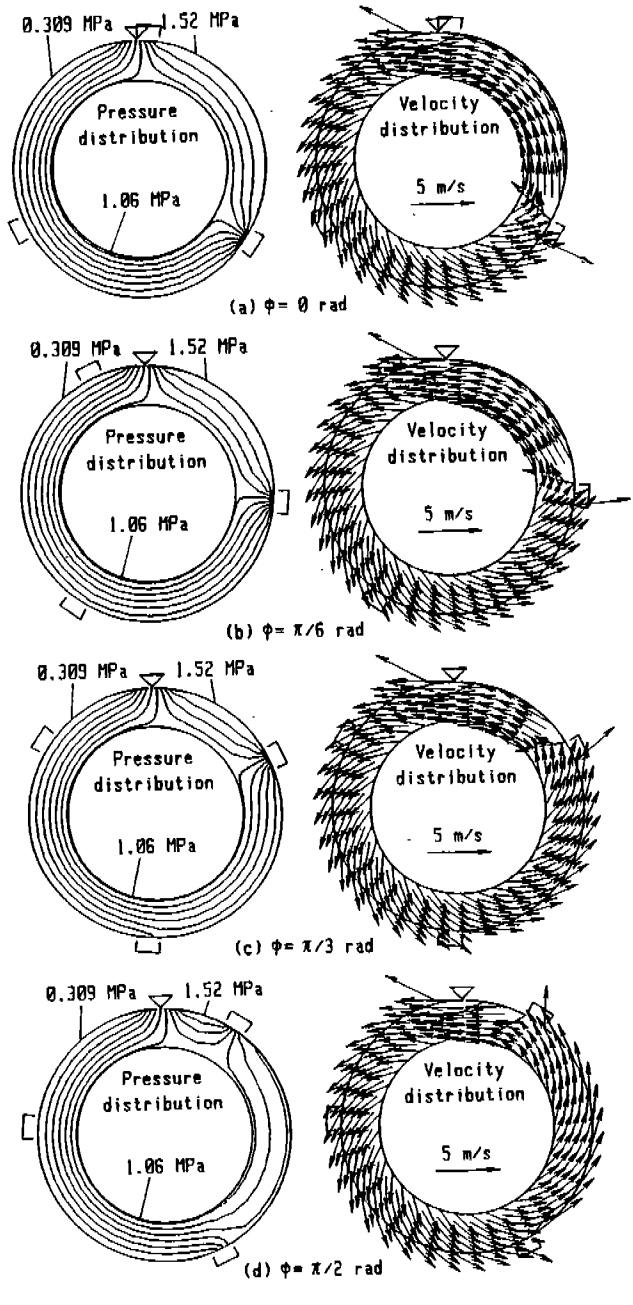

Figure 6 Instantaneous distributions of pressure and velocity under boundary condition 1

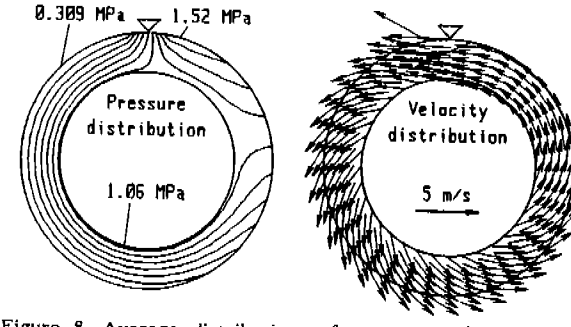

Figure 8 Average distributions of pressure and velocity under boundary condition 2

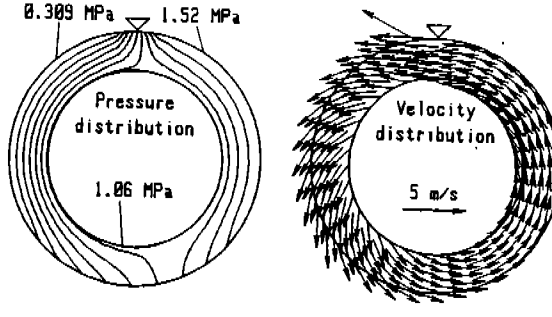

Figure 9 Average distributions of pressure and velocity under boundary condition 3

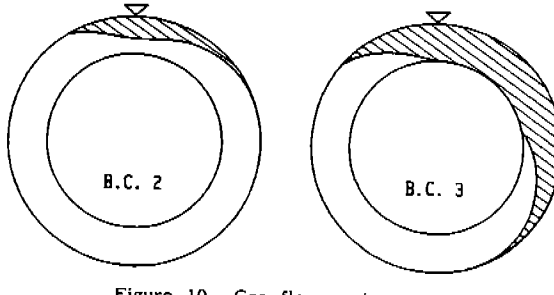

Figure 10 Gas flow region

A TECHNICAL NOTE ON THE EFFECTS OF SUCTION CHAMBER AND CELL INTERACTION ON THE SUCTION CHARACTERISTICS OF A ROTARY VANE COMPRESSOR

Dr A.B. Tramschek,
Senior Lecturer & Dean of Engineering
University of Strathclyde,
Glasgow, Scotland.

Dr K.T. Ooi
School of Mechanical and Production Engineering,
Nanyang Technological University,
Singapore.

ABSTRACT

In most sliding vane air compressors, the angular span of the suction port is usually larger than that of an individual cell. Hence two or more cells may communicate simultaneously with the suction plenum chamber during the suction process. Because of this, the suction process in this type of compressor is a continuous process and pulsation effects are small compared to those found in reciprocating compressors. This paper illustrates a theoretical study of the suction characteristics of a sliding vane compressor by accounting for the effects of the interaction between the "cell-in Question" and its neighbouring cells (during the suction process) as well as the suction plenum chamber. The variations of pressure, temperature and air mass flow into and/or out of each of the neighbouring cells and the suction chamber during the suction process are shown and discussed together with those of the "cell-in question".

INTRODUCTION

In the construction of certain sliding vane compressors, a suction plenum chamber is frequently located between an air intake valve and the suction port as shown in Figure 1.

The suction plenum of such a compressor is sometimes called the air intake valve chamber since it is the place where the intake valve is housed. The existence of an intake valve in the suction plenum does not improve the suction characteristic but provides a non-return valve mechanism when the compressor is stopped. It prevents high pressure fluid from escaping through the low pressure side of the machine via the suction port. In some machines this valve acts as part of a hydraulically actuated servo control system which closes the air intake port when the compressor is running off load.

A previous attempt [1] to model this type of machine, showed that a simple model which assumed that the suction plenum was volumetrically large compared to the active cell volume, gave good overall agreement between predicted and measured results. When modelling the suction process without considering the existence of a suction plenum, the nominal suction conditions were taken as constant and set equal to atmospheric conditions. This paper shows the influence of the presence of the suction plenum on the modelling results. It also shows the effects of cell interactions during the suction process.

Suction Characteristic

Any interaction between the cells influences the suction characteristic to some extent and depends mainly on the relative volume of the suction plenum and the active cells. In the following sections the influence of the air intake valve, the suction plenum and the interaction of the neighbouring cells during the suction process predicted by a theoretical model are discussed.

The analysis which follows applies to an existing compressor model or to machines with a similar configuration. A schematic diagram of the machine is shown in Figure 2 which illustrates the arrangement between suction valve, suction plenum and the compressor working space. Point 'A' and point 'B' represent the suction port opening and closing position respectively.

In the present study of an eight vane machine the cell angle is i.e. 45° and the circumferential span of the suction port is 79°. Close examination of the suction port dimensions given above shows that during the suction process a maximum of three cells and at least two cells may communicate simultaneously with the suction plenum. This means that in addition to the cell in question, there is at least one other cell which is also communicating with the suction plenum. The existence of these neighbouring cells and the interaction between them during the suction process is termed cell interaction. To model the compressor as a whole and its suction plenum in particular, interaction during the suction process must be considered.

Theoretical Model of The Suction Plenum

The existing suction model formed part of the mathematical model describing the complete compressor and used the following criteria:-

a) The process occurring in the suction plenum was assumed to be adiabatic, i.e. $Q=0$.

b) The plenum chamber has a fixed volume, i.e. $dV_p = 0$ and means that the work done term associated with the plenum is zero i.e. $W=0$.

c) For the present study, perfect sealing was assumed to exist between the plenum and the outside world, i.e. no leakage flows out of or into the plenum. This assumption is justified because the pressure difference between the suction plenum and its surrounding is small.

d) A quasi steady process is assumed for the flow through the suction plenum and means that at any particular instant the unsteady flow through the suction plenum can be treated as steady.

e) The flows into and out of the plenum chamber are assumed to behave as one dimensional isentropic flows through an orifice. An effective flow area is introduced by using a discharge coefficient with the area calculated from the actual geometry of the port.

f) Air behaves as ideal gas.

Figure 3 shows a control volume which was used to represent the suction plenum of the compressor. From the above assumptions, the primary activity which occurs is mass flow into and out of the control volume. There is massflow through the air intake valve m_i, mass flow out of the suction plenum through the suction port m_e into the cell in question, and mass flow caused by cell interaction effects m_{ci}.

Considering the control volume as an entity, from the Law of Conservation of Energy the following equation may be obtained:-

$$\frac{dQ}{dt} + \Sigma\left(\frac{dm}{dt}C_i T\right)_i - \frac{dW}{dt} + \Sigma\left(\frac{dm}{dt}C_e T\right)_e + \frac{d}{dt}(mu), \qquad \ldots(1)$$

This equation is solved simultaneously with the mass conservation equation i.e.:-

$$dm_i - dm_e = dm, \qquad \ldots(2)$$

Solving equations (1) and (2) simultaneously for a fixed volume plenum chamber together with the equation of state for an ideal gas and accounting for the effects of cell interaction yields,

$$\frac{dP_p}{dt} = \frac{\gamma R T_i}{V}\frac{dm_i}{dt} - \frac{\gamma R T_p}{V}\frac{dm_o}{dt} \pm \frac{\gamma R}{V}\left(\Sigma\left(T_T\frac{dm_T}{dt}\right) + \Sigma\left(T_L\frac{dm_L}{dt}\right)\right) \quad \ldots(3)$$

$$\frac{dT_p}{dt} = \frac{T_p}{P_p}\frac{dP_p}{dt} - \frac{RT_p^2}{P_pV_p}\frac{dm_p}{dt} \quad \ldots(4)$$

$$\left(\frac{dm_p}{dt}\right) = \frac{dm_i}{dt} - \frac{dm_o}{dt} \pm \Sigma\frac{dm_T}{dt} \pm \Sigma\frac{dm_L}{dt} \quad \ldots(5)$$

i) Suffix T denotes properties of a group of cells which is at the trailing side of the cell in question with respect to the direction of rotor rotation and which communicate with the suction plenum during the suction process.

ii) Suffix L denotes properties of a group of cells which is at the leading side of the cell in question with respect to the direction of rotor rotation and which communicate with the suction plenum during the suction process.

iii) Suffices i and o denote massflow and the properties of the air entering and leaving the cell in question only.

FURTHER SIMULATION ASSUMPTIONS

Calculations were performed for the following conditions:-

i) With the air intake non return valve free to move instantaneously, depending on the pressure differential across the valve, i.e. If $P_{ATM} > P_p$ the valve would be fully open where for $P_p > P_{ATM}$ the valve would be closed.

ii) Ignoring cell interaction effects.

iii) Accounting for cell interaction effects.

The initial conditions in the suction plenum were taken as T= 25°C and P = 1.01325 bar (760 mmHg) with the intake valve closed.
Effective air intake valve flow area - $C_d(\pi/4)((d_v)^2-(d_r)^2)$
where C_d = 0.6, d_v = 32mm, d_r = 10mm.
The atmospheric condition was taken as at T_{ATM} = 20°C and P_{ATM} = 1.01325 bar, where C_d is the discharge coefficient, and d_v and d_r are the valve port and the valve rod diameter respectively.

Calculations were performed for various suction plenum chamber volumes, ranging from 1000 mm³ to 8000 mm³.

DISCUSSION OF RESULTS

Plenum Chamber Conditions

Two distinct sets of calculations were performed. The first excluded interaction of neighbouring cells and the second took the effects of cell interaction into consideration.

a) Plenum Pressure And Temperature Variation

Figure 4 shows the comparison of variations in the plenum pressure during the suction process, both neglecting and accounting for the effects of the cell interaction. When the plenum chamber is interacting only with the cell in question, the condition in the plenum chamber is greatly dependent on the variation of the size of the suction cell, where the latter is a function of the cell angular position. The sudden decrease in the pressure of the plenum chamber to a value of 100800 N/m², is caused by mass flow out of the chamber into the cell, when the suction port is first uncovered. This causes the pressure in the plenum chamber to drop

to a level which is lower than the atmospheric pressure and hence causes the intake valve to open and permits the induction of air from the atmosphere into the plenum chamber through the air intake valve. This process causes the plenum chamber pressure to recover. As the mass flow into the cell and the mass flow into the plenum chamber are of a similar magnitude, the plenum pressure stays reasonably constant. This is shown in the later stage of the suction process.

A more realistic consideration of the suction process accounts for the interactions between the plenum chamber, the neighbouring cells and the cell-in-question.

Because the volume of the plenum chamber is fixed, and also because of the assumption of an adiabatic process occurring in the plenum chamber, the chamber pressure is primarily influenced by the **incoming** and the **outgoing** mass flow. The temperature of region from which a mass flow originates also has an influence although in the present study this temperature influence was discounted.

The pressure oscillations are caused by the rate of change of the mass in the plenum chamber i.e. the difference between the mass flow into and out of the plenum chamber. It is shown in figure 4 that the calculated plenum pressure which takes into account cell interaction is always lower than that in the case without cell interaction. This effect is caused by the additional mass flow into the neighbouring cells.

The temperature variation in the suction plenum chamber is shown in figure 5. It may be seen that the temperature variation is very small, (less than 0.4°C whereas the corresponding pressure variation is approximately 800 N/m² (~8cmH_2O). Figure 5 shows that the plenum temperature variation accounting for cell interaction effects oscillates about the plenum temperature with no cell interaction effects. By comparing figures 4 and 5, it may be seen that the temperature variation is in phase with the pressure variation. The relative magnitude of the two governing terms in the rate of change of temperature equation, i.e. the pressure and mass flow terms controls the plenum chamber temperature variation as follows, i.e.

$$\frac{dT}{dt} = \frac{T}{P}\frac{dP}{dt} - \frac{T}{M}\frac{dM}{dt}$$

$$dT = T\left(\frac{dP}{P} - \frac{dM}{M}\right)$$

if dM/M<dP/P then dT/T is in phase with dP/P whilst if dM/M>dP/P then the reverse is also true.

b) Mass Flowrates

Figure 6 shows the comparison of the variation of the mass flowrate into the cell in question both with and without cell interaction. It is clearly shown that, as the mass flow into the cell reaches its maximum value, the plenum chamber experiences the greatest pressure and temperature drop. The reason that the mass flowrate into the cell rises quickly at the beginning of the suction process is attributable to the high pressure difference across the suction port and an increasing flow area at the beginning of the suction process. The mass flowrate stays reasonably constant as the cell pressure approaches the plenum chamber pressure (and the flow area approaches a constant value). The cell mass flowrate reduces at the end of the suction process because the cell pressure very nearly equals the plenum pressure and the suction port area approaches zero as the suction port is fully covered. When accounting for cell interaction effects, it may be seen that there is a small fluctuation in mass flow at the leading vane position between 120°-140°. This would be attributable to the reduction in plenum pressure shown in Figure 4 as additional mass enters the cell adjacent to the cell in question.

Figure 7 shows the variation of mass flowrate through the air intake valve, compared to all other components of mass flow through the suction port. It may be seen that the mass flowrate term for the air intake valve is always positive which means that the valve is always open, because the plenum pressure is always less than the atmospheric pressure. It may be noticed that the mass flowrate through the air intake valve is higher than any other individual mass flowrate.

This is because the inflow through the air intake valve provides the total mass flow through the suction port. Figure 8 shows the terminologies used to describe the various mass flowrates schematically.

Figure 9 shows the variation of the mass in the plenum chamber (i.e. the sum of the mass flow out of the plenum chamber into the compressor cells minus the mass flow into the plenum chamber through the air intake valve) together with variations of the plenum pressure and plenum temperature plotted against the leading vane position of the reference cell during part of the compressor's operational cycle.

It is clearly shown that the rate of change of plenum pressure (dP/dt) is influenced by the variation of the mass flow of the chamber.

Figures 10 and 11 show the comparison of cell pressure and cell temperature with and without cell interaction. Figure 12 shows the associated comparison of the pressure volume diagram. It may be seen that there is no significant difference as far as the cell properties and the work done are concerned. It was also noticed that at least three times the computational time was required to incorporate the existence of a suction plenum into the present modelling study. The inclusion of the plenum chamber in the calculation may be considered as a big effort with but a small benefit. For many purposes the suction plenum chamber volume may be considered to be large compared with the cell volume and its presence neglected. However for the compressor which was the subject of the present study it was also noticed that a plenum chamber volume of less than 1000 mm^3 may be considered as small, and the calculations needed a very small step size to achieve convergence.

CONCLUSION

It is concluded from the present study which formed a part of K.T. Ooi's doctoral work (3) that cell interaction during the suction process produces only slight effects on the suction plenum pressure, the associated effects on the plenum temperature and mass flow are very small. The size of the plenum chamber in the present study was relatively large compared to the active cell volume and had negligible influence on compressor modelling results.

ACKNOWLEDGEMENT

The authors wish to acknowledge the support given by the Hydrovane Compressor Company Limited during the pursuit of Dr Ooi's research programme.

REFERENCES

1. Soedel, W. "Introduction to computer simulation of positive displacement type compressors". Purdue University Publication, 1972.

2. Tramschek, A.B., Ooi, K.T. "Geomtrical optimization of sliding vane compressors" European conference of development in industrial compressors. IMechE Headquarters, London, 1989.

3. Ooi, K.T. "Geometrical optimization of rotary sliding vane air compressors." Ph.D Thesis University of Strathclyde, 1989.

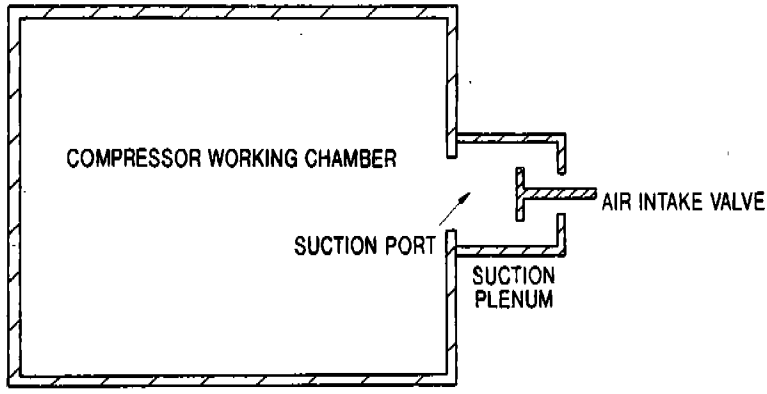

FIGURE 1. SUCTION PLENUM AND WORKING CHAMBER.

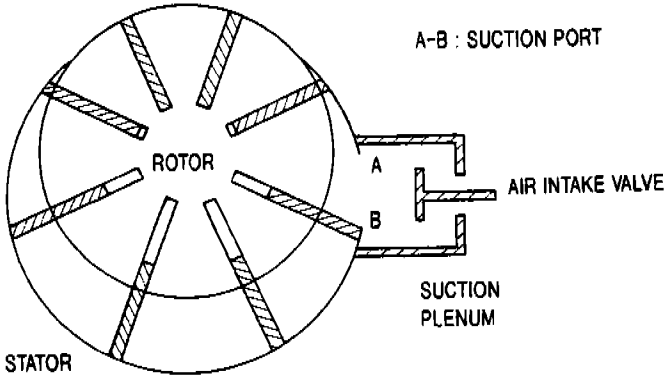

FIGURE 2. SCHEMATIC ARRANGEMENT OF A ROTARY COMPRESSOR WITH AN INLET SUCTION PLENUM

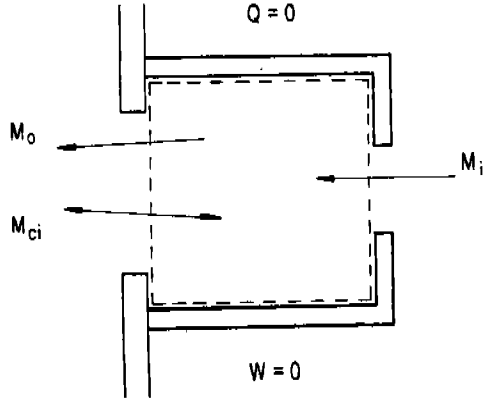

FIGURE 3. SUCTION PLENUM CONTROL VOLUME

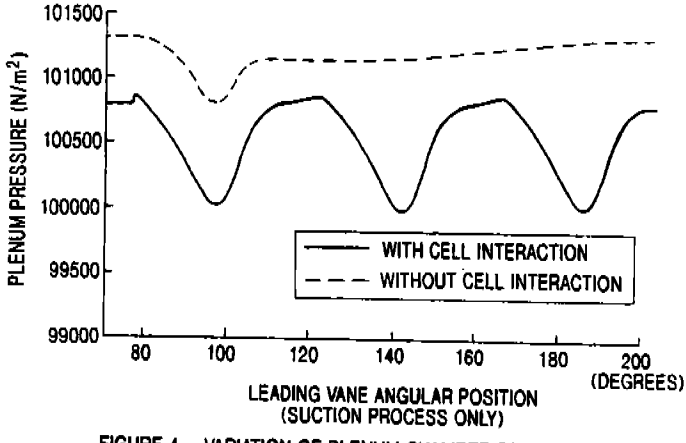

FIGURE 4. VARIATION OF PLENUM CHAMBER PRESSURE

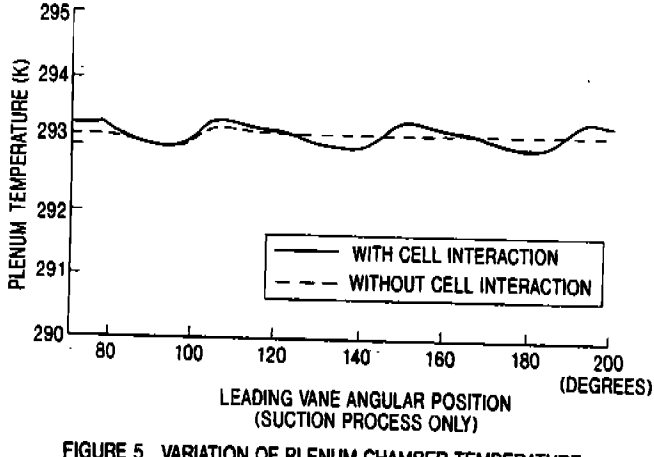

FIGURE 5. VARIATION OF PLENUM CHAMBER TEMPERATURE

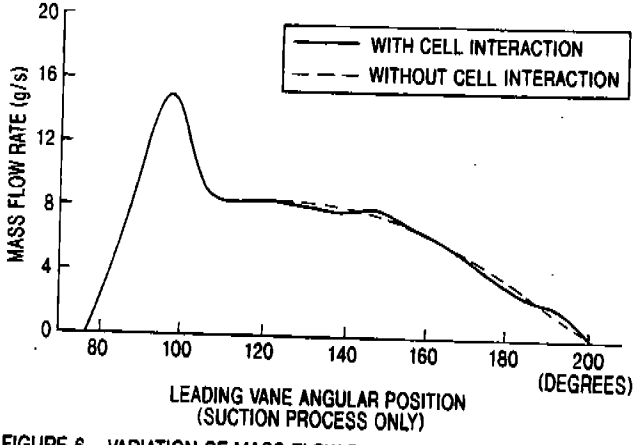

FIGURE 6. VARIATION OF MASS FLOW RATE INTO CELL IN QUESTION

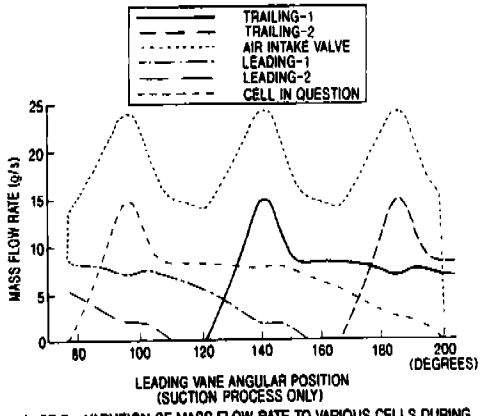

FIGURE 7. VARIATION OF MASS FLOW RATE TO VARIOUS CELLS DURING SUCTION PROCESS

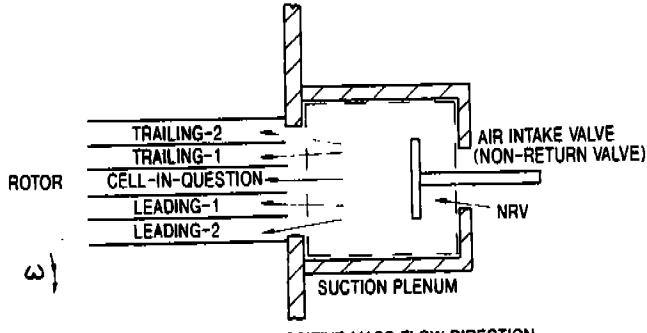

NOTE: ARROWS SHOW POSITIVE MASS FLOW DIRECTION. IN THE REAL COMPRESSOR THERE WILL BE AT MOST 3 CELLS COMMUNICATING SIMULTANEOUSLY WITH THE SUCTION CHAMBER.

FIGURE 8. MASS FLOW TERMINOLOGIES.

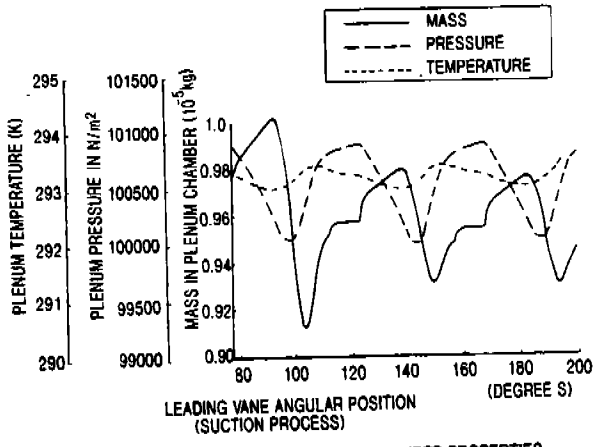

FIGURE 9. VARIATION OF PLENUM CHAMBER PROPERTIES.

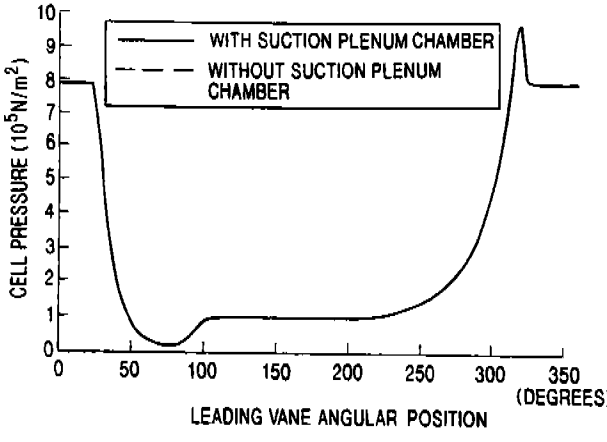

FIGURE 10. PREDICTED CELL PRESSURE WITH AND WITHOUT PLENUM CHAMBER

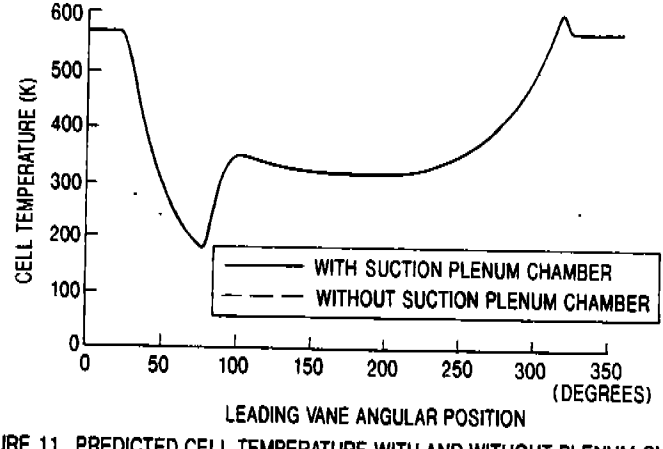

FIGURE 11. PREDICTED CELL TEMPERATURE WITH AND WITHOUT PLENUM CHAMBER

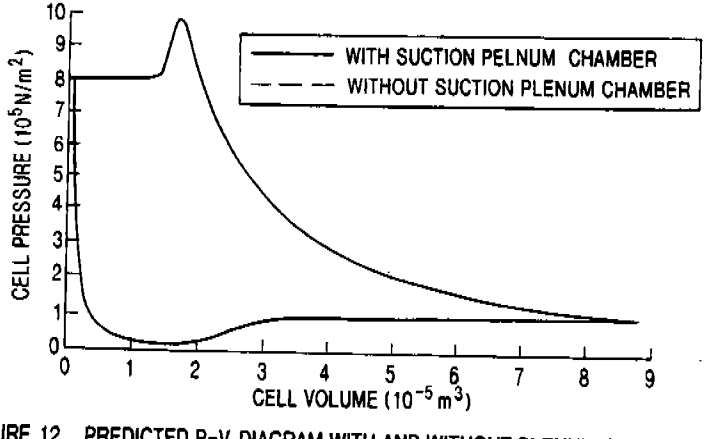

FIGURE 12. PREDICTED P-V DIAGRAM WITH AND WITHOUT PLENUM CHAMBER

EFFECTS OF PORT GEOMETRY, DIMENSIONS AND POSITION ON THE PERFORMANCE OF A ROTARY COMPRESSOR.

Dr A.B. Tramschek,
Senior Lecturer & Dean of Engineering
University of Strathclyde,
Glasgow, Scotland.

Dr K.T. Ooi
School of Mechanical and Production Engineering,
Nanyang Technological University,
Singapore

ABSTRACT

Rotary sliding vane compressors are positive displacement compressors with built-in volume ratios. Their suction and discharge processes are continuous and thus they are normally valveless machines. The suction and discharge port dimensions and positions thus critically affect the performance of the machine. The paper first presents the effects of the suction port geometry on the performance of the machine. It then follows by examining the influence of both suction and discharge port positions on the machine performance. The analysis was carried out using a theoretical model describing a circular rotor-stator configuration with radially disposed vanes, where the working fluid is air. The resulting effects on the pressure volume diagram and the instantaneous mass-angle of rotation history are shown.

INTRODUCTION

Rotary sliding vane compressors are machines with built-in volume compression ratios. Hence for given machine dimensions, the value of the pressure at the end of the compression process is predetermined by the suction pressure and the actual volume compression ratio. Matching the suction and discharge port positions with the built-in volume ratio is important in order to optimise machine performance. An experimental investigation by Kruse [1] suggested that this matching is the key to improving the machine performance. The analysis that follows examines the effects of suction port geometry and/or port positioning on the machine performance using a theoretical model [2] [3].

PORT DESIGN CONSIDERATIONS

The appropriate choice of the suction and the discharge port positions for compressors with built-in volume ratios depends very much on the variation of the cell volume. Figure 1 shows schematically a typical rotary compressor with eight vanes and table 1 shows its nominal operation conditions and its capacity. The variation of an individual cell volume is shown in Figure 2 from which it may be seen that the maximum cell volume occurs at a leading vane angular position of about 200 degrees whilst the minimum cell volume occurs at 18 degrees. These positions correspond to mid-cell angles of 177.5 degrees and 355.5 degrees respectively. Although a symmetrical rotor-stator arrangement is being considered, deviations of the above angular positions from mid-cell angles of 180 degrees and 360 degrees are caused by the inclusion of the leading vane and its slot as part of the cell volume.

For a correct port design, the maximum cell volume position should correspond to the suction port closing angle whereas the minimum volume position should correspond to the discharge port closing angle. The opening of the suction port is based on the value of the suction pressure. It is best located at the angular position where the cell pressure immediately before the suction port opens is just below the nominal suction pressure. The discharge port opening angle should correspond to the position where the cell pressure reaches a value just above the nominal discharge pressure. The latter position is always delayed for a few degrees if the operational discharge pressure of the compressor is to be varied (especially above the design pressure) as over compression losses are generally smaller than the under-compression losses in terms of their contribution to the indicated power.

EFFECTS OF SUCTION PORT CONFIGURATION

This section discusses the effects of the suction port configuration on the performance of a given compressor. Two different suction port geometries, termed the 'old' port configuration (see Figure 3(a)) and the 'new' port configuration (Figure 3(b)) were investigated, and their influence on the performance of the compressor were compared.

The 'old' suction port (Figure 3(a)) was sited on the end face of the rotor and was located between the crescent shaped gap formed between the rotor and stator. The size of the suction port is thus restricted by the dimensions of the rotor, stator and the offset between the two centres. This particular shape of the suction port produces a particular variation in the port area with respect to the variation of cell volume and influences the breathing characteristic of the compressor. Figure 3(c) shows variation of the active port areas with leading vane angular position. This shape of suction port was found to have certain disadvantages as follows:-

1. The port cross sectional area is small in the region close to the suction port opening position and hence causes a slow recovery in cell pressure during the initial suction stage. This contributes to power losses as may be seen from the pressure volume diagram in Figure 4(e).

2. The maximum width of the suction port area is limited by the dimensions of the rotor, the stator and the offset between their centres.

3. In the simulation study, it was assumed that the cell pressure is uniformly distributed throughout the whole volume of the cell. This assumption may be questionable during the suction process because air needs to flow axially through the end face of the compressor where the suction port is sited and pass along the whole length of the cell before filling the cell volume. During this process some form of axial pressure distribution would be expected and the situation would be exaggerated by a long axial flow path. A simplified simulation of the suction process may be inaccurate.

In an attempt to overcome all these problems a new port configuration was introduced. The change envisaged rectangular-like holes distributed along the stator wall, see Figure 3(b). Predicted results for the two different suction port geometries are shown in Figures 4(a) to 4(f). Figure 4(a) shows the variation of the active suction port area for the old and the new suction ports. It also shows the effects of different axial port length on the variation of the port area for the new port when axial port length varies from 6 mm to 30 mm. It may be seen that the suction port area increases directly as the axial length of the port increases. The extra port area during the initial suction stage causes the cell air mass to increase rapidly (see Figure 4(b) during the initial suction process. This effect results in rapid pressure recovery as shown in Figure 4(c) and hence improves the breathing characteristics of the compressor as reflected in pressure-volume diagram in Figure 4(e). The resulting variation on cell air temperature is also shown, Figure 4(d). Figures 4(c), 4(e) show that a further reduction in the suction loss is achieved by having a longer axial port length. Figure 4(f) compares the effects of the old and new suction port configuration on the performance of the compressor. Some increase in the free air delivery is achieved by using a new port configuration. The indicated and shaft input power decrease slightly as the axial length of the new port increases and as a result, the specific free air delivery (litre/kWs) increases. However, the benefits diminish when the axial length of the new port exceeded 25 mm. The overall advantages and the improvements stemming from the modified suction port may be summarised as follows:-

a) The machine shows a better breathing characteristic:- rapid pressure recovery during the suction process. A reduction in the indicated power was predicted.

b) The size of the suction port is no longer limited by the radii of the rotor and stator as it was before. Speaking in terms of suction port design, this feature provides greater flexibility in the selection of dimensions.

c) In practice, a shorter flow path for the air induced during the suction process should result in less suction heating and hence improve the volumetric efficiency of a machine. This effects was not included however in the theoretical model.

d) This port configuration suits better the assumption made in the simulation model that the cell pressure is always distributed uniformly in a cell. Cells may be filled quickly by the air induced because of the axially distributed and shorter flow path.

EFFECTS OF PORT POSITIONING

The effects of the suction and discharge port positions on the pressure volume diagram and the cell air mass versus leading vane angle diagram are illustrated in Figures 5 to 12. Figures 5(a) and 5(b) show the pressure volume diagram and the air mass versus leading vane angle diagram under the correct port positioning. Correct port positioning means that the suction port opens at the position where the cell pressure equals the nominal suction pressure (in reality however, a modest level of partial vacuum must exist inside the cell, to promote air flow into the cell from the suction chamber), the suction port closes as soon as the cell volume attains its maximum value. The discharge port opens as soon as the cell pressure reaches the nominal discharge pressure and closes at the position when the cell volume attains the minimum volume.

In the discussion that follows various symbols are defined:

P_s : nominal suction pressure
P_d : nominal discharge pressure
M_1 : normal residual air mass level before suction process
M_2 : normal air mass level at the end of suction process

The influence of each port-position is illustrated as follows:-

Suction port opening angle (β_s)

a) If the suction port is opened before the cell pressure reaches the nominal suction pressure, under-expansion results. This is illustrated in Figure 6(a). Losses due to this effect are shown by the shaded area in the Figure. The air mass in the cell increases gradually shortly after the commencement of the suction process. See Figure 6(b).

b) If the port is opened after the cell pressure reaches the nominal suction pressure, over expansion occurs. The cell air mass increases very rapidly in the early stage of the suction process, because of a high pressure differential across the suction port during this period. The effect is shown in Figures 7(a) and 7(b).

Suction port closing angle (β_e)

a) If the suction port is closed before the cell volume reaches the maximum cell volume position, a reduction in the cell pressure to a level below that of the nominal suction pressure occurs as the cell volume is still increasing. This premature suction port closing results in a situation where less air is induced into the machine. These effects are illustrated in Figures 8(a) and 8(b). Premature closure of the suction port results in cell pressures less than the nominal discharge pressure when the discharge port opens and backflow occurs through discharge port.

b) If the suction port is closed after the cell reaches the maximum cell volume position, air inside the cell flows out of the cell through the suction port. This effect is caused by the reduction in the cell volume after the maximum volume position attempting to produce a rise in the cell pressure. This

pressure rise is small and air flows out through the suction port at a constant nominal suction pressure. A delay in port closure results in an under compression condition and may be explained as follows.

consider $$P_2 = \left(\frac{V_1}{V_2}\right)^n P_1$$

where P_1 is the nominal suction pressure and n is a compression index. As V_1 reduces, and since V_2 is fixed for a given discharge port location the value of P_2 reduces to a value less than the nominal discharge pressure, P_d; under compression occurs. The effects are shown in Figures 9(a) and 9(b).

Discharge port opening angle (β_3)

a) If the discharge port is opened before the pressure in the cell reaches the nominal discharge pressure, under compression results. Reverse flow occurs in the initial stage of the discharge process. This is shown in figures 10(a) and 10(b).

b) If the discharge port is opened after the cell pressure reaches the nominal discharge pressure, over compression results. Air flows out of the cell during the initial stage of discharge process with a higher velocity than that of the normal condition. This is shown by the steep slope of the cell air mass-angle curve during that period. It is illustrated in Figures 11(a) and 11(b).

Discharge port closing angle (β_4)

a) If the discharge port is closed prematurely, more residual air stays in the cell at the end of discharge process. At the same time since the cell volume is still decreasing, the cell pressure rises. Less air will be delivered and less air will be induced following the re-expansion to the suction pressure. This is shown in figures 12(a) and 12(b).

b) If the discharge port is closed after the cell in question reaches the minimum cell volume position and if the cell is within the sealing arc region then this will not alter either the pressure volume diagram or the cell mass-angle diagram.

CONCLUSION

The effect of the port geometry and port positioning on the performance of a machine is significant. The analysis shows that, to optimise the machine performance, it is important to match the built-in volume ratio with the operational pressure ratio. If a machine has to operate under a wide range of operating pressure ratios, it is suggested that the discharge valve should be used, as mentioned in [1].

NOMENCLATURE

FAD (l/s)	Free air delivery
P_i(kW)	Indicated power
P_t(kW)	Shaft power
R_r(m)	Rotor radius
R_s(m)	Stator radius
TDC	Top dead centre (angular reference position, O°)
ϵ(mm)	Eccentricity between stator and rotor centres
β_1(°)	Suction port opening angle w.r.t. TDC
β_2(°)	Suction port closing angle w.r.t. TDC
β_3(°)	Discharge port opening angle w.r.t. TDC
β_4(°)	Discharge port closing angle w.r.t. TDC

ACKNOWLEDGEMENT

The authors wish to acknowledge the support received from the Hydrovane Compressor Company Limited during the period of Dr Ooi's doctoral studies.

REFERENCES

1. Kruse, H. "Experimental investigation on rotary vane compressor." Proceedings of the 1982 Purdue Compressor Technology Conference

2. Tramschek, A.B., Ooi, K.T. "Geometrical optimization of sliding vane compressors." European Conference on Developments in Industrial Compressors, IMechE Headquarters, London Oct. 1989.

3. Ooi, K.T. "Geometrical optimization of rotary sliding vane air compressors." Ph.D Thesis, University of Strathclyde, Glasgow, 1989.

Operating speed	rev/min	1450
Atmospheric pressure	bar	1.013
Atmospheric temperature	K	293
Nominal suction pressure	bar (ABS)	1.013
Nominal discharge pressure	bar (ABS)	7.91
Capacity	l/s	14.9

Table 1 Operating conditions and capacity of the compressor

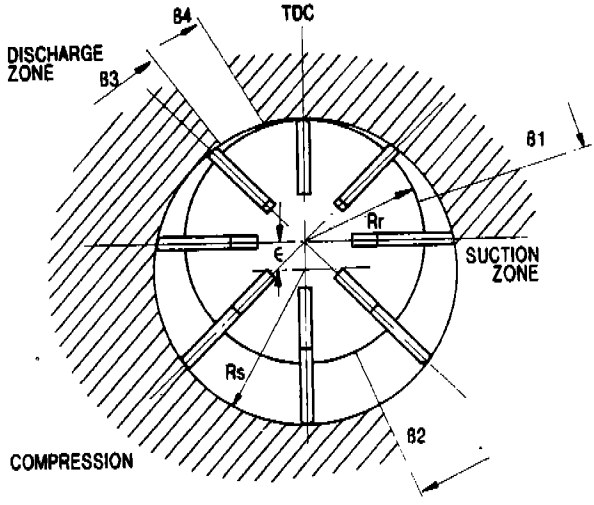

FIGURE 1. SCHEMATIC ARRANGEMENT OF A ROTARY SLIDING VANE COMPRESSOR

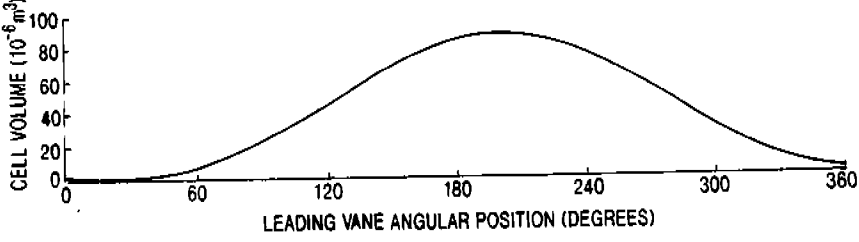

FIGURE 2. VARIATION OF CELL VOLUME.

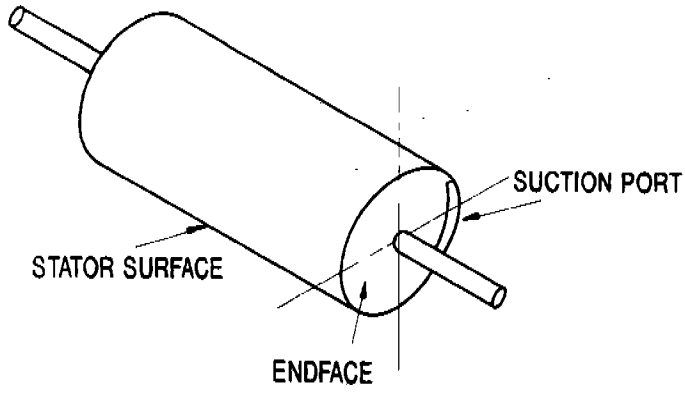

FIGURE 3a 'OLD' SUCTION PORT CONFIGURATION

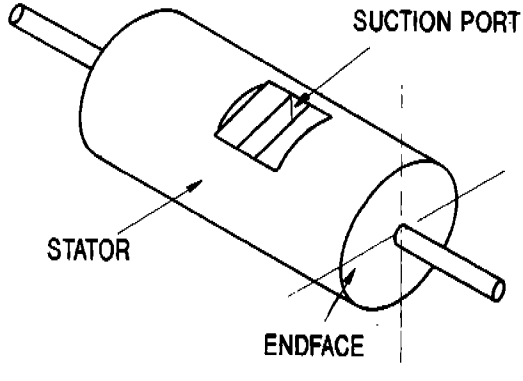

FIGURE 3b 'NEW' SUCTION PORT CONFIGURATION

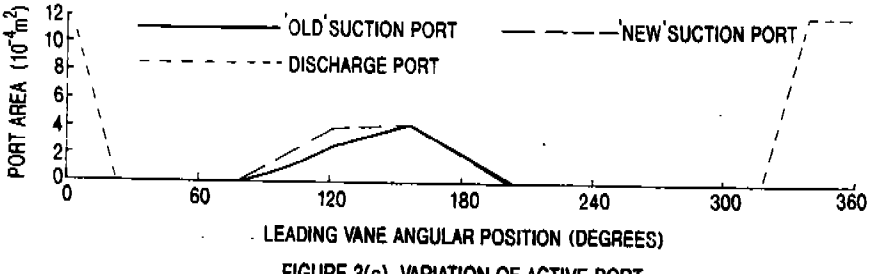

FIGURE 3(c) VARIATION OF ACTIVE PORT

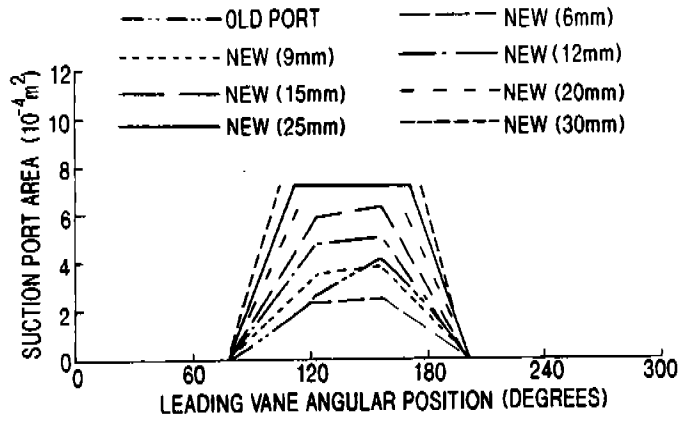

FIGURE 4(a) VARIATION OF ACTIVE SUCTION PORT AREA.

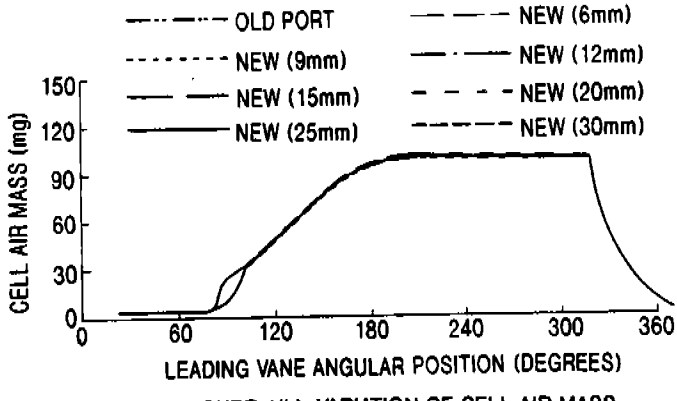

FIGURE 4(b) VARIATION OF CELL AIR MASS

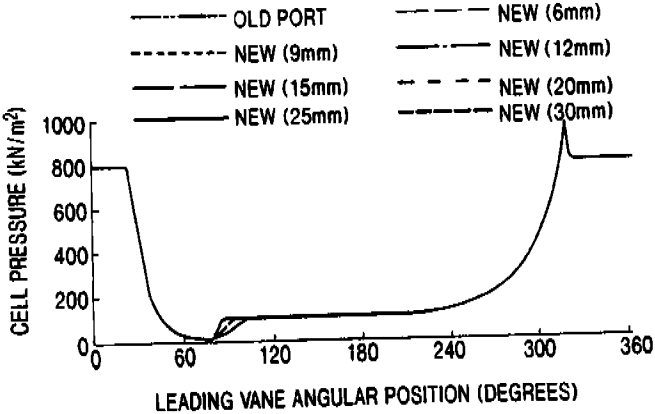

FIGURE 4(c) VARIATION OF CELL PRESSURE

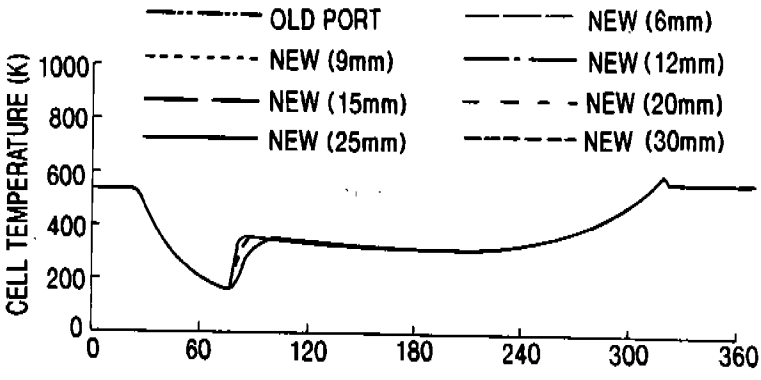

FIGURE 4(d) VARIATION OF CELL TEMPERATURE

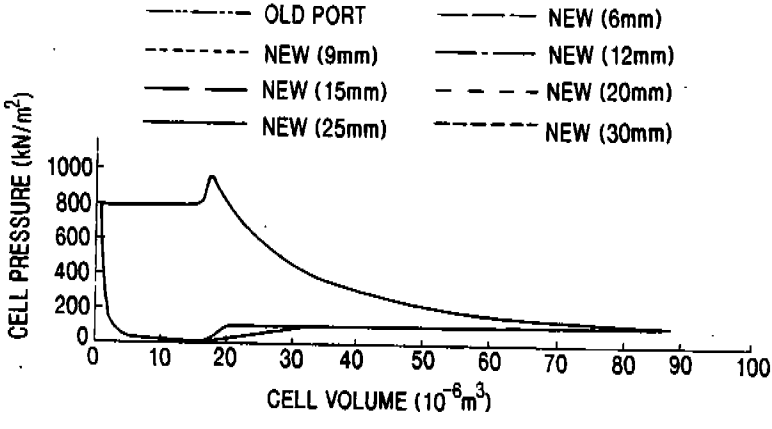

FIGURE 4(e) PRESSURE-VOLUME DIAGRAMS

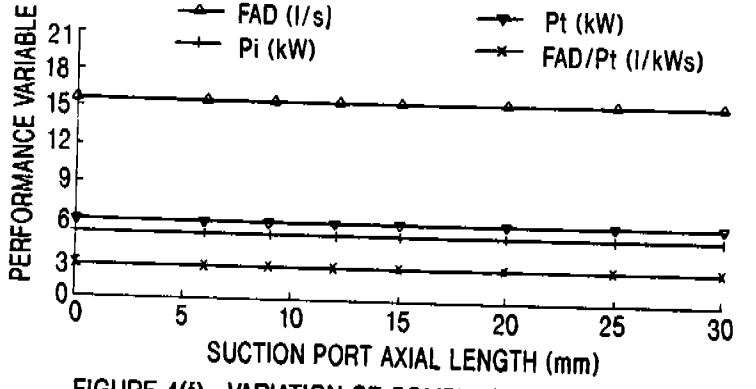

FIGURE 4(f) VARIATION OF COMPRESSOR PERFORMANCE VARIABLE WITH SUCTION PORT AXIAL LENGTH

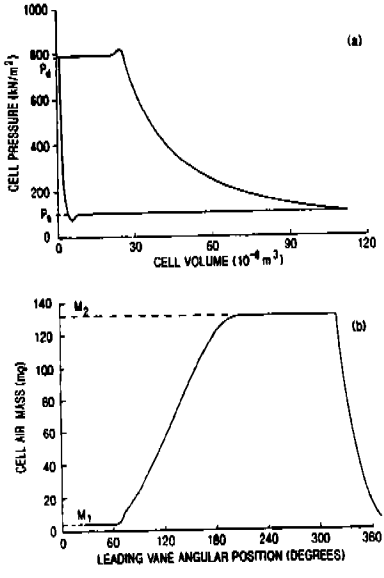

FIGURE 5. P-V DIAGRAM AND CELL AIR MASS- ANGLE DIAGRAM FOR COMPRESSOR OPERATING AT CORRECT PORT POSITIONING

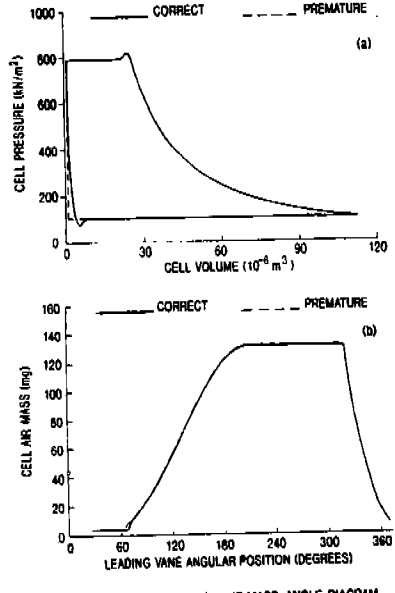

FIGURE 6. P-V DIAGRAM AND CELL AIR MASS-ANGLE DIAGRAM COMPARISON BETWEEN CORRECT AND PREMATURE SUCTION PORT OPENING

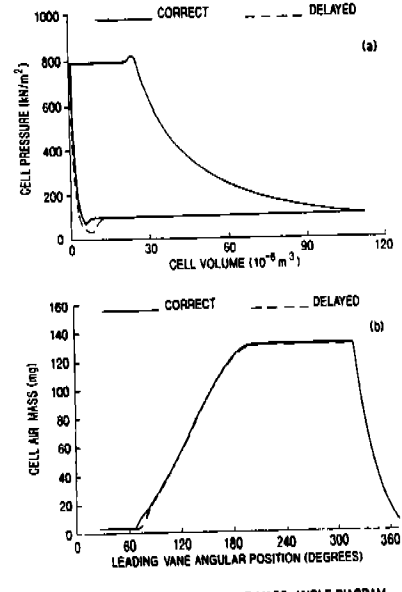

FIGURE 7. P-V DIAGRAM AND CELL AIR MASS-ANGLE DIAGRAM COMPARISON BETWEEN CORRECT AND DELAYED SUCTION PORT OPENING

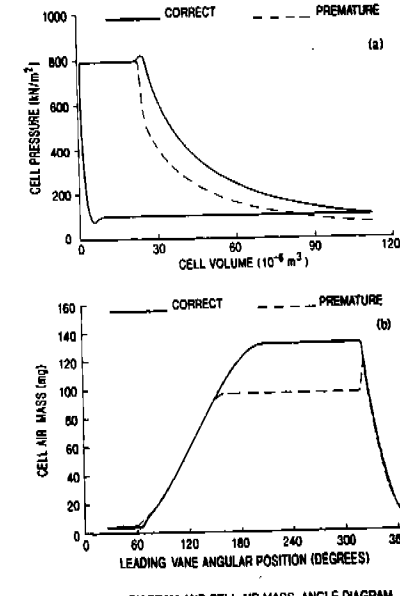

FIGURE 8. P-V DIAGRAM AND CELL AIR MASS-ANGLE DIAGRAM COMPARISON BETWEEN CORRECT AND PREMATURE SUCTION PORT CLOSING

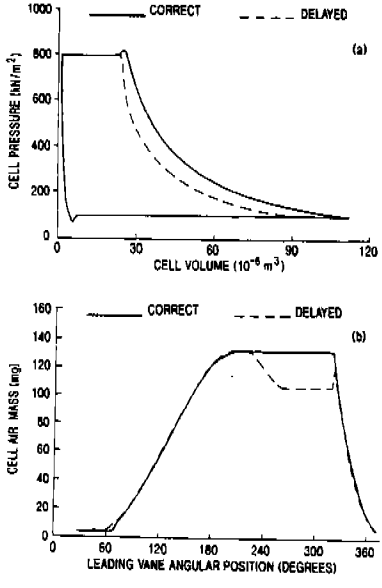

FIGURE 9 P-V DIAGRAM AND CELL AIR MASS-ANGLE DIAGRAM COMPARISON BETWEEN CORRECT AND DELAYED SUCTION PORT CLOSING

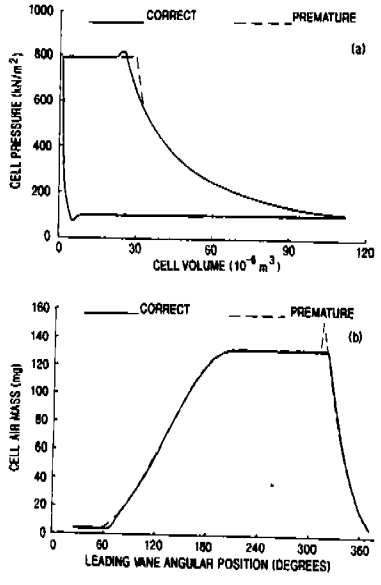

FIGURE 10. P-V DIAGRAM AND CELL AIR MASS-ANGLE DIAGRAM COMPARISON BETWEEN CORRECT AND PREMATURE DISCHARGE PORT OPENING.

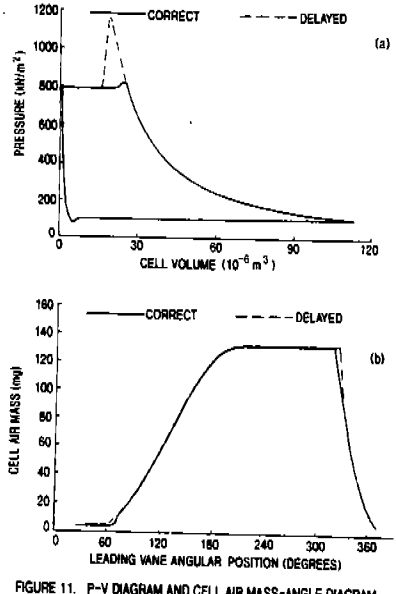

FIGURE 11. P-V DIAGRAM AND CELL AIR MASS-ANGLE DIAGRAM COMPARISON BETWEEN CORRECT AND DELAYED DISCHARGE PORT OPENING.

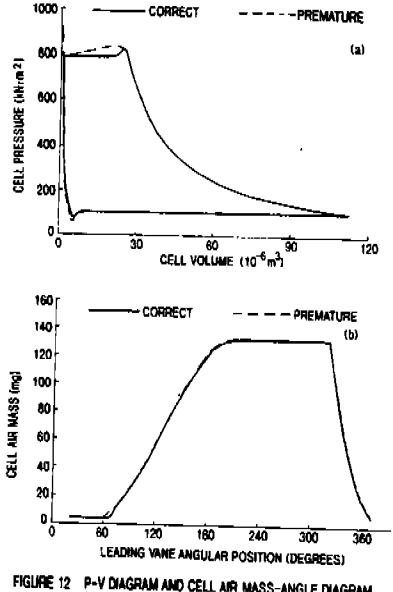

FIGURE 12 P-V DIAGRAM AND CELL AIR MASS-ANGLE DIAGRAM COMPARISON BETWEEN CORRECT AND PREMATURE DISCHARGE PORT CLOSING.

PRESSURE DISTRIBUTIONS ALONG ECCENTRIC CIRCULAR VALVE REEDS OF HERMETIC COMPRESSORS

J.L. Gasche, R.T.S. Ferreira, A.T. Prata

Department of Mechanical Engineering
Federal University of Santa Catarina
Florianopolis, SC - 88049 - Brazil

ABSTRACT

An experimentally validated analysis of the incompressible, laminar and isothermal flow in eccentric radial diffusers, representing a laboratory model of compressors valve system is numerically performed. The experimental procedures and the experimental setup are concisely described. Pressure distributions along the three-dimensional flow and the resultant axial force acting on the frontal disk are presented for various flow Reynolds numbers, different axial gaps and eccentricities. A three-dimensional bicylindrical coordinate system is used to obtain a description of the whole flow field. Certain characteristics of the velocity field are also presented.

NOMENCLATURE

D - frontal disk diameter, m
d - feeding orifice diameter, m
s - axial gap between disks, m
l - feeding orifice length, m
e - eccentricity between feeding orifice and frontal disk center lines, m
p - pressure, Pa
u, v, w - velocity components in ψ, η and z directions, m/s
ψ, η, z - bicylindrical coordinates
h - square root of the metric of the bicylindrical coordinate system, m
$\bar{p}$ - dimensionless pressure
$\bar{v}$ - mean velocity through the feeding orifice, m/s
Re - Reynolds number, $Re = \rho \bar{v} d/\mu$
F - dimensionless force on the frontal disk
Vm - mean velocity in a determined diffuser cross section, m/s
ρ - fluid density, kg/m^3
μ - absolute viscosity, kg/ms

INTRODUCTION

The operating cycle of a high speed positive displacement compressor can be described by a series of complex phenomena which show high degree of interaction and happen in a short period of time. The mathematical model used in a compressor simulation program requires the equations describing the reed dynamic behavior. Therefore it is necessary to fully understand the flow field of the gas flowing through the valve system, especially when automatic valves are employed, that is, the flow field is responsible for opening and closing those reed type valves.

Deschamps [01] and Ferreira et al. [02] have performed an experimentally validated numerical analysis of the laminar, incompressible and isothermal air flow through concentric radial diffusers with the purpose of understanding the flow through compressor valves. Deschamps [01] presents a very broad bibliographic survey related to the subject. However, as very few compressor valves systems show this type of concentricity. In order to improve the

model, getting it closer to actual refrigerating compressors valve systems, the analysis of the flow through eccentric radial diffuser, as shown in Fig. 1, is performed in this work.

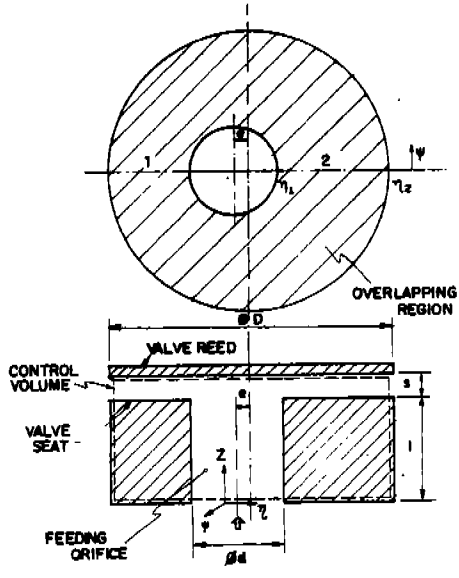

Fig. 1 - Flow geometry

It can be observed from Fig. 1 that the presence of eccentricity between the feeding orifice and the frontal disk, which is similar to a reed with parallel displacement, generates circular regions with different overlappings. This situation causes a non-uniform circumferential distribution of mass flow rate leaving the feeding orifice. The flow adjusts itself according to the solid boundaries in such a way that the main velocity component in the diffuser region, v, increases progressively from region(2) to (1). This fact produces an asymmetric pressure distribution on the frontal disk and therefore the flow is three-dimensional.

The main objective of this work is to present the numerical results of the laminar, incompressible, isothermal, steady air flow through eccentric radial diffusers. The numerical model has been validated by means of the good agreement reached with experimental pressure distributions on the frontal disk. Numerical results for the pressure distribution and the total force on the reed and also some details of the velocity field are presented. The experimental procedures and the experimental test rig are concisely described.

PROBLEM FORMULATION

The geometry of the eccentric diffuser under analysis has to be described by a bicylindrical coordinate system (ψ,η,z), as shown in Fig. 1. The air flows axially (direction z) through the feeding orifice with diameter d and length l and, after being deflected by the frontal disk of diameter D, it is forced through the gap s between disks in directions ψ and η. The disk with the feeding orifice is analogous to the valve seat and the frontal disk corresponds to the valve reed.

The hydrodynamic flow problem is governed by the continuity and Navier-Stokes equations, (1)-(4), written in bicylindrical coordinates for laminar, incompressible, isothermal and steady conditions.

$$1/h^2[\partial(\rho hu)/\partial\psi + \partial(\rho hv)/\partial\eta + \partial(\rho h^2 w)/\partial z] = 0 \qquad (1)$$

$$1/h^2[\partial(\rho huu)/\partial\psi + \partial(\rho hvu)/\partial\eta + \partial(\rho h^2 wu)/\partial z] =$$

$$-1/h\ \partial p/\partial\psi + \mu/h^2[\partial^2 u/\partial\psi^2 + \partial^2 u/\partial\eta^2 + h^2\partial^2 u/\partial z^2] +$$

$$+ \mu/h^2[2/h.\partial h/\partial\eta.\partial v/\partial\psi - 2/h.\partial h/\partial\psi.\partial v/\partial\eta -$$

$$- u/h(\partial^2 h/\partial\psi^2 + \partial^2 h/\partial\eta^2)] - \rho/h^2[uv.\partial h/\partial\eta - v^2.\partial h/\partial\psi] \qquad (2)$$

$$1/h^2[\partial(\rho huv)/\partial\psi + \partial(\rho hvv)/\partial\eta + \partial(\rho h^2 wv)/\partial z] =$$

$$- 1/h\ \partial p/\partial\eta + \mu/h^2[\partial^2 v/\partial\psi^2 + \partial^2 v/\partial\eta^2 + h^2\partial^2 v/\partial z^2] +$$

$$+ \mu/h^2[2/h\ .\ \partial h/\partial\psi\ .\ \partial u/\partial\eta - 2/h\ .\ \partial h/\partial\eta\ .\ \partial u/\partial\psi\ -$$

$$- v/h\ .\ (\partial^2 h/\partial\eta^2 + \partial^2 h/\partial\psi^2)] - \rho/h^2[uv\ .\ \partial h/\partial\psi - u^2.\partial h/\partial\eta] \qquad (3)$$

$$1/h^2\ [\partial(\rho huw)/\partial\psi + \partial(\rho hvw)/\partial\eta + \partial(\rho h^2 ww)/\partial z] =$$

$$- \partial p/\partial z + \mu/h^2[\partial^2 w/\partial\psi^2 + \partial^2 w/\partial\eta^2 + h^2\ \partial^2 w/\partial z^2] \qquad (4)$$

where u, v and w are the velocity components in the ψ, η and z directions, respectively, p is the pressure, ρ is the fluid density, μ is the absolute viscosity and h is the square root of the metric related to the bicylindrical coordinate system.

It is easily shown that h is given by

$$h = a/(\cosh\eta - \cos\psi) \qquad (5)$$

where a is the geometric parameter of the coordinate system.

The boundary conditions needed for the whole specification of the problem are given by Eqs. (6).

$$u = v = w = 0 \quad \text{for} \quad z = 1 + s;\ \eta = \eta_2\ ;\ 0 \le \psi \le 2\pi \qquad (6a)$$

$$u = v = w = 0 \quad \text{for} \quad 0 \le z \le 1;\ \eta = \eta_2\ ;\ 0 \le \psi \le 2\pi \qquad (6b)$$

$$u = v = 0 \quad \text{for} \quad z = 0\ ;\ \eta \ge \eta_1\ ;\ 0 \le \psi \le 2\pi \qquad (6c)$$

$$u = v = w = 0 \quad \text{for} \quad z = 0\ ;\ \eta_2 \le \eta \le \eta_1\ ;\ 0 \le \psi \le 2\pi \qquad (6d)$$

$$w = \partial(\rho hu)/\partial\eta = \partial(\rho hv)/\partial\eta = 0 \quad \text{for} \quad 1 \le z \le 1 + s;\ \eta = \eta_2\ ;$$

$$0 \le \psi \le 2\pi \qquad (6e)$$

NUMERICAL SOLUTION

The differential equations (1)-(4) governing the laminar flow field and the associated boundary conditions (6) are discretized using the finite volume methodology developed by Patankar [03]. The detailed discretization of all the equations is presented by Gasche [04].

The solid region of the valve seat, belonging to the calculation domain has been treated as a fluid with infinite viscosity, according to Patankar [05].

For the special case of the eccentric radial diffuser, the numerical model has to consider a zero gauge reference pressure at the diffuser outlet, that is, $p = 0$ for $1 \leq z \leq 1 + s$; $\eta = \eta_2$ and $0 \leq \psi \leq 2\pi$. In order to reach this boundary condition the control volumes at the exit of the diffuser are made sufficiently small and the main coefficient for the correction of the pressure equation, related to the SIMPLE algorithm, are made very big. Smaller control volumes, in the η direction, will guarantee a better approximation for the zero reference pressure at the diffuser outlet.

Due to the presence of very high pressure and velocity gradients, special attention has been devoted to the mesh selection in order to minimize the contribution of false diffusion. The final mesh used to generate the results in this work has 30240 nodal points, being 14 points in ψ-direction, 54 points in η-direction and 40 points in z - direction.

EXPERIMENTAL SETUP AND PROCEDURES

Fig. 2 presents a schematic general view of the experimental setup. Compressed air stored in three tanks of 0.450 m^3 each one and maximum pressure of 12 bar flowed through a 75mm diameter and 6.5m long PVC horizontal straight pipe before reaching the test section. A flow rate control valve and a calibrated orifice flow meter are mounted in the pipeline. The test section is composed by the valve seat, an aluminum disk (ϕ 150 mm, l = 28 mm) containing the feeding orifice (ϕ 30 mm), by the valve reed, a stainless steel disk (ϕ 90 mm) with a sliding bar and a small tap hole in order to measure the pressure distribution, and the positioning system used to furnish the desired location for the valve reed. The valve reed, represented in the experiment by the frontal disk, has a special feature as shown in Fig. 3. Along the horizontal reed diameter there is a sliding bar provided with a small tap hole (ϕ 0.7 mm) and an internal connecting perforation up to one of the ends of the bar and then connected to a differential pressure inductive transducer. At the other end of the sliding bar an inductive displacement transducer is attached in order to supply the instantaneous horizontal position of the tap hole. Both signals from the inductive transducers are introduced in an amplifier bridge and after to a microcomputer provided with an AD converter. All the analogic signals are adequately treated by a data acquisition program which is able to register pressure signals in intervals of 0.5mm.

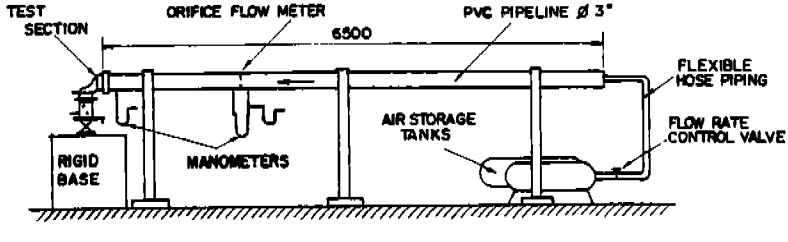

Fig. 2 - Schematic view of the experimental setup

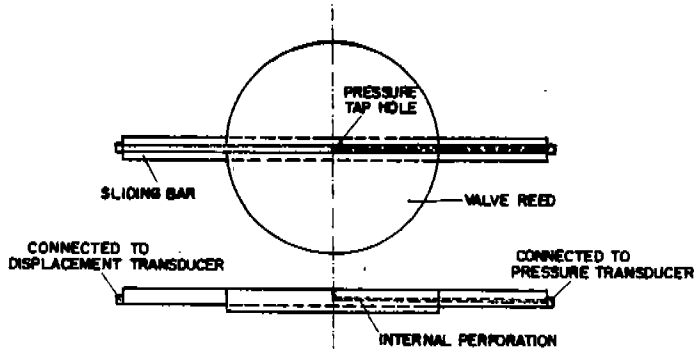

Fig. 3 - Valve reed with sliding tap hole

The reed positioning system, shown in Fig. 4, is composed by 5 moving tables. Initially, both disks have to be concentric, parallel and placed at a certain distance one from the other. Additional information regarding the experimental setup are available in [04].

Before starting to take data, some adjustments are carried out in the experimental setup. First of all the reference zero separation of the disks is determined. The frontal disk is carefully positioned using a mask drawn in the valve seat assuring the concentricity and the alignment of both disks. One steel sphere with diameter of 3.174mm glued to a fine thread is slid in different positions between the disks in order to verify their parallel displacement. Fine adjustments in the angular table produces a uniform sliding for the sphere everywhere in the gap. The final verification is made using the proper pressure distribution along the frontal disk. For the highest desired flow rate, at a certain separation between disks, the symmetry of the pressure profile is then checked. If this symmetry is not achieved within 2%, the whole procedure is repeated as many times as necessary. The accuracy in positioning the frontal disk is less than 0.01 mm.

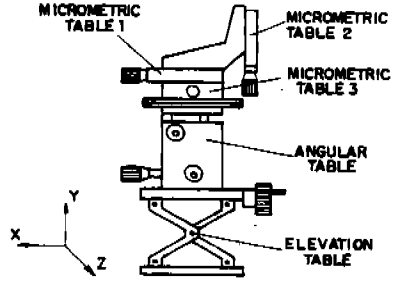

Fig. 4 - Valve positioning system

A very important aspect that has to be considered is the modification in the disks gap due to the forces produced by the pressure distribution especially for small gaps and high Reynolds numbers. Two inductive displacement transducers measured the differential displacement in both disks during the tests. Those values are used to correct the data. Table 1 shows the corrections in the

disks separation due to pressure distribution.

The main quantities measured during the experiment are: horizontal pressure distribution on the reed, mass flow rate, gap between reed and seat and eccentricity between reed and feeding orifice. The pressure distribution is measured with an inductive pressure transducer with a full scale of 0.01 bar or 0.1 bar for higher pressures.

The uncertainty associated to the experimental results reaches values on the order of 1% for the dimensionless pressure distribution on the reed, according to Holman [06]. However, if one takes into account the contribution of the uncertainty in the disks gap, due to the great influence of this distance s, the uncertainty for the dimensionless pressure distribution is less than 10%, as reported in [04].

Table 1 - Corrections introduced in disks gap for s/d = 0.01.

Re	Correction [μm]
3000	30
2500	25
2000	23
1500	18
1000	12
500	9

RESULTS

Two typical comparisons between experimental and numerical results for the pressure distribution on the reed are presented in Figs. 5 and 6. In the ordinate axis it is represented the local dimensionless pressure given by $p/(1/2\ \rho\ \bar{u}^2)$, where $\bar{u}$ is the mean velocity in the feeding orifice. In the abscissa it is plotted the dimensionless radial position r/d. The flow Reynolds number is defined as $Re = \rho \bar{u} d/\mu$. The validation of the numerical model is evident from the good comparison between experimental and numerical results.

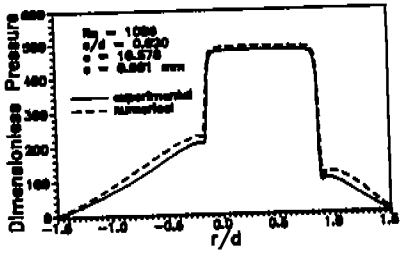

Fig. 5 - Comparison of numerical and experimental results for Re=1086, s/d=0.02 and e=10.578mm

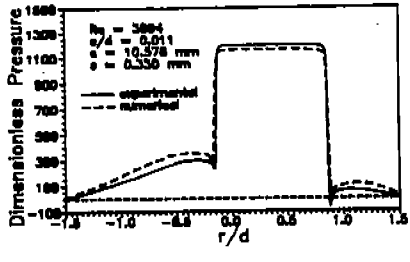

Fig. 6 - Comparison of numerical and experimental results for Re=3094, s/d=0.011 and e=10.578mm

The numerical results for the horizontal pressure distributions on the reed are presented in Figs. 7 to 12, for three different Reynolds numbers of 500, 1500 and 3000, each one for two different dimensionless gaps between disks of 0.01 and 0.03 and each one for four horizontal eccentricity values of 0, 5, 10 and 15 mm.

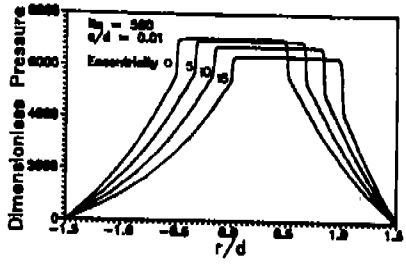

Fig. 7 - Dimensionless pressure distribution for Re=500, s/d=0.01

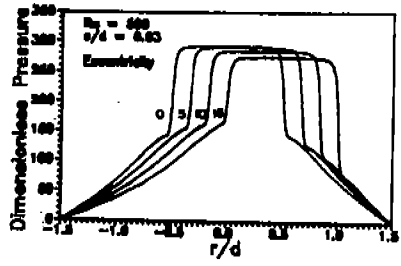

Fig. 8 - Dimensionless pressure distribution for Re=500, s/d=0.03

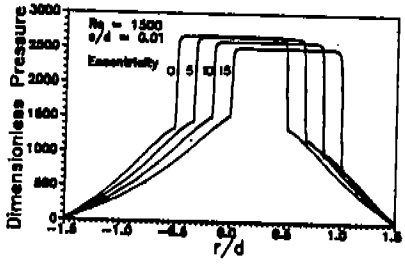

Fig. 9 - Dimensionless pressure distribution for Re=1500, s/d=0.01

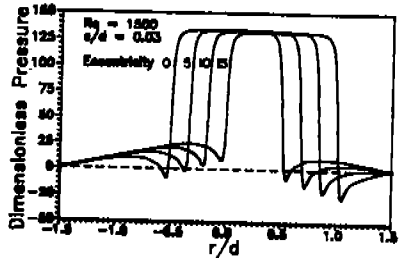

Fig. 10 - Dimensionless pressure distribution for Re=1500, s/d=0.03

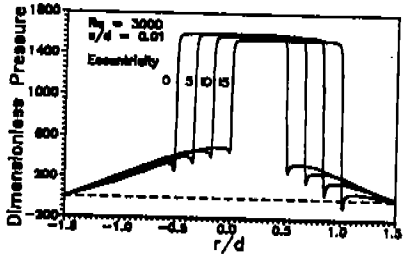

Fig. 11 - Dimensionless pressure distribution for Re=3000, s/d=0.01

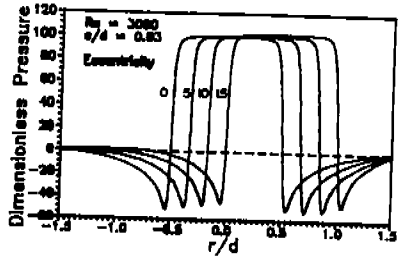

Fig. 12 - Dimensionless pressure distribution for Re=3000, s/d=0.03

The results show the great influence of the separation between disks and of the flow Reynolds numbers on the dimensionless pressure distribution, especially for s/d = 0.01. The influence of the eccentricity is relatively small. For s/d = 0.01 there is a reduction of the pressure in the stagnation region for all Reynolds numbers for all eccentricities being analyzed. This means that there is a reduction in the flow resistance due to the eccentricity. For s/d = 0.03 the same tendency is observed for Re = 500 and Re = 1500 in a smaller scale. Nevertheless for Re = 3000 it is observed an inverse tendency, that is, there is an increase in flow resistance which causes a small elevation of the dimensionless pressure in the stagnation region when the eccentricity is increased. This is due to the presence of bigger separation bubbles at the diffuser inlet, reducing the flow cross section, as shown in Fig. 16.

The integration of the dimensionless pressure distribution over the total reed area furnishes the total force caused by the flow itself. In the present work the resulting dimensionless force on the reed is given by Eq. (7).

$$F = \int_{o}^{2\pi} \int_{\eta_2}^{\eta \to \infty} p^* h^2/d^2 \; d\psi \; d\eta \qquad (7)$$

Fig. 13 presents the variation of the dimensionless force on the reed for different Reynolds numbers, and different gaps between disks when the eccentricity is varied. For both gaps under analysis there is a reasonable reduction in the dimensionless force as the flow Reynolds number increases. The influence of the eccentricity for all Reynolds numbers is very small. For s/d = 0.01 it is observed a reduction in the dimensionless force for all Reynolds numbers when the eccentricity increases. However, for s/d = 0.03 the tendency is diverse. For Re = 500, the dimensionless force is slightly reduced when the eccentricity increases, and for Re = 1500 the inverse is observed. This is due to the fact that the dimensionless pressure in the stagnation region remains almost constant while there is an increase in the local pressure in a larger region in the flow, as shown in Fig. 8. The same trend occurs for Re = 3000 where it is observed a small increase in the dimensionless pressure in the stagnation region.

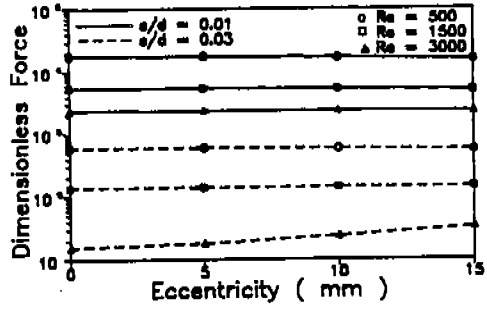

Fig. 13 - Dimensionless force on the reed

An important characteristic of the flow field is the circumferential distribution of the cross section mean velocity at the diffuser outlet Vm, as shown in Fig. 14. V_m is defined as

$$V_m = 1/s \int_{o}^{s} V_\psi \; dz \qquad (8)$$

where V_ψ is the velocity component v in a certain position ψ.

As it can be observed in Fig. 14, there is a non-uniform circumferential distribution of mass flow rate in the eccentric diffuser. This is generated by the variable flow resistance imposed by the solid boundaries. A greater solid overlapping reduces the directional mass flow rate (ψ = 0). This effect is more important for higher eccentricity values.

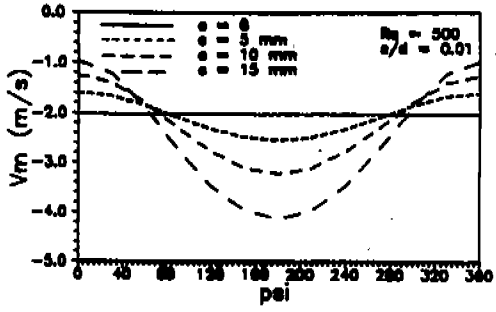

Fig. 14 - Circumferential mean velocity distribution at the diffuser outlet

The reattachment length, ΔS_η is another important parameter to get a better understanding of the flow field in the diffuser region. It defines the recirculating region caused by the effect of flow curvature at the exit of the feeding orifice. Fig. 15 presents the variation of the reattachment length as a function of flow Reynolds number for s/d = 0.01 and 0.03.

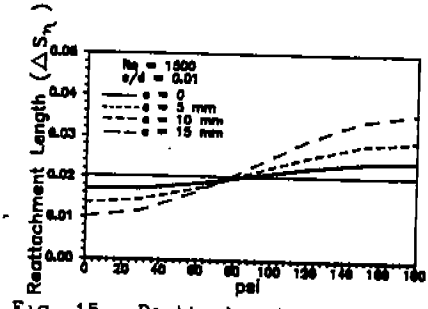

Fig. 15 - Reattachment length variation with ψ for Re = 1500, s/d = 0.01

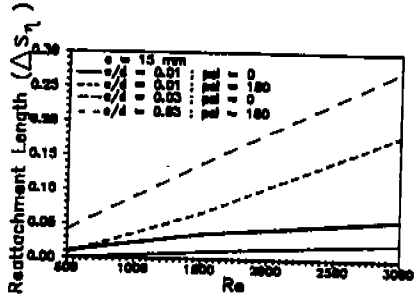

Fig. 16 - Reattachment length variation with Reynolds number

In order to improve the understanding of the pressure flow field over the reed, Figs. 17 and 18 have been prepared.

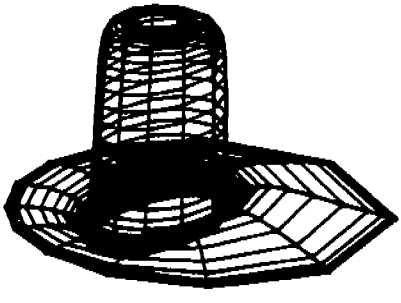

Fig. 17 - Flow pressure field for Re=1500, s/d=0.03, e=10mm

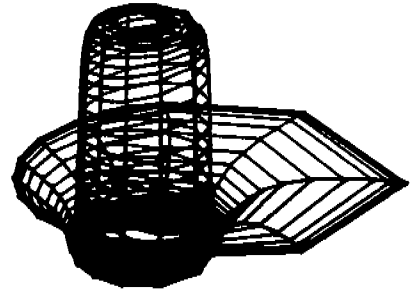

Fig. 18 - Flow pressure field for Re=3000, s/d=0.03, e=15mm

CONCLUSIONS

This paper presents an experimentally validated numerical investigation, using the method of finite volumes, of the laminar, incompressible, isothermal, steady air flow through eccentric radial diffusers. The main motivation for this work is the understanding of fluid flow and thrust in valves of refrigeration compressors.

For a certain eccentricity, it has been observed that there is a great influence of the gap between disks and of the Reynolds number on the dimensionless pressure distribution along the reed, mainly for small gaps. Besides generating a three-dimensional and an asymmetric flow field, modifying considerably the pressure and velocity fields, the eccentricity of the frontal disk does not alter significantly the dimensionless resultant force on the reed, when compared to concentric circular disks. Nevertheless the local loading on the reed used to analyze the distribution of stresses is completely modified when compared to a symmetric valve reed and therefore it should be considered.

BIBLIOGRAPHIC REFERENCES

[01] Deschamps, C.J., Laminar Fluid Flow Through Compressor Valves, M.Sc. Dissertation, Department of Mechanical Engineering, Federal University of Santa Catarina, Brazil, 1987 (in Portuguese).

[02] Ferreira, R.T.S., Deschamps, C.J., Prata, A.T., Pressure Distribution Along Valve Reeds of Hermetic Compressors, Exp. Thermal and Fluid Science, vol. 2, pp. 201-207, 1989.

[03] Patankar, S.V., Numerical Heat Transfer and Fluid Flow. Hemisphere Publ. Corp., Washington, 1980.

[04] Gasche, J.L., Laminar Fluid Flow Through Eccentric Refrigeration Compressor Valves, M.Sc. Dissertation, Department of Mechanical Engineering, Federal University of Santa Catarina, Brazil, 1992 (in Portuguese).

[05] Patankar, S.V., A Numerical Method for Conduction in Composite Materials, Flow in Regular Geometries and Conjugate Heat Transfer, Proc. 6th Intern. Heat Transfer Conf., Vol. 3, pp. 297-304, Toronto, 1978.

[06] Holman, J.P., Experimental Methods for Engineers, McGraw Hill, Tokyo, 1981.

SOME ASPECTS OF DESCRIBING PROCESSES IN SLIDING-VANE ROTARY MACHINES

Zbigniew Gnutek, Eugeniusz Kalinowski
Institute of Heat Engineering and Fluid Mechanics
Technical University of Wrocław, Wrocław, Poland

Abstract

In the paper, various methods of geometrical description of sliding-vane rotational machines, as found in publications, are considered. Choice and modification of one of them has been proposed. With regard to precise analysis, formulae have been obtained to calculate the working chamber volume for any chamber position and for any type of sliding-vane rotational machine.

Nomenclature:
A - cross-sectional area
b - vane thickness
e - eccentricity
L - length of working chamber
r - rotor radius
R - cylinder radius
V - volume
y - radial clearance
λ - angle between successive vanes
ρ - radius vector
φ - amplitude; angular coordinate
ψ - vane/rotor radius inclination angle

1. Introduction

Many publications appeared in recent years discussing theoretical and experimental results of tests on sliding-vane rotary machines (see for example [1, 2, 3, 4]). A number of methods have been used in them to describe mechanical, thermodynamic and flow processes and to carry out the geometric, kinematic and dynamic analysis of sliding-vane machines; various coordinate systems are therein applied. This makes it difficult to compare the results obtained and leads often to misunderstandings. Besides, it makes superfluous variables appear sometimes in the mathematical model.

Geometric form of sliding-vane rotational machines implies, that values required to describe the machine operation (like cross-sectional area of the working chamber, working chamber volume, lengths of linear and circular segments) are calculated approximately, approximation degree being different for particular authors. With powerful microcomputers becoming widespread, design offices and research centres are looking for precise numeric algorithms, which do not necessarily assume the form of a simple equation.

With regard to the statement made above, the authors would like to put forward a convention concerning geometric description systematization of multisliding-vane rotational machines. In the opinion of the authors, this will provide a more readable description of geometric values, as well as of phenomena and processes relevant to these machines. We also intend to point out some properties of the $Z(\varphi)$ function, particularly its ability to evaluate working chamber volume at any chamber position and for various types of multisliding-vane machines.

2. Coordinate System

In almost all publications, cylindrical coordinate system is employed for describing multisliding-vane rotary machines (Fig. 1a). The system converts into polar coordinate system (Fig. 1b) when things are being considered within the plane perpendicular to the Z axis. The choice of the Z axis is still undetermined.

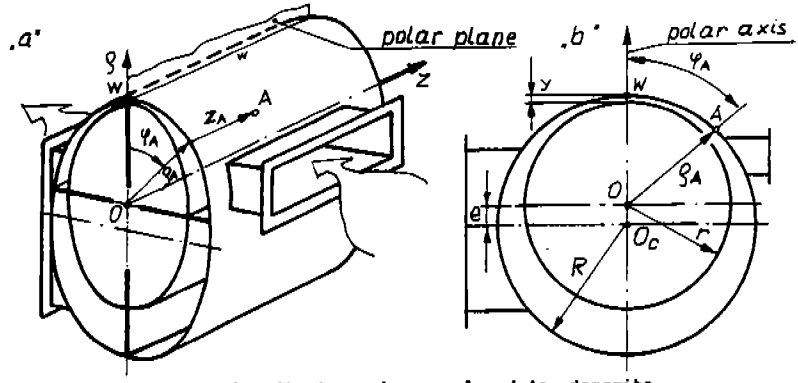

Fig. 1. Coordinate systems employed to describe multisliding-vane rotary machines
a - cylindrical, b - polar.

In some cases this is the cylinder axis [1, 2], in other the rotor axis [2]. For further analysis, the authors have adopted basically a coordinate system with the Z axis running through the rotor axis and the polar plane determined by the axis and its nearest cylinder generatrix. The z = 0 plane runs through the chamber side cover surface.

3. Arrangement of Points, Vanes and the Working Chamber in Multisliding-vane Rotary Machines

With the coordinate system adopted, the machines can be described from the geometrical point of view, i.e. position of arbitrary point, segment and figure, as well as that of the working chamber; length of a segment and arc, area of a figure and volume of a solid (working chamber, e.g.) can all be described. Also processes to which parts of the machine are exposed (movement, friction) can be specified in that way. This applies still more to the description of the thermodynamic state (p, T, i) and representation of processes, which the gas contained in the working chamber undergoes (i.e. heat exchange, flows, compression and decompression).

Fig. 2 outlines the cross-section of a multisliding-vane rotary machine. In the coordinate system adopted, the position of an arbitrary point (e.g. point C on the

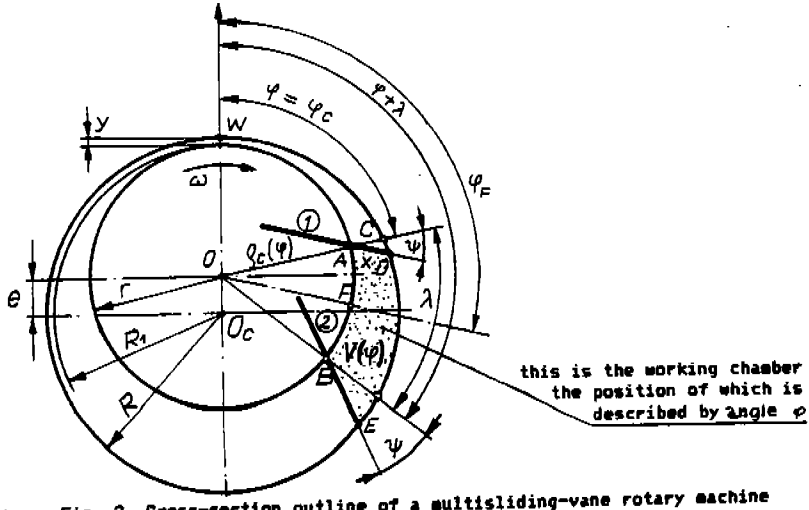

Fig. 2. Cross-section outline of a multisliding-vane rotary machine

cylinder surface) is determined by two coordinates ρ_c and φ_c. The vane position is given by specifying coordinates of either two points situated on the vane, or of vane axis/rotor surface intersection point and vane/rotor radius inclination angle. Coordinates of the (1) vane (Fig. 2) are equal $\rho = \rho_A = r$; $\varphi = \varphi_A$ and ψ. When considering a machine with constant r and ψ, then the only variable, which describes position of the vane is the vane amplitude φ. Values relating to the vane, which vary with the rotor rotation, will be thus functions of φ (e.g. $x(\varphi)$, $P_i(\varphi)$).

Position of the working chamber is usually determined in publications [1, 2] by specifying position of the bisector of the angle λ contained between vanes limiting the chamber (angle φ_F in Fig. 2). This however implies certain inconveniences, consisting in principle in necessity of two at least (sometimes three) position coordinates for one given chamber (i.e. position coordinates for the vanes and for the chamber itself). In order to avoid this complication, the author's proposal is to determine the working chamber position by means of coordinates of one of its limiting vanes and to adopt the convention that the vane in question will be thevane which "closes" the chamber in the sense of chamber movement direction (vane (2) in Fig. 2). Then the angle φ becomes the coordinate of the working chamber position and all quantities relating to the chamber and chamber medium. This convention is also useful for one- and two-sliding vane machines.

4. Working Chamber Volume

Mindful of the simplifications generally applied to calculate volume of the working chamber being in arbitrary position, the authors reconsidered the above relations. With no simplifications assumed, they derived formulae, whose applicability exceeds multisliding-vane rotary machines.

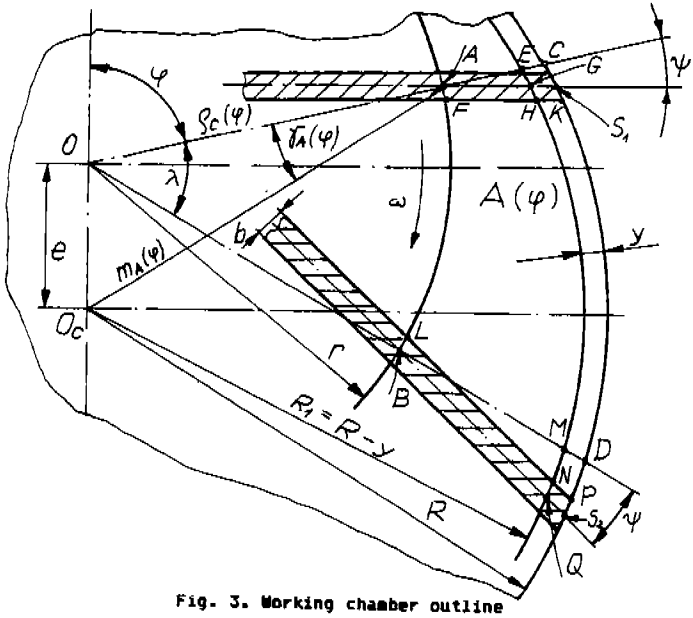

Fig. 3. Working chamber outline

Fig. 3 shows schematically a working chamber in position characterized by angle φ and specifies its dimensions necessary to calculate the chamber volume.

The working chamber volume equals to:

$$V(\varphi) = A(\varphi) \cdot L \qquad (1)$$

where $A(\varphi)$ - cross-sectional area of the chamber.

According to designations of Fig. 3:

$$A(\varphi) = A_{AEMB} + A_{BMQ} - A_{AEG} - A_{AGHF} - A_{BQNL} - A_{HKPN} \tag{2}$$

In the above formula the following members can be distinguished:

$A_{AEMB}(\varphi)$ - cross-sectional area of the working chamber for a machine with $\psi = 0$; $y = 0$; $b = 0$.

$$A_{AEMB} = R_1^2 \cdot Z_1(\varphi) \tag{3}$$

$$Z_1(\varphi) = \frac{e}{R_1}\left\{\lambda - \frac{1}{2}\left[\sin(\varphi+\lambda)\sqrt{1-\left(\frac{e}{R_1}\right)^2\sin^2(\varphi+\lambda)} + \right.\right.$$

$$+ \frac{1}{\frac{e}{R_1}} \cdot \arcsin\frac{e}{R_1}\sin(\varphi+\lambda) - \sin\varphi \cdot \sqrt{1-\left(\frac{e}{R_1}\right)^2\sin^2\varphi} +$$

$$\left. - \frac{1}{\frac{e}{R_1}} \cdot \arcsin\frac{e}{R_1}\sin\varphi\right] +$$

$$\left. - \frac{1}{2}\left(\frac{e}{R_1}\right)\left[\lambda - \sin(\varphi+\lambda)\cos(\varphi+\lambda) + \sin\varphi\cos\varphi\right]\right\} \tag{4}$$

$A_{BMQ}(\varphi)$; $A_{AEG}(\varphi)$ - areas of figures arising by inclining the vanes by an angle of φ towards the rotor radius.

$$A_{AEG} = R_1^2 \cdot P_1(\varphi) \tag{5}$$

The $P_1(\varphi)$ function is represented by the following formula:

$$P_1(\varphi) = \int_0^{\psi} \frac{1}{2}\left\{\sqrt{1-\left[\frac{a_A(\varphi)}{R_1}\right]^2\sin^2\left[\psi+\gamma_A(\varphi)\right]} - \cos\left[\psi+\gamma_A(\varphi)\right]\right\} d\varphi \tag{6}$$

Functions $a_A(\varphi)$ and $\gamma_A(\varphi)$ in the above formula are defined as follows:

$$a_A(\varphi) = R_1\sqrt{1-2\left(\frac{e}{R_1}\right)\left(1-\frac{e}{R_1}\right)(1-\cos\varphi)} \tag{7}$$

$$\gamma_A(\varphi) = \arcsin\frac{e}{R_1}\,\frac{R_1\sin\varphi}{a_A(\varphi)} \tag{8}$$

Value of $A_{BMQ}(\varphi)$ can be evaluated from equation (4) for a vane in a position described by the angle of $\varphi + \lambda$:

$$A_{BMQ} = R_1^2 \cdot P_1(\varphi+\lambda) \tag{9}$$

Vane thickness is allowed for in the formulae for $A_{AGHF}(\varphi)$ and $A_{BQNL}(\varphi)$. The sum of

the areas is equal to:

$$A_{AGHF}(\varphi) + A_{BGNL}(\varphi) = R_1^2 \cdot P_2(\varphi) \tag{10}$$

where the $P_2(\varphi)$ function is given by:

$$P_2(\varphi) = \frac{1}{2} \frac{b}{R_1} \left\{ \sqrt{1 - \left[\frac{a_A(\varphi)}{R_1} \right]^2 \sin^2 \left[\psi + \gamma_A(\varphi) \right]} + \right.$$

$$+ \sqrt{1 - \left[\frac{a_A(\varphi + \lambda)}{R_1} \right]^2 \sin^2 \left[\psi + \gamma_A(\varphi + \lambda) \right]} +$$

$$\left. - \cos \left[\psi + \gamma_A(\varphi) \right] - \cos \left[\psi + \gamma_A(\varphi + \lambda) \right] \right\} \tag{11}$$

If the rotor does not adhere closely to the cylinder, i.e. if $y \neq 0$, then the chamber cross-sectional area should be increased by $A_{HKPN}(\varphi)$.

$$A_{HKPN} = R_1^2 \cdot P_3(\varphi) \tag{12}$$

where $P_3(\varphi)$ is given by the formula:

$$P_3(\varphi) = \left\{ \lambda - 2 \frac{e}{R_1} \cos \frac{2\varphi + \lambda}{2} \sin \frac{\lambda}{2} + 2 \frac{e}{R_1} \operatorname{tg} \psi \sin \frac{2\varphi + \lambda}{2} \sin \frac{\lambda}{2} + \right.$$

$$\left. - \operatorname{tg} \psi \left[\sqrt{1 - \left(\frac{e}{R_1} \right)^2 \sin^2 \varphi} - \sqrt{1 - \left(\frac{e}{R_1} \right)^2 \sin^2 (\varphi + \lambda)} \right] \right\} \frac{y}{R_1} +$$

$$- \frac{y}{R_1} \frac{b}{R_1} \tag{13}$$

Having allowed for (2), (4), (6), (11) and (13), equation (1) assumes the following form:

$$V(\varphi) = R_L^2 \cdot \left(1 - \frac{y}{R} \right)^2 \left[Z_1(\varphi) - P_1(\varphi) + P_1(\varphi + \lambda) - P_2(\varphi) + P_3(\varphi) \right] =$$

$$= R_L^2 \cdot Z(\varphi) \tag{14}$$

where:

$$Z(\varphi) = \left(1 - \frac{y}{R} \right)^2 \left[Z_1(\varphi) - P_1(\varphi) + P_1(\varphi + \lambda) - P_2(\varphi) + P_3(\varphi) \right] \tag{15}$$

In the above formula, $Z(\varphi)$ represents relative cross-sectional area of the working chamber of an expansion-type machine (motor, compressor). The form of the equation (15) emphasizes the fact that variables λ, e/R, y/R, b/R and ψ are regarded as parameters, and the variable φ as an argument.

Evaluation of the working chamber volume in an arbitrary chamber position is thus reduced to determining the $Z(\varphi)$ value for a given angle φ from formula (15). The chamber position, when the chamber volume is already known, is found by solving a simple nonlinear equation, which can be done easily by using standard numerical procedures and microcomputers.

5. Application of Z(φ) Function to Other Machines

The Z(φ) function can be useful when evaluating other types of machines. For compression multisliding-vane rotary machines (compressors, vacuum pumps), the polar coordinate system is produced from the system presented in paragraph 2 by rotating the polar axis by an angle of $\Delta\varphi = \pi$. The Z(φ) function can then be employed, if the expression $\varphi + \pi$ is assumed as an argument.

$$V_K(\varphi) = R^2 L \cdot Z_k(\varphi) \tag{16}$$

where: $V_K(\varphi)$ - the working chamber volume of that compression-type vane rotary machine, wherein the angle φ is used to describe the chamber position.
$Z_k(\varphi)$ - relative cross-sectional area of the working chamber for this machine.

$$Z_K(\varphi) = Z(\varphi + \pi) \tag{17}$$

Solving numerous technical problems requires evaluation of area for a segment of a figure formed by two non-concentric circles (Fig. 4). If figure ABCD is assumed to be the segment in question, then its area equals to the working chamber area in the chamber position of φ'; λ amounts then to $\Delta\varphi'$. Then

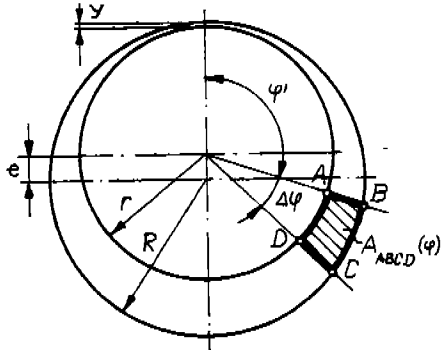

Fig. 4. Areas of figures contained between non-concentric circles

$$A_{ABCD} = R^2 \cdot Z(\varphi') \tag{18}$$

The value of $Z(\varphi')$ has been determined for a machine of a conventional number of vanes $z = 2\pi/\Delta\varphi'$. The number can assume values from within the range of $z \geq 2$.

The Z(φ) function can also be used for rotary piston machines (one-sliding vane rotational machines). To describe these machines, a polar coordinate system is usually used related to the cylinder centre (Fig. 5). If the rotor position is determined by the coordinate φ in this coordinate system, then the working chamber cross-section is represented by figure ABCD.

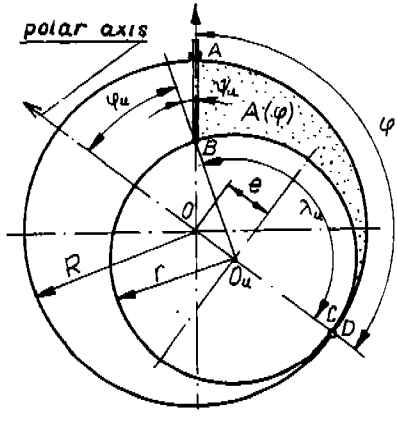

Fig. 5. Area of the figure which the vanes form in a rotary-piston machine.

To evaluate area of the figure, no more than a conventional compression machine should be analyzed with the momentary rotation axis in point Ou. The point acts also as a momentary pole, the conventional polar axis being the half-line $O_u O$. Then position of the conventional working chamber is described by the angle $\varphi_u = \pi - \varphi$. The vane is inclined to the rotor radius at the angle ψ_u. The other vane is almost completely inserted into the groove (point C). The angle between the vanes equals $\lambda_u = \varphi$. The following is true for such a chamber:

$$A_{ABCD} = A(\varphi) = R^2 \cdot \tag{18}$$

$$\cdot Z_k(\varphi_u, \psi_u, \lambda_u, e/R, b/R, \gamma/R)$$

where $Z_k(\varphi_u, \psi_u, \lambda_u, e/R, b/R, \gamma/R)$ is relative cross-sectional area of the working chamber of a conventional

vane rotational machine. Parameters φ_u, ψ_u and λ_u are functionally dependent on φ.

The $Z(\varphi)$ function would also appear in those thermodynamic relations for vane rotary machines, where working chamber volume or volume ratio is involved.

6. Final Remarks

The presented methods of describing vane rotational machines and evaluating working chamber volume have been applied by the authors in design and research studies over the machines. The microcomputer software package worked out for the purpose and the $Z(\varphi)$ function tables are intended for universal and extensive application by engineers working in the area of vane rotational machines.

7. References

[1]. Fischer R.D. "Feasibility study and hardware design of a pivoting-tip rotary-vane compressor and expander applied to a solar-driven heat pump". Proc. of the 1978 Purdue Compressor Technol. Conf. West Lafayette 1978.

[2]. Golovincov A.G. "Rotacjonnyje kompressory". Masinostrojenie, Moskva 1964r.

[3]. Gnutek Z. "Analiza procesow termodynamicznych w łopatkowych maszynach rotacyjnych", Raport Polit. Wr. I-20, SPR 24/91; 29/91; 31/91; Wrocław 1991.

[4]. Gnutek Z. "Geometryczny opis i analiza procesów tarcia, przepływów i sprężania w jedno- i dwułopatkowych maszynach rotacyjnych". Raport Polit. Wr. I-20, SPR 3/92. Wrocław 1992 r.

A COMPARATIVE STUDY OF THE REED VALVE ASSEMBLY TO OPTIMIZE COMPRESSOR PERFORMANCE

Thomas J. Fedorka, P. E.

Senior Development Engineer
The Campbell Group
Harrison, OH U. S. A.

Livingston A. Newberg

Product Manager
De-Sta-Co
Troy, MI U. S. A.

INTRODUCTION

The valve, backer and port are usually treated individually in design and through production. This limits the overall assembly performance due to the individual part restrictions. The interrelationships of the three can be optimized to improve performance in the dynamic operation of the air compressor. Consequently, this comparative study of the discharge valve assembly will show a few key ways the valve, backer and port can be changed to improve the performance of the compressor.

OBJECTIVE

The object of the comparative testing is to establish the theory that the combination of a curved dynamic backer and a peripheral flow port will improve the compressor's performance. This combination will also justify the reduction of valve thickness which will improve the compressor's dynamic response. The compressor's performance will be evaluated by monitoring the amp draw at known pressure loads. This will indicate the compressor's energy improvement using the new valve assembly compared to the old assembly.

TEST SAMPLES

In the assembly, the rectangular valve and backer parts are attached to the valve plate at one end and will operate in the cantilever mode. The valve and backer thicknesses, the backer form, and the port design were changed for each test, the rest of the compressor components remained the same. These design changes will be tested to evaluate the compressor's performance in stages. It should be noted that the dynamic curved backer and the valve are made from flapper valve steel and the valve plate is made from die cast 380 Aluminum (see Exhibit A).

TEST SEQUENCE

The three factors, valve thickness, backer thickness, and port shape, were each assigned two levels and arranged in the test matrix shown in Exhibit B. The run order was randomized and replicated to reduce biasing the data. The input voltage was maintained at a constant level while amp draw, compressor speed and free air delivery data were recorded at various pressure loads. The data was analyzed using graphical techniques and *Technicomp's TARGET-DOE* software to identify which factors affect compressor performance the most. Pressure versus volume curves were also plotted to investigate valve efficiency.

COMPARATIVE TESTS

Chart #1 compares the fixed stop with the dynamic backer using the same round port. The curved backer allowed the valve to open before it dynamically responded with the valve at the tangent point at the base of the port. The dynamic backer proved to be more energy efficient when a thinner valve and backer were used (see curve #8).

Chart #2 compares the round and teardrop ports using the same valve and dynamic backer thickness combinations. The teardrop shaped port proved to be more energy efficient than the round port at all loads. This established the theory that a peripheral flow port reduced the dynamic backer loft height and reduced the energy required to meet the dynamic loads.

Chart #3 compares the baseline fixed stop and round port with the dynamic backer, teardrop port, and thinner valves. The combination of the three changes proved to increase the response and efficiency at all pressure loads. Test #7 met the objective of optimizing the compressor performance.

CONCLUSIONS

You can optimize the operating characteristics of an air compressor by evaluating a dynamic curved backer, a peripheral type port and a thinner valve for the discharge valve assembly. Similar results could be expected by modifying the suction valve assembly; however, this will not be covered at this time. Of course, additional testing is required for each unique compressor design. This comparison proves the value of optimizing the valve assembly.

REFERENCES

1. Reineking F. C., United States Patent # 939,549, "Reed Air-Intake Regulator For Carburetors", Nov 9, 1909.

2. Sodel W., Ph.D., "Design and Mechanics of Compressor Valves" Short Course Text Book of Purdue Technical Conference, Ray Herrick Laboratories, Purdue University, 1984.

EXHIBIT A

ROUND PORT

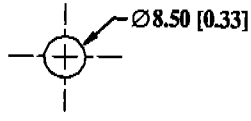

TEARDROP PORT

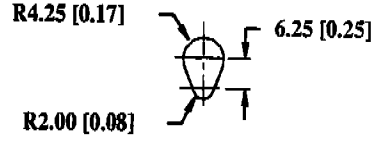

VALVE DIMENSIONS

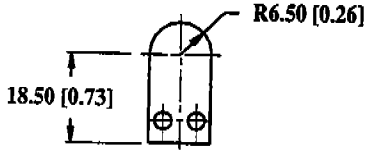

SIDE VIEW OF FLEXIBLE BACKER

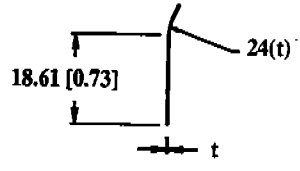

OLD (CURRENT) ASSEMBLY SKETCH

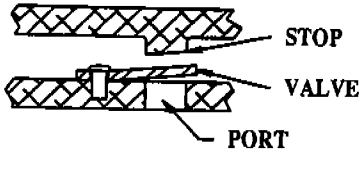

NEW (TEST) ASSEMBLY SKETCH

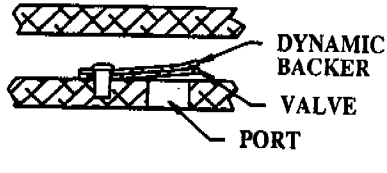

ALL DIMENSIONS ARE IN MILLIMETERS.
DIMENSIONS IN [ ] ARE INCHES.

EXHIBIT B

TEST DATA

TEST NUMBER	CANTILEVER VALVE THICKNESS	DYNAMIC BACKER THICKNESS	PORT SHAPE
A (STD)	.305 [.012]	RIGID STOP	ROUND
1	.305 [.012]	.305 [.012]	TEARDROP
2	.305 [.012]	.305 [.012]	ROUND
3	.305 [.012]	.152 [.006]	TEARDROP
4	.305 [.012]	.152 [.006]	ROUND
5	.152 [.006]	.305 [.012]	TEARDROP
6	.152 [.006]	.305 [.012]	ROUND
7	.152 [.006]	.152 [.006]	TEARDROP
8	.152 [.006]	.152 [.006]	ROUND

MEASURED DATA AT LOAD POINTS

- COMPRESSOR FREE AIR FLOW
- COMPRESSOR SPEED
- MOTOR AMP DRAW
- P-V CURVES
- INPUT VOLTAGE

ALL DIMENSIONS ARE IN MILLIMETERS.
DIMENSIONS IN [ ] ARE INCHES.

CHART #1

ENERGY IMPROVEMENT OF FIXED STOP vs. DYNAMIC BACKER

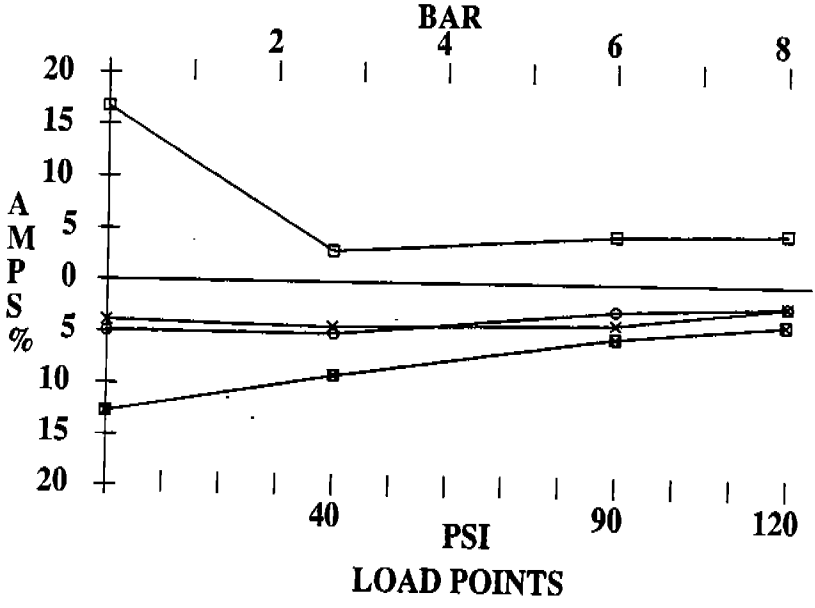

$$\text{AMPS\%} = \left(\frac{\text{STD - TEST}}{\text{TEST}} \right) 100\%$$

☒ = TEST #2

○ = TEST #4

× = TEST #6

□ = TEST #8

CHART #2

ENERGY IMPROVEMENT OF TEARDROP PORT vs. ROUND PORT

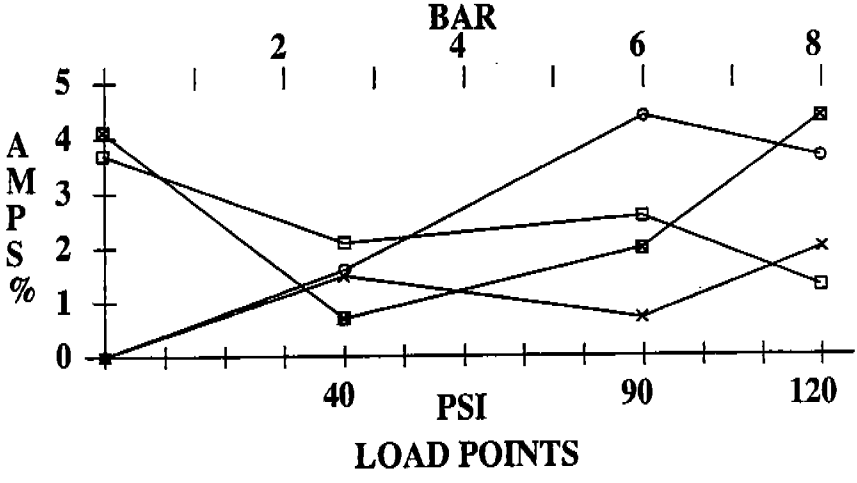

$$\text{AMPS\%} = \left(\frac{\text{ROUND - TEARDROP}}{\text{TEARDROP}} \right) 100\%$$

□ = TEST #1 vs. TEST #2

× = TEST #3 vs. TEST #4

⊠ = TEST #5 vs. TEST #6

○ = TEST #7 vs. TEST #8

CHART #3

ENERGY IMPROVEMENT OF OPTIMIZED VALVE ASSEMBLY vs. ORIGINAL VALVE ASSEMBLY

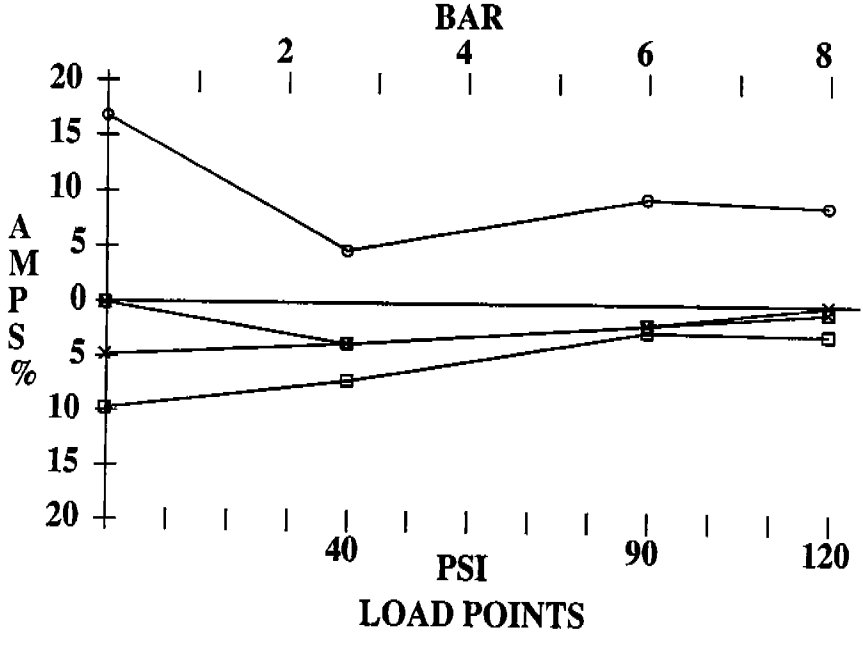

$$\text{AMPS\%} = \left(\frac{\text{STD - TEST}}{\text{TEST}} \right) 100\%$$

□ = TEST #1

× = TEST #3

⊠ = TEST #5

○ = TEST #7

NUMERICAL AND EXPERIMENTAL ANALYSIS OF THE FLOW CHARACTERISTICS THROUGH A CHANNEL VALVE

G. R. Price and K. K. Botros
NOVA HUSKY Research Corporation
Calgary, Alberta, Canada

ABSTRACT

An experimental and numerical study of compressor channel valves was performed for low pressure air flows at a Reynolds number based on the inlet slot width (Re_s)~$2x10^4$. The objective was to investigate the variation of the effective valve flow and force areas with lift. The results showed that the variation in the effective flow area with valve lift is approximately linear. The numerically determined effective valve flow areas agreed within 15% of those obtained from experimental measurements. The numerical model was then used to determine the valve flow and force areas at operating conditions prevailing in the suction and discharge of a high pressure natural gas reciprocating compressor (Re_s~$4x10^5$). The effect of increasing the Reynolds number (Re_s), over the range considered, on the effective flow area was found to be small. The effective force area decreases rapidly at small values of valve lift and gradually increases at larger lifts.

NOMENCLATURE

A_{ef}	effective force area;
A_{ep}	effective flow area;
A_t	nozzle throat area;
C_D	nozzle discharge coefficient;
C^*	critical flow factor;
h	valve plate lift;
k	turbulence kinetic energy;
L	inlet slot length;
$\dot{m}$	mass flow rate through valve;
P	gas pressure;
R	gas constant;
Re	Reynolds number;
T	gas temperature;
w	inlet slot width;
ε	dissipation of turbulence kinetic energy;
γ	isentropic exponent;
ρ	gas density;

Subscripts

d	recovered downstream of valve;
max	full valve lift;
o	stagnation conditions;
s	based on inlet slot width;
u	upstream of valve;

INTRODUCTION

The use of computer simulations to predict the magnitude and frequency of pressure pulsations generated by reciprocating compressors has become widespread[1,2,3,13]. The suction and discharge valves of the compressor do not only modify the fluctuating flow produced by the piston motion, but also interact dynamically with the associated piping system. Thus, the influence of the valves should be taken into account in the simulations if accurate prediction of the pulsation levels is required, particularly at the higher harmonics of the compressor operating speed.

A one-dimensional quasi-steady state flow equation along with a second-order ordinary differential equation (O.D.E) describing the motion of the valve plate, (i.e. a concentrated mass point with a single degree of freedom spring-mass-damping model), are typically used to characterize the valve dynamics. This quasi-steady state assumption followed from extensive experiments on large scale models of valves by Boswirth[4,5,6] which led to a one-dimensional unsteady flow equation that takes into account the gas inertia and unsteady work exchange between the gas and the valve plate. The calculations based on this equation have shown that the steady flow equation generally gives acceptable results in the absence of valve flutter. Tilting of the valve plates can occur even in completely symmetric flows[7] and hence can not be properly represented by the single degree of freedom spring-mass-damping model. More sophisticated models of the valve dynamics exist[8] which consider the valve plate with more than one degree of freedom, but they require a more complete knowledge of the flow, force and spring characteristics of a valve than was obtained from this work. Consequently, the steady flow equation and the second-order O.D.E (spring-mass-damping) were considered adequate to model the valve dynamics of the low speed, high flow compressors used in gas transmission systems. In these equations, the effective valve flow and force areas are parameters that depend on the lift and Re_S for a given compressor valve.

An experimental study was conducted on a low pressure air test loop. Pressure differentials across the valves at several fixed increments of valve lift were measured to determine the variation in the effective flow area. A numerical analysis of flow through the valves was conducted using PHOENICS[9], a commercial fluid dynamics software, to obtain both the effective flow and effective force areas at conditions similar to the experiments. The performance of the numerical model was verified by comparing the effective flow areas obtained numerically to those determined experimentally. The numerical code was subsequently used to evaluate the variation in both valve parameters with lift for operating conditions prevailing at the suction and discharge of the high pressure (thus higher Re_S) natural gas reciprocating compressors in NOVA's gas transmission system.

GENERAL EQUATIONS

The effective valve flow area relates the mass flow rate through the valve to the upstream and fully recovered downstream pressures. Using the one-dimensional steady flow equation, the effective valve flow area is calculated from the following expression for subsonic conditions[10] :

$$A_{ep} = \frac{\dot{m}}{P_u\sqrt{\frac{2\gamma}{(\gamma-1)RT_u}}\sqrt{\left(\frac{P_d}{P_u}\right)^{\frac{2}{\gamma}} - \left(\frac{P_d}{P_u}\right)^{\frac{\gamma+1}{\gamma}}}} \qquad (1)$$

The gas force exerted on the valve plate is the result of the normal pressure acting on both sides of the plate and the wall shear in the direction of valve lift. This force can be related to the overall pressure loss across the valve by an effective force area defined as:

$$A_{ef} = \frac{F_p}{P_u - P_d} \qquad (2)$$

DESCRIPTION OF CHANNEL VALVE

A suction and a discharge channel valve were taken from a reciprocating compressor station in NOVA's gas transmission network. The valves are rated at 5500 kPa for dynamic differentials and 10,350 kPa for static differentials, which make them suitable for the high pressure, natural gas applications. A photograph of the suction valve used in this study is shown in Fig.1. The gas flow enters the valves through seven parallel rectangular slots of equal width, but with varying lengths.

Each slot seats a U-shaped plate that is actuated by a stiff leaf spring. The gas leaves the valve through eight staggered slots that are similar in appearance to the entrance slots. A cross-section of a single slot and the U-shaped plate with spring are illustrated in Fig.2.

EXPERIMENTAL SETUP

Only the effect of the valve lift on the effective flow area was investigated experimentally, while the effects on the effective force area were not considered due to difficulties in measuring the lifting force acting on the plates. Plate lifts were secured for the seven slots by means of precision spacers which gave 20, 40, 60, 80 and 100% of the full lift for each slot. A schematic of the experimental setup is presented in Fig. 3. Ambient air was drawn through the test section and the pressure distributions, both upstream and downstream of the valve, were recorded. A 40D section of 6" pipe upstream of the test section ensured the inlet profile into the valve was fully developed. Pressure measurements were taken at two locations upstream (0.131 and 0.08 m) and four locations downstream (at 0.02, 0.08, 0.181 and 0.284 m). Each set of taps consists of four equally spaced static pressure taps around the circumference of the pipe. Air was drawn through the system by a vacuum pump located downstream of the test section at a constant mass flow rate maintained by the sonic nozzle. The mass flow rate was measured with a 40mm calibrated sonic nozzle, based on the following equation:

$$\dot{m} = C_D C^* A_t \frac{P_o}{\sqrt{RT_o}} \qquad (3)$$

A single pressure tap was located upstream of the nozzle in order to record the stagnation pressure used in the calculation of the mass flow rate from the above equation. The nozzles have been calibrated to an accuracy of +/- 0.5%. Pressures were measured with a large U-tube water manometer to an accuracy of 0.25%. The overall uncertainty in the effective flow areas is +/- 1.0%.

COMPUTATIONAL STUDY

Computational simulations were performed using PHOENICS (v1.5) to calculate the flow field through the channel valves at several different valve lifts. The code was run on an IBM 320H RISC workstation. The effective flow area was calculated from eqn.(1) using the numerically determined pressure field; the upstream and fully recovered downstream pressures. The lifting force acting on the valve plates was obtained by integrating the normal pressure acting on the front and back of the valve plate along with the wall shear stress in the direction of valve lift. The effective force area was then calculated using eqn.(2).

In this study the time-averaged forms of the Navier-Stokes and continuity equations were solved along with the standard k-ε model of turbulence[12] on a two-dimensional computational grid. The two-dimensional simplification was made as the length of the valve slots was large compared to the width ($14<L/w<19$ for the seven slots). Additionally, only half of one slot, from the center of the valve plate to the plane of symmetry of the flow produced by the adjacent slot, was modeled. This assumption is justified due to the symmetrical nature of the flow produced by the adjacent slots for the channel valve geometry. Finally, the flow through the valves was assumed to be isothermal and incompressible since the Mach number through the computational domain was below the compressible limit ($M<0.3$), except in the case of very small valve lifts ($M\sim0.4$) where the compressibilty was neglected.

Computational Grid

A body-fitted coordinate system was employed to generate a computational grid that adheres to the walls of the tapered slot in the valve and the rounded edges (r~1 mm) of the valve plate. The computational domain starts 14 mm upstream of the inlet into the valve slot, while the outlet of the domain was placed 46 mm downstream of the valve exit. The locations of the inlet and outlet boundaries were determined by trial and error in order to minimize the influence on the flow field in the vicinity of the valve plate and allowed the exiting flow to re-develop. A non-uniform grid was generated which is fine in the lift gap and becomes increasingly coarse away from the valve plate.

The grid contained 50 cells parallel to the slot width and 300 cells in the overall flow direction. The influence of grid size was investigated by solving the flow field through a finer grid (100x500 cells) at maximum plate lift for the suction channel valve. The effective flow and force areas were within 3% of that obtained with the coarser mesh. The computational grid used in this study for the suction channel valve at maximum lift is shown in Fig.4.

Boundary Conditions

Along the inlet boundary of the computational domain, a uniform velocity profile was specified based on the average velocity through all seven slots. The turbulent kinetic energy, k, and rate of dissipation of this energy, ε, were set to uniform profiles characteristic of the upstream flow. The sensitivity of the results to the inlet turbulent profiles is small. The no-slip condition at the walls was specified indirectly using the standard wall function approach[12]. At the outlet of the domain the gradient of the velocities and turbulent quantities were set to zero.

COMPARISION OF EXPERIMENTAL AND COMPUTATIONAL RESULTS

Low Pressure Air

The effective valve flow areas, calculated both numerically and from experiment, are presented in Figs.5 and 6.for the suction and discharge channel valves, respectively, at $Re_S \sim 2x10^4$. The effective flow area is normalized by the inlet slot area shown in Fig. 2 for each channel valve. The experimental and numerical data are fitted to third degree polynomials by least-squares regression. Both methods predict a direct linear relationship between the effective flow area and the valve plate lift at values of $h / h_{max} < 0.6$, i.e. the effective flow area increases with increasing lift. However, the numerical simulations predict a leveling of the effective flow area before maximum lift is obtained. The agreement between the two approaches is quite good, within a maximum of 15%. Although no direct comparision with literature is possible for this particular valve geometry and Reynolds numbers, there is general agreement in the tends shown here and results from other papers[14,15].

Computational Flow Field

The flow field in the valve lift gap for low pressure air in the suction channel valve at 100 and 20% of the maximum plate lift are shown in Fig.9. At maximum plate lift, a large recirculation zone, or separation bubble, develops along the inlet valve face in the plate lift gap. The bulk flow is deflected by the valve plate into the outlet slot. At small values of the plate lift (20%), the flow is accelerated and deflected 90 degrees in a relatively short distance. This suppresses the formation of the recirculation zone along the inlet face and a separation wake in the outlet slot as the high momentum jet cannot remain attached along the curvature of the valve plate. In this case, the Mach number of the flow in the gap is approximately equal to ~0.4, thus compressibility effects should be taken into account (which was neglected in the present work). The radius of the valve plate edge (r) was found to have an effect on the results. The radius was measured by a crude tracing technique and found to be ~1 mm which was used in all the cases presented here. Additional simulations showed that changing the curvature of the rounded edge ($0<r<2$ mm) could change the numerically calculated effective flow and force areas by ±5%.

High Pressure Natural Gas

The effective valve flow and force areas for high pressure natural gas, calculated from the numerical simulations, are presented in Fig.7 for the suction channel valve and Fig.8 for the discharge channel valve. The effect of increasing the Reynolds number of the flow through the valve to $Re_S \sim 4x10^5$ slightly increases the effective flow area for a specified plate lift. This is expected as the boundary layers in the lift gap become thinner with increasing Reynolds number and the losses are dominated more by inertia[14] . The effective force area is equal to the valve inlet slot area at zero lift. As the valve plate lift increases, the effective force area decreases because the negative pressure distribution along the outer edge of the valve plate overrides the positive pressures near the center. Eventually, as the lift increases further the negative pressures near the edges of the valve plates, needed to deflect the flow, are reduced and the effective force area increases. The numerical model predicts this trend, however the accuracy of the numerically determined lifting

forces on the valve plates needs verification with measurements. The relative magnitude of the wall shear was less than 10% of the normal pressure force for the cases considered.

CONCLUDING REMARKS

Detailed flow field through reciprocating compressor channel valves were determined using a commerical code (PHOENICS). The computations were first performed on low Reynolds number flow through the valves, and compared with actual measurements obtained with a low pressure air test loop. Good agreement between the two results gave confidence in the computation technique, which was then applied to a higher Re at conditions prevailing in high pressure natural gas compression. It was demonstrated that the influence of the Re on the effective flow area in this study was rather small. The computation also revealed values for the effective force area at different valve lifts which is required for any valve dynamic and pulsation simulation.

ACKNOWLEDGMENTS

The work presented here is part of a research program sponsored by NOVA CORPORATION OF ALBERTA and permission to publish it is hereby acknowledged. Thanks are also due to Drs. W.M. Jungowski and R.K. McBrien of NOVA HUSKY Research Corporation for their invaluable discussions.

REFERENCES

1. R. Singh, W. Soedel, "A Review of Compressor Lines Pulsation Analysis and Muffler Design Research Part II - Analysis of Pulsating Flows", Proceedings of the 1974 Purdue Compressor Technology Conference, pp.112-123.

2. W. Jungowski, J. Piechna, "Computation of a Cooperation Between Reciprocating Compressor and Complex Piping System Including Mufflers", Proceeding of the 1982 Purdue Compressor Technology Conference, pp.389-394.

3. D. Woolatt, "A Pulsation Calculation Algorithm Well Suited for Use with Valve Dynamics Calculations", 1990 International Compressor Engineering Conference at Purdue, pp.354-361.

4. L. Boswirth, "Valve Flow Experiments with Enlarged Models", 1986 International Compressor Engineering Conference at Purdue, pp.28-44.

5. L. Boswirth, "Non Steady Flow in Valves", 1990 International Compressor Engineering Conference at Purdue, pp.664-673.

6. L. Boswirth, "Theoretical and Experimental Study on Valve Flutter", 1990 International Compressor Engineering Conference at Purdue, pp.674-698.

7. L. Boswirth, "Flow Forces and the Tilting of Spring Loaded Valve Plates", Proceedings of the 1980 Purdue Compressor Technology Conference, pp.185-197.

8. W. Soedel, E. Navas, B. Kotalik, "On Helmholtz Resonator Effects in the Discharge System on a two-Cylinder Compressor", Journal of Sound and Vibration, 30 (3), 1973, pp.263-277.

9. J. Ludwig, H. Qin, D. Spalding, "The PHOENICS Reference Manual", CHAM Report TR/200, 1989, Software Version 1.5.

10. W. Soedel, "Design and Mechanics of Compressor Valves", R.W. Herrick Laboratories, Purdue University, West Lafayette, Indiana, 1984.

11. S. Patankar, "Numerical Heat Transfer and Fluid Flow", Hemisphere Publishing Co., New York, 1980.

12. B. Launder, D. Spalding, " The Numerical Computation of Turbulent Flows", Computer Methods in Applied Mechanics and Engineering, 3 (1974), pp.269-289.

13. K.K. Botros, W.M. Jungowski, W. Studzinski, J. MacLeod, "Influence of Flow in Pulsation of Gas Pipeline Installations", Proceedings of Gas and Liquid Pulsations in Piping Systems - Prediction and Control, Institute of Mechanical Engineers, London, U.K., December 1-2, 1988.

14. L. Boswirth, "Theoretical and Experimental Study on Flow in Valve Channels", Proceeding of the 1982 Purdue Compressor Technology Conference, pp.38-53.

15. R. Ferreira, J. Driessen, "Analysis of the Influence of Valve Geometric Parameters on the Effective Flow and Force Areas", 1986 International Compressor Engineering Conference at Purdue, pp.632-646.

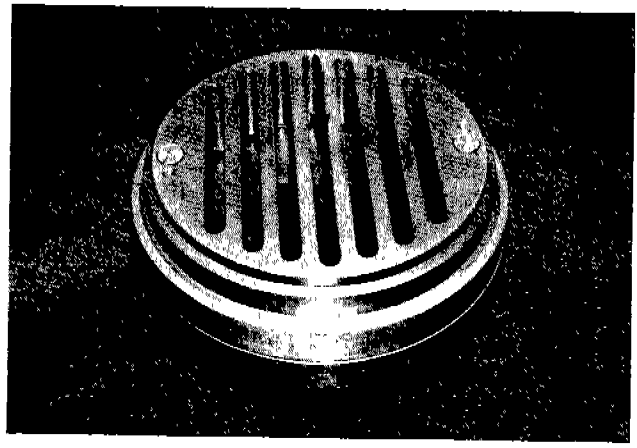

Fig.1. Photograph of Suction Channel Valve

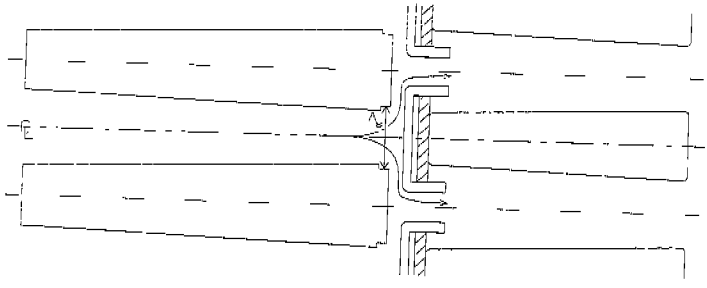

Fig.2. Cross-section of Channel Valve

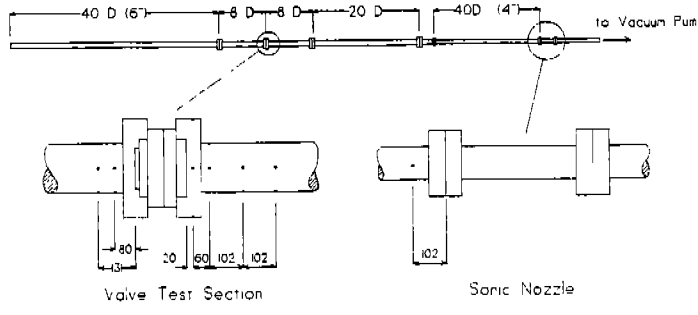

Fig.3. Schematic of Experimental Setup

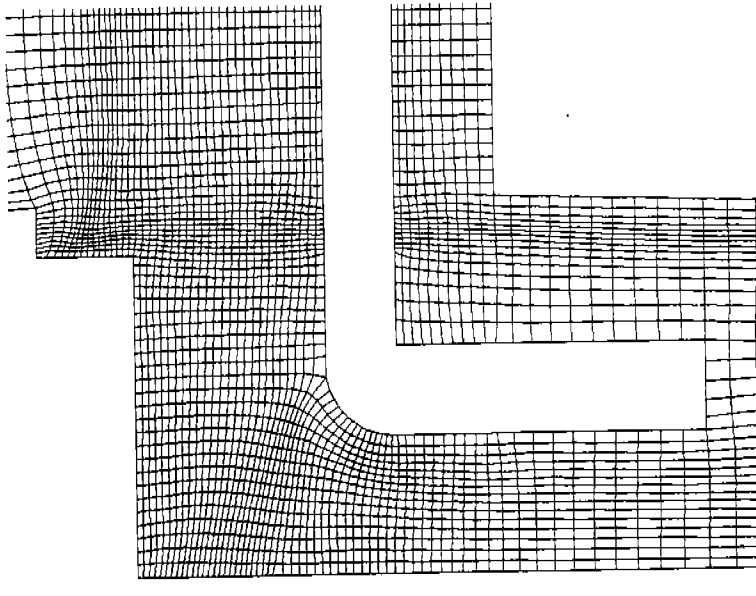

Fig.4. Computational Grid in Valve Plate Region

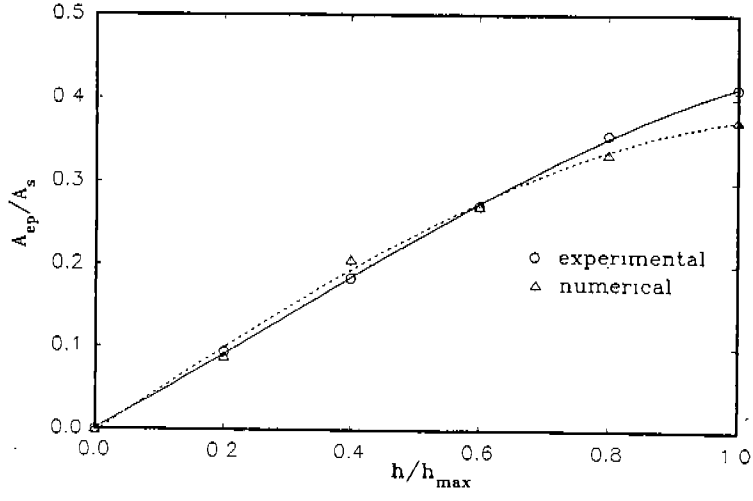

Fig.5. Effective Flow Area vs. Lift for Suction Channel Valve with Low Pressure Air ($Re_s \sim 2x10^4$)

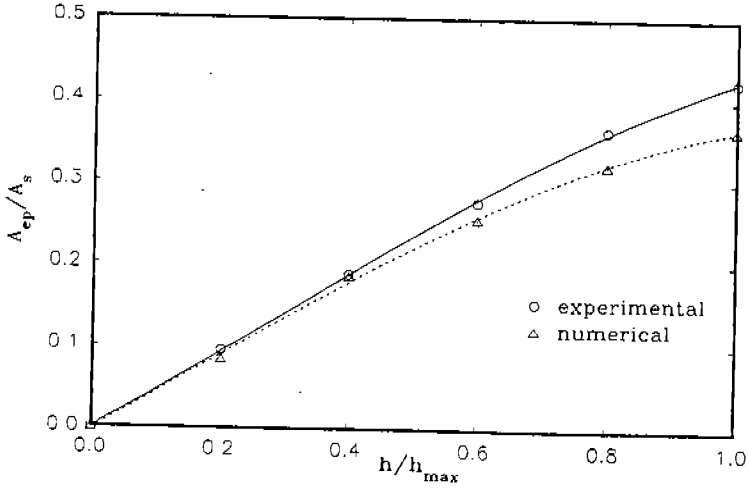

Fig.6. Effective Flow Area vs. Lift for Discharge Channel Valve with Low Pressure Air ($Re_s \sim 2x10^4$)

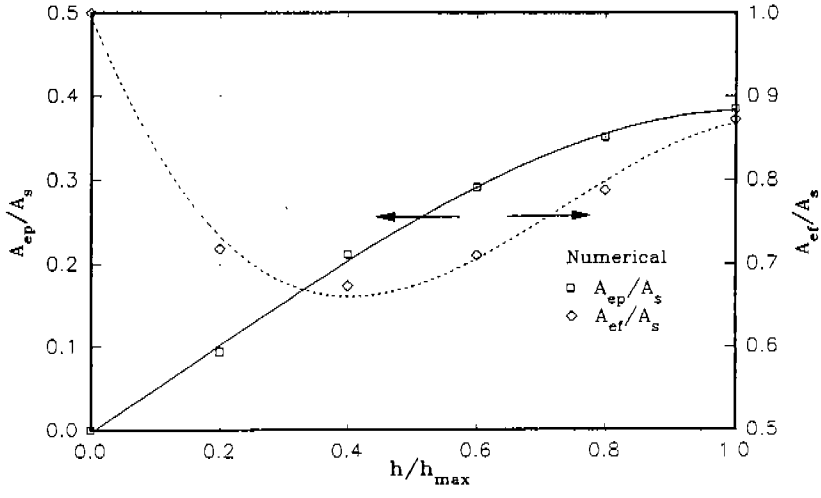

Fig.7. Effective Flow and Force Areas vs. Lift for Suction Channel Valve with High Pressure Natural Gas ($Re_s \sim 4x10^5$)

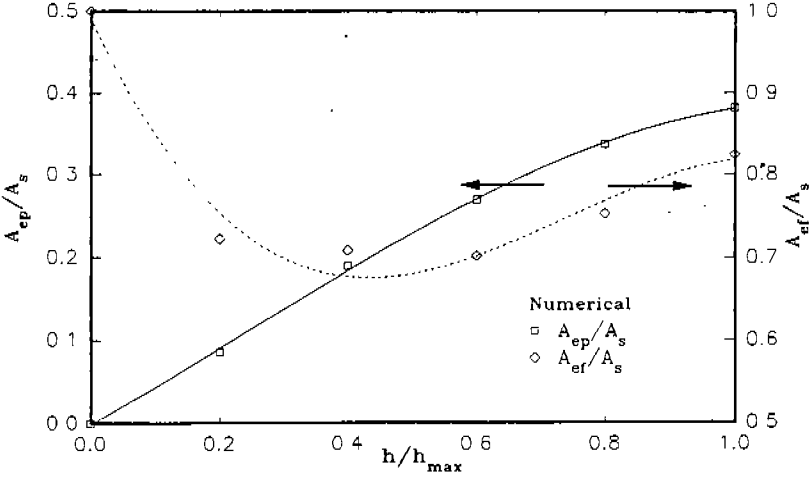

Fig.8. Effective Flow and Force Areas vs. Lift for Discharge Channel Valve with High Pressure Natural Gas ($Re_s \sim 4x10^5$)

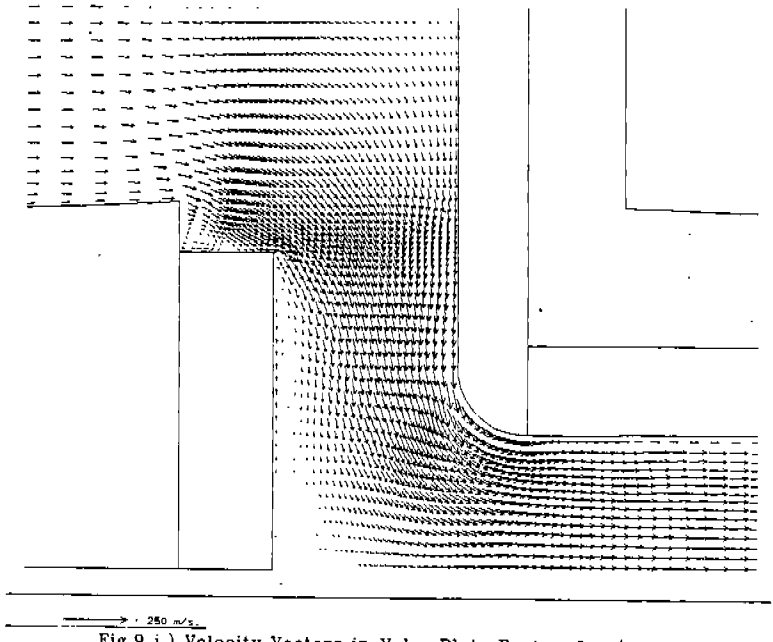

Fig.9 i.) Velocity Vectors in Valve Plate Region @ h/h_{max} = 1.0 for Low Pressure Air ($Re_s \sim 2x10^4$)

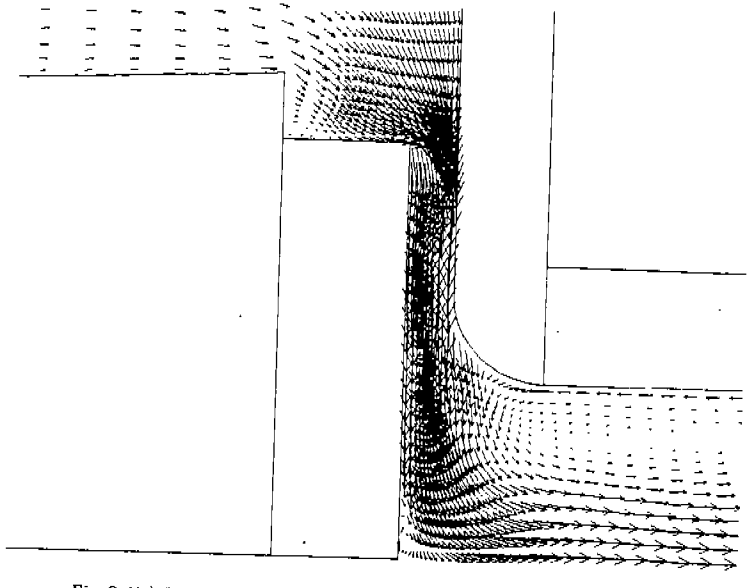

Fig.9 ii.) Velocity Vectors in Valve Plate Region @ h/h_{max} = 0.2 for Low Pressure Air ($Re_s \sim 2x10^4$)

CFD AND LDA STUDIES OF FLOW THROUGH A PLATE VALVE.

Dr A.B. Tramschek, Senior Lecturer & Dean of Engineering
University of Strathclyde,
Glasgow, Scotland.

A. Nasr, Research Assistant
University of Strathclyde,
Glasgow, Scotland

ABSTRACT

For many years compressor designers have utilised the results gained from steady state tests on valve assemblies to assist in compressor design processes and have employed various analytical models derived from experimental programmes. The present paper reports a continuation of this process, in that results derived from computational studies involving the PHOENICS computational fluid dynamics (CFD) code were able to be compared with experimental results based on conventional pressure measurements and Laser Doppler Anemometry (LDA) velocity measurements.

Computer analyses and experimental measurements were undertaken for a rotationally symmetric plate valve system with air as the working fluid. The working fluid was treated as an ideal gas with a simple relationship between its pressure, density and temperature. Calculations and measurements were performed for valve lift/valve port diameters in the range $0 < h/d < 0.2$, and valve plate diameter/valve port diameter ratios in the range $0 < D/d < 2.8$. The valve port diameter used throughout the tests was 25mm. Flow upstream of the valve was essentially a stagnation flow and overall system pressure ratios were in the range $1.0 > Pd/Pu > 0.75$, where Pd was generally the prevailing atmospheric pressure. Velocity and pressure distributions were obtained and used to demonstrate the degree of agreement between calculated and measured quantities and also to reveal the extent of the separation zone formed immediately downstream of the valve port exit plane.

Pressure distributions were measured using 30 or more pressure tappings distributed over the wall surfaces bounding the flow. Laser Doppler Anemometry techniques were used to measure radial components of fluid velocity in the gap between the valve plate and the adjacent fixed wall.

CFD calculations were made using various energy dissipation mechanisms. Flows were analysed on the basis of constant laminar viscosity, constant eddy kinematic viscosity and ultimately the $\kappa-\epsilon$ turbulent energy creation and dissipation model.

A comparison of calculated and measured velocity distributions and the extent of the resulting separation zone revealed that the calculated results appeared to suppress circulation and perhaps implied that a false diffusion mechanism was playing too significant a role in the calculations.

Attempts were made to mitigate this effect by modifications to the calculational schemes and the present paper shows the degree to which these attempts have been successful.

INTRODUCTION

Compressor designers have long recognised the crucial role that valves play in the operation of many positive displacement compressors and as a result there is available a wealth of literature (1) showing the important criteria that designers must consider when selecting reliable, efficient, economic to manufacture valve systems for use in compressors. The literature draws together the experiences of those who have designed, manufactured and operated compression machinery as well as those who have modelled either analytically or experimentally partial or complete compressor systems. Those familiar with the field will know of the diversity of contributions - models ranging from the most rudimentary to those using state of the art computational techniques - experiments ranging from those using the simplest of tools to those employing the latest developments in sensors and signal processing. This present paper fits into this pattern in that it brings together computational and experimental work on a simple plate valve arrangement. It reports on the use of a highly developed fluid dynamics code PHOENICS (2) in association with a Laser Doppler Anemometry investigation of the flow through an

axially symmetric disc valve. As a result, it has been possible to compare calculated and experimentally derived velocity and pressure distributions at various locations throughout the valve system. The study was performed for a series of steady state operating conditions as the resulting data can be employed in a quasi steady fashion when modelling the dynamic behaviour of compressor systems.

VALVE GEOMETRY

An extremely simple geometry was chosen for the study in that the valve comprised a single circular disc placed directly over a circular hole in a valve plate. The gap between the disc and the valve plate could be varied in a precise manner. The complete valve assembly formed the upper surface of a cylindrical chamber which was connected via a diffuser, pipework system, orifice meter and regulating valves to a compressed air supply. Air passing through the valve was discharged directly to the atmosphere. Details of the system are shown in Figure 1.

The diameter d of the hole (valve port) in the valve plate was 25 mm and a series of valve discs of different diameter D was manufactured such that D/d values in the range $1.04 \leq D/d \leq 2.8$ could be provided. Work reported in this paper relates to the use of a D/d value of 2.4. A gap adjusting mechanism allowed the gap (valve lift) h between the valve disc and the valve plate to be set at fixed values in the range $0.04 \leq h/d \leq 0.16$.

Some 30 pressure tappings were incorporated into the apparatus via a series of small holes in the valve disc and valve plate surfaces in the vicinity of the valve port. Details of the pressure tapping points are shown in Figures 2a, 2b, and 3.

WORKING FLUID AND OPERATING CONDITIONS

Experiments were performed in a laboratory having a compressed air supply capable of delivering air at 15 bar (gauge) pressure to the regulating and control valves upstream of the valve flow rig. The air supply temperature was typically in the range 10 to 20°C.

Control valves allowed the pressure in the cylindrical chamber upstream of the valve assembly to be held steady at pressures in the range $0 \leq P_{chamber} \leq 2$ bar gauge.

For calculational purposes air was treated as an ideal gas having the simple equation of state $P=\rho RT$. Values for the transport properties Cp, μ, k were taken from standard tables at the corresponding pressure and temperature conditions. Flow through the valve was assumed to be adiabatic.

EXPERIMENTAL TECHNIQUES

Pressure Measurements

Pressure measurements were made using a water filled multi tube manometer whose tubes were individually connected to the pressure tappings distributed throughout the apparatus. By photographing the manometer it was possible to get an instantaneous picture of the fluid levels in some 30 manometer tubes and thereby obtain pressure distributions in the valve assembly and the orifice flow metering system. The use of the photographic technique enabled slight variations in the valve plenum chamber pressure during a test run to be accommodated. Details of the pressure tapping locations are shown in Figures 2 and 3. Pressure tappings were made in the lower surface of the valve disc, the upper surface of the valve plate and in the valve port. The flow was assumed to be rotationally symmetric and the tapping points on the valve disc and valve plate were located at different radii on a spiral path in order to facilitate connections and eliminate interference.

An attempt was made to ensure that an adequate number of closely spaced holes would exist in regions where significant pressure gradients were expected with the number and location of the holes being guided by the preliminary predictions of the PHOENICS computer code.

Pressure measurements were made for a number of flow rates determined by the relative values of the plenum chamber and atmospheric pressure levels and a combination of both D/d and h/d values. The monitored values for the plenum chamber pressure and the lowest pressure indicated by one of the tapping points would indicate that the flow had not choked.

Velocity Measurements

A commercially available Laser Doppler Anemometer system was used to measure the radial component of fluid velocity at different locations in the gap between the valve disc and the valve plate. Laser anemometry is a non intrusive technique and the presence of beams of laser light does not disturb the basic flow pattern. The technique does however require the mounting of an appropriate laser beam and photomultiplier system with a facility to traverse the focus of the laser beams to desired locations. Since the technique relies on the scattering of light from flow borne particles it was necessary to seed the flow with a supply of oil particles of less than 5 micron diameter.

The valve flow rig exhibits rotational symmetry and hence by choosing to traverse the laser beam probe parallel to a given diametral line a complete range of radial locations could be covered. By adjusting the vertical location of the traverse plane, measurements could be effected for different points in the gap between the valve disc and the valve plate.

Figures 4 and 5 show details of the probe mounting and traversing system. In the system employed, two laser beams lying in a plane parallel to that of the valve disc intersect to produce interference fringes on the measuring diameter. Seeding particles moving with the flow cross the interference fringes and bursts of scattered light can be detected by a photomultiplier system thereby allowing the radial component of the flow velocity to be measured.

EXPERIMENTAL RESULTS

Velocity Measurements

Velocity measurements were made at radial locations corresponding to important regions of the pressure profiles. Thus three distributions were obtained for the central region of the flow directly above the valve port, see Figures 6a,6b,6c.

Six further locations were used to illustrate significant features of the flow in the valve disc - valve plate gap, see Figures 7a,7b,7c. Results from these locations illustrate, flow separation, flow reattachment and flow recirculation and their disposition relative to the position at which minimum pressures are recorded. Such results provide useful information about the shape, extent and strength of the resulting recirculating flow regions and provide valuable evidence by which to judge the validity of results calculated by computer codes such as PHOENICS.

Pressure Measurements

Figure 8 shows a typical radial pressure variation for the gap region. Results taken from the tappings on the valve disc show high pressure values in the centre of the disc. The pressure remains reasonably constant until a radius corresponding to the valve plate port hole radius is reached. For further outward radial movement the pressure decreases rapidly to a minimum value before recovering to attain the prevailing atmospheric pressure value at the edge of the disc. Results taken from tappings on the valve plate show corresponding behaviour where disc and plate results co-exist. The valve plate results lie slightly below the valve disc results in the central part of the system but converge with the disc results at the outer region of the disc.

For a given gap (h/d ratio) the radial pressure profile is preserved for a range of flow rates corresponding to a succession of upstream plenum pressures. The maximum pressure values recorded in the centre of the disc rise whilst the minimum value in the gap decreases further as the flow rate is increased. The location of the point of minimum pressure does not appear to move. Figure 8 illustrates these points. There is general agreement between the trends shown by pressure and velocity measurements and simple predictions based on the application of Bernoulli's equation for flow along a given streamline. At the centre of the flow the velocity is essentially axial in direction and the pressure

on the disc surface corresponds to the stagnation pressure for the flow. At the edge of the valve port the flow has taken on more of a radial characteristic, local velocities have increased and the pressure has fallen. At slightly greater values of radius increased radial velocities are associated with further reductions in pressure. As the edge of the valve disc is approached a diffusion process associated with increasing flow area results in reduced velocity and increasing pressure levels.

CALCULATED RESULTS

The PHOENICS computer code is a generalised CFD code which solves the discretized form of the governing fluid dynamic equations see Patankar (3).The PHOENICS computer code was used to obtain calculated results for a series of cases for which corresponding experimental evidence had been collected. Thus set values of d, D/d, h/d were employed together with known values of downstream pressure, upstream pressure, upstream temperature and system flow rate. Density variations in the flow were accommodated by a simple ideal gas representation of the equation of state i.e. $P=\rho RT$. A constant value of 1×10^{-5} kg/ms was adopted for the viscosity of air.

PHOENICS gives users the facillty to activate a variety of turbulent kinetic energy production and dissipation models as part of the calculational process and this paper presents the results of the exercise of two such models. The first set of calculations employed only a constant value laminar viscosity (μ) approach. The second set of calculations employed the full blown $\kappa-\epsilon$ turbulent kinetic energy creation and dissipation terms in addition to normal viscous dissipation effects. Results for the constant laminar viscosity case show a recirculation region which lies well downstream of the corner of the valve port and which has a different location, shape and size to those revealed by the corresponding experimental pressure and velocity measurements – see Figure 9 (calculated) and Figure 8 (measured).

The calculated radial pressure profile does not exhibit the same degree of pressure reduction in some parts of the flow as was observed in practice.

Similar comments apply to the calculated velocity values. The inbuilt solution techniques ensure that the calculated pressure and velocity values are consistent. However the agreement between measured and calculated velocities varies according to which region of the flow is being considered. Calculated and measured radial velocity components agree in central region of the valve port where the flow is contracting and no significant energy dissipation is occurring, see Figures 6a, 6b, 6c.

Similar comments apply to pressure and velocity components calculated using the $\kappa-\epsilon$ routines within PHOENICS.

Neither the simple constant viscosity treatment nor the $\kappa-\epsilon$ turbulent kinetic energy process adequately predicted the pressure and velocity fields in the gap region where separation, reattachment and recirculation occurs. The $\kappa-\epsilon$ calculations caused the centre of the recirculation zone to move upstream towards the port corner but reduced its size considerably. The inclusion of turbulent kinetic energy consideration (into the calculations) had made the flow appear to be more viscous than it really is. Figure 10 illustrates these effects.

Careful examination of the experimental and calculated results prompted the authors to question whether a false diffusion mechanism associated with the form of the PHOENICS calculations was responsible for the discrepancies.

False diffusion effects, Raithby (4), are known to occur with many difference schemes in flow fields where the resultant velocity vector at particular points in a flow field is inclined at 45° to the directional axes of the calculational grid. The effect is amplified as the fluid velocity increases. The valve geometry currently being studied contains all the ingredients where false diffusion effects associated with the calculational schemes embodied in the PHOENICS code might be expected to be present. A 90° change in the direction of the main flow field inevitably means that in parts of the flow field the velocity vectors will be inclined at 45° to the principal grid directions. Small gaps between the valve disc and the valve plate are associated with significant fluid velocities. False diffusion

effects are less noticeable with low velocity flows. Figure 12 shows results for a two dimensional plane geometry at a greatly reduced flow rate. In this case the centre of the predicted recirculation zone has moved upstream and is closer to the port corner.

The PHOENICS computer code contains a facility which permits the user to introduce user developed routines (2) into parts of the code thereby allowing alternative schemes to be deployed.

In its standard form the PHOENICS code uses equations linking cell variables with the corresponding values in neighbouring cells via the components of fluid velocity normal to the cell surfaces. The upwind difference formulation employed is known to introduce false diffusion effects for flows inclined at 45° to the principal grid orientations. To overcome this effect a modification was introduced which allows greater account to be taken of the variable values in cells lying in a direction along which the fluid has travelled.

At the time of writing this paper coding modifications had been effected for the plane cartesian X-Y coordinate system and further coding changes were being put in train to handle the axi-symmetric R-Z system.

The efficacy of the modifications was tested by undertaking a comparison of modified and unmodified PHOENICS calculated results with experimental results obtained by Duggins (5), (6) in a 2 dimensional large scale model of a plate valve employing water as the fluid medium.

The unmodified PHOENICS results show generally good agreement with Duggins experimental results. This is partially attributable to the low velocity throughout the flow field and the viscosity of the fluid medium (water), Figure 11.

The modified calculations have raised the upstream pressure level slightly and caused a further reduction in pressure immediately downstream of the corner of the flow. This is precisely the form of change needed to bring about a better match between the calculated and measured results for the rotationally symmetric system being studied by the authors.

CONCLUSIONS

Whilst very considerable advances have been made in the development of calculational and experimental techniques used to study fluid flows, it must however be recognised that difficulties can still arise when computer codes employing difference schemes are applied to geometries where very sudden changes in flow direction are involved. Research workers performing fluid dynamic calculations on the types of flow and geometrical arrangements found in compressor valve systems would be well advised to pay attention to the effects of "false diffusion" which may be present in any calculational scheme that they might employ.

REFERENCES

1. Soedel, W. "Design and Mechanics of Compressor Valves", Purdue University, 1984.
2. Rosten, H.I., Spalding D.B., "PHOENICS User Manual" CHAM TR200 (1987).
3. Patankar, S.V. "Numerical Heat Transfer and Fluid Flow" Hemisphere, 1980.
4. Raithby, G.D. "Skew Upstream Differencing Scheme for Problems in Fluid Flows" Comp. Methods. Appl. Mech. Eng. 9 (153-164) (1976).
5. Duggins, R.K. "A Potential Flow Model for a Closed Separation Region." Proc. I.Mech.E., Volume 182, Part 3H, 1967-68.
6. Duggins, R.K. "A Study of Flow in a Plate Valve." Ph.D Thesis, University of Nottingham, 1962.

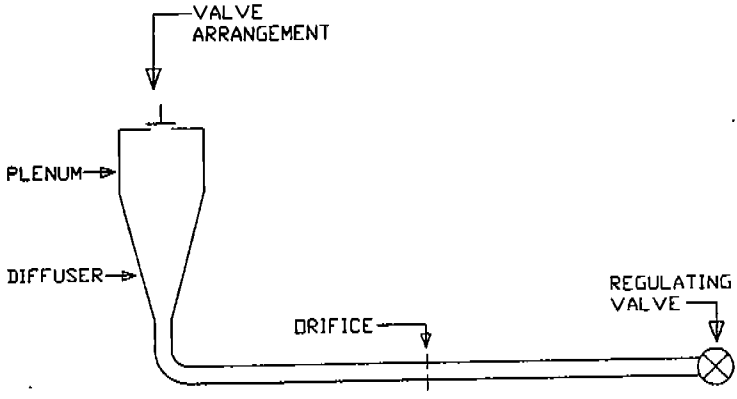

(FIG. 1) LAYOUT OF THE TEST RIG.

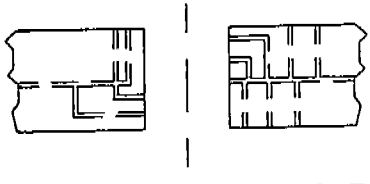

(FIG. 2A) PRESSURE TAPPINGS IN THE PORT AREA.

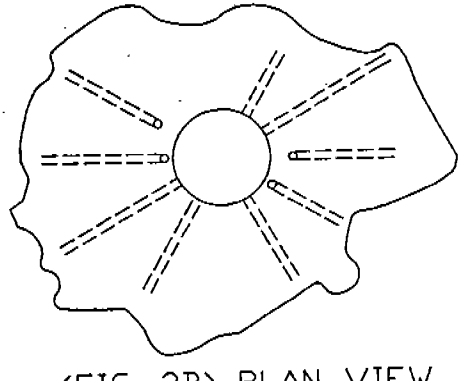

(FIG. 2B) PLAN VIEW FOR THE PRESSURE TAPPPINGS IN PORT.

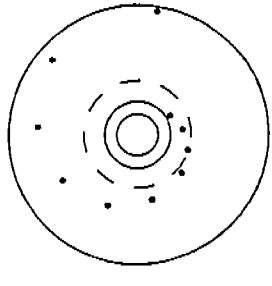

(FIG. 3) PRESSURE TAPPINGS IN THE VALVE DISC.

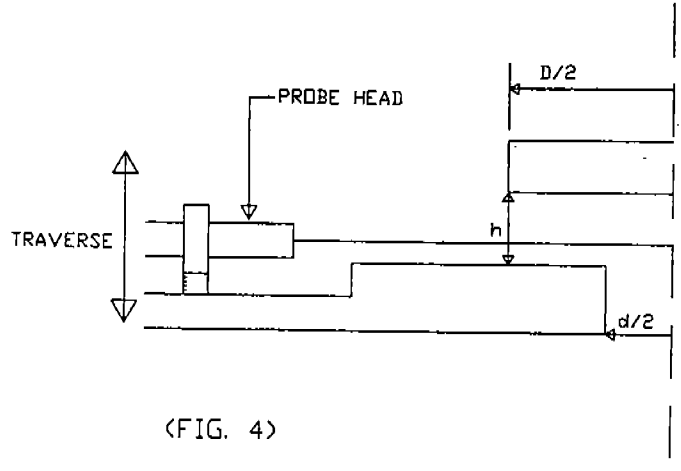

(FIG. 4)

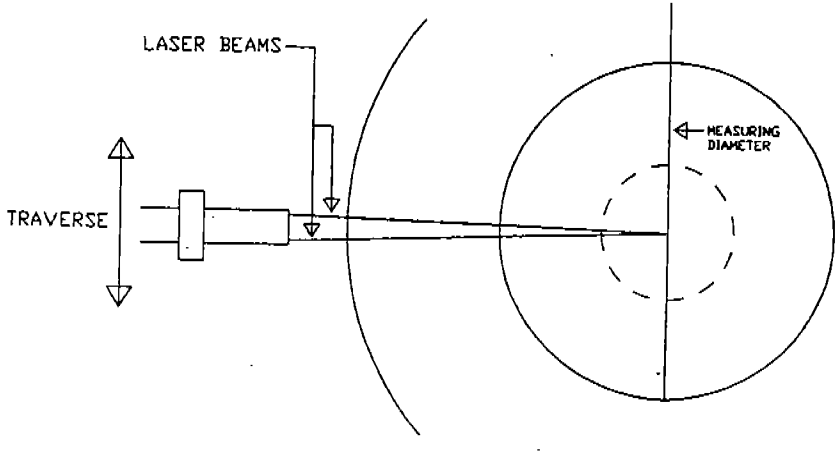

(FIG. 5)LASER DOPPLER VELOCITY MEASUREMENTS.

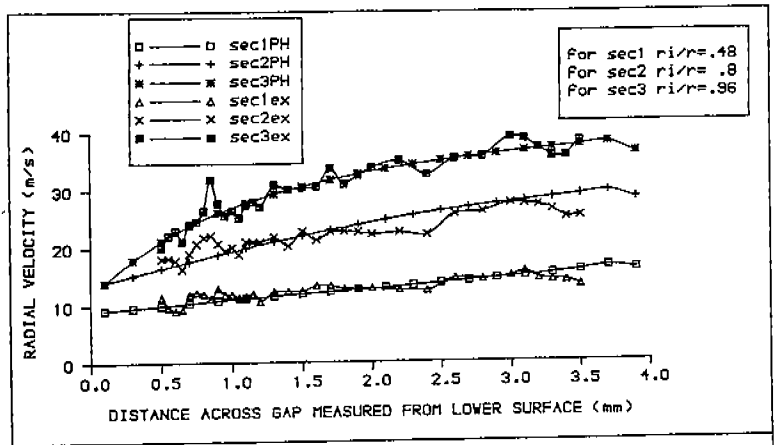

(FIG.6A) COMPARISON OF MEASURED AND CALCULATED RADIAL VELOCITY FOR 4 mm GAP

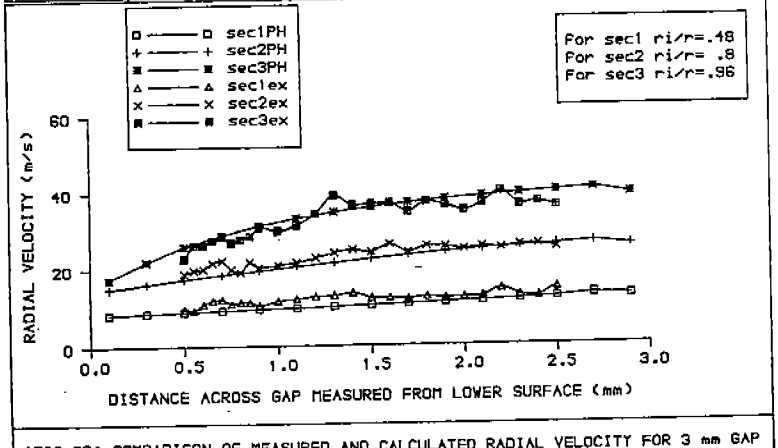

(FIG.6B) COMPARISON OF MEASURED AND CALCULATED RADIAL VELOCITY FOR 3 mm GAP

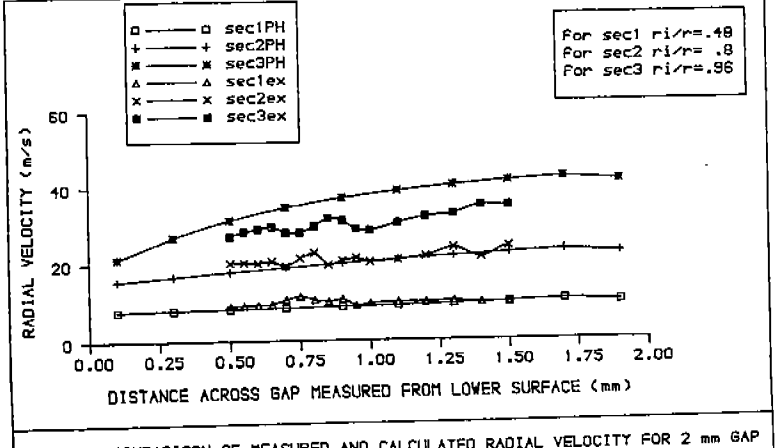

(FIG.6C) COMPARISON OF MEASURED AND CALCULATED RADIAL VELOCITY FOR 2 mm GAP

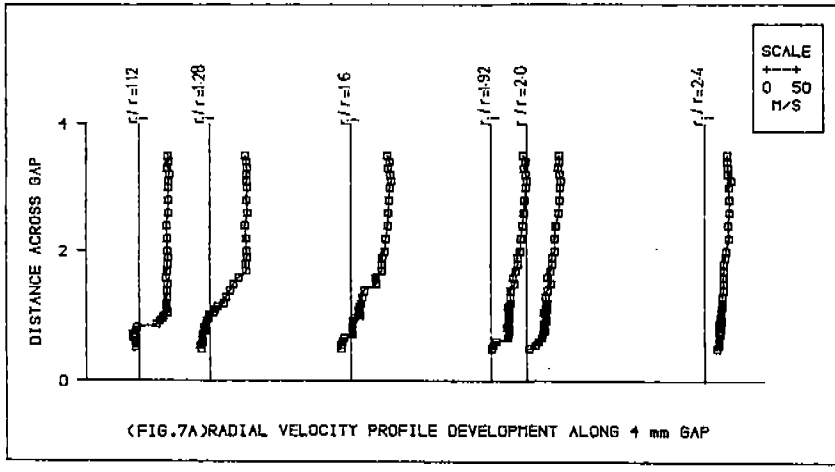

(FIG.7A)RADIAL VELOCITY PROFILE DEVELOPMENT ALONG 4 mm GAP

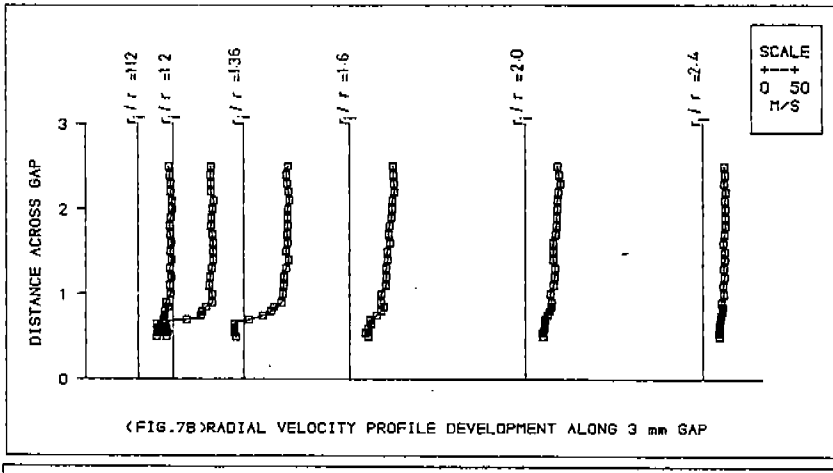

(FIG.7B)RADIAL VELOCITY PROFILE DEVELOPMENT ALONG 3 mm GAP

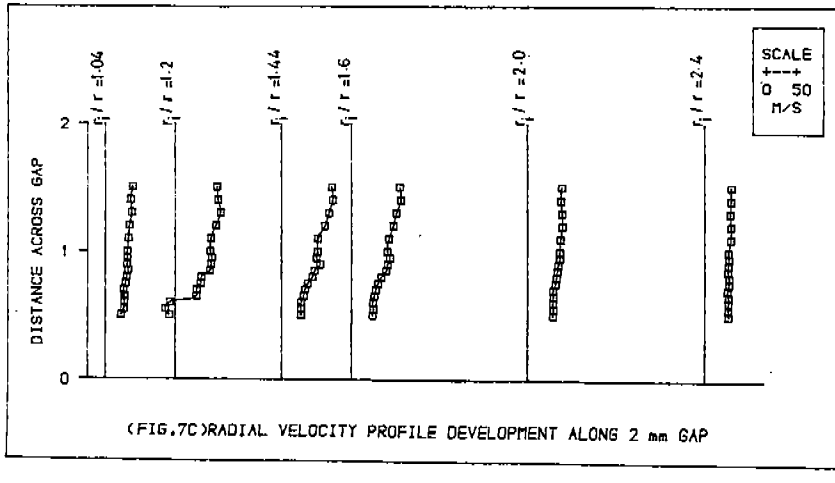

(FIG.7C)RADIAL VELOCITY PROFILE DEVELOPMENT ALONG 2 mm GAP

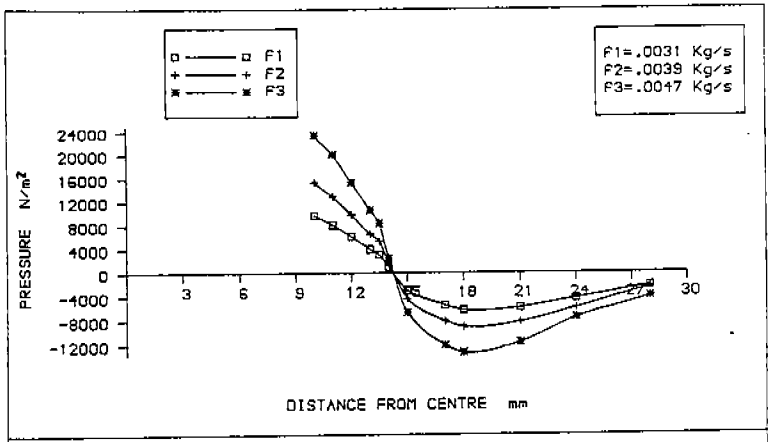

(FIG.8A)EXPERIMENTAL PRESSURE DISTRIBUTION OVER DISK D/d =2.4,h=4 mm

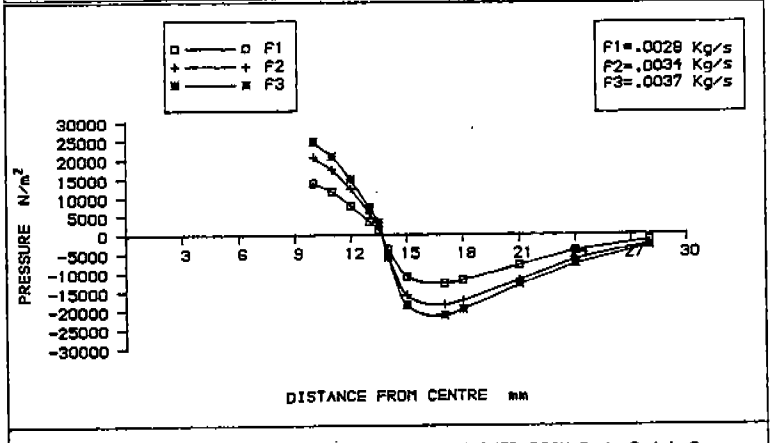

(FIG.8B)EXPERIMENTAL PRESSURE DISTRIBUTION OVER DISK D/d =2.4,h=3 mm

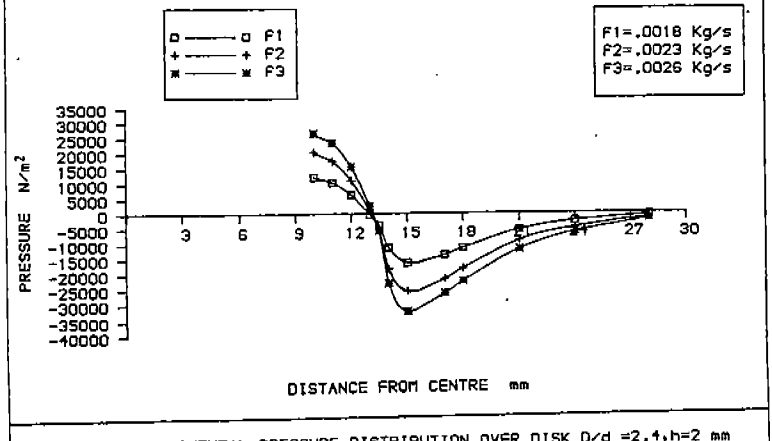

(FIG.8C)EXPERIMENTAL PRESSURE DISTRIBUTION OVER DISK D/d =2.4,h=2 mm

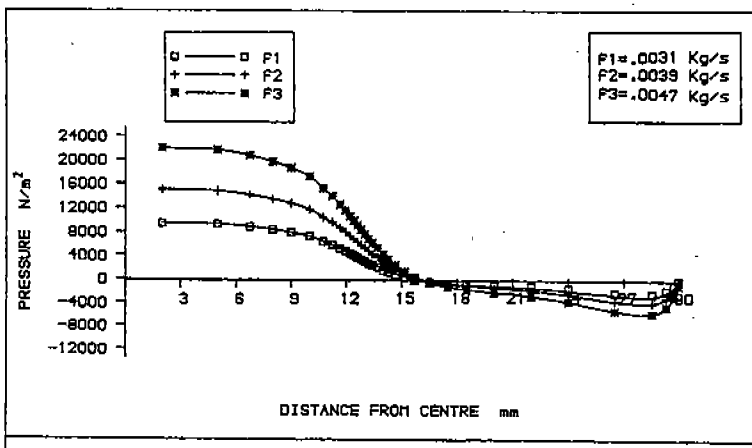

(FIG.9A)CALCULATED PRESSURE DISTRIBUTION OVER DISK,LAMINAR, D/d =2.4,h=4 mm

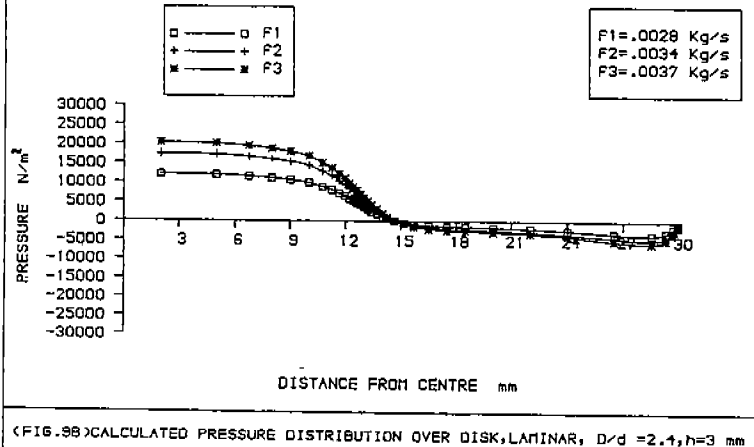

(FIG.9B)CALCULATED PRESSURE DISTRIBUTION OVER DISK,LAMINAR, D/d =2.4,h=3 mm

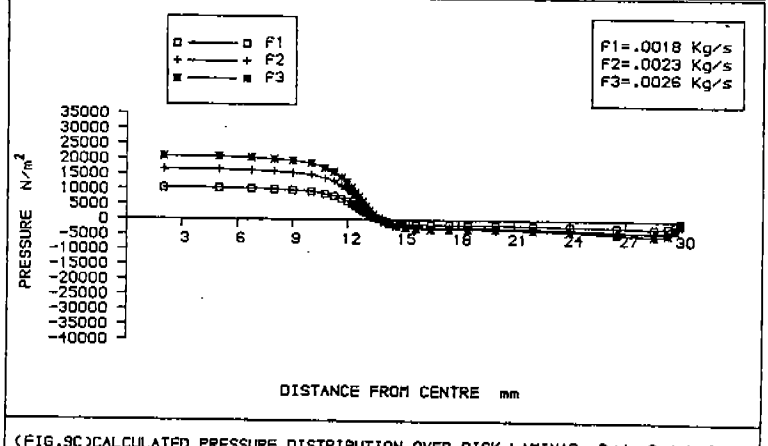

(FIG.9C)CALCULATED PRESSURE DISTRIBUTION OVER DISK,LAMINAR, D/d =2.4,h=2 mm

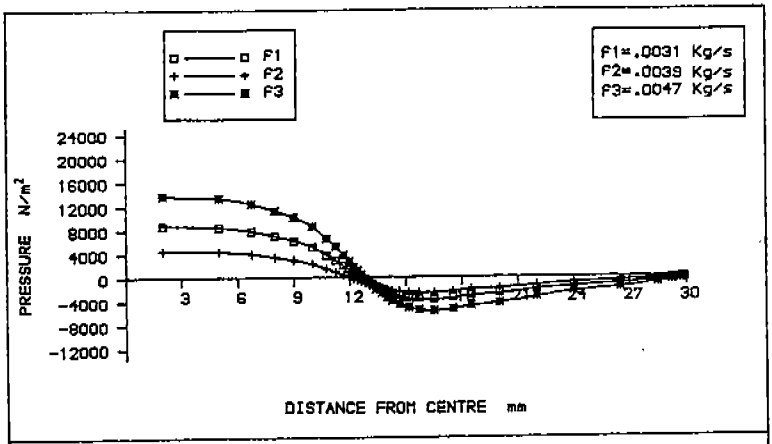

(FIG.10A)CALCULATED PRESSURE DISTRIBUTION OVER DISK,K-E, D/d =2.4,h=4 mm

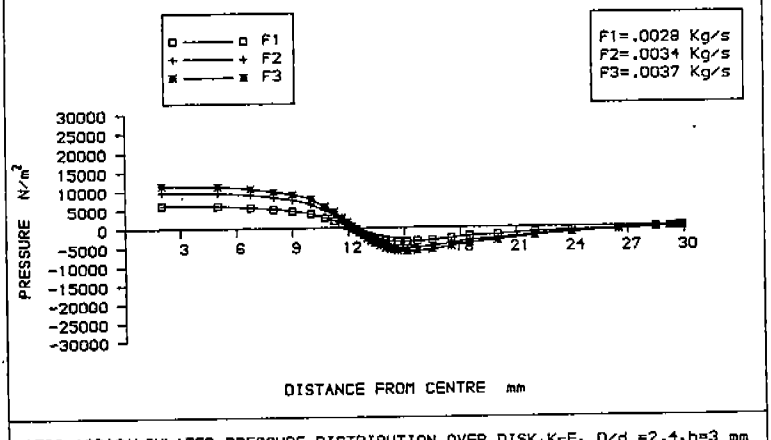

(FIG.10B)CALCULATED PRESSURE DISTRIBUTION OVER DISK,K-E, D/d =2.4,h=3 mm

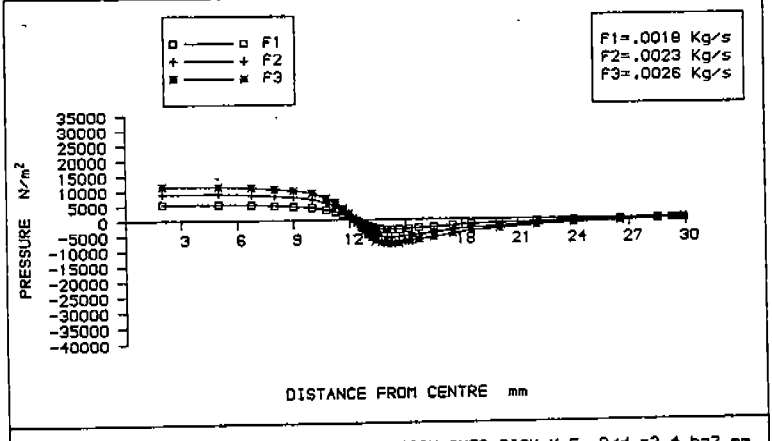

(FIG.10C)CALCULATED PRESSURE DISTRIBUTION OVER DISK,K-E, D/d =2.4,h=2 mm

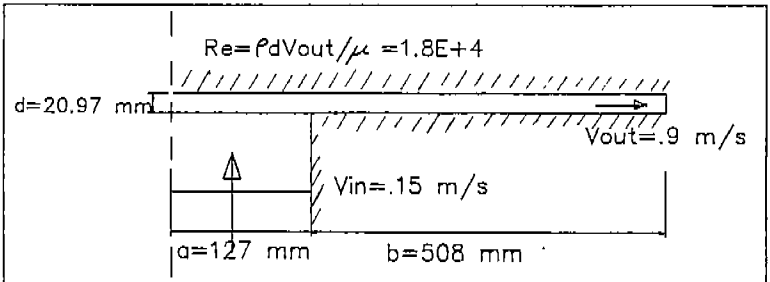

(FIG.11) PRINCIPAL DIMENSIONS OF TWO DIMENSION WATER FLOW MODEL.

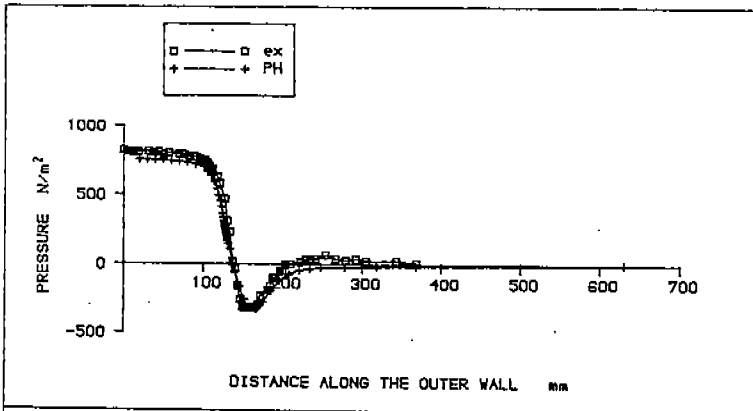

(FIG.12A)COMPARISON BETWEEN EXPERIMENT AND STANDARD PHOENICS

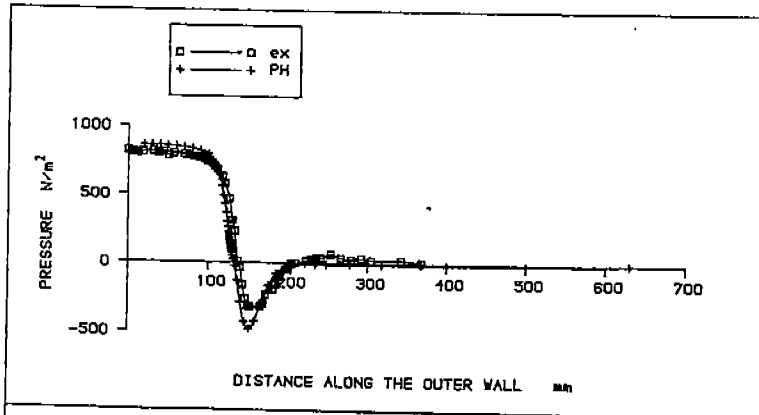

(FIG.12B)COMPARISON BETWEEN EXPERIMENT AND MODIFIED PHOENICS

"DEVELOPED MATHEMATICAL MODEL OF THE SELF-ACTING VALVES OF THE RECIPROCATING COMPRESSOR AND ITS APPLICATION FOR TONGUE VALVES "

M. ŁUSZCZYCKI, P. CYKLIS, J. ŻELASKO
Department of Thermodynamics and Heat Machines Measurements,
Technological University of Cracow (Poland)

ABSTRACT

In the paper an extended mathematical model of compressor self-acting valves has been presented. The model provides a better possibility of a more precise analysis of the valve action, in particular collisions between the working plate and valve stop or seat. An elasto-plastic model of collision has been introduced. A method of the application of the mathematical description for both plate valve and valve with deformable working element has also been presented. The description of valve operation has been used on a simulation model of gas and refrigerating compressor. In the model the heat exchange in the cylinder and medium loss due to the leakage have been considered. The medium has been described individually by a selected equation of state of real gas. The dynamic effect of the installation has also been taken into account on the basis of the acoustic model. The model has been verified in experimental tests of small gas and refrigerating compressors with inlet tongue valves.

INTRODUCTION

Numerous investigations in the field of air, gas and refrigerating compressors carried out in our Department were the basis to work out a universal, one-dimensional model describing the processes occurring in the reciprocating compressor. The complex model describing thermodynamic gas in the compressor cylinder, taking into consideration the influence of installation have been worked out. The analysis showed that while creating the reciprocating compressor simulation model special attention should be paid to working valves dynamics. Hence in the mathematical description of the valves operation all the most important phenomena determining their work have been considered. The mathematical model has been worked out for plate valves most frequently used in a new types of compressors . The worked out model of valves, though one-dimensional can be successfully adopted for different type of valves with deformable working element such as tongue or channel valves which are frequently used in small or medium refrigerating compressors.

DESCRIPTION OF PROCESSES IN RECIPROCATING COMPRESSOR CYLINDER.

The mathematical model of valve action presented in this paper is an integral part of a complex model of the compressor, based on the I law of thermodynamics for the medium in the cylinder. The medium has been treated as real gas, and both the effect of leakage and heat exchange in the cylinder have been taken into account. After introducing differentiation with respect to crank angle φ one obtains the equation describing thermodynamic changes in the cylinder in the form:

$$\frac{dT}{d\varphi} = \frac{1}{m c_v}\frac{dQ}{d\varphi} - \frac{h}{m c_v}\frac{dm_t}{d\varphi} - \frac{h}{m c_v}\frac{dm_n}{d\varphi} + \frac{h_{cs}}{m c_v}\frac{dm_s}{d\varphi} - \frac{h}{m c_v}\frac{dm}{d\varphi} -$$

$$-\frac{T}{m\,c_v}\left[\frac{\partial p}{\partial T}\right]_v\frac{dV}{d\varphi}+\frac{vT}{m\,c_v}\left[\frac{\partial p}{\partial T}\right]_v\frac{dm}{d\varphi} \qquad (1)$$

In this equation the following notation has been used on T - temperature, p - pressure, v - specific volume, h - enthalpy, m - mass, h_{cs} - enthalpy of the medium entering the cylinder through suction valve, c_v - specific heat.

$\frac{dm_s}{d\varphi}$; $\frac{dm_t}{d\varphi}$; $\frac{dm_n}{d\varphi}$ - mass flow through suction, discharge valves and leakage, respectively

Equation (1) has been supplemented by the mass balance and kinematic relationship for compressor volume $V(\varphi)$. In our model the working medium can be treated as both ideal gas described by Clapeyron's equation and real gas describedby equation of state, adequate for the given medium. The refrigerant properties have been defined on the basis of Redlich-Kwong-Soave equation of state, introduced in the form of computer library.

The method of calculation of heat exchange rate in the cylinder has been based on the relations given in [7]. In the presented model this dependence has been made more complete by introducing, on the basis of global energy balance for cylinder wall, an iterative formula for calculating its mean temperature $T_{śc_i}$:

$$T_{śc_i}=\frac{\int_0^{2\pi}\frac{dQ_{i-1}}{d\varphi}(\varphi)d\varphi+2\pi N_f}{2\pi A_z k_{ch}}+T_m \qquad (2)$$

where: index i denotes i-th crankshaft revolutism, N_f - power lost on friction in cylinder, A_z - area of outer surface of cylinder cooled by refrigerant, k_{ch} - substitute of overall heat transfer coefficient which does not consider convection coefficient from cylinder side.

The heat loss due to leakage in cylinder piston system has been described in a simple form experimentally confirmed given in [3]. In the program there has also been included the possibility of valve leakage simulation, which so far has been neglected.

Installation of the gas under compression is a wave-guide, which can be modeled as a system of series connected tubes of various diameters. The calculation of the run of changes in a pressure pulsation in this installation requires a solution of the partial differential equations which describe pulsating flow of gas with equivalent boundary conditions taken into account. The equations describing pulsating flow of gas in a straight pipeline of constant cross-section are considered below. These equations are derived by means of various simplifying assumptions on the basesof equations of movement, equation of continuity and equation of state Assuming that the gas density is constant and equal to its mean value with respect to time and linearizing nonlinear resistance expression, this equation can be presented in the following form:

$$\begin{cases} -\dfrac{\partial v}{\partial t} = \alpha \dfrac{\partial p}{\partial x} + \gamma v \\ -\dfrac{\partial p}{\partial t} = \beta \dfrac{\partial v}{\partial x} \end{cases} \qquad (3)$$

where: $\alpha = \dfrac{A}{\rho_o}$, $\beta = \dfrac{\rho_o a^2}{A}$, $\gamma = \dfrac{\lambda w_o}{2D}$;

Symbol p denotes here variable pressure of gas, t - time, D - internal diameter of pipeline, a - sonic gas velocity, λ - friction losses factor, w_o - mean analytical gas velocity, A - cross-sectional area of the tube, ρ_o - mean gas density, v - variable volumetric velocity. The equations of non stationary flow have been solved on the basis of electro-acoustic analogy. This made it possible to solve this problem on the PC computer taking into consideration also multicylinder interaction problem.

GENERAL DYNAMIC MODEL OF COMPRESSOR SELF-ACTING VALVES

The movement of valve working plate with mass m (fig.1) can be described by equation:

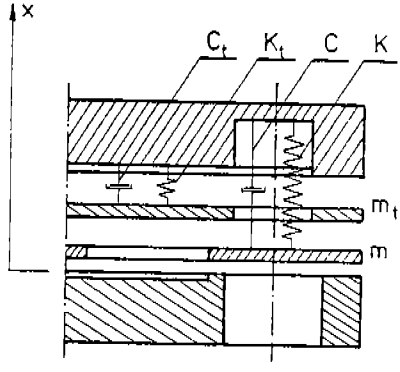

Figure 1. Phisical model of the self-acting valve.

$$\left[m + m_t H(x-x_t)\right]\ddot{x} + \left[C(\dot{x},x) + C_t(\dot{x},x)\,H(x-x_t)\right] + \left[K(x) + K_t(x)H(x-x_t)\right] = \qquad (4)$$

$$= F_s - F_{10}\delta(x) + F_{1,1}\,\delta(x-h) + F_{1t}\delta(x-x_t) + S_0(R_0,\dot{x}_-)\delta(x) + S_-(R_1,\dot{x}_+)\delta(x-h)$$

In this equation the effect of dumping plate with mass m_t has been considered by introducing Heafiside function H(x), nonlinear force of elasticity K(x) and nonlinear force of dumping C(x,ẋ). Sticking of the working plate to seat F_{10}, valve stop F_{11} and dumping plate F_{1t} have also been taken into account. Moreover, collision impulse forces S_0 and S_1 depending on coefficient of restitution R_1 and velocity before collision have been introduced. A two-parameter model of collision has been adopted. The flow force F_s on the valve plate has been determined on the basis of dependencies commonly adopted for the given type of valve, or on the ground of results of static tests.

Eq. (4) has been derived for plate valves but it is possible to extend this method for mathematical description of valve working plate dynamics. To make its application possible a method of calculating equivalent forces and concentrated masses has been worked out for this type of valves. As follows from both theoretical solutions [2] as well as experiments (Table I) the tonque valve plate vibrates when the valve is being opened with a frequency higher than the frequency of first harmonic of free vibrations. This means that the tonque valve plate should be treated as a vibrating system in which the vibration frequency is determined by cyclic rebounds of the valve plate tip against stop A method of calculating equivalent forces and concentrated masses is based on the assumption that the equivalent mass is concentrated at the seat geometric center and that the stream pressure is applied at the same point. Until contacting the valve stop the working plate behaves as a fixed rod loaded by a concentrated force It is assumed that the part of the rod off the point of force application is not deformed until it gets into contact with the stop. From the moment it contacts the stop, the plate is treated as a rod of length l fixed on one side, and on the other side support is rotational and slideable, loaded by a concentrated force (fig. 2).

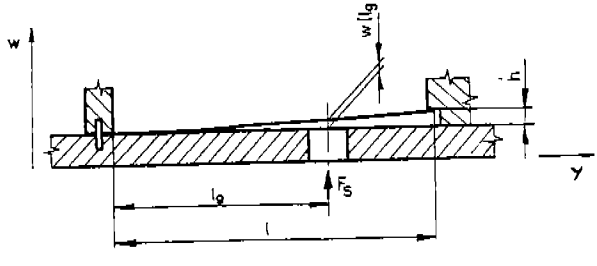

Figure 2. Scheme of a tongue valve plate

Depending on the relation between the stream pressure and elasticity, its tip may be torn away from the stop when the valve is opened, or it may remain in contact all the time. The values of forces induced by the plate elasticity vary in particular phases of its deformation. The numerical values of these forces can be defined experimentally or calculated on the basis of dependencies from the theory of elasticity. On the ground of this theory it is also possible to determine the lift at any point of the plate at any point of time.

As a result of elasticity force the valve plate, after reaching the maximal deflection, makes effort to return to its primary position. The height of displacement of the tip of the valve plate reaching the valve stop w(l) is equal to the maximal valve lift h and could be expressed by the formula:

$$h = w(l) = w(l_g) + w'(l_g)(l - l_g) \qquad (5)$$

in which the heigh of valve displacement at the point of flow force action is

denoted as $w(l_g)$ and:

$$w(l_g) = \frac{F\, l_g^3}{3\, E \int_0^{l_g} \frac{J(y)}{y}\, dy} \qquad (6)$$

where: E - Young's modulus, J(y) - moment of inertia of valve plate in cross-section y, $w'(l_g)$-value of first derivative of function describing the plate shape as l_g point

Formula (5) makes it possible to calculate the displacement of the reduced at the concentrated mass at the moment the valve tip reaches the limiter.

The reduced mass has been calculated on the basis of conventional mechanical relation of the displacement equilibrium:

$$m_r = \frac{\sum_{i=1}^{n} m_i\, w(l_i)}{w(l_g)} \qquad (7)$$

In this equation m_i denotes the mass of tongue valve part with the displacement $w(l_i)$. The m_i values depends on the shape of the cross section in the corresponding fragment of valve plate The value of the reduced mass depends on the phase of valve movement. The calculated reduced values of mass m_r and displacement w(l) correspond with the values m, m_t, and x in equation (4).

To describe the state of medium flowing through the valve various equations of state can be applied. Most commonly the flowing medium is treated as ideal gas. The authors treat the medium flowing through the valve as real gas described by equation:

$$p = \frac{\sigma(p,T)\, R\, T}{V} \qquad (8)$$

the coefficient of compressibility σ being selected seperately for medium mean parameters for inlet or outlet valve. The flows through valves have been calculated on the basis of Costagliola's equations, derived with the assumption that the flow is steady. However to improve the model also the inertia of gas in the valve gap has been considered especially during opening and closing the valves. It has been decided to introduce the correction for gas inertia based on the assumption that the pressure difference on the valve gap changes in a linear way during the time that elementary mass of gas flows through the gap.

EXPERIMENTAL VERIFICATION OF THE SIMULATION PROGRAM WORKED OUT

The verification of the above presented mathematical model and the computer simulation program based on this model have been carried out on the basis of experimental investigations of two refrigerating compressors SAF-23 and SAF-5 of Polish make. Both compressors have been equipped with suction tongue valves (fig. 3) and discharge channel valves. The investigation has been carried out within a very broad range of variations of compressing ratios determined by standard temperatures of coolant vaporization and condensation. During the tests the pressure pulsations in the cylinder and valve plate displacement have been registered. The valve plate displacements have been recorded using our own construction capacitance transducer, coupled with the traditional measurement system consisting of the feeder, amplifiers

and oscilloscope. The graph of plate displacements in the function of crank angle obtained on the oscilloscope screen have been photographed. In fig.4 the displacement of chosen point of the suction valve for both compressors obtained by measurements and simulation have been compared.

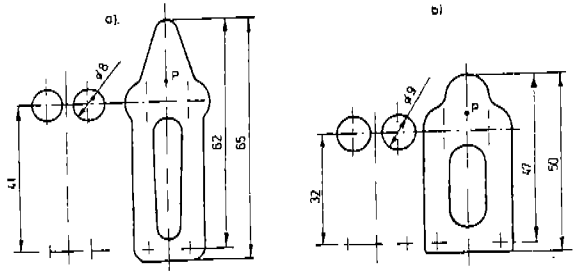

Figure 3. Shapes of suction valve tongue plates of a)SAF-23 compressor, b) SAF-5 compressor

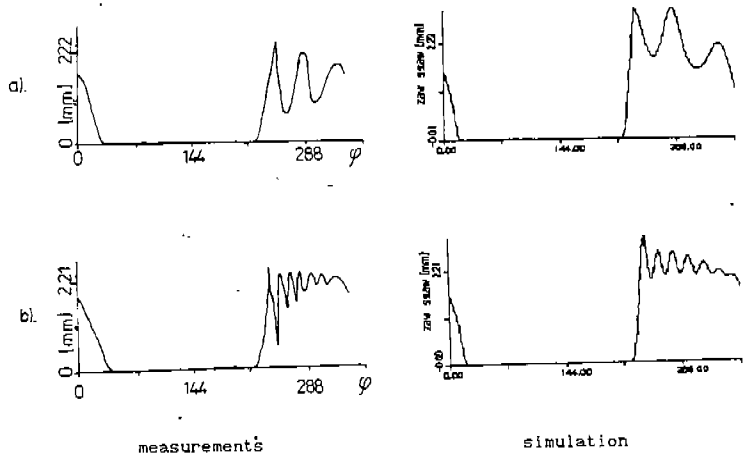

Figure 4. Displacement of chosen point of suction valve obtained by measurements and simulation. a) SAF-23, b) SAF-5.

In case of the SAF-23 compressor the used working medium used was air. This made it possible to define precisely the coefficients of medium flow through valves, by means of static tests, and besides it facilitated experimental registration of the valve plate displacement. In case of the SAF-5 compressor the investigations have been carried out using R-12 as a working medium, which allowed us to confirm the universality of the worked out model. Relatively simpler investigations of the SAF-23 compressor while pumping air, allowed us to carry out experiments over a broad range of working parameters. The tests have been made using valve plates with different thickness and the same shape. In fig.4a. the displacement of the valve plate for the recommended working parameters are shown. During compressor tests working in conditions significantly different from recommended ones the oscillations of a higher amplitude occurred. The valve plate worked with alternate collisions

with valve seat and stop. The same kind of movement has been achieved by means of computer simulation.

Pressure pulsations in valve chambers have a fundamental influence on the valve work. That is why while comparing registered and calculated valve plate displacements also pressure changes in the cylinder and valve chambers should be compared.

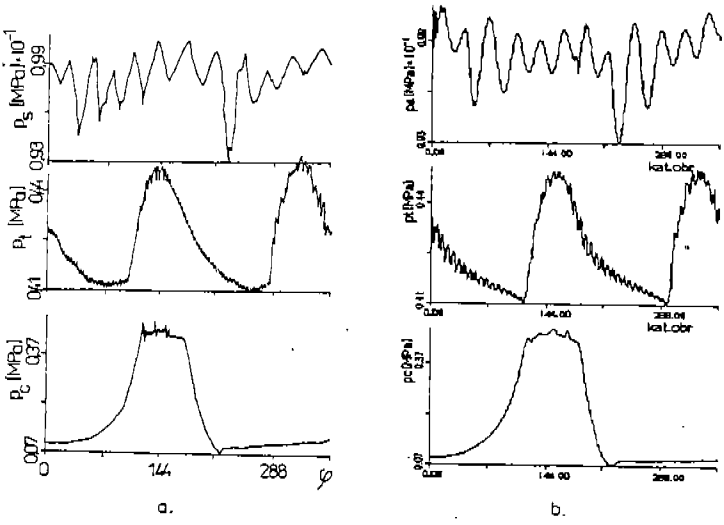

Figure 5. Pressure changes in the cylinder and valve chambers of SAF-23 compressor. a) measured b) calculated.

In fig.5 registered and calculated pressure pulsations in the cylinder and suction and discharge valve chambers for SAF-23 compressor are shown. They have been registered for the same working conditions as diagrams of suction valve displacements shown in fig.4a.

Interesting information could be provided by dynamic tests of the valve plates, carried out outside the compressor and especially its self-frequency oscillation tests. The results of test which have been carried out for suction valves of SAF-23 compressor are given in Tab.I.

TABLE I.

Oscillation frequency of the tongue valve.

Type of plate	Natural frequency of tongue valve [Hz]			Frequency of tongue valve during its work in compressor [Hz]	Remarks
mode	I	II	III		
"a"	45	290	320	----	without pin
	43	282	310	about 110	with pin
"b"	80	495	-	about 320	without pin

For the plate "a" from fig.3a the results of experiments for standard valve plate

and the plate with pin, which is the inner screen of the capacitor, are shown. The oscillation frequency of the valve plate during its work in the compressor has been calculated on the basis of the experimental results. What needs attention is the fact that the frequency of plate vibration during its functioning in the valve is about 2.5 - 4 times higher than the original frequency of natural vibrations of this plate determined by means of an oscillator. It follows both from the change of the oscillation character from the moment that the plate reaches its limiter, as well as the effect of collision itself. This confirms the results of theoretical works done by the authors earlier on the effect of rebound from the limiter and seat on the frequency of working plate vibrations in the valve shown in /3/. Those results have been used for working out the presented model.

CONCLUSION

On the basis of the investigations it can be stated that the presented mathematical model describing the functioning of compressor automotive valves is universal in character. It can be easily adapted for description of functioning of various types of compressor valves. An example of such an adaptation for an automotive suction tongue valve of a small refrigerating compressor has been demonstrated in this paper. The presented model of valve plate displacements, in which the frequency of its vibrations is determined by the phenomenon of cyclic rebound of its tip from the limiter,is closer to reality than the clasical model which does not cover such rebounds. An advantage of our model is the fact that it makes it possible to estimate the impulse forces of the working plate colliding with the limiter and seat. The model, together with the description of the phenomena in the compressor cylinder and adjoining installation, allows an analysis of valves acting during compressor work with various cooling media. The properties of these coolants can be described by means of individually selected equations of state for real gas.

REFERENCES

1. P. Cyklis: Mathematical model of real thermodynamic changes in cylinder of reciprocating compressor. Ph. D. Thesis, Tech. Un. of Cracow (1991) (in polish).
2. P. Cyklis, M. Łuszczycki, J. Żelasko: Influence of the dynamics of automotive valves on the energy loss in reciprocating compressor. II Symph. Energetic Poblems in Mechanics, Szczyrk, (1989) pp.45-52, (in polish).
3. J. Young., Zu'bi A. A.,Mac Laren J. F. T.: Piston leakage in hermetic refrigeration compressors. IIR Congress, Venice 1979.
4. S. Lawson, R. J. L. Mc Laren : An Approach to computer modeling of Reciprocating Compressor. Proc. of the 1984 Int. Comp. Eng. Conf. - at Purdue, West Lafayette, pp. 139-147.
5 M. Łuszczycki : Dynamic investigations of suction valves in a small refrigerating compressor. Proc. of the 1978 Purdue Comp. Tech Conf., West Laffayette, pp. 382-388.
6. M. Łuszczycki, J. Żelasko: Influence of dynamics of suction tongue valve on reciprocating compressor work. Proc. of XIV Thermodynamics Symph., Kraków (1990) pp. 468-475, (in polish).
7. Van der Meer J. S., S. W. Brook, S. Touber: Computer simulation of the reciprocating compressor with cyclic heat transfer - a usefull tool? IIR Congres, Sophia 1982.
7. E. H. Ng, A. B. Thramschek, J. F. T.Mc Laren : Mathematical modeling of a multicylinder refrigerating compressor using Helmholtz resonator and acoustic wave technique. II R. Congress, Paris (1983).
8. R. Singh, W.Soedel: Mathematical modeling of multicylinder compressor discharge system interactions. Journal of Sound and Vibration, Vol. 63, No 1 (1979).

CALCULATING MOOEL AND EXPERIMENTAL INVESTIGATION OF GAS LEAKAGE

Yuan Xiuling	Chen Zhiming	Fan Zhen
Professor	Research Engineer	Lecture
Refrigeration Division	Screw Research Lab.	Cryogenic Division

Xi' an Jiaotong University
Xi' an, P. R. China

ABSTRACT

In this paper, a new mathematical model to calculate gas leakage in small clearance is established. In the model, viscous force and inertia force are considered at the same time. Theoratical analysis and experimental results show that the calcuating results coincide well with the experimental results.

NOMENCLATURE

h	height of passage (m)
h_{min}	the smallest height of passage (m)
k	specific heat ratio
P	pressure (Pa)
p_1	pressure in high pressure cavity (Pa)
p_2	pressure in low pressure cavity (Pa)
R	universal gas constant (J/kg. k)
Q	volume flow rate (m^3/h)
r	piston radius (m)
T	temperature (k)
T_1	temperature in high pressure cavity (k)
u	partial veloceity along x direction (m/s)
w	partial velocity along z direction (m/s)
μ	kinetic viscosity ($N. s/m^2$)
ρ	density of gas (kg/m^3)
ξ	compressibility coefficient

INTRODUCTION

Gas leakage is an important factor affecting the performance of compressor. If more accurate equation is found to calculate leakage, we could do it better to predict compres-

sor's performance.

In many cases, leak—passage is composed of two curved surface with same length. This kind of leaking passage is unfolded as figure 1. For calculating the gas leakage through this kind of passage, nozzle flow model was used in most of literatures[1,2,3,4,5]. The precondition of this model is that the effect of viscous friction on flow is neglected. In other literatures[6], it is suggested to use viscous flow model. In this kind of model, the effect of inertia force on flow is neglected. In fact, because gas is easy to compress and it leaks through small clearance, both viscous force and inertia force have the equivalent influence on gas leakage.

In this paper, a new mathematical model is presented in which viscous force and inertia force are considered at the same time. The calculating results are compared with those of experiments. The comparison shows that the new calculating model is more accurate than nozzel flow model or viscous flow model. The accuracy of calculation is improved greatly.

FLOW FIELD ANALYSIS AND FUNDAMENTAL EQUATIONS

The leaking passage is shown in figure 1. When gas leaking occurs, the high pressure gas first flows into passage through section 1—1, then passes a small clearance channel in which section area is changing, and last flows out of passage through section 2—2. Because the width of passage is same and it is far bigger than height of passage, the flow field could be considered as uniform along y direction and be handled as two demension flow field. Navier—Stocks equation can be simplifed as following:

$$\rho(u\frac{\partial u}{\partial x}+w\frac{\partial u}{\partial z})=-\frac{\partial p}{\partial x}+\frac{\partial}{\partial x}\{\mu[2\frac{\partial u}{\partial x}-\frac{2}{3}(\frac{\partial u}{\partial x}+\frac{\partial w}{\partial z})]\}+\frac{\partial}{\partial z}[\mu(\frac{\partial w}{\partial x}+\frac{\partial u}{\partial z})] \tag{1}$$

$$\rho(u\frac{\partial w}{\partial x}+w\frac{\partial w}{\partial z})=-\frac{\partial p}{\partial z}+\frac{\partial}{\partial z}\{\mu[2\frac{\partial w}{\partial z}-\frac{2}{3}(\frac{\partial u}{\partial x}+\frac{\partial w}{\partial z})]\}+\frac{\partial}{\partial x}[\mu(\frac{\partial w}{\partial x}+\frac{\partial u}{\partial z})] \tag{2}$$

Since the height of passage changes slightly, the pressure change in x direction can be considered far bigger than that along z direction, i. e. $\frac{\partial p}{\partial x}\rangle\rangle\frac{\partial p}{\partial z}$. From numerical analysis, it can be known that each item in eq. (2) has the same order, so the change of gas momentum in z direction can be neglected. In addition, because the clearance is very small, the change of velocity u along z direction is far bigger than that along other directions, i. e. $\frac{\partial u}{\partial z}\rangle\rangle\frac{\partial u}{\partial x}$, $\frac{\partial u}{\partial z}\rangle\rangle\frac{\partial w}{\partial z}$, $\frac{\partial u}{\partial z}\rangle\rangle\frac{\partial w}{\partial x}$. From numerical analysis as above, it can be deduced that $\frac{\partial^2 u}{\partial z^2}\rangle\rangle\frac{\partial^2 w}{\partial z\partial x}$, $\frac{\partial^2 u}{\partial z^2}\rangle\rangle\frac{\partial^2 u}{\partial x^2}$, so eq. (1) can be simplified as following:

$$\rho(u\frac{\partial u}{\partial x}+w\frac{\partial u}{\partial z})=-\frac{\partial p}{\partial x}+\frac{\partial}{\partial z}(\mu\frac{\partial u}{\partial z})$$

In order to simulate leaking mathematically, we put forward some assumptions:

1. Pressure is uniform in z direction on every section.

2. Flow process is an adiabatic process.

According to above analysis and assumptions, the following fundamental equations of gas leakage are gained:

momentum eq. $$\rho(u\frac{\partial u}{\partial x}+w\frac{\partial u}{\partial z})=-\frac{\partial p}{\partial x}+\frac{\partial}{\partial z}(\mu\frac{\partial u}{\partial z}) \tag{3}$$

continuity eq. $$\frac{\partial}{\partial x}(\rho u)+\frac{\partial}{\partial z}(\rho w)=0 \tag{4}$$

state eq. $$p=\xi R\rho T \tag{5}$$

process eq. $$p/\rho^{k}=C \tag{6}$$

CALCULATING MODEL ESTABLISHING

On the basis of assumption (1), volumetric flowrate of gas through unit width is

$$Q=\int_{o}^{h}udz \tag{7}$$

The viscosity of gas is a function of pressure and temperature: $\mu=\mu(p, T)$, i. e. $\frac{\partial \mu}{\partial z}=0$, so momentum eq. (3) is simplified as

$$\rho(u\frac{\partial u}{\partial x}+w\frac{\partial u}{\partial z})=-\frac{\partial p}{\partial x}+\mu\frac{\partial^{2}u}{\partial z^{2}} \tag{8}$$

In small clearance passage, the fluid film of gas is very thin, so inertia item in above equation can be averaged along z direction, we get

$$\rho(u\frac{\partial u}{\partial x}+w\frac{\partial u}{\partial z})=\frac{\rho}{h}\int_{o}^{h}(u\frac{\partial u}{\partial x}+w\frac{\partial u}{\partial z})dz$$

Taking above equation into eq. (8) and arranging it

$$\frac{\partial^{2}u}{\partial z^{2}}=\frac{1}{\mu}\frac{\partial p}{\partial x}+\frac{\rho}{\mu h}\int_{o}^{h}(u\frac{\partial u}{\partial x}+w\frac{\partial u}{\partial z})dz \tag{9}$$

The right of above equation is a function of x only, i. e.

$$\frac{\partial^{2}u}{\partial z^{2}}=f(x) \tag{10}$$

Utilizing boundary conditions

$$\begin{cases}u(x,o)=0\\u(x,h)=0\end{cases}$$

Integrating above eq. twice

$$u=\frac{z(z-h)}{2}\cdot f(x) \tag{11}$$

Taking u into eq. (7)

$$Q=-\frac{h^{3}f(x)}{12} \tag{12}$$

Obviously, in order to calculate leakage rate Q, the frist step is to find the expression of f(x). we calculate the partial derivative of x and z, aiming at eq. (11)

$$\frac{\partial u}{\partial x}=\frac{z(z-h)}{2}\frac{\partial f(x)}{\partial x}-\frac{zf(x)}{2}\frac{\partial h}{\partial x} \tag{13}$$

$$\frac{\partial u}{\partial z} = \frac{(2z-h)f(x)}{2} \tag{14}$$

Developing eq. (4)

$$\rho\frac{\partial u}{\partial x} + u\frac{\partial \rho}{\partial x} + \rho\frac{\partial w}{\partial z} = 0 \tag{15}$$

Calculating partial derivative of x, aiming at eq. (6)

$$\frac{\partial \rho}{\partial x} = \frac{kp}{\rho}\frac{\partial \rho}{\partial x} \tag{16}$$

Taking eq. (6), eq. (16) into eq. (15), we get

$$\frac{\partial u}{\partial x} + \frac{\partial w}{\partial z} + \frac{u}{kp}\frac{\partial p}{\partial x} = 0$$

Taking eq. (13) into above equation

$$\frac{\partial w}{\partial z} = \frac{zf(x)}{2}\frac{\partial h}{\partial x} - \frac{z(z-h)}{2}\frac{\partial f(x)}{\partial x} - \frac{z(z-h)f(x)}{2kp}\frac{\partial p}{\partial x} \tag{17}$$

Integrating above eq. and using boundary condition: $w(x, o)=0$, we get

$$w = \frac{z^2 f(x)}{4}\frac{\partial h}{\partial x} - \frac{1}{2}\left(\frac{z^3}{3} - \frac{z^2 h}{2}\right)\left(\frac{\partial f(x)}{\partial x} + \frac{f(x)}{kP}\frac{\partial p}{\partial x}\right) \tag{18}$$

Taking above expressions of u, $\frac{\partial u}{\partial x}$, $\frac{\partial u}{\partial z}$ and w, i. e. eq. (11), (13), (14), (18) into eq. (9), then integrating and arranging them

$$\frac{\partial^2 u}{\partial z^2} = \frac{\partial p}{\mu \partial x} + \frac{\rho h^3 f(x)}{\mu}\left(\frac{h}{60}\frac{\partial f(x)}{\partial x} + \frac{f(x)\partial h}{24\partial x} + \frac{hf(x)}{120kp}\frac{\partial p}{\partial x}\right) \tag{19}$$

Removing f(x) from eq. (5), (10), (12), (19) and arranging them, we get

$$\frac{\partial p}{\partial x} = \frac{\dfrac{12\mu\xi Q}{h^3} - \dfrac{6\xi pQ^2}{5RTh^3}\dfrac{\partial h}{\partial x}}{\dfrac{6\xi Q^2}{5kRTh^2} - 1} \tag{20}$$

Eq. (20) is the mathematical model established in this paper, i. e. the differential relation of pressure change with leakage rate, pressure, temperature and geometrie parameters of the passage.

Using numerical method to solve above equation, we can get the value of leakage and pressure distribution in flow field under defined condition.

EXPERIMENT

Experimental device scheme is shown in figure 2. The construction of experimental part is shown in figure 3, working media are R12 and R22 respectively. The frist step is to charge liquid freen into vessel 1 and heat it. The vessel pressure is kept at desired value by adjusting heat power. Next open the valve v1, high pressure gas goes into dry filter 3, water and oil are absorbed. Then gas is heated to a determined temperature by superheater 4. Finally, gas goes into part 5 where circumferential leaking occurs. In this paper, the effect of high pressure and smallest clearance on leakage is studied experimentally aiming at R12 and R22 respectively. In order to avoid the effect of surrounding temperature on the

leakage, the whole experimemtal part is soaked in a constant—temperature—water sink. In order to ensure that leaking gas goes only through clearance of radius direction, we sealed other passages where gas may leak.

COMPARISON AND DISCUSSION ABOUT CALCULATING RESULTS AND EXPERIMENTAL RESULTS.

In order to compare under the same conditions, the calculating results of three models and the results of experiments are all shown in figure 4,5. We named model A for that established in this paper, model B for nozzle flow model and model C for viscous model. Obviously, the calculating results of model A is the best comparing with the experimental results.

From figure 4, it can be known that when pressure difference between high pressure cavity and low pressure cavity is small, the calculating results of model A and C are similar and accuration. In this case, the change of gas velocity in leaking fluid field is small, the inertia force in this time is small and can be neglected. On the contrary, the effect of inertia foree is bigger than that of viscous force, the calculating results of model A and B are more accurate than that of model C.

From figure 5, we can see that when clearance is small, the calculating results of model A and C are similar to experimental results, but when clearance is big, the results of model C are not so good. The reason is that when clearance is small, the divalent derivative of gas partial velocity u (along x direction) is very big in the direction of passage height, so viscous item is bigger than inertia item, the latter can be neglected. Under the condition of big clearance, the conclusion is opposite. When the clearance is in middle size, the results of model A and C all are not so idea.

On the whole, because model A contains the effect of viscous force and inertia force at the same time, its calculating results is the smallest and the best comparing with experimental results. While the pressure difference and clearance is small, the effect of viscous force is dominant, the intention of curve A is similar with that of curve C. As the pressure difference and the clearance is big, the effect of inertia force is dominant, the trend of curve A is similar with that of curve B. But when pressure difference and clearance is in middle value, the effect of viscous force and inertia force are almost same, the trend of curve A is between that of curve B and C.

CONCLUSIONS

1. Comparing with the nozzle flow model and viscous flow model, the new calculating model which considers viscous force and inertia force at the same time is great developed. The accuracy of its calculating results is improved obviously. Both the nozzle flow model and viscous flow model have positive deviation.

2. When clearance and pressure difference are small, the effect of viscous force on

leaking flow is bigger than that of inertia force, on the contrary, the effect of inertia force is dominant.

REFERENCES

[1] W. Reed and J. F. Hamiltion, " Internal Leakage in Sliding Vane Rotary Compressors", Purdue Comp. Tech. Conf., 1980.

[2] P. N. Pandeya and W. Soedel, "Rolling Piston Type Rotary Compressors with Special Attention to Friction and Leakage", Purdue Comp. Tech. Conf., 1978.

[3]I. Chu and T. Shiga, "Piston Type Rotary Compressor", Purdue Comp. Tech. Conf., 1978.

[4]J. L. Caillat, " A Computer Model for Scroll Compressor", Purdue Comp. Tech. Conf., 1988.

[5]Kenji Tojo, "Computer Modeling of Scroll Compressor with Self Adjusting Back—Pressure Mechanism", Purdue Comp. Tech. Conf., 1986.

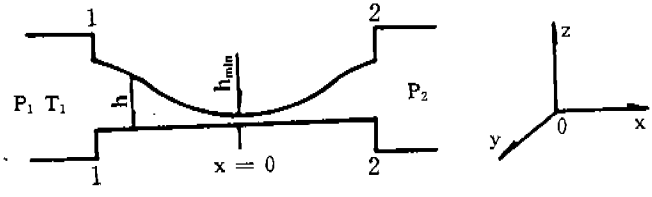

Figure 1. Simplified leaking passage

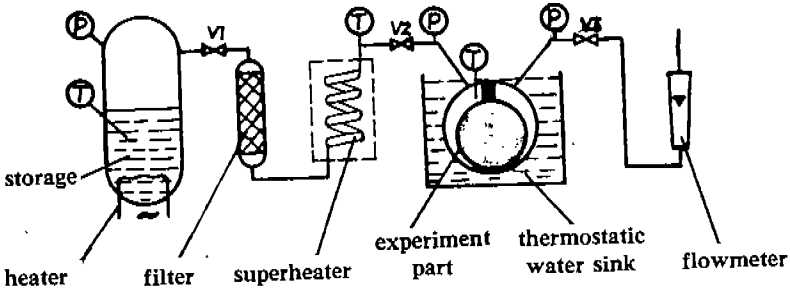

Figure 2. Schematic diagram of experimental set.

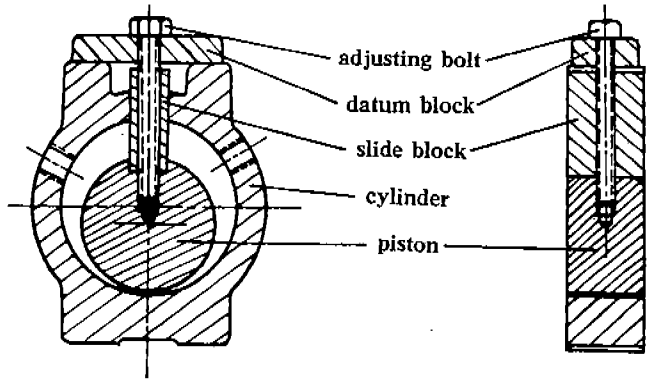

Figure 3. Schematie diagram of the construction of experimental part

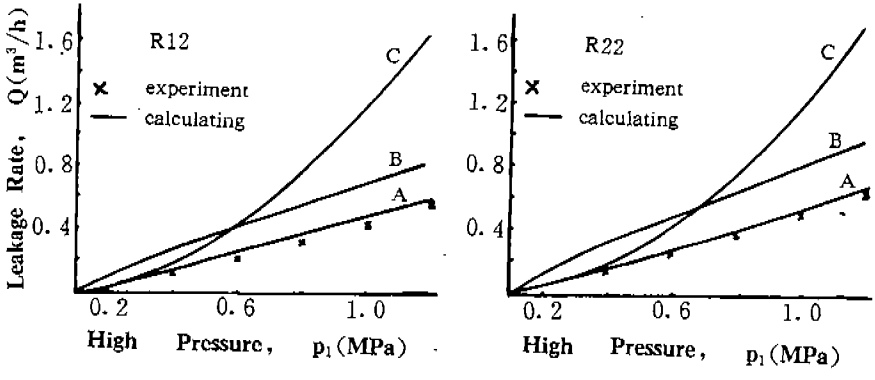

Figure 4. Effect of high pressure on leakage rate

$p_2 = 0.098MPa$ $h_{min} = 10\mu m$ $T_1 = 323k$

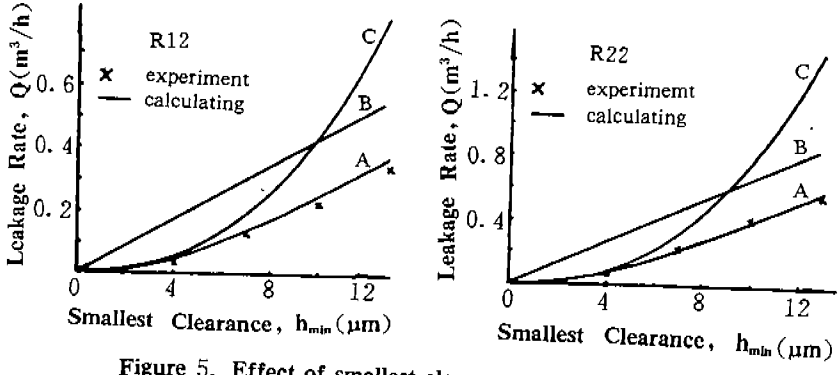

Figure 5. Effect of smallest clearance on leakage rate

$p_2 = 0.098MPa$. $T_1 = 323k$

A STUDY OF THE VIBRATION REDUCTION OF ROLLING PISTON TYPE ROTARY COMPRESSOR

Takao Yoshimura *
Takashi Koyama *
Ichiro Morita *

Masanori Kobayashi *
Toshio Uetsuji **

* *Compressor Research Laboratory, Corporate Engineering Division, Matsushita Refrigeration Company, Fujisawa, Kanagawa, Japan 251*

** *Refrigerating and Air Conditioning Systems Research Laboratory, Corporate Engineering Division, Matsushita Refrigeration Company, Higashiosaka, Osaka, Japan 577*

ABSTRACT

In general, the vibration of rolling piston type rotary compressors is greater than that of reciprocating compressors because the compressor-motor unit is fixed to the shell. It is therefore necessary that refrigerators utilizing rotary compressors incorporated a vibration-proof design.

This paper refers to the experimental vibration reduction study of rotary compressors (horizontally installed) for household refrigerators and other appliances. The vibration of rotary compressors consists of the rotational vibration caused by the speed variation of the shaft and of the imbalance vibration caused by the mass imbalance in the rotation system. There are various methods for reducing the rotational vibration. This study researched the dynamic damper. It will be shown that the dynamic damper, using a helical extension spring applied to the outside of the shell, is effective in reducing vibration. In regards to the imbalance vibration, this paper researched the influence of the number of correction planes and the accuracy of the balancing.

INTRODUCTION

The vibration of the compressor-motor unit itself is substantially smaller than that of reciprocating compressors because rolling piston type rotary compressors do not have such a large reciprocating inertia force as that of reciprocating compressors. The actual vibration of the shell section, however, is greater than that of a reciprocating compressor. This is because, for a reciprocating compressor, the compressor-motor unit is dampened by means of springs, and on a rotary compressor, in contrast, the vibration of the compressor-motor unit is transferred directly to the shell

In rotary compressors, therefore, the reduction of both noise and vibration are very important. For this reason, in rotary compressors for air conditioning, two cylinder compressors have come into wide use. But in rotary compressors for household refrigerators, it is the real state that the vibration reduction of a compressor itself has not so much been studied.

This paper refers to the result of the experimental study of the vibration reduction method for rotary compressors by the cause of vibration.

STRUCTURE

Fig.1 shows the structure of Matsushita's horizontal rotary compressor for household refrigerators. A motor-stator is shrink-fitted directly to the shell, and the compressor-motor unit is weld-fitted to the shell through the main bearing whose outer circumference is round. The vibration of the compressor-motor unit, therefore, is transferred

directly to the shell resulting in the generation of vibration and noise.

VIBRATION OF ROTARY COMPRESSOR

The vibration of a rotary compressor can be divided into 3 forms: (1) rotational vibration caused by the speed variation of the shaft, (2) imbalance vibration caused by the mass imbalance in the rotation system, and (3) reciprocative vibration caused by the reciprocation inertia force due to the vane reciprocating movement.

Firstly, the levels of the respective vibration forms of current rotary compressors (displacement: 5 cm^3 class) were compared with each other by a modal analysis. As shown in Fig.2, the vibration level rate of each vibration form, that is, rotational vibration : imbalance vibration : reciprocative vibration is 4 : 1 : negligible. Rotational vibration is the most serious.

It is therefore the most important to reduce the rotational vibration. There are various methods for reducing the rotaional vibration. This study was made on a dynamic damper as a vibration reducing method, which does not lower the efficiency and maintains compactness and lightness.

In addition, another study was made on the correlation between the accuracy of the balancing and the imbalance vibration, which is considered to be a serious problem where the rotational vibration is reduced.

STUDY OF ROTATIONAL VIBRATION REDUCTION

Application of Dynamic Damper to Compressor

In general, the application of a dynamic damper to a compressor can be expressed as a vibration form of a series of two degrees of freedom. That is, it is expressed as the vibration proof supporting system considered to be a series of one degree of freedom to which a dynamic damper of a series of one degree of freedom is added.

Generally, the vibration damping effect of the dynamic damper can be determined from the following equations.

Natural angular frequency of body

$$\omega_1 = \sqrt{\frac{k_1}{m_1}}$$

Natural angular frequency of dynamic damper (when c=0)

$$\omega_2 = \sqrt{\frac{k_2}{m_2}}$$

Body amplitude ratio

$$M_x = \frac{X_1}{X_0} = \frac{(\frac{\omega_2}{\omega_1})^2 - (\frac{\omega}{\omega_1})^2}{(1-\frac{\omega}{\omega_1^2})(\frac{\omega_2^2}{\omega_1^2}-\frac{\omega^2}{\omega_1^2}) - \mu \cdot \frac{\omega_2^2}{\omega_1^2}\frac{\omega^2}{\omega_1^2}}$$

$$X_0 = \frac{F_0}{k_1} \qquad \mu = \frac{m_2}{m_1}$$

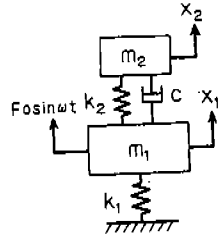

In general, as shown in Fig.3(a), dynamic dampers are used to avoid the resonance frequency which may become a problem. In compressors, however, because K_1 of a vibration proof supporting system is extremely lessened, the compressor may not be resonated at operating frequency. Therefore, the dynamic damper is not used for avoiding resonance but for reducing vibration by letting it damp the vibration of a compressor itself as shown in Fig.3(b).

Study on A Wide Variety of Dynamic Damper

In applying dynamic dampers to compressors, larger vibration damping effect and wider band of vibration damping effect (frequency area in which vibration is damped by adding a dynamic damper) are preferred. The reason for the above is because there is the dispersion of the resonance frequency of the dynamic damper itself and also it may be used for both 50Hz and 60Hz operation. Moreover, it is naturally required to secure reliability. Based on these matters, the authors studied some types of dynamic dampers.

A dynamic damper consists of a mass, spring, and damper, and it is important how to set the spring and damper in particular. Because of a wide variety of dynamic dampers, the following four types were studied: the rubber type, coil spring type, beam type, and helical extension spring type utilizing the lateral bending of a contact spring having initial tension shown in Fig.4. For these studies, an exciter was used in the experiments. Fig.5 shows the vibration damping characteristics (vibration characteristics with dynamic damper / vibration characteristics without dynamic damper) in each type. The experiments revealed that in the rubber type, although a maximum quantity of the vibration damping effect was inferior to that of other types, the effect band is broad and excellent. As shown in Fig.6, however, the variation of resonance frequency to that of temperature is extremely large. This seems to be caused by the variation of the spring constant due to the change of the hardness of the rubber caused by the change in temperature. And this will harmfuly affect the stability and long period reliability of the compressors. The coil spring type provides us with a large maximum damping effect but an effect of a narrow band. In the beam type damper, damping effect characteristics are excellent, but there is a problem in reliability. The damping effect characteristics in the helical extension spring is the most excellent, but even in this type, a problem involves the variation of the resonance frequency due to the exciting force as shown in Fig.7. It is considered that this change occurs because the lateral spring constant exhibits a nonlinear characteristic due to the exciting force, because of the utilization of the lateral bend of the contact spring having an initial tension force. However, by setting the resonance frequency of the damper to the value at the time when the compressor is highly loaded, the vibration can be prevented from amplifying. Since the effect band of this type is broad, it is considered that a comparatively stable vibration damping force can be obtained.

The authors concluded from the results mentioned above that the herical extension spring type is the best considering the stability, reliability, and effect.

Application of Helical Extension Spring Type Dynamic Damper to Compressor

It is the specifications of mass (i.e., weight and shape), the specification of springs (i.e., wire diameters, mean diameter, number of turns and the initial tension force) that is the most important for determining the vibration damping effect and resonance frequency in a helical tension spring type dynamic damper. Fig.8 shows the variation of the vibration damping characteristic while the initial tension varies in the case of the same spring constant. As the initial tension is smaller, the resonance frequency becomes low, and the vibration damping effect also becomes small. This reveals that the initial tension is an important factor for determining a resonance frequency and vibration damping effect.

In addition, there are the following three factors affecting the vibration damping effect other than that mentioned above: the dimension α between the vibration center and the center of gravity of mass, dimension β between the spring fixing position (the position where spring force works to cancel compressor vibration) and the

center of gravity of mass, and dimension γ between the center of vibration and the position where the spring is fixed. Fig.9 shows the diagram of the dimension α , β , γ .

Since the rotational vibration reduction is equivalent to the torque variation reduction, the vibration damping effect is proportional to the generated spring force and the dimension γ . Moreover, the generated spring force is proportional to the inertia force of mass which is determined by the dimension α . Consequently, as the vibration damping effect is proportional to the dimension α , γ , the internal installation of a dynamic damper in a compressor, which means the dimension α , γ is smaller, is not effective. In that case, only the vibration damping effect up to 15% is expected according to our research. A large extent of the vibration damping effect is only expected to be achieved when installed externally.

On the other hand, the dimension β is an important factor which affects the buckling of the spring. The generated spring force and the resonance frequency change nonlinerly when the spring is buckled. Therfore, it is necessary to decide the dimension β without the buckling of the spring under all operating conditions.

Effect of Application to Refrigerator in Field

Based on the aforementioned result, the authors evaluated the vibration reduction effect with the helical extension spring type dynamic damper externally installed to a refrigerator in the field. Fig.10 and Table 1 show the result. Excellent vibration damping effect could be obtained, and the degree of reduction reached near the level of imbalance vibration.

The vibration of the rotary compressor of the refrigerator in the field includes the vibration caused by the resonance of the system piping in the radial direction other than rotational vibration. Since when the system piping is resonated, the generated spring force works so as to reduce large rotational vibration in the dynamic damper, the phase relation to the rotational vibration at the position where the dynamic damper is installed becomes important. In the case of the same phase, the vibration in the radial direction is also dampened, but in the case of the reverse phase, the vibration in the radial direction increases.

STUDY OF IMBALANCE VIBRATION REDUCTION

The rotational vibration becomes the most serious problem in the vibration of a rotary compressor. It could be reduced to the extent of the level of imbalance vibration by externally applying the helical extension spring type dynamic damper. So, in the imbalance vibration, we examined the influence of the number of correction planes and the accuracy of the balancing as it pertains to imbalance vibration.

Balancing Concept of Rotary Compressor

Fig.11 shows the arrangement of balance weights in a horizontal rotary compressor. In order to balance the eccentric section of a shaft and piston, in general including the case in our company, two-plane balancing (two balance weights) are used by means of the balance weights M2 and M3. This time, adding the weight M4, three-plane balancing (three balance weights), by which the weight reduction of the balance weights M2 and M3 is possible, were also studied. If the direction of gravity of balance weights is completely same or opposite to the eccentric of the shaft, the ratio of the imbalance moment in each correction plane can be shown in Table 2. It means good balancing that each ratio of the imbalance moment (Cn) gets near 1.

Fig.12 shows the characteristics of the ratio of the imbalance moment (Cn) in two-plane balancing. The weight of M2 is adjusted by

the number of steel sheets; and the number of steel sheets determines C3 approximately. And when the number of steel sheets (M2) is constant, C2 is determined automatically by determining C1. That is, in this study the evaluation of the number of steel sheets (M2) and the ratio of the imbalance moment C1 was made.

Balancing Study Specifications

A study was made on both of (1) evaluation of shaft behavior and bearing deformation and (2) vibration evaluation of a compressor, regarding the models different weights and the arrangement of balance weights. The models on which the study was made are as follows:

Model A:two-plane balancing	(M2, M3);Balance removal weight(C1=1.3)
Model B:two-plane balancing	(M2, M3);Balance adjusting weight(C1=1.1)
Model C:three-plane balancing	(M2,M3,M4);Balance adjusting weight(C1=1.1)
Model D:non imbalance	(M1 to M4 none, with rotor)

Rotation Characteristics of Rotor

The authors, first of all, measured the shaft behavior and bearing deformation of the shaft and bearing arrangement in the compressor by means of the bearing test machine. Fig.13 shows the structure of the bearing test machine and measuring method. As shown in the Fig.13, the same test bearings (main bearing and sub-bearing) as those of a compressor are fixed to the bearing test machine. In addition, the test shaft is connected to the inverter motor so that the motor may be driven at any speed. An eccentric section is mounted on the test shaft and a rotor is also mounted. An eddy current type gap sensor was used to measure shaft behavior and bearing deformation in the X axis and Y axis directions. Fig.14 shows an example of the measuring result of the rotation locus (position a) of the rotor. As shown in Fig.14, the rotation locus of the rotor becomes like a circle.

As a result of the above-mentioned measurement in the models aforementioned, the following were disclosed.

(1) In a horizontal rotary compressor, even if the balance is adjusted perfectly by two-plane balancing, the rotation of the rotor is 62/80μm(50/60Hz).

(2) The rotation of the rotor is 41/47μm(50/60Hz) by adjusting balance by three-plane balancing. This is 40% reduction.

Imbalance Vibration Characteristics

Fig.15 shows the imbalance vibration measuring results in the compressor of the models A to D. It also shows the imbalance vibration characteristics (60Hz) to the ratio of the imbalance moment C1. As a result, when the ratio of the imbalance moment C1 is 1.1 or less, compared to non imbalance, imbalance vibration is nearly the same level, about 16% to the rotational vibration. But, when the ratio of the imbalance moment C1 becomes 1.3, the imbalance vibration increases up to about 82% to the rotational vibration. These results reveal that imbalance vibration increase on the ratio of the imbalance moment C1, similar to a curve of a secondary degree.

Fig.16 shows the characteristics of the imbalance vibration predicted based on the measuring result of the vibration of compressors of the models A to D. Fig.16 also disclose the following matters: When comparison is made between two-plane balancing and three-plane balancing, it is cleared that both the rotation of the rotor and imbalance vibration in three-plane balancing is smaller than those in two-plane balancing at the same operation frequency. And the difference between the two becomes remarkable during the rotation at high speed in particular. (Ⅰ and Ⅲ points ⟷ Ⅳ and Ⅴ points)

When comparison is made between the two at C1=1.1 and 90Hz, the rotation of the rotor is 165/78μm (two/three-plane balancing), and the imbalance vibration is about 29/19% to the rotational vibration. (Ⅲ

point ⟷ V point). Therefore, the imbalance vibration under 90Hz in three-plane balancing is the same level as at 60Hz in two-plane balancing. (I point ⟷ V point)

The collection of aforementioned result are as follows.

(1) The rotation of the rotor and the imbalance vibration of the compressor can be suppressed to a minimum by making the ratio of the imbalance moment C1 within a range of 1±0.1.

(2) Even in three-plane balancing, the imbalance vibration is not improved at an operation frequency of 60Hz or less compared to that in two-plane balancing. That is, even in two-plane balancing, imbalance vibration can be suppressed to a minimum by sufficiently balancing. At an operation frequency of over 60Hz, however, the effect of the reduction of imbalance vibration is large in three-plane balancing.

CONCLUSION

A study was made to reduce rotational vibration and imbalance vibration which become a problem in particular in horizontal rotary compressors for household refrigerators. Regarding rotational vibration, by externally installing a helical extension spring type dynamic damper to a compressor, rotational vibration was reduced to nearly the level of imbalance vibration at an operating frequency of 50/60Hz. Regarding imbalance vibration, it was clarified that at an operating frequency of 60Hz or less in particular, even in two-plane balancing, the imbalance vibration can be suppressed at the same level as in three-plane balancing by conducting sufficient balance adjustment. But three-plane balancing can reduce the rotation of the rotor, more than two-plane balancing, and it is effective for improving reliability between shaft and bearings. In addition, at a higher operation frequency over 60Hz, the reduction effect of imbalance vibration owing to three-plane balancing is large.

REFERENCE

1. Imaichi, K, Ishii, N., al., "Vibration Analysis of Rotory Compressors," Proceedings of the Purdue Compressor Technology Conference, July 1982, pp.275-282.
2. C.M. Harris & C.E. Crede, "Shock and Vibration Hand Book".
3. Itami, T., et al.,"Estimation of Bearing Load of Rolling Piston Type Rotary Compressor under High Speed Operation" Proc. Purdue Int. Compressor Engineering Conference, Vol.2, Aug.,1986, pp.477-493.
4. Hattori, H.,t al.,"Dynamic Analysis of a Rotor-Journal Bearing System for Twin Rotory Compressor" Proc. Purdue Int. Compressor Engineering Conference, Vol.2, July, 1990, pp.750-760.

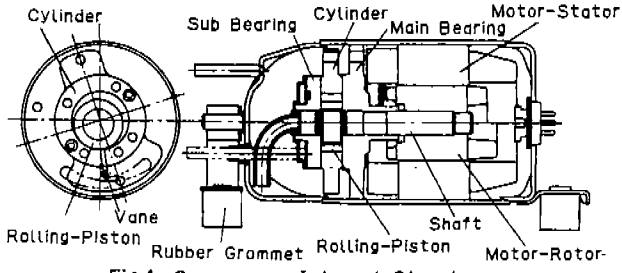

Fig.1 Compressor Internal Structure

	ROTATIONAL VIBRATION	IMBALANCE VIBRATION	RECIPROCATIVE VIBRATION
VIBRATION FORM	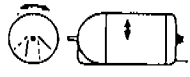	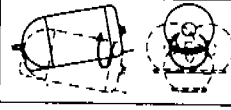	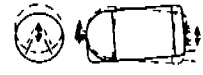
VIBRATION LEVEL RATE	4	1	NEGLIGIBLE

Fig.2 Vibration Form and Vibration Level Rate

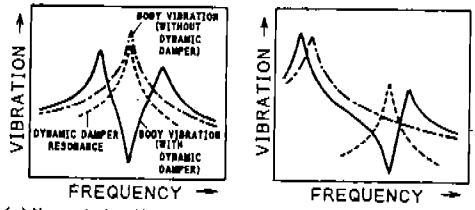

(a) Normal Application of Dynamic Damper (b) Application of Dynamic Damper to Compressor

Fig.3 Dynamic Damper Application

	RUBBER TYPE	COIL SPRING TYPE	BEAM TYPE	HELICAL EXTENSION SPRING TYPE
FORM	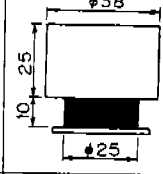	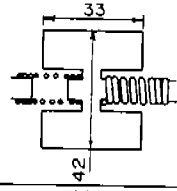	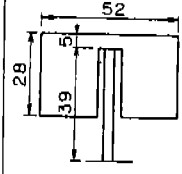	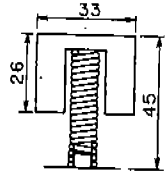
MASS	weight 220g	weight 195g	weight 240g	weight 230g
SPRING & DAMPER	·material :NBR ·hardness:65 (Hs)	·material:piano wire ·diameter of wire :φ1.4mm ·mean coil diameter :φ8.4mm ·number of turns :4	·material:piano wire ·diameter of wire :φ2.9mm ·length :39mm	·material:piano wire ·diameter of wire :φ2.0mm ·mean coil diameter :φ7.2mm ·number of turns :15 ·initial tension :78.4N

Fig.4 Type of Dynamic Damper

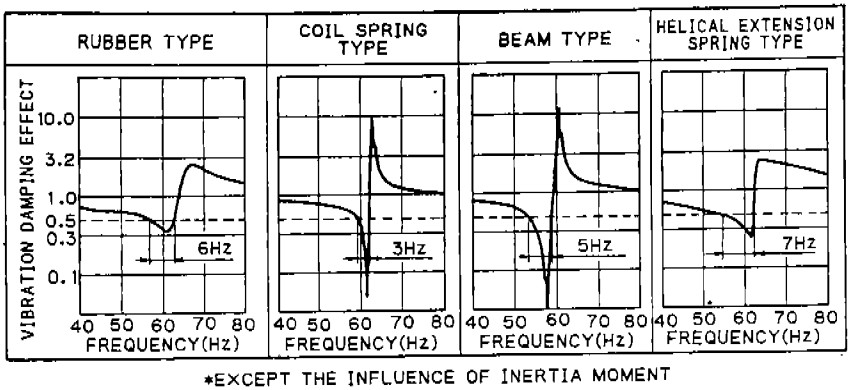

*EXCEPT THE INFLUENCE OF INERTIA MOMENT

Fig.5 Vibration Damping Characteristic by Type

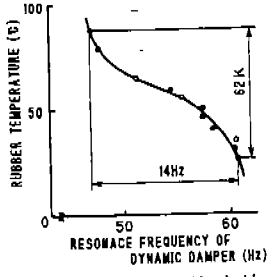

Fig.6 Temperature Variation of Rubber Type-Resonance Frequency Variation Characteristic

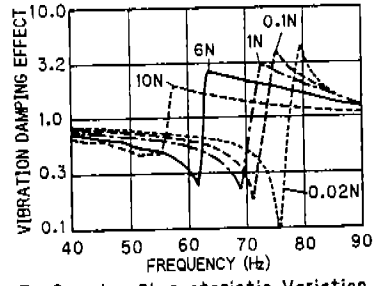

Fig.7 Damping Characteristic Variation Caused by Exciting Force Variation of Helical Extension Spring type Dynamic Damper

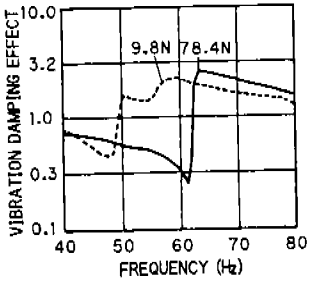

Fig.8 Vibration Damping Characteristic Variation at the Time of Change of Spring Initial Tension

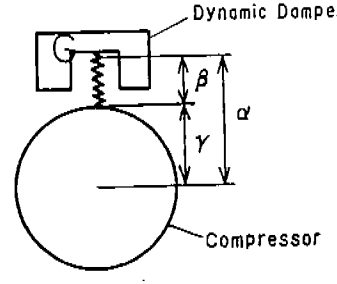

Fig.9 Diagram of Dimension α, β, γ

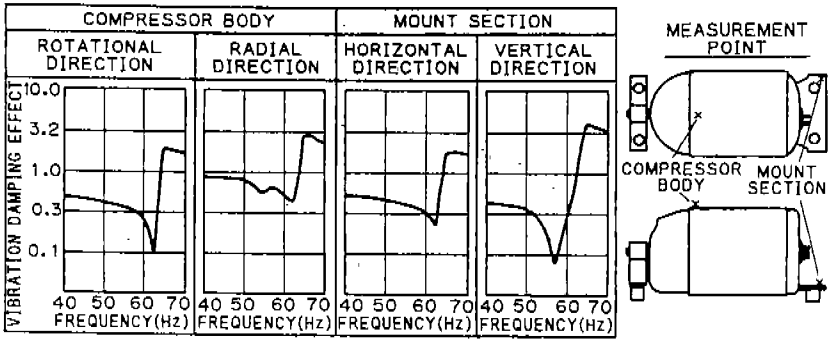

Fig.10 Household Refrigerator in Field Vibration Damping Characteristic in Applying Helical Extension Spring Type Dynamic Damper

Table.1 Household Refrigerator Vibration Damping Effect in Applying Helical Extension Spring Type Dynamic Damper

		IN 50Hz OPERATION	IN 60Hz OPERATION	IN MAX. EFFECT
COMPRESSOR BODY	ROTATIONAL DIRECTION	57%	70%	91%
	RADIAL DIRECTION	17%	47%	55%
MOUNT SECTION	HORIZONTAL DIRECTION	53%	65%	77%
	VERTICAL DIRECTION	63%	80%	92%

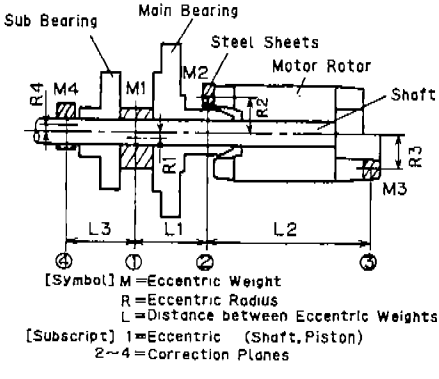

Fig.11 Balance Weight Arrangement

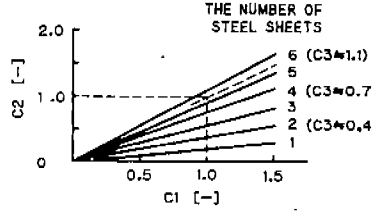

Fig.12 The Ratio of Imbalance Moment Characteristics

Table.2 The Ratio of Imbalance Moment(Cn)

Two-Plane Balancing	$C1=M3\cdot R3(L1+L2)/(M2\cdot R2\cdot L1)$ $C2=M3\cdot R3\cdot L2/(M1\cdot R1\cdot L1)$ $C3=M2\cdot R2\cdot L2/\{M1\cdot R1(L1+L2)\}$
Three-Plane Balancing	$C1=\{M3\cdot R3(L1+L2)+M4\cdot R4\cdot L3\}/(M2\cdot R2\cdot L1)$ $C2=\{M3\cdot R3\cdot L2+M4\cdot R4(L1+L3)\}/(M1\cdot R1\cdot L1)$ $C3=\{M2\cdot R2\cdot L2+M4\cdot R4(L1+L2+L3)\}/\{M1\cdot R1(L1+L2)\}$ $C4=\{M1\cdot R1\cdot L3+M3\cdot R3(L1+L2+L3)\}/\{M2\cdot R2(L1+L3)\}$

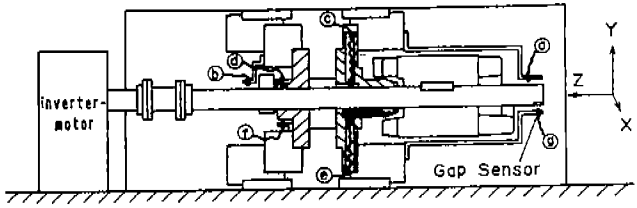

ⓐ : Measuring of Rotation Diameter of The Rotor Top
ⓑ,ⓒ : Measuring of Shaft Behavior of the Sub Bearing Side.
ⓒ,ⓓ: Measuring of Shaft Locus in the Main,Sub Bearing.
ⓔ,ⓕ: Measuring of Main,Sub Bearing Deformation.
ⓖ : Measuring of Crank Angle.

Fig.13 Test Equipment(Bearing Test Machine)

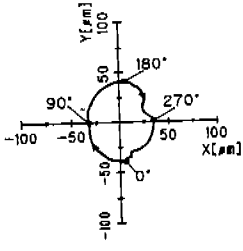

Fig.14 Rotor Top Locus (3500r/min)

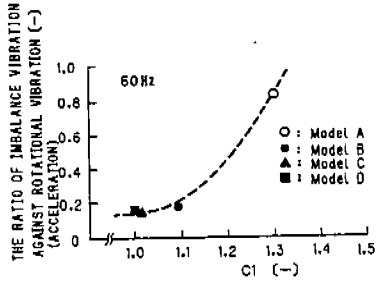

Fig.15 Measuring Result of Imbalance Vibration

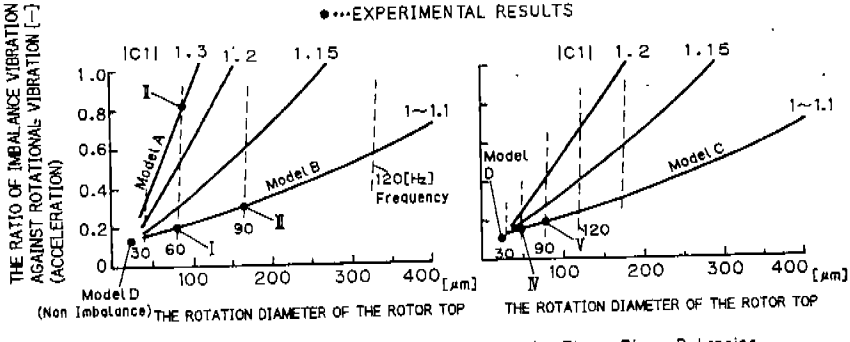

(a) Two-Plane Balancing (Steel Sheets : 5pieces)

(b) Three-Plane Balancing (Steel Sheets : 4pieces)

Fig.16 Imbalance Vibration Characteristics

STATIC AND DYNAMIC CALIBRATION OF A TRIAXIAL FORCE GAGE FOR MONITORING THE STRUCTUREBORNE FORCES WITHIN A FREON COMPRESSOR

D. L. Young, Graduate Research Assistant
L. D. Mitchell, Randolph Professor of Mechanical Engineering

Virginia Polytechnic Institute and State University
Department of Mechanical Engineering
Blacksburg, VA 24061-0238

INTRODUCTION

Reciprocating freon compressors are commonly used in air conditioning and heat pump applications. Compressor manufacturers are interested in understanding how internal structural and acoustical energy travels to become acoustical energy outside of the sealed shell. Basic understanding of this nature will allow new designs to be developed that will be quieter than present units. Three key areas for analysis are the motor / crankcase assembly, the acoustic and structural transmission paths between this assembly and the shell, and the acoustic radiation behavior of the shell among other things. The identification of the transmission paths requires measurement of the compressor assembly forces on the shell. The most dominant paths should be the support springs and the freon in the shell. The freon path is easily measured with a pressure transducer but measurement of the forces from the springs is difficult without modification of the compressor.

INSTALLATION

The Kistler 9251A triaxial force gage was chosen to measure the interaction forces between the compressor support springs and the shell. These forces, if measured, can be correlated to the acoustic output of the compressor to determine the importance of the individual paths and can also be used to drive a finite element model of the compressor. The force gage shown in Fig. 1 is 0.945 in (24 mm) square with a height of 0.394 in (10 mm). It is a charge-mode piezoelectric transducer which can measure both axial and two lateral forces passing through the support springs. This force gage has a force range of 2200 lbf (9800 N) in compression and 1100 lbf (4900 N) in shear with the standard 5600 lbf (25,000 N) preload. It can withstand the freon environment and the AC field produced by the motor during compressor operation. The main disadvantages of this force gage are the required preload, the possibility of large moments at startup cracking the quartz crystals, and the modifications in the compressor necessary for installation.

A typical compressor has two identical support springs that rest on brackets spot welded to the side of the shell (see Fig. 2) and a centering spring at the top that rests against a mount which is spot welded to the top of the shell (see Fig. 3). It was a challenge to devise the mounting assemblies necessary for the force gages without significantly stiffening or mass loading the shell. Kistler approved a 3750 lbf (16,700 N) preload for our application in order to measure the lateral forces and improve its tolerance to the high moments at compressor startup. The mating surfaces must be as smooth and plane as practical. A small boss was machined on each of these surfaces to fit within the recesses at the edge of the mounting hole in the force gage (see Fig. 1, Isometric view only) to aid in alignment during installation and to ensure the transmission of the lateral forces to the transducer. Stops were also installed to limit the compressor motion at startup to limit the startup moments.

The standard lower spring support bracket is shown in Fig. 2. The spring retaining post was removed and the assembly shown in Fig. 4 was installed in its place. The threaded force gage mount fits inside of the bracket in place of the spring retainer post and was silver soldered to the end of the bracket. The disk at the top of this mount provides the required

mating surface for the force gage and rests on top of the modified bracket. The spring mount that fits on top of the transducer mimics the old post. It has straight sides up to the height of the original post minus the force gage height and platform thicknesses. It then slopes back to the center at approximately 10 degrees to avoid contact with the spring. The extra height ensures that the spring cannot hop off the mount. A 0.25 in Allen head bolt fits through the spring mount and force gage with the transducer mount serving as the nut. In order to keep the compressor in the same position relative to the bracket, three of the four dead coils at the base of the stock springs were removed to account for the added height from the force gage installation.

The top spring mount was more difficult to design. The standard top spring retainer is shown in Fig. 3. The assembly that was installed in its place is shown in Fig. 5. A 0.25 in thick threaded disk was silver soldered to the top of the shell to provide a solid base for the force gage. The spring mount was designed to be similar to the original spring retainer with enough clearance in the center to allow a 5/16 in hex-head bolt to be installed. The four holes in the side of the spring mount help reduce the weight. The top spring has no dead coils so the spring well in the motor cap was deepened to allow for the extra height of the force gage installation.

STATIC CALIBRATION

The unloaded sensitivity calibrations for the transducers were used when applying the preload. Once the transducers are preloaded these sensitivity values are no longer valid. Since the standard Kistler preload and hardware were not used in this application, a static calibration needed to be performed as described by Soom and Kubler [4].

The static calibration was performed using several weights ranging from 1 lbf (4.448 N) to 8.66 lbf (38.52 N). Limited clearance inside the shell prevented some weights from being used in all of the calibrations. The weights were either set on or hung from the force gage along one of its primary axes. The charge amplifier was set to the long time constant to allow time to read the voltage output from a digital voltmeter before significant decay. The amplifier was reset and if there was not any significant drift in the voltage readings the force gage was unloaded and the steady-state voltage value was recorded. A number of values were taken with each weight and averaged. These averaged values were used in the linear regression fit of the charge sensitivity. The lateral sensitivity values were averaged to find a single sensitivity value for both of these axes. A typical sensitivity calibration for all three axes is shown in Fig. 6.

DYNAMIC CALIBRATION

An impact test was then performed to verify the force gage dynamic calibration. This type of dynamic test requires an instrumented modal hammer which has a built-in force gage and a multi-channel fast Fourier transform (FFT) analyzer. For this type of calibration the spring mount was impacted with a modal hammer along a primary axis of the force gage. The FFT analyzer is set to trigger on the impulse from the hammer and records the time responses of both the hammer and triaxial force gage or accelerometer. These time responses are Fourier transformed into the frequency domain. The individual channel spectra and cross spectra between the channel are averaged over several impacts to improve accuracy. The cross spectrum and auto-spectrum are used to determine the frequency response function (FRF) between the hammer force and the force gage output. This FRF is the dynamic calibration of the transducer. The time responses from an impact test is shown in Fig. 7 and the averaged auto spectrums are shown in Fig. 8. The stiffness of the tip on the hammer and the compliance of the structure limit the frequency range of an impact test. The impulse in the time response narrows as the combined stiffness of the tip and structure increases. As the impulse narrows, the frequency range required to represent it increases and the quality frequency range of the data is generally the -10 dB point in the force autospectrum. The coherence between the input and output is also used as a reference to indicate FRF quality and possible bias error in the frequency response function.

The frequency response function between the hammer impact on the spring mount and the force gage response was expected to be smooth with a rise in sensitivity as the transducer assembly reached its first resonance frequency. The actual response as shown in Fig. 9 turned out to contain a number of apparent resonances beginning at approximately 800 Hz. The time response values showed an impulse for the modal hammer and the impulse followed by a ringing from the triaxial force gage indicative of its functioning as an accelerometer. Several impact tests were then performed attempting to correlate the force gage response to the accelerations of the spring mount or the support bracket. The frequency response between the force gage and an accelerometer mounted perpendicular to the shell on the end of the lower bracket under the force gage shown in Fig. 10 indicated that the distortion in the direct impact calibration was due to the effects of the force gage assembly being mounted on a light dynamic structure and in turn it acting as an accelerometer. The hammer impact was on the outside of the shell at a spot of high curvature which has a lower compliance and should yield a wider frequency range of the impact. This was the only axis and mount that exhibited a fairly clean correlation between the force gage and accelerometer. This means that the spring adapter mass was acting like an inertial mass on top of a force gage. This combination made an accelerometer. The remaining comparison for accelerometer to force for the other directions had many peaks in their frequency response functions. This did not conclusively attribute the peaky FRF from the direct impact calibration shown in Fig. 9 to the dynamic forces from the relative motion between the spring mount and the support bracket.

Another test was devised to verify that the transducer assembly was acting like an accelerometer on a light dynamic structure. A solid steel cylinder with a diameter of 4.0 in and a height of 7.5 in was machined and threaded to accept the 0.25 in bolt used in the side compression mounting spring force gage assemblies. This cylinder weighed approximately 25 lb and should serve as inertial base for the test. This cylinder was estimated to have it first transverse resonance above 12 kHz which is above our frequency range of interest. Axial modes were significantly above this frequency. One of the side force gages and its spring mount were removed and fastened to this cylinder. A direct impact test on the spring mount produced the smooth FRF shown in Fig. 11 which was originally expected. This helped validate the hypothesis that the distortion in the frequency response from a direct impact of the force gage was a result of the shell and bracket response showing up as inertial forces in the triaxial force gage. The force gage was then removed and reinstalled on the support spring bracket and recalibrated statically.

It should be apparent from the above work that the triaxial force gage installation has an acceleration sensitivity. Using the experiments with the accelerometer to force gage companson when mounted on the flexible shell, one can determine the various force gage sensitivities to acceleration. The inertial mass above the side spring mount force gage is approximately 0.10 lbm (44 gm) which agrees with the FRF in Fig. 10. This means the force gage has an acceleration sensitivity along this axis of 0.1 lbf/g (0.44 N/g). The acceleration sensitivity should be the same for the other axes with the peaks in the other force gage to accelerometer frequency response functions the result of angular acceleration.

CONCLUSIONS

The Kistler 9251A triaxial force gage can be very useful in measuring interaction forces between structures. The modifications necessary to install it require planning to minimize local stiffening and mass loading effects. In-situ static calibration will be necessary when the standard preload and preload hardware are not used. A dynamic calibration using an instrumented hammer can be used to verify the static calibration value and to determine the acceleration sensitivity of the force transducer assembly. When the force transducer is measuring the interaction forces between two structures the acceleration sensitivities may be insignificant. However, as is the case here the acceleration-based inertia forces of the spring mounts are true forces being "felt" by the shell so that they must be accepted as a true excitation force.

RECOMMENDATIONS

The use of the Kistler 9251A triaxial force gage on light dynamic structures needs more study. The hypothesis that the peaky FRF is the result of an inertial mass on top of a force gage needs to be verified. The good correlation between the radial force measurement and the acceleration of the bracket help verify this but does not conclusively prove it. An acceleration sensitivity study in conjunction with a modal survey of the structure may identify and quantify the acceleration sensitivity and the structural vibration modes responsible for the peaks.

ACKNOWLEDGEMENTS

The authors wish to acknowledge the encouragement and financial support of Bristol Compressors, Bristol, VA and Virginia's Center for Innovative Technology (CIT), Herndon, VA. Special thanks go to Mr. D. Gilliam of Bristol Compressors, Dr. K. Blurton of CIT., and J. Kubler of Kistler Instrument Corp. Consultation and cooperative research by Profs. C. J. Hurst, and C. E. Knight is also appreciated.

REFERENCES

1. Anonymous, "Operating Instructions - Quartz Force Transducer for 3 Components Type 9251A," Kistler Instrument Corporation, B6.9251e ed. 12.68.

2. Bristol Compressors, Inc., Production Drawing No. 230050, April 25, 1989.

3. Bristol Compressors, Inc., Production Drawing No. 209022, December 11, 1989.

4. Soom, Andres and Kubler, John, "Measurement of Dynamic Forces," Kistler Instrument Corporation Paper, K20.220.

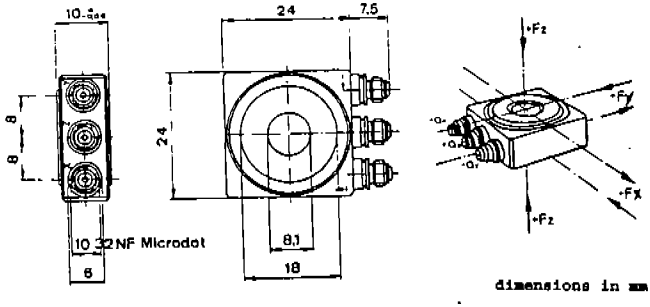

Fig. 1: Kistler 9251A triaxial force gage
(After [1])

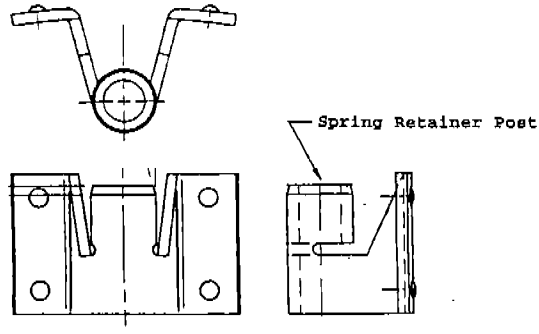

Fig. 2: Standard side spring mounting bracket
(After [2])

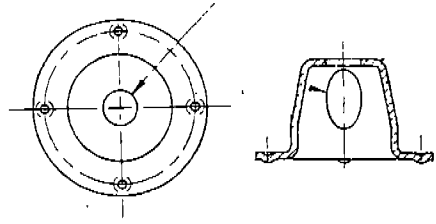

Fig. 3: Standard top spring retainer
(After [3])

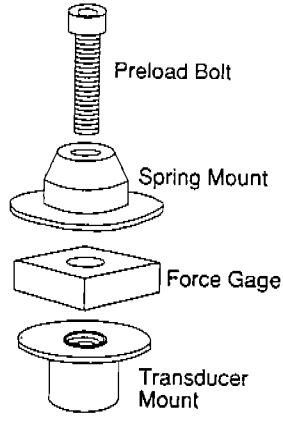

Fig. 4: Side spring force gage assembly

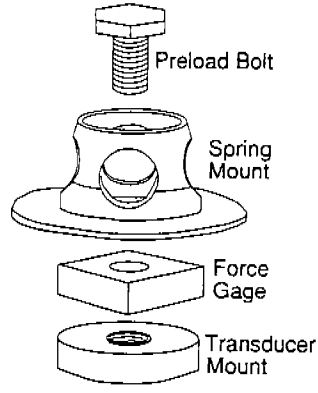

Fig. 5: Top spring force gage assembly

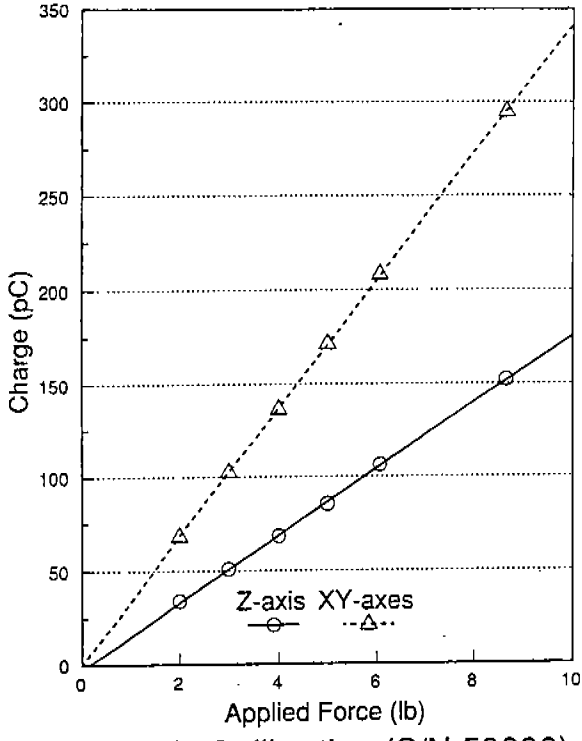

Fig. 6: Static Calibration (S/N 50090)

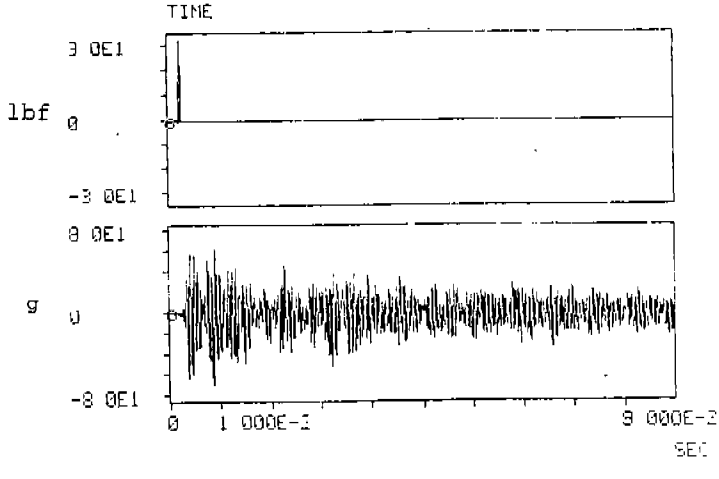

Fig. 7: Time responses from an impact test

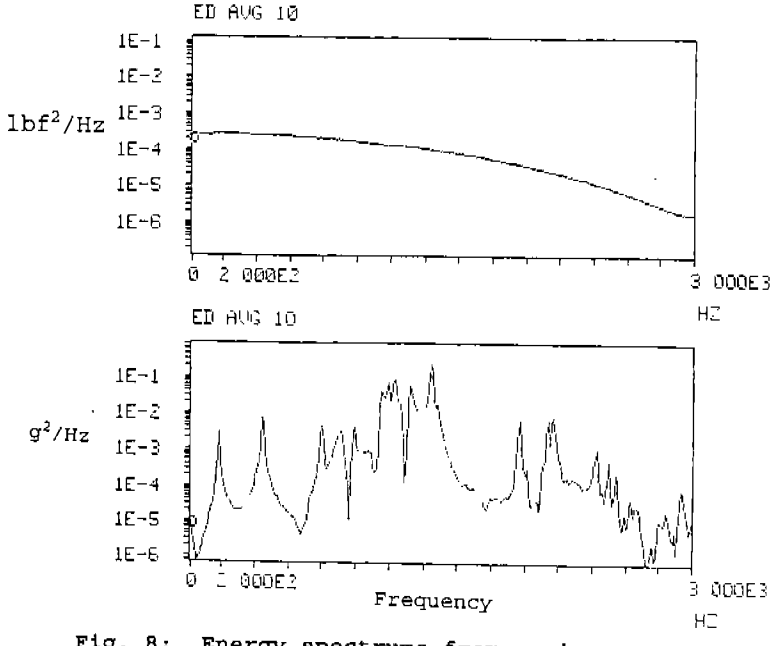

Fig. 8: Energy spectrums from an impact test

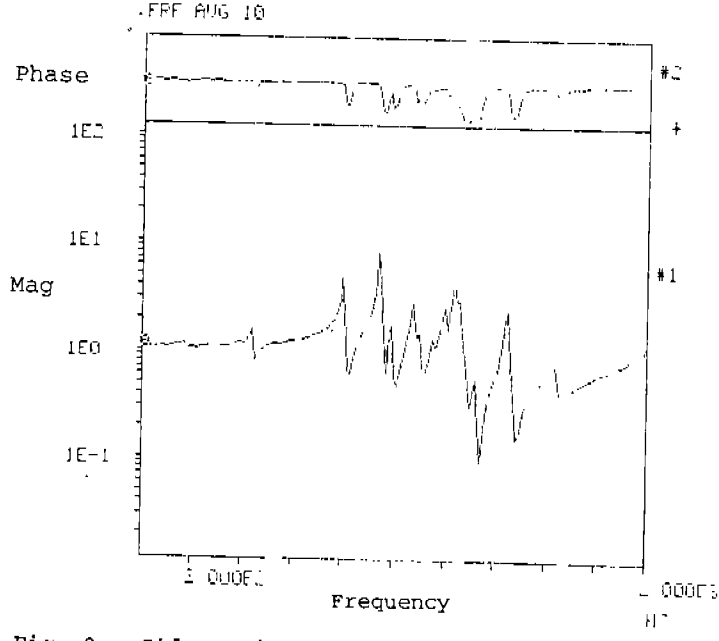

Fig. 9: Side spring mount FRF from direct impact

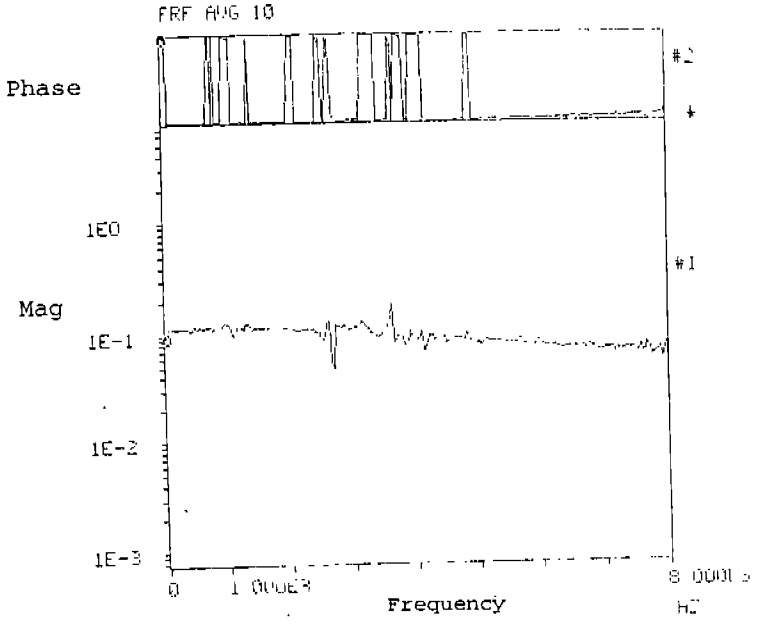

Fig. 10: Force gage to accelerometer FRF

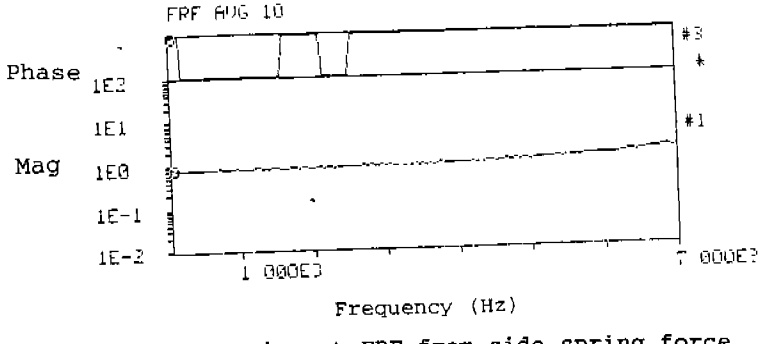

Fig. 11: Direct impact FRF from side spring force gage assembly mounted on the cylinder

MODAL ANALYSIS OF A COMPRESSOR SHELL AND CAVITY FOR EMITTED NOISE REDUCTION

M. Bucciarelli, F. Giusto
Zanussi Elettromeccanica S.p.A., Research and Development Department, Pordenone Italy.

V. Cossalter, M. Da Lio, P. Gardonio
Department of Mechanical Engineering, University of Padova, Italy.

ABSTRACT

This work concerns the design of a domestic refrigerator compressor for noise and vibration control.
Sources of noise and vibrations and the mechanisms of their propagation to the environment are first reviewed in the introduction.
The following sections then focus on the vibrations of the gas in the cavity inside the compressor shell and on the vibrations of the shell itself.
An interpretative model of modes of vibration of the shell is also given, showing that modes can be classified in two groups: those involving side walls and those involving end-caps.

INTRODUCTION

The request for systems of refrigeration with better performance, both in terms of energy consumption, and in terms of the vibrations generated and the noise spread into the surroundings, has been acquiring more and more importance. As a result of such demanding requirements, the planning and design of compressors need put greater emphasis on noise control and this demands the use of more and more sophisticated techniques, both experimental and theoretical. Furthermore, considering the recent EEC regulations and instructions concerning the reduction of chlor-fluor-carbides in the atmosphere, a further effort in noise control is necessary since the thermodynamic cycles with the new fluids are less favourable from this point of view.

In a conventional compressor, noise is substantially caused mainly by the shell which (stimulated by the springs, by pressure fluctuations of the refrigerating fluid, by the discharge piping and by the lubricating oil) vibrates and spreads the noise into the surroundings.

Figure 1 shows a scheme of the mechanisms which generate vibrations, their mechanisms of transmission, and the parts of the compressor which, by transforming the vibrations into pressure waves, make up the sources of sound which radiate towards the immediate surroundings.

The vibrations originate substantially from the motion of the compressor body suspended elastically and from the pressure fluctuations of the refrigerating gas present in the intake and discharge.

The compressor is set in motion by the forces due to: the unbalancing of the rotating parts, the forces deriving from the masses with alternating (piston) or alternating and rotatory (connecting rod) motion, and, to a lesser degree, the impulse forces caused by the closure of the valves and by magnetic forces.

The pressure waves, which spread into the intake and discharge piping, are instead produced by the thermodynamic compression cycle and valve action. In fact the valves open and close at the same frequency as that of the rate of rotation, and since their motion is impulsive rather than harmonic, pressure fluctuations with consistent superior harmonic components are generated. Such fluctuations first excite certain acoustic modes of the cavity, and then the shell containing it.

Another important source of excitation is represented by the turbulence and by the release of eddies generated in the cavity and in the intake and discharge pipes.

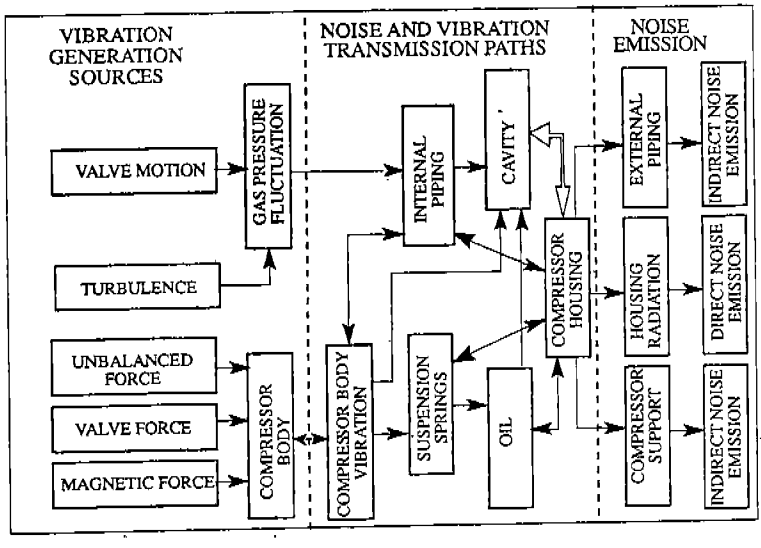

Fig. 1 - Scheme of vibration and noise generation and transmission.

Figure 2 shows a typical noise spectrum.

As can be observed from the figure and from what other authors [1,2,3] have already pointed out, three fields of frequency can be identified:

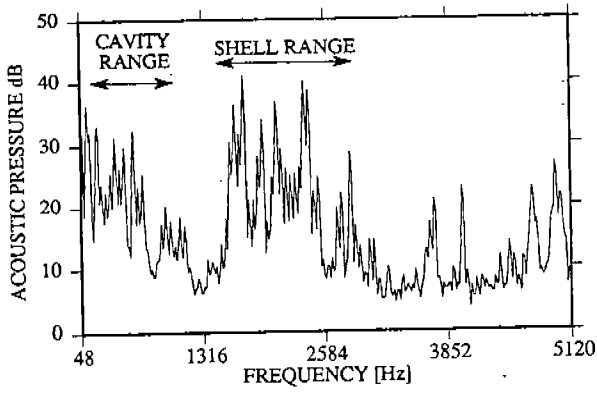

Fig. 2 - Typical noise spectrum of a conventional type of compressor.

- low frequencies (under 1000 Hz): low frequency noise is related to the rigid vibrations of the shell, caused by the fluid pulsing in the cavity in which it is contained and by the forces transmitted through the discharge pipe and the suspension springs of the compressor body;
- medium frequencies (1200-2600 Hz): This interval is dominated by the fluids (refrigerating and lubricating) contained in the cavity; this kind of excitation gives rise to flexure vibrations of the shell and they mainly come from intake gas pressure fluctuations. The unbalancing of the rotating shaft, whose basic critical speed is in this range produces stimuli which should not be neglected;
- high frequencies (above 2500 Hz): high frequency noise is caused by the vibrations originating from the impulsive action of the valves and from turbulence. Such vibrations are transmitted to the shell by the compressor suspension springs and by the discharge pipe of the re-

frigerating gas. Besides narrow band noise above 2500 Hz can be generated by magnetic-acoustic effects of the electric motor.

This work investigated the dynamic behaviour of the cavity and of the containing shell with an aim to evidencing the importance of their influence on the noise emitted. Both the cavity and the shell have been modeled with finite elements and then the relative eigenvalues and autovectors were determined. Modal analysis was performed by varying some parameters, such as cavity dimension, oil level, shell thickness and curvature radii, with an aim to pointing out their importance on the values of the natural frequencies and on the modal shapes.

MODAL ANALYSIS OF THE CAVITY

The cavity, delimited by the compressor body and by the containing shell, was modeled with 191 finite elements; the modal analysis, conducted with the ADINAT code, was performed on the assumption that the cavity contained freon at 60° C.
Figure 3 shows the first 28 natural frequencies of the cavity of a traditional compressor; the figure points out the modal density which is about 20 modes per 1000 Hz. Figure 4 schematically represents the first eight vibration modes. The broken lines indicate the positions of the nodal planes. In the figures relative to modes 5 and 6 the arrows indicate the shifting of the nodal lines starting from the bottom and going to the top of the compressor.

It can be noted that the first mode presents ventral zones (longitudinal extremities of the cavity) corresponding to the positions where the maximum pressure variations are verified. The basic frequency value depends on the distance between the points of maximum pressure (equal to about twice the wave- length) and so, it is hardly influenced by small variations in form carried out on the cavity.

In fact, there is no significant altering of the basic frequency when the cap is lowered, in such a way that the maximum distance between the compressor body and the shell is less than 10 mm. The most important effect is the decrease of the spectrum density at low frequencies (from 9 modes under 1000 Hz in the nominal shell to 5 in the case of the lowered cap). Raising the cap by 50 mm takes the spectrum density at the lower frequencies to 11 modes under 1000 Hz. Similar effects are produced by lowering or raising the oil level.

The analyses carried out have shown that the values of the natural frequencies are not substantially altered by small variations in form compatible with production requirements.
It should be noted that it is nevertheless advisable to reduce the gap between the compressor body and the shell in order to increase the modal damping values. The suppression of the undesired effect of some modes seem possible only with the use of suitable acoustic resonators [4].

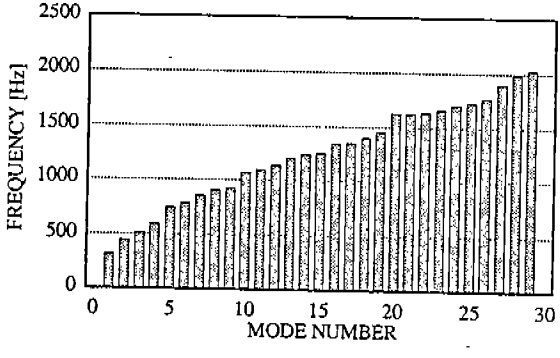

Fig. 3 - Natural frequency of the cavity of the conventional compressor.

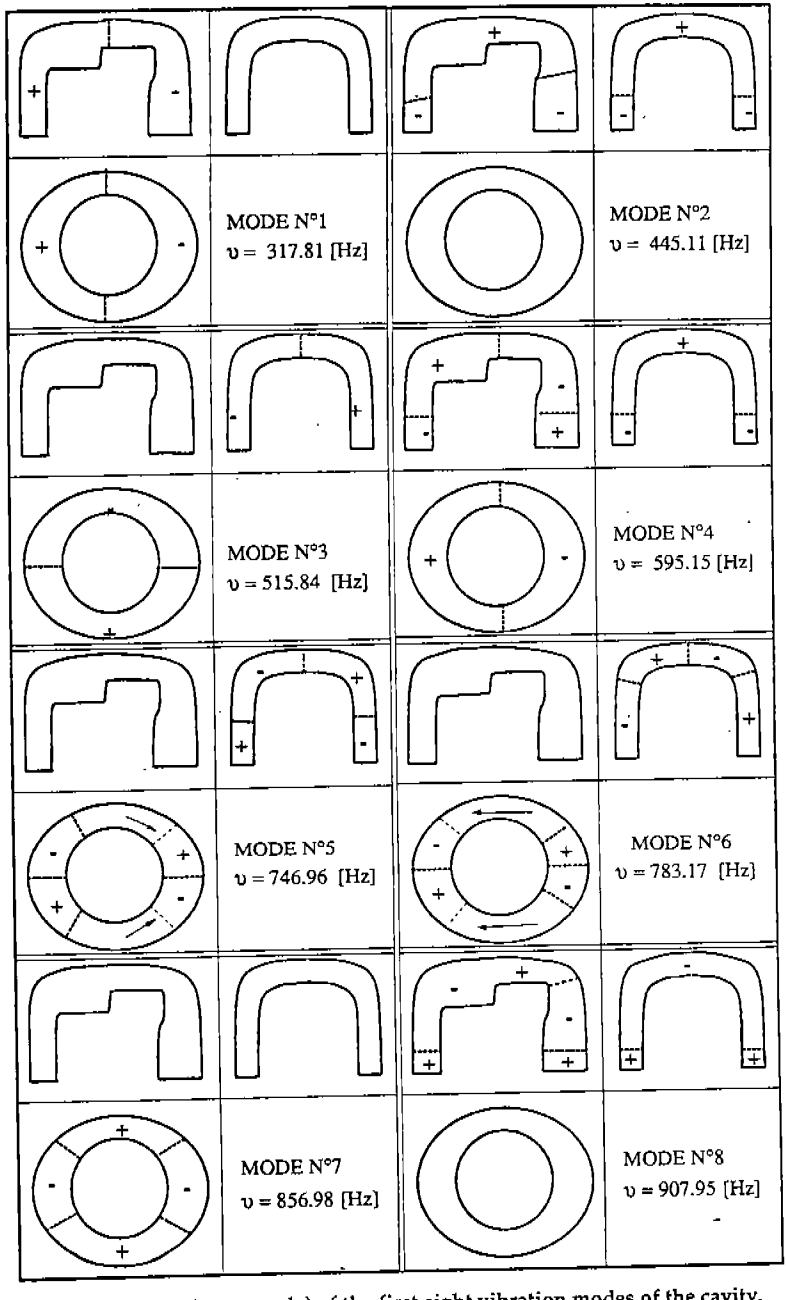

Fig. 4 - Scheme (not to scale) of the first eight vibration modes of the cavity.

CLASSIFICATION OF THE SHELL MODES

The review of the computed modal shapes of the shell (see next section), indicated that they belong to two classes (at least in the range of frequencies investigated here):
- Class 1 shows large displacements in the lateral pseudo-cylindrical portion of the housing, while the end-caps remain practically undeformed. This was called the *class of cylindrical modes* (Fig. 5).
- Class 2 shows large displacements at the domed end-plates, without involving the cylindrical body. This was called the *class of end-cap modes* (Fig.6).

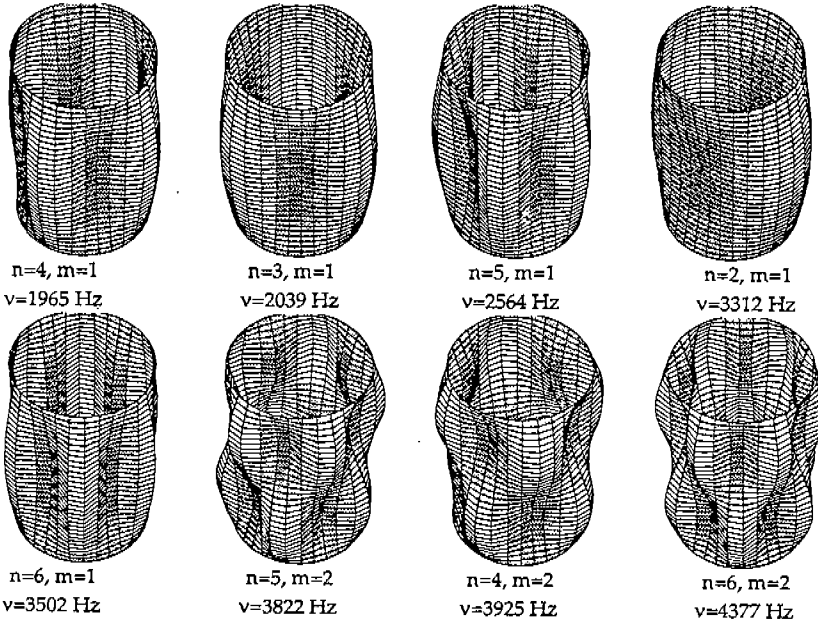

Fig.5 - Class of *cylindrical modes*.

The very existence of the two classes means that end-caps and cylindrical body are weakly coupled (coupling weakness is probably due to the high stiffness of the fillets linking the cylindrical body to the caps). The weakness of coupling allows us to explain the cylindrical modes in terms of the modes of an 'equivalent' tube (regardless of the presence of the caps) and, in their turn, the end-cap modes in terms of the modes of an 'equivalent' circular domed plate.

Closed-form solutions are available for tubes of circular cross-section, simply supported or clamped at both ends and for circular domed plates clamped at their boundary [5].

Fig.5 displays the first 16 modes of a tube simply supported at both ends. Height is equal to the height of the shell; radius is equal to the geometric mean of the two radiuses of the cylindrical part of the shell.

Because of the circularity of the cross-section of the tube, modes are in groups of two, sharing the same eigenvalue. They are characterized by two wave numbers: n, the number of half-waves in the circumferential direction, and m, the number of half-waves in the axial direction. Fig.7 shows eigenvalues as a function of n, for a given m. Frequency does not monotonically increase with n because the constraints applied at the ends of the tube (owing to its finite length) primarily affect the modes of vibration with low n. As Fig.5 shows, for $m = 1$, the minimum frequency is attained when $n = 4$; for $m = 2$ this is attained when $n = 5$.

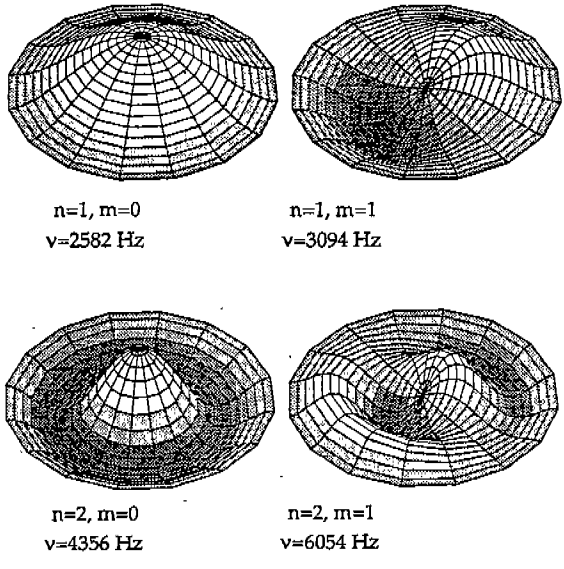

Fig. 6 - Class of *end-cap modes*.

Fig.6 shows the modes of vibration of a circular domed plate clamped at its boundary. The radius of the plate is the same as that of the tube above, and the radius of curvature of the dome is equal to the mean radius of curvature of the actual caps. As for the tube, the modes of vibration are characterized by two wave numbers (again called n and m).

The eigenvalues are also shown in Fig.7, together with the eigenvalues of the tube. Since the former increase more rapidly than the latter, we find fewer end-cap modes than cylindrical modes (up to the same frequency value).

The eigenvalues of a spherical shell with the same volume (and mean thickness) of the actual shell are also reported in Fig.7, to show the potential benefits of good shell shape design.

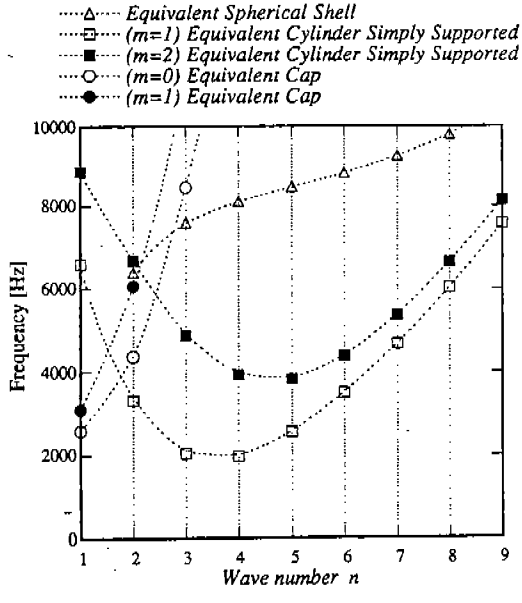

Fig. 7 - Eigenvalues of 'equivalent' spherical shell, domed end-plates and cylindrical body.

MODAL ANALYSIS OF THE SHELL

The seven figures 8A-B-C-D-E-F-G represent the natural frequency values of the first twenty modes of vibration of the shell according to different geometrical configurations.

In the figures the kind of vibration mode is also indicated with symbols: the first letter S indicates a symmetric mode, letter A an antimetric mode, the first number (n) shows the number of half-waves in the circumferential direction, and the second (m) shows the number of half-waves in the axial direction. The letters T and B indicate modes characterized by deformations at the top and at the bottom respectively.

As a reference the shell with a constant thickness of 2 mm was assumed (fig. 8A). Based on the results of the numeric analyses the following considerations can be made.

An increase of 25% in the shell thickness (fig. 8B) increases the natural frequency values of the first 20 vibration modes by an average of 10.7% and the fundamental frequency by 8.6%; a more substantial increase of 50% (from 2 to 3 mm) involves an 18.9% increase in the natural frequencies and a 14.6% increase in the fundamental frequency (fig.8C). These results agree with the values supplied by the approximate formula proposed in [6].

The stiffening weld ring, obtained by interference coupling of the cap with the lower part (10 mm x 5 mm), increases the value of the first 20 natural frequencies by 2.0% (fig. 8D) while the fundamental frequency increases by 2.6%.

A substantial increase in shell rigidity, and therefore of the natural frequency values was obtained by inserting double curvature surfaces (fig. 8E) which, for the same internal dimensions, involved a 5.5% increase in the shell overall length and a 6.6% increase in width. The natural frequencies of the first twenty vibration modes increased by 15.5% on the average and the fundamental frequency increased by 22.6%, compared to the reference (Fig. 8A) which shows simple curvature surfaces on its sides.

The double curvature must be maintained throughout the whole surface of the shell, in fact the introduction, on the bottom, of flattened areas used for facilitating the welding of the feet, caused, in the case in question, a 15% decrease of the natural frequency value.

The forming process for the shell causes variations in thickness, for example in the areas of greater shell curvature, thickness is reduced by about 20%. The natural frequency values of the shell with real thickenesses (variable from 2.5 mm to 1.8 mm) did not undergo variations of note (fig. 8F), whereas the vibration modes instead, because of the greater flexibility of the bottom, presented significant variations. For example, even the first vibration mode, type S_3-1, is already slightly coupled with the bottom.

In order to study the possibility of increasing the rigidity of the bottom, or of the cap, stiffening ribs were inserted, wherever the forming process permitted. The ribs inserted only on the cap (visible in fig. 6D) raised the natural frequency of the first mode, which only interests the cap, by about 300 Hz (fig. 8G).

Figures 9A-B-C show some typical modes of vibration.

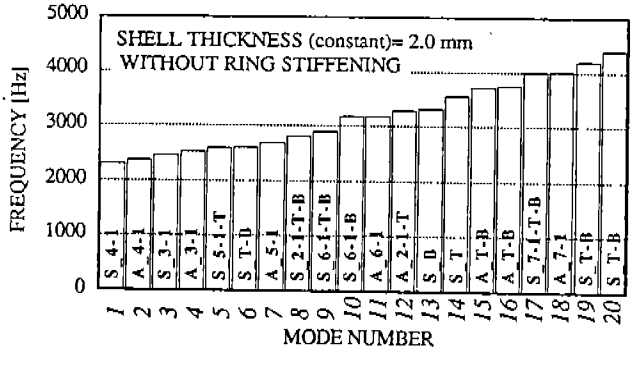

Fig. 8A - Natural frequencies and type of modes of a shell having constant shell thickness and without ring stiffening due to welding seam.

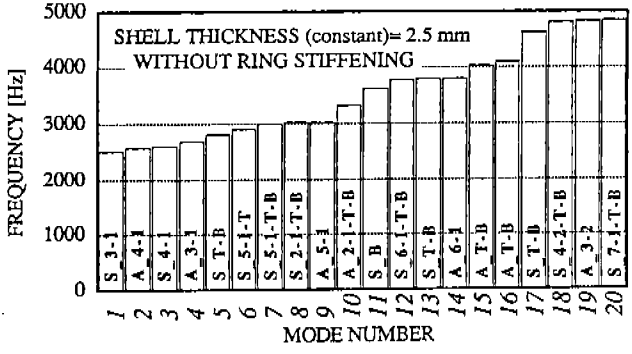

Fig. 8B - As the previous figure with shell thickness constant and equal to 2.5 mm.

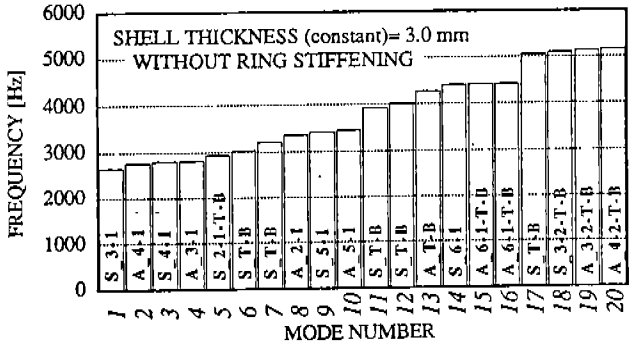

Fig. 8C - As the previous figure with shell thickness constant and equal to 3.0 mm..

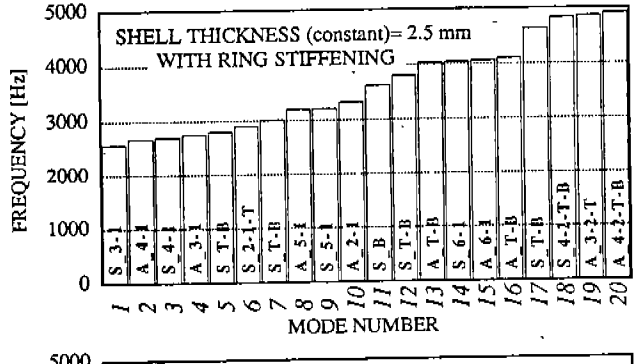

Fig. 8D - Natural frequencies and type of modes of a shell having a ring stiffening due to the welding seam (thickness=5.0 mm, width= 10 mm)

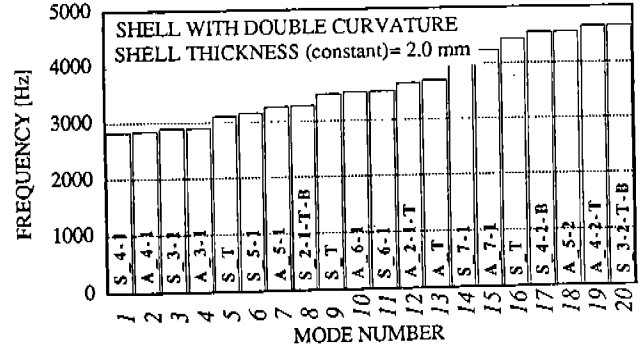

Fig. 8E - Natural frequencies and type of modes of a shell having surfaces with double curvature ranging from 30 mm to 300 mm.

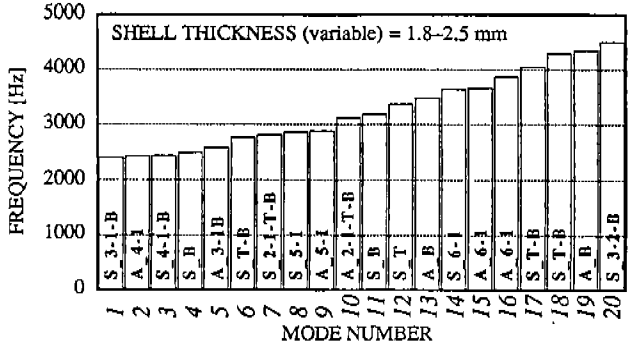

Fig. 8F - Natural frequencies and type of modes of a shell having variable shell thickness.

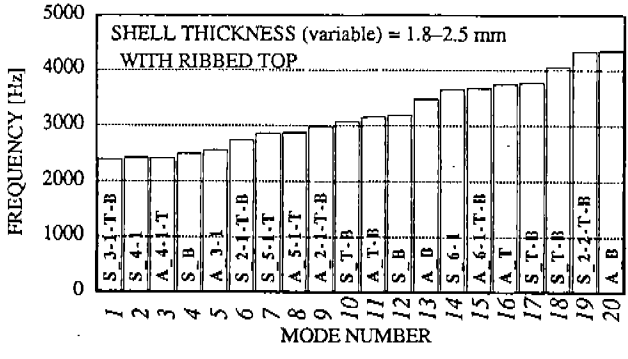

Fig. 8G Natural frequency and type of modes of a shell having a rib applied on the top.

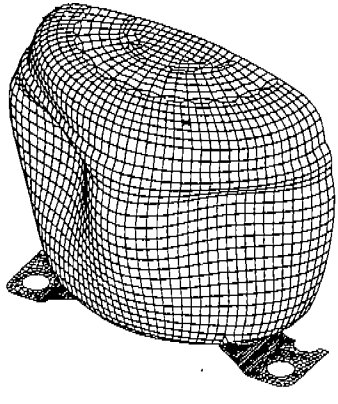

Fig. 9A - First symmetric eigenmode shape of case 8F (type of mode S_3_1-B).

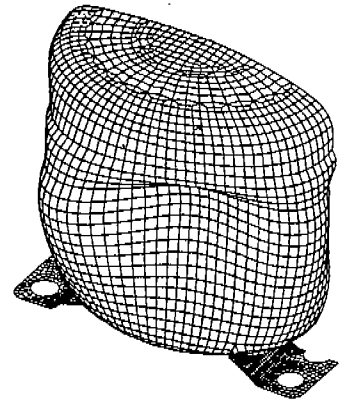

Fig. 9B - First antimetric eigenmode shape of case 8F (type of mode T_4_1).

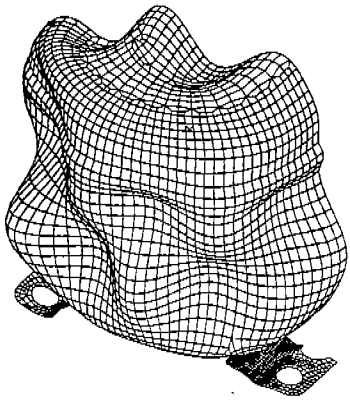

Fig. 9C - 20th symmetric eigenmode shape of case 8G (type of mode S_3-2-B).

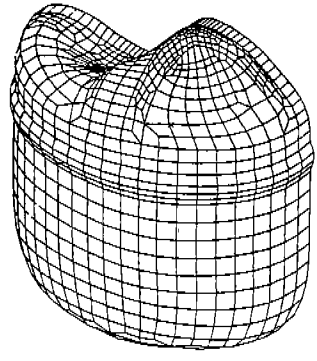

Fig. 9D - 10th symmetric eigenmode shape of case 8G (type of mode S_T-B).

CONCLUSIONS

In this work the authors have presented some results on the numerical studies performed on the cavity and shell with an aim to optimizing their acoustic behaviour.

The study on the influence of the form of the cavity on the vibration modes has shown that small variations of form do not substantially alter the values of the natural frequencies.

The study carried out on the shell has pointed out the possibilities of increasing its rigidity by means of operations that can be easily carried out and that are compatible with production requirements.

A final remark concerns the importance of the interpretative scheme for improved product quality. Knowledge of the existence of the two classes of modes and, above all, knowledge of how much natural frequencies can be increased by moving toward spherical-like shapes (Fig. 7) states an interesting and important guide-line for development.

REFERENCES

1 N. TSUJIUCHI, T. KOIZUMI: "Vibration and Noise Reduction of Household Refrigerator Using Modal Component Synthesis Technique". Proceedings of the 1990 International Purdue Compressor Conference; 1990, pp. 917-924.

2 K. TOJO, S. SAEGUSA: "Noise Reduction of Refrigerator Compressor". Proceedings of the 1980 International Purdue Compressor Conference; pp. 235-242, 1980.

3 D. C. LOWERY: "An Improved Shape for Hermetic Compressor Housing". Proceedings of the 1984 International Purdue Compressor Conference; pp. 285-290, 1984.

4. F. J. FAHY AND C. SCHOFIELD "A note on the interaction between a Helmholtz resonator and an acoustic mode of an enclosure". Journal of Sound and Vibration, n. 72, pp. 365-378, 1980.

5 W. SOEDEL, "Vibrations of Shells and Plates". Marcel Dekker Inc., New York, 1981.

6 MAU-PIN HSU W. SOEDEL "How Do Compressor Shells Vibrate and How Should They Be Designed". Report N. 0852 Ray W. Herrick Laboratories, 1986.

EXPERIMENTAL MODAL ANALYSIS OF A NEW SHELL FOR DOMESTIC REFRIGERATION COMPRESSORS.

M. Bucciarelli & F.M.Giusto

Zanussi Elettromeccanica S.p.A., Research and Developement Department, Pordenone Italy.

ABSTRACT

This paper reports about experimental investigations conducted on shells for domestic refrigeration compressors: the main goal was to state the benefits in noise reduction obtainable with shells having surfaces of high curvature.

Measurement data was collected and analysed employing experimental modal analysis techniques which are briefly described.

The results obtained from the experimental modal analysis have been useful to understand the noise emission mechanism and to tune a finite element model of a new shell for hermetic compressors to be employed in appliances utilizing ozone friendly refrigerants.

NOMENCLATURE

X	Input signal
Y	Output signal
H	Frequency response function
G_{xx}	Positive frequency autospectrum
G_{xy}	Positive frequency crosspectrum
γ_{xy}^2	Coherence function

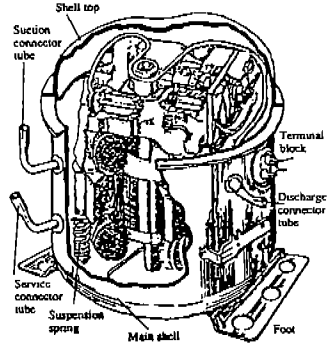

Fig.1 - A typical reciprocating compressor.

INTRODUCTION

Frequency response function measurements were taken on a compressor shell consisting in a hermetic container made of two metal parts joined under static pressure and welded together along a closed curve. These two parts which the shell is made up of, are two circular or oval cylindrical bodies with domed end plates of rather complicated curvature.

Usually the zones of the shell surface are called, in a self-explanatory way, Bottom , Top and Side Walls; in the following text they will be referred to by these names.On the Side wall surface four holes are made: three of small diameter for welding Bundy or Copper tubes,the fourth, slightly bigger one, is used to weld the electrically insulated plug of the power supply of the compressors electrical motor (the terminal block of figure 1). Furthermore, on the Bottom of the shell two thick metal sheets of rather simple geometry are welded, usually at suitable points to fasten the compressor to the refrigerator cabinet.

Once the compressor is closed inside its shell and is in a steady running condition, it is the shell surface that emits most of the sound (called Noise) and that gives it the characteristic signature ,i.e.:the shape of the Noise Spectrum. For this important reason a large amount of the development work for a new compressor shell is devoted to the analysis of the acoustic behaviour of the shell by means of experimental and theoretical Modal Analysis.

For the development of the new compressor shell a step by step method was followed: first of all a Finite Element Model was made from a shell having all the requirements of good geometry for noise reduction purposes, once a reasonable shape was found, Experimental Modal Analysis was carried out on a prototype shell and results were compared in the effort to get a more accurate model and to achieve better results.

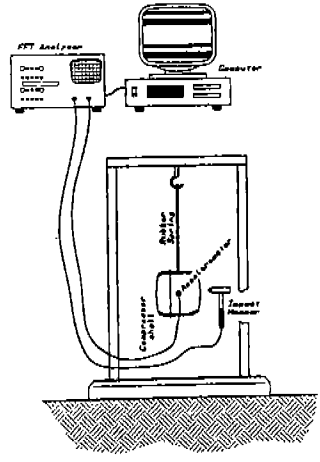

Fig.2 - Experimental apparatus.

EXPERIMENTAL DATA ACQUISITION

Experimental modal analysis was carried out on an empty closed shell with a built-in electric plug but without connection tubes.

The experimental apparatus is shown in figure 2:soft rubber strings were used to suspend the shell; a piezo-electric 1-gram accelerometer (with charge amplifier) measured accelerations; and an impact hammer with built-in force transducer excited the structure. An alternative method of excitation, based on an electrodynamic shaker, was also tried, but the impact hammer gave better performance and was ultimately preferred.

The choice of measurement and excitation points was made by exploiting the a priori knowledge of the existence of two classes of modes: the former primarilly involving the side walls, the latter the bottom and top. Measurement points were placed on the three major cross-sections of the shell: the first cutting the cylindrical part of the housing,the second placed in the plane of symmetry (cutting top and bottom caps), and the third normal to the other two.

Excitation points were placed at the intersections of the three cross-sections and on the "fillets" joining top and bottom to side walls.

The transducers were calibrated one respect to the other and International Standard Units were used. Tests were carried out to identify the frequencies of the rigid body modes of the system (shell - rubber spring - heavy beam).

By employing the impact tecnique, no overlapping of the rigid body modes frequency with the shell modes frequency was detected, the former being far apart from the latter. Modal testing was carried out on different cross sections of the structure and Frequency Response Functions (FRFs) were collected for an amount of 200 points on the shell. Coherence funtions were carefully examined to control the input signal when it had too low an energy and when the frequency resolution was too poor, in the attempt to improve the quality of the measurements. Another fact we kept in mind was the following: the whole set of mode shapes of the shell could not be fully excited by an input signal acting upon those points which allowed an exciting spectrum of constant and rather flat energy density all over the frequency bandwidth of interest. On the other hand, input points which allowed the excitation of the low frequency modes of the shell, yielded a set of FRFs that over-estimated the resonances located in the high frequency region of the spectrum of interest.

For this reason a compromise was made: sets of FRFs were collected consisting of four subsets, each belonging respectively to four

different reference points: two lying on a flat surface and two on the high curvature "fillets".
Acquired data, usually inertance, was stored in the following format:

$H_{xy} = G_{xy} / G_{xx}$ for the Frequency Response function, assuming noise at output and maintaining G_{xx} as costant as possible;

$\gamma_{xy}^2 = |G_{xy}|^2 / G_{xx} * G_{yy}$ for the Coherence function.

A smoothing window was selected and applied to output signals to fullfil the requirements of a correct FFT application for the response time frame length.
Several tests were effected with different frequency resolutions and bandwidth setups. Finally, it was found satisfactory to employ an eight hz resolution for a 4096 hz frequency baseband.This setup allows a better storage of data blocks in the Computer System when the number of actual FFT lines is taken into account. Figure 3 shows a FRF and Coherence function for an 8 hz resolution. By examining the whole set of stored FRFs a preliminary selection of the frequency range and of the candidate resonances was accomplished.It seemed the best choice to limit the frequency interval of our analysis between 2000 and 3500 hz and to focus our efforts on the evaluation of modal parameters for peaks located around the frequencies that are listed in table 1. With this approach, the most important range of sound emission of the compressor was taken into account, being absolutely certain that no resonances were present below 2000 hz in the FRFs spectra. On the other hand, input signals, acquired with the impact tecnique, showed a decreasing slope in energy density beyond 3500 hz, preventing enough excitation through the structure.

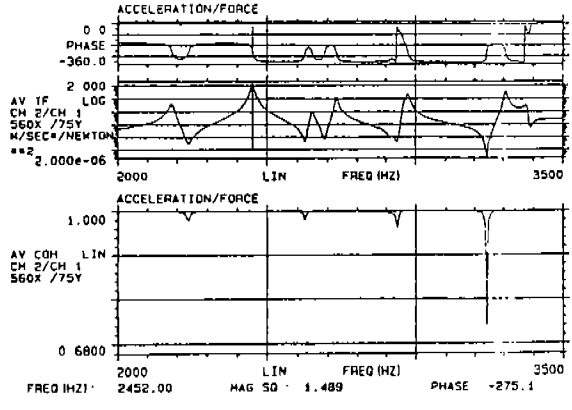

Fig.3 - An example of frequency response function and corresponding coherence function.

When all the collected sets of FRFs were found to be reasonably self-consistent all the data was transferred to the computer system for the application of the subsequent modal parameters and shapes extraction method. Various modal parameter extraction tecniques for Multi Degrees of Freedom Systems were in turn applied.Surprisingly, no method showed itself to be thoroughly decisive, neither for its ability to resolve all the resonances that were present in the Modal Indicator Function, nor (in many cases) for the evaluation of the residues, so that the analytical function was in close resemblance with the measured FRFs.

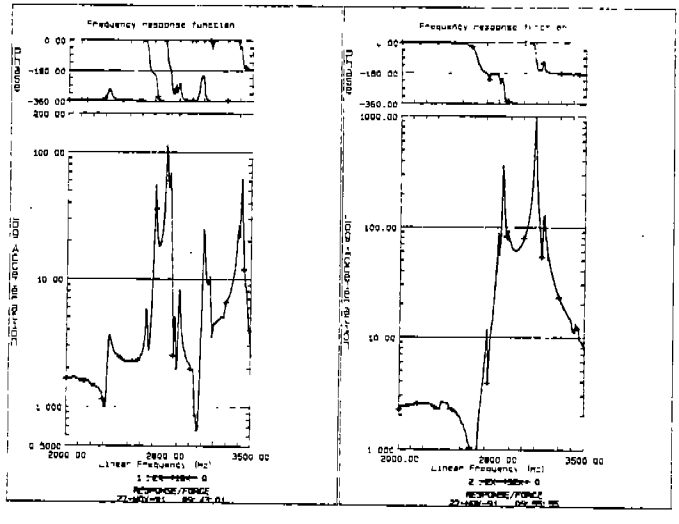

Fig.4 - Typical FRFs for side walls and domed end caps.

What seemed critical was the difference between the frequency response functions measured on the cylindrical (barrel-shaped) part of the shell and those measured on the top and bottom (spherical) parts.

As can be seen from figure 4 the FRFs are varied; the first shows well separated peaks as is typical of the barrel-shaped side walls; the second shows tight coupled peaks in a narrow frequency band.

At last we were confident with the results that a typical single degree of freedom approach gave us. The Circle Fit method, implemented in our computer, was then used.

This method,as is well-known,is based on the fact that a plot of the out-

of-phase components versus the in-phase components traces a circular arc in an Argand plane (imaginary versus real parts plane) for each resonance.

A circle is therefore fitted to the data in a narrow frequency range around the resonance frequency.Resonance frequency and damping can be estimated by determining the greatest angle between two data points along the circle. Estimation of residue is based on the diameter of the circle (amplitude) and its location in the Argand plane (phase).

Table 1 reports frequencies, maximum amplitudes and dampings of the first six modal parameters which have been extracted.

Figures 6.a and 6.b show the first four mode shapes involving the whole shell.Shapes are shown for the three typical cross-sections plotted in figure 5.

MODE NUMBER	FREQUENCY [HZ]	DAMPING	TYPE
1	2336	.06	CYLINDICAL
2	2807	.14	CYL /SPH
3	2831	09	SPHERICAL
4	2877	.04	CYL./SPH.
5	3108	03	CYL /SPH
6	3162	.68	SPHERICAL

Table 1 - Natural frequencies and dampings of the first 6 modes.

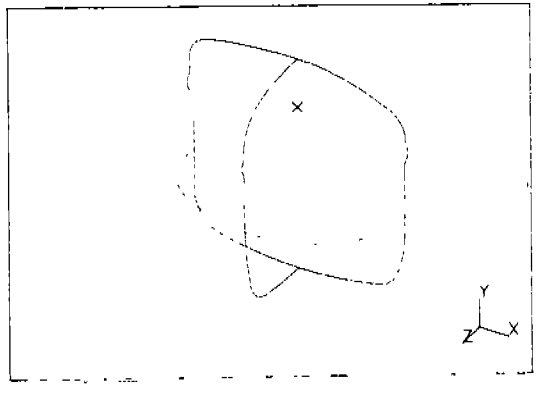

Fig.5 - The three cross-sections of the shell.

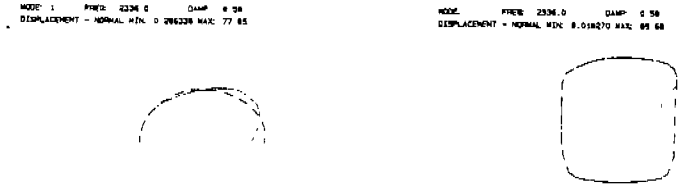

Fig.6.a - The first mode shape of the shell; only two cross-section are involved.

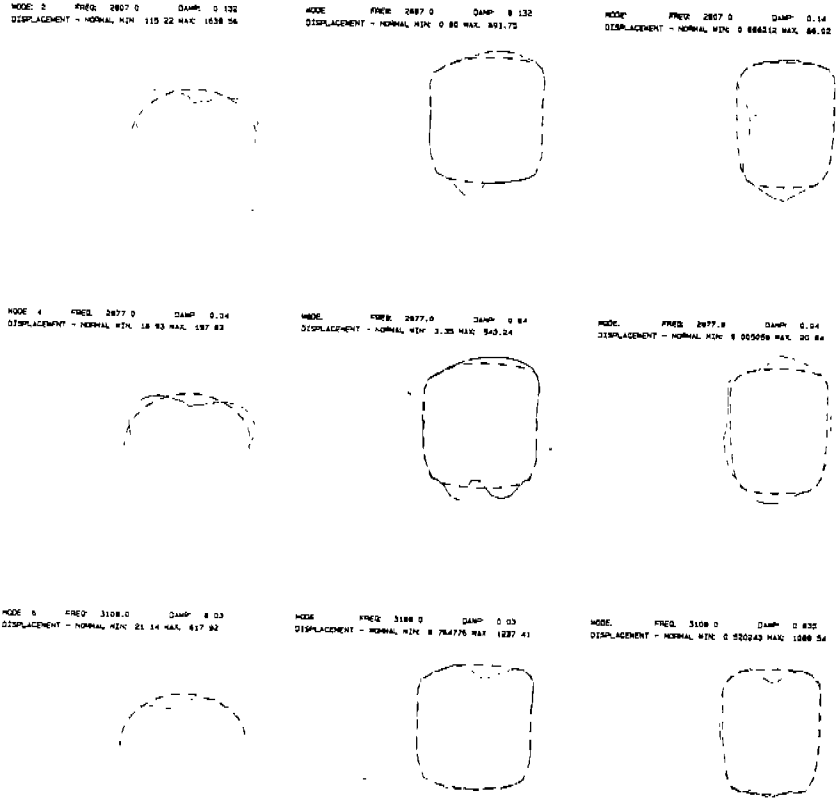

Fig.6.b - The three other mode shapes involving the whole shell.

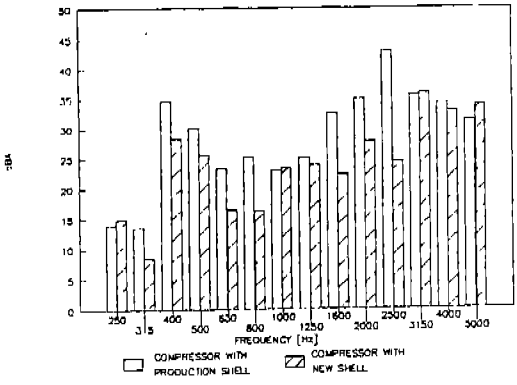

fig.7 - Comparison of SPW of the same compressors with old and new shell.

CONCLUSIONS

Initial experimental analyses did not use any form of a priori knowledge about modes. This lead to less effective placing of measurement and excitation points. They were placed all over the shell. The three-dimensional structure of the data thus collected required more measurement locations,was more difficult to interpret, and gave less information. Numerical simulation, and above all the availability of an interpretative scheme, greatly benefited experimental analysis. this lead to the definition of the three meaningful cross-sections and of the most useful excitation locations. A point to be stressed is the difficulty encountered in correctly identifying the splitted modes of the oval shell. It seems that the second and the fourth mode of fig. 6.b are the first two splitted modes of the oval cross section of the shell.

A final remark concerns the importance of the attained results.

As can be inferred from the plot at figure 7, our new developed shell has improved the acoustic performance of Zanussi Elettromeccanica SpA compressors. This characteristic is especially useful for those compressors to be employed with new refrigerants which are supposed to be ozone friendly. Such a plot was obtained by comparing the sound power levels of the same set of compressors (tested by standard acoustic measurements) with the old shell and ,subsequently, with the new one. As the graph shows, the best results have been obtained between the 1600 and the 2500 hz range represented in third octave bands.In this

range the new shell appears to be particularly effective. Overall, the accomplished improvement has permitted a reduction in sound power level by 2 dBa, with the same compressors inside the new shell. Such a result seems promising for the future use of our new compressor shell.

REFERENCES

1) EWINS, D.J.:
Modal Testing Theory And Practice
Research Studies Press, Letchworth, Hertfordshire, England

2) I-DEAS TEST USER'S GUIDE
Structural Dynamics Research Corporation, Milford. Ohio

3) MAU-PIN HSU, SOEDEL W.:
Experimental Measurements On Natural Frequencies And Mode Shapes Of Compressor Shell.
Purdue University, West Lafayette, Indiana

4) MAU-PIN HSU, SOEDEL W.:
How Do Compressor Shell Vibrate And How Should They Be Designed.
Purdue University, West Lafayette, Indiana

5) SOEDEL W.:
"Simple Mathematical Models of Mode Splitting of Hermetic Compressor Shells That Deviate From Axisymmetry".
Proceedings of the 1980 Purdue Compressor Conference, 1980, pp.259 - 262.

THE ROLE OF ESTIMATING THE STIFFNESS OF ROLLING ELEMENT BEARINGS, IN THE ANALYSIS OF SEMI-HERMETIC,TWIN-SCREW COMPRESSORS.

Uri Shapiro

SKF Engineering & Research Centre, Nieuwegein, The Netherlands

INTRODUCTION

The clear trends in rotating machinery design and construction are towards lighter and stiffer machines, and faster rotational speeds. Most machines suffer from some degree of mass imbalance, which is a major source of rotating forces. At high speeds these forces increase dramatically, and may excite resonances of the rotating machinery and the housing of the machine, causing those parts of the machine to vibrate. A stiff housing tends to absorb little of the vibration energy and therefore would act as a sound emitter, thus justifying the common opinion which regards rotating machines as potential noise and vibration generators.

The Twin-Screw Compressor

The compressors discussed in this paper typically consist of a male and female screw rotors, parallel to each other in close proximity, and supported by rolling element bearings. The female rotor is driven by the male through the screw lobe so that they are accurately synchronised. Both screw rotors are loaded radially and axially by forces generated from the gas flow. For better efficiency twin-screw compressors are constructed with tight clearance between the two screws. This design requires that excessive vibration of the rotors be avoided because it may lead to mutual hammering of the screws and consequently noise and accelerated wear. Therefore it may prove profitable to engage rotor dynamics analysis methods early in the design stage to predict the performance of the rotors. Such methods are able to foresee pitfalls, to simulate alternative solutions and to evaluate them prior to the actual manufacture of a test model. In this way the time and costs of correcting deficiencies may be dramatically reduced.
Two types of twin-screw compressors will be addressed here, with somewhat different assemblies:

(a) 'Open Shaft' - The rotors system is assembled into a massive housing with a flexible coupling to the drive motor on the protruding end of the male rotor. So the male rotor is driven by a power unit external to the compressor.

(b) 'Semi-Hermetic' - An electric motor is integrated into the compressor in such a way that the electro-rotor is mounted on the screw rotor. This is mostly an overhang part of the rotor, and therefore undergoes greater bending deflection than type (a).

Rotor Dynamics Performance

Each rotor of the twin-screw compressor orbits (whirls) in addition to rotating about its undeformed centre-line. The whirl orbit of a perfectly isotropic rotor in a vertical position would be a circle, otherwise it can take any form [1][1]. When the rotor whirls at the speed of rotation it is called 'synchronous' whirl, and otherwise 'asynchronous' whirl. Synchronous forward whirl is mostly a kinematic phenomenon caused by the forces generated by mass imbalance. Synchronous reverse , and asynchronous whirl are dynamic phenomena analogous to beam vibration. Thus dynamic whirl is associated with a form of bending of the rotor, referred to as a 'natural whirl mode shape', in short 'whirl mode', seen by a stationary observer as a vibrating beam. The frequency [Hz] at which the rotor whirls in a specific mode shape is named the 'natural whirl frequency' with reference to that mode, or in short the 'whirl frequency'. Sometimes the whirl frequency is called the 'whirl speed' and is then in [r/min].

[1]The numbers in square brackets refer to the List of References.

Every machine possesses an infinite number of whirl modes of the various bending shapes and their corresponding frequencies. The mode shapes and their natural whirl frequencies depend on the dynamic properties (mass and stiffness distribution) of the individual rotor. These properties depend in turn on the manufacturing tolerances of all the rotor components (e.g. mounting fits, bearing location,), which may vary slightly from one compressor to another. The variations, however small, lead to natural whirl frequencies which differ from those predicted for the nominal design, hence may differ from one compressor to another.

Vibration Excitation

It should be pointed out, however, that a rotor vibrates in a natural mode of whirl only if it is excited to resonate, i.e. in the presence of a forcing function with a frequency in close proximity to that mode. The most common case of excitation are the radial forces arising from mass imbalance of the rotors. As the speed of rotation of the rotor [r/min] approaches one of its natural whirl speeds (in [r/min] = [Hz] x 60) these forces excite the mode into resonance. The speed at which a mode is excited is called a 'critical speed', and the ratio of the whirl speed to the rotational speed is called the 'vibration order' (in short 'order') so that excitation by mass imbalance has order #1. A shaft with asymmetric cross-section caused by a keyway may give rise to excitation of order #2. Thus a keyway may excite a natural whirl mode at a speed of rotation which is half the whirl speed of that mode. This concept will be substantiated and further discussed later in the text with the help of practical examples.

AN APPROACH TO THE ANALYSIS

Rotor dynamics analysis is normally motivated by the desire to avoid the risk of operating at a critical speed within the rated speed range of the compressor. Such analysis can be used to simulate the operating conditions and predict the dynamic performance of each of the rotors, and to evaluate the effect of design changes. The focal point of the analysis is the analytical model representing those features of the real compressor of interest in this analysis. In general these are the mass and stiffness distributions, and the boundary conditions, i.e. the supports of the rotor.
The analysis presented herein deals only with the male screw rotor of both twin-screw compressor types: the open-shaft and the semi-hermetic.

The Rotor Dynamics Models

The rotor dynamics model of the Open Shaft screw rotor described below closely resembles many twin-screw compressor designs. This type is introduced to facilitate a discussion of the analytical model verification against experimental data, further in the text.

A Cartesian coordinate system is defined with the Z-axis along the undeformed centre-line of the screw rotor, and the Y-axis in the direction opposite to gravity (Fig. 1). The rotor has a rotational symmetry (also the screw approximately), so that the model consists of a series of cylinders of various lengths and diameters [2]. It is assumed to be elastic radially and rigid axially[2]. The screw segment of the rotor is modeled with a diameter representing its bending stiffness. Since it is smaller than the screw diameter, the rest of its mass is modeled as a point mass. The remaining parts of the screw rotor which do not add to its stiffness are also lumped as point masses (denoted m) at relevant locations on the rotor. The rotor is supported by five rolling-element bearings modeled as springs (denoted k) as shown in the stick model. They are arranged so that the angular-contact ball bearings (ACBB) k_1, k_2, and k_3, carry exclusively thrust load, while the cylindrical roller bearings (CRB) k_4 and k_5 support only radial loads.

[2]The reasons for the assumption of a rigid body in the axial sense are as follows:

a) The rotors in these compressors are mostly robust, they have a relatively large diameter as compared to the short length.

b) The natural frequency of the flexural axial mode of vibration would be well above the range of interest of the analysis.

The inner rings (IR) of the four bearings at the left end of the rotor are rigidly clamped axially onto the shaft, thereby contributing to its bending stiffness, and are therefore considered a solid part of it.

In the analysis the axial Z-axis, and the radial X-axis and Y-axis are all assumed decoupled[3] from each other. Thus the model consists of three, mutually independent sub-systems:

(a) An elastic rotor with 2-Degrees-of-Freedom in the X-Z plane, supported by the spring constant of the CRBs in the X-direction;
(b) A similar rotor in the Y-Z plane, supported by the orthogonal spring constants of the same bearings in the Y-direction;
(c) A mass-spring sub-system with Single-Degree-of-Freedom in the Z-direction and the axial stiffnesses of the ACBBs.

Bearing Stiffness Computation

The stiffness of a rolling-element bearing arises from the resistance of the material of the mating elements to elastic deformation at the contact [3]. The factors controlling it are grouped as:

a) Internal Geometry - Dimensions of the elements and the clearance, contact angle, and the number of rolling elements;
b) Rotor Assembly - Mounting fits, shaft stiffness, mounting resilience, and the force or displacement of the axial or radial preloading;
c) Operating Conditions - Shaft speed, the applied loading component acting on each bearing, and the azimuth orientation of the rolling elements relative to the load vector.

The bearings' stiffnesses are computed with a three-dimensional quasi-static[4] analytical model of the complete rotor, in the steady-state. The rotor is assumed to operate at a constant speed and loading by the gas forces. The computations yield a 5X5 square symmetric matrix for each bearing (Table 1.) corresponding to 3 translational and 2 rotational degrees of freedom.

Table 1. Bearing stiffness matrix[5]

k_x	k_{xy}	k_{xz}	$k_{x\alpha}$	$k_{x\beta}$
	k_y	k_{yz}	$k_{y\alpha}$	$k_{y\beta}$
		k_z	$k_{z\alpha}$	$k_{z\beta}$
			k_α	$k_{\alpha\beta}$
				k_β

The elements on the main diagonal named the 'pure elements' describe the stiffness in a given coordinate, i.e. the response to a force or moment in the same coordinate. So k_x is the stiffness in the X-direction due to a force acting in that direction. The remaining elements, called the 'coupling elements' describe the coupling between pairs of elements on the main diagonal.

[3]It is recognised that an error is introduced into the analysis through decoupling the sub-systems. This however, is of minor importance in weakly coupled systems (there are no disks), while it greatly simplifies the analysis.

[4]The term 'quasi-static' implies that the model accounts for the centrifugal forces acting on the orbiting rolling-elements but is otherwise a static model.

[5]The lower minor of the matrix is symmetric with the upper one, and therefore it need not be displayed.

In the matrix below k_{xa} is the coupling stiffness between a force acting in the X-direction and the resulting rotation about the X-axis. In the scheme of the decoupled system for rotor dynamics analysis, sub-systems (a) and (b) draw each a 2X2 square symmetric matrix from the matrix of the complete model, and sub-system (c) the pure axial stiffness term. The decoupled system is given in matrix form,

Table 2. Bearing stiffness matrix of the decoupled system

k_x	k_{xb}			
k_{bx}	k_b			
		k_y	k_{ya}	
		k_{ay}	k_a	
				k_z

A rotor of rotational symmetry where $k_x = k_y$ and $k_a = k_b$ for all the rotor supports[6] is regarded an isotropic rotor. In such a case, presumably, the respective coupling elements of sub-systems (a) and (b) are equal and these sub-systems become identical.

Rotor Dynamics Analysis

The rotor geometry and the stick model adequately describe the screw rotor for the purpose of dynamic analysis. Hence the bearing stiffnesses are computed prior to the rotor dynamics analysis to provide the necessary input data. Since in the quasi-static model the stiffness depends on the operating conditions of both load and rotor speed, these calculations are repeated for each combination of these conditions. The models used in the computations also account for mounting fits and resilience, and assembly errors. However the present stiffness computations and rotor dynamics analysis were conducted with the nominal data, without considerations of the manufacturing tolerances and possible assembly errors.

The bearing arrangement of the male screw rotor described above is designed so that the ball bearings carry exclusively the thrust load. They contribute, therefore, only to the axial stiffness of the rotor. The radial loading is supported by the CRBs which have radial clearance, hence their stiffnesses are expected to be anisotropic. This can be observed from the computation results tabulated below, comparing the two radial stiffness components of a bearing.

Table 2. Computed CRB stiffness [N/mm]

Bearing #4		Bearing #5	
k_x	k_y	k_x	k_y
543417	356512	400142	393084

[6]The support is defined to include the entire chain of springs from the shaft centre-line to ground.

The rotor dynamics analysis was used to predict the whirl modes and the associated whirl frequencies of the screw rotor within the frequency range 0-1000 Hz, tabulated below.

Table 3. Natural whirl frequencies [Hz]

Mode #0	Mode #1		Mode #2	
Z-axis	X-Z	Y-Z	X-Z	Y-Z
951	507	504	939	872

Evidently each of the radial whirl modes occurs twice, once in the X-Z plane and once in the Y-Z plane at different whirl frequencies, as could be expected for an anisotropic rotor. The results of the modal analysis are presented in the form of mode shapes of these modes (Fig. 2). The whirl frequencies of modes #1 are nearly identical and their mode shapes are similar, so that mode #1X only is shown in the diagram. The difference between the shape of modes #2X and #2Y is most pronounced at the left end of the rotor.

This may seem as though the rotor undergoes relatively larger radial bending deflections in the Y-direction than in the X-direction, at that end of the rotor. It should be noted, however, that different mode shapes have been normalised to their maximum deflection.

Model verification

Clearly it is strongly recommended to verify the analytical model before using it to evaluate the rotor dynamics performance of a compressor design. In the case under discussion the compressor has been operational so that some test data were available for comparison with the analysis. The signal was recorded from an accelerometer attached to the compressor successively at two locations,

1) On the housing, facing the male screw close to bearing #4, and pointing radially;
2) On the housing of bearing #5 close to the drive end, pointing axially.

The test data of the radial accelerations are presented in a diagram of the Frequency Response Function (Fig. 3). The curve consists of many spikes which seem to be super-imposed on a 'ridge' of a peak-amplitude plot shown by a dashed line. Further examination of the diagram reveals that the spikes are integer multiples of the rotational speed of the rotor, and their side-bands. Thus they can be regarded as a kinematic phenomenon depending mainly on the speed. The 'ridge' represents the dynamic characteristics of the compressor, including the screw rotors, as 'seen' by the accelerometer. Three of the computed whirl frequencies of Table 3 are depicted on the diagram by the vertical lines, and seem to support that hypothesis.
However assessment of the validity of the analytical model requires a more detailed examination of its characteristics. The main factors to be considered in interpreting the test data are outlined below:

1) Vibration excitation - For a screw rotor to vibrate in a natural mode of whirl, the mode must be excited to resonate. That occurs when the frequency of excitation, e.g. gear mesh, and the natural whirl frequency nearly coincide. This concept is presented in a Campbell diagram (Fig. 4) in the form of a critical speed map where the excitation frequencies are denoted by their orders. The horizontal lines represent the natural whirl modes, denoted by their number and coordinate. The frequency response function (Fig.3) can be thought of as a cross-section of the Campbell diagram at the operating speed 3550 r/min. It can be observed that modes #0 and #2X are excited by order #16, and mode #2Y by order #15, all at that speed.
2) Whirl mode shapes - The radial vibration forces are transmitted to the housing and sensor through the two CRBs #4 and #5 (Fig. 1). They are positioned at low response points relative to mode #1, and high response relative to modes #2.

The above observations indicate good agreement between the test data and the model.

DYNAMIC ANALYSIS

The Semi-Hermetic Rotor Model

The semi-hermetic compressor is similar to the open-shaft compressor and is modeled in much the same way (Fig. 5). From a rotor dynamics viewpoint, this rotor differs from the former type mainly by the electro-rotor mass carried on an overhung part of the rotor [4]. The structure of this mass and its mounting lead to the conclusion that it does not contribute to the bending stiffness of the rotor. Therefore the mass is lumped on the shaft at three points: m_2, m_3 and m_4, as displayed by the stick model.

Rotor Dynamics Analysis

The natural whirl frequencies and the associated mode shapes were computed for the male screw of the semi-hermetic compressor, at the rotor speed 3550 r/min. The frequencies are tabulated below,

Table 4. Natural whirl frequencies [Hz]

Mode #0	Mode #1		Mode #2		Mode #3	
Z-axis	X-Z	Y-Z	X-Z	Y-Z	X-Z	Y-Z
726	147	146	735	709	805	785

The modal survey is presented in a diagram (Fig. 6) of the mode shapes, and the rotor model for reference. The effect of the electro-rotor mass can be observed by comparing the modal survey of the open-shaft with that of the semi-hermetic rotors. For all the modes shown the latter type displays the maximum bending deflection at the drive end, as would be expected. Such mode shapes run the risk of the electro-rotor contacting the stator when operating close to a critical speed.

Critical Speed Problem

The rotor dynamics analysis has pointed at the risk that the whirl frequency of modes #3X and #3Y occur in close proximity to the operating speed of the male screw rotor 3550 r/min. That prediction is related to the event that excitation order #13.5 may be present in the compressor. The data obtained by computation were used to construct the critical speed map (Fig. 7). It can be observed that the horizontal lines representing these modes intersect with the line of order #13.5. That gives rise to the risk of critical speeds excitation at 3490 r/min (#3Y) and 3578 r/min (#3X). Observations of this kind in the development phase of the compressor are normally followed by searching for ways and means to eliminate that risk. This involves introducing design modifications which lead to re-distribute the mass and stiffness, thereby shifting the whirl frequencies. The variety of options for design solutions is only limited by the requirements of the compressor process, or by the imagination of the engineers. One of the options, seemingly simple to implement, is examined here from the rotor dynamics viewpoint. In this modified design an attempt is undertaken at redistributing the radial stiffness of the rotor by shifting bearing k_5 towards the electro-rotor. The effect of the design change was examined through rotor dynamics analysis. The analysis indicates that both modes were shifted away from the operating speed, with mode #3Y further down to 3464 r/min and mode #3X higher up at 3649 r/min. Evidently now the critical speed is caused by order #14.4 exciting mode #3X. This is shown on the diagram (Fig. 7) with the shifted whirl modes marked in brackets.

DISCUSSION

The Role of the Bearing Stiffness

The compressor was described in terms of the analytical model of the screw rotor for the purpose of rotor dynamics analysis. The bearing stiffness was shown to affect the whirl modes and frequencies of the rotor significantly.

It was demonstrated that, for a given screw rotor, both the spring constant and its location determine the whirl frequency. The importance of the bearing' stiffness is, however, relative to the whirl mode shape for the following reasoning,

a) Rigid-body modes - For a rotor which may be assumed rigid (see footnote 2) the only source of elasticity is provided by the bearings. Hence the bearing stiffnesses completely dominate these whirl modes and their frequencies.

b) Flexural modes - The influence of the bearing stiffness depends here on the bending stiffness of the rotor relative to the bearings, and on the bearing positions relative to the mode shape. It can be shown that the rotor stiffness is connected to the bearing stiffnesses in series. The nature of such a combination is that the softer one dominates.
Thus in the case of the twin-screw compressors with fairly stiff screw rotors, the bearing stiffness predominates.
The reference to the mode shape can best be explained with the help of the modal survey (Fig. 2). It can be seen that mode #1 displays hardly any bending deflection at the location of bearing #4. Hence this bearing has a negligible effect on the shape and frequency of mode #1, while mode #2 is strongly influenced by it. Comparison of modes #2X and #2Y shows that bearing #4 is the main source of the rotor anisotropy.

Estimating Bearing Stiffness

The analysis presented in sections 2 and 3 was, as mentioned, conducted with respect to the nominal manufacturing and assembly specifications of all the rotor components. Moreover, both manufacturing tolerances and assembly errors may influence the performance of the compressor considerably. In this section we examine the effect of some of the common mounting errors of bearings on estimating their stiffness and consequently on predicting critical speeds.

Axial Preloading

In general ball bearings are preloaded axially by the constant force of a spring mechanism, or by displacing one bearing, of a pair, relative to the other. Since the stiffness of these bearings depends strongly on the spin speed of the rotor it cannot be determined by static measurement. It is, therefore, necessary to rely on indirect estimates using measurements and computations, and finally verify the rotor dynamics model by comparison to test data. The effect of an erroneous estimate of the force of axial preloading on the whirl frequency was examined analytically. Results are presented in a Campbell Diagram for an error of 12.5% either below or above the nominal value (Fig. 8). The graphs demonstrate that the error of estimating the whirl speed diminishes with the speed[7], but still remains within a band of 4% at the operating speed.

Radial Clearance

The stiffness of Cylindrical Roller Bearings (CRB) depends on the internal radial clearance, in particular the orthogonal stiffness (k_y). Some of the causes of reduced clearance in the assembly of the compressor are an oversize shaft or an undersize bore of the bearing housing. Reducing the radial clearance of CRBs leads to a lower load on the individual rollers, thereby stiffer contact between the rollers and the raceways.

Eventually the bearing is stiffer and the radial natural frequency becomes higher. The extent of the effect of this assembly error can be illustrated with the help of a computed example. The radial clearance of two different CRBs with average pitch diameter of about 60 mm was reduced by 0.1 mm, and the increase of the bearing stiffness was computed.

[7]The reader would arrive at a similar observation from Fig. 4 of [3].
The results are tabulated below as the percentage change of the bearing stiffnesses from those with the nominal radial clearance.

Table 5. Computed increase [%] of CRB stiffness for reduction in radial clearance of 0.1 mm.

Bearing #4		Bearing #5	
k_x	k_y	k_x	k_y
9.7	24.6	17.4	19.6

The table shows that an assembly error of this kind may result in a significant error in predicting the natural whirl frequencies of the compressor.

Bearing Misalignment

One of the common reasons for this particular mounting error lies in the spring used for applying the constant force of axial preloading to ball bearings. These bearings in the twin-screw compressors discussed in the paper, were arranged to carry pure thrust loads. In this configuration the load is equally distributed among all the rolling elements, and the axial bearing stiffness is a maximum. For a misaligned bearing the load is no longer evenly distributed so that the bearing stiffness drops, and consequently also the natural whirl frequency. The model of the open-shaft compressor was used to illustrate the pronounced effect that may follow from a minor degree of misalignment. In that design (Fig.1) the back-up bearing #1 with 40 mm outer diameter was misaligned by tilting its outer ring an amount of 0.2 mm. This led to a lower natural frequency for the axial rigid-body mode, as could be expected. The simulation results for that model at half the applied load are tabulated below, with the whirl frequencies at the nominal mounting condition for reference.

Table 6. The effect of assembly errors on the axial whirl frequencies [Hz].

Condition	Male rotor speed [r/min]		
	10	2500	3550
Nominal	879	875	856
Misalignment	807	780	769

Also here, as for the other assembly errors, that error would lead to a substantial divergence of the test data from the computed data.

CONCLUSIONS

An approach has been described to rotor dynamics analysis of twin-screw compressors equipped with rolling-element bearings. It was shown with the help of case studies that the stiffness of the bearings can considerably influence the rotor dynamics behaviour of the screw rotors. A verified analytical model with correctly estimated bearing stiffness may be used to advantage to predict the performance of the compressor. That activity may help to reduce the risk of operating under resonant conditions and hence also to reduce noise and vibration levels.

However, the stiffness of rolling-element bearings can not be measured directly because it depends on the operating conditions and on possible assembly errors. One way of estimating bearing stiffness is to extract it from rotor dynamics analysis [5] by comparison with test data and with the knowledge of the bearing properties. Clearly, the effect of errors in the assembly must be allowed for in such estimates.

ACKNOWLEDGMENT

The author wishes to thank Dr. H.H. Wittmeyer, Managing Director of SKF Engineering & Research Centre BV, for permission to publish this paper.
Thanks are due to H. Saletti and R. Pamlin of Svenska Rotor Maskiner (SRM) Sweden, for making available compressor design and test data. The usefull discussions with Dr. J. Tripp of SKF Engineering & Research Centre, and H.H. Wallin of SKF Industries USA, are acknowledged with thanks.

LIST OF REFERENCES

[1] Nelson H.D. and Glasgow D.A., A quick graphical way to analyse rotor whirl, Machine Design, October 1976, pp. 124-130.

[2] Nelson H.D. and McVaugh J.M., The dynamics of rotor-bearing systems using finite elements, ASME Tran., J. Engrg. Indus., Vol. 98 No. 2, May 1976, pp. 593-600.

[3] Shapiro U., Rotor dynamics analysis of screw compressors fitted with rolling element bearings, SRM Technical Screw Compressor Conference 1992, May, Stockholm, Sweden.

[4] Wang K.W., Shin Y.C. and Chen C.h., On the natural frequencies of high-speed spindles with angular contact bearings, Proc. Inst. Mech. Engrs, Vol. 205 1991, Pt C: J. Mech. Engrng Sc pp. 147-154.

[5] Kraus J., Blech J.J. and Braun S.G., In Situ determination of rolling bearing stiffness and damping by modal analysis, ASME Tran., J. Vib., Acoust., Stress, and Reliability in Design, Vol. 109, July 1987, pp. 235-240.

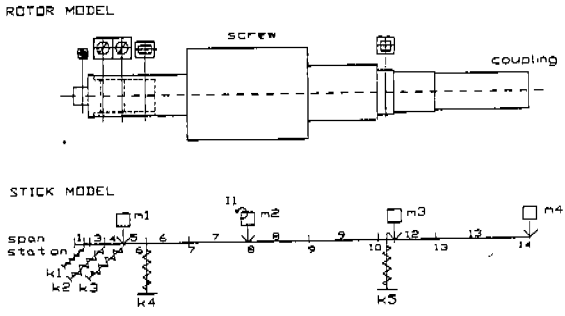

Fig 1 The male screw rotor of the twin-screw, open-shaft compressor modeled for rotor dynamics analysis

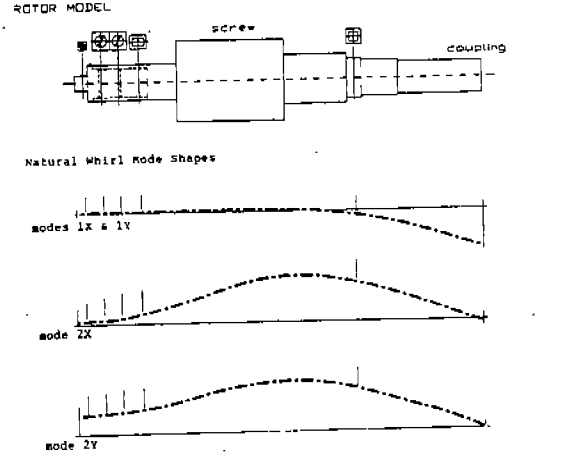

Fig. 2 Modal survey of the bending modes of the male screw of the twin-screw, open-shaft compressor using the analytical model.

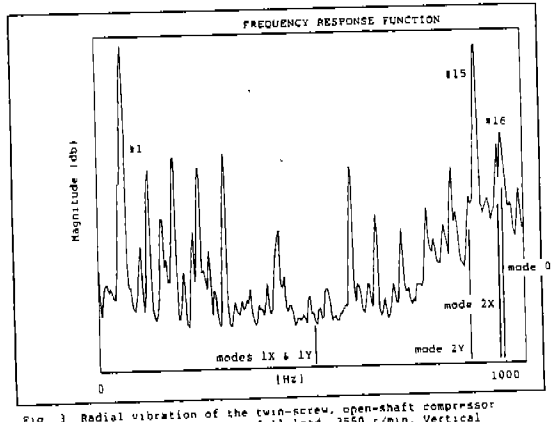

Fig 3 Radial vibration of the twin-screw, open-shaft compressor recorded during test at full load, 3550 r/min. Vertical lines indicate predicted whirl modes and frequencies. Courtesy Svenska Rotor Maskiner (SRM), Stockholm, Sweden.

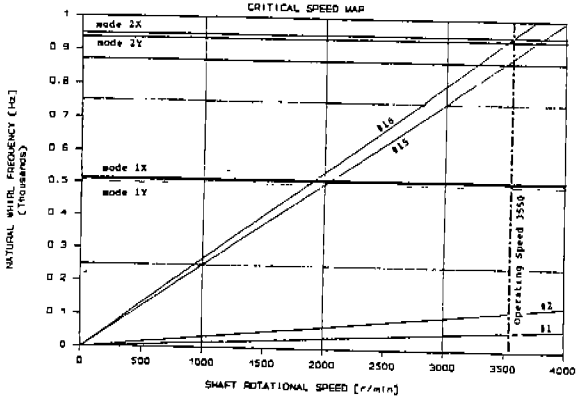

Fig. 4 The risk of critical speeds of the twin-screw, open-shaft compressor. Diagram constructed from computed data.

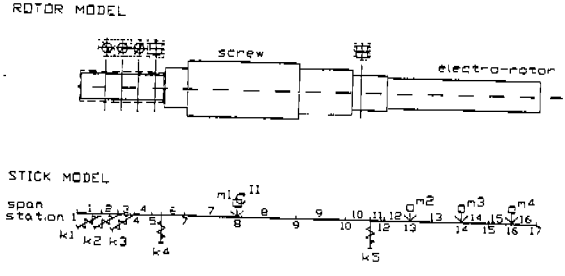

Fig. 5 The male screw rotor of the twin-screw, semi-hermetic compressor modeled for rotor dynamics analysis

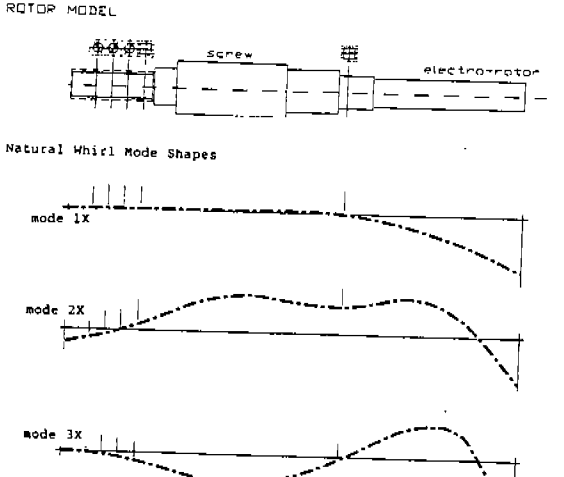

Fig. 6 Modal survey of the bending modes of the male screw of the twin-screw, semi-hermetic compressor using the analytical model.

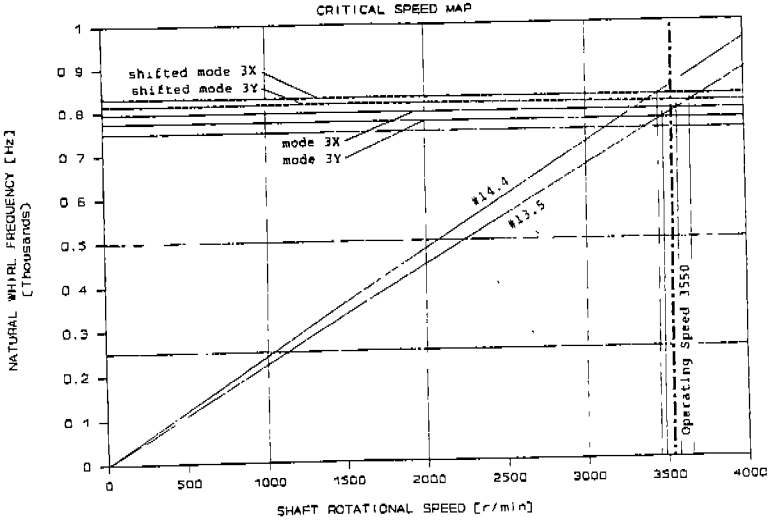

Fig. 7 The risk of critical speeds of the twin-screw, semi-hermetic compressor. Diagram constructed from computed data.

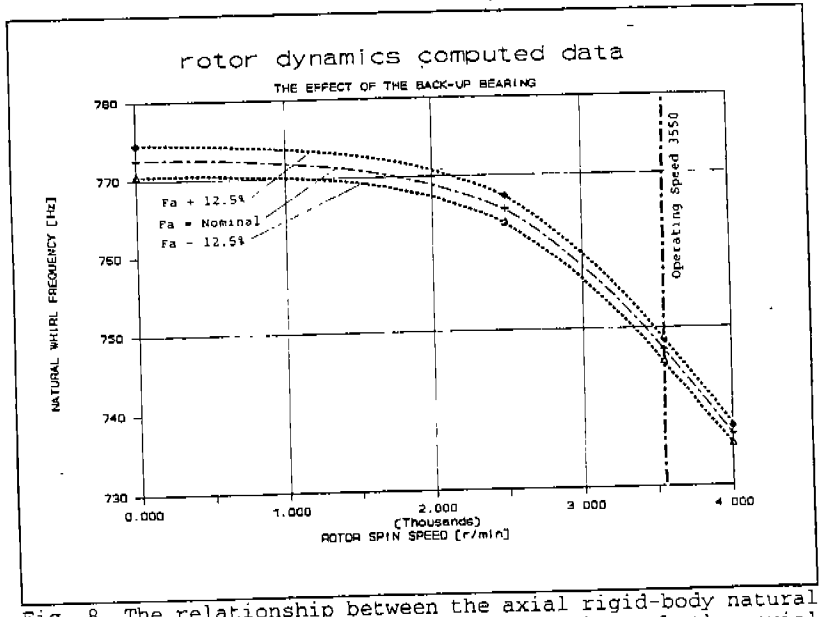

Fig. 8 The relationship between the axial rigid-body natural frequency and the spin speed, as function of the axial preloading of the back-up bearing.

A REVIEW ON FIXED-PERCENTAGE TOLERANCES FOR COMPRESSOR PERFORMANCE PARAMETERS

K.W. Yun
United Technologies Carrier Corp.
Syracuse, New York 13221 U.S.A.

ABSTRACT

Applying a fixed-percentage tolerance band to compressor performance parameters is a common practice in the industry. While finding the practice reasonable, its pitfalls are reviewed from the customer's as well as the compressor manufacturer's standpoint. Energy efficiency ratio needs to be controlled separately from capacity and input power, although it is derived from the two. Depending on the purpose, different levels of fixed percentages are suggested. Statistically, a bivariate normal distribution can be assumed for typical performance parameters. A set of 102 paired bivariate data for capacity and input power from an actual production audit has been statistically analyzed to verify that actual data generally fit the suggested distribution. Correlation analysis shows a slight positive correlation between capacity and input power against the assumed theoretical randomness.

INTRODUCTION

Besides cost, delivery, quality, and reliability factors, acceptance of a compressor at any given time is judged by its performance. Criteria or parameters for compressor performance are usually capacity (BTU's or calories per hour), input watts, energy efficiency ratio (EER), sound pressure level (SPL) and vibration. Among these, EER is not an independent parameter in the sense that it is derived indirectly as the ratio of capacity to input power. Among these criteria, the first three are the most commonly used ones.

PRACTICES IN THE INDUSTRY

Product evaluation, production audit and quality control deal with these parameters for control purposes. Original equipment manufacturers use them in accepting product performance. In the compressor manufacturing industry, it is common practice to allow a fixed-percentage tolerance band to the published or nominal value of a given performance parameter. Certainly, nothing is particularly wrong with the practice and it has served the industry fairly well.

Accepting the practice as a sound one, we should establish its theoretical basis and statistical significance verified with data generated in an actual production environment.

CUSTOMERS' AND MANUFACTURERS' PERSPECTIVES

Let us examine the fixed-percentage tolerance band not just from the manufacturer's point of view, but also from the customer's. First, from the manufacturer's point of view, the fixed-percentage tolerance band is a practical control tool in product assurance. The rule is simple enough to be popularly applied. Where product model proliferation is the case it is quite a convenient control scheme. On the other hand, there are some pitfalls. One of the pitfalls is the "as long as within $\pm$ x percent" syndrome. As actual mean value deviates from the published nominal value, the risk of performance fallout increases. Another pitfall is that the fixed-percentage rule is not very flexible as nominal performance of mass produced compressors could have a cyclic trend. A normal production environment sees both short-and-long-term shifting trends. Application of the rule without respect to time perspective is not a rational approach.

Next, from customer's point of view, it is difficult to reject product shipped as long as the product performance falls into the tolerance band. Customers could make a case based on statistical analysis of performance of product shipped, but to prove performance deficiency is realistically a difficult task. First, customers have limited time and resources or lack the capability to determine the deficiency to the required accuracy. An argument based on poor performance in an air conditioning system has an inherent limitation. Poor performance does not necessarily come from poor compressor performance.

SCOPE OF CONTROL PARAMETERS

Performance parameters controlled by manufacturers are usually capacity, input power, energy efficiency ratio, sound pressure level, and vibration. Of these, the first two or three are ones looked at as product assurance control for good reasons. On the other hand, as noise gets customers' increasing attention, sound and vibration, primarily sound level, acts as an important control parameter.

A relevant issue which arises here is whether we should also control EER as long as capacity and input power are controlled. The answer is a definite yes. First, as air conditioning system EER is scrutinized as a requirement, it is only fair for the manufacturer to control EER. One might argue that EER is not an independent parameter, that capacity and input power determine the value. However, if only capacity and power are controlled within a fixed ± 5 percent limit, otherwise unacceptable products with -10 percent of the nominal EER, could result in being accepted (Point 'A' in Figure 1).

Fig.1 Control Limits for Performance Parameters

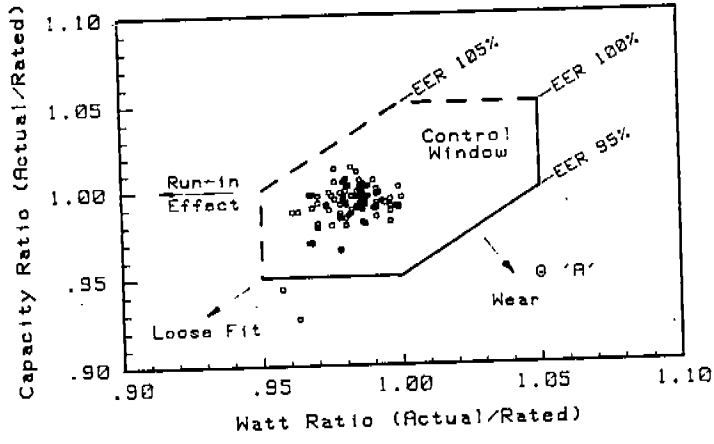

Certainly, this cannot be a satisfactory situation. EER should also be controlled as a separate parameter. The next question is concerned with the proper percentage. The same ± x percent limit, such as ± 5 percent, is reasonable, as the statistical analysis of the production data will show in later discussion.

There are, however, two points which should be discussed further. First, the three solid lines of bottom boundaries of the "control window" define the definite control limits. These are the minimum capacity and EER and the maximum watts. The other three dotted lines of the

upper boundaries may seem somewhat questionable limits. One might argue: why limit better performance? The limits should still be enforced as performance beyond these limits are practically not feasible even with a well-designed compressor and controlled manufacturing. Furthermore, the limits are also helpful as an alert to possible testing errors. If the mean performance shifts from the published nominal value as shown in Figure 1, then the window may have to be shifted. The second point of concern is with the shift of data points or the control window. The three arrows point to the general directions of shift for effects of run-in (or break-in), loose assembly fits, and mechanical wear of internal parts.

SOUND AND VIBRATION AS CONTROL PARAMETERS

As pointed out earlier, these parameters are getting ever-increasing attention. Applying a control limit to these parameters is a more complex matter. For example, setting a limit in overall sound pressure level (SPL) does not necessarily provide a satisfactory control of sound quality. Frequency content is often more important than the overall SPL value. It is tempting to use a fixed-percentage upper limit for these parameters too, but one must recognize that SPL represents a proportional number and a fixed-percentage cannot represent a true control limit. It is more appropriate to use a specific upper SPL limit, not a nominal SPL plus a fixed-percentage. In addition to this limit, specific controls on frequency content may be set.

"GOOD" FIXED-PERCENTAGE AS A CONTROL LIMIT

Accepting the fixed-percentage control limit as a popular, reasonable, and useful approach, the next question is what should the control limit be. Without taking a survey in the industry, $\pm$ 5 percent is known as a "good" limit and widely practiced. Despite the possible lack of a theoretical basis for the control limit, we regard the limit as a reasonable compromise between customer's and manufacturer's needs. The control range encompasses reasonable variations in manufacturing factors (variability in parts, machining, assembly, and testing errors). The actual production audit data in this paper proves the presumption.

The next question is if the same control limit is appropriate for both rating a compressor and providing samples for the customer's unit development. For these special purposes, one can make a good case for a tighter tolerance requirement. For compressor performance rating purpose, a good practice is to select samples with performance which approaches the mean nominal values as closely as possible. Note that the published value may not be the same as the actual nominal value. There is no sense to select intentionally a biased sample, as production is controlled within a fixed range. For a customer sample, it is important not to send a "good looking" biased sample. This will only hurt the customer and manufacturer later. Since the manufacturer must live up to the performance represented by the sample shipped, the sample should represent the nominal production performance. Thus, a tighter range, such as $\pm$ 2.5 or 3 percent is reasonable for customer sampling purposes.

STATISTICAL ANALYSIS OF PERFORMANCE PARAMETERS

As we are dealing with statistical performance data, it is appropriate to consider a statistical analysis of such data. Starting with capacity, input power and EER as control variables, we shall first characterize the variable, then suggest an appropriate statistical distribution function. The assumed distribution function will then be verified with actual production data.

Data to be examined - To examine an actual production situation, we shall analyze the production audit data of a rolling piston-type rotary compressor model. The 102 sets of raw-score data cover 28 weeks of production by a certain compressor manufacturer.

Measured Performance Variables - The data is in the form of paired capacity and input power data. The set of measured 102 pairs constitutes a bivariate data. Figure 2 depicts the data in a scatter diagram.

Fig.2 Performance Audit Data

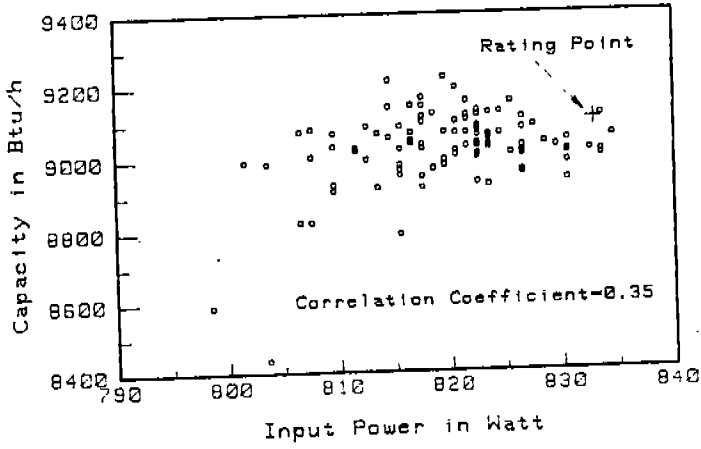

In this particular case, mean capacity and input power are slightly shifted from the rated mean values. This does not necessarily justify a change in the rated performance as one must look at production performance from long-term time perspective.

The locus of points in the scatter diagram provides an insight into the functional relationship that exists between the variables. As the EER is a resultant number from the other two parameters, basically we have bivariate data sets. The bivariate data represents data that occurs in ordered pairs. If we assume that the two variables are normally distributed (which is a reasonable assumption in light of the analysis to follow), we are dealing with a bivariate normal distribution.

Capacity and input power are interdependent on each other in that more capacity requires more power. However, the issue here is not a functional relationship between two parameters. Rather, we are interested if variations of the two parameters in products are independent or not. While it may be possible to prove it one way or the other from a theoretical standpoint, it would be more direct to test out a hypothesis statistically with actual data. While the result obtained from this set of data cannot be universally applied to other types of compressors or manufacturers, it gives a clue for statistical interferences.

Both variables are assumed to be random variables and must be free to vary. Values of one variables occur at random, depending on the production unit randomly selected in the sample. Both variables have equal status. It is convenient to think of the bivariate normal distribution as a three-dimensional surface, such as shown in Fig 3.

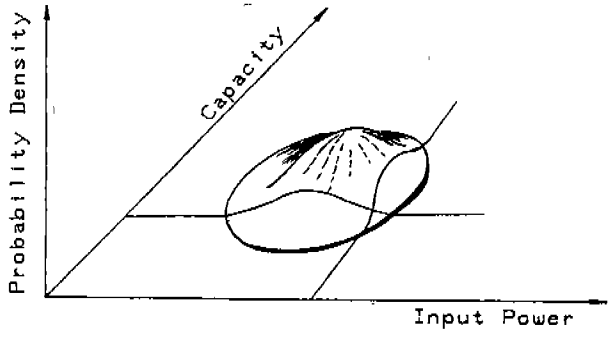

Fig.3 Bivariate Normal Distribution

In the three-dimensional diagram, the exact shape of this figure, which looks like a fireman's hat, will depend on how closely the variables are related. Here, we can see that:

(i) The frequencies are concentrated in a elliptical area with the major axis inclined upward to the right. There are no very low capacity with high power nor very high capacity with very low power.

(ii) The frequencies pile up along the major axis, reaching a peak near the center of the distribution. They thin out around the edges vanishing entirely beyond the borders of the ellipse.

Assumed Distribution Function - Capacity and input power vary together in a joint distribution. If the form of the joint distribution of two variables, X and Y, is normal, the joint distribution is a bivariate normal distribution. A special joint distribution of X and Y is assumed in making statistical inferences in simple correlation analysis - a bivariate normal distribution. If we slice the surface at any level of Y or X, the shape of the resulting cross sections are normal.

To start with, it is a reasonable assumption that the paired variables will a bivariate normal distribution function. A bivariate normal distribution means that each of two variables is distributed about the other normally. Because of the nature of the bivariate normal distribution, the values of either of the variables are distributed normally for a fixed value of the other variable. This distribution has five parameters, mean and standard deviation for each variable and the correlation coefficient, ρ, of which r is an estimator. The parameter, ρ, measures the closeness of the population relation between X and Y; it determines the narrowness of the ellipse containing the major portion of the observations.

Actual Distribution Function - To prove that we are indeed dealing with a bivariate normal distribution, we must show that each of capacity, input power, and the resultant EER variables has a normal distribution. This can be readily proved by first converting the frequency distribution into a cumulative frequency distribution, then plotting it on special normal paper.

All three variables are found indeed to be normal distribution. Thus, the bivariate data meets all requirements to be bivariate normal distribution.

Correlation analysis - The objective of a correlational study is to determine the strength of a relationship between paired observations. The correlation indicates the extent to which values of one variable are related to values of another variable. Though the regression analysis can provide essentially the same information that a correlation analysis does, we are not interested in a regression analysis here. Correlation focuses solely on the strength of the relationship. In the correlation model we assume that both X and Y values differ from sample to sample.

We want to find a measure, namely, the coefficient of correlation here, which will show us the degree of this covariability. The correlation coefficient is an index of the degree of this covariability. The population correlation coefficient ρ and its sample estimate r are intimately connected in the bivariate normal distribution.

The computed covariability between the two variables is 0.35. This lies between no covariance ($\rho=0$) and perfect covariablity ($\rho=+1$), both variables varying in the same direction (the plus sign). Then sample correlation coefficient $r=0.35$ gives the 95% confidence interval for ρ, $+0.16 < \rho < +0.51$. A positive relationship between two variables means that high value of capacity are paired with high values of input power, and low values of one with low values of the other. Correlation is a measure of linear relation only; it is of no use in describing nonlinear relations.

Test of Hypothesis that $\rho=0$ We wish to test the hypothesis that $\rho=0$ with a two-sided test and significance level of 0.05. A table of the normal distribution says that the region of significance is $z > 1.96$ and $z < -1.96$. For sample $r=0.346$ for a sample batch of 102 cases,

$$z=r\sqrt{n-1}=0.346\times10.05=3.48$$

As $z=3.48$ is in the region of significance, the hypothesis is not tenable and the sample estimate is significant. Thus, we must reject the hypothesis: $\rho=0$.

What this means is that there is a slight positive correlation between capacity and input power. Thus, the variables measured are not perfect random variables. However, this is not too surprising in view of various factors which might affect perfect randomness.

DETERMINANTS OF PARAMETER VARIABILITY

Variability in performance results from multiple sources. Variations exist in part dimension, assembly clearances, fits, and testing errors. We also recognize "break-in" run as a variable.

(i) **Time Variability** - How compressor is "broken in" and how long it is run are known determinants. The facts that input power decreases with run time and capacity varies only slightly suggest that the distribution shifts horizontally in Figure 2. This will increase EER.

(ii) **Manufacturing Assembly** - The tightness of component fit-up in assembly affects drag of mating parts and gas leakage, thus affecting input power and capacity.

(iii) **Testing Errors** - It is not clear how much of the variation in the data may be due to testing errors. We should recognize that measured performance variables are subject to errors in measurement. That is, we really observe values with testing

error included. Testing errors are independently and normally distributed with their own mean zero and respective variances. It is quite possible, however, that different cases can bias the inherent random nature of testing errors.

CONCLUSION

Fixed-percentage tolerance band to compressor performance parameters are commonly used in the industry, and the practice is reasonable. The "as long as within $\pm x\%$" syndrome without considering statistical implication and manufacturing variability is not rational. A tighter tolerance band for customer samples is justified. Along with capacity and input power, energy efficiency ratio needs also be controlled, although it is derived from the two. Statistically, a bivariate normal distribution can be assumed for typical performance parameters. Characteristics of such distribution describes actual production audit data. A set of 102 paired bivariate data, capacity and input power, from an actual production audit has been statistically analyzed. The actual data generally fits well to the assumed bivariate normal distribution. Correlation analysis, however, shows a slight positive correlation between capacity and input power. This suggests that a strict randomness lacks in the production data.

APPLICATION OF THE ECONOMIC ELASTICITY CONCEPT TO COMPRESSOR PERFORMANCE PARAMETERS

K.W. Yun
United Technologies Carrier Corp.
Syracuse, New York

ABSTRACT

Introducing the economic concept of elasticity, elasticity coefficients involving performance variables of compressors can be defined. Such a coefficient compares the percentage change in one variable with the percentage change in another. Using the published performance of three types of similar capacity compressors a total of twenty elasticity coefficients is computed. The computed coefficients are then classified into three general groups. Two specific coefficients, capacity elasticity of power and power elasticity of EER, are selected for further analysis. Also discussed is the former coefficient as a function of compression ratio. Finally, compressor run time, type of compressor, operating condition and compression ratio are cited as factors affecting elasticity values.

INTRODUCTION

Performance variables or parameters of a compressor include capacity, input power, energy efficiency ratio. And design, manufacturing and quality factors determine their values. Knowing qualitative interrelationship among these variables is not good enough in checking compressor performance. Given a set of performance values, a quantitative analysis of the interrelationship among the parameters is a prerequisite for performance improvements. In this effort, an analytical technique in economics is introduced. Also shown are results of applying the economic concept to various types of compressor and operating conditions.

THE ECONOMIC CONCEPT OF ELASTICITY

In economic studies, demand or supply curves which relate price to quantity demand or supplied are of a significant importance. Related to these curves, the economic concept of elasticity is widely used to express the responsiveness of quantity demand to price changes. Price elasticity coefficient of demand (supply) expresses the responsiveness. The coefficient compares the percentage change in quantity demanded with the percentage change in price.

Numerically, a typical demand curve passes through all three ranges, $|E| < 1$, $|E| = 0$, $|E| > 1$. Elastic (inelastic) demand means that over a given portion of the demand curve, a lower price would result in a proportionately larger (smaller) increase in quantity and increased (decreased) revenue. Unit elasticity means that a change in price would result in proportionate change in quantity with no change in revenue or total expenditure.

MATHEMATICAL EXPRESSION OF THE ELASTICITY CONCEPT

Mathematically, the concept bases the idea on the ratio of the percentage change in one variable to the percentage change in another. The general definition of Y elasticity of X, Ey, is percentage change in X divided by percentage change in Y.

To express the elasticity, we start with the expression of percentage change in variable X:

$$\text{Percent change in } X = \frac{\text{Amount changed in } X}{\text{Average of } X_1 \text{ and } X_2} = \frac{\Delta X}{X_0} = \frac{X_2 - X_1}{\frac{X_1 + X_2}{2}} \qquad (1)$$

where X_1 represents the X before the change, X_2 after the change, and X_0 being average of X_1 and X_2. Note the convention of using the midpoint of the variable range as a basis for calculating the percentage.

Likewise, using the same convention as above:

$$\text{Percentage change in } Y = \frac{\text{Amount Changed in } Y}{\text{Average of } Y_1 \text{ and } Y_2} = \frac{\Delta Y}{Y_0} = \frac{Y_2 - Y_1}{\frac{Y_1 + Y_2}{2}} \qquad (2)$$

The Y Elasticity of X is then:

$$E_y = \frac{\text{Percentage change in } X}{\text{Percentage change in } Y} = \frac{(1)}{(2)} = \frac{\frac{\Delta X}{X_0}}{\frac{\Delta Y}{Y_0}} = \frac{\Delta X}{\Delta Y}\frac{Y_0}{X_0} \qquad (3)$$

The above formula is an arc elasticity. As ΔY approaches to 0, the arc elasticity becomes point elasticity. The definition of point elasticity then becomes:

$$E_y = \frac{dX}{dY}\frac{Y_0}{X_0} \qquad (4)$$

where $[\Delta X/\Delta Y]$ transforms to $[dX/dY]$ as ΔY approaches to 0 in the limit.

CHARACTERISTICS OF THE ELASTICITY

There are several important characteristics to note in the elasticity formula:

(i) Elasticity is a relative measure, and the values range from minus infinity to plus infinity. Though it is customary in economic analysis to drop the negative sign, in our engineering analysis we shall not do so as the $\pm$ sign carries an important significance.

(ii) A positively [negatively] sloped curve yields a positive [negative] value for elasticity.

(iii) The formula (3) for computing elasticity consists of two parts - one representing slope $\Delta X/\Delta Y$ and the other position; the point (Y_0/X_0)at which the measurement is being taken. Thus one cannot look at a curve and determine its elasticity at a given point without referring to Y and X axes. This is because both the slope and position of a curve determine elasticity at any given point on the curve.

THE IMPORTANCE OF ELASTICITY

If elasticity is nothing more than another way of describing the shape and position of demand curves, it would not deserve much attention. What makes elasticity an important concept is not so much its descriptive usefulness as its analytic usefulness. The importance of

elasticity comes from three factors: magnitude, direction (± sign) of elasticity value, and magnitude of the resultant parameter from the product of the two variables. The sections following discuss significance of each of these three factors.

CALCULATION OF ELASTICITY COEFFICIENTS

We shall apply the concept of elasticity to compressor performance to different types of compressors - rotary-type compressor of one manufacturer, and reciprocating as well as scroll-type of the other manufacture. Published data from three types of compressors, with an approximate capacity of 24,000 btuh (6,050 kcal/hr) are used to calculate elasticity coefficients.

Computation of different elasticity coefficients uses a total of five performance parameters. Selected performance variables are EER in addition to capacity, input power, mass flow rate and amperage which compressor manufacturers publish. Out of 20 different possible elasticities, one half of them are just inverse of another. Furthermore, close intra-parameter relationship (such as capacity and mass flow rate) result in basically same values of elasticity. The following table summarizes classification of coefficients in three arbitrary ranges:

Y ELASTICITY OF X

\ X Y \	X=Capacity	Power	EER	Mass Flow	Amperage
Y=Capacity	-	I	U	U	I
Power	S	-	S	S	U
EER	U	I	-	U	I
Mass Flow Rate	U	I	U	-	I
Amperage	S	U	S	S	-

where I: Insensitive (Inelastic) $|E| \approx 0 - 0.5$

U: Unitary $|E| \approx 0.5 - 1.5$

S: Elastic (Sensitive) $|E| \approx 0 - 0.5$

Among the above elasticity, we shall examine the following two elasticity coefficients for further analysis.

CAPACITY ELASTICITY OF POWER INPUT

When we wish to express a relationship between two variables, such as compressor capacity and power input, functionally we can show how one variable changes with movements in the other. How sensitively power changes as compressor capacity changes is one of our interests as it relates to compressor energy efficiency ratio. Thus, we are interested in the characteristics of the capacity elasticity of power input.

We define the elasticity as the percentage change in power input as a result of percentage change in compressor capacity. Denoting capacity elasticity of power as Ec:

where W and C stand for input power and compressor capacity respectively. Input power is elastic when the percentage change in input power is greater than the percentage change in

$$E_c = \frac{\text{Percentage change in power input}}{\text{Percentage change in capacity}} = \frac{\frac{\Delta W}{W}}{\frac{\Delta C}{C}} = \frac{\Delta W}{\Delta C}\frac{C}{W} \qquad (5)$$

capacity i.e., when $\Delta W/W$ is greater than $\Delta C/C$, in elastic when $\Delta W/W$ is less than $\Delta C/C$, and unitary when $\Delta W/W$ is equal to $\Delta C/C$.

The elasticity varies with operating condition as one might suspect. For a given (reciprocating) type of compressor, values of Ec are plotted (Fig 1) over the compressor operating range.

Capacity elasticity of input power is inelastic over the wide operating range. The elasticity decreases with increasing evaporating temperature (Te) and approaches to zero at near 50°F (10°C). This observation for certain compressors relates to the decreasing slope of input power curves with Te. As Te decreases the coefficient converges to a certain value (0.4 in this case). This observation is not obvious from data or performance curves; one must compute the coefficient to find this type of characteristic.

Fig.1 Capacity Elasticity (Ec) of Input Power

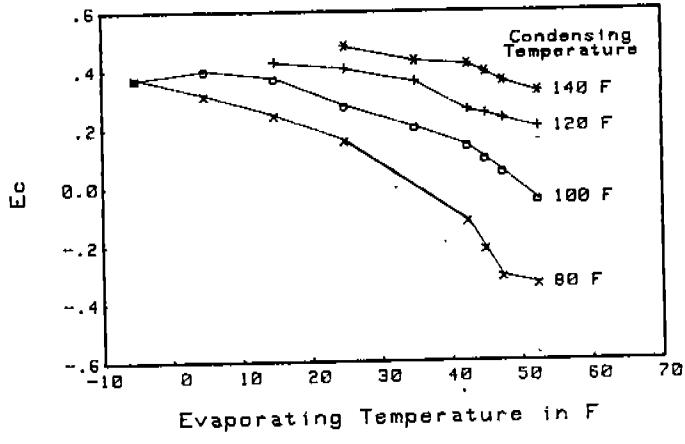

When the different types of compressors are compared, there are differences. Despite the differences among them, they are still all inelastic. However, the plus/minus sign of the values is significant as it says that input power varies in the opposite direction from capacity change.

POWER ELASTICITY OF ENERGY EFFICIENCY RATIO

We define power elasticity of EER as the percentage change in EER as a result of percentage change in input power. Denoting elasticity of efficiency as Ew:

$$E_w = \frac{\text{Percentage change in EER}}{\text{Percentage change in W}} = \frac{\frac{\Delta R}{R}}{\frac{\Delta W}{W}} = \frac{\Delta R}{\Delta W}\frac{W}{R} \qquad (6)$$

where R and W stand for EER and input power respectively.

Efficiency is elastic when the percentage change in EER is greater than the percentage change in input power - i.e. when $\Delta R/R$ is greater than $\Delta W/W$, inelastic when $\Delta R/R$ is less than $\Delta W/W$, and unitary when $\Delta R/R$ is equal to $\Delta W/W$.

Unlike the capacity elasticity of input power (Ec), the power elasticity of EER (Ew) provides a more useful analysis. Capacity being calculated as the power input multiplied by EER, a change in power can have one of three effects on capacity, depending on the shape and position of the curve. If EER changes by a larger (smaller) (same) percentage than power input, so that capacity increases (decreases) (remains unchanged) as the power decreases, EER is said to be elastic (inelastic) (unit elastic).

The fact that capacity is the product of power and EER explains why capacity responds in such a fashion to power changes. Which way the product of these two, that is, capacity, goes depends upon which changes the most (figured as a percentage). Compressor will lose capacity by a power if EER (demand) is relatively inelastic, higher EER for lower capacity. It tells something about capacity. Whether power elasticity of EER for a specific compressor is elastic or inelastic is very important because resultant net capacity change of increasing or decreasing power hinges on the elasticity.

The power elasticity of EER is quite elastic as shown in Fig 2 for given (reciprocating) type of compressor. It becomes even more elastic at high Te and low condensing temperature (Tc). This means that EER becomes very responsive (elastic) under high mass flow condition. On the other hand, the coefficients approach to a certain value (1.5-2 in this case) at low Te regardless of Tc. In other words, percentage changes in input power and EER stay at a fixed ratio at low Te.

Fig.2 Power Elasticity (Ew) of Energy Efficiency Ratio

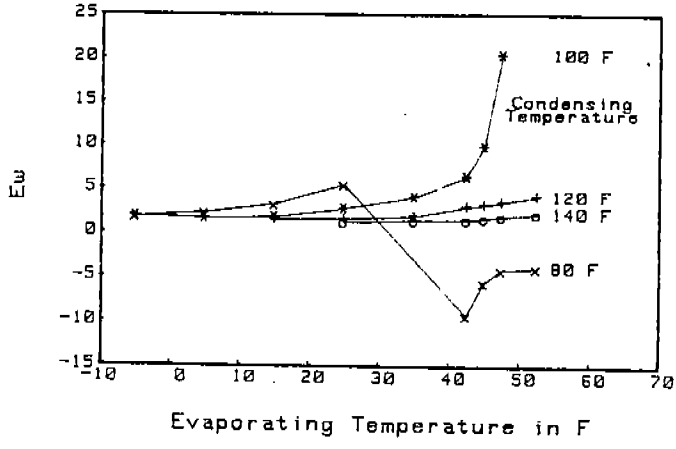

To illustrate differences in the capacity elasticity, three types of compressors, rotary, reciprocating, and scroll, are compared. Figure 3 shows the elasticity values as a function of Te at a fixed Tc. The elasticity coefficient is quite elastic with increasing trend with Te. Though the one odd-looking curve may be an accuracy problem with data, the importance of the opposite sign remains.

Fig.3 Power Elasticity (Ew) at a Fixed 100 F Condensing Temperature

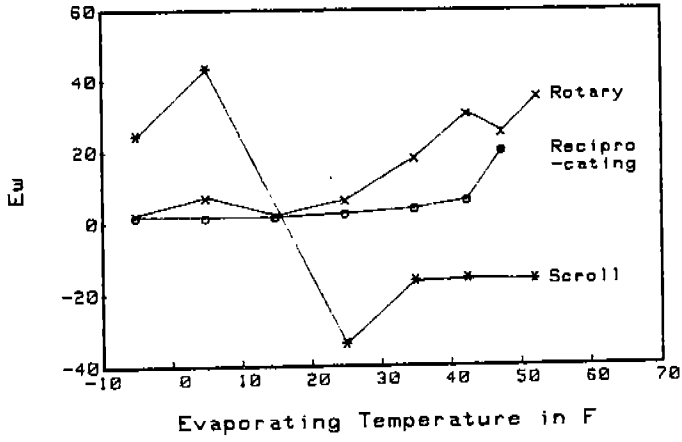

ELASTICITY AS A FUNCTION OF COMPRESSION RATIO

Compression ratio being an important factor for compressor performance, it will be intuitively interesting to examine an elasticity as a function of compression ratio. Figure 4 plots the calculated capacity elasticity, Ec as a function of compression ratio. The curves all show positive slopes, but each type of compressor distinguishes itself from the other two.

Fig.4 Capacity Elasticity (Ec) as a Function of Compression Ratio

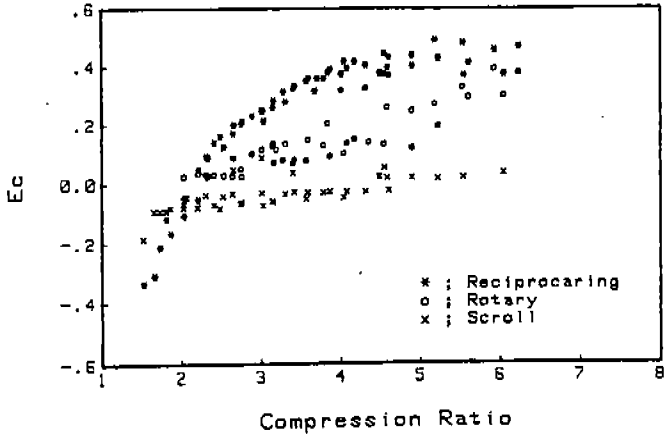

FACTORS AFFECTING MAGNITUDE OF ELASTICITY

Time perspective - Time perspective influences elasticity. Consider that initial break-in run results in reduction in input power during early break-in run. The time span could range from a few hours to weeks, somewhat depending on the running condition of the compressors.

Type of Compressor - The type of compressor does differentiate the magnitude of elasticity and direction of changes in some cases.

Operating Condition - The operating condition of the compressor affects both magnitude and rate of change in elasticity as shown in Figure 1.

Compression Ratio - Figure 4 illustrates the effect of compression ratio on elasticity.

CONCLUSIONS

The economic concept of elasticity can be applied to compressor performance variables. Out of the 20 elasticity coefficients possible from five performance variables capacity, input power, mass flow rate, energy efficiency ratio, and electrical current, one half of them are inverse relationship with respect to the other half. Given an elasticity coefficient, the value varies widely over the operating range of compressor. Though the magnitude of the computed values is roughly similar, the types of compressors show different characteristics with elasticity coefficients.

Capacity elasticity of input power is inelastic over a wide operating range. The elasticity approaches zero at an evaporating temperature of near 50°F (10°C) for the case examined. The elasticity coefficient curves as a function of compression ratio are all positively sloped, but each different type of compressor distinguishes itself from the other two. On the other hand, the power elasticity of EER becomes very elastic at high evaporating and low condensing temperatures. That means that EER becomes very responsive (elastic) under high mass flow condition. Compressor run time, type of compressor, operating condition, and compression ratio are factors which effect elasticity coefficients.

OPTIMAL DESIGN OF AN ACCUMULATOR IN A ROLLING PISTON TYPE ROTARY COMPRESSOR

Moonchang Choi, Song Choi, Hyunwook Lee *

CONSUMER ELECTRONICS RESEARCH L1 LABORATORY GOLDSTAR CO., LTD.
327-23, GARIBONG-DONG,GURO-GU,SEOUL,152-020 KOREA
* ROTARY COMPRESSOR DESIGN DEP. GOLDSTAR CO., LTD.
#1,2BLOCK,MOK-DONG,CHANGWON-SI,GYUNGNAM,641-310 KOREA

KEY WORDS :DESIGN OF EXPERIMENTS, EFFECTIVE FACTOR, INTERACTION, MAIN FACTOR, INDEPENDENT FACTOR, THE TABLE OF ORTHOGONAL ARRAYS,TWO-WAY FACTORIAL DESIGN, LINE AND DOT DIAGRAM, ANALYSIS OF VARIANCE, CONFIDENCE INTERVAL

ABSTRACT

The suction process of a rotary compressor comes with gas pulsation by the rapid and cyclic suction. Because it has an effect on suction loss and mass flow rate, the gas pulsation acts as an important factor on EER. Especially the structure of an accumulator is related to the condition of gas pulsation. So the purpose of this paper is to do an optimal design by using "design of experiments" of an accumulator. We used design of experiments to find the main factors by two-way factorial design with the table of orthogonal arrays. And by using the main factors and interactions, the experiments for optimal design were worked.

1. INTRODUCTION

It is generally well known that the accumulator of rolling piston-type rotary compressors is designed to prevent the suction of liquid refrigerant and the noise by the gas pulsation which is unavoidable in high speed compressors. So the geometry of an accumulator affects on the gas pulsation, and it changes not only noise level but also energy efficiency. Therefore if we make use of the gas pulsation, we can induce the overcharge of refrigerant gas in the suction process. By the fact that the overcharge reduces the suction loss and increases the volumetric efficiency, it increases the energy efficiency ratio(EER) on the whole.

Even though a lot of research has been done for the improvement of EER, there are few papers related to the accumulator. For this reason, we tried to find which design factors are effective on the performance of a compressor by experiments. And with that result, we decided the optimal geometry of an accumulator . First for the extraction of effective factors, we used 60Hz, 7400 Btu/hr class rotary compressors of the room airconditioners of GOLDSTAR CO.. By using experiments, the most effective factors on EER were found by design of experiments. The design of experiments means a planning method of experiments. It plans experiments, data acquisition, management of statistical data,analysis of data to get the most effective and maximum informations by the minimum experiments. The extracted effective factors and interactions were different for cooling capacity, input power and EER respectively. We were especially interested in EER in this research. After the extraction of effective factors we decided optimal geometry on the basis of found factors by using the trial and error method. For the reliability of experiments, we made test sets that could change only accumulators without changing main parts of a compressor.

2. EXTRACTION OF EFFECTIVE FACTORS

2.1. EXPERIMENT AND ANAYSIS BY DESIGN OF EXPERIMENTS

In Fig.1, seven design factors which might be affective to the performance ware selected. With the factors, design of experiments was conducted even considering interactions. Totally 16 cases of experiments were performed after selecting an appropriate line and dot diagram of the table of orthogonal analysis with two-way factorial design. In the line and dot diagram points mean effective factors and lines represent interactions. Table 2 shows dimensions and shapes of the factors. For the error estimation of a calorimeter, a compressor's performance was measured many times in a test condition. And the result was fairly good with the experimental error of 0.2 %.

2.2. EXPERIMENTAL RESULTS

Table 4 shows the results of experiments conducted randomly. After the analysis of variance, the effectiveness of each factor was determined with the confidence interval of 97.5 %. Table 5 gives the results of the effectiveness, and Table 6 is an analysis table for the direction of design. By Table 5, factors affecting the capacity, input and EER were different each other. The volume of the body , the diameter and the interaction (of the length and the diameter) of the L-Tube were found to be most effective factors.

BODY

The length and the diameter of a body did not affect on EER independently. But the volume of the body, the interaction of the length and the diameter of the body, were known to be much affective. By this fact, the volume of a body seems to be an effective factor for the performance by causing the pulsation of suction gas. In Table 6, it could be known that there is a critical point or volume which is the lowest in EER. But this point can not be fixed, because the point may vary with the capacities or characteristics of compressors.

L-TUBE

The L-Tube's diameter as an independent factor was effective, but the length was not. And the interaction of the length and the diameter, i.e., the volume, was also effective. Also, the length of the L-Tube interacted with the diameter of the body. Reflecting on the facts mentioned above, we can see that the L-Tube has complicated relation with the body. As shown in Table 6, when the length of the L-Tube is proportional to the diameter of the body there was a tendency to increase EER.

3. OPTIMAL DESIGN

Above mentioned effective factors were extracted from the conventional compressors of GOLDSTAR CO.. With the extracted factors we made experiments by varying effective dimensions of accumulators for now-developing compressors.

3.1. DIMENSION DEVELOPMENT FOR OPTIMAL DESIGN

The diameter of the L-Tube is constrained to the suction diameter of a cylinder. The diameter of an accumulator body is required as small as possible considering the setting in an air-conditioner. Based on the facts mentioned above, we developed dimensions of accumulators as follows.

i) Accumulator body

After fixing the diameter as 47.5, we developed the volumes of accumulators by changing the length.

ii) L-Tube

The diameter of the L-Tube was fixed as 15.8 by considering the suction diameter of a cylinder. So we varied the length only.

iii) Screen & screen holder

To decrease pressure loss as possible, screen mesh of 100x100, 0.1 was used. Screen holder of type 1 in Table 2 was selected.

3.2. EXPERIMENTAL RESULTS AND OPTIMAL DESIGN OF ACCUMULATORS

Experimental results were shown in Fig. 3 and Table 7. According to the results, there was difference of EER over 1 % even for a few experiments.As the length of the L-Tube is increased, cooling capacity and input power are reduced and EER is increased. Especially the reduction of input power by the increase of the length of the L-Tube may result from the effect of pressure pulsation even though the suction friction loss increases. By these factors the variation of EER is not trivial, so we should take account of them in the design of an accumulator. The appropriate design process of an accumulator is as follows.

1) To decide the volume of a body and the diameter of L-Tube by considering the compressor specification and system.

2) To decide the diameter and the length of the body. If possible, long length and small diameter will be available. Because the diameter of the body is less effective on EER than the volume of the body itself is. So the length can be designed within a wider range of variation in a decided volume.

3) To decide the L-Tube's length by trial and error method with varing the L-Tube's length.

If design of experiments is applied, the number of times of experiments will be reduced.

4. CONCLUSION

1) By changing the dimensions and shape of an accumulator, the increase of EER above 1 % compared with the conventional accumulator was gotten.

2) Most effective factors on EER are the volume of the body and the length of the L-Tube among the various design factors and the interactions of an accumulator.

3) Design of experiments was applied in designing an accumulator in view of improvement of EER.

REFERENCE

1. 박성현,"현대 실험 계획법",민영사,1990.

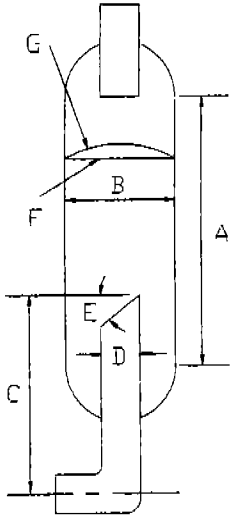

Fig. 1 Factors of accumulator

Table 1. Latin Square

sample number	1	2	3	4	5	6	7	8	9	10	11	12	13	14	15
1	0	0	0	0	0	0	0	0	0	0	0	0	0	0	0
2	0	0	0	0	0	0	0	1	1	1	1	1	1	1	1
3	0	0	0	1	1	1	1	0	0	0	0	1	1	1	1
4	0	0	0	1	1	1	1	1	1	1	1	0	0	0	0
5	0	1	1	0	0	1	1	0	0	1	1	0	0	1	1
6	0	1	1	0	0	1	1	1	1	0	0	1	1	0	0
7	0	1	1	1	1	0	0	0	0	1	1	1	1	0	0
8	0	1	1	1	1	0	0	1	1	0	0	0	0	1	1
9	1	0	1	0	1	0	1	0	1	0	1	0	1	0	1
10	1	0	1	0	1	0	1	1	0	1	0	1	0	1	0
11	1	0	1	1	0	1	0	0	1	0	1	1	0	1	0
12	1	0	1	1	0	1	0	1	0	1	0	0	1	0	1
13	1	1	0	0	1	1	0	0	1	1	0	0	1	1	0
14	1	1	0	0	1	1	0	1	0	0	1	1	0	0	1
15	1	1	0	1	0	0	1	0	1	1	0	1	0	0	1
16	1	1	0	1	0	0	1	1	0	0	1	0	1	1	0
	C	E	CE	D	CD	ED	AB	B	BC	G	CG	F	CF	AC	A

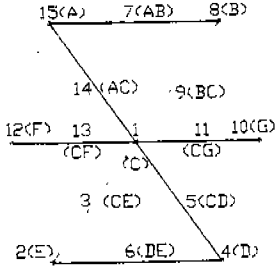

Fig. 2 Line and dot diagram

Table 2. The dimension and shape of each factor
unit [mm]

FACTOR	O - TYPE	1 - TYPE	REMARKS
A	90	120	Body length
B	50.8	65	Body diameter
C	90	130	L-tube length
D	9.52	12.7	L-tube diameter
E	0°	45°	Section angle
F	Ø0.23,0.18 100 x 100	Ø 0.1 100 x 100	Screen mesh
G			Screen holder type

TERMS \ NUMBER			1	2	3	4	5	6	7	8	9	10	11	12	13	14	15	16
BODY		ø	50.8	65	50.8	65	50.8	65	50.8	65	50.8	65	50.8	65	50.8	65	50.8	65
		L	90	120	120	90	120	90	90	120	120	90	90	120	90	120	120	90
L TUBE	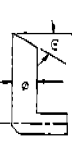	θ	0	0	0	0	45	45	45	45	0	0	0	0	45	45	45	45
		ø	9.52	9.52	12.7	12.7	9.52	9.52	12.7	12.7	9.52	9.52	12.7	12.7	9.52	9.52	12.7	12.7
		L	90	90	90	90	90	90	90	90	130	130	130	130	130	130	130	130
SCREEN	 MESH DIAMETER ø MESH #	ø	0.23 / 0.18	0.1	0.23 / 0.18	0.1	0.1	0.23 / 0.18	0.1	0.23 / 0.18	0.23 / 0.18	0.1	0.23 / 0.18	0.1	0.1	0.23 / 0.18	0.1	0.23 / 0.18
		#	30 × 160	100 × 100	50 < 160	100 × 100	100 × 100	30 < 160	100 × 100	30 < 160	30 × 160	100 < 100	30 × 160	100 × 100	100 < 100	30 < 160	100 × 100	30 × 160
HOLDER	 A B	type	A	B	B	A	A	B	B	A	A	B	B	A	A	B	B	A

Table. 3 Development of parts for experiment

Table 4. Experimental data for the extraction of effective factors

NO.	C C A P	INPUT	E E R
1	99.14	99.48	99.64
2	100.28	100.28	99.98
3	100.14	100.32	99.81
* 4	100.00	100.00	100.00
5	99.87	100.72	99.15
6	99.31	100.51	98.82
7	102.55	99.96	102.59
8	101.30	100.16	101.14
9	101.31	101.50	99.82
10	102.15	102.39	99.75
11	99.31	99.54	99.77
12	100.78	99.44	101.34
13	102.08	101.74	100.25
14	103.51	101.74	101.62
15	99.37	101.85	99.62
16	100.38	99.32	101.06

* *Reference Accumulator*

Table 5. Results from analysis of variance

T E R M S		CCAP	INPUT	EER
BODY	LENGTH			
	DIAMETER	△		
	LENGTH x DIAMETER	○	△	◎
L TUBE	LENGTH	○	○	
	DIAMETER	△	◎	○
	LENGTH x DIAMETER	◎	◎	○
	SECTION ANGLE	○		△
BODY DIA. x L-TUBE LEN.		○		○
SCREEN HOLDER			○	
BODY LEN. x L-TUBE LEN.			△	

◎ *Very effective*
○ *Effective*
△ *May be effective*

Table 6. Analysis of variance of expected values

1) A x B (BODY LENGTH x BODY DIAMETER = BODY VOLUME)

	A0		A1		SUM
B0	* 1, 7, 11, 13	**39.139	3, 5, 9, 15	38.763	77.902
B0	4, 6, 10, 16	38.884	2, 8, 12, 14	39.317	78.201
SUM	78.023		78.08		156.103

2) D (L-TUBE DIAMETER)

D0	1, 2, 5, 6, 9, 10, 13, 14	77.745	156.103
D1	3, 4, 7, 8, 11, 12, 15, 16	78.358	

3) C x D (L-TUBE LENGTH x L-TUBE DIAMETER = L-TUBE VOLUME)

	C0		C1		SUM
D0	1, 3, 5, 7	39.035	9, 10, 13, 14	39.06	77.745
D1	3, 4, 7, 8	39.264	11, 12, 15, 16	39.094	78.358
SUM	77.949		78.154		156.103

4) B x C (BODY DIAMETER x L-TUBE LENGTH)

	B0		B1		SUM
C0	1, 3, 5, 7	39.035	2, 4, 6, 8	38.914	77.949
C1	9, 11, 13, 15	38.867	10, 12, 14, 16	39.287	78.154
SUM	77.902		78.01		156.103

※ A0 , A1 , B0 ..... C1 : Refer to the table 2.

* : Sample number

** : Sum of EER for those sample numbers

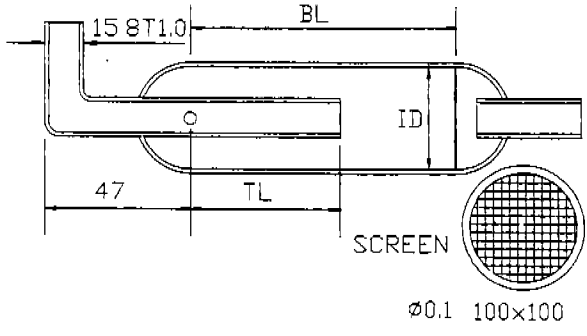

Fig. 3 Dimension developments of accumulator

Table 7. Dimensions of extracted factors for experiments

	I D(mm)	B L(mm)	T L(mm)	INPUT	C C A P	E E R
	55.0	113	103	98.86	99.80	100.22
*	61.5	160	103	100.00	100.00	100.00
	47.5	120	70	99.99	100.50	100.54
	47.5	120	80	99.76	100.33	100.58
	47.5	120	100	98.97	99.30	100.28
	47.5	120	120	98.55	99.11	100.53
	47.5	140	100	98.97	99.11	100.93
	47.5	140	120	99.61	100.06	100.51
	47.5	140	140	98.61	99.57	100.96

* *Reference dimension*

OPTIMUM HEIGHT AND BORE OF ROTARY COMPRESSOR FOR OBTAINING HIGH EER

by

TAKASHI MAEKAWA[1], NOBUYUKI KATO[2]
[1] Engineer,Small Compressor Division,DAIKIN INDUSTRIES.LTD,
[2] Chief Engineer,Small Compressor Division,DAIKIN INDUSTRIES.LTD,
1000-2 OHTANI OKAMOTO-CHO KUSATSU JAPAN

ABSTRACT

In order to minimize the tolerance of theoretical analysis, we conducted the test with many kinds of prototypes to obtain actual performance data. We made 19 different kinds of rolling piston type rotary compressors with identical piston dispracement and obtained actual EER. Cyliner height H and bore D are thought to be dominant factors for determining the rotary compressor performance We, therfore, conducted the test varying H and D, and adjusted the test data using multiple regulation analysis to investgate what really determines the performance. The result showed that the smaller the product of H and D, the higher the efficiency. If the product of H and D is constant, large D results in a small increase of eccentricity and the reliability increases. However, large D results in a large diameter compressor.

INTRODUCTION

Recently in Japan, small size scroll compressors (approx.1/2 to 1.5KW) have made their apperance in the field of residential air conditioners. However, owing to their advantages and the development of improvements, rotary compressors are still in use. In addsion, the recent restriction on SEER has lead the research into a higher EER compressor.

The capacity of a compressor follows its suction volume which is determined by some of the major dimensions such as eccentricity ε,cylinder height H and cylinder bore D. Therefore, a compressor of same suction volume can be designed with various combinations of these dimensions.The power reqired for gas compression and the friction force on the sliding face vary by these combinations and accordingly the mechanical efficiency also varies.

Therefore,the determination of these dimensions is essential for obtaining higher efficiency. It is well known that the simulation based on kinematic equations,the equations of motion of the moving element, using the repetition method enables us to predict the performance and the efficiency over a wide range of dimensional variation. Though there are some investigations on optimum combinations, they are mainly based on only mechanical friction.(*1)

In addition, some of the recent investigations,in order to be more practical,deal with performance in relation not only to mechanical friction but also to the overall factors of leakage, overheat, pressure losses and motor loss. Thus the simulasion accuracy has become higher.(*2)

However, we found that these investgations are not yet sufficient for performance prediction with higher accuracy. Therefore, we investigated how these dimensions influence the performance by testing 19 different kinds of prototypes. We conducted the test with these same suction volume compressors and confirmed the

total efficiency and its tendency. In order to obtain only the influences of these dimensions, we minimized the tolerance of machining component and the error of measurement during the test. For the evaluation of performance, we also used several other ways than EER for expressing efficiency. For processing data with some errors, we used the multiple regulation analysis for investigating how these dimensions affect performance.

DETERMINATION OF DIMENSIONS FOR PROTOTYPE

For our experiment we made totally 19 compressors with same suction volume. (Vsuc=51.3cc/rev) Sixteen of them have different combinations of dimensions , and another 3 of them have same combination of dimensions of No.7 but different shaft diameters. The specification of these prototypes are shown in Table 1. Unless the relasion ($Rin-\varepsilon > drshaft/2$) is satisfied. a shaft and a roller cannot be assembled.

Where Rin ;Inner radius of roller, drshaft ;diameter of rear shaft

As a result.there were some prototypes with small rear shaft diameter and crank pin diameter (roller inner diameter). The purpose of prototype No.18, No.19 and No.20 which have different shaft diameters is for investigating the infuluence of rear shafts and pins.

With regards to the Table 1, the prototypes shown in horizontal lines have same cylinder Bore D ,those shown in vertical lines have same cylinder height H, and those shown in diagonal lines have same eccentricity ε. For simplifying the fabrication of prototypes, the following component dimensions are made the same;

The thickness of brade (4.7mm) , Top radius of the brade
Brade spring , Motor (including rotor weigt baranser)
Casig (shell height ,radius) , Discharge valve,valve stopper
Front shaft diameter(ϕ 2 8)

A crank pin and rollar were used to adjust the centrifugal force. A spacing piece was inserted to adjust the spring load. Oil was charged to the upper level of cylinder. The compressor components were machined with high accuracy to maintain every clearance within a small tolerance (actual result was within $\pm 5\mu$).

DEFINITIONS OF EACH EFFICIENCY

$$EER = Q / W0 \quad \text{---------- (1)}$$

$$= G0 \cdot \Delta ie / W0 \quad \text{---------- (2)}$$

$$= \frac{W1}{W0} \cdot \frac{W2}{W1} \cdot \frac{WGmax}{W2} \cdot \frac{G0 \cdot \Delta ie}{WGmax} \quad \text{------- (3)}$$

in addition

w3 : minimum work per unit flow rate (1 Kg/h)

$W3 = G0 * w3$: minimum work of actual flow rate

$$w3 = WGmax / Gmax \quad \text{---------- (4)}$$

$$\therefore \; WGmax = Gmax \cdot w3 \quad \text{---------- (5)}$$

where:

- Q : actual capacity (Kcal/h)
- G0 : actual mass flow rate (Kg/h)
- Δie : specific enthalpy increase during evaporation process (Kcal/Kg)
- W0 : motor input (Watts)
- W1 : motor shaft output (Watts)
- W2 : P-v gas compression work per cycle
  = area (1' 2' 3' 4') · N/60 · g (Watts) (Fig.1)
- N : RPM of the motor (rpm)
- P : cylinder inner pressure (Kg/mm^2)
- Vc : cylinder volume (m^3)
- $g = 9.8$ (m/s^2)

WGmax : minimum power of P-V diagram required to compress the maximum cylinder volume gas

= area (1 2 3 4) N · g/60

$= (n/n-1) \cdot PsVc\left[(Pd/Ps)^{n-1/n}-1\right] N \cdot g/60$

n : average polytropic index which is to be applied to above euation n = 1.115 (for R22)

$$\therefore EER = \frac{W1}{W0} \cdot \frac{W2}{W1} \cdot \frac{WGmax}{W2} \cdot \frac{G0 \cdot \Delta ie}{WGmax} \quad \cdots\cdots (6)$$

$$= \frac{W1}{W0} \cdot \frac{W2}{W1} \cdot \frac{WGmax}{W2} \cdot \frac{G0 \cdot \Delta ie}{Gmax \cdot w3} \quad \cdots\cdots (7)$$

$$= \eta mot \cdot \eta mec \cdot \eta cid \cdot \eta v \cdot \Delta ie / w3 \quad \cdots\cdots (8)$$

Where the definition of each efficiency is as follows

- $\eta mot = W1/W0$; motor efficiency
- $\eta mec = W2/W1$; mechanical efficiency
- $\eta cid = WGmax/W2$; P-V indicator efficiency
- $\eta v = G0/Gmax$; volumetic efficiency

$\Delta ie/w3$: represents max EER
at the condition te5/tc55℃, R22, max EER=3.73
(in ASHRAE cond. max EER=4.14)

We further deffine another efficiencies as follows:

- $\eta c = \eta mec \cdot \eta cid \cdot \eta v$; compressor mechanical efficiency
- $\eta t = \eta mot \cdot \eta mec \cdot \eta cid \cdot \eta v$; total compressor efficiency
- $\eta d = \eta mec \cdot \eta cid$; indicator mechanical efficiency

$$EER = 3.73 \cdot \eta mot \cdot \eta mec \cdot \eta cid \cdot \eta v \quad \cdots\cdots (9)$$

$$= 3.73 \cdot \eta mot \cdot \eta c \quad \cdots\cdots (10)$$

$$= 3.73 \cdot \eta t \quad \cdots\cdots (11)$$

While, for the mass flow rate

WG0 : minimum work per actualflow rate G0 (Kg/h) (=W3)

$$WG0 = w3 \cdot G0 \quad \cdots\cdots (12)$$

$$= \frac{WGmax}{Gmax} \cdot G0 = WGmax \cdot \frac{G0}{Gmax} \quad \cdots\cdots (13)$$

$$= WGmax \cdot \eta v \quad \cdots\cdots (14)$$

$$\therefore WGmax = WG0/\eta v = w3/\eta v \quad \cdots\cdots (15)$$

Each loss of work is defined as follows

Motor loss = $W0-W1=(1-\eta mot)\cdot W0=\Delta Wmot$ ----- (16)

Friction loss = $W1-W2=\Delta Wmec$ ----- (17)

Compression loss = $W2-WGmax=\Delta Wc$ ----- (18)

Leakage loss = $WGmax-WG0=\Delta Wl$ ----- (19)

Above definition is similar to that of shown in refference(*4)
From reference (*5) we assume that EER is defined as follows

$$EER=\frac{W1}{W0}\cdot\frac{W2}{W1}\cdot\frac{W3}{W2}\cdot\frac{G0\cdot\Delta ie}{W3} \quad \text{----- (20)}$$

$$=\eta mot\cdot\eta mec\cdot\eta comp\cdot 3.73 \quad \text{----- (21)}$$

and then $\eta comp = W3/W2 =$ Compression efficiency

In our definition $\eta comp = \eta cid\cdot\eta v$ ----- (22)

In reference (*5), $\eta comp$ is defined without separating ηcid and ηv. However we devided $\eta comp$ into two terms ηcid and ηv. And then ,in reference (*5), (total) compressor efficiency is defined as follows

$$\eta t=\eta mot\cdot\eta mec\cdot\eta comp \quad \text{----- (23)}$$

Both of two (*4,*5) did't explain cleary the relation between EER and above efficiencies. And equation (8) is sligtly different from eq.(26) of refference(*3).

TEST RESULTS

1.Factors which affect EER

We investigated the various variables (see note) affect the capacity Q, input W and EER by using multiple regulation analysis.(*6,*7) The tendency of the data of No.4 and No.12 are different from the others. We assumed that something were wrong and eliminated them from our evaluation. The data of No.18, No.19 and No.20 show no big difference between that of No.7. This is because the major dimensions of No.18,No.19 and No.20 are exactly the same with those of No.7 except for the shaft diameters. Therefor, we used 14 datas for the analysis.

Note : $\underline{H*D}$, $\underline{H*(D+2R_o)}$, D, H, ε, D^2, D^3, H/D, $(H/D)^2$, D^2*H

We found that the underlined variables are the most influential.

In oder to accurately measure the influence of major dimensions, motor efficiency was measured separately as a motor itself. As a result,

(1) The variable (H*D) and the force to pressurize gas (Fp) affect the EER and ηd much more than any other variables (D, H, ε, D^2, D^3, H/D, $(H/D)^2$, $(H/D)^3$ or D^2*H). We obtained the following experimental equations values.

$EER=1.208-1.953*H*D$ correlation factor $r=-0.74$ ---(24)

$\eta d=1.07-0.00011*Fp$ .. .. $r=-0.85$ ---(25)

(Fig.4 and Fig.5)

From the above equations, we find that the smaller the (H*D),the higher the EER.

Note : Correlation factor indicates how much it affects EER.

$r=\pm 1$:It has perfect relation.

± 0.8 :It has considerable relation.

± 0.6 :It has some relation.

± 0.5 :It may have some relation.

(2) The smaller the (H*D), the larger the capacity Q.
We obtained the following experimental equation.

$$Q = 1.10 - 0.0829 * H * (D + 2R0) \qquad r = -0.52 \quad --- \quad (26)$$

(Fig.6)

2. Infuluence of clearance on EER.

We conducted the test of prototype No.7 with 44 different clearances to investigate its influence on EER.(*10) The test results show that though the clearance is maintained within the tolerance of $\pm 5\ \mu$, this tolerance affects EER. By using the regulation analysis we obtain the following equation (27) and (28).

$$Q(\text{Kcal/h}) = B0 + B1(CR) + B2(CR)^2 + B3(CR)^3 + B4(CB) + B5(CB)^2 + B6(CB)^3 \quad --- \quad (27)$$

$$W(\text{watts}) = C0 + C1(CR) + C2(CR)^2 + C3(CR)^3 + C4(CB) + C5(CB)^2 + C6(CB)^3 \quad --- \quad (28)$$

where

Bn,Cn ;coefficient of reguration.
CR ;clearance between roller and cylinder height ceiling
CB ;clearance between vane and cylinder height ceiling

To evaluate the data on the same clearance , we compensated the EER of each compressor using these equations. In addtion, the all values of EER was divided by those of the prototype No.7 so that they can be evaluated on the dimensionless level. The test result of the relation of(H*D) and EER are shown in Fig.2 and the simulation results in Fig.3.

The tendency of the simulation results corresponds with that of the test results. However, there are some differences in absolute values. Therefore, it is not yet allowable to predict the performance only with simulation.

3. Relation between volumetic efficiency and indicator mechanical efficiency.

The larger the volumetic efficiency ηv, the larger the indicator mechanical efficiency ηd. We obtained the following experimental equation.

$$\eta d = 0.5 + 0.48 \eta v \qquad r=0.55 \quad ---------- \quad (29)$$

FUNDAMENTALS FOR DESIGNING COMPRESSOR WITH HIGHER EFFICIENCY

1) Under the condition of same (H*D), it is favorable to enlarge D, because the reliability improves due to the small increase of eccentricity ε and less blade friction.

However, the large D results in the large diameter of a compressor casing. Therefore, within the allowable limit of casing diameter, it is favorable to increase D. Fig.8 is a chart prepared for the compressor design. The chart is based on an experimental equation which gives the influence of (H*D) on EER.

2) In order to improve EER, it is necessary to improve either each efficiency (see note) or the product of these efficiencies. (Fig.9) (*8,*9)

Note: ηmot ; motor efficiency, ηmec ; mechanical efficiency
ηcid ; P-V indicator efficiency, ηv ; volumetic efficiency

In Fig.9, the compressor under study is fixed in a bolted shell and it has the same dimensions as the No7. And from the P-V diagram the indicator efficiencies ηcid and the mechanical efficiency ηmec are calculated. At this time we use the motor efficiency ηmot which is gained separately in hot condition.

As rotational speed increase, ηmec decrease rapidly and ηv, ηcid , indicate a quadratic curve. Compressor mechanical efficiency; ηc is gained from power of all those three efficiencies. Fig.9 shows compressor mechanical efficiency; ηc has a maximum value at 60 Hz. If we wish to change the maximum point to another higher Hz , We must design the compressor which has another different each efficiencies. Of course, in the case of higher rotational speed , some especial efforts must be made. We should pay attension to valve, clearance , amount of oil, motor, so on.(*11,*12)

In oder to improve EER for an inverter controlled compressor, it is essential to design a comprssor to give the highest EER at the frequency most often used througout the whole year.

3) The smaller the (H*D) , the higher the total efficiency. If (H*D) is maintained small, the force to pressurize gass (FP) becomes small and accordingly the journal loss becomes small.
Fig.10 shows the tendency of the other manufacturers' compressors. With the years, the compressor technology innovated. It shows that their tendency of the (H*D) is becoming smaller and the efficiency has increased. We assume that this is affected by the small (H*D).

4) As a result , we improve the efficiency of a 3/4 Hp size dual cylinder rotary compressor by reducing 20 % of H and achieved 2 % of EER increase. In addition to this, we added other improvement and increased EER. This compressor is now in production.

CONCLUSION

1. In oder to obtain high efficiency, it is essential to reduce the product of H and D.

2. However , small (H*D) results in large eccentricity ε and lowers the reliability. The allowable reliability limit needs to be investigated.

3. The total compressor efficiency ηt can be divided into
   motor efficiency ; ηmot, mechanical efficiency ; ηmec,
   indicator efficiency ; ηcid and volumetic efficiency; ηv.

   In oder to improve EER , it is necessary to either improve each efficiency or improve the product of these efficiencies.

REFERENCES

1. Ishii,N.,et al.,
"Optimum Combinasion of Dimensions for High Mecanical Efficiency of a Rolling-Piston Rotary Compressor,"
Proc.Purdue Int. Compressor Engineering Conference,
July.,1990 ,Vol.2,pp.418-424.

2. Yanagisawa ,T.,
"The behavior of roling piston and Mechanical Loss in Rotary Compressor,"
Trans.Japan Soc.Mech.Engs.(in Japanese),Series C,
Vol.48,No.435,1980,pp 1854-1861.

3. Prakash Pandeya,Werner Soedel
"A GENERALIZED APPROACH TOWARDS COMPRESSOR PERFORMANCE ANALYSIS"
Proc.Purdue Int. Compressor Engineering Conference,
July.,1978 ,pp.135-143.

4. Matszaka,T.,Nagatomo,S.,
"ROLLING PISTON TYPE ROTARY COMPRESSOR PERFORMANCE ANALYSIS."
Proc.Purdue Int. Compressor Engineering Conference,
July.,1982 ,pp.149-158. Toshiba Major Appliance Produce Eng.Labo.

5. KEIJU SAKAINO,et.al.,
"SOME APROACHES TOWARDS A HIGH EFFICIENT ROTARY COMPRESSOR,"
Proc.Purdue Int.Compressor Engineering Conference,
July.,1984 ,pp.315-322. Mitsubish Electric Corporation

6. MICRO SYSTEMS Co.Ltd."Elementaly Statistical Analysis Program,"1985

7. Okuno Tadakazu,et.al.,"Multivariate Data Analysis in a Technology,"
Printed in Japan by Nicka Giren,1986

8. Iida,S.,et al.,
"Efficiency Improvement in Rotary Compressor,"
Mitsbishi Hevy Ind.Technical Report,Vol. 20,No.3,1983-5, pp29-37

9 L.Sakitani,J.Koiwa,T.Maekawa,
"Performance Evaluation of Hermetic Refrigeration Compressor Using Torque Mesurement Method". Proc.Purdue Int.Compressor Engineering Conference,
Aug.,1986,VOL.1 ,pp.228-241. Daikin Industries.LTD.

10. Janghee Lee,Tae sik Min
"Performance analysis of rolling piston type rotary compressor"
Proc.Purdue Int. Compressor Engineering Conference,
July.,1988,Vol.1,pp.154-162. Daewoo Electronics Co.,Ltd.

11. Hiroshi Iwata,Akio Sakazume,and Kenziroh Yokoyama
"Loss Analysis of Rolling-Piston Type Speed Controlled Rotary Compressor"
Trans.Japan Soc.Mech.Engs.(in Japanese),Series B,
Vol.51,No.465,June,1985,pp 1736-1741. Hitachi,Ltd.

12. B.Sakurai,Dr.J.F.Hamilton
"THE PREDICTION OF FRICTIONAL LOSSES IN VARIABLE-SPEED ROTARY COMPRESSORS"
Proc.Purdue Int. Compressor Engineering Conference,
July.,1984,Vol.1,pp.331-338. Toshiba Corpration and Purdue University

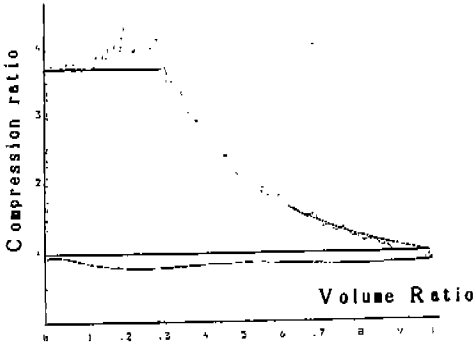

Fig. 1 P-V Diagram

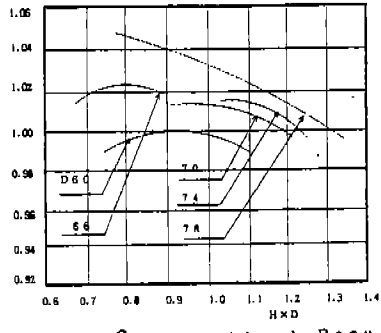

Fig. 3 Analytical Result

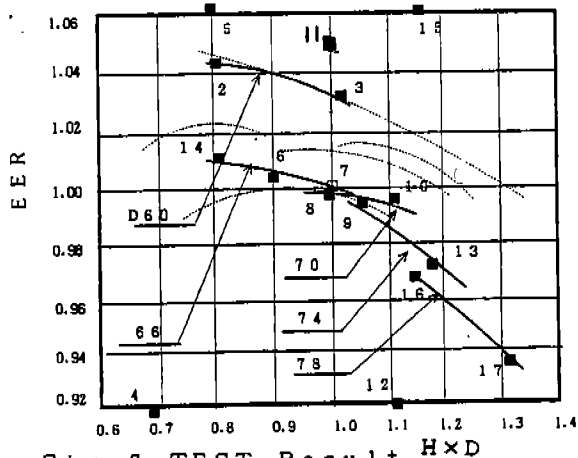

Fig. 2 TEST Result

TABLE 1. SPECIFICATION OF TEST COMPRESSOR
Main Front shaft dia ¢28, Crank pin dia¢40

		1	2	3	4	5	6	7	8	9	10
	H / D	35	40	41.73	44.16	45	46.89	50	52.8	52.84	55.83
1	56							(☆1)			
2	60					☆2					☆3
3	66	☆4	☆5			☆6		★7			
4	70						☆8	☆9	☆10		
5	74				☆11			☆12		☆13	
6	78	☆14		☆15				☆16			☆17

☆18 Ria shaft dia ¢22, Crank pin dia ¢40
☆19 Ria shaft dia ¢20, Crank pin dia ¢40
☆20 Ria shaft dia ¢20, Crank pin dia ¢34

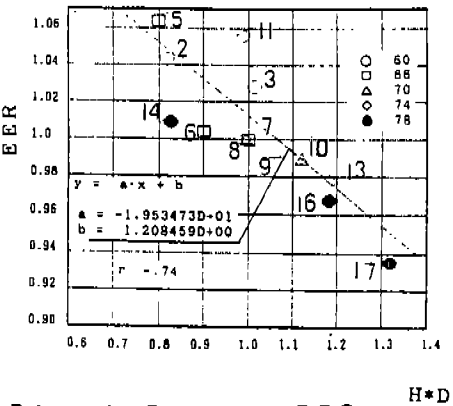

Fig. 4 Regulation EER vs. H*D

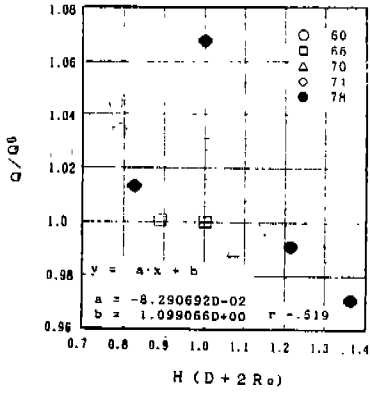

Fig. 6 Q vs. H (D + 2 Ro)

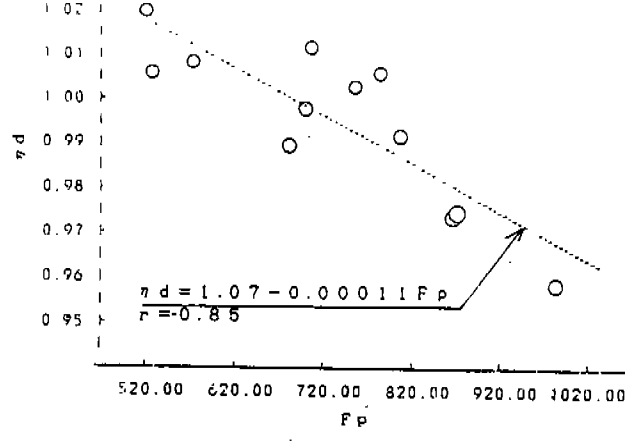

Fig. 5 Regulation ηd vs. Fp Kg

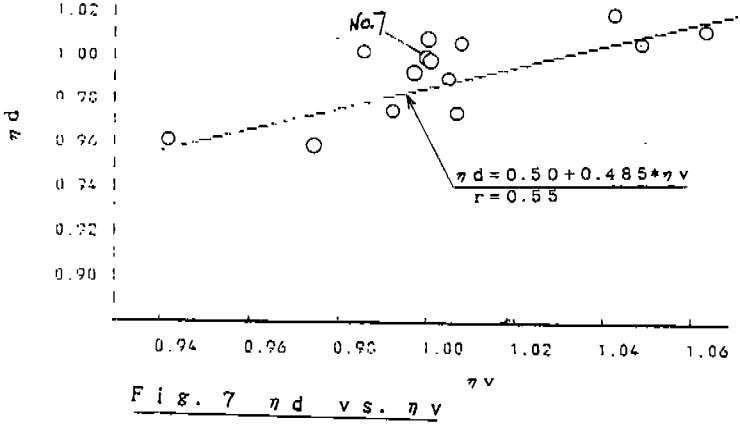

Fig. 7 ηd vs. ηv

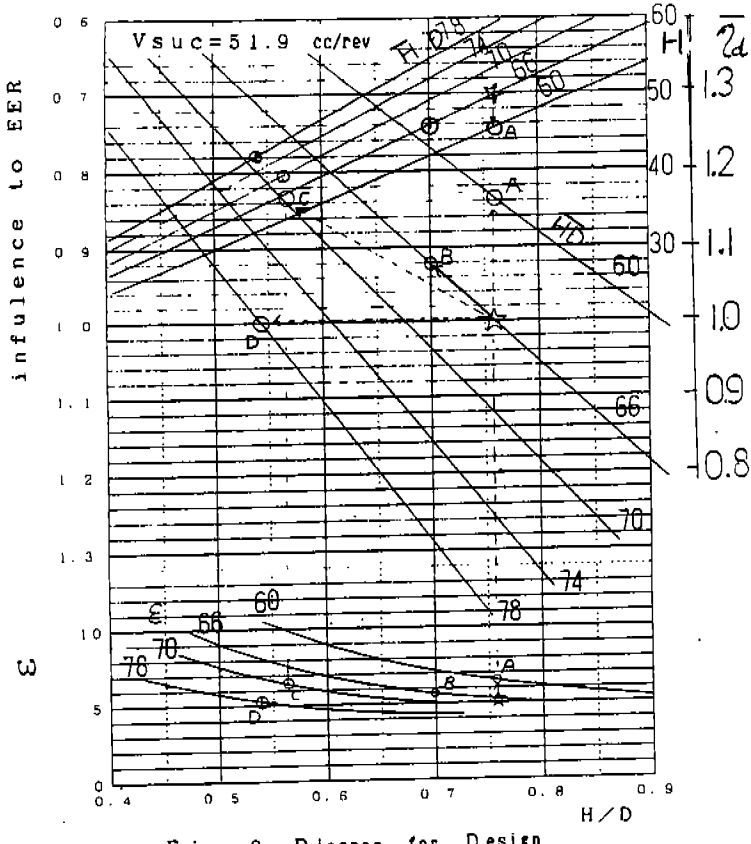

Fig. 8 Diagram for Design

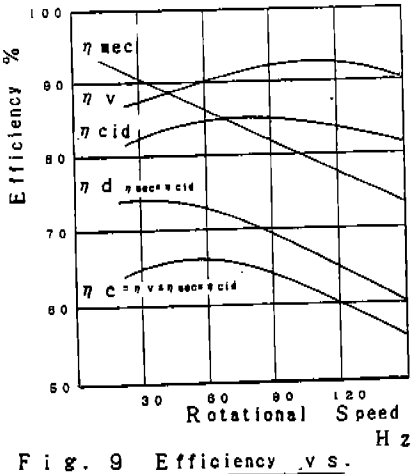

Fig. 9 Efficiency vs. Rotational Speed

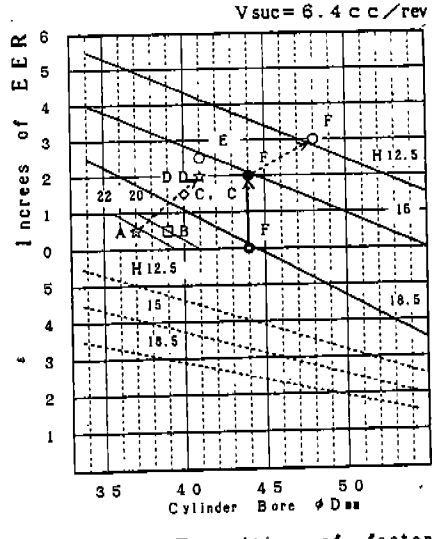

Fig. 10 Transition of factor

OPTIMIZATION OF INTER–COOLER IN RECIPROCATING COMPRESSOR

Lu Ya–dong, Sun Si–Ying, Yan Cai–qiu, and Yang Shao–Kai
Department of Power Machinery, Xi'an Jiao–tong University, Xi'an,
Shaanxi Province, The People's Republic of China

ABSTRACT

Based on the energy balance law and the mass balance law in thermodynamics, a mathematical model on the transient heat exchange process of the inter–cooler is established. Then a model on optimization of the cooler is proposed in which the objective function is the total entropy generation rate (TEGR), giving consideration to both the heat transfer and the flow resistance in the cooler. Finally, the results of the optimization on the structure size and the operating parameters are searched for the cooler. The feasibility of the simulating model and the reliability of the optimizating results have been proved by the experiments in a compressor.

INTRODUCTION

In order to increase the economy and reliability of multi–stage compressor during operation, studies on the inter–cooler of compressor should be paid attention to in addition to studing the compressor itself. From the standpoint of the whole compressor system including the compressor, inter–cooler, and later–cooler, the authors have conducted the simulation of the transient heat transfer and the optimization of the structure for the inter–cooler. In combination with our previous publications[1,2], the computer aided design for compressor system can be realized.

The shell–and–tube cooler with baffles is widely used in engineering. In the present paper, a mathematical model on the transient heat exchange of a counterflow shell–and–tube cooler has been established on the basis of the energy balance law and the mass balance law in thermodynamics. By using the flow path analysis method, the heat exchange coefficient for the shell side in the reference[2] is revised, thus the accuracy of the calculation is improved. At the same time, by means of the finite difference method, the numerical solutions for the gas inside the tube, the cooling water in the shell side, and the temperature in the tube wall are obtained, and the change rule of temperature with the time and the spacial position is determined in the heat exchange period. On this basis, a model on optimization of the cooler is proposed in which the objective function is the total entropy generation rating (TEGR), giving consideration to the two important factors, that is the heat transfer and the flow resistance in the cooler, and especially emphasising its research on energy quality. Finally, the results of optimization on the structure size and the

operating parameters are obtained for the cooler by using the flexiable tolerance optimization method. Moreover, the experiments have proved the feasibility of the simulating model, and the reliability of the optimizating results.

MATHEMATICAL SIMULATION OF HEAT EXCHANGE PROCESS

A shell –and–tube cooler with baffles is shown schematically in Fig.1. Fig.2 shows the heat exchange model of the cooler, where high–temperature fluid is the air inside the tube, and the low–temperature fluid is the cooling water in the shell side. The following assumptions are made for the model.

(1) Thermal conductance is ignored;
(2) Thermal resistance of tube wall is ignored;
(3) The shall is adiabatic;
(4) The thermal capacity rates $(cm)_h$, and $(cm)_c$ is the two fluids are constant as are the thermal conductances $(hA)_h$, and $(hA)_c$, and the thermal capacity rate $(Cm)_w$ in the tube wall.

Based on the first law of thermodynamics, the heat exchange element of the cooler should meet the following equations[3]

For the tube wall,

$$(cm)_w \frac{\partial T_w}{\partial t} = (hA)_h (T_h - T_w) + (hA)_c (T_c - T_w) \tag{1a}$$

For the fluid inside the tube,

$$(hA)_h (T_w - T_h) = (A_x \rho c)_h U_h \left(T_h + \frac{\partial T_h}{\partial x} L \right) - (A_x \rho c)_h U_h T_h + (A_x \rho c)_h L \frac{\partial T_h}{\partial t} \tag{1b}$$

For the fluid in the shell side,

$$(hA)_c (T_w - T_c) = (A_x \rho c)_c U_c \left(T_c - \frac{\partial T_c}{\partial x} L \right) - (A_x \rho c)_c U_c T_c + (A_x \rho c)_c \frac{\partial T_c}{\partial t} \tag{1c}$$

The heat exchange coefficients, h_t , for the fluid inside the tube are separately calculated on such two cases, as the turbulent zone and the transitional zone. That is

when $R_{et} > 10^4$

$$h_t = 0.023 \frac{\lambda}{D_{ti}} R_{et}^{0.8} P_{rt}^{1/3} \left(\frac{\mu}{\mu_w} \right)^{0.14} \tag{2a}$$

when $2100 < R_{et} < 10^4$

$$h_t = h' + \frac{R_{et} - 2100}{10000 - R_{et}} \left[0.023 \frac{\lambda}{D_{ti}} R_{et}^{0.8} P_{rt}^{1/3} \left(\frac{\mu}{\mu_w} \right)^{0.14} - h' \right] \tag{2b}$$

$$h' = \left[3.66 + \frac{0.085 G_{Zt}}{1 + 0.047 G_{Zt}^{2/3}} \left(\frac{\mu}{\mu_w} \right)^{0.14} \right] \frac{\lambda}{D_{ti}}$$

In the present studies, the heat exchange coefficient in the shell side is calculated by Bell–Delaware method[4], in which the effect of the gap and pass–by caused by the baffles is in consideration.

$$h_s = h_i (J_c J_l J_b J_r J_s)$$

where h_i is the heat exchange coefficient of the tube core. J_c, J_l, J_b, J_r, and J_s are the revised factors

The initial condition of the equation is that

$$T_{wi}^{j} \simeq T_{wi}^{j+z}$$

where z is the number divided equally in on period. For the boundary condition, the change of air temperature at the inlet with time is

$$T_{h\,in}^{j} = f(t)$$

and the cooling water temperature at the inlet is assumed to be a constant

$$T_{cin}^{j} = \text{const}$$

Having dispersed the equation group (1), the transient temperature change of the gas inside the tube with the time and spacial position is solved by using Jacobi iterative method, as shown in Fig.3. Thus , it is proved that the gas temperature of the inter–cooler in the reciprocating compressor is definitely not a constant, but is a pulsating value. The two peaks occurred in the figure is caused by the two cylinders in the compressor. Fig.4 shows the curved surface of transient temperature of the cooling water in the shell side. It is indicated that the temperature of cooling water slightly increases with the direction of the cooler length, but is independent on the time.

MATHEMATICAL MODEL OF COOLER OPTIMIZATION

Objective Function

At present there are many indexes to evaluate the performance of the heat exchanger. Among them the temperature efficiency, heat exchange efficiency, and the number of transfer units, et al., are often used. However, in these indexes the heat transfer is separated from the flow resistance, and the quality of the energy is not concerned. What index can be used to consider both the quantity and quality of the heat transfer and the flow resistance, and the optimum value can be searched? The authors consider that the total entropy generation rating is available. Thus, the TEGR is considered as the objective function in this optimizating model.

In order to evaluate the economy of the cooler, the TEGR as an index is a benefit, but with a certain expense. The benefit of the cooler is the heat exchange quantity, Q. The expense is the useful energy loss caused by the compressor and water pump and the heat transfer due to the temperature difference. Thus, the TEGR can be expressed by

$$Y_s = T_o [\Delta \dot{S}_{\Delta t} + n_t \Delta \dot{S}_{\Delta Pt} + n_s \Delta \dot{S}_{\Delta Ps}] / \dot{Q} \qquad (3)$$

where

$\Delta \dot{S}_{\Delta t}$ — entropy generation rate caused by the temperature difference;

$$\Delta \dot{S}_{\Delta t} = C_{pa} \dot{M}_s ln(T_{so} / T_{si}) - C_{pt} \dot{M}_t ln(T_{ti} / T_{to})$$

$\Delta \dot{S}_{\Delta Pt}$ — entropy generation rate caused by the pressure loss inside tube;

$$\Delta \dot{S}_{\Delta Pt} = 2\dot{v}_t \Delta P_t / (T_{ti} + T_{to})$$

$\Delta \dot{S}_{\Delta Ps}$ — entropy generation rate caused by the pressure loss in the shell side;

$$\Delta \dot{S}_{\Delta Ps} = 2\dot{v}_s \Delta PS / (T_{si} + T_{so})$$

n — conversion factor in which the power expense caused by the pressure loss is converted to the useful energy loss. The sub t, and s express the tube side and the shell side separately.

$$n_t = 1 / \eta_{ce} \cdot \eta_m \cdot \eta_c$$

$$n_S = 1 / \eta_{ce} \cdot \eta_m \cdot \eta_p$$

where

η_{cc} — relative efficiency from Carnot circulation to effective circulation;

η_m — efficiency of electrical power system;

η_c — efficiency of compressor;

η_p — efficiency of pump;

$\dot{Q}$ — heat transfer quantity per unit time

Eq.(3) expresses the useful energy expended per unit heat transfer quantity in the cooler. The smaller the Y_s value, the better the economy of the cooler.

Strategic (Design) Variables

In the present work, the optimization on the cooler consists of the structure size optimization, and operating parameter optimization. For the former, the vector of the strategic variable can be expressed by

$$X_1 = [x_1, x_2, x_3, \cdots, x_8]^T = [D_{to}, L_{te}, L_g, D_S, L_{bc}, B_c N_b, N_{tt}]^T$$

where $B_c = L_{hcb} / D_S$,

$N_b = (L_{to} - 2L_{ts} - L_{bi} - L_{bo}) / L_{bc} - 1$

N_{tt} — number of tube

Other symbols are shown in Fig.1.

For the latter, the vector of the strategic variable is expressed by

$$X_2 = [x'_1, x'_2, x'_3]^T = [n, p, \dot{M}_s]^T$$

where n, p, are $\dot{M}_S$ are the rotatory speed of compressor, discharge pressure, and the flow quantity of cooling water, separately.

Restrained Condition

(1) The restrained condition for optimization structure size of the cooler:

for the inequality restraint

$g_i(X_1) \geqslant 0 \qquad i = 1,2,\cdots,18$

$$g_1 = \frac{20}{D_{to}} - 1.0 \qquad g_2 = \frac{D_{to}}{5} - 1.0 \qquad g_3 = \frac{L_{to}}{D_S} - 2.5$$

$$g_4 = 1.5 - \frac{L_{tp}}{D_{to}} \qquad g_5 = \frac{L_{tp}}{D_{to}} - 1.15 \qquad g_6 = \frac{Z_{oo}}{D_s} - 1.0$$

$$g_7 = \frac{D_s}{40} - 1.0 \qquad g_8 = 15 - \frac{D_s}{D_{to}} \qquad g_9 = \frac{D_S}{D_{to}} - 5.0$$

$$g_{10} = \frac{D_s}{L_{bc}} - 1.0 \qquad g_{11} = \frac{L_{bc}}{D_s} - 0.20 \qquad g_{12} = \frac{0.5}{B_c} - 1.0$$

$$g_{13} = \frac{B_c}{0.10} - 1.0 \qquad g_{14} = \frac{0.78 D_{otl}^2}{c_1 L_{tp}^2} - N_{tt} \qquad g_{15} = \frac{N_{tt}}{7} - 1.0$$

$$g_{16} = \frac{\Delta P_{tmax}}{\Delta P_t} - 1.0 \qquad g_{17} = \frac{\Delta P_{smax}}{\Delta P_S} - 1.0 \qquad g_{18} = \frac{Q}{Q_{min}} - 1.0$$

for the equality restraint

$$h_j(X_1) = 0 \qquad j = 1$$

$$h_1 = N_b + 1 - \frac{L_{to} - 2L_{ts} - L_{bi} - L_{bo}}{L_{bc}}$$

(2) The restrained condition for optimizating operating parametr of the cooler:

for the inequality restraint

$$g_i(X_2) \geqslant 0 \qquad i = 1,2,\cdots,8$$

$$g_1 = \frac{600}{n} - 1.0 \qquad g_2 = \frac{n}{100} - 1.0 \qquad g_3 = \frac{8}{p} - 1.0 \qquad g_4 = p - 1.0$$

$$g_5 = \frac{25}{M_s} - 1.0 \qquad g_6 = \frac{M_s}{25} \qquad g_7 = \frac{\Delta P_{tmax}}{\Delta P_t} - 1.0 \qquad g_8 = \frac{\Delta P_{smax}}{\Delta P_s} - 1.0$$

Pressure Loss

In the tube side, the pressure loss is the sum of the pressure loss during the gas going through the straight tube part, and the pressure loss at the inlet and outlet. The expression is that

$$\Delta P_t = \frac{4 f_t \dot{M}_t L_{to} N_{tp}}{2\rho_t D_{it}} \left(\frac{\mu}{\mu_w}\right)^{-0.14} + 1.5\frac{\dot{M}_N^2}{2\rho_t}$$

In the shell side the pressure loss includes the pressure loss (ΔP_c) of the pure transverse flow in the zone between the tops of the baffles, the pressure loss (ΔP_w) in the window of the baffles, and the pressure loss (ΔP_i) at the end of the cooler, as shown in Fig.5. The expression is that[4]

$$\Delta P_s = \Delta P_{bi}(N_b - 1)R_b R_l + N_b\left[(2 + 0.6N_{tcw})\frac{\dot{m}_\omega}{2\rho_s} \times 10^{-3}\right]R_l + \Delta P_{bi}\left(1 + \frac{N_{tcw}}{N_{tcc}}\right)R_b R_s$$

where ΔP_{bi} is the ideal pressure loss, R_b is the revised factor, and R_e is the leakage factor.

Results of the Optimization

For the cooler size, as listed in Table 1, the operating parameters are optimized by the flexiable tolerance optimization method. The results of the optimization is shown in Fig.6 and Table 2. The optimum of the TEGR is 6.5417. Compared with the initial scheme, the value of the TEGR is reduced by a factor of 45.21%, and the pressure loss is decreased in the tube side. In addition, the perfectness K_{it} of cooling is increased from 79.24% to 89.15% by using the optimization. It is clear that optimizing the operating parameters can lead to saving energy for the compressor. In order to verify the reliability of the calculation; the experiment has been conducted in a later-cooler of an air compressor type Ⅱ ZA-1.5/8. The influence of the rotatory speed (n), cooling water quantity (M_s), and pressure ratio (E) on the TEGR and the heat exchange quantity are shown in Fig.7-9 separately. The calculation values are in agreement with the experimental results, thus it is proved that the optimizing procedure is correct.

Table 1 cooler size

Size parameter	D_o (mm)	D_S (mm)	L_{tp} (mm)	L_{bc} (mm)	L_{to} (mm)	N_{tt} (mm)	N_b	B_C	L_{bi} (mm)	L_{bo} (mm)
value	11	65	13	48	678	14	13	0.26	74	68

Table 2 The results of optimization for the operating parameters

Parameter	M_s (kg / s)	n (r / min)	E	u (W / m^2 · k)	Q (W)	Y_s	ΔP_t (KPa)
Initial Scheme	0.1667	330	5.0	163.6	1159.7	11.937	4.217
Optimum results	0.1737	250	5.99	188.9	1194.3	6.540	3.033

Parameter	ΔP_s (KPa)	T_{ti} (℃)	T_{to} (℃)	T_{si} (℃)	T_{so} (℃)	K_{tt}	/
Initial Scheme	0.199	118	25.6	19.2	19.5	79.24	/
Optimum results	0.208	113	23.5	18.2	19.6	89.15	/

The results of the optimization on the structural size of the cooler are shown in Fig.10, and Table3. The value of TEGR is reduced by a gactor of 83.39%, the useful energy loss is reduced by a factor of 63.47%, and the perfectness K_{tt} of cooling is increased by 19.54%. By using the optimization, the purpose of enhancing heat exchange and decreasing heat resistance is reached. Due to the limitation of the experimental condition, the optimum results on the structural size have not been verified.

Table 3 The results of optimization for the structural size

Parameter	D_{to} (mm)	D_s (mm)	L_{tp} (mm)	L_{bc} (mm)	L_{to} (mm)	N_{tt}	N_b	B_c	u (W / m^2 · k)	Q (w)
Initial Scheme	11	65	13	48	678	14	13	0.26	157.0	1161.7
Optimum results	13	90	15	36	605	16	13	0.24	201.4	2547.4

Parameter	Y_s	ΔP_t (KPa)	ΔP_s (KPa)	T_{ti} (℃)	T_{to} (℃)	T_{si} (℃)	T_{so} (℃)	K_{tt}
Initial Scheml	7.453	3.239	0.215	139	26.0	18.2	19.9	73.8
Optimum results	1.242	0.794	0.038	139	21.5	18.2	21.9	93.4

CONCLUSION

By means of the experiments carried out in a cooler of a laboratory compressor, the transient temperature at the inlet and outlet of the cooler and the performance parameters of the compressor have been measured. It is proved that the model on the transient heat transfer is viable, and the optimizing results in which the objective function is the total entropy generation rating is correct.

REFERENCE

(1) Ren Ting-rong, Simulation of the working processes for a reciprocating compressor, Msc Thesis, Xi'an Jiao-tong University, Xi'an, 1986.

(2) Sun Jin-ju, Computer simulation and experimental studies on the heat exchange of a cooler in a reciprocating compressor, Msc Thesis, Xi'an Jiao-tong University, Xi'an, 1989.

(3) F.E.Romie, Transient response of the counterflower heat exchanger, Journal of Heat Transfer, Transactions of the ASME, Vol.106, August, 1984, pp.620–626.
(4) E.U.Schlunder, Heat Exchanger Design Handbook, Hemisphere Publishing Corporation, 1983.

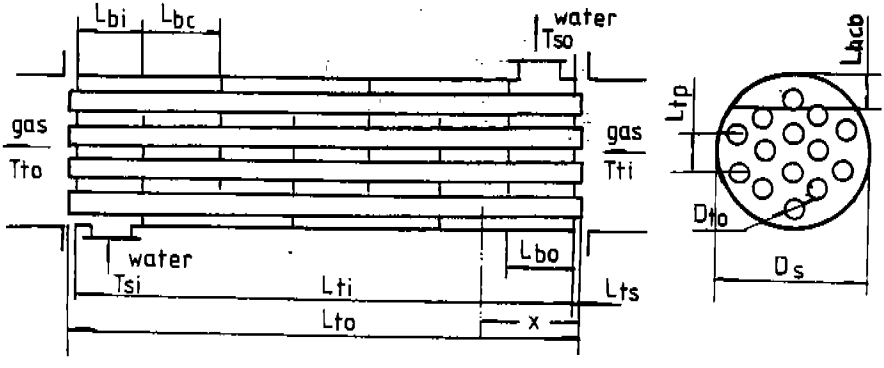

Fig.1 Schematic of the shell–and–tube cooler

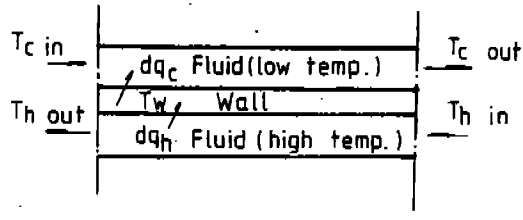

Fig.2 Heat exchange model of the cooler

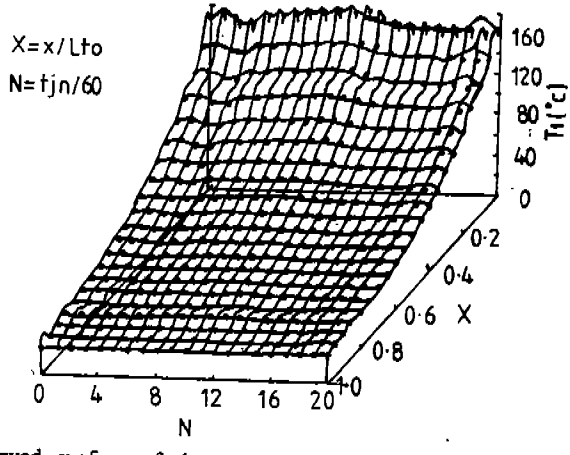

Fig.3 Curved surface of the transient temperature of the gas in the tube side with the change of time and spacial position

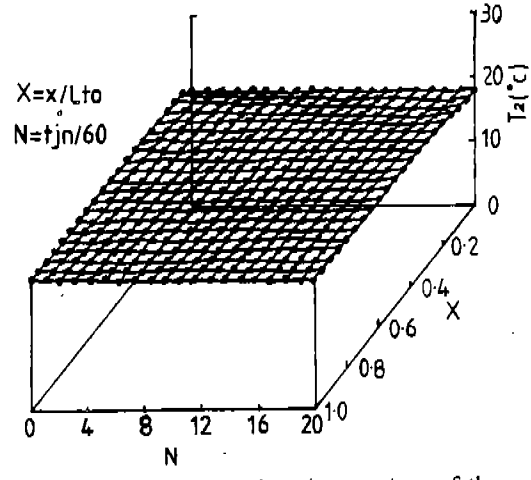

Fig.4 Curved surface of the transient temperature of the cooling water in the shell side with the change of time and spacial position

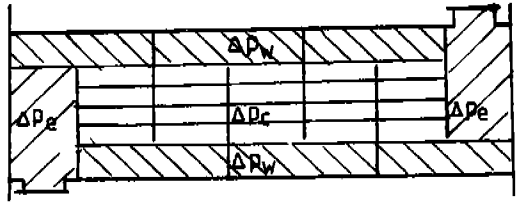

Fig.5 Distribution of pressure loss in the shell side

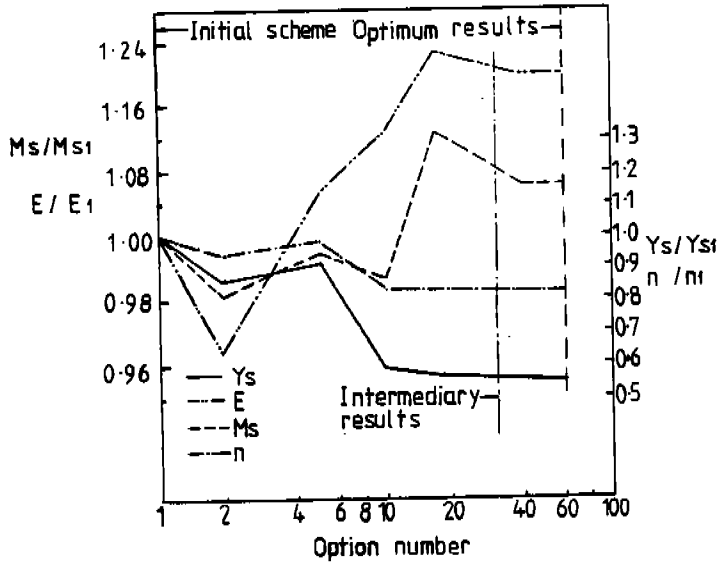

Fig.6 Optimizing results of operating parameters

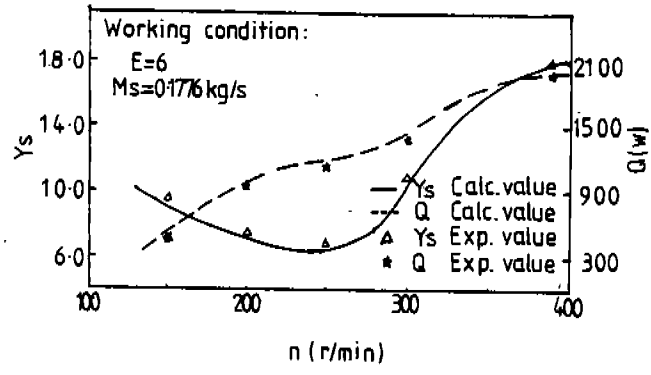

Fig.7 Relationship between Y_s and n

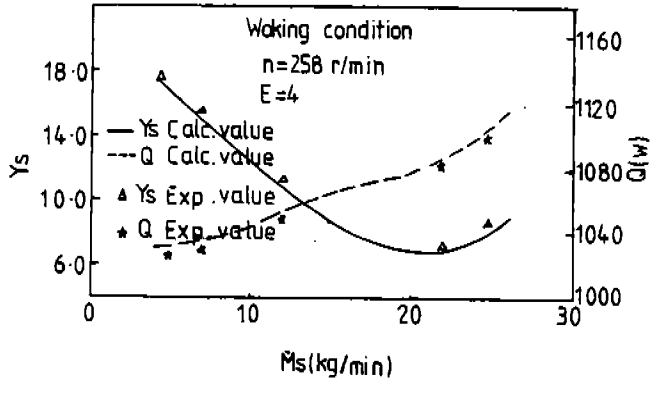

Fig.8 Relationship between Y_s and M_s

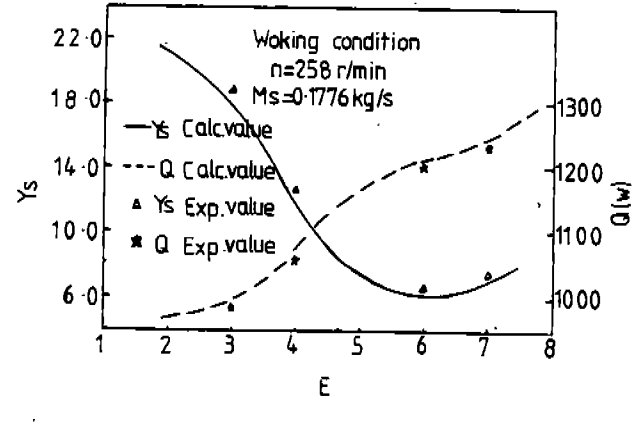

Fig.9 Relationshop between Y_s and E

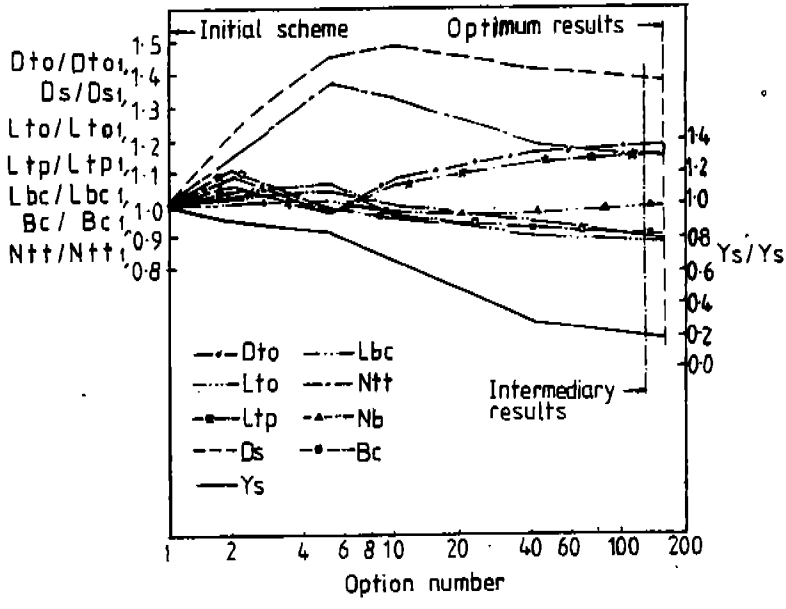

Fig.10 Optimizing results of structural size

DYNAMIC ANALYSIS AND GEOMETRICAL OPTIMIZATION OF THE DETAILS OF ROTARY COMPRESSOR WITH ROLLING PISTON

V.I.Milovanov, V.S.Limar

Odessa Institute of Low Temperatures and Power Engineering

1/3 Petra Velikogo Str., 270100, Odessa USSR phone 55-13-49

ABSTRACT:

The dynamic analysis of rotary compressor mechanism was realized by means of mathematical modelling of its operating processes with computer. The modelling procedure combined with variations of the geometrical parameters of the details proved the possible improvement of compressor efficiency and reliability. The results of modelling were used in the line of new refrigerating compressors with rolling piston manufacturing in Riga (Latvia).

NOMENCLATURE:

d_c - Diameter of internal surface of cylinder

d_e - Diameter of eccentric

d_R - Diameter of external surface of rotor

e - Eccentricity

F_{n1}, F_{t1} - Normal and tangential force components acting upon the rotor from the side of the eccentric, respectively

F_{n2}, F_{t2} - Normal and tangential force components acting upon the rotor from the side of cylinder wall

F_{n3}, F_{t3} - Normal and tangential components of the pressure force which the vane exerts on the rotor

F_{FR} - Resultant force of the refrigerant pressure exerted upon the t^{vane}

F_p - Force of the refrigerant pressure on the back edge of the vane

F_{SR} - Force of the compressed spring exerted upon the back edge of the vane

F_v - Force acting upon the vane from the side of the rotor

F_1, F_2 - Normal force components acting upon the vane from the side of cylinder

P - Resultant force of the refrigerant pressure exerted on the rotor

P_M - Mechanical power which compressor consumes

p_m - Conditional unit pressure in the conjugation passage which rotor surface runs

V_R - Velocity of external rotor surface

ε_i - Instantaneous angular acceleration of the rotor

Δ_1 - Instantaneous value of the clearance between the rotor and eccentric

Δ_{1min} - Minimum operation clearance in the sliding bearing: rotor - eccentric

Δ_2 - Instantaneous value of the clearance between the rotor and the cylinder

ν - Dynamic viscosity of the oil lubricating

$(\pi-\varphi)$ - The angle between the vectorof the forces F_{n1} and F_{n2}

ψ - The angle of rotation of the cylinder radius connecting its centre with the point of contact of the rotor and cylinder, relative to X -axis

ω - Rotational speed of the shaft
ω_R - Rotational speed of the rotor
ω_{RE} - Rotational speed of rotor relative to eccentric: $\omega_{RE_i} = \omega - \omega_{R_i}$

INTRODUCTION

The trend of using new refrigerants (R134a, R22 instead of R12) in the domestic, commercial and transport refrigerating units caused the thorough study of the rotary compressor with a rolling piston as the corresponding increase in the load exerted upon the rotor may result in excessive wear of the contacting surfaces. The same are the inner surface of a rotor and the edge of a vane.

To solve the problem of analyzing the forces acting in the mechanism was possible, and corresponding velocities of the contacting surfaces were defined. In spite of all this compressor efficiency is considered to be one of the most important subjects. This paper describes how mathematical modelling of dynamic processes in rotary compressors was realized with computer to optimize dimensions of the main details of the mechanism. As a result, a highly effici ent, reliable and compact refrigerating rotary compressor was developed.

CRITERIA OF OPTIMIZATION

There is a number of demands that define the relative standard of a compressor. The main of them are the following:
1.The compressor efficiency is to be as high as possible in a wide range of temperature conditions of refrigerating unit.
2.The reliability and the safety as well as the longevity of a compressor are to be high and long as possible.
3.The weight and dimensions indexes are to be minimal.
4.The standard of noise and vibration is to be as low as possible.

Performance of the mentioned demands is not to be accompanied by sharp rise of compressor cost. The terms "high or long or low as possible" mean objective limitations superimposed by the concrete conditions: the possibility of using inexpensive materials and accessive technology.

It is known that the mentioned demands are contradictory but computation of a simple optimal ratio for these demands is hardly possible because of its different nature. Count of each demand in economical calculations is possible and, in our opinion, it is expedient to optimize the mechanism conformably to each demand independently of the others.

Main criterion of optimization

Proceeding from such an environment that energy efficiency im-

provement is strongly desired the compressor efficiency is considered as the main criterion of optimization.

Side by side with the coefficient of fullness defining the power effectiveness of a compressor, in practice it is customary to evaluate the efficiency of the whole refrigeration units as energy efficiency ratio, i.e., refrigerating capacity C to input power:

$$E.E.R. = \frac{C}{P_c + P_v} \qquad (1)$$

where P_c, P_v is the input power of a compressor and that of a ventilator, respectively, W.

Even if SI is used the shortcoming of EER is evident as its value depends on evaporating and condensing temperatures hampering to compare tests results which are run in different temperature ranges. Therefore, it is more preferable to use the exergy efficiency ratio η_{EX} that is exergy of cold E_{CL} to input power [1]:

$$\eta_{EX} = \frac{E_{CL}}{P_c + P_v} \qquad (2)$$

where

$$E_{CL} = \left(\frac{T_o}{T_{EV}} - 1\right) \times C.$$

T_o – Ambient temperature, ^oK (3)

T_{EV} – Evaporating temperature, ^oK

It follows from equation 1, 2 and 3 that energy and exergy efficiency ratios are linked to each other with the temperature coefficient (if SI is used):

$$\eta_{EX} = E.E.R. \times \left(\frac{T_o}{T_{EV}} - 1\right) \qquad (4)$$

The second criterion of optimization

High efficiency of a compressor is to be in concord with its reliability and longevity. It is known that by excessive wear the most vulnarable contacting surfaces of a mechanism are the inner surface of a rotor (rolling piston) and the edge of a vane. That is linked with the main pecularity of a rolling piston compressor mechanism in which the sliding velocity of a rotor and an eccentric is not a garanteed value but it is determined by friction forces exerted upon the rotor.

As the conjugation rotor – eccentric may be considered a sleeve bearing; therefore, all theoretical working out and experimental data for sleeve bearings may be applied to investigation of this conjugation.

The well-known condition to secure the liquid flow friction in a journal bearing may be defined by the inequality

$$\Delta_{1min} \geq 2(R_{z1} + R_{z2}) \qquad (5)$$

where

$\Delta_{1\,min}$ - Minimal fluid-dynamic clearance in the conjugation

R_{z1}, R_{z2} - Medium heights of micro-roughness of a journal and an insert, respectively.

The greater value Δ_{1min} defines the reliable run not only in the rotor-eccentric conjugation but also, to a certain extent, it determines the wear intensity of a vane edge. The thing is that Δ_{1min} depends not only on the load F_{n1} but on rotational speed of a rotor to an eccentric ω_{RE} which determines friction loss in the conjugation vane - rotor.

Therefore, the value Δ_{1min} is accepted as the second criterion of optimization.

Other criteria of optimization

As the sliding velocity of the rotor to the vane is comparatively not essential and rigidness of the details is sufficient the vibration of a vane and a rotor or high frequency noise are hardly possible. Therefore, minimal compressor dimensions and mass are linked chiefly with values of the main and second criteria.

The special criterion of optimization is to be accepted to form the vane edge profile and to find its width. It is possible to to consider that wear intensity of a vane edge is directly proportional to multiplication of contact tension and sliding velocity in the conjugation rotor - vane: $\sigma_H \times V_R$.

GEOMETRICAL OPTIMIZATION OF THE MAIN DETAILS OF A COMPRESSOR MECHANISM

Simulation of dynamic processes in the compressor mechanism

Main details dimension ratios in a rotary compressor mechanism not only determine values of forces and relative velocities of contacting surfaces defining friction losses but also are connected with steadiness of mechanism work, its reliability and longevity. Decreasing the rotor sliding velocity relative to an eccentric causes decreasing the fluid-dynamic clearance in this conjugation and at the moment of maximal load a contact and even adherence of the surfaces become possible that may cause the damage of a compressor.

To optimize dimensions of the main details of the mechanism in accordance with criterions mentioned above the model of dynamic

processes in a compressor was worked out. One revolution of the compressor shaft was divided into small angles and a special programme provided the computations of instantaneous values of the forces acting upon the rotor and the vane. The computable schemes to define these forces at any angle of the shaft turn ψ are shown in Fig.1, 2 and 3.

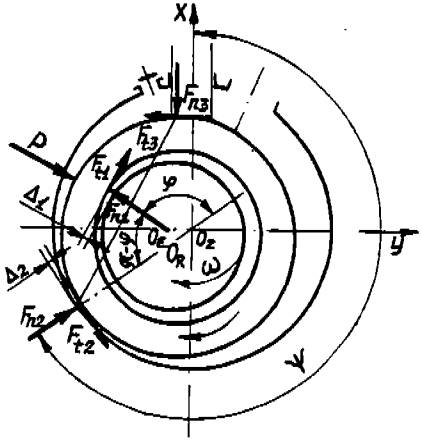

Fig.1.Calculation scheme for the forces exerted upon the rotor

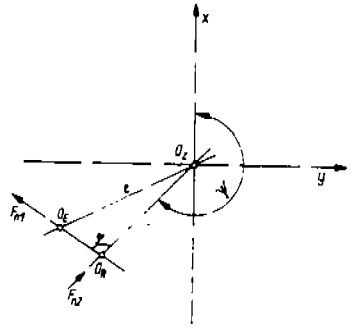

Fig.2. Layout of the rotor, eccentric and cylinder geometrical centres

In accordance with the D'Alamberian principle two equations were written down by projecting the forces, acting upon the rotor and its inertial force - on X and Y axes and one equation of the torques (Fig.1).

$$\Sigma F_{iX} = 0$$
$$\Sigma F_{iY} = 0 \qquad (6)$$
$$\Sigma M_{iO} = 0$$

On deriving the system of equations it was assumed that the mechanical trajectory of a rotor is represented by the circumference with the centre of a cylinder and the instantaneous radius value ($R_C - R_R - \Delta_2$) where:

Δ_2 - Instantaneous value of a clearance between the rotor and the cylinder

R_C , R_R - Radii of the cylinder and of the external surface of the rotor, respectively.

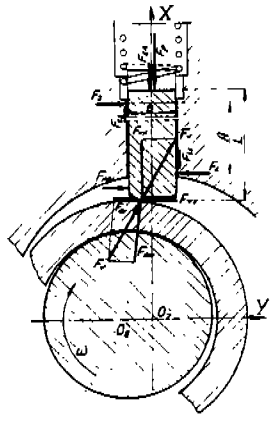

Fig.3. Calculation scheme for the forces exerted upon the vane

On the rotation of the shaft the angle of an eccentric turn advances the angle of a rotor shifting ψ (Fig.1() by a certain value.$(\pi - \varphi)$. The angle $-\varphi$ can be expressed by applying the trigonometrical function, because the sides of triangle having the tops which serve as centres of the rotor O_R , of the eccentric O_E and that of the cylinder O_C (Fig.2) are expressed by the geometrical sizes of the rotor, cylinder and the functional clearances. On adding the term Δ_1 we obtain:

$$\Delta_2 = R_C - R_R - \frac{e \sin\left\{\pi - \varphi - \arcsin\left[(R_1 - R_2 - \Delta_1)\frac{\sin\varphi}{e}\right]\right\}}{\sin\varphi} \qquad (7)$$

where

R_1, R_2 - Radius of the internal rotor surface and that of the eccentric surface, respectively.

The value of Δ_1 can be determined by applying the existing methods of computation for the sleeve bearings [2]:

$$\Delta_{1\,min} = \xi\left(R_1 - R_2\right) \qquad (8)$$

where

ξ - Relative eccentricity of a sliding bearing which is defined in dependence of the bearing stress, C_F , and of the relative length of the journal: $L/(2R_2)$.

Instantaneous rotational speed of a rotor is a result of action of instantaneous angle acceleration ε_i and the previous value of this speed $\omega_{R(i-1)}$:

$$\omega_{Ri} = \omega_{R(i-1)} + \varepsilon_i \times \Delta t \qquad (9)$$

where

Δt - The time of ε_i action

J_R – Rotor moment of inertia

$$\varepsilon_i = \frac{F_{t1} R_1 - F_{t2} R_R - F_{t3} R_R \, sign\left[\omega(R_c - R_R - \Delta_2)\cos\psi + \omega_{i-1} R_R\right] R_R}{J_R}$$

Fig.4 presents an example of the usual plot of modelling parameters. The comparatively slight rotor velocity relative to the vane edge V_3 and the corresponding length S_R that a rotor passes has been confirmed experimentally by means of accelerated filming.

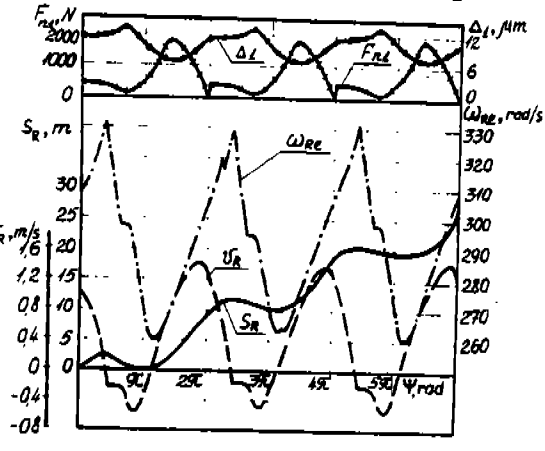

Fig.4. Change of the modelling parameters with the angle of shaft turn ψ ($R22$, $V_0 = 13 cm^3 (0.793 in^3)$, $t_0 = -10°C$ (14°F), $t_c = 55°C$ (131°F))

Modelling of vane dynamic

A block of equations of forces and torques similar to the equations (6) was derived in accordance with the computable scheme shown in Fig.3. Unifyed with the algorithmus described above the common block of these equations made it possible to learn in details the reciprocity of a rotor and a vane. As a result, we saw a good accordance with the modelling and experimental data. Fig.5 shows a usual plot of unit friction power $\sigma_H \times V_3$ in the contact of a vane edge and a rotor. The integrating value of this function during one revolution of the shaft was taken into account by optimizing the vane edge form and its thickness.

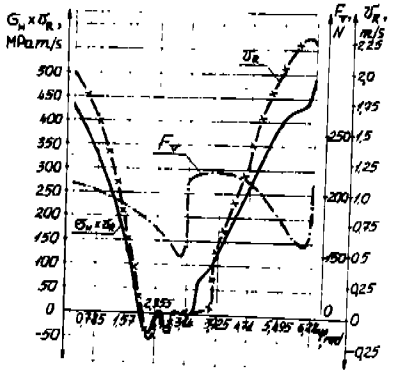

Fig.5. Change of the force of interaction between the vane and the rotor F_V, velocity of external rotor surface V_R and unit friction power $\sigma_H \times V_R$ with angle of shaft turn ψ ($R22$, $V_0 = 13 cm^3$, $t_0 = -15°C$ (5°F), $t_c = 30°C$ (86°F), $d_c = 48 mm$ (1.89"), $e = 4 mm$ (0.16"))

Main results of geometrical optimization of the details

The described above dynamic analysis and modelling the processes in a rotary vane compressor with a computer is especially efficient due to the good possibility to optimize tne mechanism varying values of geometrical parameters.

The following main problems are picked out in the number of solving ones:

- Ascertainment of the optimal value of the eccentricity
- Ascertainment of the optimal value of an eccentric diameter
- Ascertainment of the optimal value of a cylinder opening diameter
- Ascertainment of the optimal values of the vane thickness and its edge radius.

Such values have been ascertained conformably to a number of new rotary compressors with the following cylinder volumes: 7(0.427), 8.5(0.519), 11(0.671), 13(0.793) cm^3 ($inch^3$). There are two modifications of a compressor intended for R134a and R22. R22. The motor speed is 3000 r.p.m. in all units.

As a result of modelling the detailed information about interdependence of the parts dimensions and reliability of the most vulnarable conjugation rotor - eccentric is found. Separate curves are shown in Fig.6, 7 and 8.

The plot in Fig.8 proves that values Δ_1 and P_M are practically not changed with the value of an external rotor surface parameter d_R (cylinder volume V_0 is fixed). That may be resumed with an important practical conclusion: the external diameter of a rotary compressor is determined chiefly by motor size.

The optimization of the vane thickness B and radius of its edge r has shown that there is an optimal ratio of these values: $\frac{r}{B} \approx 2$. The thickness $B = 6mm(0.236i)$ is taken for all the compressors.

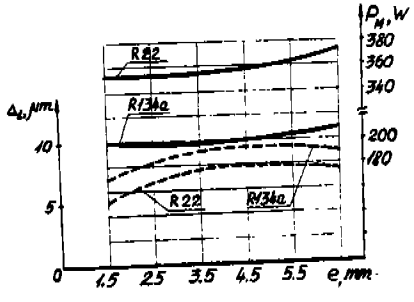

Fig.6.Change of minimal operating clearance between rotor and eccentric $\Delta_1 min$ and input of mechanical power P_M with the value of eccentricity e ($V = 13\ cm^3$ ($0.671\ i^3$), $t = -15°C$ (5F), $t_c = 30°C$ (86°F))

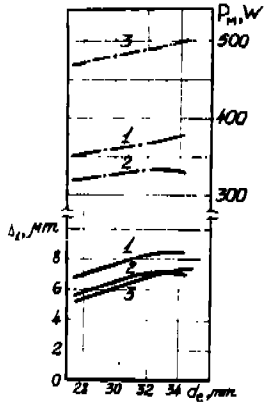

Fig.7. Change of minimal operating clearance between rotor and eccentric Δ_{1min} and input mechanical power P_M with the value of eccentric diameter d_E (V_o=13cm^3, 1-R12, t_o=+5°C (41°F), t_c=55°C (131°F); 2-R502, t_o=-35°C (-31°F), t_c=55°C (131°F); 3-R22, t_o=-10°C t_c=55°C (131°F))

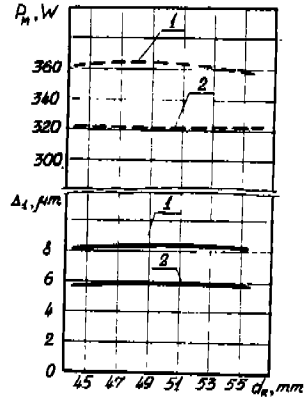

Fig.8. Change of minimal operating clearance between rotor and eccentric Δ_{1min} and input mechanical power P_M with the external rotor diameter d_R (V=13cm^3, 1-R12, t_o=+5°C (41°F), t_c=55°C (131°F); 2-R502, t_o=-35°C (-31°F), t_c=55°C (131°F))

New Riga refrigerating compressors

Optimal dimensions of the main details of the mechanism found descriptively were realized in the number of new compressors developed at Riga compressor factory. These units are characterized by the improved efficiency, small-size and lightweight formation (20% reduction over the conventional), higher reliability even if ecology safe R22 is used as well as by low noise and vibration level.

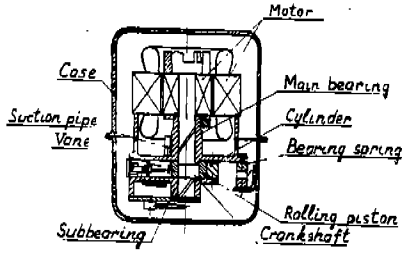

Fig.9. Sectional view of Riga compressor

The basic structure of the compressor is shown in Fig.9. Some of its specification and performance factors are listed in Table 1 indicating that in all the compressors the high efficiency

has been achieved at standard temperatures: evaporating t_o=-15°C(5°F) condensing t_c = 30°C (86°F), suction t_s = 20°C (68°F).

Table 1

Capacity R134a W (BTU/h)	Power Supply (ph-Hz-V)	E.E.R. W/W (BTU/W)	Exergy efficiency ratio η_{ex}
315 (1,075)	1 - 50 - 220	2.3 (7.85)	0.312
400 (1.365)	1 - 50 - 220	2.3 (7.85)	0.312
500 (1.706)	1 - 50 - 220	2.3 (7.85)	0.312
630 (2.150)	1 - 50 - 220	2.3 (7.85)	0.312

There is a certain drop in efficiency because of the accepted mo motor cooling scheme with a refrigerant at suction pressure and low temperature, respectively. It is known that the discharge pressure in this case means decrease of heat exchange irreversibility loss caused by less temperatures difference of the refrigerant and the motor coil windings. But in the reviewed compressors suction pressure in the case secures noise reduction in a simple and reliable design. The sizes and assembly dimensions of the new compressors are shown in Fig.10.

Low noise and vibration level

Inside the sealed case the compressor is supported by 3 bearing springs that reduces noise and particularly vibration so pecular to rotary compressors due to its light weight. A jet type muffler in the suction line with the said bearing springs together make it possible to obtain the noise level not more than 45dB at 1 m from the shell surface and vibration index 100dB.

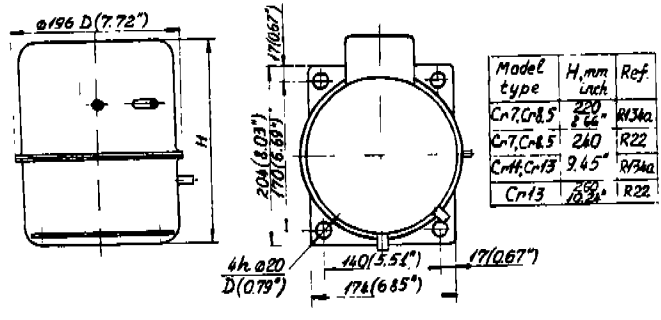

Fig.10. Dimensional Sketch

CONCLUSIONS

New highly efficient and reliable rotary compressors were developed through investigations of relationship between dimensions of main parts and values of criteria of optimization. The noise and vibration level were considerably reduced due to bearing springs supporting the mechanism inside the case.

REFERENCE

1. Brodianski V.M., Medovar L.E. About Exergy Conception in Refrigeration. Kholodilnaya Tekhnika, N5, 41-47 (1961), Moscow, Rus.

2. Orlov P.I. Mechanical Engineering , Vol.2. Moscow, 1977, 574 pp, Rus.

INFLUENCE OF SUCTION LINE ON COMPRESSOR PERFORMANCES

GIOACCHINO MOZZON (Research Engineer)

CARLO GENONI (R&D Manager)

COMPRESSOR DEVELOPMENT DEPARTMENT

WHIRLPOOL ITALIA s.r.l - Cassinetta (ITALY)

1 ABSTRACT

This paper deals with an experimental application of the supercharging phenomenon in the small reciprocating compressors.

The idea is to exploit the resonance condition of the gas contained within the suction line in order to make the suction phase more efficient.

The paper begins with a brief explanation about the basic theory, then takes into account the outcome of the tests and eventually offers the key to limit the noise emission.

2 INTRODUCTION

The technical evaluation of reciprocating compressor performances is based on the analysis of a few parameters like the specific capacity (cooling capacity over displacement), the efficiency and the noise.

The trend of the market is to require a global optimization of the product , especially under the thermodinamic point of view.

To increase the specific capacity many practical solutions have been implemented but other potential sources of improvement can be exploited.

Among them there is the so called *supercharging effect* that can increase to about 10 % the mass flow in the cylinder by introducing a resonance of the intake line.

The purpose is to find the length of the intake pipe so that, during the opening cycle of the suction valve, an overpressure takes place and aids the intake phase.

In other words, the pipe length must be calculated in order to produce pressure waves that in one cycle arrives at the open end and comes back at the valve with a positive amplitude.

In the following sections the tube has been handled by considering the valve side as a close end and modelling the pipe length in such a way as to reach the resonance condition with a frequency double the fundamental frequency of the valve opening.

One must understand that the resonance in the gas tube could produce more noise.

For this reason, it is has been necessary to design new suction mufflers ,helped by a computer software calculating the Insertion Loss of the system.

#3 BASIC THEORY

The gas behaviour in the suction line has been handled by considering it as a separated element in the whole system.

The object of this study is to tune the natural resonance of the gas tube at 100 Hz, i.e. double of the fundamental harmonic.

The meaning of the tuning is to produce an overpressure and then an extra boost of the gas located in front of the suction valve.

The theory that gives the final formula to size the intake pipe is based on the *electromechanics analogy*.

The principle of this theory is to reduce the gas tube to a mechanical system composed of mass,spring and damper.

In a complete mechanical system (fig.1) the forces balance gives the expression

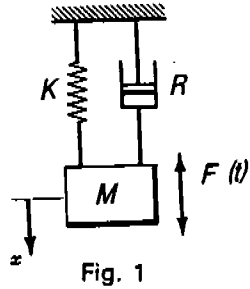

Fig. 1

$$Ft() = Fi + Fr + Fk \qquad (1)$$

F(t) = forcing force

Fi = inertia force

Fr = dissipative force

Fk = elastic force

The equation (1) can be also written as :

$$F(t) = M\,du/dt + Ru + K\int u dt \qquad (2)$$

where u = vibration velocity

M = mass

Rm = damping factor or mechanical resistance

K = spring stiffness = 1/ Cm with Cm = compliance

The solution of the equation (2) describes the oscillating motion.

Then a mechanical system can be reduced to an equivalent electric circuit in the following way.

A general electric circuit (fig.2) is composed of a generator (electromotive force), a resistance , an inductance and an electric capacity.

Applying the Ohm's Law and taking the derivative with respect to the time the equation is

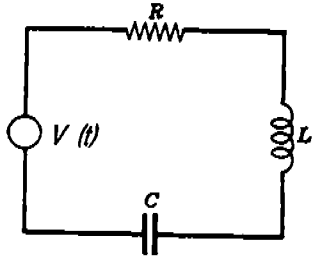

Fig. 2

$$V(t) = L\, di/dt + Ri + 1/C \int i\,dt \qquad (4)$$

where V(t) = electromotive force

i = current

L = inductance

R = resistance

C = capacitance

The solution of the equation (4) gives the current i as a function of the time.

If the equations (4) and (2) are compared, the following correspondence can be done

Mechanical System	**Electric Circuit**
Forcing Force F (t)	*Electromotive Force V (t)*
Vibration velocity u	*Current I*
Mass M	*Inductance L*
Mechanical Resistance Rm	*Resistance R*
Elastic Constant K = 1/Cm	*Inverse Capacitance 1/C*

By considering the effective values and introducing the impedance term Z we have for the electric circuit

$$Z = V / I = \sqrt{R^2 + X^2} = \sqrt{R^2 + (\omega L - 1 / \omega C)^2} \quad (5)$$

where X is the Reactance $= \omega L - 1/\omega C \quad (\omega = 2\pi f)$

The condition

$$X = 0 \qquad \omega L = 1 / \omega C$$

is called resonance condition.

Similarly, for the mechanical system, we can write

$$Zm = F / U = \sqrt{Rm^2 + (\omega L - 1 / \omega X)^2}$$

where Zm is the mechanical impedance

The correspondence between the two systems belonging to two different fields can be expanded to a third system.

The acoustic model is represented by the gas tube and the equivalent mechanical system can be obtained.

The tube is open at one side and disturbed at the other side.

The disturbance is caused by the valve motion and produces continuous pressure changes in the pipe.

The gas tube presents a mass, an elastic constant due to the property that behaves like a spring and a damping factor, or resistance, taking into account the energy dissipation (fig.3).

Applying the equation (2) to the new model is

$$f(t) = M\, du/dt + Rmu + K\int u dt \quad (7)$$

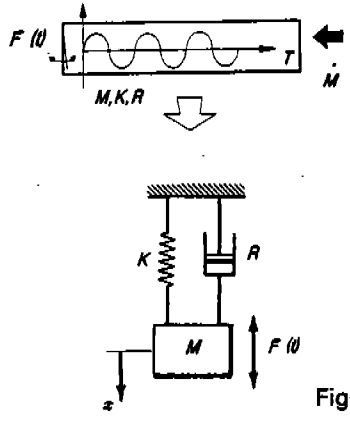

Fig. 3

where f(t) = valve motion disturbance

u = vibration velocity

M = mass of the gas tube

Rm = mechanical resistance

K = gas stiffness = 1/Cm

If we consider the pressure p, the previous equation becomes :

$$\Delta p(t) = (M/S)du/dt + (Rm/S)u + (1/CmS)\int udt \qquad (8)$$

and with the effective values

$$P = j\omega(M/S)U + (Rm/S)U - jU/(\omega CmS) =$$

$$= (Rm/S)U + jU(\omega M/S - 1/(\omega CmS)) \qquad (9)$$

Introducing the term Q, acoustic flowrate,

$$Q = US$$

we may write the equation (9) in the form

$$P = (Rm/S^2)Q + jQ(\omega M/S^2 - 1/(\omega CmS^2)) \qquad (10)$$

Now we can define

$Ra = Rm/S^2$ = Acoustic Resistance

$Ma = M/S^2 = \rho L/S$ = Acoustic Mass

$Ca = CmS^2 = V/(\rho c^2) = SL/(\rho c^2)$ = Acoustic Compliance

For analogy, the acoustic impedance Za is

$$Za = P/Q = \sqrt{Ra^2 + Xa^2}$$

where Xa = Acoustic Reactance = $\omega Ma - 1/(\omega Ca)$

The resonance condition arises when the acoustic reactance Xa is = 0,then

$$\omega Ma = 1/\omega Ca$$

$$\rho\omega L/S = \rho c^2/(\omega LS)$$

$$\omega = c/L \qquad f = c/(2\pi L) \qquad (11)$$

Then the pipe length will be

$$L = c/(2\pi f)$$

4 EXPERIMENTAL PROCEDURE. RESULTS

The experimental application of the theory has been faced with a preliminary bench test, with its aim to confirm the theoretical data.

In this test , an open compressor with a variable length of the suction pipe was taken and a manometer set in the discharge line.

Thus, a valve allowed to control the the flow coming out from the compressor and discharged in the air (fig. 4)

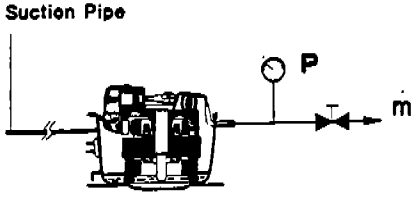

Fig. 4

Since the test was carried out in air, the pipe length was sized with reference to the corresponding sound speed.

Then , after the reaching of a steady temperature in the suction pipe, a pressure measurement has been done for each pipe length.

The resonance phenomenon was expected with an increase of pressure in the discharge pipe , as a consequence of higher flow rate.

In fig. 5 the pressure changes versus the pipe length are reported and where the value is highest the best condition are achieved.

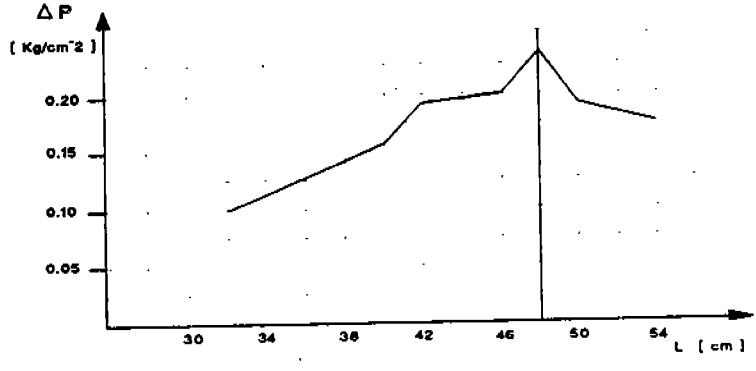

Fig. 5

Then, considering the R12 application,the pipe length was fixed.

The tests were carried out at the calorimeter and special prototypes , having a transducer near the suction valve and different pipe lengths, were used.

The transducer allowed a continuous monitoring of the gas pulsations and the corresponding graphs are reported below.

In fig.6, pulsations of the standard configuration of suction mufflers are represented and it can be noticed how flat the pressure is before the valve opening , due to the mufflers and passages damping.

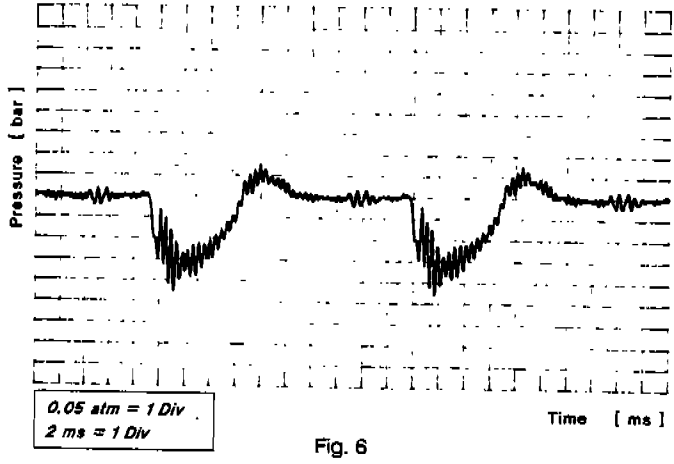

Fig. 6

If a pipe is taken, a completely different outline is obtained and this is because the resonance conditions arise., even if no tuned with the fundamental frequency.

Consequently , the amplitude of the gas pulsations are bigger and the resonances waves can be noticed (fig. 7-11).The closer the gas resonance frequency is with the double of the fundamental harmonic, the higher are the amplitudes of the gas pulsations.

The best situation can be considered with the length between 24 cm and 27 cm.

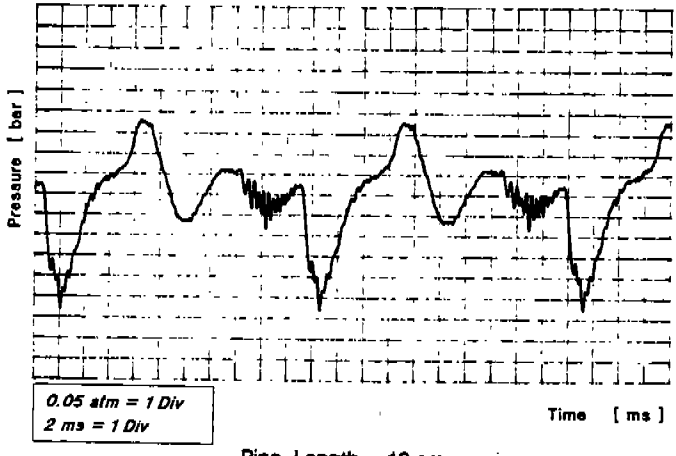

Pipe Length = 12 cm

Fig. 7

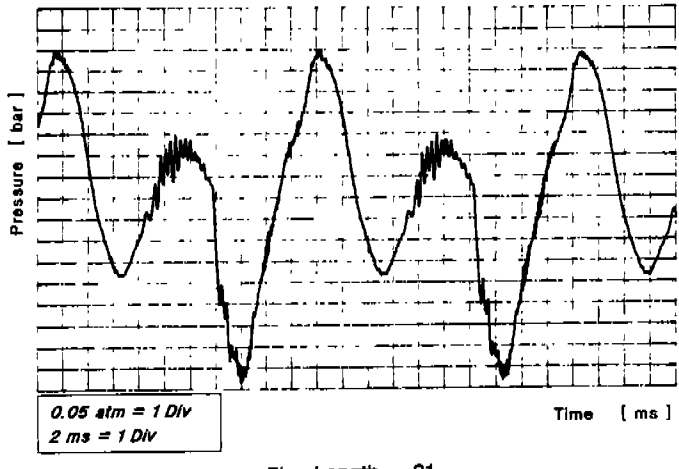

Pipe Length = 21

Fig. 8

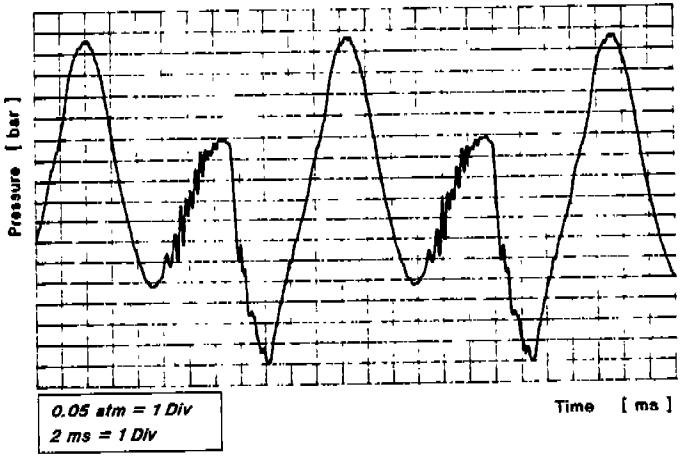

Pipe Length = 24 cm

Fig. 9

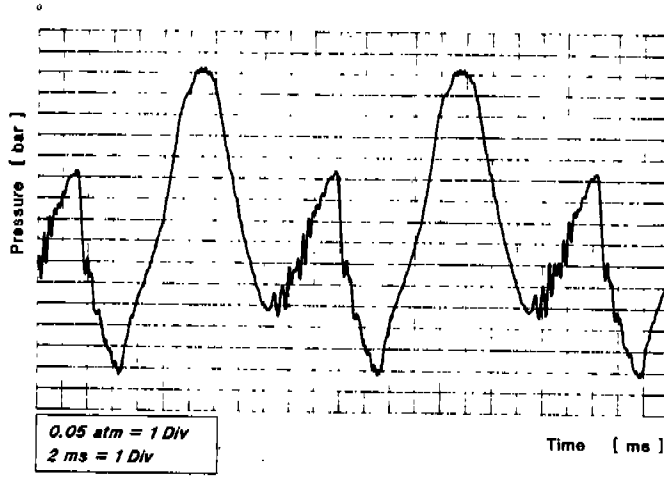

Pipe Length = 27 cm

Fig. 10

#5 NOISE CONTROL

By experience , the noise range affected by the suction line is below 1000 Hz and it plays an important role in the overall noise generation mechanism of reciprocating compressors.

A support for the investigations is provided by existing computer simulation programs.

In our case, a Fortran program allows the calculation of the frequency spectrum of noise ,due only to the suction gas pulsations.

The main aim of this study is to find out a new geometry of the mufflers , when the long suction pipe is applied.

The acoustic properties of the mufflers can be represented by the INSERTION LOSS , defined as :

$$I.L. = W1 / W2 \quad or \quad I.L. = 10 \, Log \, W1 / W2 \quad (db)$$

where W1 = sound power of the system without mufflers

W2 = sound power of the system with mufflers inserted.

The mufflers have been reduced to an equivalent cylindrical pipe with a length equal to the physical distance between the input and the output of the muffler and a radius calculated considering the volume of the pipe equal to the real volume.

In the following graphs, three different suction lines are compared.

The first concernes the standard configuration (fig.11), whereas the others two are with the long pipe,the former without any specific design (fig. 12), and the latter with two Helmotz Resonators to damp a few frequency peaks (fig.13).

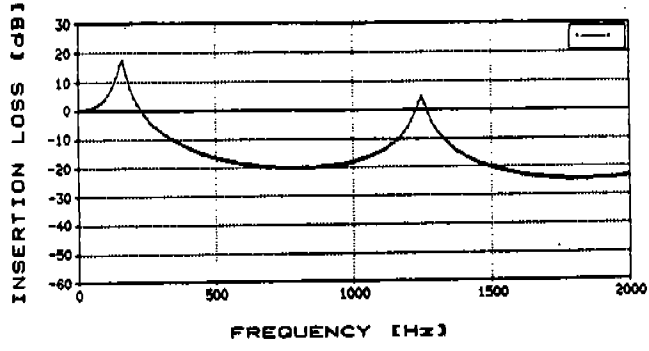

Fig. 11

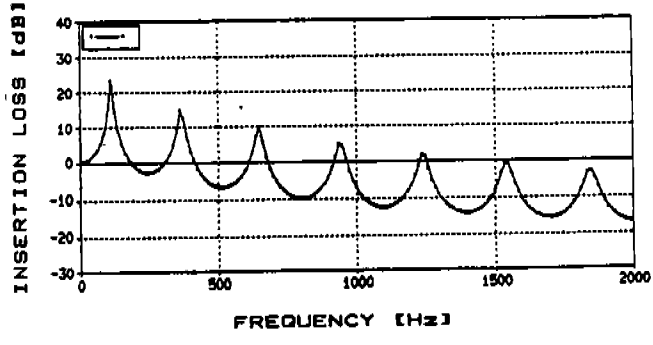

Fig. 12

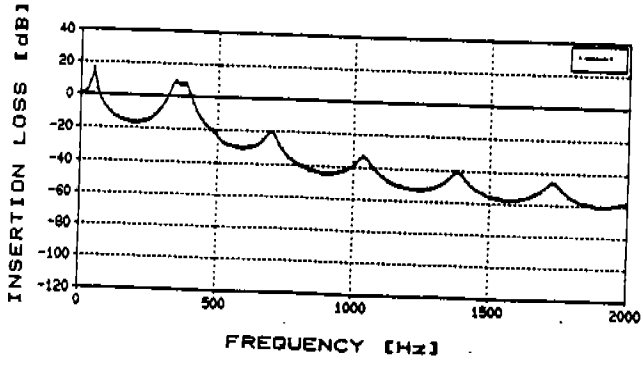

Fig. 13

#6 CONCLUSION

The outcome of this study have shown the validity of the supercharging effect.

The great increase of the specific capacity has been followed by a limited increase of input power and therefore the efficiency of the compressors improved.

Particular attention must be dedicated to the suction muffler design in order to dampen the noise without influencing the resonance phenomenon.

Further investigations have been planned to optimize this application.

#7 REFERENCES

The effect of inlet piping system on the reciprocating compressor work..

M.Luszczycki, Purdue 1990

Design and mechanics of compressor valves. W.Soedel,

Ray W.Herrick Labs. School of Mechanical Engineering , Purdue University 1984.

Modeling Temperatures in High Speed Compressors for the Purpose of Gas Pulsation and Valve Loss Modelling

Zheji Liu, Graduate Research Assistant
Werner Soedel, Professor of Mechanical Engineering
Ray W. Herrick Laboratories
School of Mechanical Engineering
Purdue University
West Lafayette, IN 47907

ABSTRACT

The effects of compressor speed variation on the heat transfer inside a speed controlled compressor were investigated in this study. Based on the lumped capacitance method, the temperatures of the compressor components, the oil, and the refrigerant gas within the shell were modeled and simulated on a relative scale. A different heat transfer coefficient correlation was developed to evaluate the convective heat transfer rate between the compressor cylinder wall and the gas inside it. The refrigerant gas mass loss at different compressor speeds and how the compressor speed affects the suction gas heating were discussed.

1. Introduction

Power is consumed in each compression cycle to increase the enthalpy of gas through the compression performed by the piston inside the compressor cylinder. Cool gas enters the cylinder, and then leaves the cylinder at a much higher temperature. Hot gas circulates inside the hermetic shell and warms up other components in the shell. In addition, because of friction losses and motor losses, mechanical energy and electrical energy are converted into thermal energy, which can be considered as heat sources supplying energy to compressor parts. According to the heat transfer modes, the overall heat transfer inside the compressor system can be classified as: convection due to gas and oil circulation, conduction between the connected components, and radiation from internal components to the shell and from the shell to the surroundings.

Of the overall heat exchange of the compressor system, the heat transfer of most concern happens in the suction side of the compressor. From the moment when gas enters the suction pipe until the gas is trapped in the cylinder volume and compression is about to start, the gas continuously picks up heat from the suction passage and the cylinder wall, which is called suction gas heating. Because of suction gas heating, the gas expands and its density is decreased. Since the volume of the suction chamber is fixed, the lighter gas means less mass is pumped, and, therefore, volumetric losses occur without reducing the amount of energy required for compression.

The heat transfer rate between the compressor cylinder wall and the gas is one of the factors which affects the thermodynamic processes inside the cylinder. Therefore, the heat transfer between the cylinder wall and the gas during both the expansion and the compression process needs to be studied. The heat transferred between the cylinder wall and the gas has effects on the compressor power consumption and discharge temperature.

However, the study of the heat transfer in the compressor cylinder and the suction passage can not be isolated. The temperatures of the cylinder wall and the suction passage are needed to determine the heat flow rate in these regions. Since heat flows from one compressor component to another, the temperatures of these components are interactively related and have to be solved simultaneously. So, the overall heat transfer model is indispensable.

The compressor shaft rotation speed also affects the heat transfer both in the cylinder and in the suction passage. Intuitively, the faster compressor speed would mean less time for heat transferring to the gas from the suction passage and the cylinder wall, and therefore reducing the effects of suction gas heating. However, the increase of compressor speed also causes more power wasted into heat through friction and motor losses per unit time, and in the same time, causes larger convective heat transfer coefficients due to faster gas flow, so the heat transfer is elevated from this point of view. The net effect of the speed variation on heat transfer is very complicated and can only be determined by resorting to the computer simulation.

2. The Lumped Capacitance Method

The temperature distribution inside the compressor system is very complicated. Even in a single component, for example, the cylinder case, the temperature could be different from one place to another. It is beyond the scope of this research to study the spatial temperature distributions of the compressor components.

Based on the consideration that the spatial fluctuations of the temperatures are relatively small, comparing with the average temperatures of the solids, it is assumed that the temperature in each solid and oil is spatially uniform at any instant during the transient process. This is called the lumped capacitance method [1]. It implies that temperature gradients within the solid and the oil are negligible.

Using the lumped capacitance method, uniform temperatures are assigned to the compressor components, as shown in Figure 1, and are described as follows:

T_{comp} = Bulk temperature of the compressor and the rotor, combining the cylinder case, the vane, the roller, the shaft, and the motor rotor as one lumped mass.

T_{oil} = Bulk temperature of the oil.

T_{shelld} = Bulk temperature of the lower part of the shell, or of the shell section below the oil level.

T_{shellu} = Bulk temperature of the upper shell and the stator, combining the shell section above the oil level and the motor stator as one lumped mass.

T_{pipe2} = Bulk temperature of the suction pipe segment exposed to the outside, located between the compressor shell and the accumulator.

T_{accu} = Bulk temperature of the accumulator and the suction pipe segment inside the accumulator, which are considered as one lumped mass.

3. Heat Transfer in the Suction Passage

The suction passage of the rolling piston rotary compressor is actually a circular pipe, as shown in Figure 2. The convection heat transfer coefficient for turbulent flow in a uniformly circular pipe is [1]

$$h_p = 0.023 \frac{k}{D} Re_D^{0.8} Pr^{0.4} \tag{1}$$

where k is the thermal conductivity of the gas inside the pipe, D is the diameter of the pipe, Re_D is the Reynolds number of the gas, and Pr is the Prandtl number of the gas.

The average value of the Reynolds number Re_D for flow in the circular pipe is [1]

$$Re_D = \frac{4\dot{m}_{ave}}{\pi D \mu} \tag{2}$$

where $\dot{m}_{ave}$ is the average mass flow rate of the suction gas during the suction process, and μ is the dynamic viscosity of the gas.

If the whole suction pipe is divided into three segments as shown in Figure 2, then, according to Section 2, the temperatures of the three segments of the pipe are respectively T_{accu}, T_{pipe2}, and T_{comp}. Applying the principle of energy conservation to each of the gas control volume inside the three segments of the pipe yields

$$h_p \pi D L_1 \left(T_{accu} - \frac{T_s + T_{s1}}{2} \right) = \dot{m}_{ave} c_p (T_{s1} - T_s) \tag{3}$$

$$h_p \pi D L_2 \left(T_{pipe2} - \frac{T_{s1} + T_{s2}}{2} \right) = \dot{m}_{ave} c_p (T_{s2} - T_{s1}) \tag{4}$$

$$h_p \pi D L_3 \left(T_{comp} - \frac{T_{s3} + T_{s2}}{2} \right) = \dot{m}_{ave} c_p (T_{s3} - T_{s2}) \tag{5}$$

where L_1, L_2, and L_3 are the lengths of the three segments of the pipe, c_p is the constant pressure specific heat of the gas, T_s is the temperature of the gas entering the suction pipe, T_{s1} and T_{s2} are the down stream gas temperatures of the control volume 1 and the control volume 2, as shown in Figure 2, and T_{s3} is the temperature of the gas entering the cylinder volume.

The component temperature T_{accu}, T_{pipe2}, and T_{comp} will be calculated in Section 5. When they are known, the gas temperature T_{s1}, T_{s2}, and T_{s3} can be solved from Equations (3)-(5).

4. Heat Transfer Between the Cylinder and the Gas Within it

The instantaneous heat transfer between the compressor cylinder walls and the gas within the cylinder is due to the turbulent motion of the gas relative to the walls. The velocity of the gas consists of two components [2]. The first component is due to the motion of the compressor cylinder volumes

relative to the cylinder walls. The second one is the squishing velocity caused by the cylinder volume geometry change. However, the squishing velocity is very difficult, if not impossible, to predict, because of the complex configuration of the cylinder volume and its variation from one type of compressor to another. Therefore, modeling the heat transfer inside the cylinder is much more difficult than that inside the suction pipe. Not like the heat transfer inside the pipe, there is no general and accurate formula or correlation for the convection heat transfer coefficient between the cylinder walls and the gas in the cylinder of a rolling piston rotary compressor.

A fair amount of work has been done on the prediction of the heat transfer between cylinder walls and the gas inside a cylinder. Adair [3] is the first one who investigated the instantaneous heat transfer between the cylinder and the gas within a reciprocating compressor. He presented his heat transfer coefficient correlation as follows

$$h_c = 0.053 \frac{k}{D_e} Re^{0.8} Pr^{0.6} \tag{6}$$

$$D_e = \frac{6 \text{ cylinder volume}}{\text{cylinder surface area}} \tag{7}$$

$$Re = \frac{\rho D_e \left(\frac{D_e}{2} \omega_g \right)}{\mu} \tag{8}$$

where ρ is the density of gas, ω_g is the characteristic angular velocity. However, Recktenwald's results [4] cast considerable doubt on the validity of the heat transfer correlation obtained by Adair. By using the so called multinode model, he found that the heat transfer rate between the cylinder walls and the gas within the cylinder of a reciprocating compressor is an order of magnitude larger than that predicted by the Adair correlation.

Yanagisawa [5] applied both the Adair correlation and the McAdams correlation to the heat transfer between the cylinder walls and the gas in the cylinder of a rolling piston rotary compressor. The McAdams correlation was first used by Atesmen [2] on the rotary combustion engine. It is expressed as

$$h_c = 0.023 \frac{k}{D_h} Re^{0.8} Pr^{0.4} \tag{9}$$

where D_h is the instantaneous hydraulic diameter of the combustion chamber. In the combustion chamber of the rotary engine, the fuel-air mixture velocity relative to the housing is more complicated than the gas velocity in the compressor cylinder. Besides the velocity component due to the motion of the chamber relative to the housing and the squishing velocity component caused by the changing chamber geometry, there is a third velocity component induced by the expanding combustion products in between the flame fronts. Therefore, the effective fuel-air mixture velocity Atesmen used in the McAdams correlation is three times the velocity of the chamber relative to the rotary combustion engine housing. Without any modification, Yanagisawa borrowed the above correlation for the rolling piston rotary compressor, although the gas velocity in the compressor cylinder does not consist of the component of flame front velocity as in the rotary combustion engine. He adopted

$$h_c = 0.023 \frac{k}{D_h} \left(\frac{u D_h}{\nu} \right)^{0.8} \left(\frac{\nu}{\kappa} \right)^{0.4} \tag{10}$$

$$D_h = r_1 = \text{cylinder radius} \tag{11}$$

$$u = 3 \omega r_1 \tag{12}$$

where ν is the kinematic viscosity, κ is the thermal diffusivity, ω is the angular velocity of the compressor shaft, and u is the effective velocity of the gas.

The Adair correlation was developed for the reciprocating compressor whose geometry is quite different from that of the rolling piston rotary compressor. The McAdams correlation is primarily for the heat transfer between a pipe and the fluid within it, and does not reflect the effect of the curved geometry of the rolling piston rotary compressor cylinder volume on the heat transfer. Therefore, a different heat transfer coefficient correlation is used in this study. Since the crescent shaped volume inside the rolling piston rotary compressor is similar to a spiral tube with rectangular cross section, the convection heat transfer correlation for curved channels of rectangular cross section [6] is applied to the heat transfer inside the rolling piston rotary compressor cylinder. The correlation is

$$h_c = 0.025 \frac{k}{D_h} Re^{0.8} Pr^{0.4} \left(1.0 + 1.77 \frac{D_h}{r_{ave}} \right) \tag{13}$$

where r_{ave} is the average value of the cylinder radius r_1 and the roller radius r_2. As the compressor shaft rotates, the cylinder volume geometry is changing, so is the hydraulic diameter D_h. Since the physical properties of the gas, such as density, thermal conductivity, and dynamical viscosity, are all

functions of the pressure and the temperature in the cylinder, the instantaneous value of Reynolds number Re and that of Prandtl number Pr are all changing from one location of the cylinder volume to another.

The gas velocity is a very important factor of the heat transfer coefficient. As mentioned in the beginning of this section, the velocity of the gas inside the rolling piston rotary compressor cylinder is made up of two components. As predicted by Atesmen, the relative magnitude of the velocity component due to the motion of the cylinder volume relative to the cylinder is of the same order as the squishing velocity component caused by the cylinder volume geometry change. So, It is assumed that the characteristic velocity of the gas is

$$u = 2\,\omega r_1 \tag{14}$$

The instantaneous value of the hydraulic diameter D_h of the crescent shaped cylinder volume is

$$D_h = \frac{4\,V(\alpha)}{A_c(\alpha)} \tag{15}$$

where the cylinder volume $V(\alpha)$ and the volume surface area $A_c(\alpha)$ can be calculated by using the geometrical relations of the compressor.

Using the above characteristic velocity and the hydraulic diameter, the Reynolds number is obtained as

$$Re = \frac{\rho\, u\, D_h}{\mu} \tag{16}$$

and the Prandtl number can be calculated by the relation

$$Pr = \frac{c_p\,\mu}{k} \tag{17}$$

Finally, the heat transfer rate from the cylinder walls to the gas inside the cylinder can be expressed as

$$\dot{Q} = h_c\, A_c(\alpha)\,(T_{comp} - T)$$

$$= 0.025\,\frac{k}{D_h}\,Re^{0.8}\,Pr^{0.4}\left(1.0 + 1.77\,\frac{D_h}{r_{ave}}\right)A_c(\alpha)\,(T_{comp} - T) \tag{18}$$

5. Governing Equations of the Compressor System Temperatures

The temperatures of some compressor components, such as the cylinder temperature, and the temperatures of the three segments of the suction pipe, are needed in determining the heat transfer both in the cylinder and in the suction passage. As mentioned in Section 1, all the compressor component temperatures must be solved simultaneously, because they are coupled to each other through the heat flowing between them.

Thus, the presented results are based on the lumped capacitance method introduced in Section 2 and the following assumptions:

(1) The heat transfer induced by oil circulation throughout the compressor system is neglected.
(2) The motor losses is considered as a heat source inside the stator, or the upper shell-stator lumped mass.
(3) Friction losses are considered as a heat source inside the compressor cylinder, or the compressor-rotor lumped mass.
(4) An average heat transfer coefficient is used for the overall convection heat transfer between the gas inside the shell and the compressor components.
(5) The properties of the gas inside the shell, such as temperature, pressure, etc., are uniform, as they are inside the cylinder.
(6) Ideal gas relations are applicable to the gas inside the shell.

The heat flow diagram [7] of the compressor system is shown in Figure 2. The bulk temperatures of the lumped mass were defined in Section 2, and the rest of the symbols used in Figure 1 are described below:

T_{amb} = Temperature of the ambient surrounding the compressor shell.
T_{gas} = Bulk temperature of the refrigerant gas inside the shell.
R_1 = Average thermal resistance between the oil and the lower part of the shell.
R_2 = Average thermal resistance between the oil and the compressor.
R_3 = Average thermal resistance between the lower shell and the compressor.
R_4 = Average thermal resistance between the upper shell and lower shell.
R_5 = Average thermal radiative resistance between the upper shell-stator lumped mass and the compressor-rotor lumped mass.
R_6 = Average thermal convective resistance between the gas inside the shell and the compressor-rotor lumped mass.

R_7 = Average thermal resistance between the oil and the upper shell-stator lumped mass due to the fact that part of the windings in the stator is immersed in the oil.

R_8 = Average thermal convective resistance between the gas inside the shell and the oil.

R_9 = Average thermal convective resistance between the gas inside the shell and the upper shell-stator lumped mass.

R_{10} = Average thermal resistance between the upper shell and the accumulator.

R_{11} = Average thermal resistance between the outside surface of the lower shell and the surrounding medium.

R_{12} = Average thermal resistance between the outside surface of the upper shell and the surrounding medium.

R_{13} = Average thermal resistance between the lower shell and the suction pipe segment exposed to the outside, located between the compressor shell and the accumulator.

R_{14} = Average thermal resistance between the compressor and the suction pipe segment exposed to the outside.

R_{15} = Average thermal resistance between the suction pipe segment exposed to the outside and the surrounding medium.

R_{16} = Average thermal resistance between the suction pipe segment exposed to the outside and the accumulator.

R_{17} = Average thermal resistance between the accumulator and the surrounding medium.

$\dot{Q}_m$ = Rate of heat released by the compressor motor.

$\dot{Q}_{ave}$ = Average heat flow rate from the compressor cylinder walls to the gas inside the cylinder.

$\dot{Q}_{friction}$ = Rate of heat generated by friction in the compressor.

$\dot{Q}_{pipe1}$ = Rate of heat picked up by the gas from the pipe segment 1, as shown in Figure 2, when the gas flows through the suction passage.

$\dot{Q}_{pipe2}$ = Rate of heat picked up by the gas from the pipe segment 2, as shown in Figure 2, when the gas flows through the suction passage.

$\dot{Q}_{pipe3}$ = Rate of heat picked up by the gas from the pipe segment 3, as shown in Figure 2, when the gas flows through the suction passage.

C_{comp} = Thermal capacity of the compressor-rotor lumped mass.

C_{oil} = Thermal capacity of the oil.

C_{shelld} = Thermal capacity of the lower shell.

C_{shellu} = Thermal capacity of the upper shell-stator lumped mass.

C_{pipe2} = Thermal capacity of the suction pipe segment exposed to the outside.

C_{accu} = Thermal capacity of the accumulator and the suction pipe segment inside the accumulator.

C_{gas} = Thermal capacity of the gas inside the shell.

$\dot{m}_2$ = Mass flow rate of the gas exiting the shell.

h_2 = Enthalpy of the gas exiting the shell.

h_0 = Average enthalpy of the gas flowing out of the discharge port.

All the thermal capacities, except that of the gas, can be treated as constants. By summing up the heat flow rates at the node points of Figure 3, the energy balance equation of each lumped mass can be obtained, expressed as

$$\frac{d}{dt}(T_{comp}) = \frac{1}{c_{psteel} m_{comp}} \left(-\frac{T_{comp} - T_{shelld}}{R_3} + \frac{T_{gas} - T_{comp}}{R_6} - \frac{T_{comp} - T_{oil}}{R_2} - \frac{T_{comp} - T_{pipe2}}{R_{14}} + \frac{T_{shellu} - T_{comp}}{R_5} + \dot{Q}_{friction} - \dot{Q}_{ave} - \dot{Q}_{pipe3} \right) \tag{19}$$

$$\frac{d}{dt}(T_{oil}) = \frac{1}{c_{poil} m_{oil}} \left(\frac{T_{comp} - T_{oil}}{R_2} - \frac{T_{oil} - T_{shelld}}{R_1} + \frac{T_{shellu} - T_{oil}}{R_7} + \frac{T_{gas} - T_{oil}}{R_8} \right) \tag{20}$$

$$\frac{d}{dt}(T_{shelld}) = \frac{1}{c_{psteel}\, m_{shelld}}\left(\frac{T_{comp} - T_{shelld}}{R_3} + \frac{T_{oil} - T_{shelld}}{R_1} + \frac{T_{shellu} - T_{shelld}}{R_4} - \frac{T_{shelld} - T_{pipe2}}{R_{13}} - \frac{T_{shelld} - T_{amb}}{R_{11}}\right) \quad (21)$$

$$\frac{d}{dt}(T_{shellu}) = \frac{1}{c_{psteel}\, m_{shellu}}\left(\frac{T_{gas} - T_{shellu}}{R_9} - \frac{T_{shellu} - T_{accu}}{R_{10}} - \frac{T_{shellu} - T_{comp}}{R_5} - \frac{T_{shellu} - T_{oil}}{R_7} - \frac{T_{shellu} - T_{shelld}}{R_4} - \frac{T_{shellu} - T_{amb}}{R_{12}} + \dot{Q}_m\right) \quad (22)$$

$$\frac{d}{dt}(T_{pipe2}) = \frac{1}{c_{psteel}\, m_{pipe2}}\left(\frac{T_{comp} - T_{pipe2}}{R_{14}} + \frac{T_{shelld} - T_{pipe2}}{R_{13}} - \frac{T_{pipe2} - T_{amb}}{R_{15}} - \frac{T_{pipe2} - T_{accu}}{R_{16}} - \dot{Q}_{pipe2}\right) \quad (23)$$

$$\frac{d}{dt}(T_{accu}) = \frac{1}{c_{psteel}\, m_{accu}}\left(\frac{T_{shellu} - T_{accu}}{R_{10}} + \frac{T_{pipe2} - T_{accu}}{R_{16}} - \frac{T_{accu} - T_{amb}}{R_{17}} - \dot{Q}_{pipe1}\right) \quad (24)$$

where

c_{psteel} = Specific heat of steel
c_{poil} = Specific heat of the oil
m_{comp} = Mass of the compressor and the rotor
m_{oil} = Mass of the oil
m_{shelld} = Mass of the lower shell
m_{shellu} = Mass of the upper shell and the stator
m_{pipe2} = Mass of the suction pipe segment exposed to the outside
m_{accu} = Mass of the accumulator, including that of the suction pipe segment inside the accumulator

The mass of the gas inside the shell is not a constant during the transient process. Its rate of change is

$$\frac{d}{dt}(m_{gas}) = \dot{m}_{ave} - \dot{m}_2 \quad (25)$$

Applying the principle of energy conservation to the gas inside the shell yields

$$c_{vgas} m_{gas} \frac{d}{dt}(T_{gas}) + c_{vgas} T_{gas}(\dot{m}_{ave} - \dot{m}_2) = -\frac{T_{gas} - T_{shellu}}{R_9} - \frac{T_{gas} - T_{comp}}{R_6} - \frac{T_{gas} - T_{oil}}{R_8} + \dot{m}_{ave} h_0 - \dot{m}_2 h_2 \quad (26)$$

or

$$\frac{d}{dt}(T_{gas}) = \frac{1}{c_{vgas}\, m_{gas}}\left[-\frac{T_{gas} - T_{shellu}}{R_9} - \frac{T_{gas} - T_{comp}}{R_6} - \frac{T_{gas} - T_{oil}}{R_8} + \dot{m}_{ave}(h_0 - c_{vgas} T_{gas}) - \dot{m}_2 T_{gas}(c_{pgas} - c_{vgas})\right] \quad (27)$$

where c_{pgas} is the constant pressure specific heat of the gas inside the shell, c_{vgas} is constant volume specific heat of the gas inside the shell, and m_{gas} is instantaneous mass of the gas inside the shell.

The heat rate released by the motor, $\dot{Q}_m$, depends on the efficiency of the motor. It is expressed as

$$\dot{Q}_m = (1 - \eta_{motor})\, W_{in} \quad (28)$$

where η_{motor} is the motor efficiency, and W_{in} is the power input to the motor. Both of them are usually given.

Without studying the friction in the compressor in detail, the heat rate generated by friction can be approximated by the following relation

$$\dot{Q}_{friction} = (1 - \eta_{mech})\,\eta_{motor} W_{in} \tag{29}$$

where η_{mech} is the mechanical efficiency of the compressor. It can be empirically determined.

The heat transfer rates from the suction pipe segments to the suction gas, $\dot{Q}_{pipe1}$, $\dot{Q}_{pipe2}$, and $\dot{Q}_{pipe3}$, are respectively the terms on the left sides of Equations (3)-(5), which have been determined in Section 3.

Equation (19)-(25) and Equation (27) form a group of first order differential equations. The temperatures of the compressor system can be obtained by numerically solving those equations.

6. Results and Conclusions

Typical outputs are plotted in Figures 4-6. Three interpretations can be obtained from Figure 4. Firstly, the temperatures of the compressor-rotor lumped mass, the oil, the lower shell, the upper shell-stator lumped mass, and the shell gas go up with the increase of the compressor shaft rotation speed. Since the piston work required to complete one cycle does no change much, it follows that the faster the compressor shaft rotates, the more power is consumed, and the more energy is converted to heat per unit time for the given motor efficiency and mechanical efficiency factors. Secondly, the temperature of the upper shell-stator lumped mass is higher than that of the shell gas at high rotation speeds. This suggests that the refrigerant gas works as a kind of coolant for the motor. Thirdly, at higher speed, the transient process of the compressor system temperatures converges to steady state faster in time.

As discussed in the last paragraph of Section 1, the compressor speed has two direct effects on the heat transferred from the cylinder to the gas inside it. The higher speed reduces the time for heat to transfer from the cylinder to the gas per cycle, but enhances the convection heat transfer coefficient. Besides this, an indirect effect of higher speed on the heat transfer is through the fact that it causes the compressor metal temperature to increase, as shown in Figure 4. By carefully examining the cylinder gas temperature comparisons at different rotation speeds, as shown in Figure 5, we find that the cylinder gas temperature increases when the speed is increased. This can be further verified by checking the instantaneous mass curves of the cylinder gas, as shown in Figure 6. Less mass of gas is pumped into the cylinder per cycle at the higher speed. So, we conclude that at higher speed, suction gas heating is more severe, which causes a larger amount of mass loss.

Acknowledgement

Support of this research by the Toshiba Corporation is gratefully acknowledged.

References

[1] Incropera, F.P., and Dewitt, D.P., "Introduction to Heat Transfer", John Wiley & Sons, 1990.

[2] Atesmen, K.M., Trans. ASME, Ser. C, Vol. 97, No. 2, P. 288, May, 1972

[3] Adair, R.P., M.S. Thesis, Purdue University, 1972.

[4] Recktenwald, G.W., Ramsey, J.W., and Patankar, S.V., "Prediction of Heat Transfer in Compressor Cylinders", Proceedings of the 1986 Purdue Compressor Technology Conference, pp. 159-174.

[5] Yanagisawa, Tadashi, et al., "A Study on Suction Gas Heating in a Rolling Piston Type Rotary Compressor", Bulletin of the JSME, Vol. 27, April, 1984, pp. 741-748.

[6] "Handbook of Single-Phase Convective Heat Transfer", Wiley, 1987

[7] Dhar, M., Ph.D Thesis (Major professor, W. Soedel), Purdue University, 1978.

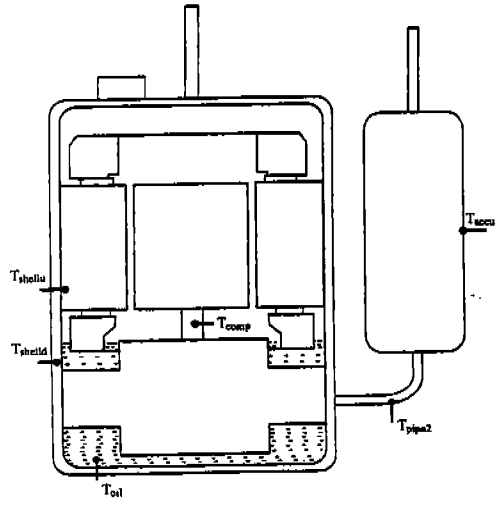

Fig.1 Bulk Temperatures of the compressor system

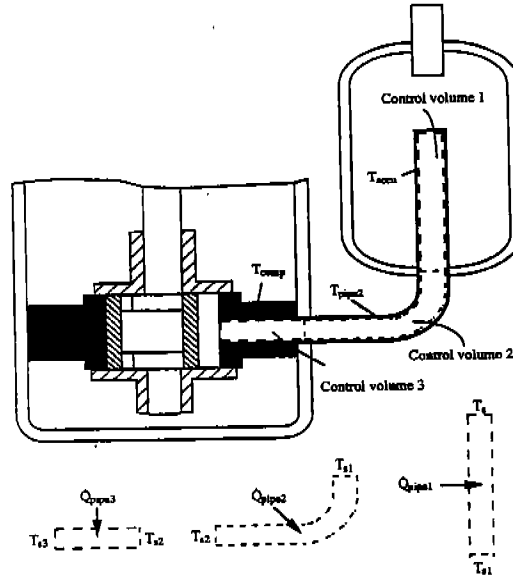

Fig.2 Heat transfer model of the gas in the suction pipe

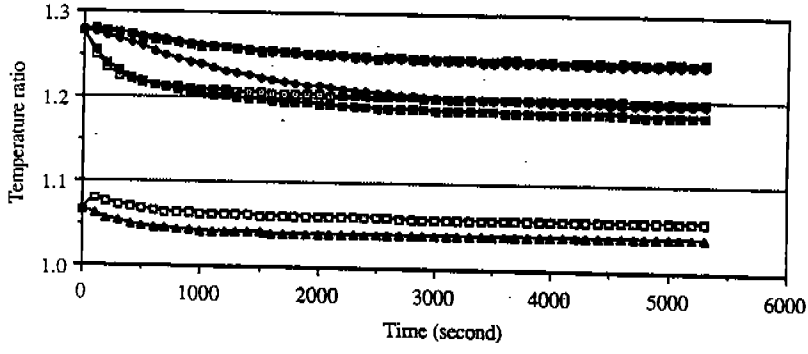

(a) At the rotation speed of 1800 rpm

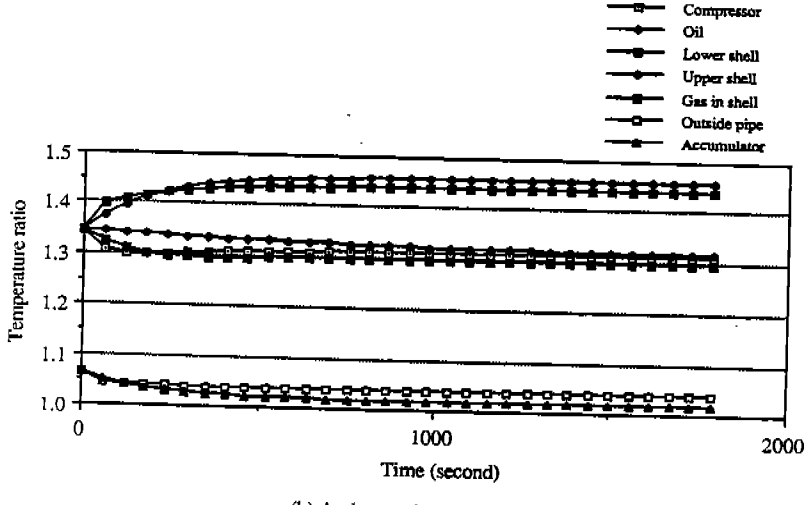

(b) At the rotation speed of 9000 rpm

Fig.4 The ratios of compressor system temperatures at different speeds to a reference temperature

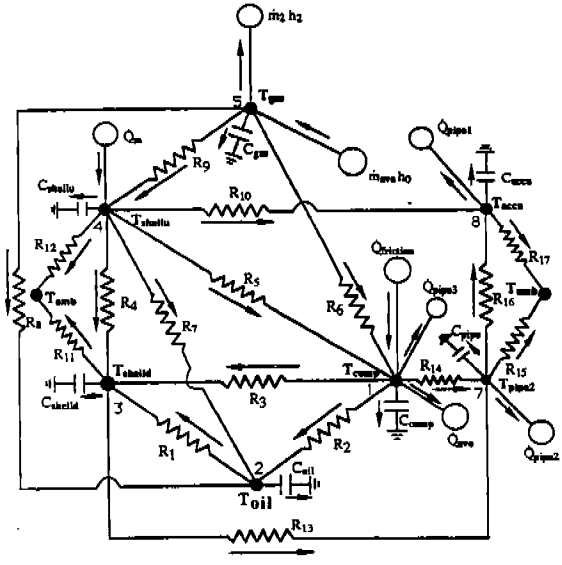

Fig.3 heat flow diagram of the compressor system

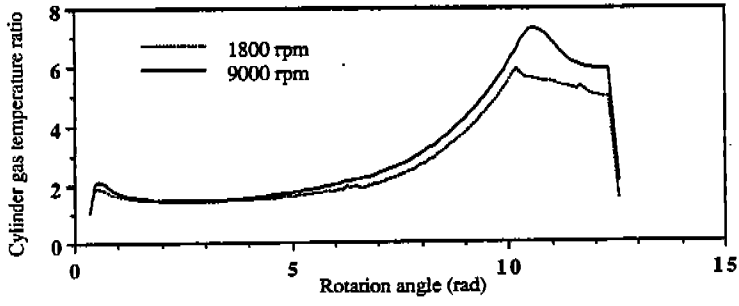

Fig. 5 The ratio of cylinder gas temperature at different speeds to a reference temperature

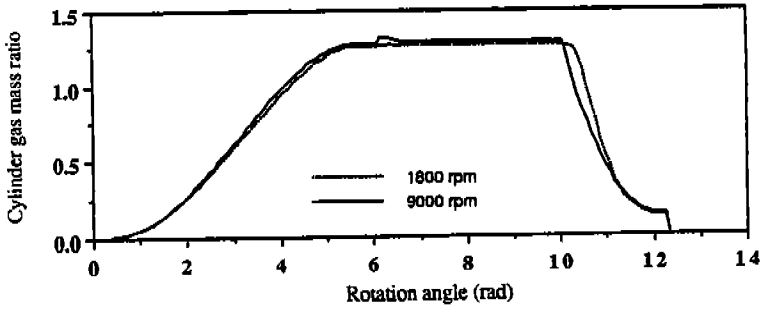

Fig. 6 The instantaneous cylinder gas mass ratio at different speeds

FAST RESPONSE TEMPERATURE MEASUREMENTS IN A RECIPROCATING COMPRESSOR

B.G. SHIVA PRASAD
DRESSER-RAND, EPCD
PAINTED POST, NY 14870

ABSTRACT

Mathematical modeling of the dynamic processes in a compressor involves a knowledge of the various forms of energy exchange occurring in the system. Heat transfer to and from the gas is one such. Any detailed modeling of the heat transfer process would require a detailed knowledge of the temperature variations resolved to temporal scales at least as fine as the finest generated by the dynamics of the valves and their interaction with the cylinder and piping. This paper presents measurements of gas temperature inside the cylinder and valve chambers made with a new type of thermocouple sensor which can meet the fast response requirements. The measurements were used to predict the effect of suction gas heating on capacity loss which agreed quite well with direct capacity loss measurements.

INTRODUCTION

The ever increasing demand for improving energy efficiency and pollution control has fueled lot of research on the understanding of the dynamic processes in machinery including reciprocating compressors and its application to analytical modeling. In reciprocating compressors, until recently , the heat transfer process had assumed a back burner role. This was partly because of the notion that heat transfer has very little impact on the performance of a reciprocating compressor and partly due to the difficulty in modeling the complex heat transfer processes. Even determination by experiment is also not an easy task, since it is very difficult to isolate its effects.

Most of the work on heat transfer effects have been done in the area of refrigeration compressors. Meyer and Thompson [1] have studied heat transfer effects on the performance of refrigeration compressors by using a steady state modeling of the complete system. They particularly studied the impact of inlet system design on heat transfer effects. The comparison of the results of their model with experimental data indicated reasonable agreement and suggested that the discrepancies could perhaps be reduced by considering the unsteadiness in the heat transfer process occurring inside the cylinder. Pandeya and Soedel [2] have derived a simple relationship for the change in mass flow rate expressed as a function of the magnitude of suction gas heating using thermodynamic principles. Adair, Qvale and Pearson [3] have provided a correlation for the instantaneous heat transfer across the cylinder based on dimensionless quantities with constants derived from their experimental data. Jacobs [4] has reported measurements of the important losses in a compressor. In addition, he observed the benefit of cooling of the suction gas on volumetric efficiency increase. He also indicated that a suction gas heating of 10^{0}F would reduce the volumetric efficiency by approximately 2 %. On the other hand, Brok, Touber and Vander Meer [5] provided credence to the conflicting opinion about the extent of influence of heat transfer on volumetric efficiency decrease by suggesting that the impact (was only 2.5 % for the compressor they modeled) is only nominal.

Lee and Smith [6] have measured instantaneous temperature inside the cylinder in order to understand the heat transfer

mechanism and its impact on volumetric efficiency loss. Hanjalic and Stosic [7] have also made measurements of instantaneous temperature and pressure inside the cylinder in order to understand the dynamic processes occurring inside the cylinder and to develop a mathematical model for simulating the compressor for aiding the designer. Gerlach and Berry [8] have assessed heat transfer losses by force fitting experimentally measured discharge temperature to their mathematical simulation of the compressor. The capacity loss based on their heat transfer estimate agreed quite well with their direct measurements, thus giving credence to their heat transfer model. They also obtained reasonable agreement between their predicted and measured variation of cylinder gas temperature over the cycle. Of all the reported temperature measurements in a compressor, Lee and Smith appear to be the only ones who have used a sensor with a very fast response (1 msec.). Their probe design which is similar to the commercially available bare wire thermocouple sensor with an exposed loop of the bare wire thermocouple is difficult to make and does not appear to be rugged. In addition, since the thermocouple bead is only 0.5 mm away from its supporting tube, it is likely to disturb the flow. Commercially available thermocouple probes, although more rugged are more sluggish and do not have a response faster than 10 - 20 msec. The other techniques which can provide the fast response required, like the optical techniques using laser induced fluorescence, are not easily adaptable to measurement inside a compressor and also involve sophisticated and expensive instrumentation. All these problems were overcome by designing a new thermocouple probe similar to the hot-wire probe and was successfully employed in this investigation for making temperature measurements.

This paper reports measurements of instantaneous temperatures inside the cylinder and suction and discharge valve chambers of the first stage of a two stage, double acting compressor. Other measurements for assessing the compressor performance including the p-v diagram, heat rejection to cooling water and compressor capacity were also taken. Since the main objective was to assess the effect of suction gas heating on capacity loss, the capacity was carefully monitored right from the instant of time the compressor was started from cold condition. The measurement of the total suction gas heating together with an assessed variation of capacity as a function of suction gas heating enabled the estimation of total capacity loss due to suction gas heating. The results are compared with the expression given by Pandeya and Soedel [2] based on suction gas temperature increase alone.

PROBE DESIGN AND CONSTRUCTION

In addition to fast response, ease of fabrication, ruggedness and applicability for point measurement were some of the other considerations kept in mind during the design of the probe. To get that fast response, it was obvious that it should be of the exposed junction type. The commercially available ribbon type thermocouple, in addition to not being able to meet the response requirement is also not well suited for point measurements. Also, in a turbulent environment, the large drag forces might induce vibrations and even snap the wire. Using a round wire thermocouple in the form of a loop as done by Lee and Smith is difficult for construction, particularly if the wire diameter is reduced to 0.0005 in. for obtaining a faster response. Further, the loop need to be big enough to reduce disturbance to the flow near the bead. But making it bigger makes it more fragile. To satisfy all these conflicting requirements, a new design similar to that of the hot-wire probe was conceived.

The tips of two 0.015 in. diameter wires of Chromel and Constantan served both as sensor supports as well as lead wires for the thermocouple (see fig. 1). These leads were passed through the two holes of a 1/16 in. diameter ceramic tube (approximately 2.25

ins. long) and glued to it using OMEGA CC high temperature cement. The exposed lead wires on the other side were covered with insulating sleeves which can withstand temperatures up to 600°F. The ceramic tube itself was passed through a 0.25 in. outside diameter stainless steel tube and glued to it using the high temperature cement. A 0.0005 in. diameter Chromel-Constantan bare wire thermocouple was spot welded to the tips of the supports, taking care to keep the bead at the middle and welding the Chromel wire to the Chromel support and the Constantan wire to the Constantan support. This unique construction similar to a hot-wire probe helped retain the complete fast response (the response is expected to be better than the probe designed by Lee and Smith which had a time constant of 1 msec.) capabilities of the bare wire thermocouple, while keeping errors due to conduction and radiation very small.

INSTRUMENTATION

The measurements were done in a two stage, single cylinder, double acting compressor running at approximately 900 rpm. The suction pressure was atmospheric and the discharge pressure was 110 psig. All measurements were mainly confined to the head end of the first stage cylinder.

Chromel-Constantan was chosen as the thermocouple material because of its high sensitivity. The voltage output by the thermocouple was directly recorded using a 4 channel NICOLET oscilloscope using 3mv/cm and 500 sec/point sensitivities which were good enough to discern the variations over the cycle clearly. Thus the need for using additional signal conditioning instrumentation which also adds noise was avoided. The compensation for the cold junction (both of which were exposed to the room temperature) was done by adding the room temperature which was monitored. The oscilloscope sweep was triggered by the signal from an optical encoder which was synchronized to occur at the top dead center.

Two probes were installed inside the cylinder, one near the center of the head and the other at the exit of the suction valve. Probes were also installed in the suction and discharge valve chambers just above the valve. Signals from 4 transducers at a time were recorded simultaneously on a floppy disc. Temperatures at various points along the flow path were also monitored using OMEGA J type thermocouples. The capacity was monitored by measuring the pressure drop across an orifice installed in the inlet pipe. The p-v card was recorded using a PFM 2000 cycle analyzer.

RESULTS AND DISCUSSION

Figure (2) shows the p-v and t-v cards. One can observe that the cylinder gas temperature variation follows a pattern similar to that of the pressure. Figures (3) - (5) show the effect of compressor heating up on the cylinder gas (at the center of the head) and suction and discharge valve chamber temperatures. All of them showed a significant increase in temperature as the compressor heated up. Also, the two independent samples shown for each of the parameters showed good agreement indicating that there was very little cycle to cycle variation. One can observe from the simultaneous traces of fig. (6) that the gas heated up significantly (approximately 50°F) as it entered the cylinder through the suction valve and inside the cylinder itself during the suction stroke. Thus at the end of the experiment, out of the total suction gas heating of 66°F, most of it occurred inside the cylinder with only a small part occurring in the suction pipe and cylinder passages. Figure (6) also shows the effect of valve opening, which results in an increase in gas temperature in the valve chambers, followed by cooling due to the ingestion of cold suction gas in the case of the suction valve and mixing with the relatively cooler discharge gas in the case of

the discharge valve. Figure (7) which shows simultaneous traces of gas temperature inside the cylinder at the center of the head and also near the suction valve indicates the extent of spatial nonuniformity in the temperature distribution inside the cylinder. This observation is in conformity with the earlier observations reported by Lee and Smith [6] and Adair et al [3].

One of the important objectives of temperature measurement inside the cylinder was to assess the extent of suction gas heating and then predict the capacity loss resulting from it. Capacity was also monitored to verify this prediction. Assessing suction gas heating based on gas temperature in the suction valve chamber will not give the total suction gas heating, because the in-cylinder regenerative heat transfer makes a significant contribution to the heating process. This was also demonstrated by the present experimental data taken after the compressor had attained thermal equilibrium, which showed approximately $42^{\circ}F$ temperature raise in the suction valve and the cylinder compared to $24^{\circ}F$ in the suction pipe and cylinder passages. Hence the trapped charge temperature inside the cylinder at the end of the suction stroke was used for assessing the total suction gas heating.

Figure (8) shows the capacity loss and fig. (9) the suction gas heating as a function of time. Both of them showed a very rapid rate of variation as the compressor started from cold condition and appeared to settle after about 3 hours of operation. The initial rate of loss of capacity was so rapid that it would have been erroneous to assume the first reading of capacity (which could only be taken after a few minutes of switching the compressor on) to represent the maximum value and basing the total capacity loss on that. The correct way would be to establish a functional relationship between the capacity loss and the suction gas heating and then use it to compute the capacity loss for the observed total suction gas temperature increase. Figure (10) shows such a graph of capacity loss against suction gas temperature increase which was derived from figs. (8) and (9). The correlation appears to be very closely linear.

Capacity loss was also computed from the measured total suction gas temperature increase using the expression given by Pandeya and Soedel [2]. Table (1) provides a comparison of the capacity loss obtained using the correlation shown in fig. (10) with that computed from suction gas heating and also from direct capacity monitoring compared with rated capacity. The agreement between all the three methods is very good.

The present experimental data has demonstrated the enormous influence of suction gas heating on compressor performance at least for the compressors of the type used in the experiment. It has also shown that because of the rapid rate of decrease of capacity during the start up and initial running of the compressor, the capacity measurement alone will not help in assessing the capacity loss due to suction gas heating. Simultaneous measurement of cylinder gas temperature and its use in establishing a correlation between suction gas heating and capacity loss is required for determining the capacity loss due to suction gas heating. The paper has thus underlined the importance of cylinder gas temperature measurement and demonstrated its measurement using a newly designed fast response thermocouple probe.

CONCLUSIONS

The investigation provided a new design for the thermocouple probe to meet the fast response characteristics and the ruggedness required for making temperature measurements inside the cylinder. The temperature measurements inside the cylinder not only indicated a significant spatial nonuniformity but also a large suction gas heating. The capacity loss due to suction gas heating obtained from the established correlation between suction gas temperature increase

and capacity loss agreed very well with that computed from total suction gas temperature increase as well as direct monitoring of capacity.

Further work is in progress to make use of these temperature measurements for understanding the heat transfer mechanism and formulating a model enabling prediction of its effects on compressor performance.

ACKNOWLEDGEMENTS

The author would like to thank Mr. Donald Draper and Dr. Derek Woollatt for the encouragement, support and guidance provided throughout this work. The author would also like to gratefully acknowledge the time and effort of the Dresser-Rand Development Laboratory group, namely Mr. Richard Ellison, Mr. Edward Frazzini and Mr. Bill Glosick.

REFERENCES

1] Meyer, W.A. and Thompson, H.D., 'An Analytical Model of Heat Transfer to the Suction Gas in a Low-side Hermetic Refrigeration Compressor', Proceedings of the 1990 Purdue International Compressor Engineering Conference, West Lafayette, Indiana, pp. 898-907, 1990.

2] Pandeya, P. and Soedel, W., 'On Suction Gas Heating in Hermetic Compressors (A Technical Note)', Proceedings of the 1978 Purdue Compressor Technology Conference, July 1978, West Lafayette, Indiana, pp. 144-147, 1978.

3] Adair, R.P., Qvale, E.B. and Pearson, J.T., 'Instantaneous Heat Transfer to the Cylinder Wall in Reciprocating Compressors', Proceedings of the 1972 Purdue Compressor Technology Conference, West Lafayette, Indiana, pp. 521-526, 1972.

4] Jacobs, J.J., 'Analytical and Experimental Techniques for Evaluating Compressor Performance Losses', Proceedings of the 1976 Purdue Compressor Technology Conference, West Lafayette, Indiana, pp. 116-123, 1976.

5] Brok, S.W., Touber, S. and van der Meer, J.S., 'Modelling of Cylinder Heat Transfer - Large Effort, Little Effect?', Proceedings of the 1980 Purdue Compressor Technology Conference, West Lafayette, Indiana, pp. 43-50., 1980.

6] Lee, K. and Smith, J.L., 'Time Resolved Mass Flow Measurement for a Reciprocating Compressor', Proceedings of the 1980 Purdue Compressor Technology Conference, West Lafayette, Indiana, pp. 51-57.

7] Hanjalic, K. and Stosic, N., 'Some Aspects of Laboratory Testing and Computer Modelling of Two-stage Compressors with Inter and After Cooling', Proceedings of the Institution of Mechanical Engineers, London, pp. 11-19, 1978.

8] Gerlach, R.C. and Berry, R.A., 'Effect of Heat Transfer and Related Variables on Compressor Performance', Proceedings of the Fourth Annual Reciprocating Machinery Conference, San Antonio, Texas, 1989.

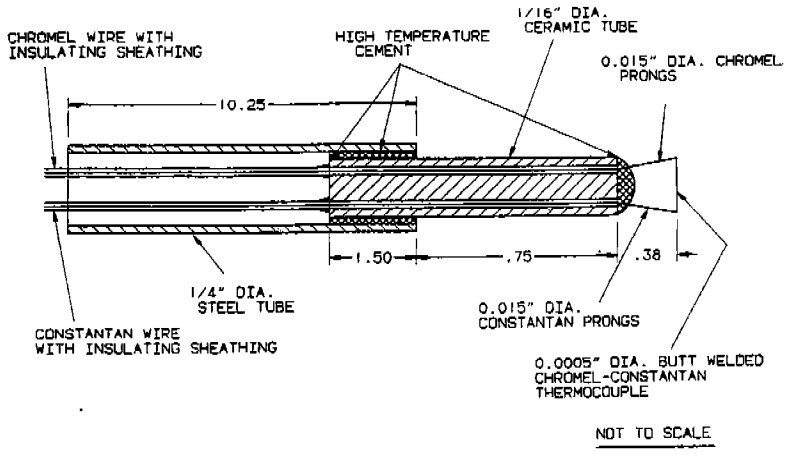

FIG.(1) PROBE FOR INSTANTANEOUS TEMPERATURE MEASUREMENT

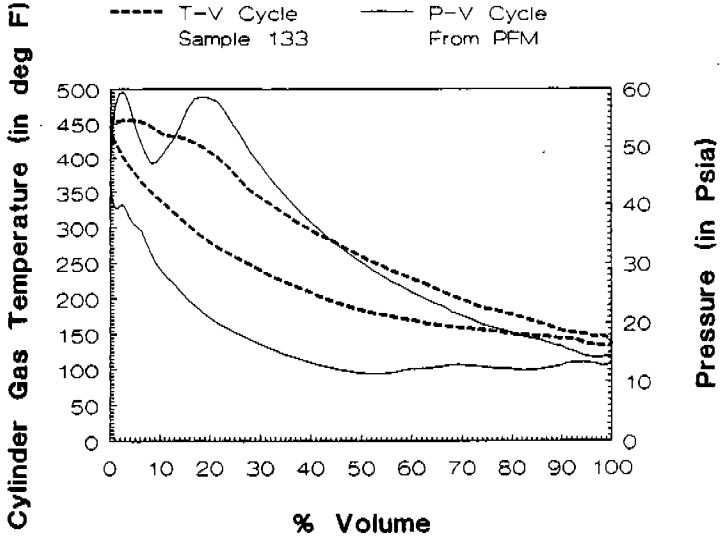

Fig. (2). Comparison of T-V and P-V Cycles after 3.5 Hours of Operation

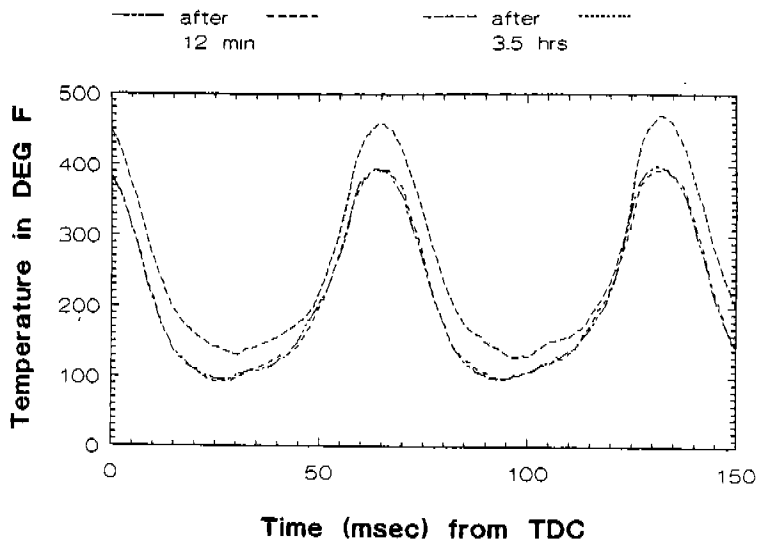

Fig. (3). **Effect of Compressor Heating up on Cylinder Gas Temperature at the Center of Head**

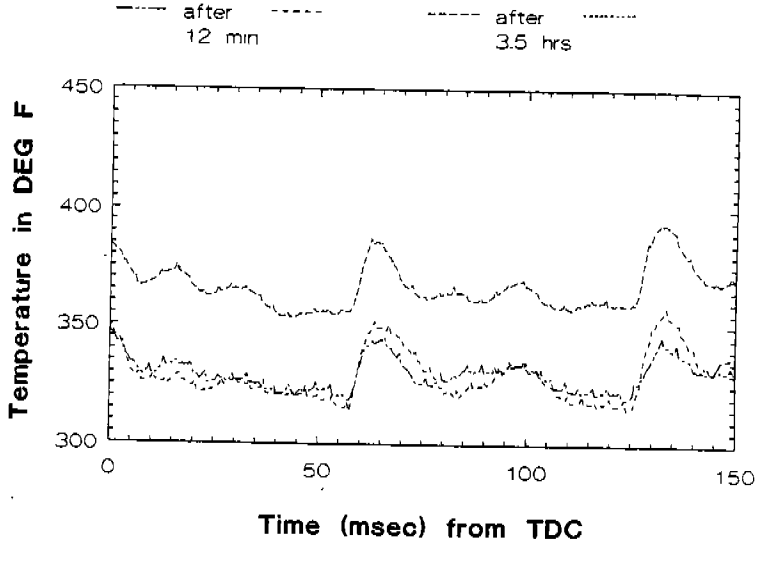

Fig. (4). **Effect of Compressor Heating up on Discharge Valve Chamber Gas Temperature**

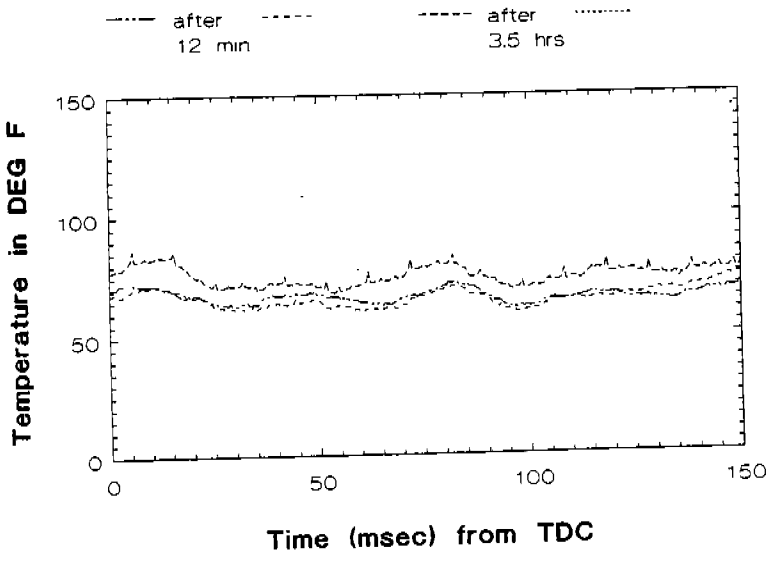

Fig. (5). Effect of Compressor Heating up on Suction Valve Chamber Gas Temperature

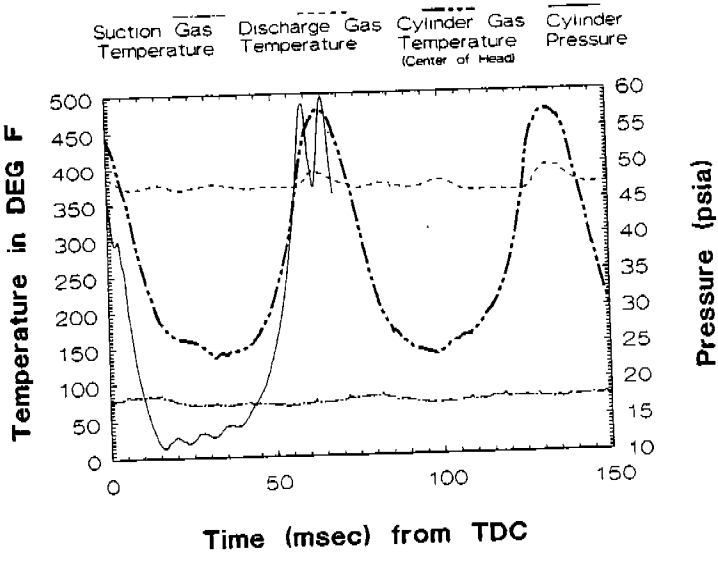

Fig. (6). Simultaneous Traces of Gas Temperature and Pressure inside the Cylinder and Valve Chambers

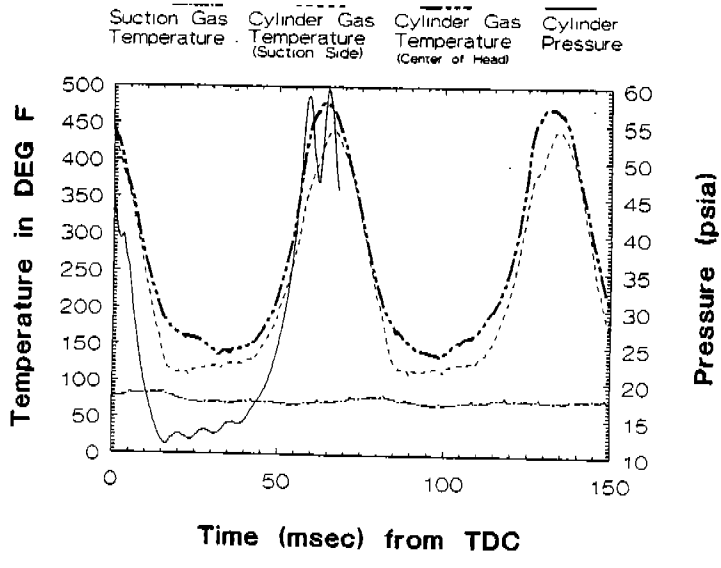

Fig. (7). Simultaneous Traces of Gas Temperature and Pressure inside the Cylinder and Valve Chambers

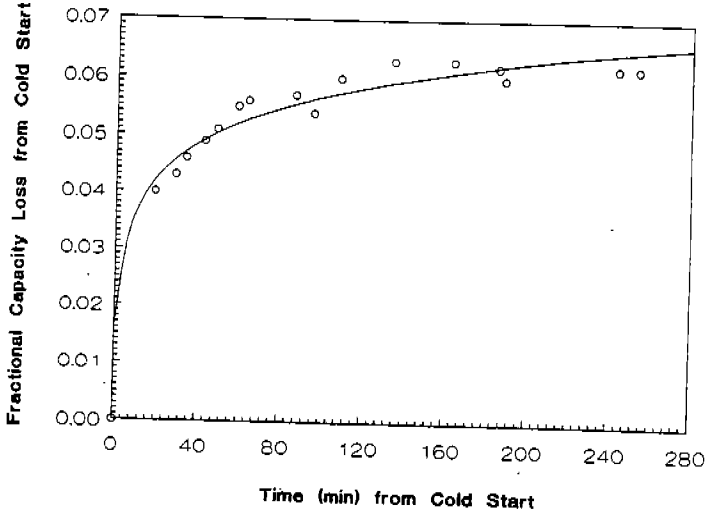

Fig. (8). Measured Capacity Loss Variation with Time

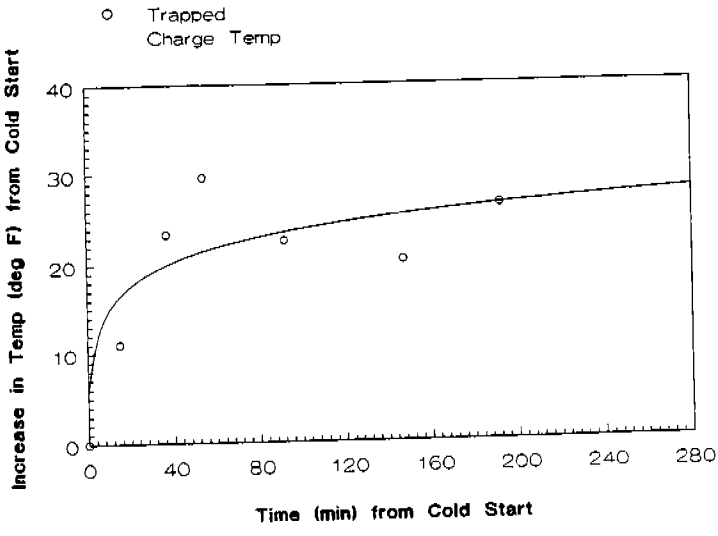

Fig. (9). Variation of Suction Gas Heating with Time

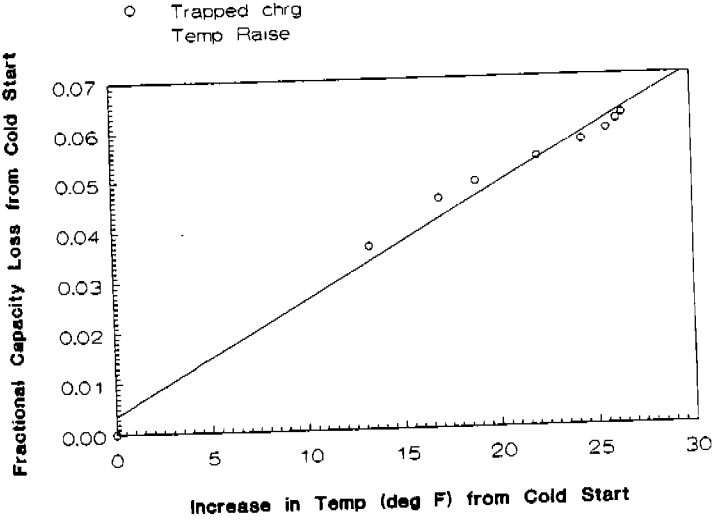

Fig. (10). Correlation of Capacity Loss with Suction Gas Heating

METHOD USED	CAPACITY LOSS	
	8 min After Start	At End of Expt
SUCTION GAS TEMPERATURE INCREASE	56 F	66 F
CAPACITY LOSS BASED ON RATED CAPACITY	12.6 %	17.1 %
FROM RESULTS OF MONITORING CAPACITY	12.9 %	15.2 %
CAPACITY LOSS BASED ON SUCTION GAS TEMPERATURE INCREASE	12.9 %	15 %

Table (1). Comparison of Measured and Computed Capacity Loss

Separation of Suction Gas from the Discharge Gas and Benefits of Feeding the Gas Directly to the Crankcase

Prasanta K. Roy and Michael A. Di Flora
Bristol Compressors, Bristol, VA (U.S.A)

ABSTRACT

Despite its advantageous characteristics, the separation of suction gas from the discharge gas and utilization of polymer suction and discharge valves has only recently been attempted due to the difficulties in manufacturing and the lack of availability of suitable polymers. However, in recent years, production technique and polymer materials have been greatly improved.

Advances in design and manufacturing engineering have led to the introduction of the Inertia compressor. Using gas seperation and polymer valves it is possible to achieve high efficiency and reliability under a wide range of compression ratios. For this reason, the Inertia compressor is very suitable and highly efficient for the application of heat pump air conditioners.

INTRODUCTION

After the Energy Crisis, energy conservation has been the most important topic in the field of air conditioning. In the United States, the regulation of system efficiency started in 1992. Besides the legal demand, air conditioners with higher efficiency have been required from the distributors to meet the customer's needs concerning energy savings.

In such a situation, there came a strong demand for higher efficiency compressors, because the improvement of compressor efficiency is the most economical method to increase unit efficiency in spite of technological difficulties. Thus, most compressor manufacturers have been eagerly improving conventional compressors and developing new ones.

The Inertia compressor is a new generation of reciprocating compressor, separating suction gas from the discharge gas and utilizing polymer suction and discharge valves.

In the standard reciprocating refrigeration compressor the normal route of the suction gas flow is through a cylinder head that is divided into two chambers, suction and discharge. The suction gas picks up heat from the discharge chamber, raising its temperature prior to entering the cylinder. Also, the pressure decreases as it passes through the suction chamber (the small suction port area in the valve plate) and the restricted opening of the suction valve.

In the Inertia compressor the cylinder head is exclusively utilized for high side pressure and temperature. This arrangement reaps the benefits which will be discussed below.

Because the suction gas flows directly into the piston suction ports, which are separated from the hot discharge gas in the cylinder head, the valve plate and discharge valve assembly contain hot exiting gas only.

DESIGN FEATURE

The suction gas enters through the suction tube, flows into the housing and through an opening in the motor cap. From the motor cap, the inlet gas is routed through the left and right side suction tubes, through the plastic manifolds, into the crankcase side ports, and into the piston suction port areas. (Fig. 1) Because the suction gas is separated from the discharge gas, it does not conduct any heat from the discharge chamber, therefore, its temperature is much lower as shown in the temperature profile (Fig. 2).

This gas separation design incorporates suction ports in the piston body and a polymer suction valve on the sculptured top of the piston. The suction gas flows smoothly into the piston ports and through the 360° opening of the suction valve (Fig. 3).

Another special feature of the design incorporates the use of a polymer discharge valve with a deeper head in the steel valve plate assembly (Fig. 4). This reduces the cylinder clearance volume by ~ 50%. The larger volume head facilitates smoother flow and exit of the high temperature and pressure discharge gas.

CALCULATION

Volumetric Efficiency η_υ:

$$\eta_\upsilon = \frac{m_a}{m_t} = \frac{\text{Actual mass of new gas entering the compressor per stroke}}{\text{Theoretical mass of gas represented by the displacement volume and determined at the pressure and temperature at the compressor inlet}}$$

$$= \frac{\text{Actual lbs/hr}}{\text{Theoretical lbs/hr}} = \frac{\text{Actual volume rate}}{\text{Theoretical volume rate}}$$

$$= \frac{\text{CFM } (ft^3/min) \times 1728\ (in^3/ft^3)}{in^3/rev \times rev/hr}$$

Check Units:

$$= \frac{\text{BTU/Hr} \times \upsilon \text{ suction } (ft^3/lb) \times 1728\ (in^3/ft^3)}{in^3/rev \times \text{RPM (rev/min)} \times \Delta h \text{ (BTU/lb)} \times 60 \text{ (min/hr)}}$$

where υ suction = specific volume at compressor inlet, ft^3/lb (=1/density)

Δh = [Enthalpy (superheated) at compressor inlet temperature - Enthalpy (saturated liquid) at expansion valve], BTU/lb.

From refrigerant -22 chart, at 45°F evaporator, and 130°F condenser:

15° subcooling (130-15) results in 115°F at expansion valve

h @ 115°F saturation liquid at expansion valve = 44.065 BTU/lb

υ @ 65°F = 0.64106 cu. ft/lb

h @ 65°F = 112.128 BTU/lb

Δh @ 65°F = 112.128 - 44.065 = 68.063 BTU/lb

$$\eta_v = \frac{\text{BTU/Hr} \times \text{suction } (ft^3/lb) \times 1728\ (in^3/ft^3)}{in^3/rev \times \text{RPM (rev/min)} \times \Delta h\ (\text{BTU/lb}) \times 60\ (\text{min/hr})} \quad \text{Equation 1}$$

$$= \frac{\text{BTU/Hr} \times \upsilon \text{ suction} \times 28.8}{in^3/rev \times \text{RPM} \times \Delta h} \quad \text{Equation 2}$$

Therefore, η_υ (ARI) @ 65°F return gas (ARI rating point) $= \frac{\text{BTU/Hr} \times .64106 \times 28.8}{in^3/rev \times 3500 \times 68.063} = \frac{\text{BTU/Hr}}{12902.9\ in^3/rev}$ Equation 3

$$\text{Mass flow rate} = m\ (\text{lbs/hr}) = \frac{\text{BTU/Hr}}{\Delta h(\text{BTU/lb})} \quad \text{Equation 4}$$

Therefore, $m = \frac{\text{BTU/Hr.}}{68.063}$ @ 65°F return gas ARI rating point

From equation 3, $\eta_\upsilon \propto \frac{1}{in^3/rev}$, BTU/Hr = constant between standard and inertia pumps.

Therefore, η_υ is higher if the displacement is lower or BTU/in^3 is higher, which is the case of inertia pumps.

CONCLUSION

In the Inertia compressors, the separation of suction gas from the discharge gas with the utilization of polymer suction and discharge valves results in the following benefits:

a. Lower suction temperature (Fig. 2)

b. Reduced clearance volume (Fig. 5)

c. Higher volumetric efficiency, η_v (Fig. 6)

d. Higher BTU/cu. in. (Fig. 7)

e. Higher EER. (Fig. 8)

ACKNOWLEDGEMENT

The authors would like to acknowledge the substantial contribution to this paper by David Gilliam and Hugh Stringer. The authors also wish to thank Bristol Compressor's upper management for their support and permission to publish this paper.

REFERENCES

[1] ASRAE Handbook, Fundamentals, 1.9

[2] Thermodynamics - J.P. Holman

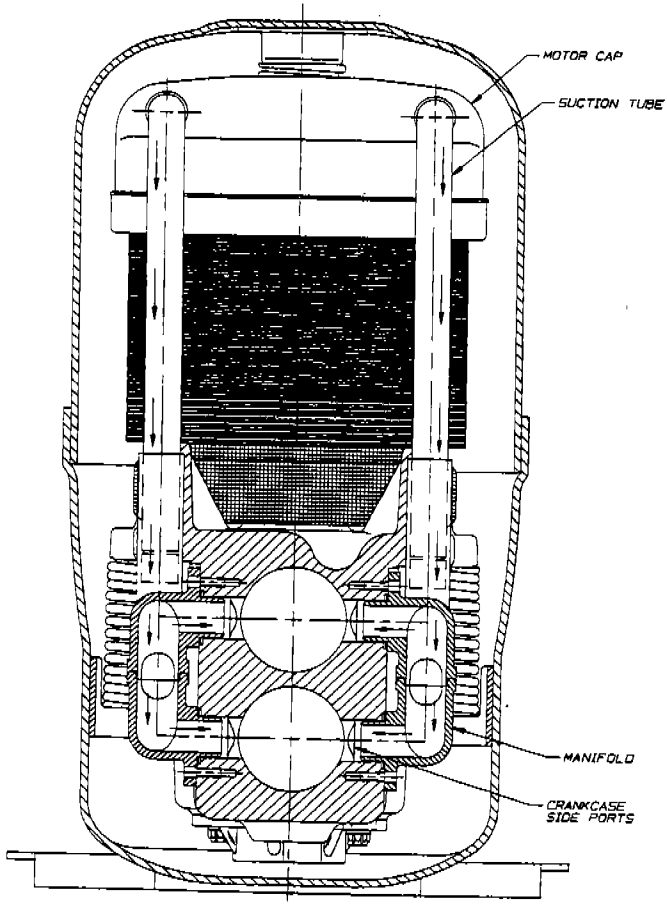

FIG. 1

Temperature Profile
at ASRE/T (ARI in Parenthesis)

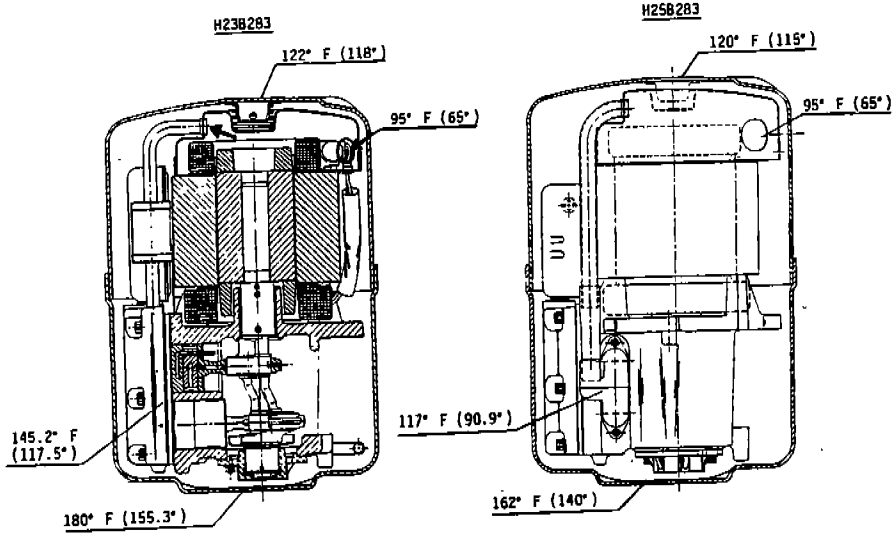

FIG. 2

Bristol Compressors

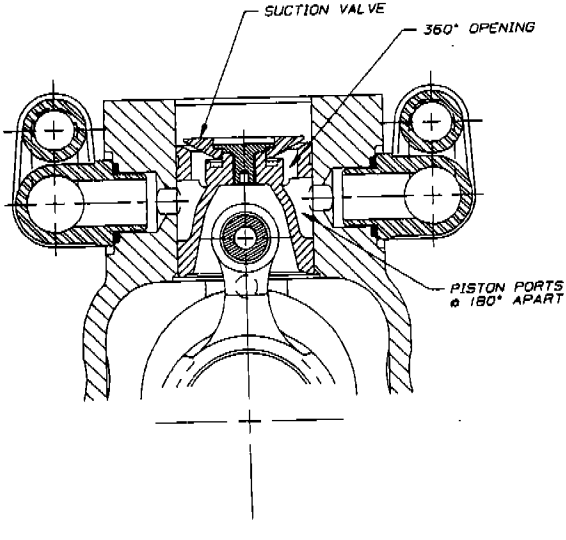

FIG. 3

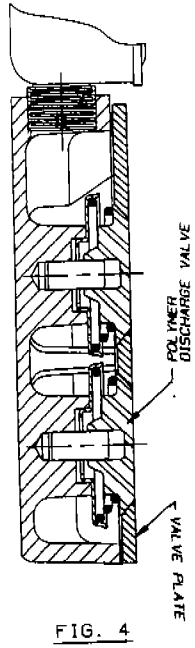

FIG. 4

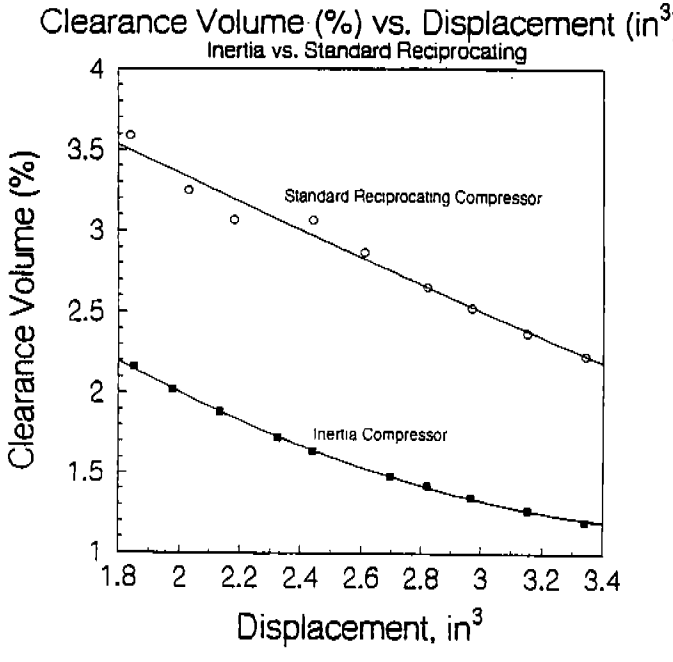
Clearance Volume (%) vs. Displacement (in3)
Inertia vs. Standard Reciprocating
Clearance Volume (%)
4
3.5
3
2.5
2
1.5
1
Standard Reciprocating Compressor
Inertia Compressor
1.8
2
2.2
2.4
2.6
2.8
3
3.2
3.4
Displacement, in3

FIG. 5

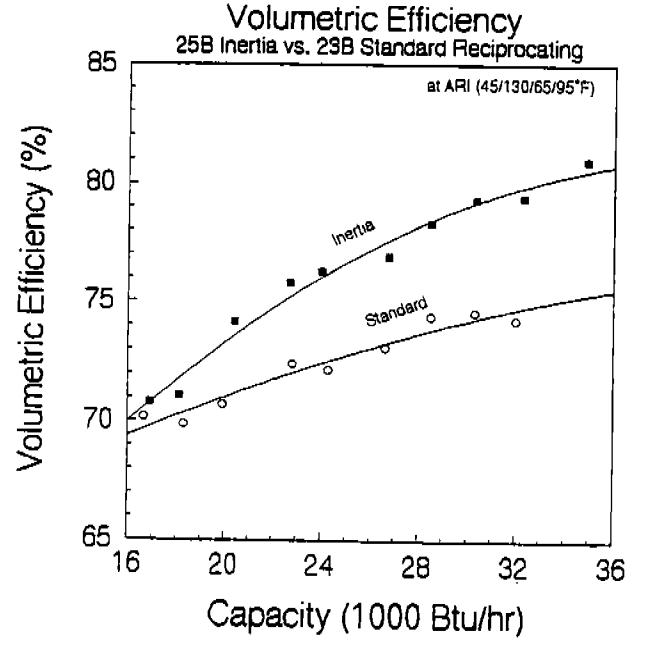
Volumetric Efficiency
25B Inertia vs. 23B Standard Reciprocating
at ARI (45/130/65/95°F)
Volumetric Efficiency (%)
85
80
75
70
65
Inertia
Standard
16
20
24
28
32
36
Capacity (1000 Btu/hr)

FIG. 6

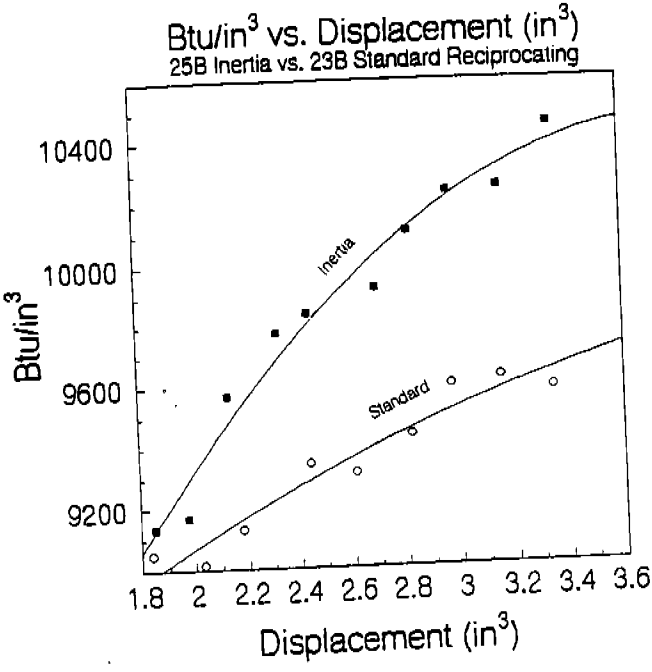
Btu/in3 vs. Displacement (in3)
25B Inertia vs. 23B Standard Reciprocating
10400
10000
9600
9200
Btu/in3
Inertia
Standard
1.8 2 2.2 2.4 2.6 2.8 3 3.2 3.4 3.6
Displacement (in3)

FIG. 7

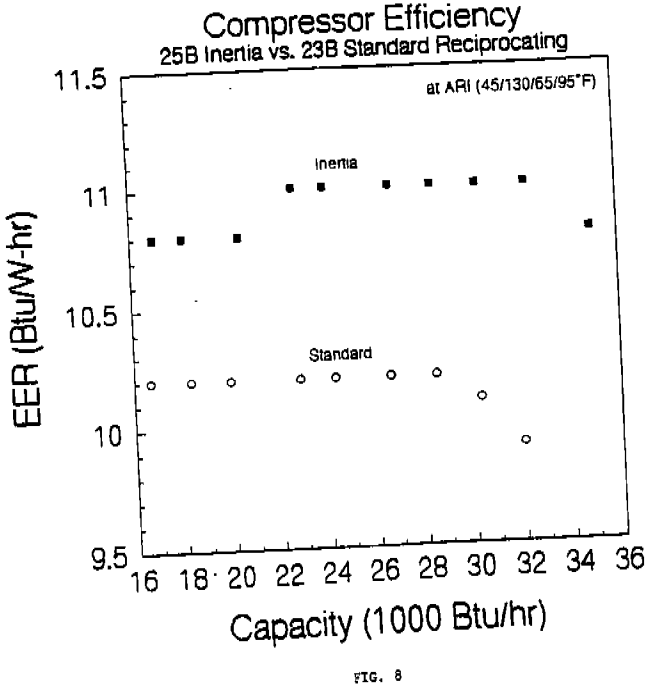
Compressor Efficiency
25B Inertia vs. 23B Standard Reciprocating
at ARI (45/130/65/95°F)
11.5
11
10.5
10
9.5
EER (Btu/W-hr)
Inertia
Standard
16 18 20 22 24 26 28 30 32 34 36
Capacity (1000 Btu/hr)

FIG. 8

HEAT TRANSFER MODEL OF A ROTARY COMPRESSOR

Sisir K. Padhy
General Electric Company
Appliance Park 5-2North, Louisville, KY 40225

ABSTRACT

Energy improvements for a rotary compressor can be achieved in several ways such as: reduction of various electrical and mechanical losses, reduction of gas leakage, better lubrication, better surface cooling, reduction of suction gas heating and by improving other parameters. To have a better understanding analytical/numerical analysis is needed. Although various mechanical models are presented to understand the mechanical losses, dynamics, thermodynamics etc.; little work has been done to understand the compressor from a heat transfer stand point. In this paper a lumped heat transfer model for the rotary compressor is described. Various heat sources and heat sinks are analyzed and the temperature profile of the compressor is generated. A good agreement is found between theoretical and experimental results.

NOMENCLATURE

D_i	inner diameter
D_o	outer diameter
D_{mf}	upper bearing plate outer diameter
Δx	conduction length
$\dot{Q}$	rate of heat transfer
S_i	heat generation within element i
$\Delta \dot{E}$	change in internal energy
D_{case_i}	case inside diameter
D_{case_o}	case outside diameter
$A_{i,j}$	coeffients of the simultaneous equations [coefficients of the matrix]
h_r	effective radiation heat transfer coefficient
ε	emissivity
h_4	heat transfer coefficient between the case inside and the gas above the stator/rotor
h_∞	heat transfer coefficient of the case and outside
z_1	height of the case above the stator
z_2	height of the stator
B_i	known parts of the system equations
$\dot{m}$	mass flow rate of the gas
$\dot{W}$	rate of work done
σ	Stefan-Boltzmann constant

ΔT	temperature difference
T_i	temperature of i-th element
$H_{i,j}$	thermal conductances
k_i	thermal conductivity of i-th element
$N_u = \frac{hL}{k}$	average nusselt number
$Gr = \frac{g\beta\Delta TL^3}{\nu^2}$	Grashof number, g acceleration due to gravity, β volumetric thermal expansion coefficient, ν kinematic viscosity
h	heat transfer coefficient
$Pr = \frac{c_p\mu}{k}$	Prandtl number, c_p specific heat
$Ra = Gr.\ Pr$	Rayleigh number
$Re = \frac{\rho vx}{\mu}$	Reynolds number, ρ density, v velocity, x length, μ viscosity
t	case thickness
Ta	Taylor number

1. INTRODUCTION

Rotary Compressors have been used in refrigerators and room airconditioners for several years. The enforcement of strict energy regulations for the power consumption as well as the goal of the CFC (the present refrigerant) removal by the year of 1995, are driving the design methodology of compressors to take new shapes. To achieve these goals the key is to understand the mechanics of the system and to develop analytical techniques to analyze the effect of various geometry, clearances, material properties, and temperature in the system. This understanding will lead to an optimum design of the compressor from energy, reliability, and economics stand point.

The rotary compressor is a high side compressor with all the components exposed to either lubricant oil or the hot compressed gas. The temperature profile as well as the heat transfer among the components of the compressor play a critical role on the reliability as well as energy efficiency. The suction gas heating has been of interest since it has an adverse effect on the energy rating of the compressor. Again an understanding of various heat transfers between the components, both qualitatively as well as quantitatively will help the designer to do design modifications that will result a compressor with improved reliability ands the energy rating. Another area of interest can be the effect of the temperature on the bearings dynamics of the compressor.

2. PREVIOUS WORK

The understanding of the heat transfer of a rotary compressor involves compressor dynamics, mechanical and electrical losses, thermodynamic analysis, lubrication, & determination of heat transfer coefficients for the various interfaces of the compressor. Although works have been reported in the areas of dynamics, mechanical losses, lubrication (a complete theoretical study by the author [1] recently) and thermodynamics of the compressor, no work has been reported for the heat transfer of the rotary compressor except for an internal report of General Electric company.

Brok et al. [2] reported their research on the cylinder heat transfer for an reciprocating compressor. Applying simple overall thermodynamic analysis and mathematical modeling of the

cylinder, suction chamber and discharge chamber they conclude that the heat transfer has a lesser effect on performance as opposed to the standard belief of higher effect. Kawai et al [3] discussed improvement in performance with the reduction of suction gas. The efficiency improvement of 6 to 10% is reported by modifying the suction muffler of an reciprocating compressor. Meyer and Thompson [4,5] carried out research both analytically and experimentally only for the suction gas of an reciprocating hermetic compressor. A steady state analysis was done. Heat transfer correlations were adapted from literature and some are experimentally determined. As a part of the same research Srikanth and Thompson [6] carried out a flow visualization study to evaluate the gas flow pattern inside a hermetic reciprocating compressor. Their conclusions are again to modify the muffler design for improved efficiency. Adair et al [7] studied the instantaneous heat transfer between the cylinder wall and the gas of an reciprocating compressor. They proposed a new correlation based on their experimental work. In an recent study Recktenwald et al [8] and Recktenwald [9] investigated the same heat transfer using numerical methods. The GE internal report [10] describes a lumped heat transfer model for a rotary compressor. However all the components of the compressor are not modeled and some experimental heat transfer coefficients are used. The present work models the compressor in total, to use better theoretical correlations and to produce a more accurate model.

3. PRESENT WORK

The present work deals with a lumped (averaged) parameter formulation of the heat transfer for a rotary compressor. The laws governing the system are said to be lumped if the their terms are independent of space and to be distributed if the terms depend on space[11]. The fundamental laws governing the system in the present discussion are conservation of mass, and first law of thermodynamics. The conservation of mass is given by

$$\dot{m} = 0$$

and the first law of thermodynamics is given by

$$\Delta \dot{E} = \dot{Q} - \dot{W}$$

In the present case there are interactions between more that one lumped mass and the law of conservation of mass for *i*-th element is

$$\sum_{j=1}^{n} \dot{m}_{j,i} = \sum_{k=1}^{m} \dot{m}_{i,k} + \frac{d\mathrm{M}_i}{dt}$$

where *j*'s represent the elements from which the mass flows to *i-th* element and *k*'s represent the elements to which mass flows from element *i*. M_i represents the instaneous mass of the element *i*. Similarly the first law of thermodynamics for the *i-th* element becomes

$$\dot{Q}_i + \sum_{j=1}^{n} \dot{m}_{j,i} h_{j,i} = \dot{W}_i + \sum_{k=1}^{m} \dot{m}_{i,k} h_{i,k} + \frac{d(\mathrm{M}_i u_i)}{dt}$$

Although the inlet and exit enthalpy of the element are different an averaged value is used in the calculations.

The principal modes of heat transfer considered inside the rotary compressor are conduction and convection, and radiation is neglected. For the compressor case outside free and forced convection are considered in addition to the radiation. The conduction heat transfer is

$$\dot{Q} = \frac{k_i A_i \Delta T}{\Delta x}$$

The convective heat transfer is given by

$$\dot{Q} = h_i A_i \Delta T$$

and the radiative heat transfer equation is

$$\dot{Q} = \varepsilon\sigma A\left(T_i^4 - T_\infty^4\right)$$

Writing an effective heat transfer coefficient as

$$h_r = \varepsilon\sigma\left(T_i + T_\infty\right)\left(T_i^2 + T_\infty^2\right)$$

the radiative heat transfer equation becomes

$$\dot{Q} = h_r A\left(T_i - T_\infty\right)$$

All these equations can be conveniently represented by introducing the concept of thermal conductance and the general equation for heat transfer becomes

$$\dot{Q} = H_i \Delta T$$

H is calculated from actual geometry, thermal properties of elements and heat transfer coefficients.

The total rate of heat transfer to an element i can be written as the sum of heat transfer from other elements either to the element or from the element, and the rate of heat generation S within the element.

$$\dot{Q} = \sum_{j=1}^{n} H_{j,i}\left(T_i - T_j\right) - \dot{S}_i$$

A steady state analysis is carried out and the equations became

$$\sum_{j=1}^{n} \dot{m}_{j,i} = \sum_{k=1}^{m} \dot{m}_{i,k} \qquad \text{as } \frac{dM_i}{dt} = 0,$$

$$\dot{Q}_i + \sum_{j=1}^{n} \dot{m}_{j,i} h_{j,i} = \dot{W}_i + \sum_{k=1}^{m} \dot{m}_{i,k} h_{i,k} \qquad \text{as } \frac{d\left(M_i u_i\right)}{dt} = 0$$

and

$$\dot{Q} = \sum_{j=1}^{n} H_{j,i}\left(T_i - T_j\right) - \dot{S}_i = 0$$

Heat addition to the element is considered positive and the heat transfer from the element is considered negative. Internal heat generation (including frictional heat generation) are considered positive.

The lumped and isothermal elements of the compressor are selected such that they conform with the natural geometric boundaries. These boundaries include solid parts, fluid masses and flow paths. Applying first law of thermodynamics and conservation of mass to the elements of the compressor a system of equations are formulated. These equations are solved by Gauss-Jordan method to calculate different element temperatures. The rest of this section deals with describing the system of equations, the solving procedure, the equations for the calculation of heat transfer coefficients, and the electrical and mechanical losses.

3.1 System of Equations

The formulation of the system of equations is described in the following paragraphs. The compressor is divided into 22 elements [Figure 1] and these elements are modeled yielding 22 equations. For example element 1 is presented here.

Element 1: Case portion above the stator

This element is connected to the outside of compressor, to the gas above the stator inside the compressor and to the case element that is attached to the stator. The energy balance gives

$$H_{1,2}\left(T_1 - T_2\right) + H_{1,\infty}\left(T_1 - T_\infty\right) + H_{1,22}\left(T_1 - T_{22}\right) = 0$$

or

$$T_1\left(H_{1,2} + H_{1,\infty} + H_{1,22}\right) - H_{1,2}T_2 - H_{1,\infty}T_\infty - H_{1,22}T_{22} = 0$$

This can be written in the following form, with the A's as the matrix elements to solve the

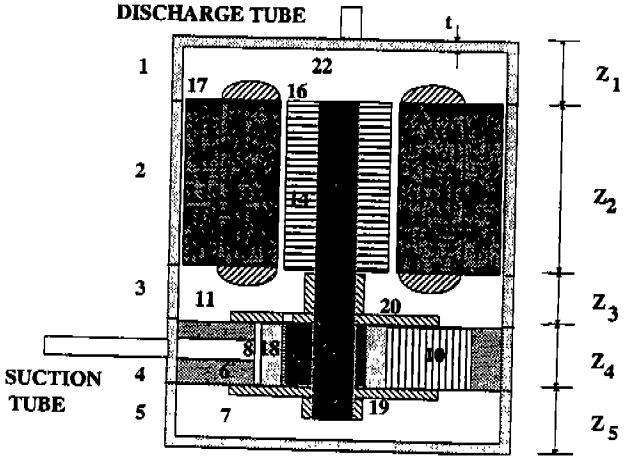

[Figure 1. Compressor Schematic with 22 elements are shown except the compressed gas (Element 9). The element names are described in Table 1.]

simultaneous equations.

$$A_{1,1}T_1 + A_{1,2}T_2 + A_{1,22}T_{22} = B_1$$

Where

$$A_{1,1} = H_{1,2} + H_{1,\infty} + H_{1,22}\ ,\quad A_{1,2} = -H_{1,2}\ ,\quad A_{1,22} = -H_{1,22}\ ,\quad B_1 = H_{1,\infty}T_\infty$$

$$H_{1,2} = k_1\pi\left(D_{caseo}^2 - D_{casei}^2\right)/4z_2\ ,$$

$$H_{1,\infty} = \pi\left(h_r + h_\infty\right)\left(D_{caseo}z_1 + \left(D_{caseo}^2 - D_{casei}^2\right)/4\right)$$

$$H_{1,22} = h_4\pi\left(D_{caseo}\left(z_1 - t\right) + \left(D_{casei}^2 - D_{dis}^2\right)/4 + D_{dis}t\right)$$

Similarly the other elements are modeled. In general the equations can be represented as

$$\sum_{j=1}^{n} A_{i,j}T_i = B_i$$

where

$$A_{\substack{i,j\\ j\neq 2}} = -H_{i,j}\ ,\quad A_{i,i} = \sum_{j=1(j\neq i)}^{n} H_{i,j}$$

and B is the heat quantity that may be the heat transferred to the sorrounding or the mechanical losses or may be the electrical losses.

3.2. Heat transfer coefficients calculation

3.2.1. Case outside

The compressor is placed in the cabinet of the refrigerator or an air conditioner unit. Depending on the air flow on the compressor the heat transfer can be natural convection or forced convection in addition to the radiation. Modeling the compressor as a cylinder in cross flow to the air stream the forced convection correlation used is [13]

$$N_u = 0.3 + \frac{0.62\,\mathrm{Re}^{1/2}\,\mathrm{Pr}^{1/3}}{\left[1+\left(\frac{0.4}{\mathrm{Pr}}\right)^{2/3}\right]^{3/4}}\left[1+\left(\frac{\mathrm{Re}}{282000}\right)^{5/8}\right]^{4/5}$$

for $10^2 < \mathrm{Re} < 10^7$; $\mathrm{Pe} > 0.2$

The following equation is used for the free convection [13]

$$N_u = \left[0.6 + \frac{0.378 Ra^{1/6}}{\left\{1+(0.559/\mathrm{Pr})^{9/16}\right\}^{8/27}} \right]^2$$

for $10^{-5} < \mathrm{Ra} < 10^{12}$

and the heat transfer coefficient is calculated as

$$h = \frac{N_u k}{x}$$

In calculating the radiation heat transfer, the temperature of the case is unknown. Hence a temperature is assumed to be close to the gas temperature coming out of the compressor.

3.2.2. Oil sump heat

The heat transfer between the case and oil is very complicated. The heat transfer between the oil and the vertical case portion is modeled as free convection as the oil circulating through the compressor mechanism comes down to the sump and there is a continuous motion. However as the shaft rotates, the bottom portion of the case is subjected to both free and forced convection. The oil velocity in the sump is calculated knowing the volume rate of oil flow [previous paper] through the shaft. The equation for the vertical portion is [14]

$$N_u = 0.68 + \frac{0.67 Ra^{1/4}}{\left[1+(0.492/\mathrm{Pr})^{9/16}\right]^{4/9}}$$

for $\mathrm{Ra} < 10^9$

Otherwise the following formula is used

$$N_u = 0.825 + \frac{0.387 Ra^{1/6}}{\left[1+(0.492/\mathrm{Pr})^{9/16}\right]^{8/27}}$$

For the bottom circular disk for free convection the equation used is[15]

$$N_u = 0.818\,\mathrm{Pr}^{0.034}\, Ra^{0.2}$$

and for the forced convection

$$N_u = 0.664\,\mathrm{Re}^{0.5}\,\mathrm{Pr}^{1/3}$$

The overall mixed convection Nusselt number is calculated as follows;

$$(N_u)^3_{total} = (N_u)^3_{forced} + (N_u)^3_{free}$$

3.2.3. Suction tube heat transfer calculation

In one cycle the rotary compressor compresses the gas as well as draws the gas into the suction chamber. Knowing the volume of gas, and the diameter of the suction tube portion inside the cylinder as well as outside the compressor, the velocity of the gas is determined and Reynolds number is calculated. This is a case of flow through pipes and the Nusselt number is calculated using the following correlation[15]. For laminar flow

$$N_u = 4.36$$

and for turbulent flow

$$N_u = 5 + 0.015\,\mathrm{Re}^a\,\mathrm{Pr}^b \; ; \quad \text{for } 0.1 < \mathrm{Pr} < 10^5 \text{ and } 10^4 < \mathrm{Re} < 10^6$$

where $a = 0.88 - \frac{0.24}{4+\mathrm{Pr}}$, $b = 0.3333 + 0.5e^{(-0.6\mathrm{Pr})}$

3.2.4. Suction Chamber heat transfer coefficient

The suction chamber is modeled as a circular duct and the hydraulic diameter is evaluated. The velocity in the chamber is calculated from the mass flow rate which is known from the calorimeter tests. No swirl effects are assumed in the suction chamber. The Nusselt number are calculated using correlations described in 3.2.3.

3.2.5. Compression chamber heat transfer coefficient

There are no correlations reported in literature for the heat transfer coefficient calculation for the rotary compressor. The gases involved in heat transfer at high temperatures and undergo a rapid physical change. Further difficulty is introduced by the uncertainties of gas flow patterns, the state of boundary-layer developments as well as the complexities induced by the change of compression volume boundaries. In absence of more exact data the following equation is used for the calculation of Nusselt number [7] although it was originally formulated for reciprocating compressors.

for laminar: $N_u = 4.36$

for turbulent: $N_u = 0.053\,\mathrm{Re}^{0.8}\,\mathrm{Pr}^{0.6}$

where the Reynolds number is calculated using the swirl velocity. The swirl angular velocity is taken to be twice that of shaft angular velocity[7]. The compression chamber is modeled as a circular duct and the hydraulic diameter is used in calculation of the Reynolds number.

3.2.6. Stator and case channel heat transfer coefficient

The volume of gas flow through the channel is determined with known volume rate of flow from the compression chamber (In the present the compression volume is calculated using ideal gas law and polytropic coefficient of 1.16[16]). As the gas flows through the channel and rotor gap, volume flow rate is calculated for each of them knowing the cross sectional areas of the channel and the gap. The effect of heat interaction in gap as well as in the channel, on the gas is neglected. The velocity of flow and the Reynolds number is calculated using the hydraulic diameter concept. Depending on the Reynolds number the Nusselt number is calculated from the formulations described in section 3.2.3.

3.2.7. Heat transfer coefficients in rotor and stator gap

The calculation of heat transfer coefficient in the rotor gap has been of great interest for many years [17-26]. Although many experimental works are undertaken, no attempts have made to simulate theoretically the heat transfer rates for the combined effects of rotation and axial flow[26]. The flow field in the gap is complicated by the onset of vortices and axial flow velocity. In the compressor, the stator is fixed while the rotor rotates. The radial velocity is determined from the angular speed while the axial velocity in the present case is calculated from the volume rate of flow through the gap. The calculation of Nusselt number involves mean radius, axial Reynolds number, Taylor's number, and critical Taylor's number. The following correlations are used in the present work.

$N_u = 4.294\sigma^{0.4845}$; for $1 < \sigma < 4.817$

and $N_u = 5.08\sigma^{0.3507}$; for $\sigma > 4.817$

where $\sigma = Ta/Ta_{cr}$, $Ta = \frac{\omega^2 r_m \delta^3}{\nu^2}$, $Ta_{cr} = \frac{\omega_{cr}^2 r_m \delta^3}{\nu^2}$, $\omega_{cr}^2 = \frac{\pi^4 \nu^2 r_m}{S\delta^3 r_i^2}$

$\delta = r_o - r_i$, $r_m = (r_o + r_i)/2$

and $S = 0.0571\left(1 - \frac{0.652\delta}{r_i}\right) + 0.00056\left(1 - \frac{0.652\delta}{r_i}\right)^{-1}$

These correlations cover a very good range of axial Reynolds number of about 250 to 1000. In the present work the axial Reynolds number is approximately 720.

3.2.8. Heat transfer coefficient between the gas above the cylinder and rotor bottom

The compressed gas emerges from the clearances of the volume cup and comes in contact with the rotor bottom. The rotation of the rotor induces velocity in the gas. The effect of the axial velocity impinging the rotor bottom is neglected. The Reynolds number is calculated using an average radial velocity of the rotor which is calculated utilizing mean diameter concept. The formula used for the calculation of Nusselt number is adapted from Kreith[27].

$$N_u = \frac{\mathrm{Re}\,\mathrm{Pr}\left(\sqrt{C_{dr}/2}\right)}{5\mathrm{Pr} + 5\ln(5\mathrm{Pr}+1) + \sqrt{2/C_{dr}} - 14}$$

where $C_{dr} = \frac{1}{-2.05 + 4.07\log_{10}\mathrm{Re}\sqrt{C_{dr}}}$

and C_{dr} is solved numerically using Newton-Raphson [28] method.

3.2.9. Copper winding of Stator and the gas above the cylinder

The location of copper winding is very close to the rotor and hence the gas velocity at copper windings will be fairly same that of the gap. Hence the heat transfer coefficient is taken as same as that of the rotor gap.

3.2.10. Heat transfer coefficient between the stator bottom and the gas above cylinder

The velocity of the gas near the rotor is equal to the radial velocity of the rotor . Assuming a swirl motion in this chamber, the velocity of the gas is assumed to be equal to the rotor velocity. This value is used to calculate the Reynolds number. The heat transfer is modeled as a flat plate and the following correlations [14] are used.

$N_u = 0.664\,\mathrm{Re}^{1/2}\,\mathrm{Pr}^{1/3}$; for $\mathrm{Re} < 10^5$

$N_u = \mathrm{Pr}^{1/3}\left(0.037\,\mathrm{Re}^{0.8} - 850\right)$; for $10^5 < \mathrm{Re} < 10^7$

and the heat transfer coefficient is determined as

$$h = \frac{N_u k}{(D_o - D_i)}$$

3.2.11. Heat transfer coefficient between the case and the gas above cylinder

As it is not known how the gas behaves in the space below the stator and above the cylinder, the gas and case interaction is modeled as gas flowing to the case perpendicularly. The velocity of the gas is taken as the rotor velocity value as described in section 3.2.10. Following Schlichting [29] the equation becomes

$$N_u = \frac{\mathrm{Re}^{1/2}\,\mathrm{Pr}^{1/2}}{\sqrt{0.5\pi}}$$

3.2.12. Heat transfer coefficients between the gas above cylinder and cylinder

As the cylinder has three kidney shaped ports, it is more complicated to calculate the heat transfer coefficient accurately. In the present work the cylinder is modeled as a circular disk and the heat transfer is modeled as a flat plate heat transfer for this particular calculation. The velocity of the gas above the cylinder is taken to be equal to the rotor velocity assuming swirl is there. The equations governing the heat transfer coefficient [14] are

$$N_u = 0.664\,\mathrm{Re}^{1/2}\,\mathrm{Pr}^{1/3}; \qquad \text{for } \mathrm{Re} < 10^5$$

$$N_u = \mathrm{Pr}^{1/3}\left(0.037\,\mathrm{Re}^{0.8} - 850\right); \text{ for } 10^5 < \mathrm{Re} < 10^7$$

and the heat transfer coefficient is determined as

$$h = \frac{N_u k}{\left(D_{case} - D_{mf}\right)}$$

3.2.13. Heat transfer coefficient between the upper bearing plate and the gas above the cylinder

The analysis is same as that described in section 3.2.12 except that the cylinder dimensions are replaced by the bearing plate dimensions. The velocity of gas is again taken to be the rotor radial velocity.

3.2.14. Heat transfer coefficient between the stator top, rotor top, copper winding, shaft top and the gas above stator/rotor

The analysis is same as that of the gas above cylinder and the stator/rotor bottom and copper winding. The velocity of gas is calculated from continuity of mass. However for the heat transfer calculation for the rotor and the shaft top, velocity is taken as the rotor velocity and Kreith's formula is used.

3.2.15. Heat transfer coefficient between the case above the stator and the gas above the stator/rotor

The gases coming from the rotor gap, stator channel mix in this chamber. The gas flows to the condenser through the discharge tube which is connected to this chamber. Using continuity of mass the velocity in the chamber is evaluated. The heat transfer is modeled as a flat plate heat transfer and the equations used are described in section 3.2.12.

3.2.16. Contact resistances

The stator is shrink fit to the case and similarly is the rotor to the shaft. The contact stresses are evaluated knowing the interfearance of the contacting surfaces. The contact pressure is calculated [30] and the contact resistance is found from heat transfer hand book [31]. The contact pressure is given by

$$p = \frac{\eta}{b\chi}$$

where

$$\chi = \frac{1}{E_i}\left(\frac{b^2 + a^2}{b^2 - a^2} - \nu_i\right) + \frac{1}{E_o}\left(\frac{c^2 + b^2}{c^2 - b^2} - \nu_o\right)$$

and a is the radius of the hole of the inner member, b is the radius of contact surface, c is the radius of outer surface, E's are the youngs modulus for innet and outer members, ν's are the poisson's ratio, and η is the radial interference.

3.2.17. Thermal conductivities

The thermal conductivities are adapted from various sources [31,32].

3.3. Mechanical and Electrical Losses

Mechanical losses in the rotary compressor have been described in the literature extensively [33,34] and also they can be found from fundamental principles [35]. Electrical losses on the other hand depends on the configuration and mass of the components and is usually provided in forms of charts from the manufacturer. For the present work the electrical losses, i.e. iron and copper losses are determined from the data of the particular motor used in the compressor. However the bearing losses should be modified by a correcting factor for the turbulent case. If P_l is the loss at laminar condition then the loss P_t at turbulent condition becomes[35]

$$P_t = 0.039\,\mathrm{Re}^{0.57} P_l, \qquad \text{for Re} > 1600$$

It is assumed that all the work transforms into heat. The present work accounts for the mechanical losses occur at the upper bearing plate journal, lower bearing plate journal, the journal bearing between the shaft eccentric and the roller, upper and lower thrust bearing losses, vane side, vane top and bottom losses, vane and roller loss at the contact surface, roller and bearing plate losses, and the loss at stator and rotor gap. In addition to these mechanical losses copper and iron losses at the motor is also included in the analysis.

3.4. Implementation

A computer code is developed for the heat transfer analysis of the compressor. The architecture of the computer program is shown in Figure 2. The program code is developed in FORTRAN and it consists of more than 2000 lines of code. In the main program the data is declared, and the thermal conductances and the system equations are coded. There are five subroutines in this program executing

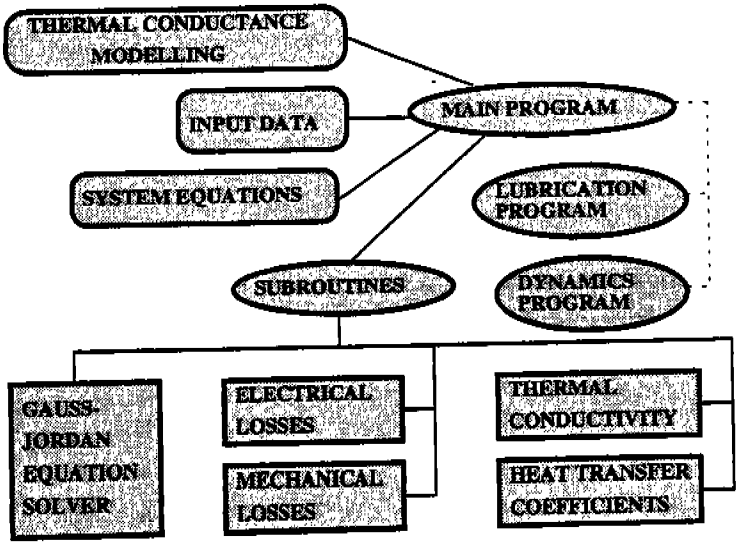

[Figure 2. Program Architecture]

the tasks of simultaneous equation solution, electrical loss calculation, mechanical loss calculation, providing values of thermal conductivity of the components used in compressor, and heat transfer coefficients calculations. Some inputs for this program are generated using the Lubrication and Dynamics computer programs. The simultaneous linear equations are solved using Gauss-Jordan method.

The input to the program are the ambient temperature, the power consumption of the compressor, the gas temperature at the inlet to the compressor, pressure ratio, the exit gas temperature, and the amount of air flow over the compressor. The outputs of the program include the temperatures at various location and heat transfer between components.

3.5. Verification and Discussion

To verify the theoretical prediction a compressor is modified to attach 24 thermocouples at various locations. The experiment was carried out on a calorimeter and various temperatures are measured [Figure 3]. The experimental data is compared against theoretical predictions and a good agreement is found. Table 1 describes the theoretical as well as experimental temperatures (in degree Fahrenheit) at various locations.

[Figure 3. Experimental setup with airflow over compressor using a fan]

It is found that the case temperature above the stator/rotor differs that of experimental measurement by approximately 8 degrees. This is attributed to the fact that the heat transfer due to radiation is calculated assuming a temperature of the case which is ten degrees higher than that of the exit temperature. In calculating the oil sump temperature, a more accurate determination of velocity profile of the lubricant oil can be done using computational fluid dynamics and at present this is not done. Otherwise a good agreement between the thoery and experiment is found.

Element Number	Element Name	Theoretical temperature	Experimental temperature
1	Case above the stator top	176.21	184.71
2	Case attached to the stator	197.56	192.82
3	Case between stator and cylinder	196.03	192.03
4	Case attached to the cylinder	191.98	191.41
5	Case portion attched to the oil sump	187.08	188.84
6	Cylinder	200.45	198.25
7	Oil sump	192.00	197.64
8	Suction gas in the cylinder	125.38	123.11
9	Compressed gas in cylinder	237.51	231.89
10	Vane	202.31	Not measured
11	Gas above cylinder	200.44	203.44
12	Stator copper windings	200.03	198.33
13	Stator iron	198.07	195.28
14	Rotor	200.88	Not measured
15	Shaft above upper bearing	200.89	Not measured
16	Gas at rotor gap outlet	200.46	195.28
17	Gas at channel outlet	199.9	198.55
18	Roller	203.04	Not measured
19	Lower bearing plate	201.72	202.8
20	Upper bearing plate	201.66	205.21
21	Shaft in the bearings	201.74	Not measured
22	Gas above the stator/rotor	199.68	196.48

[Table 1. Comparision of theoretical and experimental results]

4. CONCLUSION

A lumped mass model for the rotary compressor is developed. System equations are developed using the thermal conductance concept. Heat transfer coefficients are calculated from the empirical/theoretical equations adapted from various sources. No empirical correction factors are introduced into the system equations. Mechanical as well as electrical losses are considered as heat addition to the system. A computer code is generated to predict the temperature of the compressor at various locations and a good agreement is found with the experimental data.

ACKNOWLEDGMENT

The author is indebted to Mr. J. J. O'Neill, Manager-Compressor & Refrigerant Systems Design, for his many valuable discussions, help and encouragement; without which the publication of this paper might not have been possible. The author wish to thank his academic advisor Prof. S. N. Dwivedi at West Virginia University for his technical discussions. The author appreciates the help of Dr. Robert Bergholz at GE-Air Craft Engines in explaining his prior work. Thanks to our technicians Mr. Robert Smith and Mr. James O'Dell for their excellent work on the experiments. Special thanks to Mr. R. Mark Schreck, General Manager-Refrigeration and Dr. William J. Sheeran, Vice President-Technology for their encouragement and for allowing the paper to be published.

REFERENCES

1. Adornato, V., Padhy, S. K. & Herzog, R. R.," Theoretical Modeling of Lubrication System of a Rotary Compressor", To be Published in *Proc. of the International Appliance Technical Conference*, Purdue University, 1992.
2. Brok, S. W., Touber, S. & van der Meer, J. S., "Modeling Cylinder Heat Transfer - Large Effect, Little Effect?", Proc. of the Purdue Compressor Technology Conference, pp. 43-50, Purdue University, 1980.
3. Kawai, H., Nishihara, H., Hamada, K. and Nakapka, S., "The Development of High Efficiency Compressor by Reducing Suction Gas Temperature", *Proc. of the Purdue Compressor Technology Conference*, pp. 222-228, Purdue University, 1982.
4. Meyer, W. A. & Thompson, H. D., "An Experimental Investigation into Heat Transfer to the Suction Gas in a Low-Side Hermetic Refrigeration Compressor", *Proc. of International Compressor Engineering Conference*, pp. 908-916, Purdue University, 1988.
5. Meyer, W. A. & Thompson, H. D., "An Analytical Model of Heat Transfer to the Suction Gas in a Low-Side Hermetic Refrigeration Compressor", *Proc. of International Compressor Engineering Conference*, pp. 898-907, Purdue University, 1988.
6. Srikanth, R. & Thompson, H. D., "How the Design of the Suction Return Affects Compressor Efficiency", *Proc. of International Compressor Engineering Conference*, pp. 615-622, Purdue University, 1988.
7. Adair, R. P., Qvale, E. B. and Pearson, J. T.," Instantaneous Heat Transfer to the Cylinder Wall in Reciprocating Compressors", *Proc. of the Compressor Technology Conference*, pp. 521-526, Purdue University, 1972.
8. Recktenwald, G. W., Ramsey, J. W. & Patankar, S. V., "Prediction of Heat Transfer in Compressor Cylinders", *Proc. of International Compressor Engineering Conference*, pp. 159-174, Purdue University, 1986.
9. Recktenwald, G. W., " A Study of Heat Transfer Between the Walls and Gas Inside the Cylinder of a Reciprocating Compressor", Ph. D. Dissertation, University of Minnesota, 1989.
10. Bergholz, R. F. & Caney, R. D., Jr., "Refrigeration Compressor Model", *G.E. Internal Report*, 1984.
11. Arpaci, V., Conduction Heat Transfer, Addison-Wesley, Reading, MA,1966.
12. Schneider, P. J., Conduction Heat Transfer, Addison-Wesley, Reading, MA,1955
13. Incropera, F. P. & De Witt, D. P., Fundamentals of Heat & Mass Transfer, 3rd Edition, John Wiley & Sons, New York, 1990.
14. Holman, J. P., Heat Transfer, 6th Edition, McGraw-Hill, New York, 1986.
15. Burmeister, L. C., Convective Heat Transfer, John Wiley & Sons, New York, 1983.
16. Jastor, H., G.E. CR & D, Personal Discussions, 1991.
17. Bjorklund, I. S. and Kays, W. M., "Heat Transfer Between Concentric Rotating Cylinders", *Trans. of ASME, J. of Heat Transfer*, pp. 175-186, August 1959.
18. Becker, K. M. & Kaye, J. ," Measurements of Diabatic Flow in an Annulus with an Inner Rotating Cylinder", *Trans. of ASME, J. of Heat Transfer*, pp. 97-105, May 1962.
19. Gazley, C., " Heat Transfer Characteristics of Rotational & Axial Flow Between Concentric Cylinders", *Trans. of ASME, J. of Heat Transfer*, pp. 79-90, Vol 80, 1958.
20. Kaye, J. & Elgar, E. C., "Modes of Adiabatic and Diabatic Fluid Flow in an Annulus with an Inner Rotating Cylinder, *Trans. of ASME, J. of Heat Transfer*, Vol 80, pp. 753-765, 1958.
21. Tachibana, F. & Fukui, S.," Convective Heat Transfer of the Rotational & Axial Flow Between Two Concentric Cylinders", *Bulletin of JSME*, pp. 385-391, Vol 7, No. 26, 1964.

22. Gardiner, S. R. M. & Sabersky, R. H.," Heat Transfer in an Annular Gap, *Int. J. of Heat & Mass Transfer*, Vol 21, pp. 1459-1466, 1978.
23. Rao, K. V. C. & Sastri, V. M. K., " Experimental Studies on Diabatic Flow in an Annulus with Rough Rotating Cylinder", Heat & Mass Transfer in Rotating Machinery (Ed. D. E. Metzger & N. H. Afgan), Hemisphere, 1984.
24. Kataoke, K. Hasioka, K., Komai, T. & Doi, H., "Mass Transfer in the Annulus between Two Rotating Cylinders", Heat & Mass Transfer in Rotating Machinery (Ed. D. E. Metzger & N. H. Afgan), Hemisphere, 1984.
25. Vahl Davis, G. de.,Leonardi, E. & Reizes, J. A., "Convection in a Rotating Annular Cavity", Heat & Mass Transfer in Rotating Machinery (Ed. D. E. Metzger & N. H. Afgan), Hemisphere, 1984.
26. Maron, D. M. & Cohen S.," Hydrodynamics and Heat/Mass Transfer near Rotating Surfaces,", Advances in Heat Transfer, Vol 21, pp. 141-183, 1991.
27. Kreith, F., Principles of Heat Transfer, 3rd Edition, Intext Educational Publishers, New York, 1973.
28. Kreyszig, E., Advanced Engineering Mathematics, 6th Edition, John Wiley & Sons, New York, 1988.
29. Schlichting, H., Boundary Layer Theory, 7th Edition, McGraw-Hill, New York, 1977.
30. Shigley, J. E. & Mischke, C. R., Standard Hand Book of Machine Design, McGraw-Hill, New York, 1986.
31. Heat Transfer Data Book, Geneum Publishing Company.
32. Materials Engineering, Dec. 1989.
33. Sakurai, B. & Hamilton, J. F., "The Prediction of Frictional Losses in Variable-Speed Rotary Compressor, *Proc. of International Compressor Engineering Conference*, pp. 331338, Purdue University, 1984.
34. Pandeya, P. & Soedel, W.," Rolling Piston Type Rotary Compressors with Special Attention to Friction & Leakage", *Proc. of the Compressor Technology Conference*, pp. 209-218, Purdue University, 1978.
35. Fuller, D. D., "Theory & Practice of Lubrication for Engineers", 2nd Edition, John Wiley & Sons, New York, 1984.

THERMAL ENERGY ANALYSIS IN RECIPROCATING HERMETIC COMPRESSORS

M. L. Todescat, F. Fagotti
EMBRACO
Empresa Brasileira de Compressores S/A
Rua Rui Barbosa, 1020 - Cx. P. D-27
89200 - Joinville, SC - BRAZIL

A. T. Prata and R. T. S. Ferreira
Federal University of Santa Catarina
Department of Mechanical Engineering
Cx. P. 476 - Florianópolis, SC
88049 - BRAZIL

ABSTRACT

In this paper the thermal energy analysis of a reciprocating hermetic compressor is performed using a computational program. The simulation model employed in the program is based on energy balances. For the refrigerant gas inside the compressor cylinder use was made of the first law of thermodynamics including time variations of the mass and energy fluxes. The required temperatures at the suction chamber, cylinder walls, discharge chamber, discharge muffler, compressor shell, and ambient inside the compressor shell are obtained from steady state energy balances at various locations within the compressor. Effective overall heat transfer coefficients were determined experimentally, except for the heat transfer between the refrigerant and the cylinder walls which was obtained from existing correlations. A companion simulation program which represents the compressor working features was used to calculate the mass fluxes at the suction, discharge, and the leakage flux. Simulation results are presented for a small compressor and compared with experimental results. Good agreement prevails indicating that the major effects affecting the thermal performance of the compressor have been considered by the proposed model.

INTRODUCTION

There are several reports in the literature concerning numerical models to predict the performance of hermetic refrigeration compressors. Those models require thermodynamic relationships to describe the behavior of the gas inside the cylinder. These relationships can be obtained either through a polytropic transformation or through an energy balance. A further aspect to be considered is the heat transfer to and from the refrigerant as it passes through the compressor. The models described in the literature differ mainly on how the two aforementioned issues are addressed. On the next paragraphs some of the major works done on compressor modelling will be reviewed.

Qvale *et al.* [1] indicated some areas where research should be done to improve the current knowledge on compressor modelling. Heat transfer on the suction and discharge lines, on the valves, and between the gas and the cylinder walls are the most important points mentioned by the authors. According to [1] the numerical models dealing with the cylinder of hermetic compressors have frequently employed the assumption of perfect gas in a polytropic process. The exponent of the polytropic equation is usually adjusted to fit experimental results. In this regard the polytropic index incorporates the combined effect of the heat transfer between gas and cylinder, friction, and deviations from the perfect gas behavior. Therefore, the influence of these effects separately cannot be detected.

Karll [2] investigated through the first law of thermodynamics the process described by a real gas inside the cylinder. He considered the cylinder as a close system undergoing exchange of heat and work with the surroundings. Prakash and Singh [3] also employed the first law of thermodynamics but assumed perfect gas behavior. The heat transfer between the cylinder walls and the gas was predicted using the correlation given by Adair *et al.* [4]. Röttger and Kruse [5] verified through their model that for the compressor performance it is important to use the equation of state for real gas but for the valve performance suffices to use the perfect

gas assumption. Ng *et al.* [6] also employed the first law of thermodynamics to model the compressor. Additionally they assumed the cylinder to be adiabatic. According to [6] the real gas model is justified only if the gas superheating at the suction is small and if the pressure ratio at the compressor is large. A simplified model based on a polytropic process was proposed by Suefuji and Nakayama [7]. The disadvantage of their model is that the suction and discharge temperatures must be known a priori. Brok *et al.* [8] have shown that in reciprocating compressors there are two major heat transfer contributions that should be carefully examined: the part of the compression power that is transferred to the external environment and that transferred to the suction gas. In [8] the heat transfer between refrigerant and cylinder walls was modelled via Adair *et al.* [4] correlation, modified by a factor to reduce the mixing inside the cylinder. This factor was adjusted to fit the experimental data. For the suction and discharge values use was made of the Dittus-Boelter correlation for turbulent flow [9]. In the suction chamber a correlation for annular concentric ducts was adopted, and for the discharge chamber a constant value of the heat transfer coefficient was employed. According to [8] the influence of the heat transfer inside the cylinder on the compressor performance is less than what is suggested in the literature. For low speed situations it was found that during compression at most 4% is gained by cooling and 3% is lost by superheating. Parise and Cartwright [10] also performed a compressor simulation including an energy balance in the cylinder. Heat transfer between refrigerant and cylinder walls was modelled using Adair *et al.* [4] correlation.

Lee *et al.* [11] proposed a simulation model emphasizing the need for a correct evaluation of the thermodynamic properties inside the cylinder. They employed both the first law and a polytropic process. According to [11] the pressure inside the cylinder is not strongly affected by different values of the polytropic exponent but the temperature showed a great dependance on the value adopted. The mass flow rate through the compressor has shown to be weakly dependant on the thermodynamic model employed. Liu and Zhow [12] obtained experimentally the temperature distribution on the cylinder lateral walls of a reciprocating compressor (averaged during a cycle) for different pressure ratios, suction temperatures and rotational speeds. They have observed that the temperature variation along the axial direction is due to heat transfer to the suction gas. The temperature variation along the circumferential direction is due to the friction between the piston and the cylinder wall and also due to the discharge location. Schary *et al.* [13] performed a compressor simulation incorporating in their model gas pulsation and a polytropic process. The numerical results were checked against experimental results an a surprisingly good agreement was achieved.

Some few works reported more elaborate models where the heat transfer inside the cylinder is evaluated through the differential form of the energy equation. Chong and Watson [14] solved the continuity, momentum and energy equations in differential form using a finite difference scheme. Their analysis assumed laminar flow and ignored the gas suction and discharge through the valves. They observed that as the rotational speed increases, the thermal boundary layer becomes so thin that heat transfer can be predicted through a conductive one-dimensional model which requires only the boundary layer thickness. More recently, Recktenwald [15] (also Recktenwald *et al.* [16]) employed two models to investigate the instantaneous heat transfer between the cylinder walls and the gas in a reciprocating compressor. One model used mass and energy balances to predict the instantaneous bulk thermodynamic properties of the gas in the cylinder. Heat transfer between the cylinder walls and the gas was calculated with Adair*et al.* [4] correlation. The other model solved the unsteady continuity, momentum, and energy equations for the gas in the cylinder using a finite volume technique. No heat transfer correlation was needed in this model. The instantaneous heat transfer predicted by the simple model using Adair *et al.* [4] correlation was an order of magnitude less than that predicted by the finite volume model indicating that instantaneous heat transfer in compressor cylinders is much greater than many researchers have assumed. The average heat transfer coefficient during a cycle calculated in [15] is at least twice bigger than the value that is predicted from Adair *et al.* [4].

The main goal of the present work is to present a model based on the first law of thermodynamics for simulating the performance of a hermetic refrigeration compressor, and in this regard shed more light on this subject. In what follows the energy balance for the refrigerant inside the cylinder is computed for each instant during the operating cycle and take into account time variations of mass and energy fluxes. For this balance the temperatures at the discharge, the discharge chamber, the suction line, the gas inside the compressor shell, the compressor shell and the cylinder are determined from steady state energy balances. Those balances require heat transfer coefficients which are obtained either from existing correlations or from experimental measurements. Similar procedure has recently been adopted by Meyer and Doyle [17-18] to develop an analytical model for the heat transfer to the suction gas in a low-side hermetic refrigeration compressor.

ENERGY BALANCES

The energy balances to be explored in this section will be developed with the aid of Fig. 1. This figure presents a schematic view of a hermetic refrigeration compressor illustrating the motor, the cylinder and piston, the discharge and suction valves, the discharge and suction chambers, as well as the compressor shell. Also shown in Fig. 1 by dashed lines are the selected control volumes chosen for the energy balances.

Energy Balance for the Gas inside the Cylinder

For the gas inside the cylinder an energy balance is computed at each instant during the operating cycle. According to the first law of thermodynamics this balance can be written as

$$Q_c + W_i = \frac{\partial}{\partial t}\int_{c.v.} \rho e d\forall + \int_{c.s.} \rho e \vec{V}.d\vec{A} \qquad (1)$$

where e is the specific energy of the gas, $\forall$ is the cylinder volume and $\vec{V}$ is velocity; Q_c is the rate of heat transferred between the gas and the cylinder walls (including piston and valve plate), W_i is the power input. The two terms on the right-hand side of eq. (1) are, respectively, the variation with time of the energy inside the cylinder and the flux of energy associated with the mass fluxes through the suction and discharge valves and with the leakage mass flow through the clearance between piston and cylinder wall. From thermodynamics considerations eq. (1) can be written as (see Todescat *et al.* [19]),

$$\frac{dT}{dt} = \frac{1}{mc_v}\left\{Q_c + \dot{m}_s(h_{sc} - h) - \frac{T}{\rho}\frac{\partial p}{\partial T}\bigg|_\rho \left[\rho\frac{d\forall}{dt} - (\dot{m}_s - \dot{m}_d - \dot{m}_v)\right]\right\} \qquad (2)$$

At each instant during the compressor cycle the temperature of the gas inside the cylinder is determined from eq. (2). The heat transfer rate, Q_c, is obtained using an effective heat transfer coefficient as,

$$Q_c = h_c A_c (T_c - T) \qquad (3)$$

where A_c is the instantaneous cylinder surface area and T_c is an effective surface temperature. In the present analysis h_c is evaluated according to three different expressions. That of Adair *et al.* [4], that of Annand [4], and a third expression obtained simply multiplying Annand's formula by a factor of three. This last correlation was used to explore the influence of higher heat transfer coefficients on the compressor performance according to what is recommended by Recktenwald [15].

All the thermodynamics properties in eq. (2), including c_v, are evaluated according to Martin-Hou equation of state for real gas [20]. The mass fluxes at the suction, discharge, and the leakage flux, $\dot{m}_s$, $\dot{m}_d$ and $\dot{m}_v$, are obtained from a simulation program which represents the working features of the compressor. This program is similar to those developed by Ussyk [21] and Ferreira [22]. The specific enthalpy of the suction gas, h_{sc}, is a function of the specified suction pressure and the unknown temperature, T_{sc}. The temperature T_{sc} as well as the other temperatures inside the compressor are obtained through specific energy balances as explored next.

Energy Balance at the Muffler and Suction Chamber

According to Fig. 1, an energy balance at the muffler and suction chamber requires that

$$Q_s = \dot{m}_s h_{sc} - \dot{m} h_s - \dot{m}_v h_{sc} - \dot{m}_{bs} h_c \qquad (4)$$

where Q_s is the heat transfer between the gas inside the chamber and that inside the compressor shell. In terms of an overall energy balance Q_s can be written as,

$$Q_s = \overline{UA}_s (T_{sc} - T_{ms}) \qquad (5)$$

in which $T_{ms} = (T_s + T_{sc})/2$; T_s is the temperature of the intake gas and T_{sc} is the temperature of the gas exiting the chamber and entering the cylinder. The mass fluxes with their respective enthalpies appearing in eq. (4) are indicated in Fig. 1. As the leakage mass flux $\dot{m}_v$, the backflow at the suction valve, $\dot{m}_{bs}$, and the mass flow rate produced by the compressor, $\dot{m}$, are obtained by the simulation program that represents the working features of the compressor as mentioned previously.

Energy Balance at the Cylinder

An overall energy balance at the cylinder along the entire operating cycle requires that,

$$Q_c = \dot{m}_s\, h_{sc} - \dot{m}_{bs}\, h_c + \dot{m}_{bd}\, h_{dc} - \dot{m}_d\, h_c + W_i + W_p - \dot{m}_o\, h_c \tag{6}$$

where Q_c is given by eq. (3).

It should be noted that eq. (1) was written for the gas inside the cylinder whereas eq. (6) represents an energy balance for a control volume that envelops the cylinder itself, including the piston. In this regard, the frictional power, W_p, was taken account in eq. (6). To calculate the mechanical losses due to friction, W_p, variation of the oil viscosity with temperature was considered.

Energy Balance at the Discharge Chamber

The energy balance performed at the suction line according to equation (4) included both the muffler and the suction chamber. For the discharge line the muffler and the discharge chamber will be considered separately. According to Fig. 1 the energy balance at the discharge chamber can be written as,

$$Q_{dc} = \dot{m}_d\, h_c - \dot{m}\, h_{dc} - \dot{m}_{bd}\, h_{dc} \tag{7}$$

where the heat transfer between the gas inside the discharge chamber and that inside the compressor shell, Q_{dc}, is expressed as,

$$Q_{dc} = \overline{UA}_{dc}\,(T_{dc} - T_{ic}) \tag{8}$$

The backflow at the discharge valve, $\dot{m}_{bd}$, is obtained via the compressor simulation program as discussed earlier.

Energy Balance at the Discharge Muffler

According to Fig. 1, an energy balance for the discharge muffler can be written as,

$$Q_d = \dot{m}(h_{dc} - h_d) \tag{9}$$

where,

$$Q_d = \overline{UA}_d\,(T_{md} - T_{ic}) \tag{10}$$

in which $T_{md} = (T_d + T_{dc})/2$; T_d is the temperature of the gas leaving the compressor and T_{dc} is the gas temperature at inlet of the discharge muffler.

Overall Energy Balance

The compressor exchanges heat with the surroundings according to its shell temperature. To obtain this temperature the following overall energy balance can be performed,

$$Q_e = \dot{m}(h_s - h_d) + W_c \tag{11}$$

where,

$$Q_e = \overline{UA}_e\,(T_b - T_{ee}) \tag{12}$$

The shell temperature is related to the gas temperature inside the compressor, T_{ic}, by simply equating Q_i and Q_e as shown in Fig. 1, that is,

$$Q_i = \overline{UA}_i\,(T_{ic} - T_b) = \overline{UA}_e\,(T_b - T_{ee}) = Q_e \tag{13}$$

Equations (4), (6), (7), (9), (11) and (13) are used to determined T_{sc}, T_c, T_{dc}, T_d, T_b and T_{ic}. Those equations are nonlinear due to the dependance of the specific enthalpy on the temperatures, and are solved simultaneously and iteratively. The required mass fluxes are obtained through the compressor simulation program. To evaluate the heat fluxes according to eqs. (5), (8), (10), (12) and (13), overall heat transfer coefficients are required. The precise determination

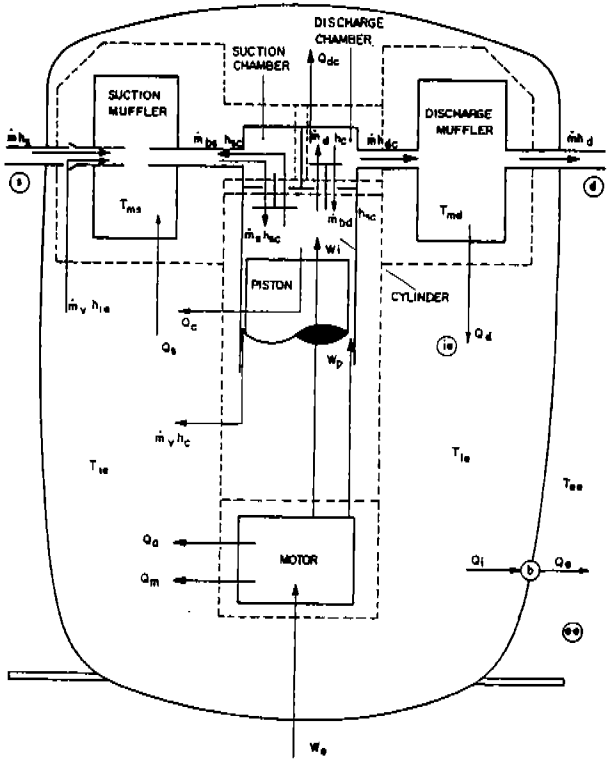

Fig. 1 -Schematic view of a hermetic refrigeration compressor ilustrating the control volumes chosen for the energy balances

of those heat transfer coefficients is a difficult task. This is so due to the complicated geometry of the parts involved as well as due to the complexity associated with the heat transfer mechanisms. Inside the suction and discharge lines, for instance, the flow is pulsated in addition to be turbulent and three-dimensional. Also, the prediction of the heat transfer between the gas inside the compressor and the compressor shell have to be made considering the presence of the lubricating oil. At present it seems to be no detailed report in the literature concerning the aforementioned difficulties. A practice that has currently been adopted is to rely on experiments in order to estimate the heat fluxes. This same procedure was used in the present work. Through temperature measurements, and knowing the compressor operating conditions, the overall heat transfer coefficients required in the present model were determined. The compressor investigated here is a small reciprocating hermetic compressor (about 1/4 horsepower) and typical values of the overall heat transfer coefficients are shown in Tab. 1.

Table 1 - Typical values of the overall heat transfer coefficients determined from experimental data [W/K]

$\overline{UA}_s$	$\overline{UA}_{dc}$	$\overline{UA}_d$	$\overline{UA}_t$	$\overline{UA}_c$
0.76	0.57	2.3	9.2	4.5

At this point the model used to simulate the thermal performance of the compressor has been completed. The temperature of the gas inside the cylinder is determined at each instant during the operating cycle using eq. (2) which was solved by a Runge-Kutta algorithm. The temperatures at the suction chamber, cylinder walls, discharge chamber, discharge muffler, compressor shell, and ambient inside compressor shell, are averaged over the cycle and are determined from eqs. (4), (6), (7), (9), (11) and (13) via Newton-Raphson. A companion program was used to evaluate the requiring friction losses and the mass fluxes. Except for the heat transfer coefficient between the gas and the cylinder walls which was obtained from correlations available in the literature, the heat transfer coefficients were determined using experimental data.

RESULTS AND DISCUSSIONS

The model presented in the previous section was used to simulate the thermal performance of a small reciprocating hermetic compressor (about 1/4 HP) subjected to the following operating conditions,

evaporating temperature	=	$-23.3^{\circ}C$
condensing temperature	=	$54.4^{\circ}C$
superheating temperature	=	$32.2^{\circ}C$
subcooling temperature	=	$32.2^{\circ}C$
ambient temperature	=	$32.2^{\circ}C$
compressor inlet temperature	=	$32.2^{\circ}C$

Table 2 explores the influence of different correlations for the heat transfer coefficient between the gas and the cylinder walls on the compressor performance. Except for the temperature of the cylinder walls, T_c, use of different correlations for the heat transfer coefficient h_c has little effect on the quantities presented in Tab. 2. Even when h_c was multiplied by a factor of three the quantities presented in Tab. 2 seem to show little reaction to that. From Tab. 2 it is also seen that the model presented here is able to predict, with good accuracy, the experimental results. Annand's correlation multiplied by three seems to yield results that are slightly better than those obtained using the two other correlations. Because of that, in what follows, use will be made of this correlation. For other conditions (not shown in Tab. 2) Annand's correlation times three also presented a better agreement with the experimental results.

Table 2 - Influence of different correlations for the cylinder heat transfer coefficient on the compressor performance

Temperatures [°C]	h_c			Experiment
	Adair	Annand	Annand (x3)	
T_{sc}	55.3	55.2	56.0	56.2
T_c	85.5	93.3	98.4	101.0
T_{dc}	138.8	138.1	138.7	140.8
T_d	88.0	87.2	86.3	88.1
T_b	64.4	64.0	64.2	65.0
$T_{\infty e}$	80.1	79.5	79.7	80.9
Power Consumption [W]	191.1	187.8	185.6	192.5
Mass Flow Rate [kg/s]	$1.949\text{x}10^{-3}$	$1.930\text{x}10^{-3}$	$1.856\text{x}10^{-3}$	$1.865\text{x}10^{-3}$
EER [Btu/W.h]	5.02	5.06	4.92	4.84

The small influence of h_c on the thermal performance of the compressor is demonstrated in Fig. 2. This figure shows the various heat transfer contributions plotted as a function of the temperature of the compressor shell, T_b. Experimentally, T_b can be varied by controlling the airflow over the compressor shell.

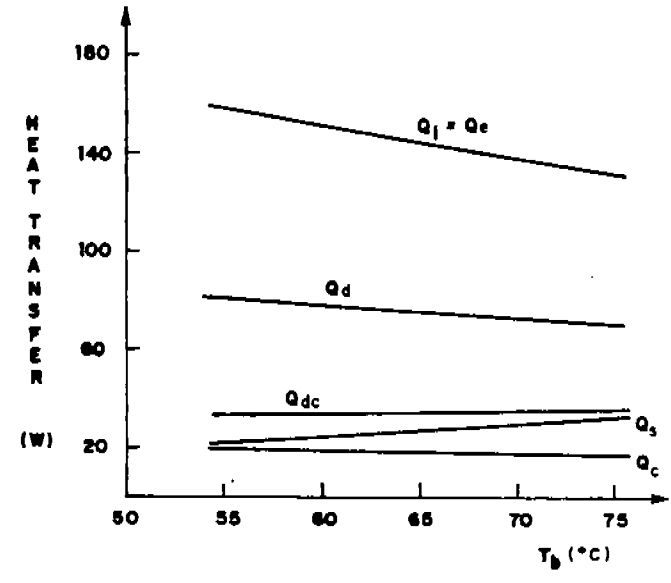

Fig. 2 - Heat transfer contributions as a function of the temperature of the compressor shell, T_b

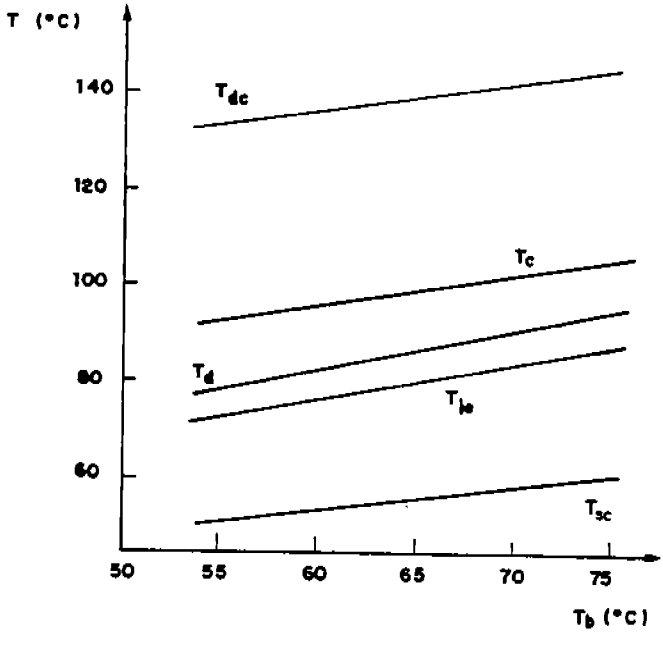

Fig. 3 - Calculated temperatures as a function of the temperature of the compressor shell, T_b

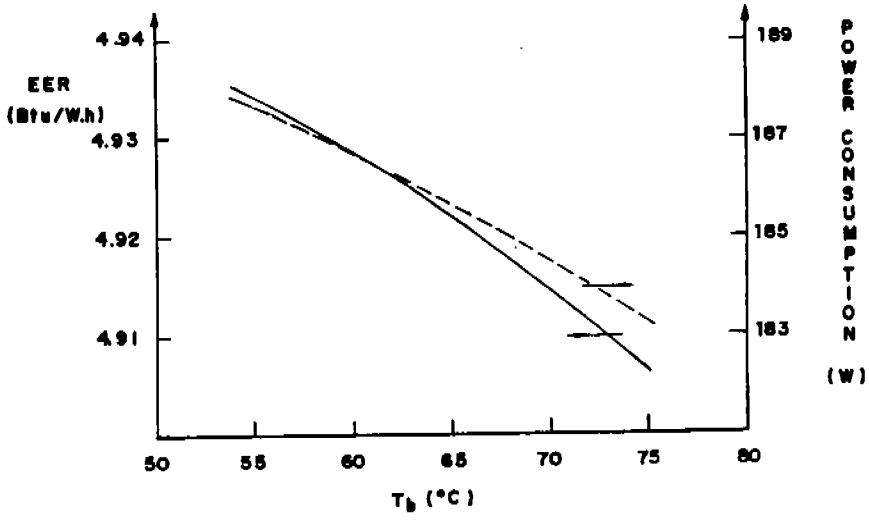

Fig. 4 - Energy efficiency ratio and power consumption as a function of the temperature of the compressor shell, T_b

From Fig. 2 it is seen that Q_e represents the least heat transfer contribution among those entering in the energy balances. Therefore, variations on Q_e are expected to have little effect on the thermal performance of the compressor. It is also seen from Fig. 2 the important role played by the heat transfer Q_e on the overall energy balance. On a relative basis, the heat transfer to the refrigerant at the muffler and suction chamber, Q , is the contribution that is more affected by changes on the temperature of the compressor shell. As T_b varies from 55 to 75^0C, Q_s increases by about 50%.

The influence of the temperature of the compressor shell on the other temperatures is shown in Fig. 3. As expected, all temperatures increase with increasing values of T_b. The increase of the refrigerant temperature at the suction line, $T_{s,r}$, represents a waste of the cooling capacity which reduces the cycle efficiency. As T_b varies from 50 to 75^0C, $T_{s,r}$ increases around 10^0C.

Results for the energy efficiency ratio, EER, and for the compressor power consumption are explored in Fig. 4. A comparison of the power consumption and the heat transfer to the surroundings, Q_e, indicates that between 70 and 80% of the power consumption is wasted as heat to the external environment. This result seems to reinforce Brok *et al.* [8] reccommendation that heat losses to surroundings should be carefully examined.

CONCLUSIONS

The present paper presents a model to perform thermal energy analysis of reciprocating hermetic compressors. The gas inside the cylinder was modelled through the first law of thermodynamics taking into account time variations of mass and energy fluxes. Steady state energy balances were used to obtain the temperatures of the compressor components and of the refrigerant at various locations along the flow path. Those balances require heat transfer coefficients which were determined either from existing correlations or from experimental measurements.

This model was used to simulate the thermal performance of a small compressor (about 1/4 horsepower). Comparisons between experimental results and those obtained with the simulation showed good agreement, indicating that the model can be successfully employed for design studies.

REFERENCES

[1] Qvale, E. B., Soedel, W., Stevenson, M. J., Elson, J.P., and Coates, D.A., "Problem Areas in Mathematical Modeling and Simulation of Refrigerating Compressors", ASHRAE Transactions,Paper 2215, pp. 75–84, 1972.

[2] Karll, B., "Computer Simulation of the Cylinder Process in a Compressor Based on the First Law of Thermodynamics", Purdue Compressor Technology Conference, pp. 18–21, 1972.

[3] Prakash, R. and Singh, R., "Mathematical Modeling and Simulation of Refrigerating Compressor ", Purdue Compressor Technology Conference, pp. 274–285, 1972.

[4] Adair, R. P., Qvale, E. B. and Pearson, J. T., "Instantaneous Heat Transfer to the Cylinder Wall in Reciprocating Compressors", Purdue Compressor Technology Conference, pp. 521–526, 1972.

[5] Röttger, W. and Kruse, H., "Analysis of the Working Cycle of Single Stage Refrigeration Compressors Using Digital Computers", Purdue Compressor Technology Conference, pp. 18–25, 1976.

[6] Ng., E. H., Tramschek, A. B., and MacLaren, J. T. F., "Computer Simulation of a Reciprocating Compressor Using a Real Gas Equation of State",Purdue Compressor Technology Conference, pp. 33–42, 1980.

[7] Suefuji, K. and Nakayama, S., "Practical Method for Analysis and Estimation of Reciprocating Hermetic Compressor Performance", Purdue Compressor Technology Conference, pp. 15–23, 1980.

[8] Brok, S. W., Touber, S., and van der Meer, J. S., "Modelling of Cylinder Heat Transfer – Large Effort, Little Effect?", Purdue Compressor Technology Conference, pp. 43–50, 1980.

[9] Incropera, F. and DeWitt, D. P., Fundamentals of Heat and Mass Transfer, 2nd edition, John Wiley and Sons, New York, 1985.

[10] Parise, J. A. R. and Cartwright, W. G. "Simulation of Reciprocating Compressors: Numerical Method and Comparison with Experimental Data", Journal of the Brazilian Society of Mechanical Sciences, Vol. 8, pp. 129–152, 1985.

[11] Lee, S., Singh,R., and Moran, M. J., "First Law Analysis of a Compressor Using a Computer Simulation Model", Purdue Compressor Technology Conference, pp. 1–10, 1982.

[12] Liu, R. and Zhou, Z., "Heat Transfer Between Gas and Cylinder Wall of Refrigerating Reciprocating Compressor", Purdue Compressor Technology Conference, pp. 110–115, 1984.

[13] Schary, M., Scheideman, F. and Singh, R., "Energy and Pressure Pulsation Predictions for Refrigeration Compressors", Simulation of Energy Systems, Part 2, pp. 173–181, 1978.

[14] Chong, M. S. and Watson, H. C., "Prediction of Heat and Mass Transfer During Compression in Reciprocating Compressors ", Purdue Compressor Technology Conference, pp. 466–472, 1984.

[15] Recktenwald, G. W., "Numerical Modelling of the Flow and Heat Transfer in the Cylinder of a Reciprocating Compressors", M. Sc. Thesis, University of Minnesota, 1984.

[16] Recktenwald, G. W., Ramsey, J. P. and Patankar, S. V., "Prediction of Heat Transfer in Compressor Cylinders", Purdue Compressor Technology Conference, pp. 159–169, 1986.

[17] Meyer, W. A. and Doyle, H., "An Analytical Model of Heat Transfer to the Suction Gas in a Low-Side Hermetic Refrigeration Compressor", International Compressor Engineering Conference at Purdue, pp. 898-907, 1990.

[18] Meyer, W. A. and Doyle, H., "An Experimental Investigation Into Heat Transfer to the Suction Gas in a Low-Side Hermetic Refrigeration Compressor ", International Compressor Engineering Conference at Purdue, pp. 908– 916, 1990.

[19] Todescat, M. L., Ferreira, R. T. S. and Prata, A. T., Thermal Balance in Reciprocating Compressors, Technical Report UFSC/EMBRACO, 1990.

[20] Reynolds, W. C., Thermodynamic Properties in SI, Department of Mechanical Engineering,
Stanford University, 1979.

[21] Ussyk, M. S., Numerical Simulation of the Performance of Reciprocating Hermetic Compressors, M. Sc. Dissertation, Federal University of Santa Catarina, Brazil, 1984.

[22] Ferreira, R. T. S., Simulation of a Reciprocating Hermetic Compressor Via the First Law of Thermodynamics, Technical Reports UFSC/EMBRACO, 1987.

LOW FLOW DISPLACEMENT COMPRESSOR: THERMODYNAMICAL PROCESS ANALYSIS

M.M.Perevozchikov, I.B.Pirumov, B.S.Chrustalyov,
K.M.Ignatiev, A.Taha

Compresssor Department, Technical University of St.Petersburg.
St.Petersburg, Russia

ABSTRACT

The present paper deals with some aspects of reciprocating low flow (V<0.2 m3/min) compressor design for the high pressure gas- or air delivery systems.

We have developed two kinds of mathematical models for calculation the parameters of gas in elements of reciprocating compressor. The major differences of approaches and restrictions for engineering purposes are discussed and illustrated by some results of numeric experiment.

INTRODUCTION

The application of the mathematical models makes it possible to investigate into the thermodynamical and gasdynamical processes in the reciprocating and rotary special-purposed compressors for gas- or air delivery systems.

Fig.1 presents the investigated double-staged reciprocating air compressor with discharge pressure of 65 bar. The main features of this kind of compressors are small dimensions (Dc < 40 mm) highly efficient low volume (Vcool < 0.3 Vst) interstage gas coolers, low number of stages (2-3) with pressure ratio within one stage up to 8 and more, sophisticately profilled flexible plates of the valves, sometimes without restrictors. Below are shown some results of mathematical modelling and the comparison of different kinds of models.

MATHEMATICAL MODELS

1. Model of the first kind.

It is well known that traditional methods of reciprocating compressor design are based on the rough mathematical models that deal with polytropic compression and expansion processes and isobaric suction and discharge processes. The loss in the valves and communicating pipelines are supposed to be constant depending on average gas velocities. The values of gas pressure and temperature are obtained with the help of a number of integral equations, comprising the parameters of a gas in different points of the pressure-volume diagram.

Fig.2 presents superimposed pressure-volume diagrams for the first and the second stages of a reciprocating compressor with a ratio Vcool / Vst1 = 0.3 (the pressure loss at suction and discharge is ta-

ken into consideration). The compressor discharge pressure is 65 bar, and the compressible gas is assumed to be perfect. We suppose that the process of heat exchange in the interstage gas cooler takes place only along the 2 - 2' line under constant specific volume until the temperatures of the gas and the cooling media level. In point 1 the gas in the cylinder of the first stage instantly mixes (adiabatically) with a portion of gas left in the cooler and the discharge valve opens.

Fig.3 shows that the discharge process from the first stage and the second stage suction are not the isobaric (p2 >> p1) throughout the investigated range of the ratio A. It should also be noted that the temperature T3 much decreases due to the effect of gas expansion and cooling during suction process, and therefore the compressor discharge temperature also decreases. The character of the ratio A influence on the temperatures (T2, T2' and T3) leads to conclusion that interstage gas heat exchanger can work either as gas cooler or as gas heater.

The slight power consumption increase at low values of A is not essential. Thus the design of a special-purposed reciprocating compressor requires taking into consideration the interstage communication volumes as well as other constructive parameters.

Unfortunately this kind of mathematical models does not deal with a number of very important aspects of actual working cycle. For example, the real values of the polytropic numbers could hardly be properly estimated because of the simultaneous effects of mass- and heat transfer during the processes 1-2, 2-2', 2'-3 (fig.2). The valve dynamics (especially when the flutter occures) is also out of consideration, and it is so far impossible to estimate the exact power consumption at the first stage discharge and the second stage suction processes because of considerable varying of gas parameters. It is neccessary to modify the mathematical model to overcome these problems.

2. Mathematical model of the second kind

The flow passage of reciprocating compressor is supposed to consist of a series of vessels of either constant or variable volume, pipelines and other communication units such as self-acting valves, control valves and safety valves that could be regarded as concentrated aerodynamic resistors. The gasdynamics equations in partial derivations and thermodynamics equations in differential form should be applied to describe the unsteady flow.

On the basis of our experimental and theoretical researches we came to the conclusion that under certain conditions (cycle frequency less than 25-30 Hz, and no resonant pressure and velocity pulsations in the pipelines) the working processes can be regarded as the quasi-static ones.

Assuming this character of processes we have developed the mathematical model of the second kind. The parameters of gas in vessels are obtained by solving the thermodynamic differential equations, while gas velocities in elements of communications are determined by pressure differences using the steady flow equations with experimentalloss coefficients. The mathematical model deals with each element of the flow passage (block) in particular. Gas leakages through piston seals and valves are omitted. The

compressible gas is perfect. To each block the followig equations can be applied:
Energy equation

$$\frac{dU_j}{d\varphi} = \frac{\alpha}{\omega} F_j (T_{wj} - T_j) + \frac{i_{j-1} m_{j-1}}{\omega} - \frac{i_{j-1} m_{j-1}}{\omega} - P \frac{dV_j}{d\varphi} \tag{1}$$

Mass flow equation

$$\frac{dM_j}{d\varphi} = (m_{j-1} - m_j) \frac{1}{\omega} \tag{2}$$

Gas density is obtained from

$$\rho_j = \frac{M_j}{V_j} \tag{3}$$

Caloric equation

$$f_1(P,T,U) = 0 \,, \; T_j = \frac{U_j}{c_v} \tag{4}$$

Gas state equation

$$f_2(P,\rho,T) = 0 \,, \; P_j = \rho_j R T_j \tag{5}$$

Enthalpy is obtained from

$$i_j = c_p T_j \tag{6}$$

Heat transfer coefficient α and wall temperature Tw are independent of time and estimated either by experimental data or by generally known methods using average mass flow through the gas cooler.

The mass flow through the j-th element of communications is obtained by following equations:
if $P_j > P_{j+1}$

$$m_j = \mu_j \rho_{j+1} F_j \sqrt{\frac{2(P_j - P_{j+1})}{\rho_j}} \tag{7}$$

or

$$m_j = \mu_j \rho_{j+1} F_j \sqrt{\frac{2k}{k-1} R T_j \left(1 - \left(\frac{P_{j+1}}{P_j}\right)^{\frac{k-1}{k}}\right)} \tag{8}$$

if $P_j < P_{j+1}$

$$m_j = 0 \tag{9}$$

The passage area of a valve at any time is defined by differential equation of valve dynamics. We have found out that the majority of valves can be regarded as single-mass system, and the corresponding equation (for discharge valve) is as follows:

$$F_j = l_j h_{j\max} \chi_j \tag{10}$$

$$\frac{d^2\chi_j}{d\varphi^2} = B_j \xi_p (P_j - P_{j+1}) - \nu_j^2 (\chi_j + \chi_{oj}) - \eta \frac{d\chi_j}{d\varphi} \tag{11}$$

It should be noted that all the neccessary integral characteristics of compressor (power consumption, temperature, flow rate etc.) are obtained as well.

RESULTS

Fig.4. presents some results of numeric experiment variants. They demonstrate the possibilities of the question. First, the unusual perfomance of the second stage discharge valve was observed. It closes prematurely and opens soon afterwards for very short phase of dischaarge due to the influence of valve chamber volume. Secondly, the simultaneons effects of unsteady heat- and mass transfer in outlet gas cooler cause under certain conditions the reverse flow in the discharge pipeline. The analysis of interstage cooler volume influence on the perfomance of compressor confirms in general the data shown on fig.3.

CONCLUSIONS

It was proved that the proper design of a reciprocating compressor can be carried out only with help of detailed mathematical model of the second kind.

The considerable decrease of compressor discharge temperature can be achieved by proper selecton of the interstage gas cooler volume.

The interstage communication volumes are much fluent on the whole compressor perfomance (especially the valve perfomances) and should not only be taken into consideration but thoroughly calculated.

It was shown that under certain conditions the gas coolers of both stages can work either as gas cooler or gas heater. There is a possibility of reverse flow achieving as much as 20 % of the direct flow maximal speed.

NOMENCLATURE

P	pressure
T	temperature
ρ	density
U	internal energy
M	gas mass
D	cylinder diameter
i	enthalpy
φ	crank angle
F	heat transfer surface
V	volume
m	mass flow
ω	angular speed
α	heat transfer coefficient
R	gas constant
C_v	specific heat at constant volume
C_p	specific heat at constant prassure
l	valve perimeter
μ	valve flow coefficient
ξ	flow force coefficient
B	gas force complex
ν	kinematic viscosity

χ dimensionless valve plate lift
χ_o predeformation of valve spring
h_{max} maximal valve plate lift
η aerodynamic damping coefficient
k isentropic coefficient (C_p / C_v)
$A_1 = V_{cool} / V_{st1}$
$A_2 = V_{st2} / V_{st1}$

SUBSCRIPTS

st - stage
cool - cooler
c - cylinder
w - wall

REFERENCE

1. Frencel M.I. "Reciprocating Compressors", Mashinostrojenije, Moscow, 1969.

2. Fotin B.S.,Pirumov I.B."Reciprocating Compressors",Mashinostrojenije, Leningrad,USSR, 1987.

3. Pirumov I.B."Valve of Reciprocating Compressor. Simulation and Optimisation",Transactions of the LPI, Leningrad, USSR, N 384, PP 83-91,1982.

4. Pirumov I.B.,Chrustalyov B.S. "Problems of dynamic valve investigations", CINTICHIMNEFTEMASH, N 306/76, USSR, 1976.

5. Ignatiev K.M., Perevozchikov M.M. "Hardware and Software Development of Experimental Reciprocating Compressor Computer" Proc. of the VI conference of compressor reseach, disign and thechology, Kazan, Rus sia,1991.

6. Perevozchikov M.M. "CAD for Development Low Flow Reciprocating Compres sor", Proc. of the VI conference of compressor reseach, design and thechnology, Kazan, Russia, 1991.

7. W.Soedel. Introduction to Computer Simulation of Positive Displacement Type Compressors. 1972 Shot Course Text, Rey W. Herrick Laboratories.

8. Kakuda M.,Kitora Y.,Hirahara T.,Yamamoto T.,"Investigation of pressure Pulsation in Suction Pipe on Rotary Compressor ", Purdue University, School of Mechanical Engineering, 1988.

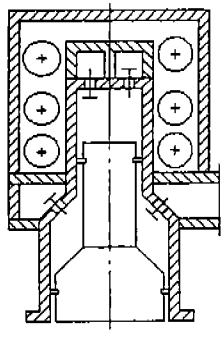

fig.1 The schematic view of the double stage compressor.

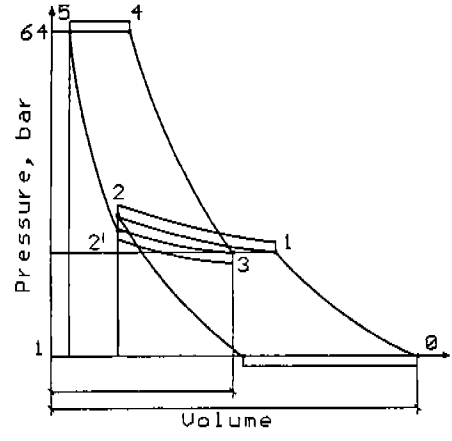

fig.2 Theoretical pressure-volume diagram.

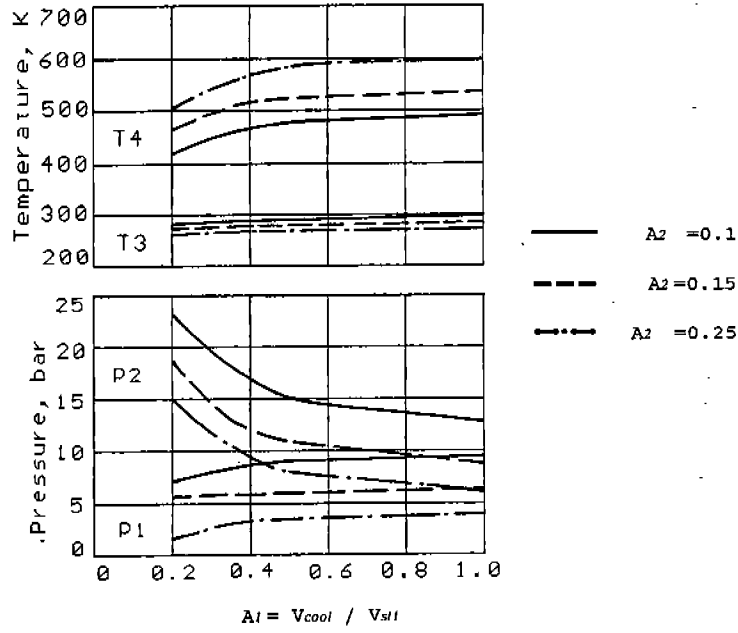

fig.3 Effect of cooler volume on the maximal and minimum pressure and temperature.

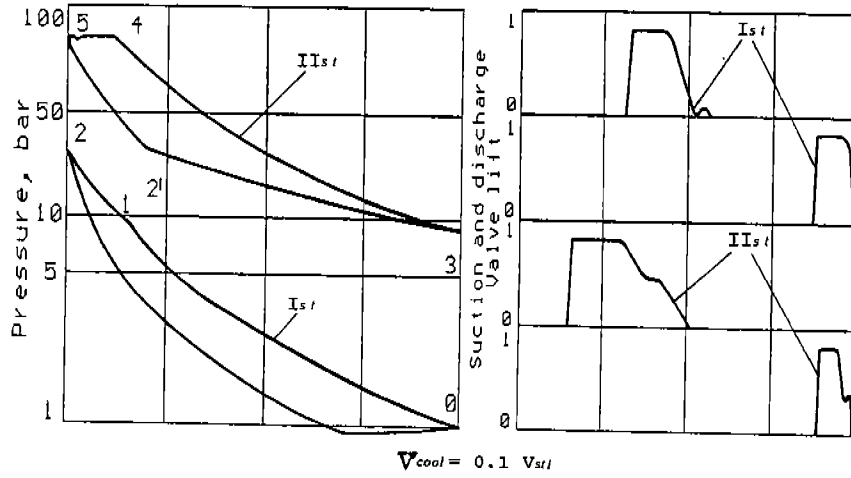

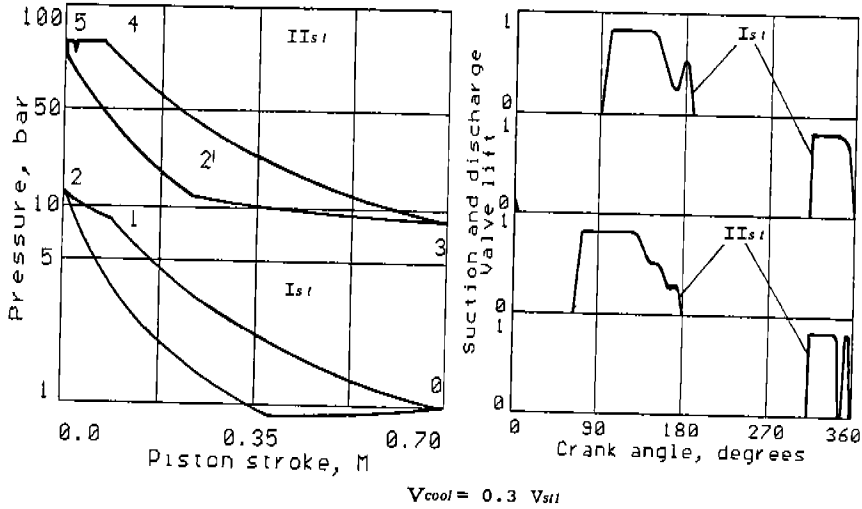

fig.4 Effect of volume cooler on the working processes.

THE EVOLUTION OF THE HIGH EFFICIENCY TWO-POLE HERMETIC COMPRESSOR

Herbert Siewert
Tecumseh Products Company

INTRODUCTION

During the last 30 years, there has been a 30% increase of efficiency of two-pole hermetic compressors. This improved performance has been in response to marketplace requirements and Government legislation. Throughout this evolution, there has been a noteworthy increase of the compressor reliability while sound and economic values have remained constant.

Presented in this paper is a tracking of this history. The increased efficiency has not been the result of improvements in any singular component. It has occurred due to small improvements in all components of the compressor. Discussed here-in are the changes of these components (ie. valving, lubrication, motors, flow path, materials, internal heat exchange and machining tolerances) and how these changes affected the overall performance of the compressor.

VALVING

The valving of a hermetic refrigeration compressor is probably the most important singular design item of the compressor. Although volumes of work have been applied to valve design, a direct approach for a universal solution has not been revealed. The early design goals were to achieve a reasonable life in bending fatigue, impact and fluid abuse while maintaining maximum flow rate requirements. The pressure drop, or efficiency of the valving system, was considered of less importance. Compressor designs with high bore/stroke ratios were favored because they resulted in sufficient cylinder cross-sectional areas for reasonable valve porting. Suction ports were normally two to three times larger than the discharge ports.

This ratio is approximately the same as the ratio of suction gas density to discharge gas density. Possibly ignored was the fact that the valve open period had a greater ratio (suction period to discharge period). This resulted in discharge valve systems having pressure drops nearly four to five times as great as the suction valve system pressure drops (1). Most early designs were either ring valves with the suction ports surrounding the discharge ports, or beam suction valves with cantilever discharge valves.

Valve design analytics were based upon the solution of second derivative displacement distribution strain equations (2). The equations ignored dampening effects (stiction) and valve inertia contributions. The flow analysis of the valving system was often based upon incompressionable fluid flow through a group of orifices. This type of analysis did not include gas dynamics or time dependent variable flow passages. These omissions, plus the affects of complex shapes, severely reduced the accuracy of the analysis.

Current valve design methodology utilizes finite element analysis techniques which result in improved predictions of dynamic valve stress levels and valve shape predictions. Shape predictions are extremely important in defining the actual, instantaneous flow areas and, thus, the pressure losses of the transient mass flow.

From these studies, it has become more and more evident that the perimeter of a valve may be of greater importance than the valve plate port area. The importance of the perimeter is readily evident when including valve lifted shape in determining the peripheral area for flow energy loss determination.

Valve action is controlled by aerodynamic drag forces, valve inertia, spring forces, fundamental resonances, gas dynamics, physical shape and stiction. Valve action analytical studies must include these items, as well as flow and dynamic performance predictions (3). Flow equations should predict the energy losses due to flow restriction. Dynamic equations should predict the time related motion of the valve. Dynamic predictions will also determine the maximum expected stress levels and instantaneous flow passages for flow energy loss predictions.

Modern valve analysis techniques for the above should include the following:

A. Modal analysis determination for natural mode shapes. These modal shapes determine the instantaneous flow passage areas.

B. Stiction of the valve to the valve plate and/or backing plate. Stiction is the dampening parameter of valve dynamic calculations. This dampening affect will the delay the valve opening and closing. These delays can result in back flow through the valve and loss of valve efficiency (4).

C. The inertia of the valve has major effects on opening and closing timing. Inertia has similar effects as stiction (ie. motion delays).

D. The valve contour is naturally needed when determining the modal shape. Alteration of the contour may be used to alter the modal shape and optimize the peripheral flow area between the valve and valve plate.

E. Though often very difficult to analyze, passage acoustical tuning can seriously affect the overall efficiency of a valving system. The timing of peak pressure waves with respect to valve opening can result in appreciable increases of cylinder entrance and exhaust flow.

LUBRICATION

The lubrication system of a compressor is, naturally, a very major item in the control of unwanted power consumption. The lubrication system will affect the peripheral losses by controlling the bearing friction. It also has a significant affect upon windage losses, cylinder friction losses and oil pump losses. Each of these items are more fully discussed in the following.

Bearing friction is a function of the oil viscosity, shaft speed and bearing load [(see figure below (5)].

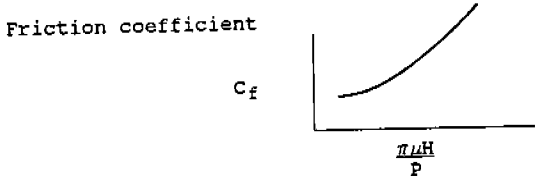

Friction losses are the result of viscous shear in the bearing oil interface and may be further defined as: $H_p = \frac{2\pi^3 \mu N^2 D^3 L}{C}$

From this, we see that the shear losses are directly proportional to the oil viscosity, vary with the second power of the shaft speed and the third power of the shaft diameter. They are also inversely proportional to the diametrical clearance when the clearance is established with respect to the required minimum oil film thickness. The lower viscosities will have a negative affect upon the load carrying capacity of the bearing

Oil viscosity is the load-carrying element in the selection of a bearing. In each application, the viscosity of the oil at the operating condition must be determined. This operating oil viscosity will then reveal whether sufficient minimum film thickness is present to support the load without asperity contact. The lower the oil viscosity, the lower the bearing viscous losses. Higher bearing temperatures result in lower viscosities. Early compressors applied oils having viscosities as high as 450 SUS, where a more current compressor utilizes oils of 150 SUS.

The shaft speed in most current compressors is nearly constant (3,500 rpm) and is, therefore, not a consideration in performance improvement to date.

The bearing diameters may have major effects on the total bearing friction contribution. This is readily seen with the third order relationship to the bearing friction losses. Adjustment of bearing diameter and bearing length (first order losses) for a given load may well result in optimizing for minimum bearing losses.

Permissible minimum oil film thickness is generally considered as a function of the opposing surface finishes. The asperities of these surfaces must be separated by the oil to have minimum friction losses. The combined finish, times a factor of 4 to 10, is normally used for a minimum thickness guideline. The total area of the asperities is the primary supporting element of the bearing. This area, related with the oil film pressures (ie. viscosity), result in the support without contact of the bearing load.

The lubrication system also becomes a major factor in controlling the friction losses of the cylinder/piston operation. Sufficient oil must be present to control these cylinder losses. Operating loss studies of reciprocating engines have shown that these cylinder loses are "number one" in the overall engine losses (6). The major contributors to cylinder losses are piston ring and piston skirt friction.

Piston ring friction losses have been defined by Stribeck as a direct function of oil viscosity and piston velocity. It also has an inverse relationship with the ring load. Piston skirt (body) friction follows a very similar relationship as ring friction where the ring load is supplemented with piston side loading. Interfacial oil film shear losses will, again, be a direct function of surface finish and clearance.

Total lubrication system oil pumping power requirements are separate and additive to the internal compressor losses. Oil circulation controls the operating bearing temperatures and also affects the windage losses. Oil pump power is $H = PQ/K\mu$, where P is the pumping pressure rise, Q the oil flow rate, K the pump efficiency and μ the oil viscosity. Naturally, excessive oil pumping for either bearing viscosity control or for the control of compressor sound levels will result in unwanted power inputs.

Although internal cranking windage losses are not a major item in determining overall compressor losses, they should be included in design considerations. These losses have been defined not only as a function of the frontal areas of the moving components, but they are affected by the oil entrainment within the cranking cavity (6).

$$H_w = \frac{Pv^2CdA}{2}$$

The density of the cranking cavity gases is directly affected by the oil gas entrainment. An increase of 10% of the oil entrainment can result in major increases of windage losses. Windage losses may outweigh friction losses if the cranking cavity oil concentration is excessive.

Overall oil entrainment in the pumped mass flow also affects the total refrigerant pumping ability of the compressor. Also, high oil pumping rates (greater than 2%) will affect system performance by reducing the heat transfer rates of the heat rejection surfaces.

MOTORS

As mentioned in the introduction, improvments in motor efficiency have been a significant contributor in the improvement of overall compressor efficiency. This is especialy true for a suction gas cooled motor where the motor losses directly cause an increase of suction gas temperature. A 20% increase of motor losses (2% reduction of motor efficiency) will result in a 14% increase of suction gas heating and a significant drop in compressor efficiency.

Single-phase motor efficiencies of 78-82% were considered quite acceptable in the early 1970's. Current high efficiency compressors have motor efficiencies in the range of 86-90%. Motor improvements that have yielded this increase are discussed below:

1. Low Loss Lamination Steel - Improved quality and reduced thickness of motor lamination steel has resulted in reduction of core losses of the laminations. Standard lamination steel has a core loss of approximately 2.7 watt/lb, while a high quality steel has a core loss of 1.7 watt/lb.

2. Lamination Insulation - Improvements in the electrical insulation between core laminations (either oxides or bondings) have resulted in reduced core eddy current losses.

3. Phase Separator and Slot Liner Insulation - Improvements of these insulations have allowed for improvement of slot fill for higher density more efficient coils.

4. Coil Compaction - Improved manufacturing methods of placing and compacting magnet wire in the slots have yielded higher density fills. High density filling has resulted in higher flux densities for the same quantity of wire (constant electrical losses), resulting in improved efficiencies.

5. Improved Magnet Wire Coating - Improved wire varnishing systems to the current two coat polyesterimide coating has also contributed to the increased slot fill of Item 4.

6. Increased Stack Height - The tendancy in higher efficiency compressors has been to apply longer stack motors for the same maximum running torque, which results in improved motor efficiency.

7. Reduced Rotor Fans - Improvements compressor efficiencies have reduced the amount of forced cooling required to maintain reasonable motor temperatures. With this reduced need for cooling, the motor windage losses have been reduced by the application of smaller rotor fans.

FLOW PATHS

Gas flow pressure losses through a compressor must be minimized to realize high efficiencies. Reduced flow restriction is often counter productive in achieving low sound levels and reduced pressure peaks. To have the best of both worlds, some of the following design techniques are being applied:

1. Through-flow side band and Helmholtz resonators for sound control. These are replacing the high flow resistance impedance muffling systems.

2. Through-flow resonance chambers for discharge pressure pulse control.

3. Increased valve travel for reduced value losses.

4. Enlarged valve ports for reduce passage losses.

5. Increased shockloop sizes for reduced pressure drops.

6. Tuned discharge systems for reducing discharge pressure pulse levels without high impedance losses.

7. Balanced flow losses of the section passages and discharge passages.

8. Non-flow restrictive motor cooling.

9. Non-restrictive liquid refrigerant scheduling.

10. Dynamic gas pressure recover.

MATERIALS

Although generally overlooked, the proper selection of materials is having important effects upon the improvement of compressor efficiency. Proper material selection can affect the motor efficiency, reduce internal heat transfer, reduce friction losses and affect dynamic responses. Some areas in which proper material selection has been effective in increasing the overall efficiency of the compressor are:

1. Low loss motor lamination steel.

2. Improved bearing materials (ie. bronze vs. aluminum; pheneolic thrust plate material; coated shafts).

3. Low thermal conductivity barriers between suction and discharge gas passages.

4. Low thermal conductivity valves.

5. Oil additives for reduced friction.

6. Improved motor insulation systems (wire coating, phase separators and slot liners).

7. Improved cutting tool material for improved finishes.

INTERNAL HEAT EXCHANGE

The transfer of heat within a compressor has been found to have major effects not only upon the compressor's capacity, but also upon its efficiency (7). Energy requirement per unit of mass flow increase with the temperature of the mass. With this in mind, control of the suction gas temperature is very essential in maintaining or increasing efficiency levels. Items which affect the suction gas temperature are:

1. Gas Passage Heat Interchange - The use of common manifolds or castings for routing the refrigerant to and from the cylinder may result in internal heat transfer from the discharge gas to the suction gas. This internal heat transfer increases the suction gas temperature, which results in an associated loss of compressor efficiency.

2. Discharge Shockloop Oil Submersion - Routing the internal shock loop through the oil sump (possibly for driving dissolved refrigerant from the oil) increases the oil sump temperature. The increased sump temperature results in an increase of heat transfer to the suction gas blanking the oil. This results in an increase of the suction gas temperature and a loss in compressor efficiency.

3. Minor Internal Leakage - Assumed "minor" internal gas leakage from the discharge plenum to the suction gas can have severe affects upon the overall compressor efficiency. Some possible sources of these minor leaks are:

   A. Valve plate porosity
   B. Gasket permeability
   C. Piston dome porosity
   D. Porous braze joints
   E. Valve seat imperfection or roughness
   G. Piston blow-by

4. Motor Efficiency - See the section on "Motor Improvements.

MACHINING TOLERANCES

Improved machining tolerances have resulted in significant improvments in the general efficiency of compressors. These tolerance improvments have involved surface finish improvmeents (bearings, journals, cylinder bores), crankshaft alignment improvements, and out-of-round control (cylinder bores, journals and bearings).

The most significant of these is the improvement of the surface finishes. The roughness of bearing journals has been reduced from an average value of 30 micro inches to a plus three sigma limit value of 16. This 16 limit results in a maintaining an average value between 10 and 12 micro inches. Surface finish reductions directly result in reducing the friction power losses as noted in the section on "Lubrication".

Production crankshaft alignment has also been improved through the application of modern automatic assembly techniques. Improved alignment results in reduced main bearing power consumption and, thus, improves compressor efficiency.

SYMBOL DIRECTORY

μ	=	Viscosity
N	=	Shaft speed
D	=	Bearing inside diamter
L	=	Bearing length
C	=	Diametrical clearance
H_p	=	Bearing heat loss
P	=	Bearing load
H_w	=	Windage losses
P	=	Gas density
v	=	Piston velocity
A	=	Piston frontal area
C_f	=	Friction coefficient
H	=	Oil pump power
Q	=	Oil pump flow
K	=	Oil pump efficiency
C_d	=	Drag coefficient
V	=	Velocity

1. 1984 International Compressor Engineering Conference "Analysis of the Effect of the Compressor Kinematics on the Valve Losses", Prakash N. Pandeya

2. Proceedings of the 1974 Purdue Compressor Technology Conference, "The Prediction of Dynamic Strain in Ring-Type Compressor Valves Using Experimentally Determined Strain Modes", J. Adams, J. F. Hamilton, W. Soedel

3. Proceedings of the 1972 Purdue Compressor Technology Conference, "Review of Simple Mathematical Models of Values in Reciprocating Compressors", J. F. T. MacLoren

4. Proceedings of the 1974 Purdue Compressor Technology Conference, "Computer Simulation of Valve Dynamics as an Aid to Design", A. M. Bredesen

5. Lubrication, Vol. 59 1973, "Lubrication Fundamentals", R. S. Feim, Fred J. Villforth, Jr.

6. SAE Technical Paper Number 920482, "Engine Friction Modeling", Rob H. Thring

7. 1978 Purdue Compressor Technology Conference, "Improved Efficiency Compressors for Air Conditioning", Tara C. Kandpal

8. 1978 Purdue Compressor Technology Conference, "Dynamic Investigations of Suction Valves in a Small Refrigerating Compressor", Marian Luszczycki

9. 1984 International Compressor Engineering Conference, "Analysis of the Effect of the Compressor Kinematics on the Valve Losses", Prakash N. Pandeya

10. SAE Technical Paper Number 920482, "Engine Friction Modeling", Rob H. Thring

INDUCTION MOTOR MODELING USING COUPLED MAGNETIC FIELD AND ELECTRIC CIRCUIT EQUATIONS

Lee W. Marriott Glenn C. Griner

Tecumseh Products Research Laboratory
3869 Research Park Drive
Ann Arbor, Michigan 48108
(313) 665-9182

ABSTRACT

Traditional design/prototype/test cycles have improved the efficiencies of small induction motors to high levels. To achieve still higher efficiencies, motor performance must be studied in a more detailed and integrated manner. The authors present a nonlinear, time-dependent computer simulaton modeling the performance of a permanent-split-capacitor induction motor. The effects of nonlinear permeability and time varying terminal voltages are included in the model. Two-dimensional finite element magnetic field equations are coupled with the electric circuit equations and solved using the Newton-Raphson and Crank-Nicholson methods. The simulation predicts main and auxiliary winding currents, induced rotor currents, hysteresis losses and motor torque as functions of time. Due to the detailed nature of the results a deeper understanding of motor performance factors, normally difficult to determine, can be obtained.

INTRODUCTION

Induction motor design involves the prediction and evaluation of performance parameters such as torque, line current and losses at any given slip and terminal conditions. These parameters can be accurately determined only with knowledge of the magnetic field distribution within the machine. Approximate analytical methods [1] have been used in the past with some success. Continued pressure to conserve energy dictates improved motor performance. This requires an even more detailed knowledge of the magnetic fields occurring within motors. Two-dimensional stationary magnetic field problems have been investigated by many authors [2,3]. The nonlinear permeability or saturation characteristics of steel require iterative methods for the solution of these problems. Tandon, Armor and Chari [4] were first to combine the Newton- Raphson technique with the Crank-Nicholson central difference scheme to solve transient field problems in electrical machines. The disadvantage of these methods is that they rely on apriori knowledge of the currents or current densities in the device.

The problem is much more complicated when current densities are unknown and terminal conditions must be considered. Potter and Cambrell [5] combined a two-dimensional finite element field solution and circuit equations to simulate an induction motor. In their work the stator field was replaced with a current sheet at slip frequency. Strangas and Theis [6] also combined the finite element field solution with circuit equations to model a shaded-pole motor. Their approach used a time-dependent grid for rotor movement. This paper expands the above techniques to model a permanent-split-capacitor induction motor. The two-dimensional magnetic field equations are combined with electric circuit equations describing end and external effects. The partial derivatives

of the combined system of equations form a Jacobian matrix which is solved by the Newton-Raphson method for each time step. Equilibrium at each time step is obtained when the derivatives of the time-dependent nonlinear magnetic field equations are satisfied. The electric circuit equations are linear ordinary differential equations appearing as constants in the Jacobian matrix. The solution advances through time by updating the time dependent terms of the Jacobian matrix and corresponding right hand side. The Crank-Nicholson finite difference method, being an implicit method, requires an inversion to solve for the unknowns in the next time step. This inversion is carried out by a complex math "sky-line" linear equation solver.

MAGNETIC FIELD EQUATIONS

The solution of the magnetic field problem is based on three of Maxwell's equations and the magnetic and electric field constitutive laws. Neglecting displacement current these equations are:

$$\nabla \times H = J \tag{1}$$

$$\nabla \times E = -\frac{\partial B}{\partial t} \tag{2}$$

$$\nabla \bullet B = 0 \tag{3}$$

$$H = \nu B \tag{4}$$

$$J = \sigma E \tag{5}$$

Where H is magnetic field intensity, B is magnetic flux density, E is electric field intensity, J is current density, ν is reluctivity and σ is an effective conductivity.

A vector potential function A is chosen such that the following relationship is satisfied:

$$\nabla \times A = B \tag{6}$$

Combining equations (1) through (6) and introducing the gradient of the scalar voltage as shown in [12], yields the time-dependent magnetic field equation:

$$\nabla \times (\nu \nabla \times A) = -\sigma \frac{\partial A}{\partial t} - \sigma \nabla V \tag{7}$$

FINITE ELEMENT APPROXIMATION OF THE MAGNETIC FIELD

The finite element method was employed to approximate the magnetic field equations. Many authors have contributed to this methodology. Some of the earliest magnetics work is attributed to Silvester and Chari [2]. The basic assumption of the method is that the vector potential within a finite element can be approximated by a linear combination of shape functions:

$$A\left(\xi,\eta\right) = \sum_{i=1}^{n} N_i\left(\xi,\eta\right) A_i \tag{8}$$

Where N_i are shape functions and n is the number of nodes in the element. Examples of shape functions may be found in the text books of Zienkiewicz [7] or Bathe [8]. Using this approximation and the minimization of the energy functional, the assembled finite element magnetic field equations become:

$$[T]\frac{\partial A}{\partial t}+[S(A)]A-[N_w]V_w-[N_b]V_b=0 \qquad (9)$$

Where $[T]$ is the global conductivity matrix, A is the global vector of vector potentials, $\frac{\partial A}{\partial t}$ is a vector of time derivatives of A, $S(A)$ is a nonlinear global coefficient matrix, $[N_w]$ is a matrix of weighting factors which distribute and convert coil voltages into element nodal current densities, V_w is the applied voltage across a length of coil lying within the lamination stack, $[N_b]$ is a matrix of weighting factors which distribute and convert rotor bar voltages into element nodal current densities and V_b is the applied voltage across a rotor bar length. The matrices and vectors given above are comprised of an assembly of element matrices, the details of which can be found in reference [12].

ELECTRIC CIRCUIT EQUATIONS

The electric circuit is characterized by two linear differential equations. The first equation sums the voltages along a rotor bar or coil and can be written as:

$$V_{applied}=V_{induced}-IR \qquad (10)$$

Where I is the current, V is voltage and R is a bar or effective coil resistance. The induced voltage along a length of a coil or rotor bar is:

$$V_{induced}=\frac{L}{A_c}\int\frac{\partial A}{\partial t}\,dS \qquad (11)$$

Substitution of the induced voltage (11) into equation (10), dividing through by the resistance and introducing $\frac{\partial A}{\partial t}$ as a vector of nodal vector potential time derivatives yields a first order differential equation which is coupled to the magnetic field equation (9).

$$-[N]\frac{\partial A}{\partial t}+\frac{\sigma A_c}{L}V-nI\bar{n}=0 \qquad (12)$$

Where $[N]$ is a matrix of Newton-Cotes integration factors, A_c is the area of a conductor, L is the length of the conductors, n is the number of conductors and $\bar{n}$ is a current direction vector for the winding.

It should be noted that this equation is dependent on the solution of the magnetic field equations for the values of $\frac{\partial A}{\partial t}$ and assumes that the applied voltage V is uniform across a coil or a rotor bar. The second equation is based on Kirchhoff's law as applied to a winding:

$$\Sigma nV\bar{n}+IR_e+L_e\frac{\partial I}{\partial t}+\frac{1}{C_{ext}}\int Idt=V_T(t) \qquad (13)$$

Where n is the number of conductors, V is the individual coil voltage, R_e is the end resistance, L_e is the end inductance, C_{ext} is the external capacitance, $\bar{n}$ is a direction vector, $V_T(t)$ is the time-dependent terminal voltage and Σ is a summation over the number of coils contributing to a winding. Notice that this equation is coupled to the first circuit equation (12) but does not directly influence the magnetic field equations. Note also that any other external impedances in series with the winding could be added to equation (13). Equations similiar to equations (12 and 13) can also be written for the rotor. Using the

method of rotor representation used by Strangas and Theis [6], rotor end ring currents and voltages are solved for rather than rotor bar voltages and currents. Rotor bar currents are then computed by summation of the appropriate end ring currents.

CRANK-NICHOLSON METHOD

The Crank-Nicholson method [9] is a numerically stable implicit central-difference scheme in which the basic assumption is:

$$A^{n+1} = A^n + \frac{\Delta t}{2}\left[\frac{\partial A^{n+1}}{\partial t} + \frac{\partial A^n}{\partial t}\right] \tag{14}$$

Combining equations (9), (12), (13) and (14) for the present (n) and future ($n+1$) time steps as shown in [12] yields the coupled finite difference magnetic field and electric circuit system of equations:

$$\begin{bmatrix} \nu[S] + \frac{2}{\Delta t}[T] & -\frac{\sigma}{L}[N_1] & 0 \\ -\frac{2}{\Delta t}\sigma[N_1]^T & \frac{\sigma A_c}{L} & -n\,\bar{n} \\ 0 & -n\,\bar{n} & -\left(Re + \frac{2}{\Delta t}Le + \frac{\Delta t}{2C_{ext}}\right) \end{bmatrix} \cdot \begin{Bmatrix} A^{n+1} \\ V^{n+1} \\ I^{n+1} \end{Bmatrix} =$$

$$\begin{bmatrix} \left[-\left[S(A) + \frac{2}{\Delta t}[T]\right]A^n\right] - [Nw]V_w^n - [N_b]V_b^n \\ \frac{2}{\Delta t}\sigma[N_1]^T A^n - \frac{\sigma A_c}{L}V^n + nI^n\,\bar{n} \\ -nV^n\,\bar{n} - \left(Re + \frac{2}{\Delta t}Le + \frac{\Delta t}{2C_{ext}}\right)I^n + V_T^{n+1} + V_T^n + \frac{2\Delta t}{C_{ext}}\sum_{i=1}^{n} I_i \end{bmatrix} \tag{15}$$

NEWTON - RAPHSON METHOD

Due to the nonlinearity of the $\nu[S]$ matrix, the finite difference system of equations must be solved using a nonlinear equation solution technique such as the Newton-Raphson method. The Newton-Raphson method is used to find equilibrium at each time step. The method is shown in the following equations:

$$\left[\frac{\partial \Psi}{\partial Var}\right]\{\Delta Var\} = \{-\Psi\} \tag{16a}$$

$$\{Var\}_{i+1} = \{Var\}_i + \{\Delta Var\} \tag{16b}$$

Where $\{\Psi\}$ is the nonlinear homogeneous equation to be solved, $\left[\frac{\partial \Psi}{\partial Var}\right]$ is the assembled Jacobian matrix rendered symmetric by algebraic manipulation of equation (15), $\{Var\}_i$ is a vector of solution variables from the previous iteration, $\{Var\}_{i+1}$ is a vector of solution variables at the new iteration and $\{\Delta Var\}$ is a vector of corrections.

The Newton-Raphson method requires repeated inversion of the nonlinear Jacobian matrix. Since the Jacobian is not positive definite, a complex math "skyline" solver was used for inversion. During each iteration the ΔVar is solved for and used to update the prediction for the unknown variables.

TORQUE

Motor torque computation using finite element methods commonly relies either on the use of the Maxwell stress tensor or the virtual work principle. The stress tensor method requires several layers of air gap elements in order to obtain accurate values of the tangential flux density. The virtual work implementation normally requires two finite element solutions whose meshes are displaced a small rotation from each other. A more elegant virtual work method was developed by Coulomb and Meiner [10]. Their method requires only a single layer of elements in the air gap and one finite element solution at each time step. The magnetic energy expression is differentiated mathematically with respect to rotation before integration over the solution space and results in the following equation for the torque contribution per unit depth of each virtually distorted element in the air gap:

$$Te = -\nu_a \left[B_X \frac{d}{d\theta}\left[\sum_{i=1}^{n} \frac{dN_i}{dY} A_i \right] + B_Y \frac{d}{d\theta}\left[\sum_{i=1}^{n} \frac{dN_i}{dX} A_i \right] \right] A_e - \left(\frac{\nu_a}{2}\right)\left[\frac{B^2}{|J|} \frac{d|J|}{d\theta} \right] A_e \qquad (17)$$

Where ν_a is the reluctivity of air, B_X, B_Y are the X and Y flux densities, θ is angular rotation, B^2 is flux density squared, A_e is the element area, $\frac{dN_i}{dY}$, $\frac{dN_i}{dX}$ are derivatives of the shape functions N_i, A_i are nodal vector potentials and n is the number of nodes in the element. Additional details of the method can be found in [10] and [12].

RESULTS

Transformer

For three reasons a transformer was selected as a model to test the computer simulation. First, a transformer is similiar to an induction motor at standstill. Therefore the generated code would be directly applicable to a motor. Second, an isolation transformer of known contruction details was available for experimental verification. Third, the transformer lends itself to a simple mesh which can be easily modified or refined as required. The transformer was a 1.2 KVA, 120 Vac, 60 hertz model with a turns ratio of 1.1 (secondary to primary) and constructed of Arnold Technologies, Inc. M-22 steel. B-H points for the steel were selected from a published curve and a ν-versus-B^2 curve was fit using cubic splines [11]. The finite element grid for one-quarter of the transformer consisted of 216 triangles and 125 nodes and the time step used was one-sixtieth of a second. Approximations for the end leakage reactances were obtained from no-load and shorted-secondary tests. The transformer model was tested under three conditions: at no-load (i.e., with secondary winding open-circuited) for computation of the magnetizing current; with shorted-secondary to predict induced voltages and currents; and with a purely capacitive secondary load. A ramped sinusoidal voltage was applied to the model to minimize the startup transient of the solution, permitting steady state to be achieved in about 2-1/2 electrical cycles. Figure 1 shows steady-state computed and experimental results for the magnetizing current of the transformer. Differences in the current waveforms are due to hysteresis effects which are not modeled. The experimental and calculated RMS values of magnetizing current are 0.84 and 0.73 amps, respectively. In the shorted-secondary test, a voltage of 3.87 volts RMS was applied. The experimental primary and secondary currents are 11.5 and 10.6 amps; calculated values are 11.5 and 10.4 amps. These results demonstrate that the method of calculating induced voltages and currents is valid.

The most interesting results on the transformer were obtained using a capacitive secondary load of 25 microfarads. Figures 2 and 3 show the primary and secondary currents for the transformer. A pronounced second harmonic caused by resonance occurs in the primary current and is properly modeled. Surprisingly, secondary current remains essentially sinusoidal and is also modeled well. A summary of the experimental and modeled results for the transformer for the three load cases is given in Table 1.

Table 1. Transformer - Three Load Cases

Load Condition	Input Voltage (Volts)	RMS Current (Amps)				RMS Output Voltage (Volts)	
		Predicted		Measured		Predicted	Measured
		Prim.	Sec.	Prim.	Sec.		
No Load	120	0.84	-	0.73	-	131.9	132
Shorted Sec.	3.87	11.5	10.6	11.5	10.4	-	-
25 Mfd Cap.	120	0.83	1.24	0.83	1.25	130	132

AC Induction Motor - Locked Rotor

A two-pole permanent-split-capacitor motor was also modeled. The stator has 24 slots and the rotor 34 bars. A finite element grid composed of 3464 triangles and 1761 nodes was used for the model. The input for the model was again a ramped sine wave voltage with time steps of one-sixtieth of a second. An outline of the motor lamination and resulting vector potential contours (flux lines) is shown in Figure 4. For reference, the main winding axis is located along the horizontal and the auxiliary winding axis along the vertical. The vector potential contours are shown at one instant in time for the locked rotor condition. A series of figures over one electrical cycle would show the contours rotating and changing in magnitude as the magnetic field revolves within the motor. The plotted vector potential is the resultant of both winding currents and currents induced in the rotor.

AC Induction Motor - Moving Rotor

The final step in code development was the creation of a time-dependent mesh to permit the rotor to rotate and to be automatically reconnected to the stator through the airgap mesh. Because the rotor nodes are moving in their own coordinate system, it is unnecessary to add the speed voltage term to Equation (8) with this technique. The solution procedure is conceptually simple but involves much bookkeeping. At each time step the nodes in the rotor are incremented through a small angle, the airgap elements between the stator and rotor reconnected, the model bandwidth minimized, electric circuit equations added to the matrices and a Newton-Raphson iteration performed. Much smaller time steps were required than for the transformer or motor at locked rotor conditions. Steps corresponding to one or two mechanical degrees were required both for computational stability and for sufficient definition in plotted results. The mesh, nodal results (i.e., vector potential and vector potential derivatives), voltages across windings and winding and rotorbar currents at each time step after steady state is reached are saved for post-processing.

It is again noted that the solution of equation (15) is time-dependent in nature and several electrical cycles must be solved to allow any startup transients to die out. Our procedure was to set rotor rotation at the desired speed and then apply a ramped sinusoidal voltage to the motor windings for the first two or three electrical line cycles. Seven to ten additional line cycles were then required to reach a quasi-steady state solution, that is, where each succeeding cycle was approximately the same as the previous cycle. Cycles will not repeat exactly due to motor slip when running at other than synchronous speed.

Post-processing for each time step consists of calculation of the magnetic field intensity, eddy currents in rotor bars, motor torque and an instantaneous power balance for the motor. The power balance includes the rate of change of magnetic energy in the finite elements, the rates of change of energy in circuit inductances and capacitor, winding I-squared-R losses and eddy current losses in rotorbars, the sum of which must equal the instantaneous input line power. Power balances within a few percent were achieved.

Motor torque at each time step is computed using the virtual work principle described previously. In contrast to Strangas and Theis [6], who used an airgap mesh composed of elements which could stretch elastically, the authors found it necessary to "lockstep" the rotor to prevent element distortion during rotation. Element distortion drastically affects the magnetic energy in the element as the element area changes and prevents accurate torque calculation. The "lockstepping" technique consists of meshing the airgap with uniform elements and rotating the mesh an integral number of airgap elements at each time step.

Calculated results from the model are instantaneous values of flux density, rotor bar currents, torques, line, main and auxiliary currents and voltages, and many others. Air gap flux densities can be plotted to check winding distributions, torques examined for alternating components, eddy current losses checked in rotor bars, etc. A plot of input power and motor output torque is shown in Figure 5 which clearly shows the alternating torque characteristic of single-phase motors. Table 2 shows representative time-averaged results together with dynamometer data where available.

Table 2. PSC Induction Motor - 230 Vac Line Volts

	3600 RPM (Synchronous)		3500 RPM (Full Load)		2900 RPM (Breakdown.)		Locked Rotor	
	Measured	Predicted	Measured	Predicted	Measured	Predicted	Measured	Predicted
Torque*	-2.1	-2.1	67	67	158	156	13-15	11.7
Line Amps	1.26	1.36	10.2	10.3	-	41.9	58-62	60.2
Line Watts	172	150	2,363	2,365	-	8,113	-	8,521
Main Amps	5.07	5.14	8.1	8.1	-	41.8	-	62.7
Main Watts	-690	-711	1,575	1,561	-	7,711	-	8,466
Aux Amps	5.02	5.24	4.4	4.6	-	2.87	3.23	3.33
Aux Watts	860	861	794	804	-	402	-	55
Aux Volts	280	-	257	262	-	141	-	23
Cap. Volts	377	397	333	343	-	214	245	250

* Torque in Ounce-Feet (11.8 oz-ft = 1 nt-m)

The modeling technique inherently accounts for motor leakage reactances such as slot, belt and zig-zag leakages [1], but not end or skew leakage, which must be included in the circuit equations. Iron losses must also be separately included in the model, but are easier to estimate with the more complete knowledge of the magnetic field quantities. Friction and windage losses must also be separately considered and corrections made to calculated currents.

CONCLUSIONS

A method of modeling magnetic devices using a two-dimensional finite element approach coupled with electric circuit equations has been developed. The finite element solution yields the time-varying magnetic field solution within the device and the circuit equations account for both end effects and external circuit elements. The governing equations have been cast in a form that allows the forcing functions to be time-varying terminal voltages. Results give not only the magnetic field solutions for the entire device, but also permit calculation of eddy currents in conductors. Another result of the solution technique is that magnetic flux density variation is calculated in every element of the mesh. Both major and minor flux reversals are modeled which permits core losses to be estimated. Experimental and predicted results for a transformer and a permanent-split-capacitor induction motor both at standstill and with moving rotor have been presented. The model and experiment are in excellent agreement in all cases.

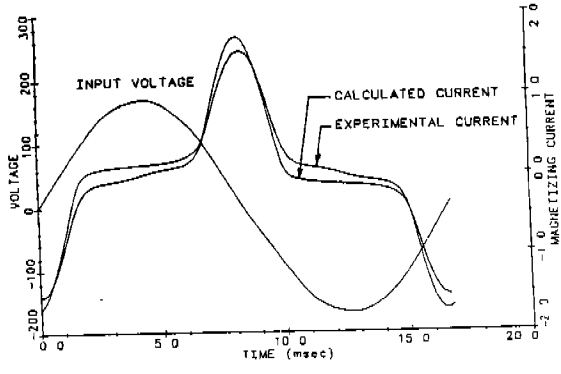

Figure 1. Transformer input voltage and magnetizing current versus time.

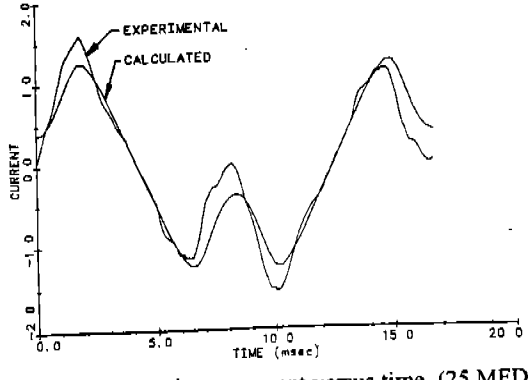

Figure 2. Transformer primary current versus time (25 MFD Capacitor).

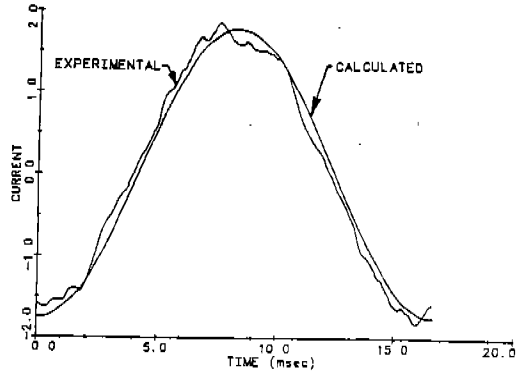

Figure 3. Transformer secondary current versus time (25 MFD Capacitor).

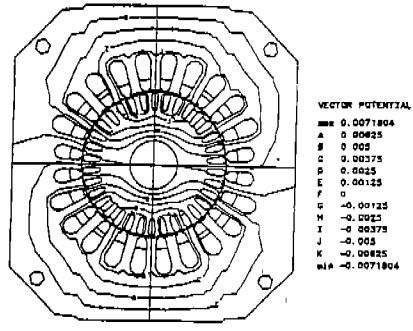

Figure 4. PSC induction motor vector potential contour plot.

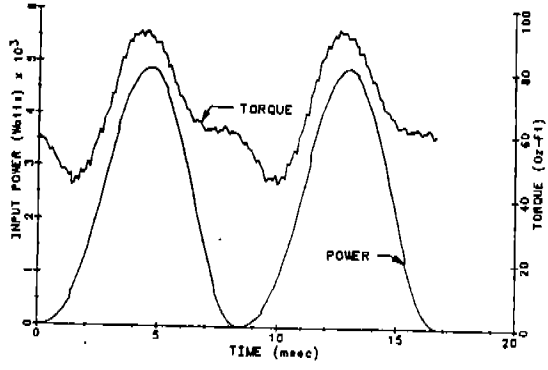

Figure 5. Calculated torque and power input for PSC induction motor.

REFERENCES

[1] C.G.Veinott, Theory and Design of Small Induction Motors, McGraw-Hill, New York, N.Y., 1959.

[2] M.V.K. Chari and P. Silvester, "Finite-Element Analysis of Magnetically Saturated D-C Machines," IEEE PES, Paper 71 TP3-PWR, 1971.

[3] S.R.H. Hoole, Computer-Aided Analysis and Design of Electromagnetic Devices, Elsevier, New York, N.Y., 1989.

[4] S. C. Tandon, A. F. Armor, and M.V.K. Chari, "Nonlinear Transient Finite Element Field Computation of Electrical Machines and Devices," IEEE Trans. PAS, Vol. 102 May 1983, pp. 1089-1096.

[5] P.G. Potter and G.K. Cambrell, "A Combined Finite Element and Loop Analysis For Nonlinearly Interacting Magnetic Fields and Circuits," IEEE Trans. MAG, Vol 19, No. 6, Nov. 1983, pp. 2352-2355.

[6] E.G. Strangas and K.R. Theis, "Shaded Pole Motor Design and Evaluation Using Coupled Field and Circuit Equations," IEEE Trans. MAG, Vol. 21, No. 5 Sept. 1985, pp. 1880-1882.

[7] O.C. Zienkiewicz, The Finite Element Method, Third Ed., McGraw-Hill, (UK), Berk shire, England, 1977.

[8] K.J. Bathe and E.L.Wilson, Numerical Methods In Finite Element Analysis, Prentice-Hall, Englewood, N.J., 1976.

[9] J. Crank and P. Nicholson, "A Practical Method for Numerical Solutions of Partial Differential Equations of Heat Conduction Type," Proc. Caub. Phil Solc. 43, 1947, pp.50-67.

[10] J.L. Coulomb and G. Meunier, "Finite Element Implementation of Virtual Work Principle For Magnetic or Electric Force and Torque Computation," IEEE Trans. MAG, Vol. 20, No. 5, Sept. 1984, pp. 1894-1896.

[11] P. Silvester, H.S. Cabayan and B.T. Browne, "Efficient Techniques for Finite Ele ment Analysis of Electric Machines," IEEE PES, Paper T73 301-0, 1973.

[12] L.W.Marriott and G.C.Griner, "Induction Motor Modeling Using Coupled Magnetic Field and Electrical Circuit Equations," Proc. of the 42nd Annual International Appliance Technical Conference, May 21-22, 1991, pp. 567-578.

TRANSMISSION LOSS AND BACK PRESSURE CHARACTERISTICS FOR COMPRESSOR MUFFLERS

by

H.J. Kim and W. Soedel
Ray W. Herrick Laboratories, School of Mechanical Engineering,
Purdue University, West Lafayette, IN 47907-1077, U.S.A.

ABSTRACT

Changing the typical definition of the transmission loss, which is the acoustic pressure amplitude ratio in a test arrangement consisting of anechoic pipes, the amplitude of the volume velocity ratio is recommended for transmission loss models of compressor mufflers. The theoretical calculation is based on the four pole parameter theory using the wave equation for each acoustic element. Transmission loss curves are plotted for typical silencer elements. Also, the amplitude and time lag of ratios of the pressure and volume velocity at the entrance of the muffler are shown, which can be used as indicators if the silencer is too restrictive to flow.

INTRODUCTION

This paper introduces a different definition of transmission loss compared to the typical one which is the acoustic pressure amplitude ratio [1].

The transmission loss is here defined as

$$\eta = \frac{Q_{in} - Q_{out}}{Q_{in}} \tag{1}$$

This definition has been used by the senior author and his students in the past, but not perhaps in the systematic presentation schema advocated here. In decibels, the transmission loss is

$$TL = 20 \log_{10}\eta = 20 \log_{10}\frac{Q_{in}}{Q_{out}} \tag{2}$$

The volume velocity has more physical meaning than the pressure in a compressor where the oscillatory valve flow is defined in terms of volume velocities.

Also, it is desirable to define the dynamic back pressures which develop in silencers and which may interfere with the proper operations of valves (valve flutter, energy loss). We define it in terms of the amplitude and time lag of ratios of the pressure and volume velocity at the entrance of the muffler, P_{in}/Q_{in}.

EXAMPLE CASE

Four Pole Parameters of Acoustic Elements

Two cases where harmonic volume velocities at the same frequency are defined at each end of a system are shown in Figure 2.

For example, the relationship between input pairs Q_{L1}, P_{L1} and output pairs Q_{L2}, P_{L2} of one acoustic tubular element, which has pipe length L_1, can be described as [2]

$$\begin{Bmatrix} Q_{L1} \\ P_{L1} \end{Bmatrix} = \begin{bmatrix} b_1 & b_2 \\ b_3 & b_4 \end{bmatrix} \begin{Bmatrix} Q_{L2} \\ P_{L2} \end{Bmatrix} = [B] \begin{Bmatrix} Q_{L2} \\ P_{L2} \end{Bmatrix}, \tag{3}$$

where $b_1=\cosh(\gamma L_1)=b_4$, $b_2=(j\omega A_1/(\rho C^2\gamma))\sinh(\gamma L_1)$, $b_3=((\rho C^2\gamma/(j\omega A_1))\sinh(\gamma L_1)$.

The four pole parameters of the second element can be described in the same way,

$$\begin{Bmatrix} Q_{L3} \\ P_{L3} \end{Bmatrix} = \begin{bmatrix} c_1 & c_2 \\ c_3 & c_4 \end{bmatrix} \begin{Bmatrix} Q_{L4} \\ P_{L4} \end{Bmatrix} = [C] \begin{Bmatrix} Q_{L4} \\ P_{L4} \end{Bmatrix}, \tag{4}$$

where $c_1=\cosh(\gamma L_2)=c_4$, $c_2=(j\omega A_2/(\rho C^2\gamma))\sinh(\gamma L_2)$, $c_3=(\rho C^2\gamma/(j\omega A_2))\sinh(\gamma L_2)$.

Combining Elements

Using boundary conditions which are $P_{L2}=P_{L3}$ and $Q_{L2}=Q_{L3}$, the four pole parameters of the whole system can be described by multiplying the two matrices. This results in

$$\begin{Bmatrix} Q_{L1} \\ P_{L1} \end{Bmatrix} = \begin{bmatrix} d_1 & d_2 \\ d_3 & d_4 \end{bmatrix} \begin{Bmatrix} Q_{L4} \\ P_{L4} \end{Bmatrix} = [D] \begin{Bmatrix} Q_{L4} \\ P_{L4} \end{Bmatrix}, \tag{5}$$

where [D]=[B]x[C].

Ratio Q_{in}/Q_{out}

If the end of the system has acoustic pressure release condition, the volume velocity ratio, which is the transmission loss, can be calculated.

$$Q_{in}/Q_{out} = Q_{L1}/Q_{L4} = d_1 \tag{6}$$

Back Pressure

The amplitude and time lag of ratios of the pressure and volume velocity at the entrance of the muffler are very important from the viewpoint of valve action and energy loss, and can be described in the same way :

$$P_{in} = P_{L1} = d_3 Q_{L4} = (d_3/d_1) Q_{L1} \tag{7}$$

$$P_{in}/Q_{in} = P_{L1}/Q_{L1} = d_3/d_1 \tag{8}$$

Presenting this information in a systematic way when classifying silencers is the main contribution of this paper. Even if the system of interest is composed of many elements, simple four pole parameters can be generated relating input and output.

TRANSMISSION LOSS CURVES FOR TYPICAL SILENCER ELEMENTS

In the following, dimensions L_1, D_1 and D_2 were kept constant unless stated otherwise. Numerically, they are : L_1=20 mm, D_2=4 mm, D_1/D_2=4. The speed of sound was C=140 m/s.

Figure 3 shows a typical expansion chamber-tail pipe design. It is noted that the silencer becomes effective above its cut-off frequency, which is a function of the tail pipe length L_2. The region of ineffectiveness in the vicinity of 1800 Hz for $L_2=L_1$ corresponds to the first organ pipe resonance in the tail pipe. The back pressure plot shows that the back pressure at the low frequency end of the plot (it is known that this is the region which controls valve motion restriction due to back pressure build-up) increases as the cut-off frequency is decreased, which illustrates the fact that acoustic criteria and valve energy efficiency are basically at odds. Of course, phasing of the back pressure is also important. Figure 4 shows what happens when the diameter of the expansion chamber is doubled. There is an improvement in transmission loss, because the cut-off frequency decreases and the magnitude of the transmission loss increases. The back pressure build-up is in general reduced, except in the vicinity of the lowered cut-off frequency. The effect of adding a second expansion chamber shows (Figure 5) approximately a doubling of transmission loss, but the cut-off frequency increases slightly. The back pressure behavior remains essentially unchanged. Adding a third expansion chamber (Figure 6) continues the trend. In Figure 7, the behavior of a side branch resonator is shown if it is attached simply to a pipe section without expansion chamber behind the valve. As one can see from the back pressure build-up, this is essentially an undesirable design. It is necessary to provide for an expansion chamber behind the valve. This is illustrated in Figure 8, where two arrangements of the side branch resonator are explored. Figure 9 answers the question whether there is an advantage in dividing the original expansion chamber of Figure 3. From a transmission loss viewpoint, this is indeed the case (except that the cut-off frequency is higher), but the back pressure build-up is much increased.

CONCLUSIONS

A different way of characterizing silencers for compressors was advocated again, which utilizes a transmission loss definition based on harmonic volume velocity reduction. This is in contrast to the normal procedure where transmission loss is defined in terms of pressure ratios, based on a "test" section with anechoic terminations.

It was also advocated that back-up pressure information needs to be examined and presented.

A few example cases were discussed.

REFERENCES

1. C. Harris, *Hand Book of Noise Control*, McGraw-Hill Book Company, Inc., 1957.
2. W. Soedel, *Gas Pulsations in Compressor and Engine Manifolds*, Short Course Text Book of Purdue Compressor Technology Conference, Ray W. Herrick Laboratories, Purdue University, 1978.

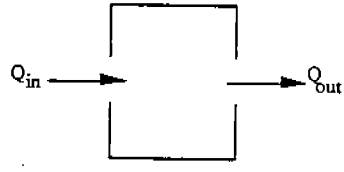

Figure 1 Acoustic element with input and output volume velocity

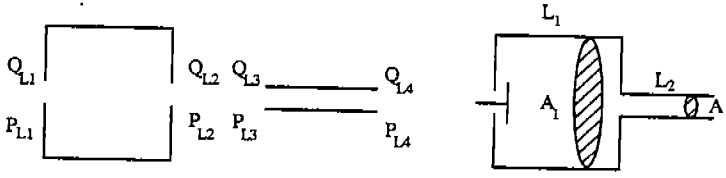

Figure 2 Two different acoustic elements

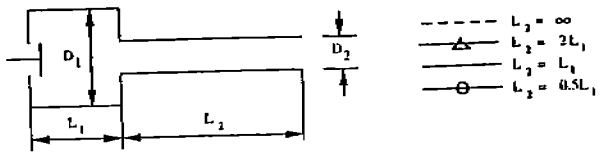

(a)

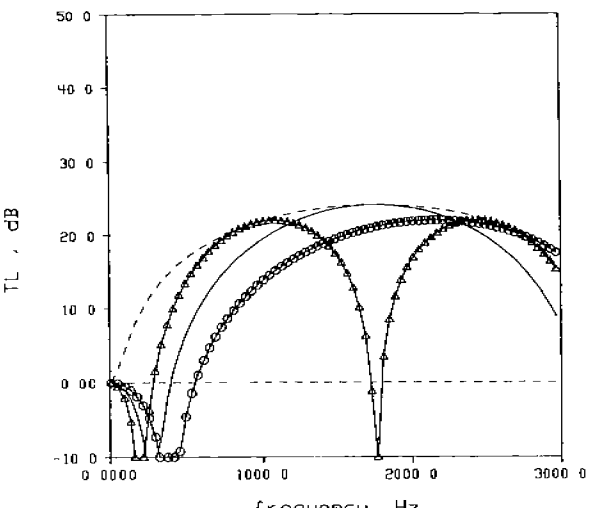

(b)

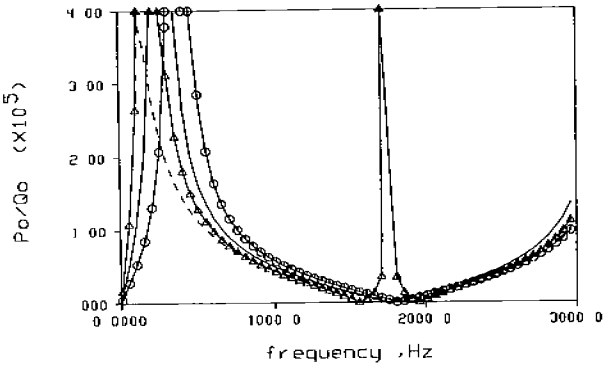

(c)

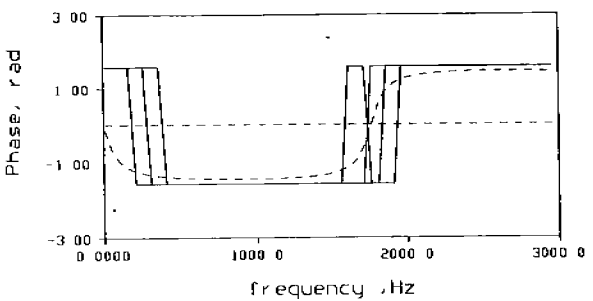

(d)

Figure 3 Typical expansion chamber-tail pipe design : (a) Dimensions, (b) transmission loss, (c) back pressure-input volume velocity ratio, (d) back pressure phasing

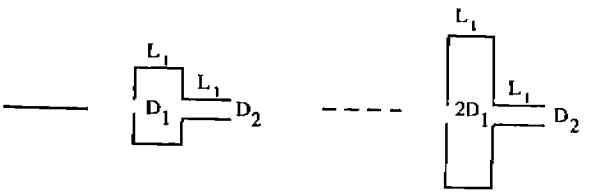

(a)

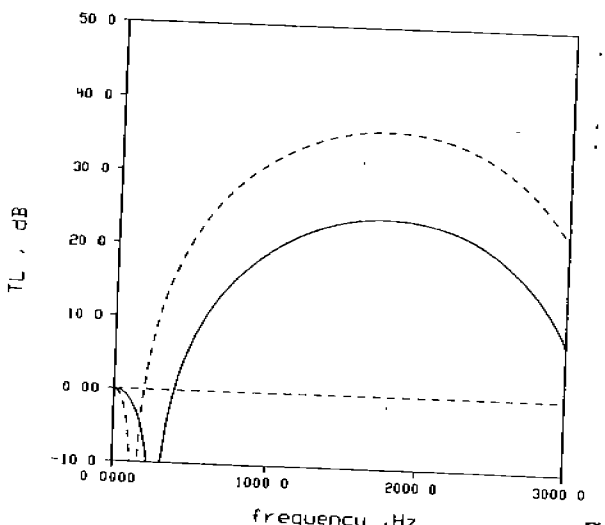

(b)

Figure 4

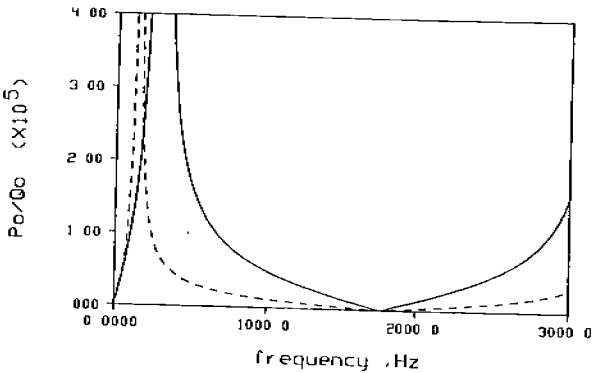

(c)

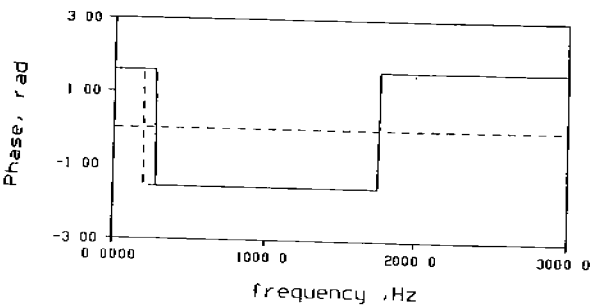

(d)

Influence of changing D_1 : (a) Dimensions, (b) transmission loss, (c) back pressure-input volume velocity ratio, (d) back pressure phasing

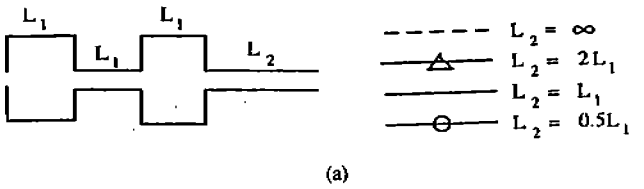

(a)

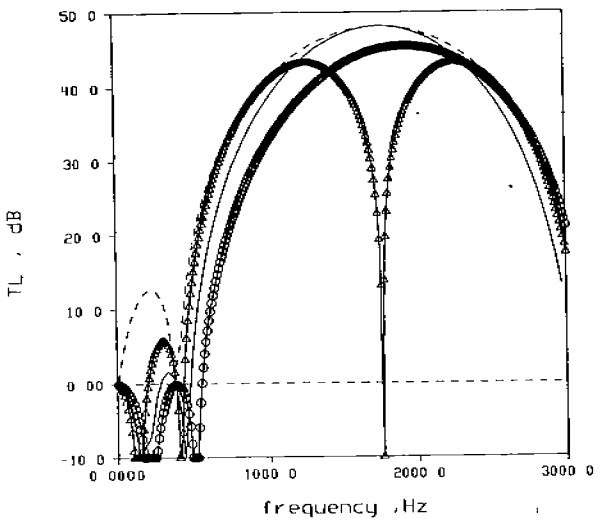

(b)

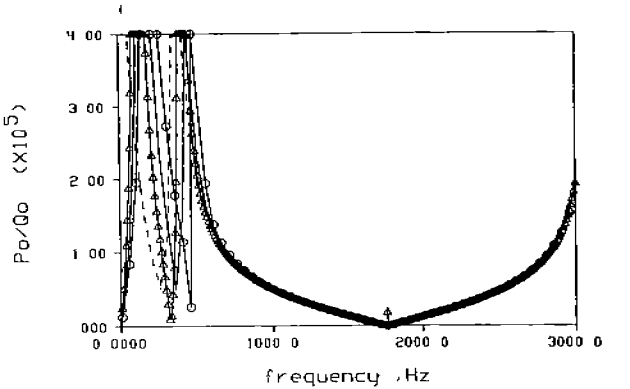

(c)

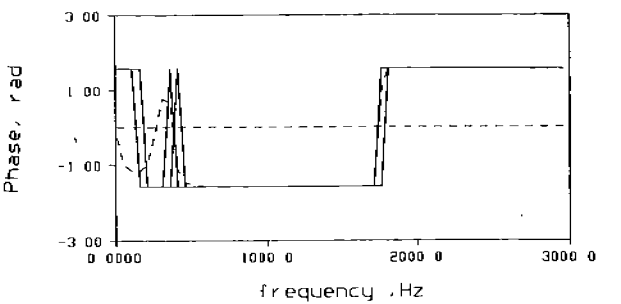

(d)

Figure 5 Two-expansion-volume muffler : (a) Dimensions, (b) transmission loss, (c) back pressure-input volume velocity ratio, (d) back pressure phasing

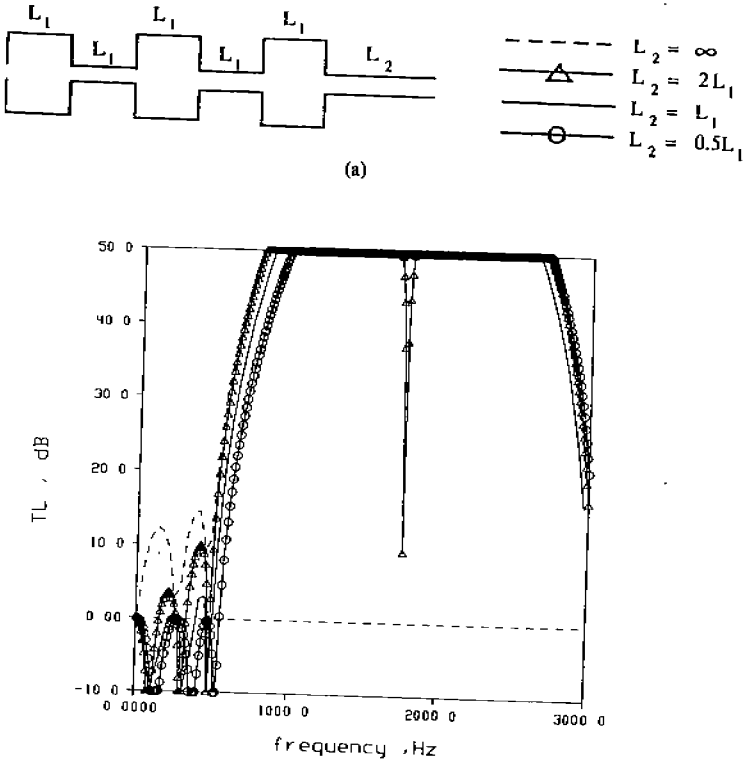

Figure 6

Three-expansion-volume muffler : (a) Dimensions, (b) transmission loss, (c) back pressure-input volume velocity ratio, (d) back pressure phasing

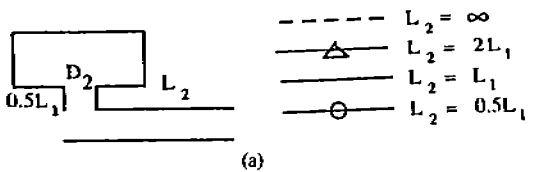

(a)

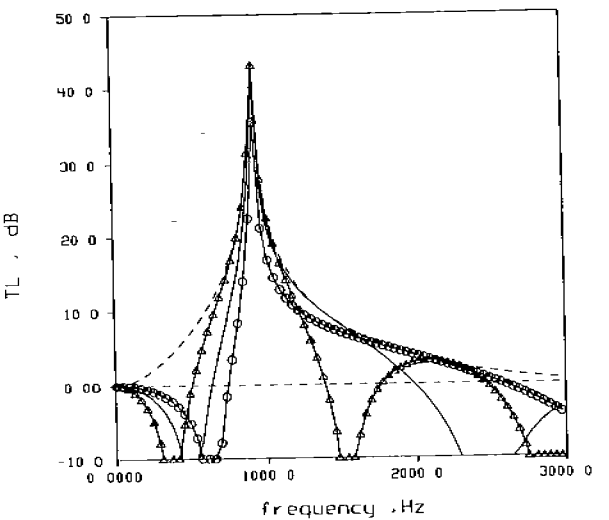

(b)

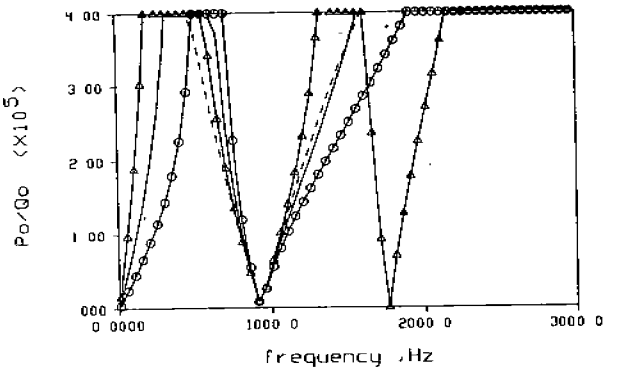

(c)

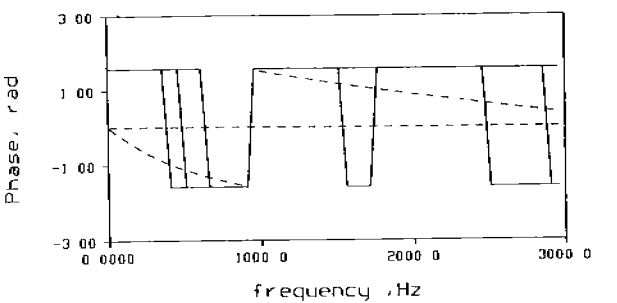

(d)

Figure 7 Behavior of tuned side branch resonator, as function of changing L_2 : (a) Dimensions, (b) transmission loss, (c) back pressure-input volume velocity ratio, (d) back pressure phasing

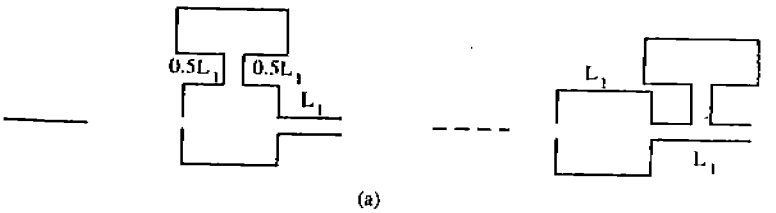

(a)

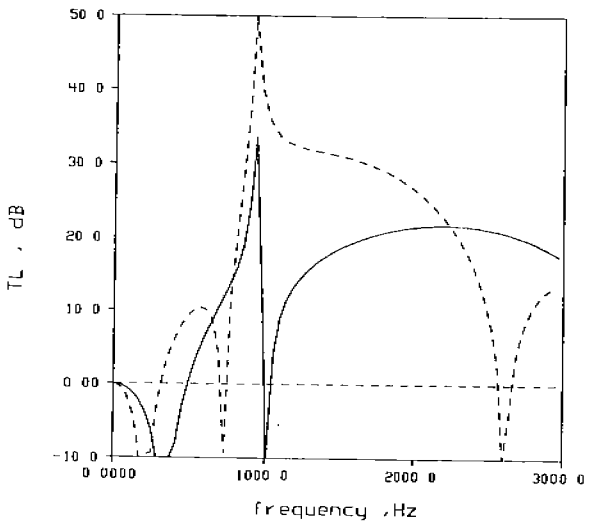

(b)

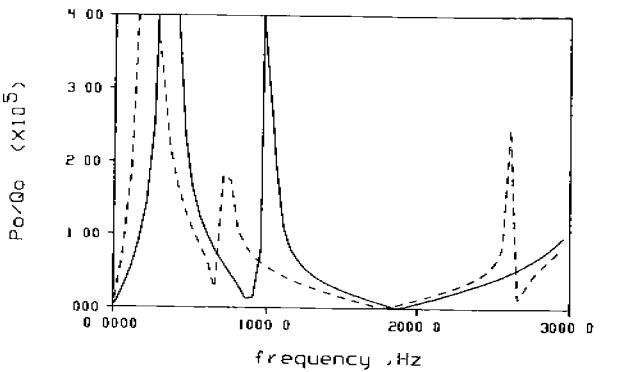

(c)

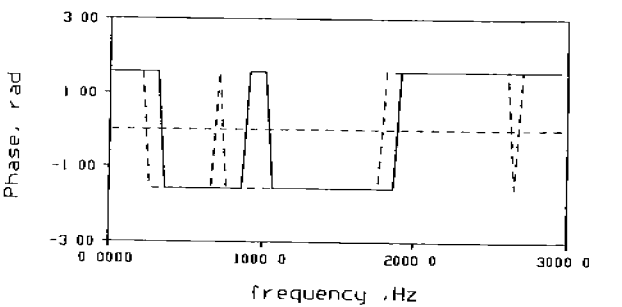

(d)

Figure 8 Side branch resonator located either off volume or off tail pipe. : (a) Dimensions, (b) transmission loss, (c) back pressure-input volume velocity ratio, (d) back pressure phasing

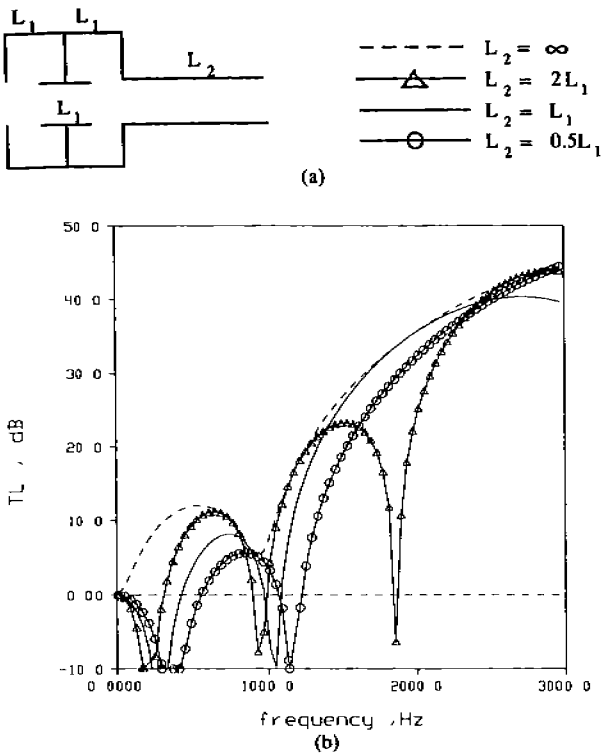

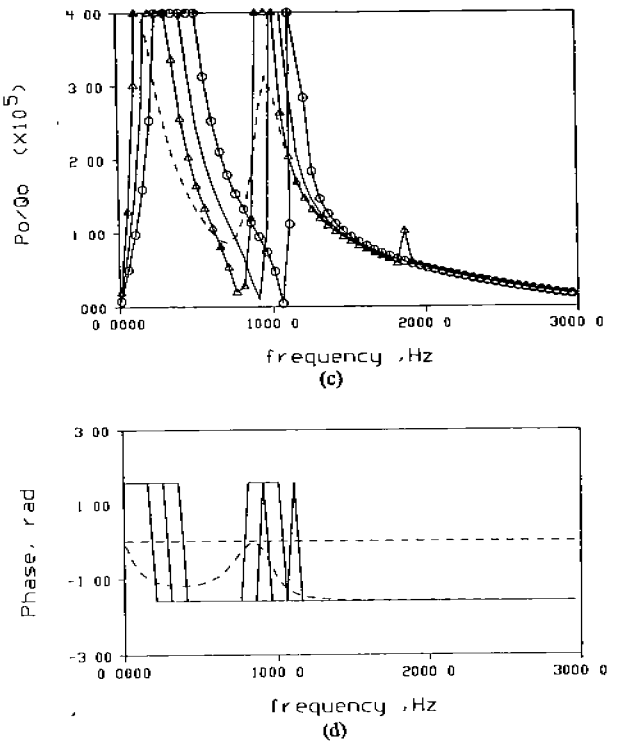

Figure 9 Influence of expansion chamber subdivision : (a) Dimensions, (b) transmission loss, (c) back pressure-input volume velocity ratio, (d) back pressure phasing

DEVELOPMENT OF A SIMPLIFIED DESIGN FORMULA FOR THE LOW FREQUENCY CUT-OFF OF A SMALL TWO VOLUME SILENCER

by

D. T. Soedel and W. Soedel
Ray W. Herrick Laboratories
School of Mechanical Engineering
Purdue University
West Lafayette, IN 47907

ABSTRACT

One of the most difficult tasks in compressor suction or discharge muffler design is to successfully attenuate very low frequencies (typically the first and second harmonic of the operating speed; 60 and 120 Hz for a 3600 RPM compressor). Design formulas for the low frequency cut-off of two-volume silencer effectiveness are developed and some design implications are discussed. The work is based on the Helmholtz approximations.

NOMENCLATURE

V_1, V_2 = volumes [m^3]
p_2, p_2 = acoustic pressures relative to ambient [N/m^2]
T_1, T_2 = temperature [^{0} K]
L_1, L_2 = corrected effective neck length [m]
$L_1 = L_{G1} + \sqrt{\pi A_1/2}$
$L_2 = L_{G2} + \sqrt{\pi A_2/2}$
L_{G1}, L_{G2} = geometric effective neck length [m]
A_1, A_2 = average cross-sectional areas of necks [m^2]
ρ_1, ρ_2 = average mass densities [Ns^2/m^4]
$\Delta V_1, \Delta V_2$ = dynamic change in volumes [m^3]
K_1, K_2 = bulk moduli [N/m^2]
D_1, D_2 = viscous damping coefficients [Ns/m^3]
C = average speed of sound [m/s]

INTRODUCTION

A frequently used configuration of a low pass filter muffler for small compressors and engines is a two volume muffler having a transfer pipe and tail pipe. While this or similar configurations have been analyzed frequently in the past, using various approaches such as lumped time domain models, four pole models based on the wave equation solution, and others, the approach to designing such a silencer has usually been to analyze a design configuration after the fact. The design method, is therefore, typically an iteration. One guesses the best proportions, analyzes the acoustic performance of the silencer, compares it to the desired performance, arrives at a new, hopefully improved design, analyzes again and so on. It is easily possible, if the designer is inexperienced, that the approach converges to an adequate design which is far from an optimal design. A second design method is automatic optimization. The problem with this is that it is often difficult to define which constraints have to be introduced. If not properly done by experienced designers, the muffler design may converge to strange proportions which may violate the physics of the theory which was the basis of the optimization program in the first place.

The third approach is to design the silencer in its approximate proportions using "rules of thumb" and experimentation. It has the potential short coming that it may become time consuming if an adequate initial design cannot be found quickly.

It is not the intent of this paper to make a case in favor of one of the three approaches. All three are of practical value. Rather, a simplified design formula is developed, following a philosophy of approach to small one volume engine mufflers developed by the authors, which will allow one to narrow the choice of several dimensional ratios by utilizing the concept of design by cut-off frequency, which is the frequency above which the silencer abates sound except for standing wave frequencies. This should be of value no matter which approach to design is used. Below the cut-off frequency, the silencer has two frequencies at which it may magnify sound. In order to accomplish this in a simple way, we confined ourselves to silencers of small enough dimensions so that at the cut-off frequency the associated wavelength is larger than approximately four times the largest muffler dimension (quarter wave criterion). This allowed us to employ the Helmholtz resonator simplifications.

The approach which will be presented allows one to start with the definition of the desired cut-off frequency of the silencer, select the dimensional ratios of a first workable design, and then to calculate the necessary tail pipe length. Subsequently this design can be improved by more sophisticated computer modeling procedures and/or experimentation.

GOVERNING EQUATIONS

This design is typically used in suction silencer design, but it can also be viewed as an approximation of a three volume muffler ending in an anechoic termination if the third volume just before the anechoic termination (for example, the shock loop which is often approximated as a pipe of infinite extension) is very large. Typically used two volume discharge muffler arrangements terminating in an "infinite" shock loop are not covered by the following, but similar design formulas can and have been developed by the authors.

Figure 1 is a schematic idealization. Neglecting the influence of mean velocity V_m, since V_m is typically much less than the speed of sound, it does not matter in what direction the mean flow is pointed. The valve (suction or discharge) provides a sum of harmonic volume velocity inputs, one of which is shown at the left.

The free body diagrams of the forces acting on the gas in the tubes are also shown in Figure 1. Any geometric shape that consists of a volume and a short neck and is filled with a compressible gas or fluid can be viewed as a Helmholtz resonator. Helmholtz realized that if a volume-neck combination is made to vibrate, it behaves essentially as if the neck is an incompressible plug that vibrates as a whole on the spring provided by the compressible gas in the volume. He found that he could analyze the resulting oscillation if he assumed that the compression process was linear. The relationship between the Helmholtz simplification and the wave equation was illustrated by Elson and Soedel [9].

Referring to the free body diagram for gas column 1 in Figure 1, the mass is

$$m_1 = L_1 A_1 \rho_1 , \tag{1}$$

the pressure p_1 in volume V_1 is (K_1 is the bulk modulus):

$$p_1 = -K_1 \frac{\Delta V_1}{V_1} , \tag{2}$$

and the change in volume V_1 is

$$\Delta V_1 = A_1 \xi_1 - A_o \xi_o . \tag{3}$$

However, ξ_o is usually not given, instead, we know that the input is a sinusoidally varying volume velocity

$$Q(t) = Q_n e^{j\omega_n t} = \{\text{either } Q_n \sin \omega_n t \text{ or } Q_n \cos \omega_n t\} . \tag{4}$$

Thus,

$$A_0 \xi_0 = \int_0^t Q_n e^{j\omega_n t} dt . \tag{5}$$

Substituting equation (5) into (3) gives

$$\Delta V_1 = A_1\xi_1 - \int_0^t Q_n e^{j\omega_n t}dt\,. \tag{6}$$

Substituting into (2) gives

$$p_1 = \frac{-K_1A_1\xi_1}{V_1} + \frac{K_1}{V_1}\int_0^t Q_n e^{j\omega_n t}dt\,. \tag{7}$$

The pressure p_2 in volume V_2 is

$$p_2 = -K_2\frac{\Delta V_2}{V_2}\,, \tag{8}$$

where

$$\Delta V_2 = A_2\xi_2 - A_1\xi_1\,. \tag{9}$$

Thus

$$p_2 = \frac{-K_2A_2\xi_2}{V_2} + \frac{K_2A_1\xi_1}{V_2}\,. \tag{10}$$

Therefore, summing up all the forces in the free body diagram for gas column 1 gives

$$p_1A_1 - p_2A_2 - D_1A_1\dot{\xi}_1 - m_1\ddot{\xi}_1 = 0\,, \tag{11}$$

or

$$L_1A_1\rho_1\ddot{\xi}_1 + D_1A_1\dot{\xi}_1 + \left(\frac{K_2}{V_2} + \frac{K_1}{V_1}\right)A_1^2\xi_1 - \frac{K_2A_2A_1\xi_2}{V_2} = \frac{K_2A_1}{V_1}\int_0^t Q_n e^{j\omega_n t}dt\,. \tag{12}$$

Next, we consider the free body diagram of gas column 2 in Figure 1, and obtain

$$L_2A_2\rho_2\ddot{\xi}_2 + D_2A_2\dot{\xi}_2 + \frac{K_2A_2^2}{V_2}\xi_2 - \frac{K_2A_1A_2}{V_2}\xi_1 = 0\,. \tag{13}$$

By defining volume velocities

$$Q_1 = A_1\dot{\xi}_1\,, \quad Q_2 = A_2\dot{\xi}_2\,, \tag{14,15}$$

and differentiating eqs. (12) and (13) with respect to time, we get

$$\ddot{Q}_1 + \frac{D_1}{L_1\rho_1}\dot{Q}_1 + \left(\frac{K_2}{V_2} + \frac{K_1}{V_2}\right)\frac{A_1}{L_1\rho_1}Q_1 - \frac{K_2A_1}{V_2L_1\rho_1}Q_2 = \frac{K_1A_1}{V_1L_1\rho_1}Q_n e^{j\omega_n t}\,, \tag{16}$$

$$\ddot{Q}_2 + \frac{D_2}{L_2\rho_2}\dot{Q}_2 + \frac{K_2A_2}{V_2L_2\rho_2}Q_2 - \frac{K_2A_2}{V_2L_2\rho_2}Q_1 = 0\,. \tag{17}$$

Defining

$$\omega_{11}^2 = \left(\frac{K_1}{V_1} + \frac{K_2}{V_2}\right)\frac{A_1}{L_1\rho_1}\,, \quad \omega_{22}^2 = \frac{K_2A_2}{V_2L_2\rho_2}\,, \tag{18,19}$$

$$\omega_{12}^2 = \frac{K_2A_1}{V_2L_1\rho_1}\,, \quad \omega_{21}^2 = \frac{K_2A_2}{V_2L_2\rho_2}\,, \quad \omega_{01}^2 = \frac{K_1A_1}{V_1L_1\rho_1}\,, \tag{20,21,22}$$

$$\zeta_1 = \frac{D_1}{2L_1\rho_1\omega_{11}^2}\,, \quad \zeta_2 = \frac{D_2}{2L_2\rho_2\omega_{22}^2}\,, \tag{23,24}$$

we may finally write

$$\begin{bmatrix}1 & 0\\ 0 & 1\end{bmatrix}\begin{bmatrix}\ddot{Q}_1\\ \ddot{Q}_2\end{bmatrix} + \begin{bmatrix}2\zeta_1\omega_{11}^2 & 0\\ 0 & 2\zeta_2\omega_{22}^2\end{bmatrix}\begin{bmatrix}\dot{Q}_1\\ \dot{Q}_2\end{bmatrix} + \begin{bmatrix}\omega_{11}^2 - \omega_{12}^2\\ -\omega_{21}^2 \quad \omega_{22}^2\end{bmatrix}\begin{bmatrix}Q_1\\ Q_2\end{bmatrix} = \begin{bmatrix}\omega_{01}^2Q_n e^{j\omega_n t}\\ 0\end{bmatrix}. \tag{25}$$

NATURAL FREQUENCIES

We set $\zeta_1 = \zeta_2 = 0$ and $Q_n = 0$. Eq. (25) becomes

$$\begin{bmatrix} 1 & 0 \\ 0 & 1 \end{bmatrix} \begin{bmatrix} \ddot{Q}_1 \\ \ddot{Q}_2 \end{bmatrix} + \begin{bmatrix} \omega_{11}^2 & -\omega_{12}^2 \\ -\omega_{21}^2 & \omega_{22}^2 \end{bmatrix} \begin{bmatrix} Q_1 \\ Q_2 \end{bmatrix} = 0 \tag{26}$$

At a natural frequency ω_n,

$$Q_1 = \bar{Q}_1 \sin \omega_n t \quad , \quad Q_2 = \bar{Q}_2 \sin \omega_n t \, , \tag{27,28}$$

where $\bar{Q}_1$ and $\bar{Q}_2$ are amplitudes of motion. Substituting eqs. (27) and (28) into eq (26) gives

$$\begin{bmatrix} -\omega_n^2 + \omega_{11}^2 & -\omega_{12}^2 \\ -\omega_{21}^2 & -\omega_n^2 + \omega_{22}^2 \end{bmatrix} \begin{bmatrix} \bar{Q}_1 \\ \bar{Q}_2 \end{bmatrix} = 0 \, . \tag{29}$$

This equation can only be zero if the determinant of the matrix is zero:

$$\begin{vmatrix} \omega_{11}^2 - \omega_n^2 & -\omega_{12}^2 \\ -\omega_{21}^2 & \omega_{22}^2 - \omega_n^2 \end{vmatrix} = 0 \, . \tag{30}$$

Solving this equation gives

$$\omega_{n1,2}^2 = \frac{(\omega_{11}^2 + \omega_{22}^2)}{2} \pm \sqrt{\left[\frac{(\omega_{11}^2 + \omega_{22}^2)}{2}\right]^2 - (\omega_{11}^2 \omega_{22}^2 - \omega_{12}^2 \omega_{21}^2)} \, . \tag{31}$$

RESPONSE RATIO

In steady state, the solutions of eq (25) must be of the form

$$Q_1 = \tilde{Q}_1 \, e^{j\omega t} \quad , \quad Q_2 = \tilde{Q}_2 \, e^{j\omega t} \, . \tag{32,33}$$

We obtain

$$\begin{bmatrix} (\omega_{11}^2 - \omega^2 + 2\zeta_1 \omega_{11} j\omega) & -\omega_{12}^2 \\ -\omega_{21}^2 & (\omega_{22}^2 - \omega^2 + 2\zeta_2 \omega_{22} j\omega) \end{bmatrix} \begin{bmatrix} \tilde{Q}_1 \\ \tilde{Q}_2 \end{bmatrix} = \begin{bmatrix} \omega_{01}^2 \, Q_n \\ 0 \end{bmatrix} \tag{34}$$

Solving for $\tilde{Q}_1$ and $\tilde{Q}_2$ and dividing the magnitude of $\tilde{Q}_2$ by Q_n gives the ratio of "output" to "input" volume velocity as

$$R = \frac{|\tilde{Q}_2|}{Q_n} = \frac{\left(\frac{\omega_{01}}{\omega_{11}}\right)^2}{\sqrt{\left\{\left[1 - \left(\frac{\omega}{\omega_{01}}\right)^2 \left(\frac{\omega_{01}}{\omega_{11}}\right)^2\right]\left[1 - \left(\frac{\omega}{\omega_{01}}\right)^2 \left(\frac{\omega_{01}}{\omega_{22}}\right)^2\right] - \left(\frac{\omega_{01}}{\omega_{11}}\right)^2 \left(\frac{\omega_{11}}{\omega_{01}}\right)^2 - 4\zeta_1\zeta_2 \left(\frac{\omega}{\omega_{01}}\right)^2 \left(\frac{\omega_{01}}{\omega_{11}}\right)\left(\frac{\omega_{01}}{\omega_{22}}\right)\right\}^2 + 4\left\{\zeta_2 \left(\frac{\omega}{\omega_{01}}\right)\left(\frac{\omega_{01}}{\omega_{22}}\right)\left[1 - \left(\frac{\omega}{\omega_{01}}\right)^2 \left(\frac{\omega_{01}}{\omega_{11}}\right)^2\right] + \zeta_1 \left(\frac{\omega}{\omega_{01}}\right)\left(\frac{\omega_{01}}{\omega_{11}}\right)\left[1 - \left(\frac{\omega}{\omega_{01}}\right)^2 \left(\frac{\omega_{01}}{\omega_{22}}\right)^2\right]\right\}^2}} \tag{35}$$

and the phase angle ϕ_2 is

$$\phi_2 = \tan^{-1} \frac{2\zeta_2 \left(\frac{\omega}{\omega_{22}}\right)\left[1-\left(\frac{\omega}{\omega_{11}}\right)^2\right] + 2\zeta_1 \left(\frac{\omega}{\omega_{11}}\right)\left[1-\left(\frac{\omega}{\omega_{22}}\right)^2\right]}{\left[1-\left(\frac{\omega}{\omega_{11}}\right)^2\right]\left[1-\left(\frac{\omega}{\omega_{22}}\right)^2\right] - \left(\frac{\omega_{21}\omega_{12}}{\omega_{11}\omega_{22}}\right)^2 - 4\zeta_1\zeta_2\left(\frac{\omega^2}{\omega_{11}\omega_{22}}\right)}, \tag{36}$$

where, for $K_1 = K_2 = \rho c^2$, $\rho_1 = \rho_2$, we have

$$\frac{\omega_{12}}{\omega_{01}} = \sqrt{\frac{V_1}{V_2}}, \frac{\omega_{01}}{\omega_{11}} = \sqrt{\frac{1}{1+\frac{V_1}{V_2}}}, \frac{\omega_{01}}{\omega_{22}} = \sqrt{\left(\frac{A_1}{A_2}\right) \Big/ \left[\left(\frac{V_1}{V_2}\right)\left(\frac{L_1}{L_2}\right)\right]}, \tag{37,38,39}$$

$$\omega_{11} = C\sqrt{\left(\frac{1}{V_1}+\frac{1}{V_2}\right)\frac{A_1}{L_1}}, \omega_{22} = C\sqrt{\left(\frac{1}{V_2}\right)\frac{A_2}{L_2}} = \omega_{21}, \tag{40,41}$$

$$\omega_{12} = C\sqrt{\left(\frac{1}{V_2}\right)\frac{A_1}{L_1}}, \quad \omega_{01} = C\sqrt{\left(\frac{1}{V_1}\right)\frac{A_1}{L_1}}. \tag{42,43}$$

The muffler will attenuate sound whenever $R < 1$. There will be two lower frequency regions where the muffler will potentially amplify sound. These regions correspond approximately to the two resonance frequencies of the muffler.

CUT-OFF FREQUENCY

It is of interest to calculate the cut-off frequency above which the muffler will be generally effective in attenuating pulsations. For this purpose, we take the situation which gives the highest value of cut-off frequency for a given set of parameters, namely when $\zeta_1 = \zeta_2 = \zeta = 0$. Setting $R = 1$ gives, from eq. (35).

$$1 = \frac{\pm\left(\frac{\omega_{01}}{\omega_{11}}\right)^2}{\left[1-\left(\frac{\omega}{\omega_{01}}\right)^2\left(\frac{\omega}{\omega_{11}}\right)^2\right]\left[1-\left(\frac{\omega}{\omega_{01}}\right)^2\left(\frac{\omega_{01}}{\omega_{22}}\right)^2\right] - \left(\frac{\omega_{12}}{\omega_{11}}\right)^2}, \tag{44}$$

where the $\pm$ sign comes from the fact that the denominator is $\pm\sqrt{(\cdots)^2} = \pm(\cdots)$. Expanding gives

$$\left(\frac{\omega}{\omega_{01}}\right)^4 - B\left(\frac{\omega}{\omega_{01}}\right)^2 + C_{1,2} = 0, \tag{45}$$

where

$$B = \left(\frac{\omega_{11}}{\omega_{01}}\right)^2 + \left(\frac{\omega_{22}}{\omega_{01}}\right)^2 = 1 + \frac{V_1}{V_2} + \left(\frac{A_2}{A_1}\right)\left(\frac{V_1}{V_2}\right)\left(\frac{L_1}{L_2}\right), \tag{46}$$

$$C_{1,2} = \left(\frac{\omega_{11}}{\omega_{01}}\right)^2\left(\frac{\omega_{22}}{\omega_{01}}\right)^2 - \left(\frac{\omega_{12}}{\omega_{01}}\right)^2\left(\frac{\omega_{22}}{\omega_{01}}\right)^2 \pm \left(\frac{\omega_{22}}{\omega_{01}}\right)^2 = 0,2\left(\frac{V_1}{V_2}\right)\left(\frac{L_1}{L_2}\right)\left(\frac{A_2}{A_1}\right), \tag{47}$$

and where $C_1 = 0$ is the value for the minus sign and C_2 is the value for the plus sign.

The solution is

$$\left[\frac{\omega}{\omega_{01}}\right]^2 = \frac{B \pm \sqrt{B^2 - 4C_{1,2}}}{2} \quad (48)$$

For example, for $A_1/A_2 = 1$, $L_1/L_2 = 1$, $V_1/V_2 = 1$, we obtain $B = 3$, $C_1 = 0$ and $C_2 = 2$. There are, therefore, four values of ω/ω_{01} at which $R = 1$: $(\omega/\omega_{01}) = 0$ and 1.73, obtained from $C_1 = 0$, and $(\omega/\omega_{01}) = 1.0$ and 1.414, obtained from $C_2 = 2$. Or, $R = 1$ exists when $\omega = 0$, ω_{01}, $1.41\omega_{01}$ and $1.73\ \omega_{01}$.

Eq. (48) is perhaps more useful if eqs. (46) and (47) for $C_1 = 0$ are substituted ($C_1 = 0$ determines the highest cut-off frequency, $\omega = 1.73\,\omega_{01}$). This gives the condition that all frequency bands are attenuated whose frequency is higher than the cut-off frequency ω_c for the $C_1 = 0$ case:

$$\omega > \omega_C\ , \quad (49)$$

where

$$\omega_C = \omega_{01}\sqrt{B} = \omega_{01}\left[1 + \frac{V_1}{V_2} + \left[\frac{A_2}{A_1}\right]\left[\frac{V_1}{V_2}\right]\left[\frac{L_1}{L_2}\right]\right]^{1/2} . \quad (50)$$

Changing ω_C[rad/s] to f_C [Hz] and solving for L_1 gives

$$L_1 = \frac{A_1}{V_1}\left[\frac{C}{2\pi f_c}\right]^2\left[1 + \left[\frac{V_1}{V_2}\right] + \left[\frac{A_2}{A_1}\right]\left[\frac{V_1}{V_2}\right]\left[\frac{L_1}{L_2}\right]\right] . \quad (51)$$

For pipe length that are much larger than $(1/2)\sqrt{\pi A}$, we may set $L_1 = L_{G1}$ and $L_2 = L_{G2}$. Thus, if "best" ratios (V_1/V_2), (A_2/A_2), (L_1/L_2) can be rationally selected, and A_1, V_1 and f_C can be selected, L_1 can be calculated.

RESULTS AND DISCUSSION

In order to understand how muffler dimensions should be selected, a large variety of cases were selected and the logarithm of the ratio R was plotted versus the ratio of the volume flow oscillation input frequency to a nondimensionalizing frequency ω_{01}.

Figure 2 shows the influence of damping, which is for most mufflers an empirical parameter. Selecting $\zeta_1 = \zeta_2$, $A_1/A_2 = 1$, $L_1/L_2 = 1$ and $V_1/V_2 = 1$, and assuming an average speed of sound, results in three curves which differ from each other mainly by the amplitudes of the two resonance peaks. The muffler is only effective in regions ω/ω_{01} where the logarithm of the transmission ratio is negative. Ignoring the small stretch between the two peaks where this is the case, the main region of effectiveness is for values of ω/ω_{01} greater than the cut-off frequency, defined by this graph.

Next, damping was held constant, as were all other parameters except for the ratio of inertia block pipe length L_1 to tailpipe length L_2. It can be seen from Figure 3 that this ratio should be as small as practically feasible, but at the same time the absolute length L_1 should also be as large as possible because L_1 is part of the nondimensionalizing frequency ω_{01}. A practical recommendation is probably to make L_1 as large as feasible and then make L_2 twice as long.

Figure 4 shows what happens when the volume ratio V_1/V_2 is varied. Also, because it is required that the absolute value of V_1 be as large as possible since it is part of ω_{01}, the result is that the total muffler volume $V_1 + V_2$ should be as large as possible. At this point in time it is recommended to make the two volumes equal, $V_2 = V_1$. The volume V_1 should ideally be several times the displacement volume of the compressor. More work is necessary to define the minimum required volume V_1, probably in conjunction with modeling the compressor itself.

Figure 5 shows what happens when the ratio A_1/A_2 is varied. This plot is not of great consequency since flow resistance considerations usually demand that A_1 should be equal to at least the maximum valve flow area and that $A_2 \geq A_1$.

Figure 6 shows the ratio R when "best" and "worst" ratios of volumes, tube length and crossectional areas are used in the range of the previous examples. It is needless to point out that "best" ratios are

subject to design constraints. The most severe constraint is usually that the overall geometric size of mufflers is severly limited.

It is obvious from the equations and figures that as lower f_C can be selected, as better it is for the average noise attenuation. The fundamental and first few harmonics corresponding to compressor speed and number of cylinders are difficult to attenuate since f_c will have to be correspondingly low. Very low values of f_c will lead to large L_1 selections. The crossectional area A_1 is determined essentially by the maximum compressor valve flow area. It cannot be much smaller. The first volume V_1 is determined by the back pressure on the valves, which is generated by the muffler. There is a minimum value for each valve design, which can be determined only experimentally or by a more complete computer simulation program. As a first rule of thumb, V_1 should be about two times the displacement volume of the compressor, but may have to be smaller due to space limitation.

A possible design procedure sequence is as follows:

(a) Select volume V_1 of the first muffler chamber as large as possible (as initial guess about two times the compressor displacement volume). The shape of the volume is relatively unimportant.

(b) Select the crossection of the inertia block tube A_1, and also the crossection of the tail tube A_2, to be approximately equal to or larger than the maximum valve flow area of the compressor. The tubes do not have to be circular. They may also deviate from being cylindrical. In this case the crossections are average values.

(c) Select the cut-off frequency f_C of the muffler. It should be as low as possible. What it should be depends on the compressor noise or gas pulsation spectrum.

(d) Select, if possible, $V_2 \cong V_1$. The shape of V_2 is relatively unimportant.

(e) Select the length of the tail tube to be at least twice that of the inertia block tube, $L_2 \cong 2L_1$. Tubes do not have to be straight.

(f) Calculate the length of inertia block pipe L_1 from eq. (51). Use an average speed of sound C which corresponds to the average temperature in the muffler.

(g) Build a prototype muffler.

(h) Measure the achieved noise reduction.

(i) Measure if there is significant power loss.

(j) If low frequency pulsations are still too high, lower the cut-off frequency f_c.

(k) If there is too much power loss, increase the first volume V_1 (if possible). But readjust L_1 (recalculate) so that the cut-off frequency is not changed.

(l) Go back to (g) and iterate between theory and experiment.

Note that this is only a very approximate approach which will allow one to design into the direction of low frequency pulsation reduction. There may be higher frequency noise bands where the silencer is not very effective because standing waves are excited in the tailpipe and other parts of the muffler. Additional experimental work and theoretical approaches, not discussed here, will have to be applied in this case.

ACKNOWLEDGEMENT

Support of this work by the COSMOS Tool and Dye Company is gratefully acknowledged.

REFERENCES

1. J. Kim and W. Soedel, "Analysis of Gas Pulsations in Multiply Connected Three-Dimensional Acoustic Cavities with Special Attention to Natural Mode or Wave Cancellation Effects," Journal of Sound and Vibration, Vol. 131, No. 1, 103-114, 1989.

2. F. Laville and W. Soedel, "Some New Scaling Rules for Use in Mufflers," Journal of Sound and Vibration, Vol. 60, No. 2, 273-288, 1978.

3. J.H. Lee, B. Dhar, and W. Soedel, "A Mathematical Model of Low Amplitude Pulse Combustion Systems Using A Helmholtz Resonator-type Approach," Journal of Sound and Vibration, Vol. 98, No. 3, 379-401, 1985.

4. B.R.C. Mutyala and W. Soedel, "A Mathematical Model of Helmholtz Resonator Type Gas Oscillation Discharges of Two-Stroke Cycle Engines," Journal of Sound and Vibration, Vol. 44, No. 4, 479-491, 1976.

5. R. Singh and W. Soedel, "Interpretation of Gas Oscillations in Multicylinder Fluid Machinery Manifolds by Using Lumped Parameter Descriptions," Journal of Sound and Vibration, Vol. 64, No. 3, 387-402, 1979.

6. W. Soedel, E. Padilla Navas, and B.D. Kotalik, "On Helmholtz Resonator Effects in the Discharge System of a Two-Cylinder Compressor, " Journal of Sound and Vibration, Vol. 30, No. 3, 263-277, 1973.

7. W. Soedel, "Designing Simple Low-Pass Filter Mufflers for Small Two-Cycle Engines," Noise Control Engineering, Vol. 10, No. 2, 60-66, 1978.

8. W. Soedel, "Gas Pulsations in Compressor and Engine Manifolds," Purdue University Publications Office, 116 pages, 1978.

9. J.P Elson and W. Soedel, "Criteria for the Design of Pressure Transducer Adapter Systems," Proceedings of the 1972 Purdue Compressor Technology Conference, pp. 390-3904, 1972.

FIGURES

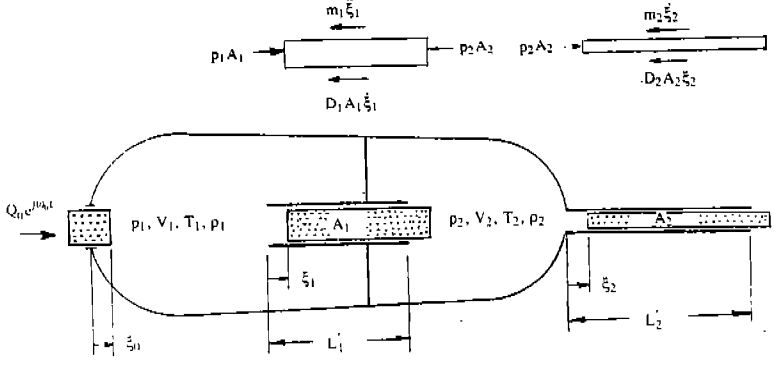

Figure 1. Two volume low pass filter muffler.

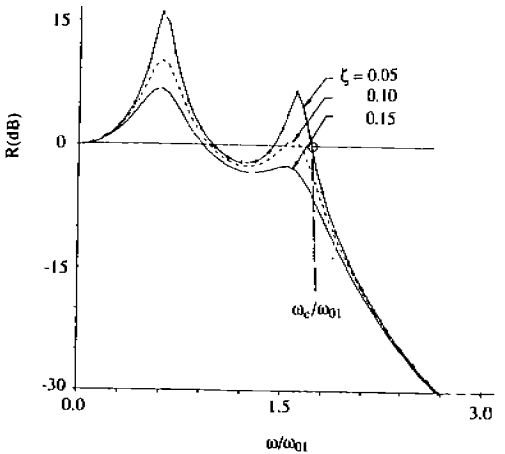

Figure 2. Influence of damping for $A_1/A_2 = 1$, $L_1/L_2 = 1$ and $V_2/V_2 = 1$.

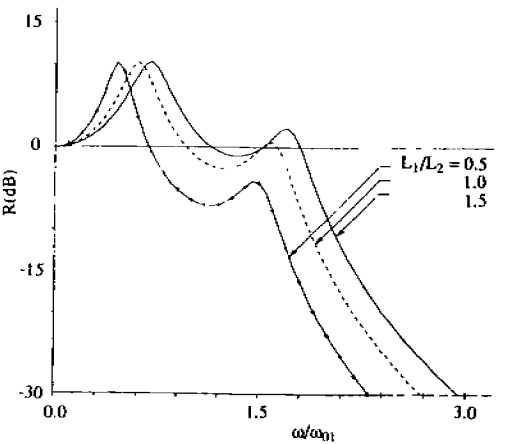

Figure 3. Influence of ratio of inertia block pipe length to tail pipe length for $\zeta = 0.1$, $A_1/A_2 = 1$ and $V_1/V_2 = 1$.

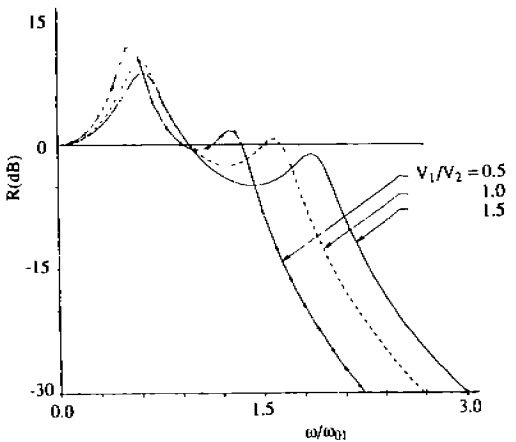

Figure 4. Influence of ratio of volumes for $\zeta = 0.1$, $A_1/A_2 = 1$ and $L_1/L_2 = 1$.

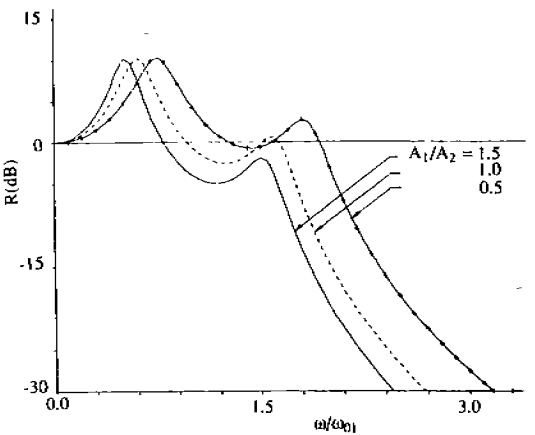

Figure 5. Influence of ratio of pipe cross-sectional area for $\zeta = 0.1$, $V_1/V_2 = 1$ and $L_1/L_2 = 1$.

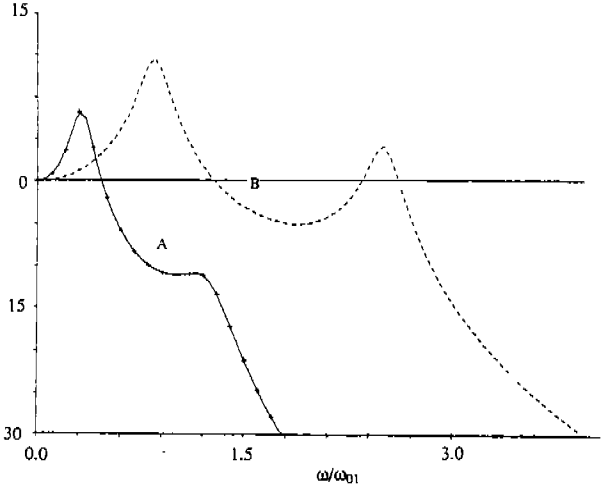

Figure 6. This figure illustrates how the two volume low pass filter muffler can vary in effectiveness when "best" ratios or "worst" ratios are selected simultaneously. Curve A is for $V_1/V_2 = 0.5$, $L_1/L_2 = 0.5$, $A_1/A_2 = 1.5$, $\zeta = 0.15$, curve B is for $V_1/V_2 = 1.5$, $L_1/L_2 = 1.5$, $A_1/A_2 = 0.5$, $k\zeta = 0.05$. However, it has to be realized that the muffler of curve A has a much larger total volume ($3V_1$) than the muffler of curve B ($1.67V_1$).

CAVITY RESONANCES IN HERMETIC COMPRESSORS : A FINITE ELEMENT APPRAOCH

AKELLA S., RAO N.J., VENKATESWARLU K., SUNDARESAN S.A

SHRIRAM REFRIGERATION INDUSTRIES LIMITED
BALANAGAR TOWNSHIP
HYDERABAD - 500 037, INDIA

ABSTRACT

A triangular prism acoustic finite element was developed based on Craggs (1) method. It has the advantage of representing shells of different shapes with changes in cross section along the length. Two sample compressors were studied for their resonant frequencies and mode shapes. Modifications to the shell or pump changed both the resonant frequencies and mode shapes. 1-D finite elements were used to find resonant characteristics of a discharge tube with area changes. Mufflers used in compressors form a different study. However, the tubes used can be designed using 1-D finite elements. Finally, a simple cubical room where the compressor/appliance is used was also analysed to detect if any problematic frequencies can be removed. It was found that acoustic damping using absorbers and baffles may be the answer than changing room dimensions.

INTRODUCTION

The noise generated by a hermetic compressor both while it is running as well as during its start and stop is a very important criterion to the customer and often becomes a selling point. The vibrations of different parts of the pump, acoustics of the gas in cavities and the discharge tube all cause shell vibrations.

Most of these factors are analysed experimentally or analytically while designing. However, some problems arise during initial production. If experimental and analytical analysis is carried out at this stage, the results are often very difficult to correlate to the causes. The available analytical techniques cannot accurately model the complex cavity resonances and mode shapes.

In this paper available finite element techniques are used to analyse the resonances that occur in the cavity between the shell and the pump, the discharge tube connecting the pump and the shell as in low side compressors, and finally the room in which the appliance is used.

Cavity resonances in refrigerant compressors was reported by Johnson and Hamilton (2). They have used an analytical approach on cylindrical shells with annular pumps and got reasonable agreement with the experimental values. However, since actual compressor cavity is not a true annulus the disagreement may be reduced by using finite element method.

A study of noise reduction of refrigerator compressors was done by Kenji Tojo et al (3). In this study analytical methods were used to get the cavity resonances. A 500 Hz noise was related to the cavity resonance. A finite element study was suggested in their paper for ease of representing the cavity and accuracy of the results.

Munjal (4) has summarised the use of finite elements for mufflers. He presented a high order 32 degree of freedom isoparametric 8 nodal element which has both pressure and its derivaties as nodal variables at each node. However, its size restricts its use on simple computers when complicated shapes of cavities are considered.

In the present study simple finite elements of three dimensions and single dimension are used as presented by Craggs (1), (5). Here pressure is used as the nodal variable and the velocity components are omitted. It gives good agreement with analytical results and is very useful in complex enclosures when using small computers.

FINITE ELEMENT ANALYSIS

One very powerful method of analysis with the advent of computers is the finite element method (FEM). Used mainly for structural analysis, it is explained among others by Zienkiewicz (6). Due to its ability to represent complicated shapes and boundary conditions, it was developed by Gladwell (7) for acoustic analysis and initial finite elements were developed by Craggs (1), (5).

In our study we started with a cubic element with pressure and its 3 derivaties (velocities) as nodal variables used by Munjal (4). The use of 32 degrees of freedom, 8 nodal hexahedral isoparametric element proved unmanageable as the number of elements increased. Use was made of simple elements described by Craggs (1), (5), which use only pressure at each nodal point. The equations for an acoustic system without any energy dissipation at the boundaries are found from the stationary value of the frequency dependent functional F, where

$$F = \int_{\text{Volume}} \left\{ \frac{1}{2} (\text{Grad } p)^2 - \frac{w}{c^2} p^2 \right\} dV + \int_{\text{Surface}} i\rho \frac{w}{2} A p^2 \, dS.$$

Here p is the pressure, ρ the density, c the speed of sound, w the frequency, i the complex operator and A the normal acoustic admittance. Setting the first variation of the functional, F, to zero leads to the Helmholtz equation

$$\nabla^2 p + (w^2/c^2)p = 0$$

together with the boundary condition at the surface

$$\text{Grad } p = -i\rho w A p.$$

The two boundary conditions possible are the hard case for which grad p = 0 and the soft case for which p = 0. Formation of different cavities is possible using cuboid and tetrahedral elements. In this analysis triangular prism elements are used.

For a single dimensional case as in discharge tube the functional 'F' is given as (5).

$$J = \frac{1}{2} \int_0^l \left(\frac{dp}{dz} \right)^2 A dz - \left(\frac{w}{c} \right)^2 \frac{1}{2} \int_0^l p^2 A \, dz.$$

the stationery value of this equation leads to the horn equation.

$$A \frac{d^2 p}{dz^2} + \frac{dp}{dz} \cdot \frac{dA}{dz} + \left(\frac{w}{c} \right)^2 A p = 0$$

together with the boundary conditions

$$A \frac{dp}{dz} = 0 \quad \text{at} \quad Z = 0 \text{ and } Z = l.$$

here p is the acoustic pressure, A cross sectional area at any z, w the radial frequency, c the speed of sound, and l the length of pipe. With this formation, varaible section pipe elements can be formed.

The formation of 3 D elements were compared with exact and reported values of a unit cube as given by (1). Formation of 1 D elements with a closed tube of unit length given in (5) was also verified.

CASE STUDIES

Three cavities are studied for their natural frequencies and mode shapes. The emphasis is on compressor cavity resonances in which two compressor cavities are analysed using triangular prism elements. The cavity temperatures will be different for high side compressors and for heat pump applications. Both samples are of low side type. The cavities are modified in both cases and the effect on the resonant frequencies is studied. The second study is of resonance in discharge tube carrying high pressure (temperature) gas from the pump to the shell. The third study is about resonances of the room in which a room airconditioner is installed. In all cases, boundaries are assumed to be rigid.

Compressor Cavity Resonance (Sample 1)

The free portion between the shell and pump is the cavity in which the suction gas is present. The shell considered is of cylindrical cavity in which the pump is positioned with the help of springs. The elevation view of the model considered is shown in Figure 1. The modification done with steps on the top shell is also shown in Figure 1. One quadrant of the annular cavities element formation, before and after modification, are shown in the figure at various longitudinal cross sections. However, the total shell annulus was used for computation. The height where the oil is present is considered as rigid and the longitudinal height is reduced by that length. The cavity frequencies depend on the temperature at which the gas is and the type of gas that is used in running the compressor. The original compressor and the modified compressor were analysed at temperatures of 15° C, 25° C and 35° C which is the normal range of operation in an airconditioner. Table 1 shows the speed of sound of different gases at the considered temperatures. The speeds are seen to increase with temperature and change with the gas used. Table 2 shows the resonant frequencies of the original cavity, and the modified cavity with the stepped top shell at different operating temperatures.

The first mode number represents the circumferential, the second the radial mode, and the third the longitudinal mode. The circumferential and longitudinal modes dominate at the lower frequencies of interest i.e. 2000 Hz. The radial frequencies, because of the short length in the cavity, generally occur above 2000 Hz. When only a quadrant of the cylinder is used the circumferential modes are badly affected. Hence the entire cylinder was considered. The lower frequencies do not change much with temperature, for mode number 200 the change is from 332 Hz to 343 Hz. However, the change for higher frequencies is more, as the frequency is proportional to w/c which is independent of temperature. For 002 mode the change is from 566 Hz to 788 Hz. For the modified compressor there is a slight decrease in the frequencies for circumferential models 200 and 400. The longitudinal mode 002 also shows a decrease in the frequencies in the modified shell. The mode numbers were fixed by looking at the mode shapes, it is possible that complicated mixed modes may have wrong numbering. In Figure 3 the effect of modification to the shell on different modes of cavity resonances is shown. The difference is more dominant at the higher combined modes like 012 and 013 where both radial and longitudinal modes are present.

Two mode shapes for modes 401 at cross-sections AA and BB are shown in Figure 4, for the original cavity. The difficulty in numbering arises due to change in the radial or circumferential mode number at a different cross-section.

Compressor Cavity Resonance (Sample 2)

The second sample study is also similar to the first except that the cross sectional area is elliptical in shape, and the annular section varying with length. The different cross sections are numbered along the length of the compressor and are shown in Figure 2 for the original, and second modification. In the first modification, the cross-section at AA is made identical to the one at BB thereby reducing the cavity volume. In the second modification, both top and bottom shells have narrowed stepped shapes as shown. The element formation of the different annular cavities in all these cases is shown in Figure 2 for half the area. Calculations too were carried with this formation to reduce computational time. As a result, asymmetric circumferential modes could not be obtained.

The frequencies for different modes and at different temperatures are shown for the original and the two modified cases in Table 3. The first longitudinal mode of 001 shows an increase and the circumferential modes 100 and 200 show a decrease in the frequencies as modifications are introduced. The changes are related to the volume of gas that is involved in that particular mode. The effect of modifications on resonant frequencies of diffeferent modes is shown in Figure 3. The circumferential modes 200, 300 and its combined mode with the longitudinal 202, 103, 203 show increase in frequencies when the second modification is done to the shell. The mode shapes at cross-section CC are shown for the original case for mode 213 at two heights in Figure 4. The first is at the transition from cross-section BB to CC and the second at the top most section. The change in the mode shape with height can be noticed.

Discharge Loop Resonances

The high pressure (temperature) gas coming out of the pump during discharge has pulsations associated with it which are reduced in a muffler. The gas with residual pulsations goes through a discharge loop before it comes out of the shell. If these pulsations happen to match the resonant frequencies of the tube there will be an increase in the gas pulsations. Simple one dimensional elements given by Craggs (5) were used to represent the discharge tube as shown in Figure 4. The resonant frequencies of the tube at different modes are given in Table 4. If any of the discharge gas pulsations coincides with the tube natural frequencies a resonance is caused. In such cases a modification of the tube may be required. The first few mode shapes are shown in Figure 4. It is seen that the modes correspond mostly to a straight closed tube. The effect of the expansion chamber is the introduction of slight cranks at that point.

Room Acoustics

The hermetic compressor is connected to an appliance and is used in a room. In this study a cubical room was considered for its acoustic resonance. Some of the frequencies which coincide with the lower frequencies of the compressor between 100 Hz and 200 Hz are shown. Because of the presence of a large number of frequencies, about 50, in this range it will be difficult to completely eliminate frequencies that are problematic. Any shifting would only be marginal and would not be effective, as there could be a similar change in the compressor noise/vibration natural frequency due to change in temperature or voltage. It is best to adopt some acoustic absorbent agent to reduce noise, if necessary. The mode shapes for a cubical room are very straight forward and mode 132 at a height of 2 meters is shown in Figure (4).

CONCLUSION

Acoustic finite elements of 3 D and 1 D type were used in finding the resonant frequencies of compressor shell to pump cavity and discharge tube. It was possible to consider complex cross-sectional changes along the length of the compressor. The method can be used to represent non circular cross-sections like the elliptical shell. Modifications to either the pump or the shell results in a shift of the resonant frequencies. Thus, any problematic frequencies could be tackled. Finally a room's acoustic behaviour, where the appliance is used, is also determined.

REFERENCES

1. Craggs A., "The use of Simple Three - Dimensional Acoustic Finite Elements for Determining the Natural Modes and Frequencies of Complex Shaped Enclosures", Journal of Sound And Vibration, 23(3) 331-339, 1972.

2. Johnson C.N., Hamilton J.F., "Cavity Resonance in Fractional HP Refrigerant Compressors", Proceedings of International Compressor Conference, pp 83-89, 1972.

3. Tojo K, et al, "Noise Reduction in Refrigerator Compressors", Proceedings of International Compressor Conference, pp 235-242, 1974.

4. Munjal M.L., "Acoustics of Ducts and Mufflers" John Wily & Sons, New York.

5. Craggs A., "A Note on the Theory and Application of a Simple Pipe Acoustic Element", Journal Of Sound And Vibration, 85(2), 292-295, 1982.

6. Zienkiewicz O.C, "The Finite Element Methods in Engineering Sciences", McGraw hill, London, 1971.

7. Gladwell G.M.L, and Zimmerman G., "On Energy and Complementary Energy Formulations of Acoustics and Structural Vibration Problems", Journal Of Sound And Vibration, 3(3), 233-241, 1965.

TABLE # 1

SPEED OF SOUND (M/S) FOR DIFFERENT GASES AT DIFFERENT TEMPERATURES

GAS	TEMPERATURES (DEG C) --->		
	15	25	35
R 12	150.2135	152.7978	155.3391
R 22	180.7996	183.9100	186.9688
AIR	340.2626	346.1165	351.8730

TABLE # 2

EIGEN VALUES AND RESONANT FREQUENCIES FOR SAMPLE # 1

MODE NUMBER	ORIGINAL				ORIGINAL				MODIFIED SHELL			
	ONLY QUADRANT				ENTIRE CYLINDER				ENTIRE CYLINDER			
C R L	w^2/c^2 (m^-2)	FRQNCY.(Hz) AT 15 C	25 C	35 C	w^2/c^2 (m^-2)	FRQNCY.(Hz) AT 15 C	25 C	35 C	w^2/c^2 (m^-2)	FRQNCY.(Hz) AT 15 C	25 C	35 C
2 0 0					133	332	338	343	126	324	329	335
0 0 1	144	345	351	357	145	346	352	358	170	376	382	389
2 0 1					313	509	518	527	339	530	539	548
4 0 0	455	614	625	635	527	661	672	683	506	647	659	670
0 0 2	546	672	684	695	566	684	696	708	500	643	654	665
4 0 1	656	737	749	762	729	777	790	803	733	779	792	805
2 0 2					809	818	832	846	936	880	895	910
0 1 2	985	903	918	934	1058	936	952	968	962	893	908	923

TABLE # 3

EIGEN VALUES AND RESONANT FREQUENCIES FOR SAMPLE # 2

MODE C R L	ORIGINAL				MODIFICATION # 1				MODIFICATION # 2			
	w^2/c^2 (m^-2)	FRQNCY.(Hz) AT 15 C	25 C	35 C	w^2/c^2 (m^-2)	FRQNCY.(Hz) AT 15 C	25 C	35 C	w^2/c^2 (m^-2)	FRQNCY.(Hz) AT 15 C	25 C	35 C
0 0 1	73	246	250	254	87	268	272	277	90	273	278	282
1 0 0	200	407	413	420	185	391	398	405	191	397	404	411
1 0 1	347	536	545	554	352	540	549	558	386	565	575	584
0 0 2	460	617	628	638	482	632	643	653	510	650	661	672
2 0 0	588	698	710	721	660	739	752	765	582	694	706	718
1 0 2	676	748	761	773	681	751	764	776	778	802	816	830
2 0 1	911	869	884	898	948	886	901	916	920	873	888	903

Sample: 1

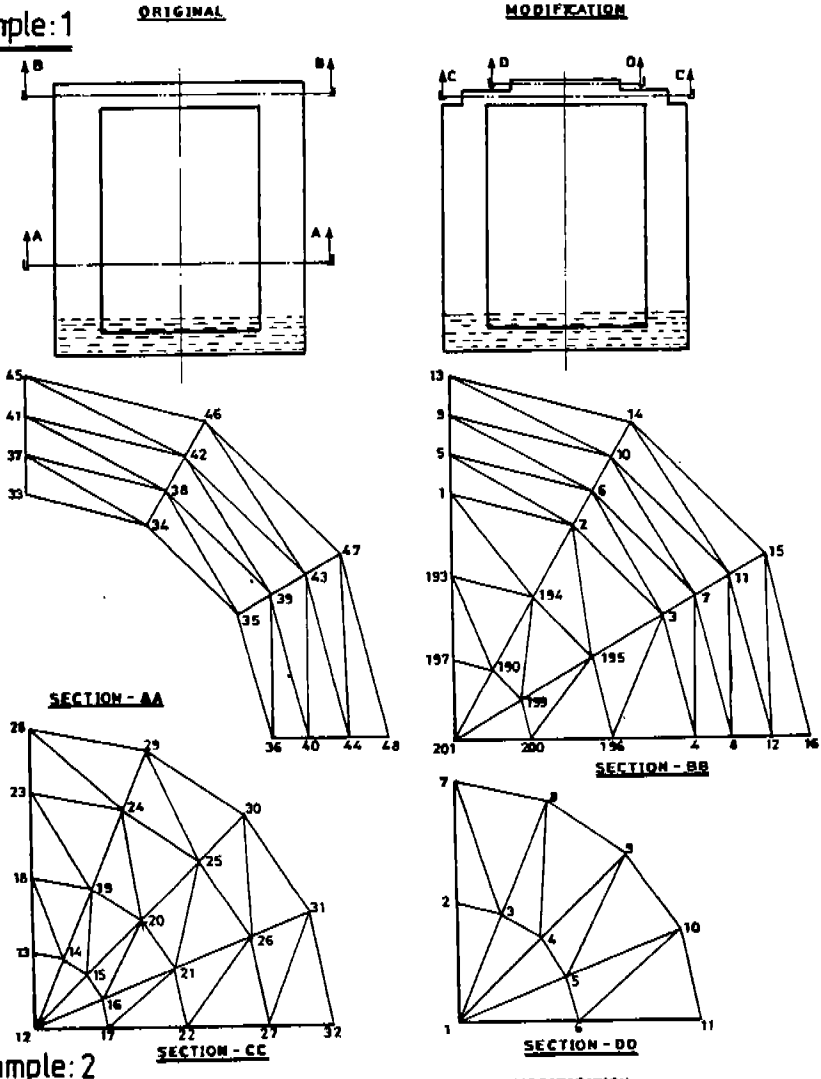

Sample: 2

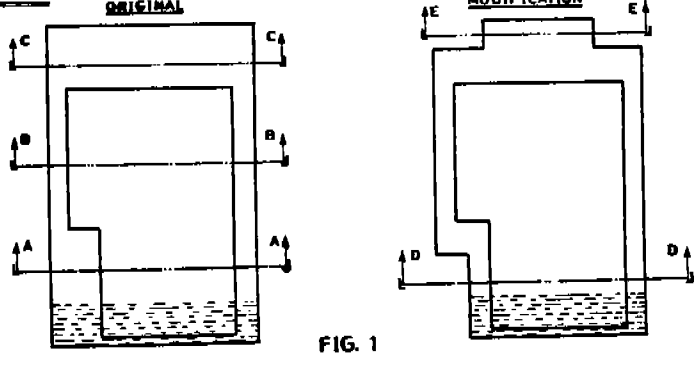

FIG. 1

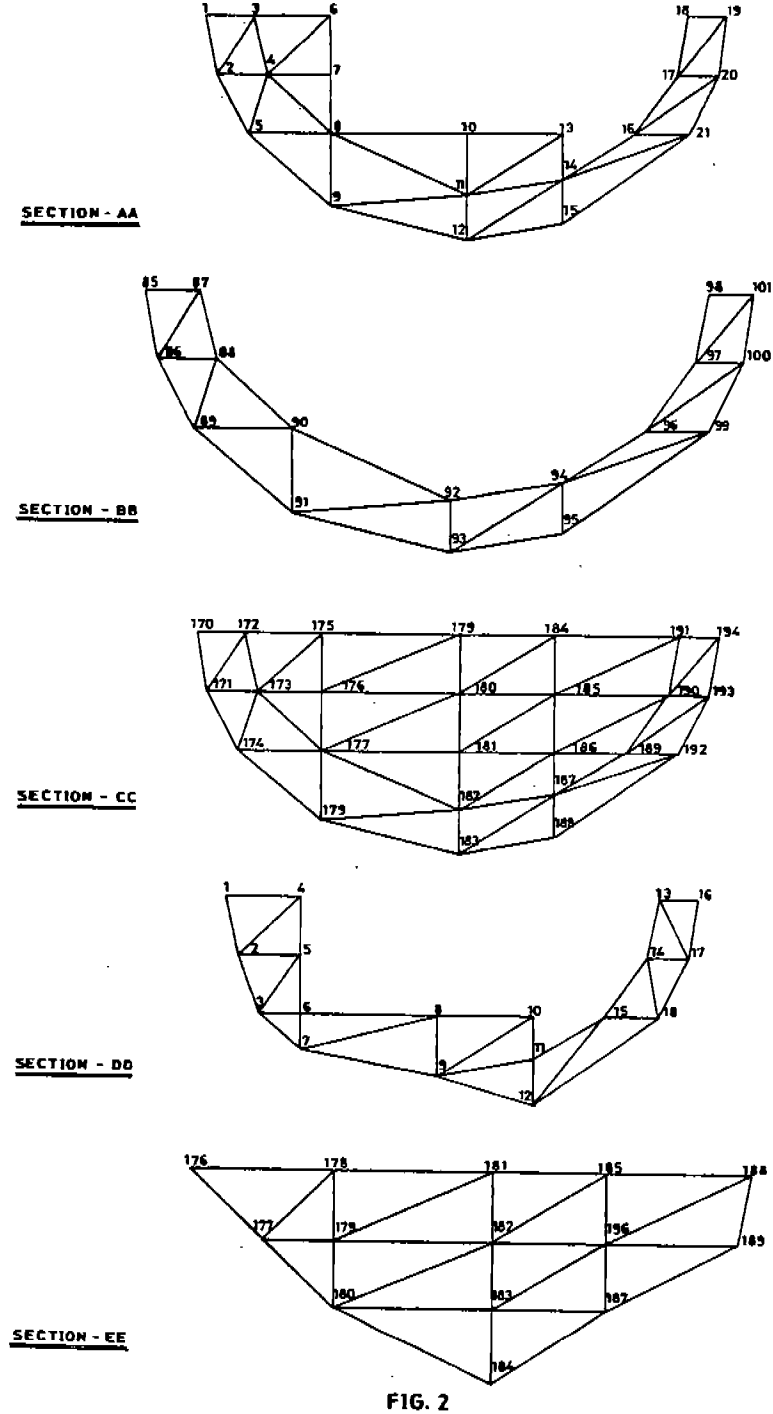

FIG. 2

CAVITY RESONANT FREQUENCIES

Sample: 1

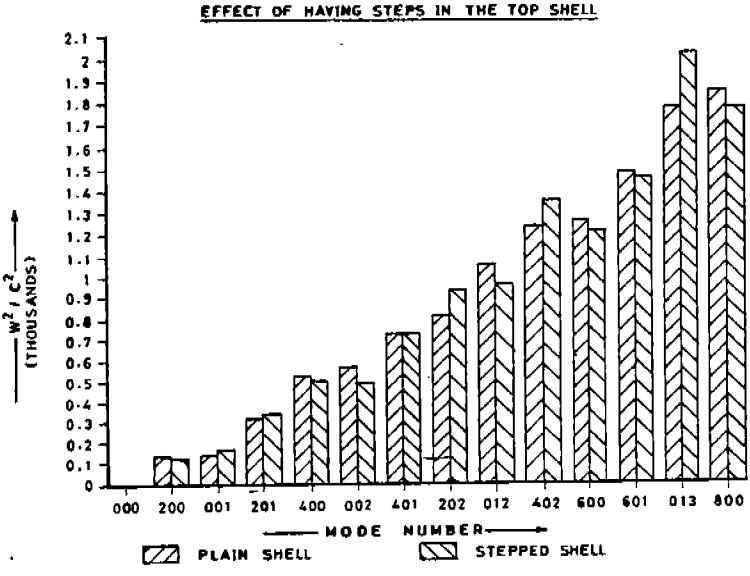

Sample: 2

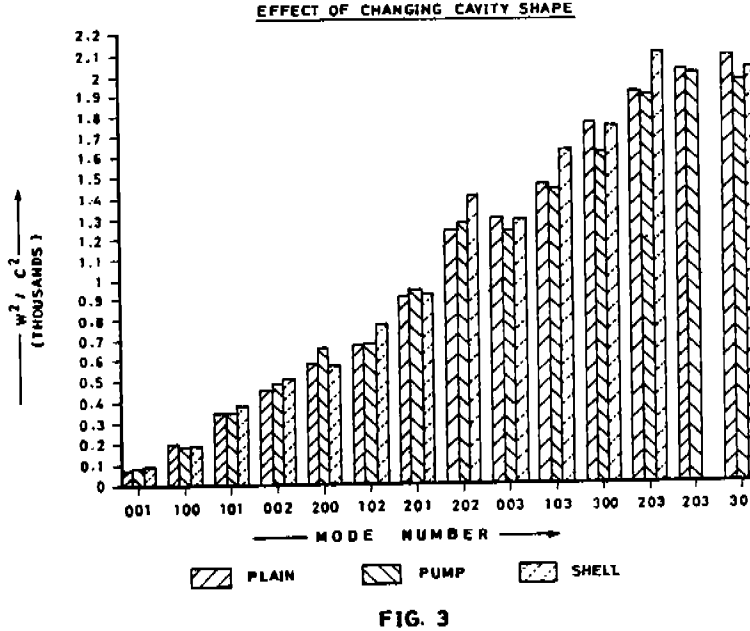

FIG. 3

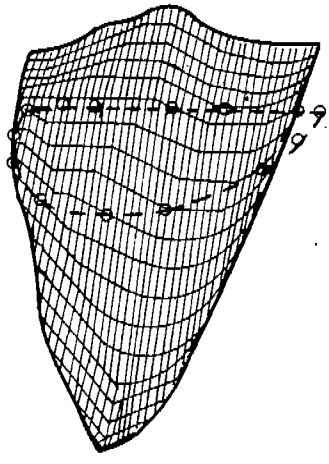

MODE : 213 C

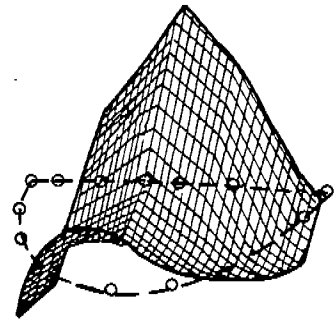

MODE : 213 C

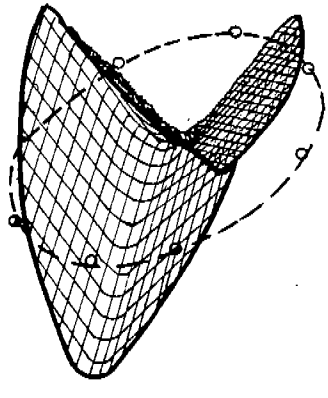

MODE : 401 B

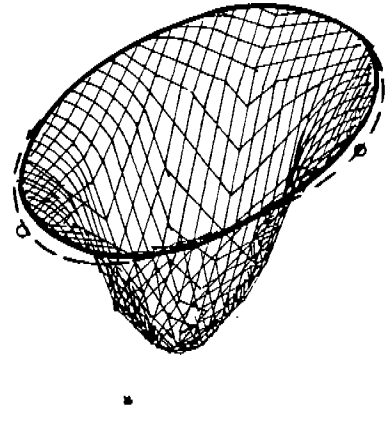

MODE : 012 B

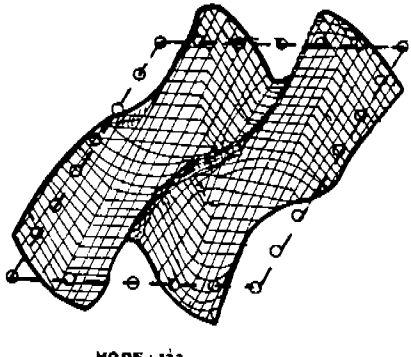

MODE : 132

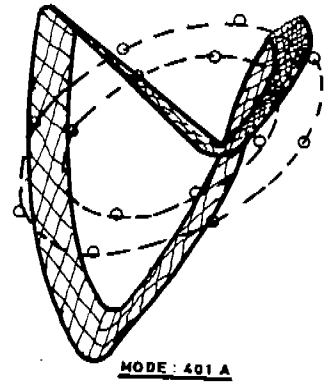

MODE : 401 A

FIG. 4

TABLE # 4

EIGEN VALUES AND RESONANT FREQUENCIES FOR THE DISCHARGE LOOP

MODE NUMBER	w^2/c^2 (m^{-2})	FREQUENCY (HZ) AT T = 85 C	100 C	115 C
1	22.0852	150.7618	153.8865	156.9490
2	82.1983	290.8520	296.8803	302.7885
3	169.56	417.7365	426.3946	434.8803
4	367.745	615.1969	627.9476	640.4444
5	490.661	710.6103	725.3386	739.7736
6	740.796	873.1524	891.2495	908.9864

TABLE # 5

SOME EIGEN VALUES AND RESONANT FREQUENCIES FOR A ROOM AT A TEMPERATURE OF 30 C

w^2/c^2 (m^{-2})	f (Hz)	w^2/c^2 (m^{-2})	f (Hz)	w^2/c^2 (m^{-2})	f (Hz)	w^2/c^2 (m^{-2})	f (Hz)	w^2/c^2 (m^{-2})	f (Hz)
4.50	117.9	6.55	142.1	8.21	159.1	10.1	176.8	12.0	193.0
4.83	122.1	6.62	142.9	8.27	159.7	10.2	178.1	12.1	193.6
4.95	123.6	6.72	144.0	8.56	162.5	10.4	179.7	12.2	194.7
5.42	129.4	7.01	147.0	9.04	167.0	10.8	182.8	12.4	195.6
5.48	130.1	7.14	148.4	9.27	169.1	11.1	185.1	12.5	196.4
5.94	135.4	7.25	149.5	9.30	169.4	11.3	186.8	12.5	196.7
6.00	136.0	7.72	154.3	9.47	170.9	11.3	187.0	12.7	198.1
6.03	136.4	7.75	154.6	9.75	173.4	11.4	187.7	13.0	200.3
6.29	139.3	7.75	154.6	9.76	173.5	11.9	191.9	13.2	202.2
6.40	140.5	8.13	158.4	9.90	174.8	12.0	192.4	13.2	202.3

MODE SHAPES FOR DISCHARGE TUBE

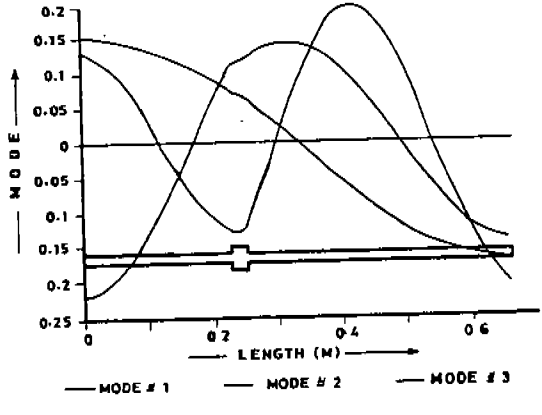

FIG. 5

APPLICATION OF FOUR POLE PARAMETERS FOR GAS PULSATION ANALYSIS OF MULTI-CYLINDER COMPRESSORS WITH SYMMETRICALLY ARRANGED GAS CAVITIES

J. Kim
Mechanical, Industrial and
Nuclear Engineering
University of Cincinnati
Cincinnati, OH 42221-0072

ABSTRACT

Analysis of a single input and single output acoustic system can be done very efficiently by utilizing the concept of four pole parameters. Although there are more than one inputs to the system, gas pulsation analysis of multi-cylinder compressors can be done by using four pole parameters if their gas cavities are arranged symmetrically about the cylinders and the phase angles between pistons are identical. Acoustic couplings between cavities and sources are able to be decoupled by considering symmetric and anti-symmetric modes separately which allows to formulate equivalent four poles of the system. It is shown that one can fully utilize the advantage of four pole parameters.

INTRODUCTION

Four pole parameters are a very useful concept for efficient analysis of a composite acoustic system because of its computational efficiency and simplicity in formulation of the acoustic equation. Therefore, they are extremely useful to be used with design programs or simulation programs. Application examples of four pole parameters for the performance analysis of compressors are found in reference [1]. Good basic discussions on the concept and derivation of four poles of some basic acoustic elements are found in reference [2]. In reference [3], a general method is discussed on how to formulate four poles of continuous systems from pressure response solutions using natural mode superposition method. The result was also applied to the system with multiply connected cavities[4].

One limitation of the four pole method is that it cannot be used for the systems with more than one input because the concept is defined for single input single output (SISO hereafter) systems. Therefore, at least to the knowledge of the author, four poles have not been used to solve the system acoustic equation of multi-cylinder compressors. Gas pulsation analysis of the multiple cylinder was first treated in reference [5] using the Helmholtz resonator approach. The method results in a matrix equation of the same form as the vibration problem of a lumped parameter system with multi-degree of freedoms. In fact, vibration analogy was used to solve multi-cylinder gas pulsation problems in reference [6]. The eigenfunction superposition method can be used to solve the equation, however formulation and computation of the equation can be quite involved as the system becomes complex.

In this paper, it is shown that four pole parameters can be used for the analysis of the multi-cylinder compressor if *the gas manifold is arranged symmetrically with respect to each cylinder and the piston has the same phasing between each other*, for which we use simply *symmetric gas manifold* from now on. This condition is not considered to limit the application value of the method seriously because gas manifolds of most of multi-cylinder compressors or engines would be designed in such a way. The basic idea and formulation method are presented using the double cylinder compressor as an example. Then the idea is extended to compressors with multiple cylinders. A brief discussion is made on how to utilize the method for the analysis of overall gas manifold system.

FORMULATION OF EQUIVALENT FOUR POLE PARAMETERS

1. Double Cylinder Compressor

Figure 1 shows a part of the gas manifold of a compressor with two cylinders. The two identical cylinder head volumes V1 and V2 are connected to a common collector volume Vc by two identical pipes p1 and p2. If the phase between two pistons is 180 degrees, the flow inputs to

the head cavities V1 and V2 are $Q_i e^{jn\omega t}$ and $(-1)^n Q_i e^{jn\omega t}$, where n=1,2,3..., and ω is the motor speed. In general, the output flow from the collector volume may enter to another acoustic system, such as an anechoic pipe or an expansion type muffler.

Figure 2 illustrates the basic idea to be used. Because of the symmetry of the system, the inputs corresponding to an even n will excite only the symmetric modes (Fig.2-a), while the inputs corresponding to an odd n will excite only antisymmetric modes (Fig.2-b). Therefore, it is possible to consider symmetric and antisymmetric inputs separately. Let us define the equivalent four pole equation of the system in Figure 1 in the same way as we do for regular SISO systems.

$$\begin{Bmatrix} Q_i \\ P_i \end{Bmatrix} e^{j\omega t} = \begin{bmatrix} A & B \\ C & D \end{bmatrix} \begin{Bmatrix} Q_e \\ P_e \end{Bmatrix} e^{j\omega t} = \begin{bmatrix} A & B \\ C & D \end{bmatrix} \begin{Bmatrix} 1 \\ Z_e \end{Bmatrix} Q_e e^{j\omega t} \tag{1}$$

where, A, B, C, and D are equivalent four poles of the system, $Z_e = P_e / Q_e$ is the acoustic impedance at the system output point e, which depends on the acoustic system to be attached to, and P_i, P_e are pressure amplitudes at the system input and output points. Unlike ordinary four poles, they define the relationship between one of the two input pairs of the system and the output pair, which is why they are named *equivalent* four poles.

(1) Symmetric Modes

First, let us look at the common collector volume Vc subjected to the symmetric inputs (n = 2,4,6..) shown in Figure 3-a. The pressure at a point r in the volume can be represented as,

$$P(r) = Q_1 f_1(r) + Q_1 f_2(r) - Q_e f_e(r) \tag{2}$$

where, $f_i(r)$ is the pressure response of the cavity at the point r to the harmonic flow input of unit magnitude at the point r_i. Pressure responses may be obtained by any experimental, analytical or numerical methods. In reference [3], pressure responses were obtained by using natural mode superposition method using analytical natural modes. Let us use $f_{ij} = f_i(r_j)$ for short notation, the first subscript meaning the input point and the second subscript meaning the response point. From the reciprocity, we also can utilize the fact that $f_{ij} = f_{ji}$. The pressure at the output point e is

$$P_e = Q_1 (f_{1e} + f_{2e}) - Q_e f_{ee} = 2Q_1 f_{1e} - Q_e f_{ee} \tag{3}$$

where the fact that $f_{1e} = f_{2e}$ was used from the symmetry. The input point pressure P_1 is

$$P_1 = Q_1 (f_{11} + f_{21}) - Q_e f_{e1} \tag{4}$$

By rearrange equation (3), we obtain

$$Q_1 = (f_{ee} / 2f_{1e}) Q_e + (1/2f_{1e}) P_e \tag{5}$$

Substituting equation (5) to equation(4),

$$P_1 = \left[(f_{ee} / 2f_{1e}) (f_{11} + f_{21}) - f_{e1} \right] Q_e + \left[(f_{11} + f_{21}) / 2f_{1e} \right] P_e \tag{6}$$

Equations (5) and (6) defines the equivalent four pole relationship of the cavity 3. Therefore equivalent four poles of the collector volume with two symmetric inputs and a single output are

$$A_c = f_{oo} / 2f_{1o} \tag{7}$$

$$B_c = 1 / 2f_{1o} \tag{8}$$

$$C_c = (f_{oo} / 2f_{1o})(f_{11} + f_{21}) - f_{el} \tag{9}$$

$$D_c = (f_{11} + f_{21}) / 2f_{1o} \tag{10}$$

The overall equivalent four poles of the system in Figure 1 for symmetric inputs are now obtained by utilizing the cascading property of four poles.

$$\begin{bmatrix} A & B \\ C & D \end{bmatrix} = \begin{bmatrix} A_{v1} & B_{v1} \\ C_{v1} & D_{v1} \end{bmatrix} \begin{bmatrix} A_{p1} & B_{p1} \\ C_{p1} & D_{p1} \end{bmatrix} \begin{bmatrix} A_c & B_c \\ C_c & D_c \end{bmatrix} \tag{11}$$

The first two matrices are regular four pole matrices of the volume V1 and the pipe p1. Equations of four poles of various acoustic elements can be found in reference [6,7]. If all the acoustic elements in the system are small enough to be treated as lumped parameter elements, the equation represents the half of the system as shown in Figure 2-c.

(2) Antisymmetric Modes

If we look at the antisymmetric input cases (n=1,3,5...) shown in Figure 2-b, we know that $Q_a = 0,\ P_a = 0$ from the geometry. Therefore, we don't have to consider these modes for the analysis of the system beyond the collector volume. The flow and pressure after the collector volume will have only the even harmonics(n=2,4,6,...).

In many cases, it is necessary to know the pressure or flow before the collector volume. For example, the pressure in V1 is the back pressure of the valve which is necessary to be known for an accurate compressor performance simulation. From Figure 3-b, the pressure at point 1 is,

$$P_1 = Q_1 f_{11} - Q_1 f_{21} = Q_1 (f_{11} - f_{21}) \tag{12}$$

Therefore, the input point impedance at the pint 1 of the collector volume becomes,

$$Z_1 = P_1 / Q_1 = f_{11} - f_{21} \tag{13}$$

The four pole relationship between the system input point and the input point of the collector volume is,

$$\begin{Bmatrix} Q_i \\ P_i \end{Bmatrix} = \begin{bmatrix} A_{v1} & B_{v1} \\ C_{v1} & D_{v1} \end{bmatrix} \begin{bmatrix} A_{p1} & B_{p1} \\ C_{p1} & D_{p1} \end{bmatrix} \begin{Bmatrix} 1 \\ Z_1 \end{Bmatrix} Q_1 = \begin{bmatrix} A_T & B_T \\ C_T & D_T \end{bmatrix} \begin{Bmatrix} 1 \\ Z_1 \end{Bmatrix} Q_1 \tag{14}$$

Equation (14) can be used to calculate the head cavity pressure as it will be shown later. From equation (12), it is also known that $Z_1 = 0$ if the collector is relatively small, therefore the pressure inside is nearly uniform. Furthermore, if all acoustic elements are small, the equation represents a Helmholtz resonator in Figure 2-d as expected. It should be noted that *large* or *small* is a relative term compared with the shortest wave length of interest.

2. Multiple-Cylinder Compressor

(1) Symmetric Modes

The previous discussion can be extended to the case of a multi-cylinder compressor. Figure 4 shows a compressor with three symmetrically arranged cylinders. From similar considerations as before, only symmetric modes contribute to the gas pulsations of the system beyond the collector volume. Notice that the modes corresponding to n=3,6,9,..are considered symmetric for the three cylinder case. For the m cylinder case, four poles of the collector volume have to be modified from equations (7),(8),(9) and (10) as follows.

$$A_c = f_{aa} / m f_{1a} \tag{15}$$

$$B_c = 1 / m f_{1a} \tag{16}$$

$$C_c = (f_{aa} / m f_{1a}) (\sum_{k=1}^{m} f_{kl}) - f_{al} \tag{17}$$

$$D_c = (\sum_{k=1}^{m} f_{kl}) / m f_1 e \tag{18}$$

(2) Antisymmetric Modes

Input point impedance of the collector volume can be obtained in a similar way as double cylinder cases. Let us look at the collector volume of the symmetric three cylinder compressor when n=1,4,5,.. as shown in Figure 5. The pressure in the volume is

$$P_1 = Q_1 + Q_2 f_{21} + Q_3 f_3 \tag{19}$$

Because $Q_2 = Q_1 e^{j2\pi/3}$ and $Q_3 = Q_1 e^{j4\pi/3}$ and $f_{21} = f_{31}$ from geometry, equation (19) becomes

$$P_1 = Q_1 (f_{11} - f_{21}) \tag{20}$$

One can notice that this is exactly the same equation as equation (12) of the double cylinder case. It can be shown that equation (12) has the same form for all antisymmetric modes of any multi-cylinder compressors with symmetric manifold. Therefore equation (13) and (14) can be used without modification for the calculation of pressure or flow before the collector volume.

APPLICATION TO THE SYSTEM ANALYSIS

1. Compressor Performance Simulation.

Gas pulsations in the compressor head cavity should be calculated to simulate compressor performance accurately because the pulsating pressure in the cavity is what the piston is working against, therefore high amplitude gas pulsations can cause performance losses, undesirable noise problems and sometimes even valve failures[2].

From the four pole equation, harmonic amplitude of the pressure in the cavity is,

$$P_i = (C + ZD) / (A + ZB) Q_i \tag{21}$$

where, a different set of four poles and impedance Z should be used for the symmetric and antisymmetric modes. For example, in the case of the double cylinder compressor in Figure 1,

equation (11) and the system impedance Z_s should be used for the symmetric modes, while equation (14) and the impedance Z_1 in equation (13) should be used for antisymmetric modes.

Q_i is the amplitude of the nth harmonic input volume flow through the compressor valve and it can be obtained by the Fourier Transform of the time series of the valve flow calculated from the previous iteration of simulation[1]. The time domain pulsating pressure in the head cavity can be obtained by adding the average pressure in the cavity p_a to the inverse Fourier Transform of the pressure amplitudes P_i.

$$p(t) = p_a + \sum_{n=1}^{N} P_i e^{jn\omega t} \tag{22}$$

Therefore, gas pulsation analysis of the multi-cylinder compressor can be handled by virtually the same procedure as the single cylinder case once equivalent four poles are obtained. Actual transform and inverse transform can be implemented extremely fast if the FFT and Inverse FFT algorithms are used.

2. Muffler Design

If a muffler is to be designed after the collector volume, one needs to consider only symmetric modes because the antisymmetric modes do not contribute to the unsteady flow beyond the common collector volume. Suppose that we want to design an expansion type muffler to be attached to the system in Figure 1, therefore that we want to obtain transfer functions before and after the muffler is used. If the muffler exit is subjected to pressure release condition, impedance Z_s in equation (1) is zero. Then, the transfer function is obtained as,

$$TF(n\omega) = Q_s / Q_i = 1 / A \tag{23}$$

where, A is the equivalent pole A of the overall system of the symmetric modes and n = m, 2m, 3m,.. and m is the number of cylinders. The transfer function of the system when the muffler is attached can be easily obtained from the new four pole obtained by multiplying one more four pole matrix representing the muffler to the system matrix without it. It also has to be noted that the transfer function defined by equation (23) is the ratio of one of the input flows to the output flow of the system.

Analysis to use a side branch type muffler can also be handled easily following to the procedure in reference [1]. Since the side branch muffler has a band filter characteristics, it will be particularly efficient for the noise control of the symmetric multi-cylinder compressors because unsteady flow harmonics are separated by much larger frequency intervals from each other compared with single cylinder compressors with the same motor speed. For example, if the compressor has four cylinders with 60 Hz motor, then the gas pulsation components beyond the head cavity would have frequencies of 240 Hz, 480 Hz, ..., instead of the harmonics at every 60 Hz of the single compressor. Therefore, it would be relatively easy to design a side branch muffler to filter out a few undesirable noise components without amplifying other frequency components.

SUMMARY

It was shown that how the concept of four pole parameters can be utilized for the analysis of multi-cylinder compressors with symmetric gas manifold. A concept of equivalent four poles was introduced to formulate the system four pole equation by considering the responses of the system to symmetric inputs and antisymmetric inputs separately. The method enables us to utilize the full advantage of the four pole parameters such as simple formulation procedure and efficient

computation in solving the acoustic equation of multi-cylinder compressors. Multicylinder compressors often have relatively large cavities and long pipes, therefore the method has another advantage because it is easier to handle continuous acoustic systems using four poles compared with other approaches.

REFERENCES

[1] J. Kim and W. Soedel, "Convergence of Gas Pulsation Simulation in Combined Time and Frequency Domain Models," Proc. of 1990 International Compressor Engineering Conference, 1990, pp 641-646.

[2] W. Soedel, "Gas Pulsations in Compressor and Engine Manifolds," Short Course Text Book of Purdue Compressor Technology Conference, Ray W. Herrick Lab., Purdue University, 1978

[3] J. Kim and W. Soedel, "General Formulation of Four Pole Parameters for Three Dimensional Cavities Utilizing Modal Expansion with Special Attention to Annular Cylinder," J. of Sound and Vibrations, Vol. 129(2), 1989, pp. 237-254.

[4] J. Kim and W. Soedel, "Analysis of Gas Pulsations in Multiply Connected Three Dimensional Acoustic Cavity with Special Attention to Natural Mode or Wave Cancellation Effects," J. of Sound and Vibrations, Vol. 131(1), 1989, pp 103-114.

[5] W. Soedel, E. Padilla-Navas, B.D. Kotalik, "On Helmholtz Resonator Effects in the Discharge System of Two Cylinder Compressor," J. of Sound and Vibrations, Vol. 30, No.3, pp 263-277, 1973.

[6] R. Singh, "Modeling of Multicylinder Compressor Discharge System," Ph.D. Thesis, Ray W. Herrick Lab., School of Mechanical Engineering, Purdue University, December 1975.

[7] J. Kim, "Simulation of a High Speed Hermetic Compressor with Special Attention to Gas Pulsations in Three Dimensional Continuous Cavities,' Ph.D. Thesis, Ray. W. Herrick Lab., School of Mechanical Engineering, Purdue University, May 1988.

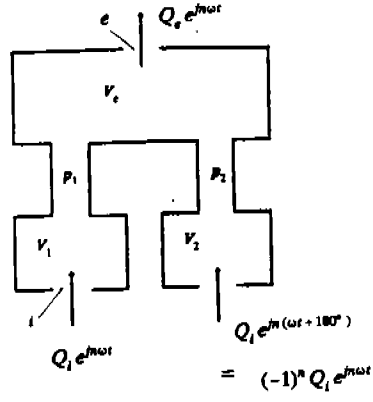

Figure 1 Double-cylinder compressor with symmetric gas manifold

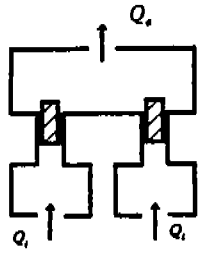

(a) Symmetric modes(n=2,4,6,..)

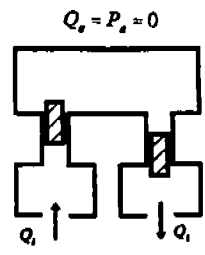

(b) Anti-symmetric modes (n=1,3,5,..)

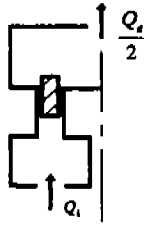

(c) Symmetric modes

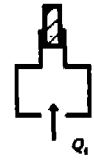

(d) Anti-symmetric modes

Equivalent systems of the lumped parameter system

Figure 2 Symmetric and anti-symmetric modes of the double-cylinder compressor

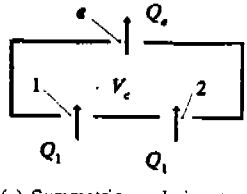

(a) Symmetric mode input

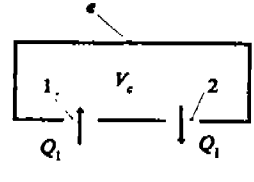

(b) Anti-symmetric mode input

Figure 3 Collector volume

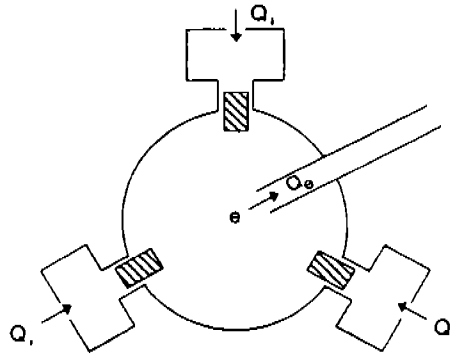

Figure 4 Symmetric mode of the three-cylinder compressor

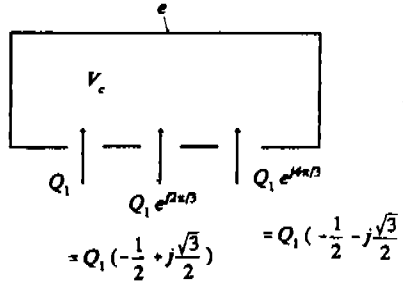

Figure 5 Collector volume with anti-symmetric inputs ; three-cylinder compressor

Appendix A

Additional papers from the 1990 International Compressor Engineering Conference at Purdue

OPENING ADDRESS BY FRED V. HONNOLD

WORLDWIDE COMPRESSOR ENGINEERING CONFERENCE

PURDUE UNIVERSITY

17-19 JULY, 1990

Every two years, we gather to share with each other a portion of what we've learned about compressors since the last meeting.

We also learn at these conferences just how much we don't yet know.

Our professional curiosity is stimulated and we return from West Lafayette energized and determined to probe even deeper into the arcane field we've chosen for study.

In the intervening time, we focus our thoughts sharply on screws, scrolls, rotaries, recips and centrifugals. We concentrate on improving seals and tolerances; improving valve or port designs; creating better gas paths; eliminating losses . . . the list goes on and on.

We live and breathe compressors.

Today I'm asking that we widen our vision -- looking beyond the narrow confines of our science to some larger issues that affect each of us in this room both on a personal and professional basis.

The fact is, they are issues we couldn't avoid even if we wanted.

Many of you are familiar with the American fable of Rip Van Winkle, the rural New Yorker who laid down one afternoon for a nap and woke up 20 years later in a vastly changed world. I'm sure that similar tales exist in almost every culture.

Although we, as engineers, work in a world of facts and scientific proof, who among us has not engaged in such fantasy? We all have asked ourselves what problems our children's children will face and how will they be solved.

Fortunately, or unfortunately, depending on how you view change, the world is changing at such a pace that we won't have to wait 20 years to find out.

Consider global warming.

Mathematical models sophisticated enough to digest and analyze the complexity of the earth's atmosphere and oceans completely, do not exist.

Neither does scientific consensus on global warming.

The Environmental Protection Agency is projecting a 3 degree centigrade increase in the earth's overall temperature by the year 2100. This could result, they say, in devastating coastal flooding as sea levels rise as much as 3 feet.

Others say CO-2 and other "greenhouse gases" in the atmopshere have nearly doubled in the last 100 years, but global temperatures have risen only a half degree centigrade -- way below other projections.

The various hypotheses have yet to be proven, but concern over the accumulation of these "greenhouse gases" -- carbon dioxide, methane, oxides of nitrogen and sulfur, and CFCs -- appears likely to result in legislation or regulation that will restrict their generation and release.

Consider atmospheric ozone depletion.

Besides being viewed as a "greenhouse gas", we're all aware of the role CFCs are believed to play in reducing levels of atmospheric ozone.

Two weeks ago in London, the United Nations Environmental Programme confirmed a total ban on CFC production by the turn of the century.

There will be a future reassessment to see if such a ban is achievable by 1997.

Those attending the UNEP conference agreed that HCFCs, like 22 and 123, are essential if the CFC phaseout is to succeed. But there also was agreement that even these compounds should be phased out by 2040 at the latest and by 2020 if possible.

There are other concerns lurking in the future, as well.

Consider the dwindling of finite energy reserves and increased electricity demand.

When those of us in developed countries flip on a wall switch, we expect electricity to flow, and it almost always does. But as the demand for electricity inches closer to the available supply, the threat of shortages appears more and more likely.

I attended a conference last month at which a major southern U.S. electric utility announced incentives for its large commercial and industrial customers to reduce, or at least shift to off-peak periods, their consumption of electricity.

In itself, that isn't too startling. Utilities have been promoting off-peak usage for years. But the size and intensity of their efforts have increased.

Rebates for the purchase of energy-efficient equipment are increasing, and no longer are utilities promoting new ways for their customers to use as much electricity as they can.

Some other speakers at the conference presented scenaria that I think shocked a few people in the audience.

The Electric Power Research Institute anticipates that 200 new medium-sized power plants will need to be built in the U.S. within 10 years to add an additional 100 gigawatts of generating capacity.

But, EPRI said, only 75 gigawatts of generating capacity are planned between now and the year 2000.

Even some of that additional capacity is in doubt as utilities face increased pressure from the public and regulators to justify each new generating plant.

The puzzle becomes even more complex as you consider the interplay among these issues.

The worldwide demand for electricity is steadily increasing.

Growth of demand is even greater in developing countries where urbanization increases energy consumption as societies shift focus from agrarian to industrial.

But meeting that demand for electricity contributes to those other problems.

Coal, in the U.S. and elsewhere, is the fuel of choice to generate that electricity.

According to the North American Electric Reliability Council, coal now generates about 43.5 percent of electricity in the U.S.

By 2000, the Reliability Council expects the percentage to fall to 41.4 percent. Regardless, coal will continue to be used far more than other fuels.

But burning coal generates greater amounts of carbon dioxide as well as oxides of nitrogen and sulfur -- all of which contribute to the threat posed by global warming.

Sulfur emissions, or course, contribute to acid rain, an environmental concern I hadn't mentioned earlier.

The push to eliminate CFCs has added another variable to the equation.

As compressor engineers, we know that most of the non-CFC refrigerants under study as possible substitutes or alternatives offer less cycle efficiency -- thus drawing more electricity input for the same output.

Add to this the efficiency penalty created by the elimination of CFC-blown insulating foam from refrigerator and freezer walls.

Of course, burning natural gas is a cleaner way to generate electricity and more natural gas is being used for that purpose, but methane is even more efficient than CO-2 at trapping heat. Stricter regulation of methane releases during production and transportation may hinder the development of gas-powered generating plants.

There are other alternatives, such as nuclear generation, solar and clean, renewable hydro-electric power, but they have their problems, too .

After the Chernobyl accident in 1987, the safety of nuclear power plants around the world is being called into question.

Both Japan and France are committed to expanding their use of nuclear power, but Sweden plans to phase out nuclear plants by 2010.

Spain, as well, has a five-year moratorium on the construction of new nuclear plants. A recent public opinion poll showed that only 30 percent of the Spanish populace favored nuclear power.

Even hydro has its problems.

The proposed "Three Gorges" project in the People's Republic of China would include a 600-foot-high dam across the Yangtze River that would provide 18 gigawatts of electricity. The dam is attractive to a country that relies mainly on coal-burning power plants.

But the social consequences would be staggering. More than a million people would be displaced from their homes. The lake created behind the dam would engulf some of the country's most scenic areas.

The news just keeps getting worse.

I wish I could paint a brighter picture of our earth's future, but doing so would be inaccurate. These problems are real and they cannot be ignored.

I assume by now you've begun to sense the direction in which I'm heading.

The air conditioning and refrigeration industries contribute to these problems. And even though issues like global warming, ozone depletion, and dwindling natural resources cannot easily be reduced to more human dimensions, we, as individual compressor engineers, must believe that we can play a significant role in their solution.

And now is as good a time as any to place one more obstacle in our path -- the requirements of the various markets we serve.

While we're keeping an eye on energy efficiency for the sake of our environment, we can't forget about things like cost, reliability, low sound levels and comfort that our customers expect.

Remember:

- Compressors dominate air conditioning system cost.
- Compressor failures dominate system repair costs.
- Compressor sound levels also dominate air conditioning and refrigeration system sound levels.

Where do we start?

The problems of global warming and dwindling natural resources available for electricity generation both hinge on increasing the efficiency with which the world uses energy.

In the air conditioning and refrigeration industries, that means increasing the efficiency of our systems and processes. And since improving compressor efficiency is generally more cost effective than increasing heat exchanger efficiency, the responsibility falls heavily on our shoulders.

We've already come a long way. Compressor efficiencies in the last 20 years have increased nearly 60 percent from 7 to 11 EER by reducing losses from friction, heat transfer, leakage and motors.

But the way people look at air conditioning and refrigeration systems is changing and will demand more of us. Let me give you some examples.

As a means of shifting peak demand so that they can postpone the construction of new generating capacity, utilities are waking up to the potentials of thermal storage.

A San Diego developer recently received more than $400,000 from a utility because he agreed to install an ice storage system to cool a 30-story office building and hotel complex.

Other utilities are paying for feasibility studies to see if thermal storage is a viable alternative to builders.

Some say thermal storage uses more energy because lower suction temperatures are required to make sub-freezing brine as opposed to chilled water at 6 degrees centigrade..

But the real savings will come when we combine ice storage with a cold air delivery system.

In standard air distribution systems, air is cooled to around 12 degrees C. But air cooled to 7 degrees reduces the volume of air needed. That means smaller ducts and reduced fan horsepower. When compared with a conventional system, cold air systems can reduce electricity consumption by 50 percent.

But these ice storage / cold air systems will really come into their own when we develop compressors with higher efficiencies at lower suction temperatures.

The focus is not only on ice storage.

Heat recovery has long been popular with commercial and industrial users, but with energy costs rising, it will also spread into the residential sector with products that integrate space cooling with domestic water heating.

Integrated products demand stronger compressors.

With the increased reliability and cost effectiveness of digital electronic controls, we also find that zoning is making a comeback in commercial systems and spreading into the residential systems.

Using energy only where and when it is necessary to maintain comfort saves our customers money, but to be effective, it requires compressors that operate efficiently over a broader range of load conditions.

So how do we get there?

I'm sure most of us have conceptualized the ideal compressor. It would have:

No valves
No torque pulses
No bearing wear
No compression chamber leakage
No heat transfer in compression
No lubricant
No over or under pressure
Minimum dynamic imbalance
Capacity matching the load

Few moving parts
Minimum sound
And intelligence

The rotating-type compressors our industry has embraced recently already possess some of these ideal characteristics. Better dynamic balance and fewer parts. Screws and scrolls don't have valves and only minimum torque pulses. But the ideal is still far ahead of us.

The papers we'll hear at this conference will move us closer to those ideals.

o We already are looking at new materials that hold the promise of improved efficiency, robustness, reliability, and reduced costs.

The cast iron and aluminum we've had around for years is good stuff and metallurgists keep making better alloys. Because of their low cost, we're bound to keep using them as substrates.

But the wear and abrasion resistance we need we'll probably get from ceramic coatings. Reliability will increase. Not only will our customers be happier, but the number of scrapped compressors out there will reduce the volume of CFCs and HCFCs released into the atmosphere.

Metallic and non-metallic composites, especially in screw and scroll compressors, will help us attack the leakage problems inherent in both systems. Abradable coatings that seat with each other may help us reduce both leakage and friction.

And when we do that, we increase efficiency.

Air conditioning and refrigeration system manufacturers spend millions of dollars each year to improve the heat transfer characteristics of our coils.

New materials, some variation of those same coatings, will help us eliminate the unwanted heat transfer within a compressor that steals efficiency.

Until now, the oil-less compressor has pretty much been a dream. But with new bearing materials, that dream is within our grasp.

Not only will compressor reliability be greatly enhanced with no lubrication system to fail, but overall system efficiency will improve as oil stops circulating with refrigerant through heat exchangers.

Oil-free compressors start looking even better when you consider the effects that some CFCs substitutes have on traditional lubricants.

o We are advancing the idea of designing electronic controls and sensors into the compressor rather than adding them as afterthoughts. Coupled with variable-speed capabilities, efficiency and reliability will improve dramatically.

Variable-speed drives offer exceptional opportunities for efficiency improvement because they allow us to more "easily" approach achievable system SEERs over 20.

Compressor efficiency increases because the variable-speed drive allows it to operate at lower pressure ratios.

When the system is operating at below maximum load, as it does most of the time, the throttled-down compressor reduces refrigerant flow.

In effect, that oversizes the evaporator and condenser coils to improve heat transfer and efficiency.

With permanent magnet, electronically commutated motors, some of the losses common to induction motors no longer exist because current isn't being used to create a field in the rotor. More efficient motors also dump less heat into the suction gas, multiplying their impact on overall compressor efficiency.

As I mentioned earlier, zoning in both residential and commercial applications calls for compressors that operate over a wider range.

Is there any reason, given the sophistication of future electronics, that we couldn't see speed variations of 30 to 1?

We're also talking about intelligence in compressors -- intelligence that lets them adapt to changing conditions, protect themselves better and diagnose their own ailments.

As a compressor ages and capacity degrades because of wear, an intelligent compressor could increase its speed to compensate. If it sensed refrigerant flooding, it would reduce speed and signal the fan motor to increase airflow over the evaporator coil.

The possibilities are limited only by our imagination and the very real marketplace constraints that require real value for money.

o Advances in manufacturing processes, such as near-net-shape casting and more precise machining, will also help us create better compressors.

Near-net-shape molding operations already have permitted the substitution of a plastic material for steel in the rotors of a twin-screw air compressor.

The challenge is to apply near-net-shaping to achieve large manufacturing cost savings for screw rotors and scroll elements in air conditioning and refrigeration compressors.

Near-net-shaping, through molding, casting or powdered metal techniques, can have a huge implication for tooling costs. Imagine eliminating $5 worth of capital depreciation from the cost of each small compressor.

We also need to improve the accuracy of our final machining. Screw rotors today are machined to tolerances of + or - 20 microns. That needs to be cut in half to stop leakage and realize full efficiency.

While maintaining accuracy, we also need to increase the speed at which metal is removed to control costs.

Computer-compensated machine tools will soon offer real-time feedback during all compressor machining processes so adjustments can be made without sacrificing time.

o More sophisticated computer modeling and simulation techniques will allow us to improve efficiency, reliability and cost before a cutting tool ever touches metal -- or plastic.

As Ray Cohen has pointed out before, it really wasn't too long ago that we even began to fully understand what was happening inside a compressor.

It wasn't until about 1960 that modern engineering methods were first applied to analyze compressor operation. With electric resistance strain gauges and piezoelectric pressure transducers, we began to gather the measurements and analytical tools we needed to develop today's mathematical models and simulations.

Today, those computer simulations are proving their worth as we optimize designs long before they are committed to metal.

Computer simulation tools are now being used to eliminate rotor chatter in twin-screw compressors. The computer can analyze variation after variation until the right rotor profile is achieved.

Purdue is now working on computer simulations that correlate a screw compressor's internal pressure pulsations with radiated sound.

When you consider the volatile regulatory environment in which we operate, these simulation tools give us the flexibility we need to respond to what may seem like overnight changes in policy. They help us shorten the time needed to progress from concept to finished product. Their importance will increase as regulatory and market demands shorten product life cycles.

Standing up here in front of the world's foremost compressor experts is like, as the American expression goes, preaching to the saved. There's not much I can tell you that you don't already know.

But if anything has become clear from this quick and admittedly superficial discussion of today's compressor technology, it's that none of us can be expected to know or do it all. In fact, such an attitude is dangerous.

The rapidity of change doesn't allow time for mistakes if we're to be successful. We need to look beyond our own workstations and involve others in the process of creating compressors.

Do we think about :

- Parts availability
- Inventory requirements
- Weight requirements
- Tolerance capability of machine tools

- Factory layout
- Fabrication cost
- Capital depreciation

Have we taken manufacturing variables into account in assessing performance?

The resolution of any technical problem, like shell vibration, can seriously affect factory throughput.

And more than manufacturing is involved. We need to consider product applications, life-cycle cost, capital investments and the applied cost over the life of the product.
This is an organizational challenge, not a technical one. But its importance can't be underestimated.

Like self-abrading coatings on moving parts, we must make sure we maintain intimate contact with other parts of our organizations or our customers' organizations. For just as we understand technical matters unknown to them, they are aware of market and regulatory forces we may not have considered.

When we tie all of this together -- new materials, powerful electronics, precise manufacturing techniques, computer simulation and the willingness to work with others, we'll achieve results that benefit our institutions, our companies, even our individual countries.

And, as I suggested earlier, our advances in compressor technology will have a broader effect.

I've done some figuring to see if I couldn't quantify what impact our efforts to improve compressor efficiency might potentially have on our planet.

Admittedly, they are rough calculations based on simple assumptions, but they illustrate my point.

Let's assume that we've develolped a new 30,000 BTU scroll compressor. New materials have reduced friction and leakage losses to a minimum. Electronics have given it variable speed and adaptive powers.

For the sake of argument, let's give it an EER of 12.5. That's 20 percent over what most compressors of this size achieve today. Over a 20-year operating life, that's a savings of 20,000 kilowatt hours. You also should remember that this compressor will maintain its efficiency longer.

What does this mean in terms of saved resources?

In today's power plants, it would take 7,000 kilograms of coal to generate that many kilowatts.

What does it mean in terms of greenhouse gases?

Burning that much coal creates about 20,000 kilograms of CO-2. Multiply the savings from one compressor by the number of compressors produced year after year and you'll see that we can have a significant impact on the problems facing our world. There also are other environmental benefits I haven't calculated.

Reduced size means less raw material. That avoids energy consumption at primary levels like mining and smelting. Lighter weight also reduces transportation costs and fuel consumption.

New materials and designs will soon allow us to substitute non-CFC refrigerants without any efficiency penalty.

Lower total costs will make the system more affordable. That's of real concern to those in developing nations to whom refrigeration can sometimes be a matter of life and death.

Insertion of these new technologies also has met our customers' demands for comfort, quiet, reliability and low cost.

I don't always remember what I read on bumper stickers, but I saw one recently in Ithaca, N.Y. whose message has stayed with me. It said simply:
"Think globally, Act locally." . . . "Think globally, Act

locally."

That's not a bad attitude to adopt in a world beset by problems that threaten to overwhelm us with their scope and complexity.

Issues like global warming, ozone depletion, the steady erosion of natural resources and the needs of millions in developing countries do seem overpowering. And there are no simple solutions, no miracle cures.

But they will be resolved.

Resolved by people with the breadth of vision to acknowledge these problems exists;

By people with the clarity of vision to see their role in creating solutions;

By people, like you, willing to focus their special talents and energy on a single aspect of the larger puzzle.

I hope some of the insights we gain during this conference will move us closer to those solutions.

Thank you.

CHANNEL RESONANT ERRORS ON P-V INDICATOR DIAGRAMS FOR RECIPROCATING COMPRESSORS

Frederick Heidrich
Mechanical Engineer
Dresser-Rand Co.
Painted Post, New York

ABSTRACT

The passage length between the cylinder pressure and the measuring transducer on commercial instrumentation will cause distorted pressure time traces. This is due to gas dynamic effects causing pressure pulsations in the indicator passage. Solutions have addressed the problem in both the time and frequency domains. The intention of this paper is to examine four of these methods in comparison to laboratory data. Then determine the most acceptable solution based upon accuracy and personal computer computational time. It was concluded that depending on the solution tools available to the analyst, both a time and frequency domain solution can satisfy the requirements mentioned above.

NOMENCLATURE

A = Cross sectional area of indicator passage (ft^2)
A_{ref} = Reference speed of sound at 14.7 psia and 60°F (ft/min)
C = Capacitance ($g_c A/c^2$)
c = Non-dimensional speed of sound (c_d / c_{ref})
c_d = Local speed of sound (ft/min)
D = Diameter of indicator passage (ft)
f = Darcy friction factor
g_c = Acceleration of gravity (ft × lbm / lbf × s^2)
i = $\sqrt{-1}$
k = Ratio of specific heats (Cp / Cv)
L = Inertance ($1/g_c A$)
l = Length of the indicator passage (ft)
n = Number of harmonics
Pd = Complex pressure at downstream conditions (psia)
P_{ref} = Reference pressure (14.7 psia)
Pu = Complex pressure at upstream conditions (psia)
Q = Complex flow rate (ft^3/min)
R = Resistance ($fQ/g_c A^2 D$)
Rg = Gas Constant (ft × lbf/lbm × °R)
t = Time it takes gas to travel from upstream to downstream conditions (sec)
$Tref$ = Reference temperature (60°F)
u = Non dimensional gas velocity (u_d / u_{ref})
u_d = Local gas velocity (ft/min)
Z = Compressibility
Zc = Characteristic Impedence
Γ = Complex propagation constant
w = Forcing function circular frequency (rad/sec)
ρ = Density (lbm/ft^3)
μ = Absolute viscosity (lbf × s/ft^2)
dx/dz = Speed of the characteristic wave

Subscripts

cyl = Conditions at the cylinder portion of the passage
$trans$ = Conditions at the transducer portion of the passage

This paper also refers to compressor tests at low ratio, low speed conditions and high ratio, high speed conditions. The low ratio, low speed condition refers to tests at a pressure ratio of 1.6 and compressor speed of 1515 rpm. The high ratio, high speed condition refers to runs at a pressure ratio of 2.5 and compressor speed of 1770 rpm (see **LABORATORY DATA**).

Please note that the Y-axis (pressure) of the graphs included in this report are given in millivolts. This is the unnormalized values of the transducer readings and will not effect the results found.

INTRODUCTION

The dimensions of a reciprocating compressor cylinder and commercial dynamic pressure indicator test equipment result in the pickup usually being installed remote from the working pressure in the cylinder bore. The dynamic pressure measurement device is connected to the working cylinder volume by a gas passage of varying designs. Gas dynamics between the inside of the cylinder and the transducer diaphragm can produce significant error in the recorded dynamic pressure trace. This translates into a distorted pressure volume diagram, error in the indicated horsepower and error in diagnosing compressor performance problems. The source of this indicated horsepower error is sometimes referred to as channel resonance.

This paper will review four methods of determining and correcting for the effects of channel resonance error. These four methods are:

1. A simple model that considers only the time for a pressure wave to move from the cylinder working volume to the indicator diaphragm.
2. A simple dynamic model that accounts for one dimensional flow in a duct of constant cross section and is solved in the time domain by the method of characteristics as published by Bradley and Woollatt in 1968.
3. A detailed dynamic model that includes acoustic damping and uses a frequency domain pressure pulsation simulation as published by H. Kammin in an ASME Pipeline Engineering Symposium in 1989.
4. A detailed dynamic model that is solved in the time domain and that includes a detailed evaluation of the physics of a reciprocating compressor including near field gas dynamics.

The paper will comment on the method that offers a balance between acceptable accuracy and relative simplicity for efficient adaptation to a personal computer environment.

TESTING PROCEDURE

The laboratory tests were conducted at the Dresser-Rand, Closed Loop facility in Painted Post, New York. For a description of this facility see reference #1. The test vehicle was a high speed, low horsepower compressor pumping nitrogen in a single stage configuration. Two passages of 6 and 12 inch lengths were designed that would allow a Ashcroft K8 transducer to be placed into the end of the passage and secured into place. Another passage of minimal length was developed to record a "channel resonant free" signal. The transducer's electric output was transmitted to one of four channels on a Nicolet 4094 Oscilloscope. A timing trace was transmitted to a different channel for top dead center definition. Each test point was recorded onto floppy disk through a disk drive connected to the oscilloscope. A BASIC computer program was written to establish communication between the oscilloscope and an IBM PC via a RS232 cable. The test data was transferred to the PC in ASCII format for later analysis and manipulation.

LABORATORY DATA

The experimental dynamic pressure data that was collected to evaluate channel resonant correction procedures was measured at two pressure ratios (1.6, 2.5) and two compressor speeds (1515, 1770 rpm) as previously noted. For each condition pressure-time traces were measured at the minimal, 6 inch and 12 inch channel lengths. For the sake of brevity, this paper will consider only the 1.6 ratio, 1515 rpm test point and the 2.5 ratio, 1770 rpm point.

The compressor cylinder pressure time diagrams plotted on graphs 1 through 4 were all measured on the outer end of the double acting cylinder. As expected, channel resonance is greater at the 12 inch passage lengths than at the 6 inch passage lengths. Also, channel resonance is greater at the low ratio, low speed condition than the high ratio, high speed condition.

The laboratory data shows that indicator passage errors

a) can redefine the expansion and compression lines and,

b) show substantial amounts of pressure pulsations on the suction and discharge events.

The effect these errors can have on compressor performance studies is important. The redefined expansion and compression lines will cause incorrect diagnosis of leakage and capacity calculations, while the pressure pulsations will cause an erroneous belief in valve dynamic problems. Both of these effects will produce an error in the indicator compressor horsepower measurement. The aim of this paper is to determine the best approach to correcting the indicator card for this channel resonant phenomena; the best approach being defined as that method that offers a balance between acceptable accuracy and relative simplicity for efficient adaptation to the personal computer.

Graph 1

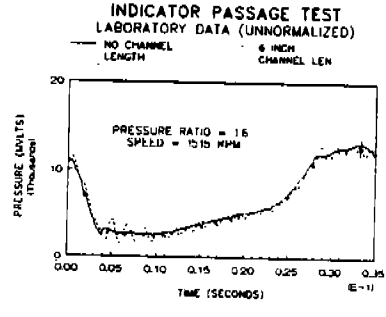

Graph 2

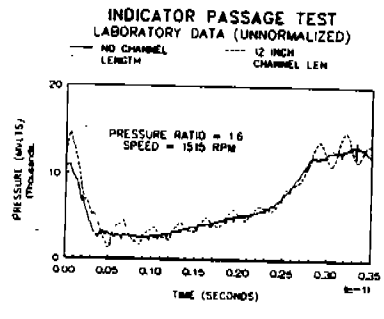

Graph 3

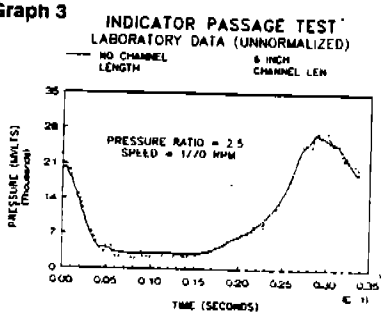

Graph 4

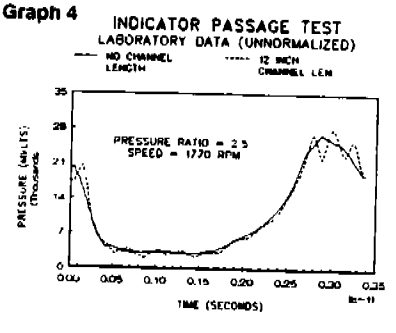

METHOD #1 : SIMPLE PHASE METHOD

Theory

The first correction method was recommended by SGA/PCRC in their 1984-10 report [2]. (SGA/PCRC has recently dropped this method of calculating indicator passage error as outlined in their 1990 test report [3]). It states that indicator passage error is a phase shift of the true indicator card or in other words the sole result of the time it takes for the gas to travel from the cylinder bore to the transducer diaphragm. This time is calculated as the length of the passage divided by the local speed of sound.

$$c = \sqrt{k g_c Z R_g T} \quad (1)$$

$$t = l / c \quad (2)$$

Observations

Graphs 5-8 show that this method did remove some of the phase shifting problems especially on the corrected 12 inch low ratio, low speed run. Unfortunately, phase shifting is only one part of the error caused by indicator passage lengths. Resonant effects are clearly present yet not corrected with this method. It is difficult to say if better results would be found at different conditions, i.e. shorter passage lengths, slower compressor speeds, different gases, etc... but it is certain this method cannot be used effectively in areas where pressure pulsations are present. If this method was assumed accurate, then faulty valve flutter diagnosis will occur. The idea of correcting phase shifting solely is an incomplete physical model. Other passageway errors must also be addressed.

Graph 5

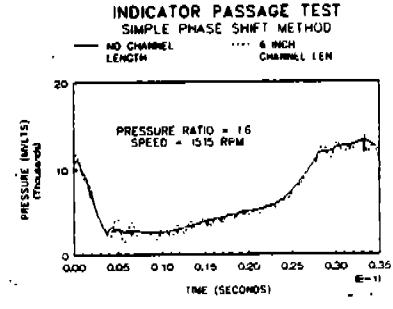

Graph 6

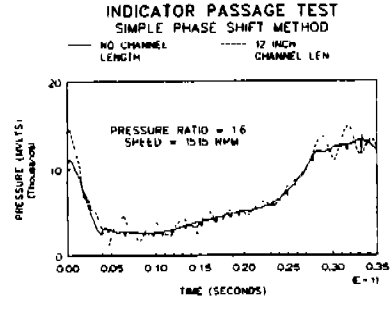

Graph 7

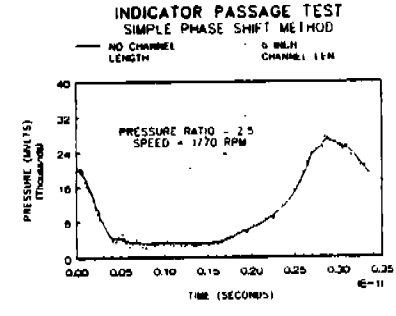

Graph 8

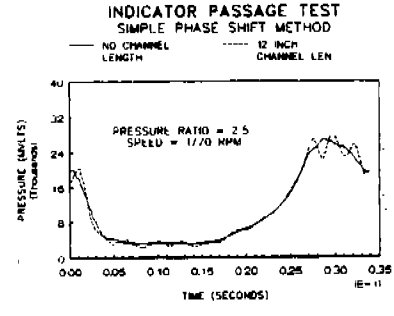

METHOD #2 : "SIMPLE" TIME DOMAIN SOLUTION

Theory

The next correction uses the method of characteristics to find a dynamic time domain solution that accounts for one dimensional flow in a duct of constant cross section[4]. The assumptions are;

1. frictionless passage
2. no substantial volume at the transducer
3. no pressure losses at the ends of the passage due to the finite gas velocity in the passage
4. the pressure wave characteristics have constant slope i.e. the gas velocity is much less than the sonic velocity.
5. homentropic flow

This method was introduced by Bradley and Woollatt in 1968 in which they concluded the preceding assumptions were reasonable based upon the scope of their testing and should not greatly affect accuracy.

The method of characteristics states;

$$c + \frac{k-1}{2} u \quad \text{is constant along} \quad \frac{dx}{dz} = u + c \tag{3}$$

and

$$c - \frac{k-1}{2} u \quad \text{is constant along} \quad \frac{dx}{dz} = u - c \tag{4}$$

Given assumption #4 is true, then the speed of the characteristics can be represented as the reference speed of sound A_{ref} and $dz/dx = +/- 1.0$. Assume that at time = 1, a pressure wave is at the transducer. Assume at time = 2, the wave reaches the cylinder. Finally, assume at time = 3, another pressure wave reaches the transducer again. Equations 3 and 4 gives;

$$c_{cyl(2)} + \frac{K-1}{2} u_{cyl(2)} = c_{trans(3)} + \frac{K-1}{2} u_{trans(3)} \tag{5}$$

and

$$c_{cyl(2)} - \frac{K-1}{2} u_{cyl(2)} = c_{trans(1)} - \frac{K-1}{2} u_{trans(1)} \tag{6}$$

Since the transducer end is considered closed, utrans(1) and utrans(3) are set equaled to zero. Adding equations (5) and (6) gives

$$c_{cyl(2)} = 0.5 \, (c_{trans(1)} + c_{trans(3)}) \tag{7}$$

Using the isentropic change of state law;

$$c = \frac{C_d}{a_{ref}} = \frac{p}{\rho_{ref}}^{(k-1)/2k} \tag{8}$$

gives;

$$P_{cyl(2)} = \left\{ \frac{P_{trans(1)}^{(k-1)/2k} + P_{trans(3)}^{(k-1)/2k}}{2} \right\}^{2k/(k-1)} \tag{9}$$

The program written to test this solution uses an array of pressure time points measured at the transducer for one full compressor cycle. The program uses a point at the transducer as time = 1. The passage length is divided by the reference speed of sound and multiplied by 2 to determine the pressure at time = 3. These two pressures are inputed into equation 9 and a value of the pressure at time = 2 is found. The new time is determined by simply adding on the passage length divided by the reference speed of sound to the original time = 1. This procedure is continued through the whole cycle.

Observations

Graphs 9-12 present the results produced from this method. Acceptable accuracy was found at both the 6 and 12 inch lengths with some minor exceptions. This method successfully filtered the channel resonance found on the cards. A small error was found at the low ratio, low speed condition on the discharge event with the corrected pressure falling below the actual pressure. This can cause a small underestimation of compressor horsepower. For the 12 inch cards, the method did not accurately correct for the compression and expansion line phase shift although it reduced the magnitude of the original loss. A misrepresented expansion or compression line will cause erroneous capacity and horsepower calculations and lead one to believe that leakage is occurring in the compressor when it is not.

The condition that had the least favorable correction was the 12 inch, high speed, high ratio card. Both channel resonance and phase shifting was present. It may be advantageous to relax some of the assumptions for passageways of greater length and for compressors of higher speeds. This was not done for this current study.

Graph 9

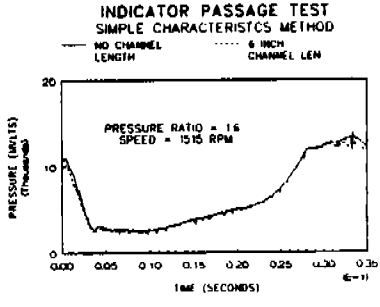

Graph 10

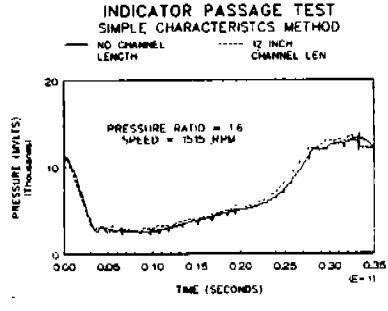

Graph 11

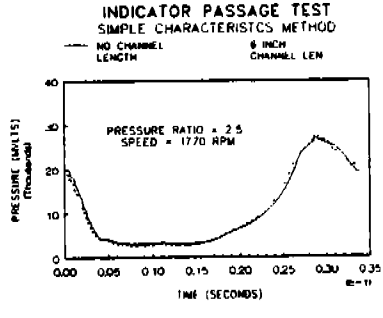

Graph 12

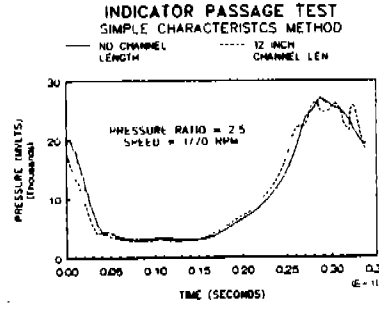

The simple time domain solution is a simple yet effective method to correct for channel resonance in short indicator passageways where resonant effects are limited. This correction requires minimal time for a solution in a PC environment.

METHOD #3 : FREQUENCY DOMAIN SOLUTION

Theory

This method is a frequency domain analysis that utilizes oscillatory forced vibrations for pressure pulsation simulation. The pressure and flow at either the upstream or downstream of the passage varies harmonically at each point in the system at the excitation frequency. The amplitude and phase of the pressures or flows change with position in the system but remain independent of time[6]. The governing equation used for this analysis is;

$$P_{cyl} = P_{trans}\cosh(\tau l) + Q_{trans}Z_c\sinh(\tau l) \tag{10}$$

$$\tau = \sqrt{wC(-wL + iR)} \tag{11}$$

Since the downstream portion of the passage is a closed end, the transducer flow (Q_{trans}) is equal to zero, thereby reducing equation (10) to;

$$P_{cyl} = P_{trans}\cosh(\tau l) \tag{12}$$

The solution method generated solves equation 12 in a number of steps. The first step is to accurately represent the original pressure time card into a series of real and imaginary coefficients (a1,a2...an,b1,b2...bn). The indicator card can then be written as;

$$P(t) = P0 + \sum_{1}^{n} a_1 \cos(wt) + a_2 \cos(2wt) + \ldots a_n \cos(nwt) + \sum_{1}^{n} b_1 \sin(wt) + b_2 \sin(2wt) + \ldots b_n \sin(nwt) \tag{13}$$

Trial and error has shown that 20 or more harmonics is sufficient to accurately define the pressure time trace. Once the series is defined, the values for the pressures for each time step can be plugged into equation 12. Using complex number FORTRAN programming, a new value for the pressure at the cylinder bore is found. These pressures are represented as a series of real and imaginary coefficients. The final step is to generate a Fourier series to convert the coefficients into a pressure time equation for all crank angles.

Observations

The results found from using this method were good. Graphs 13-16 indicate that the solution was accurately filtered out channel resonant pressure pulsations. Similar to the previous time domain solution, the lower ratio, lower speed trace showed a corrected pressure line falling lower than the actual line. As mentioned before, this can cause a small underestimation of the indicated horsepower. Another problem is an inaccurate definition of the expansion and compression traces. Once again, this error can cause a misdiagnosis of leakage effects and capacity calculations.

It should be noted that the inaccuracies found with this particular set of data are small and that the remaining errors are insignificant compared to the cards without any type of correction.

Certain assumptions with this method could effect the accuracy of the results. One such assumption is the value of the resistance variable used in the imaginary portion of the

complex function. For this particular application, a resistance value was used that is similar to the one discussed in Harlan Kammin's paper[5]. It is assumed the resistance in the passage is comprised of two parts; a part due to flow through the passage and the resistance due to the viscosity of the gas. It was reasoned that since the passage was a dead end channel, the resistance in the pipe due to gas flow was small or negligable. The equation used was;

$$R_{eq} = R_{flow} + \frac{W^2}{\rho g A C_d^2} \mu \frac{4}{3} + 1.6\,(k-1) \qquad (14)$$

For this case, it is assumed that R_{flow} equals 0 and that the Prandtl number = 1.6.

The mathematics of the solution will cause a greater amount of computational time (as compared to other methods) which should still be small with modern high speed personal computers. The downfalls associated with this method are that;

a) it will take some time to run on older, slower PC's especially if a large number of harmonics are specified and

b) it requires complex number FORTRAN programming to work correctly.

It is felt that these downfalls are small and given the accuracy of the solution well worth the extra time.

Graph 13

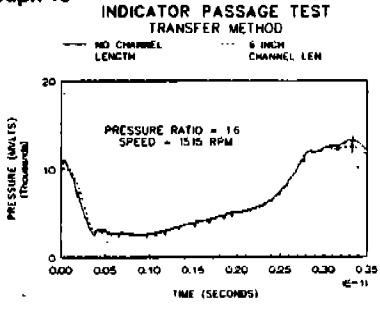

Graph 14

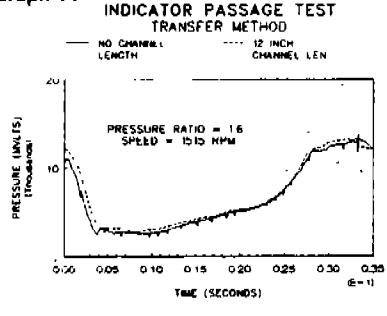

Graph 15

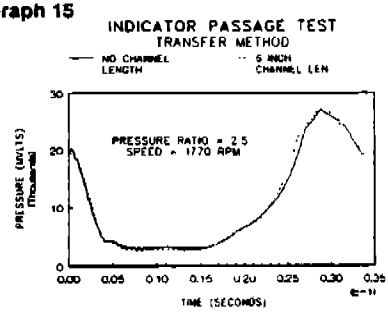

Graph 16

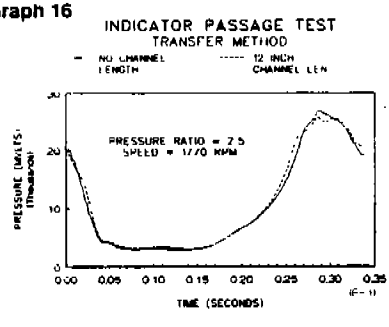

METHOD #4 : DETAILED TIME DOMAIN SOLUTION

The final method that will be addressed is a dynamic model that is solved in the time domain and includes a detailed evaluation of the physics of a reciprocating compressor near gas field conditions. This approach also uses the method of characteristics in which the

magnitude of a pressure pulsation can be calculated by using the slopes of two intersecting characteristic pressure lines. The solution is adaptable for varying lengths, diameters and friction factors.

For this particular method, a test of its accuracy cannot be discussed since the routine is a subset of a large Dresser-Rand proprietary compressor cycle simulation program. Extracting this routine to run on a PC proved not to be an easy task. For the particular cases mentioned before, the graphs 17-20, show the comparisons between what the program thought a 6 and 12 inch card should look like and the actual measured card.

As with the previous frequency domain solution, the value used for the friction term has a large effect on the results. As evident from the graphs, the program calculated larger magnitudes of pressure pulsations for the tested channel lengths. This is a direct link to the damping factor used.

Graph 17

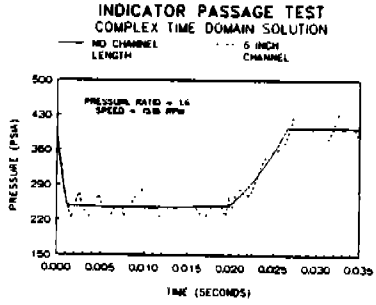

Graph 18

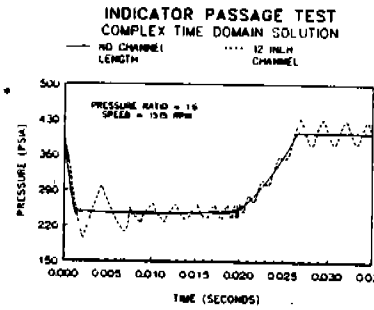

Graph 19

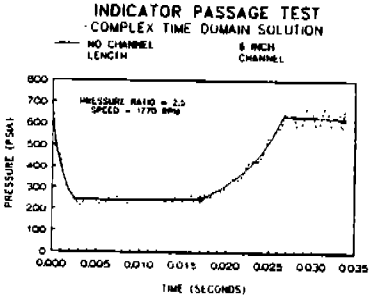

Graph 20

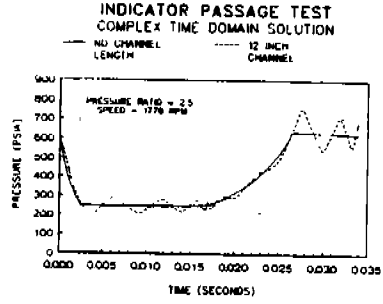

CONCLUSIONS

This paper discussed four different ways of calculating indicator passage error due to channel resonance. The methods looked at dealt with the problem in either the time or the frequency domain. Versions of both approaches offered acceptable accuracy while maintaining reasonable computational time. In cases where a high speed computer (AT or better) is not available, the simple time solution (Method #2) is recommended. The simplicity of the solution makes it extremely easy to program and relatively fast computational time on

almost any computer. If a slightly more detailed solution is desired and a higher speed computer is available, the complex frequency domain solution (Method #3) is recommended. The test results showed that overall this method offered the best results. The detailed time domain solution (Method #4) is probably the most interesting because it is part of a compressor performance calculation package that determines all other variables present in compressor performance as well as indicator passage error. The emphasis with this method is to predict performance results based on sound principles of physics and not data-fit equations. Finally, the first method did not offer acceptable results because it was an oversimplified approach to the dynamics problem. The complex frequency solution dealt with the dynamics in grater detail and thus gave better results.

The four methods presented here give four ideas for correcting indicator passage error. Some feel the error's magnitude is less than the problem of correcting it. This is not the case. Even if horsepower numbers do not greatly change with the error, erroneous diagnosis can occur. It is quite evident from the laboratory data that the channel resonance appears as valve losses and leakage past valves. Substantial amounts of time and money can be saved if both the analyst and compressor owner can distinguish between what is real and what is error.

ACKNOWLEDGMENTS

The author would like to gratefully acknowledge the time and effort of the Dresser-Rand Development Lab personnel, namely Mr. David Decker, Mr. Donald Mason and Mr. Bill Glosick. The author would also like to thank his supervisor Mr. Donald Draper, Dr. B.G. Shiva Prasad and Dr. Derek Woollatt for their technical support and guidance.

REFERENCES

1. Draper, D.C. and Briggs, K.A., "Ingersoll-Rand's Closed Loop Facility", Ingersoll-Rand Co., Painted Post, NY
2. SGA/PCRC, "Field Measurement Guidelines Compressor Cylinder Performance Summary", Report No. 8410, May 1984
3. SGA/PCRC, "Field Measurement Guidelines Compressor Cylinder Performance Summary", Report No. 8410, Third Revision, February, 1990
4. Bradley, P.G. and Woollatt, D., "Correction of Errors in Indicator Diagrams : Passage Effects", THE ENGINEER, March 9, 1968, pp. 511- 516
5. Kammin, H., "Improved Accuracy in a Digital Pulsation Simulation", ASME Book No. H00448-1989
6. Wylie, E.B. and Streeter, V.L., "Fluid Transients", McGraw-Hill, 1978, pp. 205-216

EXPERIMENTAL ANALYSIS OF A WATER-TO-WATER HEAT PUMP WITH VARIABLE SPEED SCROLL COMPRESSOR

K. Holzapfel, Consultant, Germany
V. Bruno, and V. Recchi, TECNARS, Bari Italy

ABSTRACT

As part of a broader international cooperation variable speed scroll compressors have been tested in a specially designed water-to-water heat pump test rigg at TECNARS in Bari, Italy. Experimental results for the compressor performance and efficiency are being compared to catalog data of single speed reciprocating compressors. A large number of tests were run in order to investigate effects of different voltage to frequency characteristics in the frequency inverter output. Results show a considerable impact of a properly selected supply voltage on the compressor efficiency in particular at low frequencies. Energy conservation effects when using variable speed scroll compressors in place of single speed reciprocating compressors for space heating and air conditioning applications are briefly discussed.

Introduction

Variable speed electric heat pump systems have been introduced very successfully into the Japanese residential and small commercial air conditioning market since the early 1980s. In the US, compressor and heat pump manufacturers have also investigated this technology for years and first products are available now. In Europe, only limited attention was given to this technology and heat pump manufacturers are just starting to get interested.

The work reported here forms part of a larger activity undertaken in international cooperation by 5 countries within the framework of the International Energy Agency's (IEA) R&D program. Besides Italy, represented by TECNARS in Bari, also acting as "Operating Agent" of this project, Austria, Germany, Switzerland and the US are contributing to this project. The objective of the total project is to provide the necessary basis for identifying potential benefits of advanced electric heat pump systems by means of verified APF simulation models and reliable data. At present this work is focussed on variable speed electric heat pumps.

Water-to-Water Heat Pump Test Rigg

As a basis for further analytical investigations and for validation of computer models a broad range of reliable performance data of state of the art variable speed compressors were needed. For this purpose a special compressor test rigg was developed and installed at TECNARS. The test rigg was designed as a water-to-water, or alternatively, brine-to-water heat pump equipped with temperature and pressure sensors at the inlet and outlet of each major component in the refrigerant cycle as well as in the water loops of the condenser and evaporator. In addition, mass flow metering devices are installed in both water loops and in the refrigerant cycle. All data are continuously collected and evaluated by a computerized monitoring and data evaluation system.

The expansion device is split into 4 parallel units, operated manually or automatically with conventional thermostatic expansion valve or alternatively with electronic expansion valve. The heat pump test rigg is designed for operating with compressors up to a maximum of approximately 1000 kg/h R22. A general purpose frequency inverter supplies the required compressor motor power supply at frequencies up to 150 Hz for a motor capacity up to 15 kW. The inverter allows for a free selection of the output voltage/frequency characteristic. A high-precision wattmeter is measuring the power input to the inverter, thus all inverter losses are included in the compressor energy balances.

All tests of the scroll compressors, reported in this paper, were made with the heat pump operating in well established steady state conditions. By measuring temperatures, pressures and mass flow rates simultaneously both in the refrigerant cycle, and in the water loops, a refrigerant side energy balance and a water side energy balance can be calculated for both heat exchangers, the evaporator capacity and the condenser capacity. Tests were accepted only if the difference between condenser water loop heating capacity and refrigerant side heating capacity was less than 3 percent. In general, a good agreement of both energy balances was achieved, and the difference was found to be less than 1 percent with the lower values measured on the water side. Data shown in the following diagrams are based on this water side energy balance calculation.

Two variable speed Scroll compressors, S/A and S/B, were tested with this installation. [1] In the following, experimental test results of the scroll compressors are being compared to catalog data for single speed reciprocating compressors: [2]

Type	Displacement [cm³]	Compressor Speed [rpm]
Scroll S/A	64.2	30-115 / 1800-6900
Scroll S/B	45	30-115 / 1800-6900
Reciprocating MT 100 HS	171.3	50 / 2900

Test results show a very similar characteristic for both compressors with compressor S/B resulting in a somewhat better COP. Data shown in the following are derived from performance tests of compressor S/A, since in this second test series the real rotor speed was measured, which was not done in the tests of compressor S/B.

Performance of Scroll Compressor S/A

In these tests we found the scroll compressor to compare very favorable with state of the art single speed reciprocating compressors. Diagram 1 shows the measured cooling capacity Q'ev of scroll S/A at constant 90 Hz and for comparison the cooling capacity (catalog data) of the reciprocating compressor MT 100. The reason for selecting the MT 100 for comparison is the capacity which is equal to the cooling capacity of the scroll at 90 Hz and high compression ratio, here approx. suction pressure 0.32 MPa at discharge pressure 1.7 MPa, a potential design point. Depending on the requirements of any particular application, the variable speed compressor S/A can be used in place of other single speed compressors with considerably larger or smaller capacity. Therefore, the comparison in diagram 1 and also in further diagrams is intended to show the typical differences between a inverter driven variable speed scroll compressor and state of the art single speed reciprocating compressors.

With increasing suction pressure both compressors provide a larger capacity because the increasing suction gas density theoretically causes an equally increasing refrigerant mass flow rate. As diagram 1 shows, the scroll's capacity increases considerably less than the MT 100 capacity does. This feature of the scroll is very favorable for heating applications, typically requiring increasing capacity with increasing pressure ratio. Diagram 2 shows the related values of the refrigerant mass flow rates of both compressors for 2 different discharge pressures, at 1.5 MPa and at 1.9 MPa. Not only the increasing suction pressure but also the decreasing discharge pressure has got a smaller impact on the scroll's capacity relative to the reciprocating compressor. For diagram 3, the refrigerant mass flow rate of both compressors was divided by the mass flow rate at suction pressure of about 0.32 MPa, the reference point, at which both compressors provide equal refrigerant mass flow rate (and cooling capacity). Thus, the increase of the mass flow rate relative to this "design point" is used for preparing the curves for diagram 3. Finally this increase of the mass flow rates is being divided by the respective increase of the suction gas density, according to the increasing suction pressure (at constant suction gas

superheat of 10 K). Diagram 3 now shows that the scroll compressor's increase in cooling capacity actually is almost proportional to the according increase in suction gas density, while the recip. MT 100 shows a considerably stronger capacity increase. The reason for this behavior is the design of the scroll compressor with its local separation of the suction and discharge process, and with the absence of suction and discharge valves. The result is a very stable volumetric efficiency with a comparatively low sensitivity to the operating pressure ratio.

Volumetric Efficiency

Diagrams 4 and 5 give an image of the absolute values of the volumetric efficiency of Scroll S/A, as calculated from our test results. We consider the accuracy of these values to be in the range of about 5 %, mainly due to the difficult reading of the vibration analyzer used for measuring the real rotor speed. Despite this difficulty, it can be shown that in the greatest part of the scroll compressor's operating range, the volumetric efficiency is well beyond 90 %. The relative small sensitivity to the operating pressure ratio is shown in diagram 4 and the equally small sensitivity to changes of the compressor speed in a fairly broad speed range from 40 up to 90 Hz is shown in diagram 5.

The hard characteristic of the volumetric efficiency shows that the scroll compressor cooling capacity is responding almost linear to a change in compressor speed. This is shown in diagram 6 for the whole operating speed range of compressor S/A at constant discharge pressure of 1.7 MPa, and at two different suction pressures of 0.4 MPa, and 0.6 MPa. For comparison, the two respective (in this diagram constant) capacities of the single speed reciprocating compressor are shown as well.

Coefficient of Performance, COP

Diagram 7 shows the cooling coefficient of performance, COP_cooling, for both compressors, the scroll S/A and the recip. MT 100. This comparison immediately shows a limitation to the potential replacement of single speed systems by inverter driven variable speed systems. Despite the scroll compressor's superior efficiency relative to a reciprocating compressor, its coefficient of performance including all "additional" losses caused by the frequency inverter, will hardly reach the COP achieved with a single speed reciprocating compressor, as long as the comparison is being made at the same evaporation and condensing pressure. A higher energy efficiency can therefore only be reached if the variable speed compressor's unique ability to respond to changing load requirements leads to, heat pump internal, altered operating conditions (unloaded heat exchangers) with lower operating pressure ratios. In this case, a lower than design capacity will then be provided by the variable speed system with a higher COP than a single speed compressor would be able to produce while operating at considerably lower than design load. In general, the existence of a broadly changing load therefore, is a condition for a successful application of variable speed compressors, at least in terms of energy efficiency.

As can be seen in diagram 7, the scroll S/A shows its best COP relative to the reciprocating compressor MT 100 when operating with a pressure ratio between 3 and 4. In particular lower pressure ratios produce a decrease of the scroll's COP relative to the MT 100 COP. This is due to the scroll's built-in fixed volumetric compression ratio, in this case corresponding to a pressure ratio of about 3.3. Since the valve free scroll compressor always operates with this minimum compression factor, the compressor power input can not benefit from externally possible lower compression ratios, which explains the smaller increase of the scroll's COP relative to the MT 100 when moving towards lower compression ratios.

With the relatively hard characteristic of the volumetric efficiency in a fairly broad compressor speed range, also a relatively stable COP can be expected for a broad range of compressor speed (and therefore broad capacity range) while maintaining constant evaporation and condensing pressure conditions. As Diagram 8 shows in the case of scroll S/A, the cooling COP changes by less than 10 percent if the compressor speed is varied from 40 Hz up to 90 Hz. In this speed range the compressor shows a flat COP characteristic with an optimum at around 60 Hz. Electric

losses in the compressor motor and in particular in the frequency inverter cause a rather steep decrease of the COP at low frequencies (below 30 Hz). In the high frequency range electric losses become relatively small, but the COP is reduced by increasing mechanical losses. By appropriate design of the electric motor and the inverter but also, as discussed in the next chapter by the proper selection of the voltage to frequency characteristic, the COP characteristic can be changed in order to achieve an optimum in the main operating frequency range.

Compressor Motor Power Supply Voltage Optimization

As mentioned before, the required variable frequency power supply to the compressor motor in the test rigg is being supplied by a general purpose frequency inverter (Hitachi, HFC-VWS 22 HF 3 EH). The PWM output of this inverter is very similar to the output of those inverters that are specifically designed for air conditioning applications, broadly used in Japan. These inverters, however, are operating typically with one fixed voltage to frequency characteristic as shown in diagram 9. This characteristic does not correspond to the optimal compressor power supply for two reasons: first, the voltage should continue to increase with the frequency also in the higher speed range, and second, varying load at fixed frequency require changing voltage in order to maintain maximum motor efficiency. A recent investigation at Technical University in Karlsruhe, Germany showed that a tripling of the motor load requires approximately 15 % increase of the supply voltage in order to maintain maximum motor efficiency. [3]

In our own experiments we tried to identify the optimum supply voltage for scroll S/A and S/B in a broad range of operating conditions. Diagrams 10, 11, and 12 show the impact of varying power supply voltage on heating capacity, power input, COP, and the rotor slip (in % of synchron speed), for 40 Hz (Diagram 10), 75 Hz (diagram 11), and 90 Hz (diagram 12). All diagrams are showing two curves, one for suction pressure 0.4 MPa, and a second, for suction pressure 0.6 MPa. Discharge pressure is kept constant at 1.7 MPa, superheating at 10 K, and subcooling at 5 K constant. The inverter output voltage was not actually measured throughout the tests, and the figures given in the diagrams therefore represent the set voltage selected with the inverter controls. Some deviations of the measured data from theoretically expected values can be explained by this fact, since the highly complex wave form produced by the inverter apparently changed for different settings. Some wave forms seem to be producing less and others more losses in the compressor motor. All diagrams show a similar characteristic with the sensitivity to voltage variation in general decreasing at higher frequencies. The diagrams further show that the COP maximum always is being achieved when the rotor slip is at around 2 %. Higher voltage, with all other parameters kept constant, results in a motor torque increase, a reduction of the rotor slip, and therefore, an increase of the effective rotor speed. The result is the increasing compressor capacity until the rotor almost reaches synchron speed and a further reduction of the rotor slip becomes impossible.

The experimental data available so far are not sufficient in order to identify the optimum supply voltage for changing motor load at constant frequency. Because of the rather flat optimum observed, relatively small motor load changes at constant frequency as we applied in our experiments do not provide sufficient information. For this purpose more tests with more extreme operating conditions are required. Based on the data shown in diagrams 10 to 12, the optimum voltage/frequency supply characteristic for compressor S/A has been calculated for suction pressure 0.4 MPa and discharge pressure 1.7 MPa, as shown in diagram 9.

References

[1] ASHRAE Standard 23-78, Methods of Testing for Rating Positive Displacement Refrigerant Compressors

[2] Maneurop Software Program, MSP, Version 1.1

[3] H. Späth, personal communication, Elektrotechnisches Institut, Universität Karlsruhe

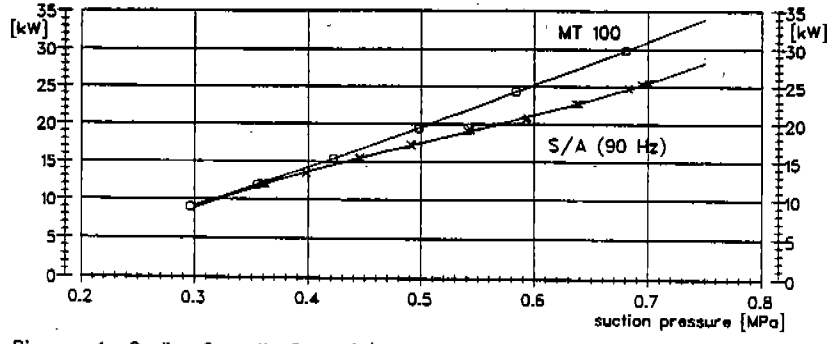

Diagram 1: Cooling Capacity Scroll S/A at 90 Hz and Recip. MT 100 HS
condenser pressure 1.7 MPa, subcool 5 K, superheat 10 K

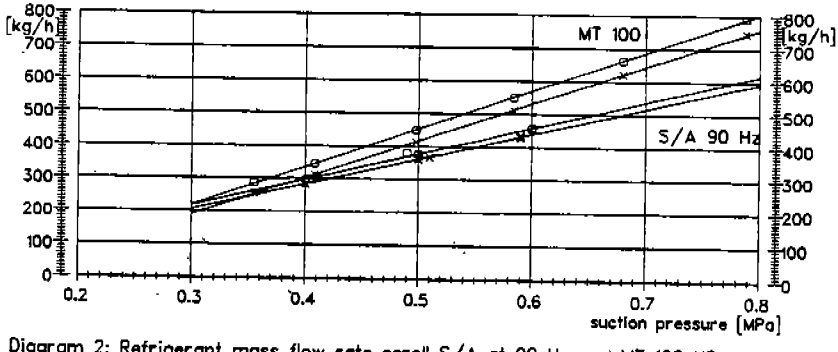

Diagram 2: Refrigerant mass flow rate scroll S/A at 90 Hz and MT 100 HS
condenser pressure: 1.5 = xx, and 1.9 MPa = oo; superheat 10K

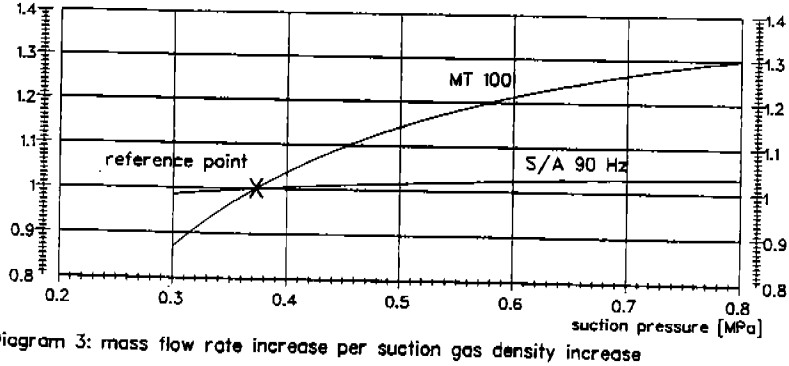

Diagram 3: mass flow rate increase per suction gas density increase

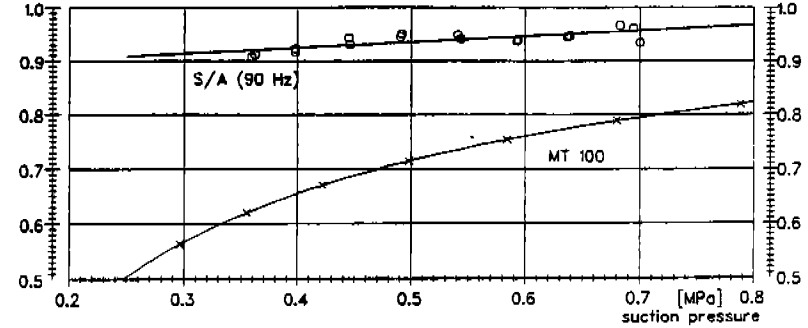

Diagram 4: Volumetric Efficiency Scroll S/A at 90 Hz and Recipro. MT 100
condenser pressure 1.7 MPa; suction gas superheat 10 K

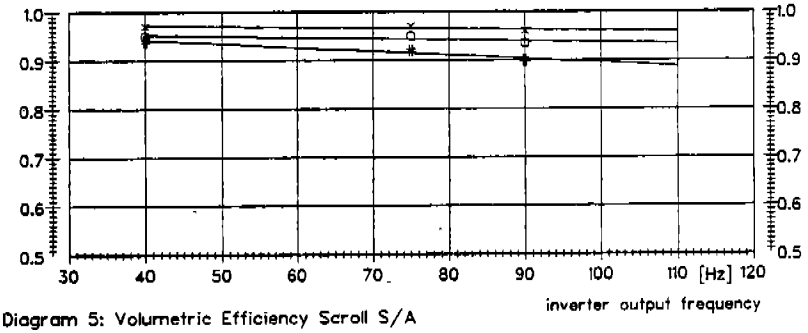

Diagram 5: Volumetric Efficiency Scroll S/A
pressure ratio (p_disch. / p_suc): x = 2; o = 3; # = 4;

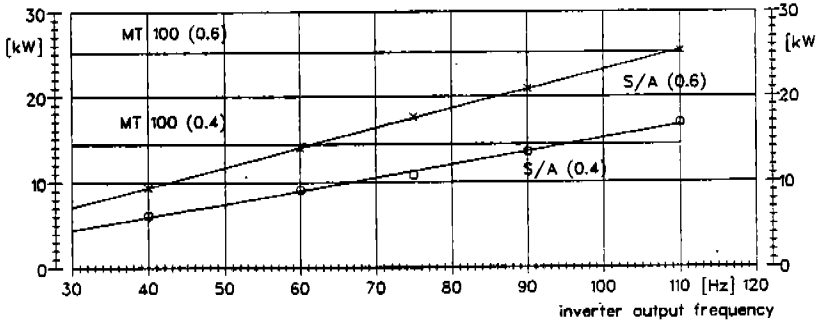

Diagram 6: Cooling Capacity Scroll S/A and Single Speed Recip. MT 100
suction pressure: o = 0.4 MPa; x = 0.6 MPa; p_disch.= 1.7 MPa

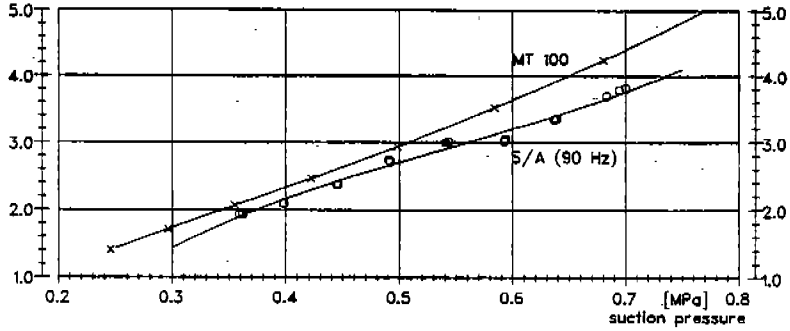

Diagram 7: COP for Scroll S/A at 90 Hz, and Recipro MT 100
condenser pressure 1.7 MPa; subcooling 5K; superheating 10K

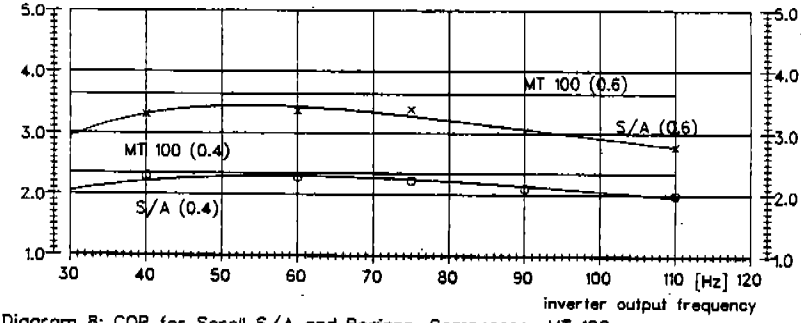

Diagram 8: COP for Scroll S/A and Recipro. Compressor MT 100
p_disch.=1.7 MPa; suction pressure: o = 0.4 MPa; x = 0.6 MPa

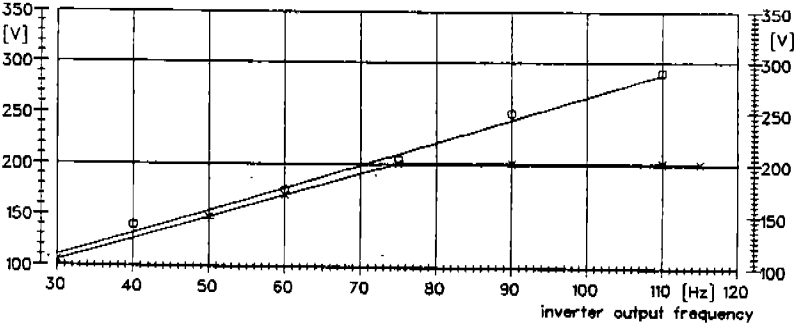

Diagram 9: Voltage versus Frequency Supply Characteristic
x = Typical for Heat Pumps in Japan; o = S/A Test Optimum

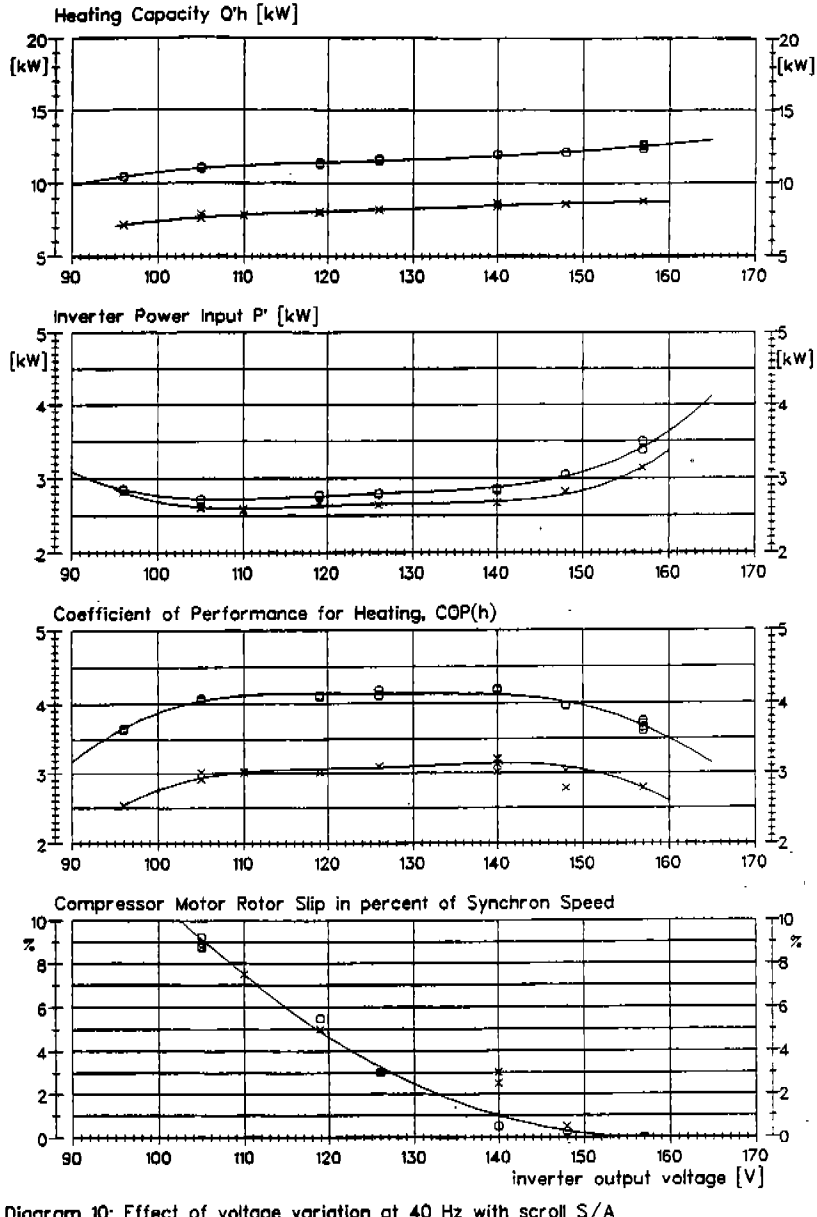

Diagram 10: Effect of voltage variation at 40 Hz with scroll S/A
p_suction = 0.4(x) MPa and 0.6(o) MPa; p_discharge = 1.7 MPa
suction gas superheating = 10 K, subcooling = 5 K

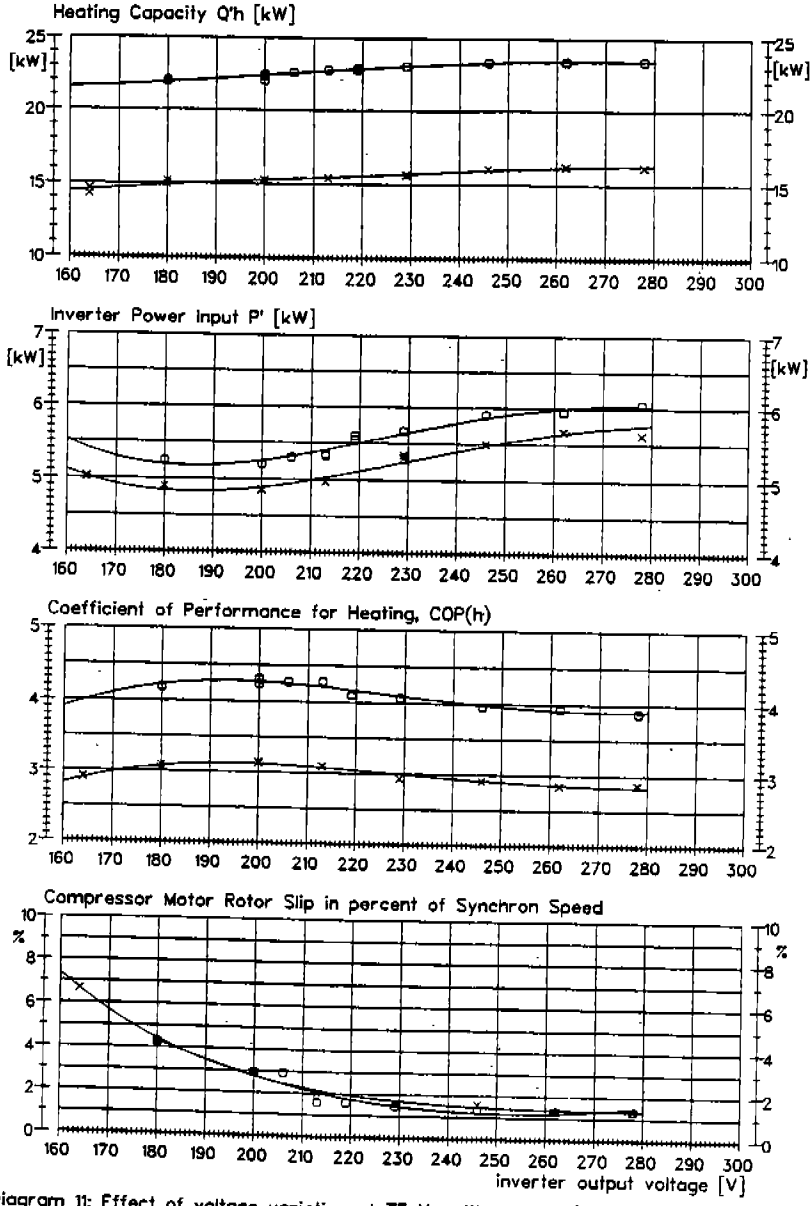

Diagram 11: Effect of voltage variation at 75 Hz with scroll S/A
p_suction = 0.4(x) MPa and 0.6(o) MPa; p_discharge = 1.7 MPa
suction gas superheating = 10 K, subcooling = 5 K

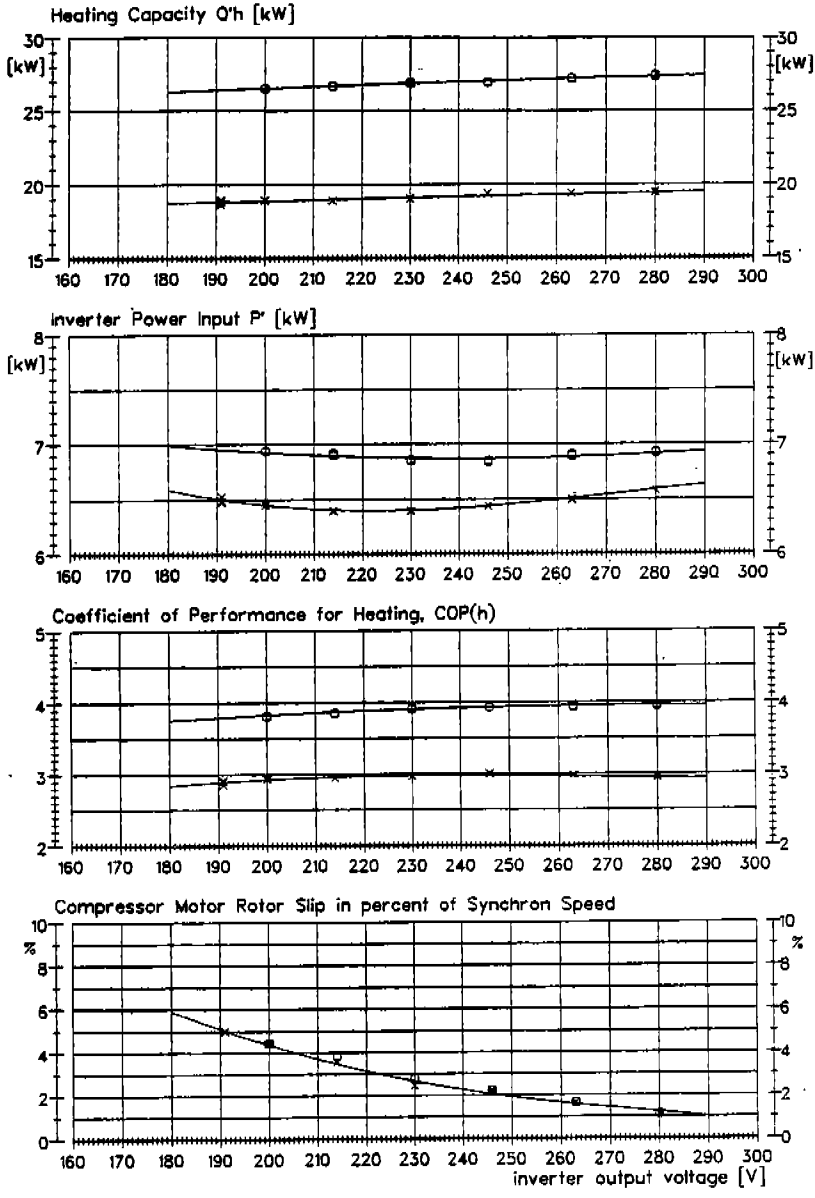

Diagram 12: impact of voltage variation at 90Hz on scroll S/A
p_suction = 0.4(x) MPa and 0.6(o) MPa; p_discharge = 1.7 MPa
suction gas superheating = 10 K, subcooling = 5 K

Cooperative Societies and Representatives

Air Conditioning Contractors of America, J. P. Norris, representative
Air-Conditioning and Refrigeration Institute (ARI), H. Phillips, representative
The American Society of Heating, Refrigerating, and Air-Conditioning Engineers (ASHRAE), J. R. Wright, representative
The American Society of Mechanical Engineers (ASME)
- Design Engineering Division, D. A. Beaty, representative
- Fluids Engineering Division, K. E. Hickman, representative

Association of Home Appliance Manufacturers (AHAM), J. Weizeorick and L. Swatkowski, representatives
Compressed Air and Gas Institute (CAGI), J. H. Addington, representative
Deutscher Kalte-und Klimatechnischer Verein (DKV), H. Kruse, representative
Gas Research Institute (GRI), S. Freedman, representative
ICI Americas Inc., T. W. Dekleva, representative
International Institute of Ammonia Refrigeration (IIAR), K. Anderson, representative
International Institute of Refrigeration (IIR), L. Lucas, representative
Japanese Association of Refrigeration (JAR), S. Hotani, representative
Japan Society of Mechanical Engineers (JSME), A. Futakawa, representative

Advisory Committee

J. Bergstrom, Uddeholm AB, Sweden
M. A. Di Flora, Vice President, Engineering, Bristol Compressors, USA
R. Dusil, President, J. N. Eberle & Cie. GmbH, Germany
E. H. Eisele, Vice President, Overseas Industrial Operations, Whirlpool Corporation, USA
A. Futakawa, Deputy General Manager of Nagasaki Workes and Manager of Development, Engineering Department, Mitsubishi Electric Corporation, Japan
K. Graunke, Manager, Research and Development, Sulzer-Burckhardt Engineering Works Ltd., Switzerland
E. Heinzelmann, Director, Research and Development, Embraco S/A, Brazil
J. J. Jacobs, Director, Commercial Compressor Engineering, United Technologies-Carrier Corporation, USA
N. J. Josiassen, Vice President, Technology, Danfoss Flensburg GmbH, Germany
E. Korfitsen, Manager, Research and Development, SABROE Refrigeration, Denmark
H. Kruse, DKV-President, Universitat Hannover, Germany
Y. Kuramitsu, General Manager, Airconditioning Systems Division, Toshiba Corporation, Japan
A. Lundberg, Vice President, Marketing and Engineering, STAL Refrigeration, Sweden
E. B. Muir, Senior Vice President, Engineering and Research, Copeland Corporation, USA
S. Olsson, Manager, Development-Strip Products, Sandvik Steel, Sweden
H. Phillips, Vice President, Engineering, Air-Conditioning and Refrigeration Institute, USA
C. F. Speich, Staff Engineer, Screw Compressor Technology, The Trane Company, USA
R. L. Swadner, Staff Engineer, Harrison Radiator Division, General Motors Corporation, USA
P. G. Szymaszek, Vice President, Engineering, Vilter Manufacturing Corporation, USA
J. K. Taulbee, Vice President, Engineering, Americold, USA
S. Touber, Faculty of Mechanical Engineering, University of Technology-Delft, The Netherlands
A. B. Tramschek, Dean, Faculty of Engineering, University of Strathclyde, Scotland
R. R. Wisner, Group Vice President, Refrigeration Engineering, Tecumseh Products Company, USA
D. Woollatt, Manager, Advanced Engineering, Dresser-Rand Company, USA
J. R. Wright, Director of Technology, ASHRAE, USA
Y. Yu, Professor and Head, Chemical Engineering Department, Xi'an Jiaotong University, P. R. China
L. Zhang, Manager, International Projects, Wuxi Compressor Works, P. R. China

4-17, 1992
e University
Lafayette, Indiana, USA

ceedings - Volume IV

2 International Compressor
ineering Conference
urdue

erence Chairman and Editor
es F. Hamilton

dinator
nond Cohen

sored by
W. Herrick Laboratories
ol of Mechanical Engineering

Proceedings of the

1992 International Compressor Engineering Conference at Purdue

Volume IV

July 14-17, 1992
Purdue University
West Lafayette, Indiana, USA

Conference Chairman and Editor
James F. Hamilton

Coordinator
Raymond Cohen

Sponsored by
Ray W. Herrick Laboratories
School of Mechanical Engineering

Table of Contents

C-1: Compressor Design

Chairperson: R. T. S. Ferreira, Federal University of Santa Catarina, Brazil

C-2: Scroll Compressor I - Performance

Chairperson: J. D. Jones, Purdue University

C-3: Compressor Valves I - Dynamics

Chairperson: J. S. Fleming, University of Strathclyde, Scotland

C-4: Screw Compressor I - Performance

Chairperson: P. G. Szymaszek, Vilter Manufacturing Corporation

C-5: Screw Compressor II - Experimental Studies

Chairperson: J. J. Jacobs, United Technologies-Carrier Corporation

C-6: Compressor Simulation

Chairperson: J. H. Kim, University of Cincinnati

C-7: Compressor Noise Control I

Chairperson: J. S. Bolton, Purdue University

C-8: Rotary Compressor I - Performance

Chairperson: C. M. Costa, Embraco, Brazil

C-9: Screw Compressor III - Geometry

Chairperson: J. Sauls, The Trane Company

C-10: Friction Effects - Tribology

Chairperson: S. K. Padhy, General Electric Company

C-11: Lubrication - Bearings

Chairperson: F. Sadeghi, Purdue University

C-12: Scroll Compressor II - Development

Chairperson: J. P. Elson, Copeland Corporation

C-13: Design - Rotary and Reciprocating Compressors

Chairperson: J. A. McGovern, University of Dublin, North Ireland

C-14: Gas Pulsations

Chairperson: L. A. Newberg, De-Sta-Co

C-15: Compressor Vibration I

Chairperson: P. E. Hansen, Danfoss-Flensburg GmbH, Germany

C-16: Alternate Refrigerants I

Chairperson: H. S. Spauschus, Spauschus Associates Inc.

C-17: Scroll Compressor III

Chairperson: J. J. Nieter, United Technologies Research Center

C-18: Compressor Valves II - Reliability

Chairperson: D. Woollatt, Dresser-Rand

C-19: Compressor Noise Control II

Chairperson: C. F. Speich, The Trane Company

C-20: Alternate Refrigerants II

Chairperson: K. Taulbee, Americold Company

C-21: Scroll Compressor IV - Design, Manufacture

Chairperson: A. Futakawa, Mitsubishi Electric Corporation

C-22: Scroll Compressor V - Loading

Chairperson: E. G. Muir, Copeland Corporation

C-23: Rotary Compressor II - Sliding Vane

Chairperson: R. Riffe, Americold Company

C-24: Compressor Valves III - Flow

Chairperson: S. Tauber, Delft University of Technology, The Netherlands

C-25: Compressor Vibration II

Chairperson: C. N. Johnson, Emerson Electric

C-26: Compressor Optimization

Chairperson: P. Davies, Purdue University

C-27: Thermal/Heat Transfer

Chairperson: G. W. Gatecliff, Tecumseh Products Company

C-28: Compressor Motor and Starters

Chairperson: D. G. Smith, Noise Cancellation Technologies Inc.

C-29: Compressor Noise Control III

Chairperson: M. Brown, Americold Company

Appendix A: Additional papers from the 1990 International Compressor Engineering Conference at Purdue

Cooperative Societies and Representatives

Air Conditioning Contractors of America, J. P. Norris, representative
Air-Conditioning and Refrigeration Institute (ARI), H. Phillips, representative
The American Society of Heating, Refrigerating, and Air-Conditioning Engineers (ASHRAE), J. R. Wright, representative
The American Society of Mechanical Engineers (ASME)
- Design Engineering Division, D. A. Beaty, representative
- Fluids Engineering Division, K. E. Hickman, representative

Association of Home Appliance Manufacturers (AHAM), J. Weizeorick and L. Swatkowski, representatives
Compressed Air and Gas Institute (CAGI), J. H. Addington, representative
Deutscher Kalte-und Klimatechnischer Verein (DKV), H. Kruse, representative
Gas Research Institute (GRI), S. Freedman, representative
ICI Americas Inc., T. W. Dekleva, representative
International Institute of Ammonia Refrigeration (IIAR), K. Anderson, representative
International Institute of Refrigeration (IIR), L. Lucas, representative
Japanese Association of Refrigeration (JAR), S. Hotani, representative
Japan Society of Mechanical Engineers (JSME), A. Futakawa, representative

Advisory Committee

J. Bergstrom, Uddeholm AB, Sweden
M. A. Di Flora, Vice President, Engineering, Bristol Compressors, USA
R. Dusil, President, J. N. Eberle & Cie. GmbH, Germany
E. H. Eisele, Vice President, Overseas Industrial Operations, Whirlpool Corporation, USA
A. Futakawa, Deputy General Manager of Nagasaki Workes and Manager of Development, Engineering Department, Mitsubishi Electric Corporation, Japan
K. Graunke, Manager, Research and Development, Sulzer-Burckhardt Engineering Works Ltd., Switzerland
E. Heinzelmann, Director, Research and Development, Embraco S/A, Brazil
J. J. Jacobs, Director, Commercial Compressor Engineering, United Technologies-Carrier Corporation, USA
N. J. Josiassen, Vice President, Technology, Danfoss Flensburg GmbH, Germany
E. Korfitsen, Manager, Research and Development, SABROE Refrigeration, Denmark
H. Kruse, DKV-President, Universitat Hannover, Germany
Y. Kuramitsu, General Manager, Airconditioning Systems Division, Toshiba Corporation, Japan
A. Lundberg, Vice President, Marketing and Engineering, STAL Refrigeration, Sweden
E. B. Muir, Senior Vice President, Engineering and Research, Copeland Corporation, USA
S. Olsson, Manager, Development-Strip Products, Sandvik Steel, Sweden
H. Phillips, Vice President, Engineering, Air-Conditioning and Refrigeration Institute, USA
C. F. Speich, Staff Engineer, Screw Compressor Technology, The Trane Company, USA
R. L. Swadner, Staff Engineer, Harrison Radiator Division, General Motors Corporation, USA
P. G. Szymaszek, Vice President, Engineering, Vilter Manufacturing Corporation, USA
J. K. Taulbee, Vice President, Engineering, Americold, USA
S. Touber, Faculty of Mechanical Engineering, University of Technology-Delft, The Netherlands
A. B. Tramschek, Dean, Faculty of Engineering, University of Strathclyde, Scotland
R. R. Wisner, Group Vice President, Refrigeration Engineering, Tecumseh Products Company, USA
D. Woollatt, Manager, Advanced Engineering, Dresser-Rand Company, USA
J. R. Wright, Director of Technology, ASHRAE, USA
Y. Yu, Professor and Head, Chemical Engineering Department, Xi'an Jiaotong University, P. R. China
L. Zhang, Manager, International Projects, Wuxi Compressor Works, P. R. China

Preface

The 1992 International Compressor Engineering Conference at Purdue (1992 ICECP) is the eleventh biennial conference of this series, which started in 1972 under the name of Purdue Compressor Technology Conference. The name change occurred in 1986 to more accurately reflect the change in the nature of the conference. The conference will be run in parallel with the 1992 International Refrigeration Conference - Energy Efficiency and New Refrigerants. The two conferences are available to attendees with registration at either one conferring attendance and proceedings privileges to both. Proceedings of the individual conferences are available as individual publications.

The goals of the conference remain the same as for the previous conferences:

- to present research and design results in positive displacement compressors,
- to review the state-of-the-art of compressor development and application,
- to educate engineers starting in the compressor field, and
- to provide an easily accessible reference for compressor engineers.

The proceedings are organized by sessions as they were presented in the conference. Papers which arrived too late for inclusion may appear in the proceedings of the 1994 conference. Appendix A of these proceedings contains late papers from the 1990 conference.

Many of the papers presented at the conference could well have fit in more than one technical session. It is advisable for the reader to scan all sessions and papers carefully for applicability to his individual interests. An author index and keyword index have been provided in addition to the table of contents to assist the reader.

The established page limit of ten pages was enforced to a reasonable degree. Papers submitted with 11 pages were usually accepted, and papers with 12 pages were accepted in very special circumstances. I recognize how difficult this page limit was for the authors, and I wish to thank them for their efforts.

On behalf of the organizing committee, I would like to thank the members of the advisory committee, the cooperating professional societies and their representatives, all authors and session chairpersons, and all industrial and academic organizations who have given assistance in many ways. I would especially like to thank Phyllis Hurst, our conference secretary; her assistant, Donna Miller; and John Wellman, the conference coordinator; for their invaluable assistance.

The 1994 International Compressor Engineering Conference at Purdue is tentatively planned for July, 1994, West Lafayette, Indiana.

James F. Hamilton
Professor of Mechanical Engineering
and Conference Chairman

Policy for Publishing Conference Papers in Archival Journals

The organizing committee recommends to all authors who have papers which satisfy the criteria for archival journal articles to submit them to such journals for publication. Because of the relatively small number of copies, publication in the proceedings of the International Compressor Engineering Conference at Purdue does not constitute prior publication as far as many journal editors are concerned. If in doubt, an inquiry should be made. In most cases, the limit of 10 pages will require the creation of an expanded journal article version, which would qualify as a new publication anyway.

The criteria for archival papers are that they should contain original, quantitative, detailed scientific materials which are placed in proper perspective relative to prior work and are supported by references to the appropriate literature. Thus, not all conference papers are suitable. Some describe present practice; or report on procedures that were applied first by someone else; or report design features which, although important to conference participants, have relatively short temporal interest.

The organizing committee requests that authors who choose to submit their papers to archival journals acknowledge that those papers were presented at the 1992 conference and send a copy of each submitted manuscript to the organizing committee.

Purdue University sponsors this conference to provide a forum for the free exchange of ideas on the engineering state-of-the-art in the compressor field. The ideas expressed are those of the author(s) and do not necessarily represent the opinions or policies of the University or the cooperating organizations. The papers are not subject to the formal review procedures of the separate cooperating organizations as they would be if they were to be published by the cooperating societies. Instead, they are subject to the review procedures of the organizing committee.

Keyword Index